UNIVERSIDADE DE LISBOA
FACULDADE DE CIÊNCIAS

A Combined Model for Tsunami Wave Propagation, Dispersion, Breaking and Fluid-Structure Interaction

" Documento Definitivo"

Doutoramento em Ciências Geofísicas e da Geoinformação
Especialidade em Geofísica

Vânia Cristina Veloso de Azevedo Lima

Tese orientada por:
Prof. Doutora Maria Ana de Carvalho Viana Baptista
Prof. Doutor Eng.º Paulo Alexandre de Avilez Rodrigues de Almeida Valente
Prof. Doutor Jorge Miguel Alberto de Miranda

Documento especialmente elaborado para a obtenção do grau de Doutor

2021

UNIVERSIDADE DE LISBOA
FACULDADE DE CIÊNCIAS

A Combined Model for Tsunami Wave Propagation, Dispersion, Breaking and Fluid-Structure Interaction

Doutoramento em Ciências Geofísicas e da Geoinformação

Especialidade em Geofísica

Vânia Cristina Veloso de Azevedo Lima

Tese orientada por:

Prof. Doutora Maria Ana de Carvalho Viana Baptista

Prof. Doutor Eng.º Paulo Alexandre de Avilez Rodrigues de Almeida Valente

Prof. Doutor Jorge Miguel Alberto de Miranda

Júri:

Presidente:

- Doutor João Manuel de Almeida Serra, Professor Catedrático e Presidente do Departamento de Engenharia Geográfica, Geofísica e Energia da Faculdade de Ciências da Universidade de Lisboa

Vogais:

- Doutor José Simão Antunes do Carmo, Professor Associado com Agregação, Faculdade de Ciências e Tecnologia da Universidade de Coimbra
- Doutor Paulo Alexandre de Avilez Rodrigues de Almeida Valente, Professor Auxiliar, Faculdade de Engenharia da Universidade do Porto, Orientador
- Doutor Joaquim Manuel Freire Luís, Professor Auxiliar, Faculdade de Ciências e Tecnologia da Universidade do Algarve
- Doutor André Bustorff Fortunato, Investigador Principal, Laboratório Nacional de Engenharia Civil – LNEC
- Doutor Rui Pires de Matos Taborda, Professor Associado com Agregação, Faculdade de Ciências da Universidade de Lisboa

Documento especialmente elaborado para a obtenção do grau de Doutor

PhD research work supported by Fundação para a Ciência e Tecnologia with grant SFRH/BD/96725/2013 and partially supported by the Research Line ECOSERVICES, integrated in the Structured Program of R&D&I INNOVMAR: Innovation and Sustainability in the Management and Exploitation of Marine Resources (NORTE-01-0145-FEDER-000035), funded by the Northern Regional Operational Programme (NORTE 2020) through the European Regional Development Fund (ERDF).

2021

Resumo

Neste trabalho de Doutoramento, um modelo de tsunami totalmente combinado (CM) foi desenvolvido através do acoplamento de 3 modelos numéricos distintos, com diferentes características, para fases particulares do ciclo de vida de um tsunami.

Os códigos computationais que compõe o modelo de tsunami totalmente combinado são o GeoClaw, um modelo não linear para águas pouco profundas, inserido no package *open-source* Clawpack, o FUNWAVE-TVD, um modelo totalmente não linear de Boussinesq, e o código OpenFOAM, um código de *Computational Fluid Dynamics* (CFD), composto por vários *solvers* e utilidades e que permite a customização e extensão de funcionalidades pré-existentes. Neste trabalho, foi utilizado em especial o *solver* olaFlow inserido no OpenFOAM. O primeiro acoplamento de modelos foi feito entre o GeoClaw com o FUNWAVE-TVD, tendo sido denominado de modelo combinado 1 (CM1). Por sua vez, a combinação do FUNWAVE-TVD/CM1 com o código CFD foi designado como modelo combinado 2 (CM2). A combinação completa dos modelos combinados CM1 e CM2 resultou no modelo de tsunami totalmente combinado CM.

Para alcançar a combinação faseada dos modelos numéricos, várias metodologias individuais de acoplamento foram abordadas, testadas e analisadas. Para o CM1, após várias tentativas, escolhemos a metodologia de acoplamento de domínio refinado com cobertura de sondas de nível, que se mostrou bastante competente na passagem de dados entre modelos numéricos. Para o CM2, foi usada a metodologia de acoplamento baseada na condição timeSeries, aplicando o waveType wavemaker e a waveTheory tveta, do módulo olaFlow.

A validação individual dos códigos numéricos e de cada modelo combinado em partes foi feita usando casos de estudo numéricos e físicos. Diversas experiências físicas foram realizadas no Laboratório de Hidráulica da Faculdade de Engenharia da Universidade do Porto, com vista estudar e gerar ondas solitárias e ondas N. As ondas N geradas foram *leading depression N-waves*, LDN. Existem ainda as *leading elevation N-waves*, as LEN, que não foram estudadas neste trabalho.

Nesta parte do trabalho, uma nova formulação teórica de primeira ordem, necessária para a geração experimental de ondas LDN, através de um sistema de geração de onda do tipo pistão, foi desenvolvida e detalhada. As expressões teóricas para a trajectória do pistão, velocidade e aceleração foram derivadas, assim como as expressões teóricas para o stroke da pá, o período de stroke e as velocidades máximas da pá. Os limites para a velocidade inicial da pá e para a aceleração foram também estabelecidos.

Na mesma fase do trabalho, foram geradas em laboratório seis ondas LDN com alturas de onda relativas entre 0.19 e 0.60. Estas ondas foram classificadas de acordo com o parâmetro de Stokes e deste modo divididas em três grupos: ondas conformes curtas quasi-Boussinesq, com $\mathrm{St} \sim 4/3$; ondas mais longas, com $\mathrm{St} > 10$; ondas com comportamento misto, com $3 < \mathrm{St} < 10$. Os resultados obtidos foram comparados com os perfis teóricos pretendidos de onda N de Tadepalli – Synolakis. Desta análise, concluiu-se que as ondas conformes curtas quasi-Boussinesq suportam uma forte transformação, tendendo para a forma de uma onda solitária, sendo seguidas de uma cava. Por outro lado, este comportamento não foi observado para as ondas mais longas, que parecem tender para uma onda LDN com forma de *bore*. Assim, as ondas mais longas apresentaram os melhores resultados quando comparadas com os perfis teóricos esperados de Tadepalli – Synolakis. As discrepâncias encontradas entre as séries temporais analíticas e experimental podem ser consequência da elevada razão entre a altura de onda e profundidade das ondas geradas. Outros autores (Goring 1978, Grilli 1997) descreveram que para as ondas solitárias a razão entre a altura de onda e a profundidade não deve exceder os 20 %, quando um método de geração de primeira ordem é utilizado.

As experiências físicas foram realizadas em várias etapas e em várias condições. Numa primeira fase, foram realizadas num canal instalado no tanque de ondas e em plano. Numa fase posterior, realizaram-se vários testes numéricos relativos à formulação de celeridade de onda a adoptar para cada tipo de onda que se pretendia gerar em laboratório. Realizaram-se ainda vários testes laboratoriais preliminares, após os quais se realizaram finalmente as experiências físicas de larga escala. Estes ensaios físicos foram feitos num tanque de ondas e numa praia composta por dois planos inclinados, um plano com inclinação 1:15 e outro plano com inclinação 1:30. Cerca de 75 conjuntos de experiências, casos de teste, foram realizados, em tanque de ondas com e sem canal e praia, em profundidades de água de 25 cm e de 50 cm, respectivamente. Após as experiências, tratamento e análise dos resultados, classificaram-se as ondas solitárias e as ondas N geradas de acordo com o seu número de Stokes. Das experiências físicas, recolheram-se, para os casos de estudo, as medições da elevação da superfície livre, as medições do *run-in* e do *run-up* e ainda as medições das pressões no obstáculo colocado no final da praia. Foram propostas leis de *run-in*, *run-up* e pressão para ondas solitárias e ondas N, respectivamente. As medições experimentais foram ainda comparadas com os resultados de simulações numéricas, com resultados satisfatórios apesar de subestimados numericamente.

Após as várias fases descritas, o modelo de tsunami totalmente combinado (CM) foi aplicado na simulação de um sismo de Mw 8.5 e tsunami, atingindo a costa Portuguesa. Os resultados da simulação mostraram a capacidade do modelo de tsunami totalmente combinado em contemplar as diversas fases do tsunami. Através de simulação 2DV com o código CFD, utilizando o perfil batimétrico e topográfico da área da marina de Cascais, foi possível observar os efeitos da vorticidade na zona posterior ao quebramar. Foi possível obter as amplitudes, velocidades e análise de pressões. Tal permitiu compreender melhor a consequência do impacto de três diferentes cenários de ondas de tsunami sobre a zona do quebramar de Cascais. Algumas conclusões considerando o impacto do tsunami foram brevemente expostas.

Os objectivos do desenvolvimento do modelo de tsunami totalmente combinado foram: (1) a conjunção das características e vantagens de cada modelo individual num único modelo, pretendendo e procurando aumentar a sua precisão e eficiência funcional, assim como o seu regime de validade, e (2) trazer ainda uma contribuição distinta na abordagem de alguns dos problemas e desafios existentes na ciência dos tsunamis, tal como a dispersão de frequência na propagação de tsunamis a longa distância, através do modelo não linear de Boussinesq, FUNWAVE-TVD, assim como a complexa propagação do tsunami em terra e as interações do fluido em escoamento com outros cursos de água e com as áreas costeiras e urbanas, através do código CFD OpenFOAM e do seu *solver* olaFlow.

O modelo de tsunami totalmente combinado combina várias e interessantes caracteríStcas de cada modelo numérico utilizado, encarando alguns dos problemas e desafios existentes na ciência dos tsunamis. Utilizando o GeoClaw, foi possível utilizar o modulo de geração de tsunamis existente no código e, ainda mais relevante, tirar partido da capacidade do GeoClaw de aplicar os refinamentos temporal e espacial adaptativos de malha estruturada em bloco, através da aplicação de resoluções de malha mais refinadas em regiões de interesse para o estudo. Esta característica foi aplicada na metodologia de acoplamento estabelecida entre o Geoclaw e o FUNWAVE-TVD, com vista obter o CM1. A dispersão em frequência na propagação de longa distância de tsunamis é tratada através da aplicação do modelo não linear de Boussinesq FUNWAVE-TVD. Para fazer a modelação dos processos *nearshore* em domínios a duas e a três dimensões e determinar a interação do tsunami com estruturas costeiras e com as áreas adjacentes, usamos o código CFD OpenFOAM e *solver* olaFlow.

O modelo de tsunami totalmente combinado alcançado neste trabalho é uma novidade, na medida em que é composto por uma sequência de modelos numéricos distintos e que inclui ainda uma componente com a capacidade de simulação numérica tridimensional. Este modelo de tsunami to-

talmente combinado (CM) e o seu conceito permitem o estudo e simulação de eventos reais de tsunami, aplicando perfis reais ou sintéticos de onda real de tsunami como condição, com o intuito de estudar e investigar o impacto e a interação do tsunami com as áreas costeiras.

Palavras-chave:

- modelo de tsunami totalmente combinado
- GeoClaw
- FUNWAVE-TVD
- OpenFOAM – olaFlow
- ondas solitárias e ondas N

Abstract

In this work, a fully combined tsunami model was developed, by coupling a sequence of 3 distinct numerical models, with different characteristics, for particular phases of the tsunami lifecycle.

The computational codes that compose the fully combined tsunami model are the GeoClaw code, the FUNWAVE-TVD code and the OpenFOAM code, via the olaFlow solver. The coupling of GeoClaw with FUNWAVE-TVD was designated as the combined model 1 (CM1) and the combination of FUNWAVE-TVD/CM1 with the CFD code was designated as the combined model 2 (CM2). The full combination of both CM1 and CM2 resulted in the fully combined tsunami model CM.

To achieve the coupling between numerical models, individual coupling methodologies were approached, tested and analysed. For the CM1, we choose a refined covered gauge domain coupling methodology and for the CM2 a timeSeries condition coupling methodology was used, which applied waveType wavemaker and the waveTheory tveta, from the olaFlow module.

The validation of the individual numerical codes and of the combined model patches was performed with both numerical and physical test cases. Several physical experiments were carried out to generate both solitary and N-waves and a novel first-order theoretical formulation, necessary to generate N-waves experimentally, by means of a piston wave generating system, was developed and detailed in this work.

The large-scale physical experiments were performed in the wave basin and in a beach composed by a 1:15 plane slope and a 1:30 plane slope. The generated solitary and N-waves were classified according to their Stokes number. Experimental free surface elevation, run-in, run-up and pressure measurements were retrieved from the physical experiments. Run-in, run-up and pressure laws were proposed for solitary waves and N-waves respectively. The experimental measurements were compared with numerical simulation results.

The objectives of the development of the fully combined tsunami model were (1) to join the advantages of the individual models in a single one, attempting to increase the accuracy, efficiency and regime of validity, and (2) to bring a contribution in the tackling of some of the existing problems and challenges of tsunami science, such as the frequency dispersion in long distance tsunami propagation, the complex tsunami on land propagation and fluid flow interactions with river courses and with the coastal and urban areas.

The fully combined tsunami model CM simulation results for a M_w 8.5 Earthquake and Tsunami hitting the Portuguese coast showed the ability of the combined model to cover all the tsunami stages. We show that with a 2DV simulation of the CFD code for the Marina of Cascais bathymetric and topographic profile it was possible to observe the vortices behind the breakwater. The analysis of the free surface elevation, velocities and pressure of the tsunami waves was performed. This allowed us to understand the consequence of three diferent tsunami waves scenarios after the breakwater zone. It was possible to draw some brief conclusions considering the tsunami impact.

The fully combined tsunami model achieved in this work is a novelty, since it is composed by a sequence of distinct numerical models, including the three-dimensional component granted by the CFD code. With this combined model, it is possible to perform the simulation of real case tsunami events and hypothetical scenarios, applying real or synthetic tsunami-type wave profiles, studying and researching the impact and the tsunami interaction with the coastal areas.

Keywords:

- fully combined tsunami model
- GeoClaw
- FUNWAVE-TVD
- OpenFOAM – olaFlow
- solitary and N-waves

Acknowledgments

This PhD research work has been financed by Fundação para a Ciência e Tecnologia, through the grant SFRH/BD/96725/2013. This PhD research work was partially supported by the Research Line ECOSERVICES, integrated in the Structured Program of R&D&I INNOVMAR: Innovation and Sustainability in the Management and Exploitation of Marine Resources (NORTE-01-0145-FEDER-000035), funded by the Northern Regional Operational Programme (NORTE 2020) through the European Regional Development Fund (ERDF).

Agradecimentos

O trabalho aqui apresentado dependeu das contribuições de várias pessoas diferentes, que de uma maneira ou de outra tornaram possível a sua concretização.

Tenho de agradecer primeiramente aos meus orientadores por terem aceite orientarem-me neste projeto e pela independência concedida na determinação do rumo do trabalho, o que me enriqueceu bastante a vários níveis.

Agradeço-lhes a disponibilidade e interesse, o esclarecimento de dúvidas e a partilha de conhecimentos científicos, a presença e amizade, e pela leitura e correções à tese.

Ao Professor Kyle Mandli, pela disponbilidade, esclarecimentos e ajuda com o GeoClaw.

Ao Professor Fengyan Shi e a Babak Tehranirad, pelos esclarecimentos relativos ao FUNWAVE-TVD.

Ao Professor Pablo Higuera, pela disponibilidade, esclarecimentos e ajuda com o OpenFOAM e olaFlow.

Ao Professor Stéphane Abadie, pela disponibilidade, esclarecimentos e ajuda com o OpenFOAM.

Ao Professor João Miguel Nóbrega e colaboradores João Oliveira e Marcelo Martins, pela disponbilidade e esclarecimentos.

À FEUP, ao CICA e a UPdigital, pela disponibilização e esclarecimentos relativos ao Grid FEUP.

Ao IDL, à Catherine Mériaux e ao Ricardo Tomé, pela disponibilização e esclarecimentos relativos aos clusters *bhuta* e *tornado*.

Ao Instituto Hidrográfico, pelo apoio na impressão e encadernação de cópias da dissertação escrita.

À Secção de Hidráulica e Recursos Hídricos do Departamento de Engenharia Civil da Faculdade de Engenharia da Universidade do Porto, pela disponibilização de espaço para realização do trabalho de Doutoramento e pelo acesso aos recursos do Laboratório de Hidráulica da Faculdade de Engenharia da Universidade do Porto.

Ao Sr. Miguel Guerra pela assistência e ajuda inestimáveis em todo o trabalho laboratorial realizado no Laboratório de Hidráulica da Faculdade de Engenharia da Universidade do Porto.

À Esmeralda Miguel, pela disponibilidade e simpatia.

À Sandra Plecha, pela amizade e companheirismo.

À minha familia, para quem estive mais indisponível do que desejável no cumprimento deste meu objectivo e a quem agradeço todo o amor, paciência, ajuda e compreensão.

À Sónia e ao Miguel, pelo companheirismo e disponibilidade.

Aos meus pais, por todo o apoio e confiança, pelos quais me sinto imensamente grata, pelos valores transmitidos, sem os quais não teria chegado até aqui, e pelo grande exemplo de trabalho e perseverança que são para mim.

Ao Manuel, por ser o melhor amigo e companheiro, por estar lá nos momentos mais difíceis deste percurso, por me ter ajudado a avançar com as suas parcas mas sábias palavras e pela sua contribuição crítica, técnica e científica.

Ao Afonso, o melhor do Mundo, pelo seu Amor e Alegria, que me deu muita força e ânimo neste percurso.

À Estela, a melhor do Mundo, pelo seu Amor e Alegria, que chegou no fim e me deu muita força e ânimo neste percurso.

A vós os três e aos meus pais, dedico especialmente o trabalho que aqui é apresentado.

The fool is the precursor to the saviour. Carl Yung

Doctor Frankenstein was the name of the man who made the monster,...wasn't he? Keith

Slow and irritated affirmative nod Ron, The Host

Já vejo o mar a crescer, onda gigante a varrer. António Variações

List of Tables

List of Figures

Notation

I - Chapters 1, 2, 3, 5, 6 and Appendices

a	wave amplitude
a^+	amplitude of the wave crest
a^-	amplitude of the wave trough
c	wave velocity
c_0	deep water wave celerity
f	wave frequency
f	Coriolis coefficient
g	gravitational acceleration
h	total water depth; still water depth
k	wavenumber
m	empirical coefficient
n	Manning's roughness coefficient
nx	number of grid columns
ny	number of grid rows
p	pressure
s	distance to the source
t	time
u	velocity component along the x-direction
$\bar{\mathbf{u}}$	depth-averaged horizontal velocity vector
$\bar{u}$	depth-averaged horizontal velocity in the x-direction
$\bar{v}$	depth-averaged horizontal velocity in the y-direction
v	velocity component along the y-direction
x	horizontal Cartesian coordinate
y	horizontal Cartesian coordinate
w	velocity component along the z-direction
z	vertical Cartesian coordinate
C_d	dimensionless bottom friction coefficient
E	average energy density per unit area
H	wave height
H_0	deep water wave height
$\mathrm{I_r}$	Iribarren number
K	empirical coefficient
L_0	deep water wavelength
L_2	L2-norm
L_{amp}	relative amplitude deviation
Lat	latitude θ
Lon	longitude ϕ

M_0	seismic moment
M_w	moment magnitude scale
R_i,R_{in}	run-in, which is the maximum inundation distance measured horizontally
R,R_{up}	run-up, which is the vertical maximum rise reached by the tsunami incident wave
R_{SW}	maximum run-up of solitary non-breaking waves (Synolakis 1987)
R_{NW}	run-up of a N-wave (Synolakis et al. 2007)
St	Stokes parameter
T	wave period
TTT	tsunami travel time
β	slope angle of the beach
ϵ	nonlinearity parameter
η	free surface elevation above a reference level
η_{obs}	observed free surface elevation
η_{num}	numerical free surface elevation
κ	generalized wavenumber
λ	wavelength
λ_0	deep water wavelength
μ	dynamic viscosity
ν	turbulent viscosity
ω	angular frequency of the wave
ρ	fluid density or volumetric mass density
σ	shallowness or dispersion parameter
τ_{xx}	stress tensor component in the x-direction on a face normal to the x-axis
τ_{xy}	stress tensor component in the y-direction on a face normal to the x-axis
τ_{xz}	stress tensor component in the z-direction on a face normal to the x-axis
τ_{yx}	stress tensor component in the x-direction on a face normal to the y-axis
τ_{yy}	stress tensor component in the y-direction on a face normal to the y-axis
τ_{yz}	stress tensor component in the z-direction on a face normal to the y-axis
τ_{zx}	stress tensor component in the x-direction on a face normal to the z-axis
τ_{zy}	stress tensor component in the y-direction on a face normal to the z-axis
τ_{zz}	stress tensor component in the z-direction on a face normal to the z-axis
υ	ratio between the water depth and the wavelength
ω	velocity of rotation of the Earth
Δt	time step
Δx	grid spacing in the x-direction
Δy	grid spacing in the y-direction
Ω_x	vorticity vector component in the x-direction
Ω_y	vorticity vector component in the y-direction
Ω_z	vorticity vector component in the z-direction

Seismic fault

d	focal depth
A	rupture area along the fault
D	average slip or displacement offset between both sides of the fault
L	fault length
W	fault width
G	shear modulus or modulus of rigidity

GeoClaw

F	fluxes
G	shear modulus or modulus of rigidity
H	bottom surface elevation relative to the mean sea level
Q_{ij}^n	cell average of solution variable in cell (i, j) at time t_n
ν	Poisson's ratio

FUNWAVE-TVD

c	wave velocity
f	Coriolis term
h	local still water depth
$\mathbf{i}^z$	unit vector in the z-direction
$\mathbf{n}$	unit vector
r	radial coordinate
r_0	radius of the sphere
u	velocity component in the horizontal ϕ-direction
v	velocity component in the horizontal θ-direction
$\bar{u}$	depth-averaged horizontal velocity in the ϕ-direction
$\bar{v}$	depth-averaged horizontal velocity in the θ-direction
$\mathbf{u_2}$	depth-dependent correction at $\mathcal{O}\left(\mu^2\right)$
$\bar{u}_{2,t}$	time derivative dispersive term
$\bar{\mathbf{u}}_\mathbf{2}$	depth-averaged $\mathcal{O}\left(\mu^2\right)$ contribution to the horizontal velocity field
$\mathbf{u}_\alpha$	velocity at reference elevation $z = z_\alpha$
z_α	reference level
A	divergence of the momentum at reference elevation $z = z_\alpha$
B	divergence of the velocity at reference elevation $z = z_\alpha$
$\mathbf{C}$	wave celerity vector
C_d	drag coefficient
C_{dw}	wind drag coefficient
Cr	Courant number
H	total local water depth
$\mathbf{M}$	horizontal volume flux
M_{glob}	global dimension in x-direction
N_{glob}	global dimension in y-direction
P	flux in the x-direction
Q	flux in the y-direction
$\mathbf{R}$	diffusive and dissipative terms (including bottom friction and subgrid lateral turbulent mixing)
$\mathbf{R}_w$	wind stress forcing
S_p	spherical coordinate correction factor
$\mathbf{U}_{10}$	wind velocity vector, at a reference height of 10 m above the sea surface
$\mathbf{V_1}$	dispersive Boussinesq term
$\mathbf{V'_{1,t}}$	time derivative dispersive term
$\mathbf{V_2}$	dispersive Boussinesq term
$\mathbf{V_3}$	represents the $\mathcal{O}\left(\mu^2\right)$ contribution $\omega \times \mathbf{u} = \mathbf{u}$
α	coordinate denoting latitude (horizontal Northerly direction)
β	constant
η	local free surface elevation
δ	shallow water nonlinearity parameter

μ	ratio between the water depth and wavelength
ω	vorticity
ϕ	coordinate denoting longitude (horizontal Easterly direction)
ϕ_0	reference longitude
θ_0	reference latitude
ρ	water density
ρ_a	air density
ε	constant
(ξ_1, ξ_2)	coordinates in the longitude and latitude directions
$\mathbf{\Psi}$	vector of conserved variables
$\mathbf{\Theta}(\mathbf{\Psi})$	flux vector function

OpenFOAM/olaFlow

$\mathbf{f_e}$	sum of all the volume forces
$\mathbf{f_R}$	resistance force exerted by the porous media
$\mathbf{f}_\sigma$	force due to the free surface tension
p	pressure
$\bar{\mathbf{u}'}$	average velocity fluctuation
C_2	inertial coefficient
K_p	media permeability
I	unit tensor
$\mathbf{T}$	stress tensor
$\mathbf{S}$	flow deformation rate tensor
$\bar{\mathbf{S}}$	deformation rate of the average flow
$alpha.water$	volume of fluid term
$prgh$	pressure term
α	volume fraction
μ	dynamic viscosity of the fluid
ν	kinematic viscosity of the fluid
ν_d	damping function used to absorb the waves
ϕ	instantaneous fluid flow variables
$\bar{\phi}$	average component of ϕ
ϕ'	fluctuation
$\overline{\phi(x_i, t)}$	Reynolds average
τ	viscosity forces tensor

Combined Model

c	wave velocity
c_1	wave celerity determined according to (5.6)
c_2	wave celerity determined according to (5.5)
$\mathbf{u}$	depth-averaged velocity vector
$\bar{u}$	depth-averaged velocity in the x-direction
$\bar{v}$	depth-averaged velocity in the y-direction
$\delta\phi$	longitude grid spacing
$\delta\theta$	latitude grid spacing
μ_{water}	dynamic viscosity of the water
μ_{air}	dynamic viscosity of the air

ρ_{water}	fluid density of the water
ρ_{air}	fluid density of the air
σ	friction coefficient between two phases

Appendices

d	still water depth
f	frequency
h	total water depth
q	non-hydrostatic pressure
q_b	non-hydrostatic pressure at the bottom
t	time
u	depth-averaged velocity in x-direction
v	depth-averaged velocity in y-direction
x	Cartesian coordinate
y	Cartesian coordinate
z	Cartesian coordinate
A	amplitude of the wave
C_d	dimensionless bottom friction coefficient
H	wave height
T	wave period
η	surface elevation measured from the still water level
κ	wavenumber
λ	wavelength
ω	angular frequency
$\tau_{xx}, \tau_{xy}, \tau_{yx}, \tau_{yy}$	horizontal turbulent stress

Notation

II - Chapter 4

a^+	amplitude of the wave crest
a^+_{obs}	observed amplitude of the wave crest
a^+_{TS}	expected amplitude of the wave crest
a^-	amplitude of the wave trough
a^-_{obs}	observed amplitude of the wave trough
a^-_{TS}	expected amplitude of the wave trough
c	wave velocity
c_0	leading ascending zero wave velocity
c^+	leading wave crest wave velocity
c^-	leading wave trough wave velocity
$\bar{c}$	weighted averaged wave velocity
$\bar{c}^*$	weighted averaged wave velocity without wg8–wg7 run
$\bar{c}_{1-4}$	average wave velocity between gauges 1 and 4
$\bar{c}_{4-5}$	average wave velocity between gauges 4 and 5
$\bar{c}_{5-7}$	average wave velocity between gauges 5 and 7
$\bar{c}_{7-8}$	average wave velocity between gauges 7 and 8
$\bar{c}_{8-3}$	average wave velocity between gauges 8 and 3
$c_{cnoidalBoussinesq}$	wave celerity of a cnoidal Boussinesq wave
d	undisturbed water depth
$f(x)$	linear regression function
g	gravity acceleration
m	elliptic parameter
s	total paddle path length
t	time
t_0	initial time instant
u	particle velocity in front of the wave-maker
$\bar{u}$	depth-averaged particle velocity
x	horizontal coordinate
x_1	horizontal coordinate for the location of the wave crest of a solitary wave at $t = 0$
x_2	horizontal coordinate for the location of the inflexion point of a N-wave at $t = 0$
D	total displacement of the paddle
F	integration function
$K(m)$	complete elliptic integral of the first kind
$E(m)$	complete elliptic integral of the second kind
P	experimental pressure exerted on a rectangular obstacle
P_{num}	numerical pressure exerted on a rectangular obstacle
Q_s	nonlinear mass flux

R^2	coefficient of determination of $f(x)$
R_i,R_{in}	run-in, which is the maximum inundation distance measured horizontally
R,R_{up}	run-up, which is the vertical maximum rise reached by the tsunami incident wave
S	paddle stroke
$S_{\min}$	minimum paddle stroke
St	Stokes number
T	apparent wave period
U_c	current speed
α	parameter relating λ and λ_B
δ	eccentricity parameter
ϵ	nonlinearity parameter
η	free surface elevation above a reference level
θ	generalized coordinate
κ	generalized wavenumber
λ	apparent wavelength
λ_B	wavelength of a Boussinesq solitary wave
ν_t	turbulent viscosity
nut	turbulent viscosity in OpenFOAM
ε	scale factor
ξ	paddle trajectory of the wave-maker
$\dot{\xi}$	paddle velocity of the wave-maker
ξ_f	final paddle position of the wave-maker
$\xi_{\max}$	maximum space travelled by the paddle
$\xi_{\min}$	minimum space travelled by the paddle
τ	stroke period
φ	integration variable
ϕ	integration variable

Physical experiments

f_1	$2 \times f_2$
f_2	ratio between δ and λ
R_{upNW}	N-wave run-up power law
R_{upSW}	solitary wave run-up power law
β_1	slope angle
β_2	slope angle

Contents

Chapter 1

Introduction

1.1 Framework and scope of study

Water waves are surface waves, composed by both longitudinal and transverse waves, which can be described as deformations of the sea surface. These waves occur at the sea surface and at the surface of other bodies of water, such as lakes, rivers and canals. Waves are typically separated into short waves, which are waves with maximum periods of around 20 s, and long waves, with periods that range from 20 s to 40 min. Short waves, also designated as deep water waves ($h/\lambda \geq 1/2$), show dispersion, which means that their wave speed depends on the wave period. Longer period waves have longer wavelengths and move faster than shorter period waves. Therefore, in opposition to short waves, longer waves or shallow water waves ($h/\lambda < 1/20$) are non-dispersive. Intermediate waves are situated between deep water waves and shallow water waves. The speed of shallow water waves depends solely on the water depth and are therefore independent of the wave period. The wave celerity c of a shallow water wave is given by

$$c = \sqrt{g \cdot h}\,, \tag{1.1}$$

where g is the gravitational acceleration and h is the water depth.

Tsunami waves are described as long, shallow water waves. A wave is characterized as a shallow water wave when its wavelength λ is much larger than the water depth h it is propagating in, so the ratio of the water depth h and the wavelength λ is very small. A common approach is to model tsunamis as solitary waves both in experimental and numerical studies. Madsen et al. (2008) discussed the solitary wave paradigm in tsunami research and concluded that, in general, tsunamis do not generate solitons in the ocean or on the continental shelf. Therefore, Madsen et al. (2008) questioned the geophysical importance of the experimental studies of breaking short solitary waves by Li (2000) and Li and Raichlen (2001, 2002, 2003). Madsen et al. (2008) stated that the breaking observed in tsunamis, before reaching the shoreline, is most likely due to short waves breaking on top of the tsunami, hence run-up will not be influenced by the breaking process. These authors also stated that combining relatively strong input nonlinearities with cnoidal or solitary theory, as performed in the previously cited experimental studies, is unrealistic in connection with geophysical tsunamis.

On the other hand, not all tsunami events are alike and reports of shoreline receding support the concept of tsunami waves with N-type shape. The concept of N-waves was introduced by Tadepalli and Synolakis (1994) and the authors suggested that a N-wave is more adequate to describe the main tsunami wave. N-waves can be described as having a leading trough, which are leading depression N-waves (LDN), or as having a leading crest, which are leading elevation N-waves (LEN). Like solitary waves, N-waves can be described by the wave height H and the water depth h.

The dispersion in tsunamis was generally disregarded in the tsunami propagation modelling, as it was believed that its contribution was neglectable. Yet, the importance of dispersive effects in tsunami propagation has increased, supported by several studies such as those by González and Kulikov (1993), Kulikov (2005b) and Horrillo et al. (2006), which presented empirical arguments on the relevance of the dispersive effects in the tsunami propagation. Also Dao and Tkalich (2007) showed how dispersion inclusion is fundamental in transoceanic tsunami simulation, as it contributes to the wave amplitude variation.

In their study, Glimsdal et al. (2013) distinguished the dispersive effects in deep water propagation and the first part of the shoaling, when earthquake tsunamis are linear, and the dispersive effects that may arise in shallow waters, effects which are connected to the nonlinearity and that originate undular bores. They found that moderate-magnitude earthquakes tend to display more dispersive tsunamis than the larger ones and observed strong directivity of the dispersion, following the amplitude directivity, due to the elongated shapes of the source regions (Glimsdal et al. 2013).

Numerical models are commonly used to simulate the several physical processes that compose the lifespan of a tsunami. The shallow water equations have shown to be competent to describe the tsunami waves characteristics throughout several flow regimes. In his thesis, George (2006) pointed out the additional computational costs of solving more computationally expensive systems, even if a more accurate numerical solution is achieved and the outcome justifies the time consumption. In the scientific modern world, time consuming numerical models can be easily disregarded, when compared to the very common computationally low-cost tsunami models available. Expeditious results with low time consuming modeling is preferred. Yet, a more complete insight and description—preferably 3D—of the coastal tsunami behaviour and inland impact is necessary, prevailing as an open challenge to the scientific community. Although many developments have been achieved in tsunami science, ultimately what is aimed is an approximate yet improved knowledge about the consequences of a tsunami in the coast, the flooding, maximum water levels, level of risk and which are the possibly protected zones along the vulnerable coastline. This is most probably possible by means of more complete tsunami models, contemplating all the lifecycle of the phenomenon, able to model all the involved physical processes—from generation to transformation, breaking and inundation—and to determine the properties and characteristics of the tsunami interaction with the coastal structures and the surrounding areas. The ultimate goal is to predict as accurately as possible the tsunami impact and avoid at all costs the loss of lives and properties.

1.2 Objectives, methods and thesis overview

The main objective of this thesis is to study and numerically implement a fully combined tsunami model CM, by parts, considering all the tsunami lifecycle stages. The development of the fully combined tsunami model is based on GeoClaw (Clawpack Development Team 2014b), a tsunami global generation-propagation model, which is part of Clawpack (Clawpack Development Team 2014a), the fully nonlinear dispersive Boussinesq (FNLB) code FUNWAVE-TVD (Shi et al. 2012b, Kirby et al. 2013) for wave propagation, breaking and inundation analysis, and the CFD code OpenFOAM (OpenCFD Limited 2019) and the OpenFoam solver olaFlow (Higuera 2019) for wave-structure impact and 3D-breaking analysis.

The individual objectives of this work are:

- to design and implement the final combined model, composed by three single open source codes;
- to study and find the theoretical formulations and assumptions necessary to achieve the

main mathematical formulations for the generation of N-waves in laboratory, by means of a piston-type wave-maker;

- to study and verify the ability to generate N-waves in the laboratory, based on the main mathematical formulations found, through the laboratory experimenting of the propagation of leading depression N-waves (LDN-waves).

  Answering this open question will enable a more complete calibration of both individual and combined models and the achievement of this objetive will contribute to the combined model validation;

- to study and evaluate the propagation, run-in, run-up and pressure impact forces of both solitary waves (SW) and leading depression N-waves (LDN-waves), by means of large laboratory-scale experimenting of SW and LDN-waves;

- to perform the numerical modelling of the case tests generated in the laboratory-scale experiments and compare the numerical results with the experimental measurements retrieved in the laboratory;

- to perform and analyse a final case study, of tsunami generation, propagation, dispersion, breaking and attack on the Portuguese coast, as well as the interaction with the existing coastal defense structures and overall coastal impact, by applying the developed final combined tsunami model CM;

- to identify and address the gaps in the understanding and perception of the tsunami propagation and tsunami waves attack on the coast—such as a better description of the tsunami waves propagation inland, as a consequence of the turbulent nature and randomness of the fluid flow involved—, its interaction with the coastal defense structures, tsunami flow in the coastal and inhabited areas and its overall coastal impact.

  It is intended that these challenges are mostly answered by applying the proposed fully combined tsunami model CM, with its 3D component description of the phenomenon.

This thesis is organized in the following manner:

- In Chapter 1, the framework and scope of study of this PhD thesis are presented, as well as the objectives, methods and thesis overview.

- In Chapter 2, the physics of tsunamis and the principles of the generation of tsunamis are presented, as well as the principles of tsunami modelling and numerical methods applied. Concepts on tsunami flow regimes and coastal interactions, from the deep ocean to the shoreline, as well as inundation and coastal interactions, are presented.

- In Chapter 3, the computational models used in this thesis are described and the results for case study applications, using each model, are presented.

- In Chapter 4, the laboratory experiments of propagation and transformation performed for solitary and N-waves are described and the principles of the generation of N-waves are presented. The comparison between the laboratory measurements of the propagation and transformation of solitary and N-waves and the numerical simulations is presented.

- In Chapter 5, the coupling methodologies applied between the numerical models described in Chapter 3 are detailed and results for several case studies, using each combined model, are presented.

- In Chapter 6, the final case study of a large earthquake event, hitting the coast of Portugal, is simulated using the final combined model CM and the tsunami event results are plotted, analysed and discussed.
- In Chapter 7, the final conclusions about the work developed in this PhD thesis are drawn and the future work is outlined.

The state-of-the-art is introduced chapter by chapter, in relation to the subject covered in each chapter.

The work of this thesis was presented and published in:

- Vânia Veloso Lima, Baptista, M.A., Miranda J.M. (2014). Tsunami impact study using the Cornell Multi-grid Coupled Tsunami Model (COMCOT). 13th International workshop on Multiscale (Un)-structured mesh numerical Modeling for coastal, shelf, and global ocean dynamics, LNEC, Lisbon, Portugal, 25-27 August 2014. http://imum2014.lnec.pt/text/program.html .
- Vânia Lima, Maria Ana Baptista, Paulo Avilez-Valente, Miguel Miranda (2016). A combined model for tsunami generation and propagation. Geophysical Research Abstracts Vol. 18, EGU2016-10028, EGU General Assembly 2016, http://adsabs.harvard.edu/abs/2016EGUGA..1810028L,https://meetingorganizer.copernicus.org/EGU2016/EGU2016-10028.pdf
- Vânia Lima, Maria Ana Baptista, Paulo Avilez-Valente e Miguel Miranda (2016). A combined model for tsunami propagation, transformation and coastal interactions. ICUR 2016, Lisboa, Portugal, 30 Junho – 2 Julho 2016, http://www.ceru-europa.pt/icur2016/ICUR2016_Proceedings.pdf .
- Vânia Veloso Lima, P. Avilez-Valente, M.A. Baptista, J.M. Miranda (2019). Generation of N-waves in laboratory. Coastal Engineering, Volume 148, June 2019, Pages 1-18, https://doi.org/10.1016/j.coastaleng.2019.02.012 .
- Vânia Veloso Lima, P. Avilez-Valente, M.A. Baptista, J.M. Miranda (2020). Laboratory and numerical studies of solitary and N- waves. *6as Jornadas de Engenharia Hidrográfica / 1as Jornadas Luso-Espanholas de Hidrografia, Instituto Hidrográfico da Marinha, Lisboa, Portugal*, 3 – 5 Novembro 2020, https://jornadas.hidrografico.pt/recursos/files/documentos/Livro_Atas_6JEH_2020.pdf .
- Vânia Veloso Lima, P. Avilez-Valente, M.A. Baptista, J.M. Miranda. Laboratory studies of solitary-like waves and N-waves. – *in preparation*.

Chapter 2

The physics of tsunamis

2.1 Introduction: What are tsunamis?

A tsunami is a series of ocean waves resulting from sudden changes in the water equilibrium position, which cause the displacement of a large volume of water. Tsunamis are described as very long water waves, which can be triggered by different kinds of natural or artificial events. The word *tsunami* comes from the Japanese language, probably because Japan has a long history of tsunami events, and is translated to English as *harbour wave*, with *tsu* standing as *harbour* and *nami* standing as *wave*. The generation mechanisms of these large waves can be related to sudden seafloor displacements—such as submarine seismic events, underwater mass movements—, internal or external disruptions of a body of water—such as landslides, volcanic activity or meteorite impacts—or any other vertical disturbance of a waterbody. The most frequent tsunami triggering mechanisms are earthquakes and landslides. Lately, more focus is being placed on landslide and especially volcanic eruption originated tsunamis. Because of their sudden occurrence, tsunamis are extremely dangerous to the coastal communities. The lifecycle of a tsunami can be shortly described by three main stages: (1) the wave generation, (2) the wave propagation and transformation and (3) the coastal impact and coastal inundation.

Munk (1950) proposed a classification of the ocean waves according to the wave period, represented in the scheme in Figure 2.1. In the figure, ocean waves and the respective generating and restoring forces are indicated and the relative energy content in the ocean surface is represented by the curve on the bottom.

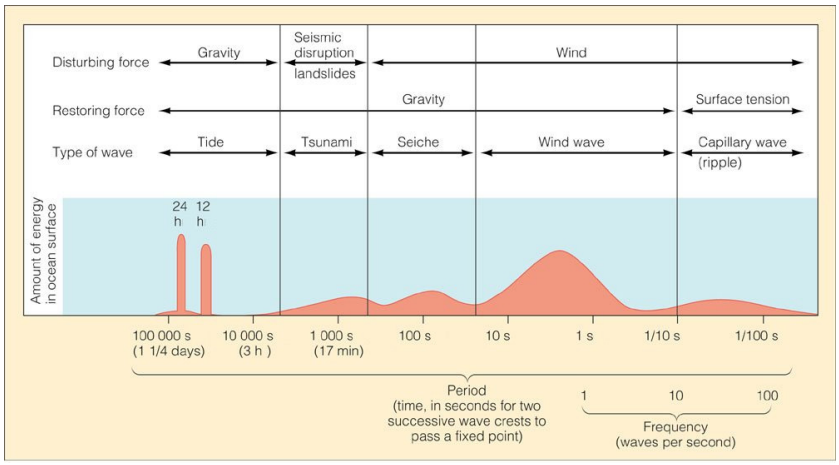

Figure 2.1: Classification of ocean waves, according to the wave period (adapted from Munk, 1950).

Waves generated by the wind typically present wave periods of 5 to 20 s and wavelengths of 100 to 200 m. Tsunami waves can present wave periods that range from minutes to hours and wavelengths of hundreds of kilometres.

2.1.1 Periodic waves

Periodic waves are characterised by specific physical characteristics, such as the wave height H, the wavelength λ and the wave period T (Figure 2.2). A periodic wave is described by two consecutive crests. The wave crest (peak) is the highest or maximum point of positive displacement of the wave, from its resting position. The wave trough, the opposite of the wave crest, is the lowest point or point of maximum negative displacement of the wave. The wave height H is the distance between the wave crest and the wave trough. The wavelength λ is the distance between two consecutive wave crests or wave troughs. In Figure 2.2, η is the water surface elevation, x is the coordinate in the direction of the wave propagation, z is the coordinate in the vertical direction, t is the time and d is the still water depth. A wave is also characterised by its wave period T, which is the time lag necessary for a wave to complete one cycle, corresponding to one full wavelength passing a stationary point. The wave frequency f is the inverse of the wave period. The wave celerity $c = \lambda/T$ is the velocity of propagation of the wave.

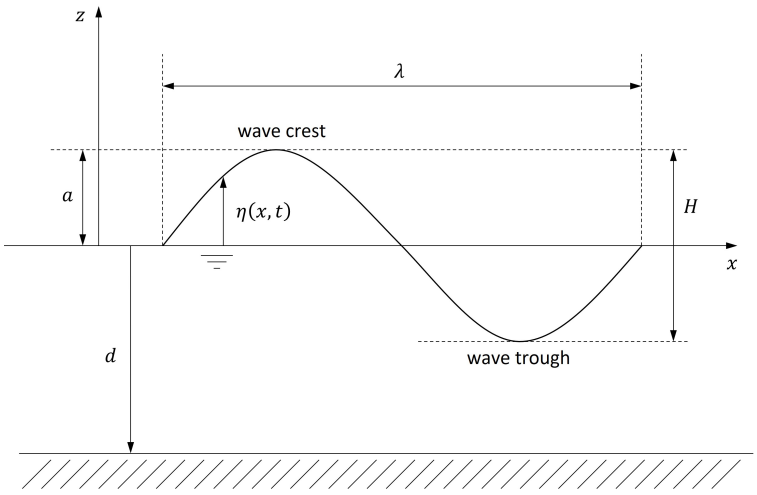

Figure 2.2: Characteristics of a periodic wave.

Frequency dispersion occurs as travelling waves of different wavelengths move with distinct wave velocities. The dispersion relation of the linear theory (Airy theory or Stokes first order theory—Dean and Dalrymple 1991) can be written as:

$$\omega^2 = g\, k\, \tanh(kh), \tag{2.1}$$

where $\omega = 2\pi/T$ is the angular frequency of the wave, $k = 2\pi/\lambda$ is the wavenumber and $h = d+\eta$ is the total water depth. Therefore, as $c = \lambda/T = \omega/k$, the dispersion relation can be written in terms of the wave celerity c as:

$$c = \sqrt{gh\,\frac{\tanh(kh)}{kh}}, \tag{2.2}$$

or

$$c = \frac{g}{\omega}\tanh(kh). \tag{2.3}$$

For deep water, $kh \to \infty$ and $\tanh(kh) \to 1$, then:

$$c_0 = \frac{g}{\omega}, \tag{2.4}$$

where the subscript 0 denotes deep water conditions.

For shallow water, $kh \to 0$, $\tanh(kh) \to 0$ and $\tanh(kh)/(kh) \to 1$, thus:

$$c = \sqrt{gh}. \tag{2.5}$$

The dispersion relation (2.2) can be re-written for the wavelength as:

$$\lambda = \frac{g\,T^2}{2\pi} \tanh(kh). \tag{2.6}$$

When kh is large, water wave propagates in deep waters. If kh is small, water depth is much smaller than the wavelength and therefore the wave propagation regime is classified as shallow waters.

In deep water, $kh \to \infty$ and $\tanh(kh) \to 1$, thus $\lambda \to \lambda_0 = g\,T^2/2\pi$, where the subscript 0 denotes deep water values. Therefore,

$$\lambda = \lambda_0 \tanh(kh). \tag{2.7}$$

Thus, the wavelength continually decreases with decreasing depth for a constant wave period.

It can be shown (Dean and Dalrymple, 1991) that the average energy density per unit area is proportional to the square of the wave height:

$$E = \frac{1}{8}\rho g H^2\,. \tag{2.8}$$

For a wave radiating at a constant depth from a generation area (see Figure 2.3), the energy between two consecutive wave crests must remain constant. As the crest length linearly increases with the distance from the source, while the wavelength remains constant, so does the energy density, E, decreases linearly with the distance from the source. Therefore, the wave height, H, slowly decreases with the distance from the source s in such a way that

$$H \propto s^{-1/2}\,. \tag{2.9}$$

Thus, a wave that at 1000 m distance from the source centre is 1 m high, would have its height reduce to less than 10 cm at 100 km from the centre and to 3 cm at a distance of 1000 km.

On the other hand, as the wave approaches a coastline, the water depth decreases. Thus, the wavelength decreases, and so does the wave celerity as the wave period remains constant. Far away from the source zone, the wave crests become straight lines, and thus the wave energy density per unit area becomes inversely proportional to the wavelength, or to the wave celerity, which for shallow water is given by expression (2.5). Assuming that there is no energy dissipation, the wave energy density becomes $E \propto h^{-1/2}$, and the wave height is $H \propto h^{-1/4}$. Thus, a wave that at a depth of 1000 m would have a height of 1 m, will become almost 4 m high at a depth of 5 m. This process is known as shoaling (see Figure 2.4).

2.1.2 Non-periodic waves

Real tsunami waves are non-periodic and nonlinear waves. They are better described as some sort of solitary wave, or as a train of almost solitary waves resulting from the fission of the leading tsunami wave. Usually, the leading tsunami wave can be described as an N-shaped wave, either with a leading trough or depression, a so-called leading depression N-wave, or with a leading crest or elevation, a so-called leading elevation N-wave (see Figure 2.5).

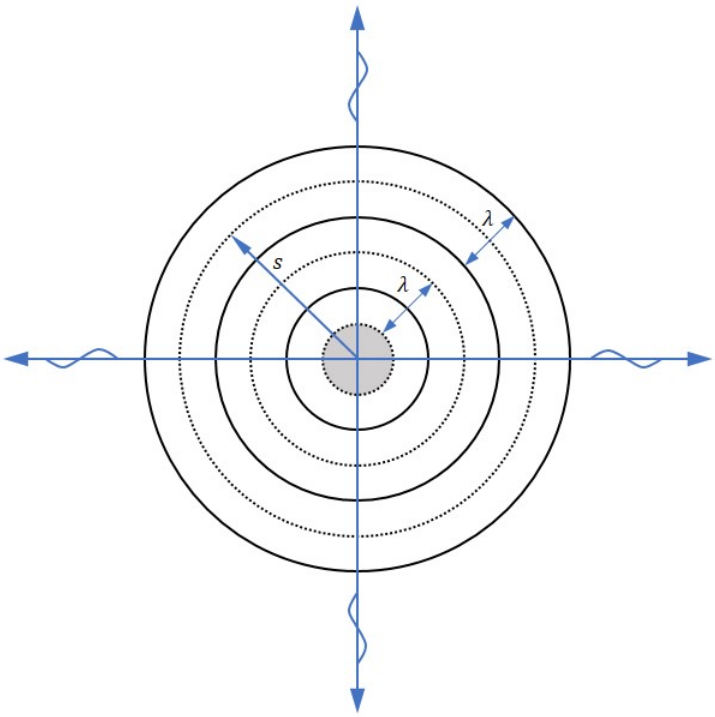

Figure 2.3: Wave radiating from a source zone (tsunami generation area).

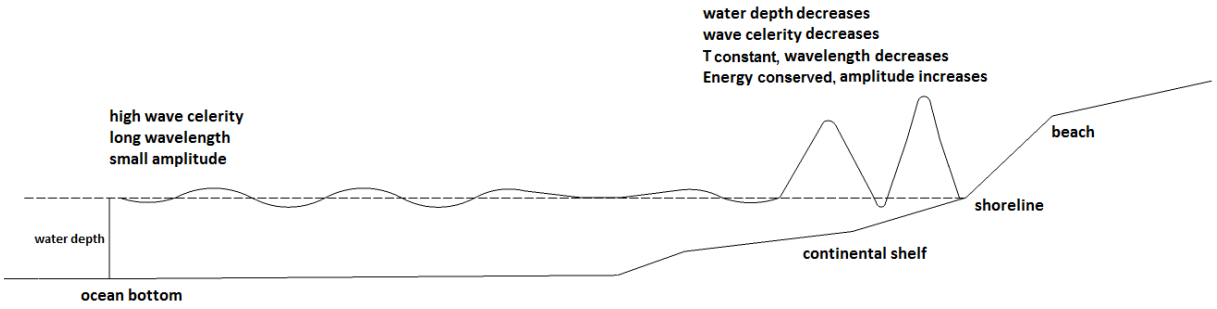

Figure 2.4: Tsunami wave propagation and the shoaling process.

The wave height H of the N-wave is obtained as $H = a^+ + a^-$, where a^+ is the amplitude of the wave crest, and a^- is the amplitude of the wave trough.

The wave celerity of a solitary wave is given at the leading order by

$$c = \sqrt{g(d+H)}\,. \tag{2.10}$$

Considering an average oceanic depth of 3700 m, it can be easily found that a tsunami wave travels at a speed close to 685 km/h, as $H \ll d$. These waves are frequently unnoticeable when propagating in the ocean because of their large wavelengths. Wind-generated waves usually present wavelengths of about 100 to 200 m, while tsunami waves can have wavelengths greater than 500 km. The wavelength and/or period of a tsunami are dependent on the type of triggering mechanism and size of the event. Tsunami wave energy loss due to bottom friction in deep waters is very small and usually it only becomes significant when the wave interacts with the continental shelf or with islands.

The arrival of the tsunami waves can be characterised by a noticeable rise or by a fall of the

coastal waters mean level. When the tsunami wave is a trough leading wave, which causes a considerable drop in the sea level, we are in the presence of a drawback phenomenon. The trough of the tsunami wave is then followed by its crest and therefore by a sudden rise of the sea level. On the other hand, when there are a train of tsunami waves, their interaction with the coast can last for a few hours. For instance, for λ = 500 km at a depth circa 4000 m, it results that c = 700 km/h, and as $c = \lambda/T$, it means that $T \sim 1$ h. For that reason, successive waves can take several hours to reach the coast.

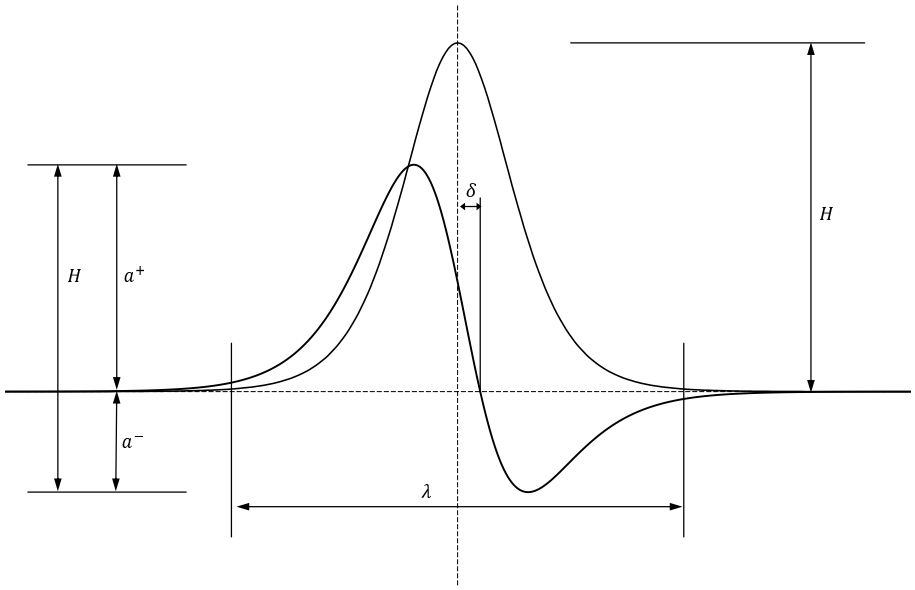

Figure 2.5: N-wave profile with wave height H and wavelength λ.

2.1.3 Tsunami generation

There are several different types of mechanisms that can trigger a tsunami event. Tsunamis can be triggered by earthquakes, landslides (underwater or sub-aerial), volcanic eruptions and other types of impact to a volume of water, such as meteorites. In this thesis, the focus will be exclusively on earthquake-triggered tsunamis. Nevertheless, for further reading on tsunamis triggered by volcanic events and tsunamis triggered by landslides, please refer respectively to Løvholt et al. (2008) and Grilli and Grilli (2013), and to Watts et al. (2003) and Tappin et al. (2014).

Earthquakes are caused by a sudden displacement (or slip) on a fault, which is a fracture zone along two blocks of the Earth's crust moving relative to each other. Although slowly, the tectonic plates are in constant movement. Tensions between the tectonic plates accumulate as they get stuck due to friction, and its energy, in the form of waves, is then released through an earthquake. Tectonic earthquakes cause the deformation of the Earth's crust and consequent shaking. The point of origin of an earthquake is called focus or hypocentre and the point at the surface directly above the focus is the epicentre (see Figure 2.6).

Some specific kinds of faults can cause earthquakes. Faults are classified according to their dip, which is the fault angle relative to the surface, and to the slip direction along the fault. Generally, faults are classified into four categories: normal faults, reverse faults (called thrust fault when having a small dip angle), strike-slip faults, and oblique-slip faults. The different types of faults are a consequence of the combination of different types of forces on the rocks. Thus, faults and earthquakes are originated by existing stresses and strains.

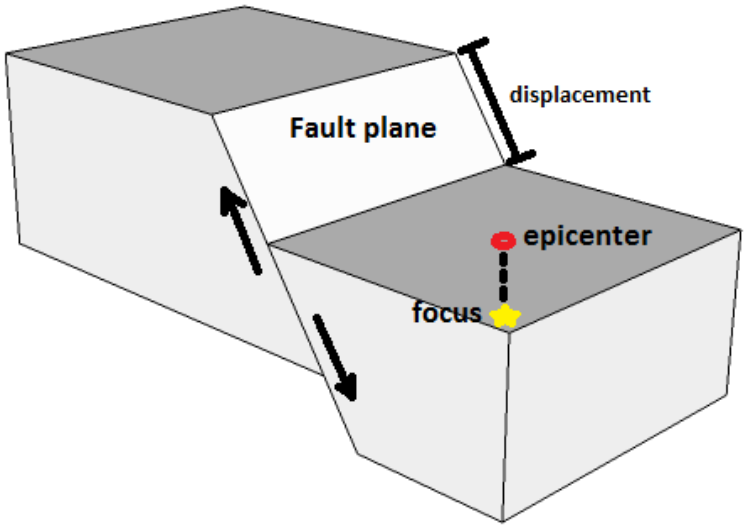

Figure 2.6: Scheme illustrating the location of the focus or hypocentre (yellow star) and the epicentre (red dot).

Following the definitions by the USGS* (see Figure 2.7):

- a strike-slip fault is a fault on which the two blocks slide past one another; it can be left-lateral or right-lateral. In a left-lateral strike-slip fault, the displacement of the far block is to the left when viewed from either side. In a right-lateral strike-slip fault, the displacement of the far block is to the right when viewed from either side;
- a normal fault is a dip-slip fault, with the block above the fault moving downward relative to the block below. It is a type of faulting which occurs in response to extension;
- a thrust fault is a dip-slip fault, with the upper block, above the fault plane, moving up and over the lower block. It is a type of faulting common in areas of compression.

Dip-slip faults move along the direction of the dip plane, and are described as normal or reverse (thrust) faults, depending on their motion. Strike-slip or transform faults move horizontally and can be classified as left-lateral or right-lateral. Oblique-slip faults are a composition of dip-slip and strike-slip motion.

Faults are characterized by several parameters (Figure 2.8), defined as:

- length L of the fault;
- width W of the fault;
- location of the hypocentre or focus;
- focal depth d, which is the depth of an earthquake hypocentre;
- slip of the fault, which is the relative displacement of formerly adjacent points on opposite sides of a fault, measured on the fault surface;
- strike, which is the trend of the line that defines the intersection between the fault and the horizontal axis or ground;
- dip, which is the angle that the fault does with the horizontal axis or the ground.

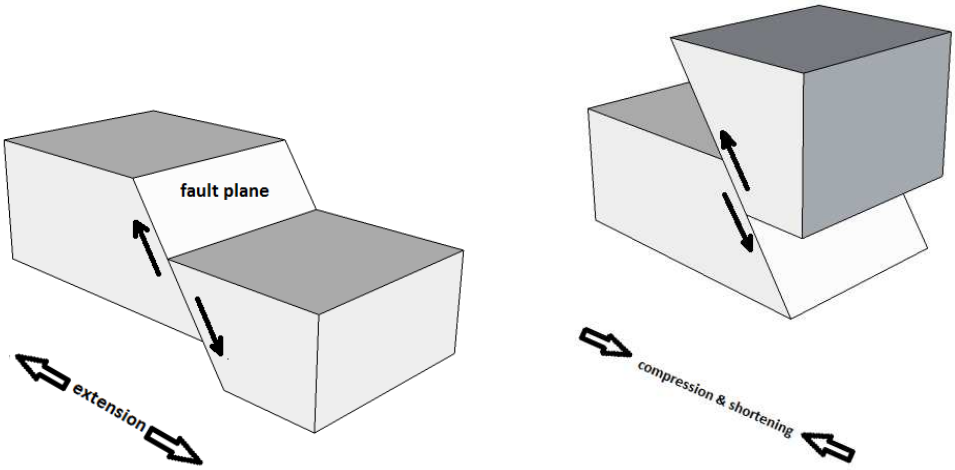

(a) Normal fault

(b) Thrust fault

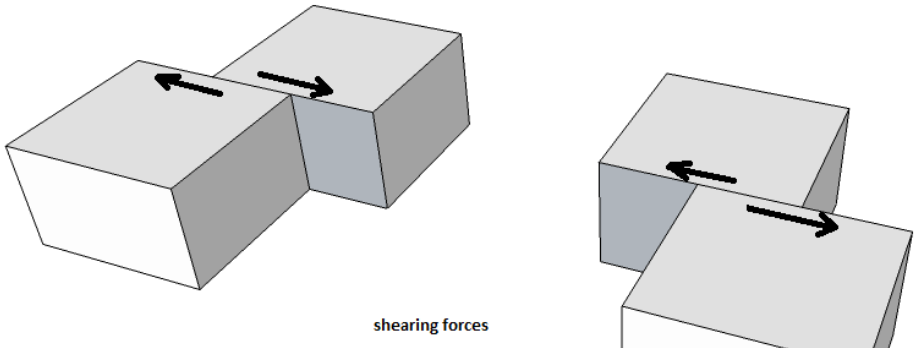

(c) Strike-slip fault

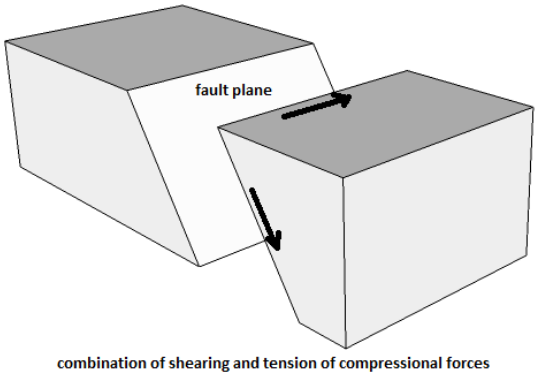

(d) Oblique-slip fault

Figure 2.7: Schemes illustrating the types of faults that generate earthquakes.

*https://www.usgs.gov/

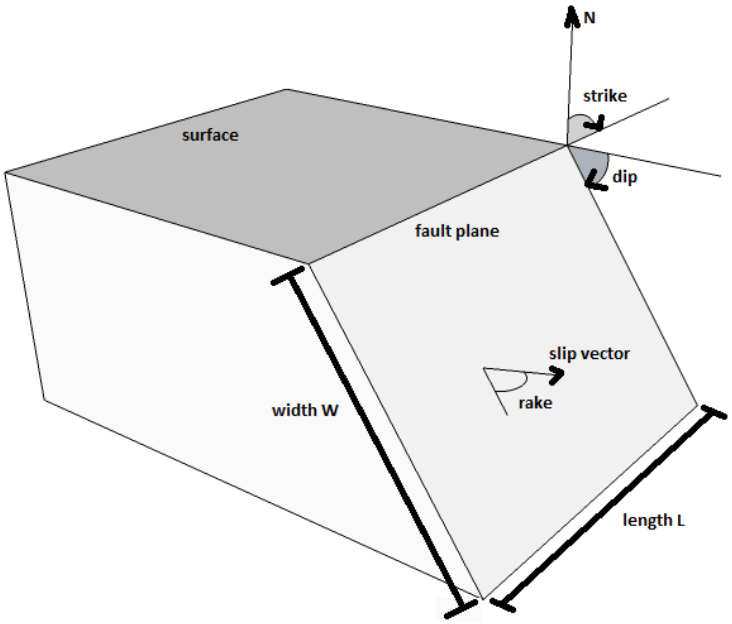

Figure 2.8: Scheme of the fault plane dimensions and geometry.

The magnitude of an earthquake is measured by the seismic moment. The seismic moment is based on the fault rupture area, the average amount of slip and the force necessary to overcome the friction between the moving blocks. The seismic moment M_0 is generally defined as (Aki, 1966):

$$\mathrm{M}_0 = GAD, \tag{2.11}$$

where G is the rigidity or resistance of a moving fault, quantified as the shear modulus of the material, A is the rupture area along the earthquake fault and D is the average slip or displacement offset between both sides of the fault (Figure 2.8). The rigidity of the Earth's crust is around 32 GPa, while the rigidity of its mantle is about 75 GPa. Nevertheless, the seismic moment is usually estimated from the amplitude spectra of the seismic waves. The non-dimensional moment magnitude scale M_w, introduced by Kanamori (1977), is a measure of the magnitude of the earthquake, translated by a number that characterises the relative size of the earthquake. It is based on the concept of the seismic moment M_0 and is often used to compare the different magnitudes of earthquakes, being specially useful for large earthquakes. Hanks and Kanamori (1979) deduced the moment magnitude M_w relation with the seismic moment M_0 as:

$$\mathrm{M}_0 = 10^{1.5\mathrm{M}_\mathrm{w}+16.1}, \tag{2.12}$$

when the seismic moment is expressed in C.G.S. units. When S.I. units are used, that relation becomes

$$\mathrm{M}_0 = 10^{1.5\mathrm{M}_\mathrm{w}+9.1}. \tag{2.13}$$

The magnitude of the earthquake event is one factor that can contribute to the tsunami generation. Most importantly, the earthquake must be of shallow depth and corresponding to an underwater event (although a tsunami could be generated by an event very close to the water and not underwater), then the sudden seafloor deformation caused by the earthquake can trigger a tsunami. As stated before, strike-slip faults cause crustal horizontal movements, and normal and thrust faults cause vertical movements. The vertical movement of normal and thrust faults can generate tsunamis: as a consequence of the seafloor bottom suddenly rising or descending, the mass

of water immediately above the seafloor is impelled to rise or descend as well, which disturbs its equilibrium, initiating the motion of the water free surface. Therefore, the most prominent type of faulting that generates tsunamis are the thrust earthquakes. Although not common, there are records of small tsunamis occurring from large ($\mathrm{M_w} > 8$) strike-slip earthquakes, such as the 12$^{\text{th}}$ January 2010 $\mathrm{M_w}$ 7.0 event at Haiti (Hornbach et al., 2010).

To determine the initial deformation of the ocean sea bottom caused by an earthquake, it is a common approach to use the elastic displacement model in a homogeneous half-space (Mansinha and Smylie, 1971; Okada, 1985). It is assumed that the bottom displacement corresponds to an instantaneous vertical displacement translated towards the free surface as an initial condition. The flow is assumed to be incompressible and the initial deformation of the ocean surface is used as the initial condition of the propagation model. However, some authors have argued about the importance of the horizontal motion of the fault in tsunami generation (see for instance Rivera, 2006), which would invalidate the shallow water hypothesis (cf. Chapter 1), as the vertical variation of the horizontal momentum would have to be taken into account. Nevertheless, the possible horizontal motion contribution is traditionally disregarded, as it is widely believed that it does not affect the ocean free surface (Synolakis et al., 1997).

Summing up, to model the tsunami generation stage, one needs to know the origin of the earthquake responsible for the tsunami and the earthquake source parameters, to determine the initial deformation of the seafloor caused by the earthquake, and finally the free surface initial position and movement of the waterbody.

2.1.4 The physics of fluid flow—3D models

2.1.4.1 The Navier-Stokes equations

To describe the flow of a fluid, two basic equations are necessary: the equation of continuity from the principle of conservation of mass, and the Navier-Stokes equations from the principle of conservation of momentum.

The continuity equation is written as

$$\frac{\partial \rho}{\partial t} + \rho \, \nabla \cdot \mathbf{u} = 0 \,, \tag{2.14}$$

where $\mathbf{u} = (u, v, w)^T$ is the velocity vector, with components u, v e w, in the x, y and z directions respectively, and ∇ is the vector differential operator given by:

$$\nabla = \left(\frac{\partial}{\partial x}, \frac{\partial}{\partial y}, \frac{\partial}{\partial z} \right) . \tag{2.15}$$

For an incompressible flow, expression (2.14) can be shown to be equivalent to:

$$\nabla \cdot \mathbf{u} = 0 \,. \tag{2.16}$$

Newton's second law of motion can be written, for a fluid particle with volume, $dV = dx \, dy \, dz$, and per unit of volume of that particle, as

$$\rho \, \frac{D\mathbf{u}}{Dt} = \boldsymbol{f} \,, \tag{2.17}$$

where $\boldsymbol{f} = \boldsymbol{f_{body}} + \boldsymbol{f_{surface}}$ is the applied force per unit volume on the fluid particle, which has been divided into body forces and surface forces. Body forces are those forces that apply to the entire mass of the fluid element and that are usually due to external forces such as gravity. Therefore, the gravitational body force is

$$\mathbf{f_{body}} = \rho \, \mathbf{g} \,, \tag{2.18}$$

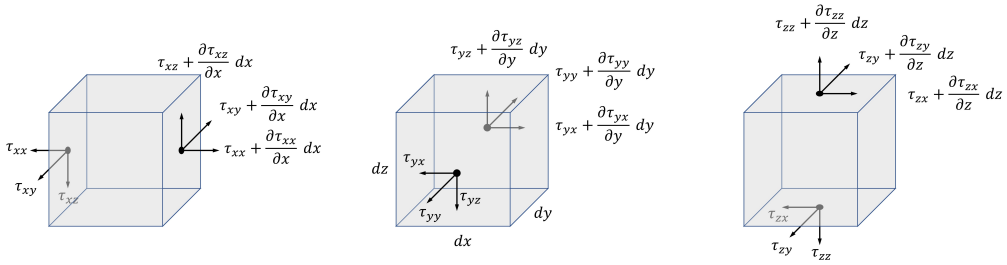

Figure 2.9: Normal and shear stresses at a fluid particle.

where $\mathbf{g} = (0, 0, -g)^T$ is the vector acceleration of gravity. The surface forces are those applied by external stresses on the sides of the element (cf. Figure 2.9). Stresses on a surface can be represented by a tensor, $\boldsymbol{T}$, given by:

$$\boldsymbol{T} = \begin{bmatrix} \tau_{xx} & \tau_{xy} & \tau_{xz} \\ \tau_{yx} & \tau_{yy} & \tau_{yz} \\ \tau_{zx} & \tau_{zy} & \tau_{zz} \end{bmatrix} . \tag{2.19}$$

Thus, the surface forces per unit volume in the x-direction, for instance, are given by:

$$f_{\text{surface},x} = \frac{\partial \tau_{xx}}{\partial x} + \frac{\partial \tau_{xy}}{\partial y} + \frac{\partial \tau_{xz}}{\partial z} , \tag{2.20}$$

which is the divergence of vector $(\tau_{xx}, \tau_{xy}, \tau_{xz})$, which is the upper row of the stress tensor. Similarly, $f_{\text{surface},y}$ and $f_{\text{surface},z}$ are the divergences of the second and third rows of $\boldsymbol{T}$. Thus, the surface force is

$$\mathbf{f_{surface}} = \nabla \cdot \boldsymbol{T} , \tag{2.21}$$

where the divergence of $\boldsymbol{T}$ is to be interpreted in the tensor sense, so that the result is a vector.

Newton's law per unit volume of fluid, equation (2.17), now becomes

$$\rho \frac{D\mathbf{u}}{Dt} = \rho\, \mathbf{g} + \nabla \cdot \boldsymbol{T} . \tag{2.22}$$

According to White (2005), the deformation law for a homogeneous and isotropic Newtonian fluid can be written as

$$\boldsymbol{T} = -p\, \boldsymbol{I} + 2\mu \boldsymbol{S} + \lambda\, (\nabla \cdot \boldsymbol{u})\, \boldsymbol{I} , \tag{2.23}$$

where p is the thermodynamic pressure, $\boldsymbol{I}$ is the identity tensor, μ and λ are two coefficients of viscosity, and $\boldsymbol{S}$ is the rate of strain tensor, given by

$$\boldsymbol{S} = \frac{1}{2} \left(\nabla \boldsymbol{u} + \nabla \boldsymbol{u}^T \right) . \tag{2.24}$$

Assuming that the flow is incompressible, then $\nabla \cdot \mathbf{u} = 0$ and the deformation law simplifies as

$$\boldsymbol{T} = -p\, \boldsymbol{I} + 2\mu \boldsymbol{S} . \tag{2.25}$$

The conservation of momentum equation for the incompressible flow of a Newtonian fluid is obtained by substituting expression (2.25) into Newton's law (2.22), resulting the so-called Navier-Stokes equation:

$$\rho \frac{D\mathbf{u}}{Dt} = \rho\, \mathbf{g} - \nabla p + 2\, \nabla \cdot (\mu \boldsymbol{S}) , \tag{2.26}$$

and the thermodynamic pressure coincides with the mechanical pressure, defined as negative normal stress numerically equal to the trace of the stress tensor, i.e.

$$p = -\frac{\tau_{xx} + \tau_{yy} + \tau_{zz}}{3} \,. \tag{2.27}$$

If viscosity, μ, can be assumed constant too and using the continuity equation (2.16), after some algebra the final form of the momentum equation becomes:

$$\rho \frac{D\mathbf{u}}{Dt} = \rho\,\mathbf{g} - \nabla p + \mu\,\nabla^2\,\mathbf{u}\,, \tag{2.28}$$

or, in a Eulerian framework, it is

$$\rho\left(\frac{\partial \boldsymbol{u}}{\partial t} + (\boldsymbol{u}\cdot\nabla)\,\boldsymbol{u}\right) = \rho\,\mathbf{g} - \nabla p + \mu\,\nabla^2\,\mathbf{u}\,. \tag{2.29}$$

2.1.4.2 The RANS equations

In turbulent flows, high frequency velocity fluctuations arise, which would require a very fine space and time discretization if the Navier-Stokes equations were used to model the fluid motion. To overcome this problem, the so-called Reynolds Averaged Navier-Stokes (RANS), or just the Reynolds equations, were proposed.

The RANS equations are obtained from a Reynolds decomposition of the instantaneous flow variables in the Navier-Stokes equations. The Reynolds decomposition is a statistical technique that separates a quantity into its time-averaged component and its fluctuation. In terms of a generic fluid flow, one can write this as:

$$\phi\,(x,y,z,t) = \overline{\phi}\,(x,y,z,t) + \phi'\,(x,y,z,t)\ , \tag{2.30}$$

where ϕ stands for the instantaneous fluid flow variable, $\bar{\phi}$ is the average component of ϕ and ϕ' is its fluctuation. The definition of the time-averaged component at a fixed position (x,y,z) and at instant t is (see for instance Erhard et al., 2010):

$$\overline{\phi}\,(x,y,z,t) = \frac{1}{T}\int_{t-T/2}^{t+T/2} \phi\,(x,y,z,t)\ dt\,, \tag{2.31}$$

where the time interval T shall be large enough so that an increase in T would not induce any change in $\bar{\phi}$.

If the generic variables ϕ and φ are considered, the Reynolds averages have the following properties:

- linearity:

$$\begin{aligned} \overline{\phi+\varphi} &= \overline{\phi} + \overline{\varphi}\,, \\ \overline{a\,\phi} &= a\,\overline{\phi}\,, \end{aligned} \tag{2.32}$$

  where a is a constant, i.e. $\overline{a} = a$;

- commutativity in derivation and integration:

$$\begin{aligned} \overline{\frac{\partial\phi}{\partial s}} &= \frac{\partial\overline{\phi}}{\partial s}\,, \\ \overline{\int \phi\,ds} &= \int \overline{\phi}\,ds\,; \end{aligned} \tag{2.33}$$

- generalized idempotency:

$$\overline{\overline{\phi}\,\varphi} = \overline{\phi\,\varphi}\,. \tag{2.34}$$

Therefore,

$$\begin{aligned} \overline{\overline{\phi}} &= \overline{\phi}\,, \\ \overline{\phi'} &= 0\,, \\ \overline{\overline{\phi}\,\overline{\varphi}} &= \overline{\phi\,\varphi}\,, \\ \overline{\overline{u}\,v'} &= 0\,, \end{aligned} \tag{2.35}$$

and the average product of two variables results in:

$$\overline{\phi\,\varphi} = \phi\,\varphi + \overline{\phi'\,\varphi'}\,. \tag{2.36}$$

The term $\overline{\phi'\,\varphi'}$ in expression (2.36) represents the covariance and is null when the variables are correlated. The correlation represents the degree of association between variables (Mesquita, 2013).

Applying the Reynolds decomposition to the velocity variables in the continuity equation (2.16), this becomes:

$$\nabla \cdot \bar{\boldsymbol{u}} = 0\,. \tag{2.37}$$

Applying the Reynolds decomposition to the velocity and pressure variables in the momentum equation (2.29) for incompressible fluid flow with constant viscosity, one gets

$$\frac{\partial \bar{\boldsymbol{u}}}{\partial t} + (\bar{\boldsymbol{u}} \cdot \nabla)\,\bar{\boldsymbol{u}} + \overline{(\boldsymbol{u}' \cdot \nabla)\,\boldsymbol{u}'} = \boldsymbol{g} - \frac{1}{\rho}\nabla\bar{p} + \nu\,\nabla^2\,\bar{\boldsymbol{u}}\,, \tag{2.38}$$

where $\nu = \mu/\rho$ is the kinematic viscosity coefficient. The momentum equation can be written as

$$\frac{\partial \bar{\boldsymbol{u}}}{\partial t} + (\bar{\boldsymbol{u}} \cdot \nabla)\,\bar{\boldsymbol{u}} = \boldsymbol{g} - \frac{1}{\rho}\nabla\bar{p} + \nu\,\nabla^2\,\bar{\boldsymbol{u}} - \nabla\left(\overline{\boldsymbol{u}'\boldsymbol{u}'^T}\right)\,. \tag{2.39}$$

The term $\overline{\boldsymbol{u}'\boldsymbol{u}'^T}$ on this equation is related to the so-called Reynolds stress, that accounts from the turbulent fluctuations of the momentum. The Reynolds stress tensor, $\boldsymbol{\tau}_R$ is defined as

$$\boldsymbol{\tau}_R = \rho\,\overline{\boldsymbol{u}'\boldsymbol{u}'^T}\,. \tag{2.40}$$

To compute the Reynolds stresses, the Boussinesq eddy viscosity hypothesis (Boussinesq, 1877) is used, according to which:

$$\frac{1}{\rho}\,\boldsymbol{\tau}_R = -2\,\nu_T\bar{\boldsymbol{S}}\,, \tag{2.41}$$

where

$$\bar{\boldsymbol{S}} = \frac{1}{2}\,\left(\nabla\bar{\boldsymbol{u}} + \nabla\bar{\boldsymbol{u}}^T\right)\,. \tag{2.42}$$

Finally, the RANS momentum equation for incompressible flow is usually written as

$$\frac{\partial \bar{\boldsymbol{u}}}{\partial t} + (\bar{\boldsymbol{u}} \cdot \nabla)\,\bar{\boldsymbol{u}} = \boldsymbol{g} - \frac{1}{\rho}\nabla\bar{p} + \nabla\left(2\,(\nu_T + \nu)\,\bar{\boldsymbol{S}}\right)\,. \tag{2.43}$$

In the remaining of this work, the average symbol in the variables is omitted, and the molecular kinematic viscosity, ν, is assumed to be much smaller than the eddy viscosity, ν_T, and thus $\nu_T + \nu \approx \nu_T$.

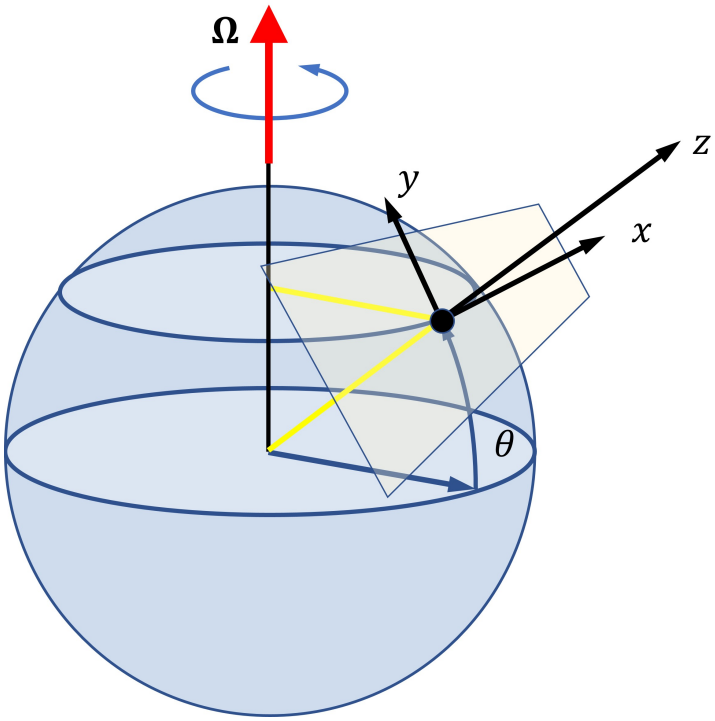

Figure 2.10: Reference frame on the surface of the Earth.

2.1.4.3 RANS equations on a rotating frame

The previous description of a fluid flow is valid on an inertial frame. The motion of water in the Earth's surface is described in a local coordinate system that rotates with the Earth around its South-North axis. A rotating frame is a non-inertial frame, and a fictitious force, the Coriolis force, must be added to the momentum equation. The Earth bounded non-inertial local frame is set up with the horizontal x-axis due East, the horizontal y-axis due North, the vertical z-axis in the upward direction, and origin at latitude θ (see Figure 2.10). Then, the Coriolis acceleration is given by (e.g. Alonso and Finn, 1972):

$$\boldsymbol{a}_C = -2\,\boldsymbol{\Omega} \times \boldsymbol{u}\,, \tag{2.44}$$

where $\boldsymbol{\Omega} = \omega\,(0, \cos\theta, \sin\theta)^T$ is the Earth's rotation vector on the local frame, and ω is the angular velocity of the Earth. The RANS equation in an Earth's bounded rotating frame is then:

$$\frac{\partial \boldsymbol{u}}{\partial t} + (\boldsymbol{u}\cdot\nabla)\,\boldsymbol{u} = \boldsymbol{g} - \frac{1}{\rho}\nabla p + \nabla\,(2\,\nu_T\,\boldsymbol{S}) - 2\,\boldsymbol{\Omega}\times\boldsymbol{u}\,. \tag{2.45}$$

When the vector product in expression (2.44) is expanded, one gets

$$\boldsymbol{a}_C = 2\,\omega\,(v\sin\theta - w\cos\theta, -u\sin\theta, u\cos\theta)^T\,. \tag{2.46}$$

In ocean dynamics, the vertical velocity, w, is small, so it can be assumed to be null. Beside that, the vertical upwards centrifugal component is very small when compared to the gravity acceleration. Therefore, the Coriolis acceleration is restricted to the horizontal plane, and the RANS equation for ocean dynamics becomes

$$\frac{\partial \boldsymbol{u}}{\partial t} + (\boldsymbol{u}\cdot\nabla)\,\boldsymbol{u} = \mathbf{g} - \frac{1}{\rho}\nabla p + \nabla\,(2\,\nu_T\,\boldsymbol{S}) + f\,\boldsymbol{u}_C\,, \tag{2.47}$$

where $f = 2\,\omega\,\sin\theta$ is the co-called Coriolis parameter, and $\boldsymbol{u}_C = (v, -u, 0)^T$.

For the sake of completeness, the time-averaged (RANS) continuity and momentum equations for the incompressible flow of a fluid in a reference frame bounded to the Earth's surface, in a scalar form, are:

$$\frac{\partial u}{\partial x} + \frac{\partial v}{\partial y} + \frac{\partial w}{\partial z} = 0, \tag{2.48}$$

$$\begin{aligned}\frac{\partial u}{\partial t} + u\frac{\partial u}{\partial x} + v\frac{\partial u}{\partial y} + w\frac{\partial u}{\partial z} = \\ -\frac{1}{\rho}\frac{\partial p}{\partial x} + \frac{\partial}{\partial x}\left(2\nu_T\frac{\partial u}{\partial x}\right) \\ + \frac{\partial}{\partial y}\left[\nu_T\left(\frac{\partial u}{\partial y} + \frac{\partial v}{\partial x}\right)\right] + \frac{\partial}{\partial z}\left[\nu_T\left(\frac{\partial u}{\partial z} + \frac{\partial w}{\partial x}\right)\right] + fv\,,\end{aligned} \tag{2.49}$$

$$\begin{aligned}\frac{\partial v}{\partial t} + u\frac{\partial v}{\partial x} + v\frac{\partial v}{\partial y} + w\frac{\partial v}{\partial z} = \\ -\frac{1}{\rho}\frac{\partial p}{\partial y} + \frac{\partial}{\partial x}\left[\nu_T\left(\frac{\partial u}{\partial y} + \frac{\partial v}{\partial x}\right)\right] \\ + \frac{\partial}{\partial y}\left(2\nu_T\frac{\partial v}{\partial y}\right) + \frac{\partial}{\partial z}\left[\nu_T\left(\frac{\partial v}{\partial z} + \frac{\partial w}{\partial y}\right)\right] - fu\,,\end{aligned} \tag{2.50}$$

$$\begin{aligned}\frac{\partial w}{\partial t} + u\frac{\partial w}{\partial x} + v\frac{\partial w}{\partial y} + w\frac{\partial w}{\partial z} = \\ -\frac{1}{\rho}\frac{\partial p}{\partial z} + \frac{\partial}{\partial x}\left[\nu_T\left(\frac{\partial u}{\partial z} + \frac{\partial w}{\partial x}\right)\right] \\ + \frac{\partial}{\partial y}\left[\nu_T\left(\frac{\partial v}{\partial z} + \frac{\partial w}{\partial y}\right)\right] + \frac{\partial}{\partial z}\left(2\nu_T\frac{\partial w}{\partial z}\right) - g\,.\end{aligned} \tag{2.51}$$

2.1.5 The physics of fluid flow—2DH models

Tsunami propagation is a special case of the general water-wave problem (Dias and Dutykh, 2007). As stated before, the propagation of water waves is governed by the so-called dynamic balance equations, the continuity equation for the conservation of mass and the Navier-Stokes equations for the conservation of momentum. The dynamic balance equations describe the motion of viscous fluids and come from applying Newton's second law to fluid motion, with the additional concept of viscous flow, as presented in the previous section. Usually the RANS equations are used, instead of the Navier-Stokes equations, and the solution of the dynamic balance equations are time-averaged flow velocity and pressure fields.

To achieve the most complete water wave description, the three-dimensional RANS equations should be applied, especially in case studies involving complex fluid flow interactions. Nevertheless, tsunami waves are in general modelled by a set of depth-integrated long wave models—the so-called 2DH (two dimensions horizontal) models—and it is common in tsunami modelling to use shallow water models (Chapter 1), and Boussinesq-type models, besides computational fluid dynamic models. Energy dissipation is included in the models, although often disregarded: Dias and Dutykh (2007) argued that there are several dissipative mechanisms present in tsunami propagation, with bottom friction being arguably the most relevant energy sink, especially in the last stages of the tsunami lifecycle.

2.1.5.1 The shallow waters equations

The Saint-Venant or shallow water equations (SWE) are a system of nonlinear quasi-hyperbolic partial differential equations (PDE), resulting from the analytical integration of the RANS equations in the vertical direction, assuming a hydrostatic pressure distribution. The shallow water equations comprise a continuity equation, and two momentum equations in the x and y directions:

$$\frac{\partial \eta}{\partial t} + \nabla \cdot \left[\Big(h + \eta \Big) \bar{\mathbf{u}} \right] = 0, \tag{2.52}$$

$$\begin{aligned} &\frac{\partial \bar{u}}{\partial t} + \bar{u}\frac{\partial \bar{u}}{\partial x} + \bar{v}\frac{\partial \bar{u}}{\partial y} + g\frac{\partial \eta}{\partial x} \\ &\quad = -C_d \, \frac{\bar{u}\,\|\bar{\mathbf{u}}\|}{h+\eta} + 2\frac{\nu_T}{h}\frac{\partial}{\partial x}\left(h\frac{\partial \bar{u}}{\partial x} \right) + \frac{\nu_T}{h}\frac{\partial}{\partial y}\left[h\left(\frac{\partial \bar{u}}{\partial y} + \frac{\partial \bar{v}}{\partial x} \right) \right] + f\bar{v}\,, \end{aligned} \tag{2.53}$$

and

$$\begin{aligned} &\frac{\partial \bar{v}}{\partial t} + \bar{u}\frac{\partial \bar{v}}{\partial x} + \bar{v}\frac{\partial \bar{v}}{\partial y} + g\frac{\partial \eta}{\partial y} \\ &\quad = -C_d \, \frac{\bar{v}\,\|\bar{\mathbf{u}}\|}{h+\eta} + \frac{\nu_T}{h}\frac{\partial}{\partial x}\left[h\left(\frac{\partial \bar{u}}{\partial y} + \frac{\partial \bar{v}}{\partial x} \right) \right] + 2\frac{\nu_T}{h}\frac{\partial}{\partial y}\left(h\frac{\partial \bar{v}}{\partial y} \right) - f\bar{u}\,, \end{aligned} \tag{2.54}$$

where h is the water depth at rest, η is the free surface elevation above the rest level, $\bar{\mathbf{u}} = (\bar{u}, \bar{v})$ is the depth-averaged horizontal velocity, with components $\bar{u}$ and $\bar{v}$ in the x and y directions, and C_d is the dimensionless bottom friction coefficient. The shallow water equations are non-dispersive as the pressure distribution is hydrostatic. The bottom friction coefficient can be related to the Manning coefficient, n, through the formula:

$$C_d = \frac{g\, n^2}{(h+\eta)^{1/3}}\,. \tag{2.55}$$

Linear wave velocity for this model is given by expression (2.5). The shallow water theory, either linear or nonlinear, is widely used and considered very suitable to model tsunami waves.

In spherical coordinates, the shallow water equations, excluding viscous terms, are written as:

$$\frac{\partial \eta}{\partial t} + \frac{1}{r\,\cos\theta}\left(\bar{u}\,\frac{\partial \eta}{\partial \phi} + \bar{v}\,\cos\theta\,\frac{\partial \eta}{\partial \theta} \right) = 0\,, \tag{2.56}$$

$$\frac{\partial \bar{u}}{\partial t} + \frac{1}{r\cos\theta}\left(\bar{u}\frac{\partial \bar{u}}{\partial \phi} \right) + \frac{1}{r}\left(\bar{v}\frac{\partial \bar{u}}{\partial \theta} \right) + \frac{g}{r\cos\theta}\left(\frac{\partial \eta}{\partial \phi} \right) - \frac{1}{r\,\cos\theta}\tau_b^{\phi} - f\bar{v} = 0\,, \tag{2.57}$$

and

$$\frac{\partial \bar{v}}{\partial t} + \frac{1}{r\cos\theta}\left(\bar{u}\frac{\partial \bar{v}}{\partial \phi} \right) + \frac{1}{r}\left(\bar{v}\frac{\partial \bar{v}}{\partial \theta} \right) + \frac{g}{r}\left(\frac{\partial \eta}{\partial \theta} \right) - \frac{1}{r}\tau_b^{\theta} + f\bar{u} = 0\,, \tag{2.58}$$

where θ and ϕ denote latitude and longitude respectively, r is the Earth radius, $\bar{u}$ and $\bar{v}$ represent the depth-averaged velocities in the θ and ϕ directions, and τ_b^{ϕ} and τ_b^{θ} represent the bottom friction terms.

2.1.5.2 The Boussinesq equations

The nonlinear shallow water equations can describe the tsunami waves from the ocean propagation up to the coastal swash. However, although the assumption of hydrostatic pressure distribution is adequate for tsunami waves, the dispersive effects, which are very important in deep water, must be

taken into account as they cause the main wave to fission, leading to the emergence of a wave train. Dispersion must be considered throughout the lifecycle of the tsunami, both in the propagation phase and in its transformation near the coast. This is supported by the observations from the 2004 Indian Ocean Tsunami (IOT), that showed dispersion in the tsunami waves propagation (Grilli et al., 2007; Horrillo and Kowalik, 2006; Watts et al., 2005).

The first wave model which included dispersive effects was obtained by Boussinesq (1872). The Boussinesq equations for solitary waves in constant depth are an extension of the Saint-Venant equations including the vertical water acceleration and thus a non-hydrostatic pressure distribution. For variable depth, Peregrine (1967) derived the Boussinesq equations using the depth-averaged velocity as variable and assuming linear variation of the vertical component of the velocity over the water depth. The linear dispersion characteristics of the Boussinesq models limit their scope of application to relatively shallow water depths, where the dispersion parameter $\sigma = kh$ is small, and to waves with weak nonlinearity. Several improved Boussinesq-like formulations are available that extend the application limits of this model (Madsen and Sørensen, 1992; Nadaoka et al., 1997; Nwogu, 1993; Schäffer and Madsen, 1995; Teng, 1997). The classical Boussinesq equations can be written as (Avilez-Valente, 2000):

$$\frac{\partial \eta}{\partial t} + \nabla \cdot \left[\Big(h + \eta \Big) \bar{\mathbf{u}} \right] = 0 \,, \tag{2.59}$$

$$\begin{aligned} &\frac{\partial \bar{u}}{\partial t} + \bar{u}\frac{\partial \bar{u}}{\partial x} + \bar{v}\frac{\partial \bar{u}}{\partial y} + g\frac{\partial \eta}{\partial x} \\ &\quad = \frac{\partial}{\partial t}\left[\frac{h}{2}\frac{\partial^2}{\partial x^2}(h\bar{u}) - \frac{h^2}{6}\frac{\partial^2 \bar{u}}{\partial x^2} + \frac{h}{2}\frac{\partial^2}{\partial x \partial y}(h\bar{v}) - \frac{h^2}{6}\frac{\partial^2 \bar{v}}{\partial x \partial y} \right] \\ &\quad - C_d \frac{\bar{u}\,\|\bar{\mathbf{u}}\|}{h+\eta} + 2\frac{\nu_T}{h}\frac{\partial}{\partial x}\left(h\frac{\partial \bar{u}}{\partial x} \right) + \frac{\nu_T}{h}\frac{\partial}{\partial y}\left[h\Big(\frac{\partial \bar{u}}{\partial y} + \frac{\partial \bar{v}}{\partial x} \Big) \right] + f\bar{v} \,, \end{aligned} \tag{2.60}$$

and

$$\begin{aligned} &\frac{\partial \bar{v}}{\partial t} + \bar{u}\frac{\partial \bar{v}}{\partial x} + \bar{v}\frac{\partial \bar{v}}{\partial y} + g\frac{\partial \eta}{\partial y} \\ &\quad = \frac{\partial}{\partial t}\left[\frac{h}{2}\frac{\partial^2}{\partial x \partial y}(h\bar{u}) - \frac{h^2}{6}\frac{\partial^2 \bar{u}}{\partial x \partial y} + \frac{h}{2}\frac{\partial^2}{\partial y^2}(h\bar{v}) - \frac{h^2}{6}\frac{\partial^2 \bar{v}}{\partial y^2} \right] \\ &\quad - C_d \frac{\bar{v}\,\|\bar{\mathbf{u}}\|}{h+\eta} + \frac{\nu_T}{h}\frac{\partial}{\partial x}\left[h\left(\frac{\partial \bar{u}}{\partial y} + \frac{\partial \bar{v}}{\partial x} \right) \right] + 2\frac{\nu_T}{h}\frac{\partial}{\partial y}\left(h\frac{\partial \bar{v}}{\partial y} \right) - f\bar{u} \,. \end{aligned} \tag{2.61}$$

The linear wave velocity of the Boussinesq model is

$$C = \sqrt{gh\,\frac{1}{1 + \frac{1}{3}(kh)^2}} \,. \tag{2.62}$$

In spherical coordinates, the Boussinesq equations, excluding viscous terms, are written as:

$$\frac{\partial \eta}{\partial t} + \frac{1}{r\,\cos\theta}\left(\bar{u}\,\frac{\partial \eta}{\partial \phi} + \bar{v}\,\cos\theta\,\frac{\partial \eta}{\partial \theta} \right) = 0 \,, \tag{2.63}$$

$$\begin{aligned} &\frac{\partial \bar{u}}{\partial t} + \frac{1}{r\cos\theta}\left(\bar{u}\frac{\partial \bar{u}}{\partial \phi} \right) + \frac{1}{r}\left(\bar{v}\frac{\partial \bar{u}}{\partial \theta} \right) + \frac{g}{r\cos\theta}\left(\frac{\partial \eta}{\partial \phi} \right) \\ &\quad + \frac{1}{r^2\,\cos^2\theta}\frac{\partial}{\partial t}\left[\frac{h^2}{6}\left(\frac{\partial^2 \bar{u}}{\partial \phi^2} + \frac{\partial^2 \bar{v}\,\cos\theta}{\partial \phi\,\partial \theta} \right) - \frac{h}{2}\left(\frac{\partial^2 (h\bar{u})}{\partial \phi^2} + \frac{\partial^2 (h\,\cos\theta\,\bar{v})}{\partial \phi\,\partial \theta} \right) \right] \\ &\quad - \frac{1}{r\,\cos\theta}\tau_b^{\phi} - f\bar{v} = 0 \,, \end{aligned} \tag{2.64}$$

and

$$\frac{\partial \bar{v}}{\partial t} + \frac{1}{r\cos\theta}\left(\bar{u}\frac{\partial \bar{v}}{\partial \phi}\right) + \frac{1}{r}\left(\bar{v}\frac{\partial \bar{v}}{\partial \theta}\right) + \frac{g}{r}\left(\frac{\partial \eta}{\partial \theta}\right) + \frac{1}{r^2}\frac{\partial}{\partial t}\left[\frac{h^2}{6}\left(\frac{1}{\cos\theta}\left(\frac{\partial^2 \bar{u}}{\partial \phi\,\partial \theta} + \frac{\partial^2(\bar{v}\cos\theta)}{\partial \theta^2}\right)\right) - \frac{h}{2}\left(\frac{1}{\cos\theta}\left(\frac{\partial^2(h\,\bar{u})}{\partial \phi\,\partial \theta} + \frac{\partial^2(h\,\cos\theta\bar{v})}{\partial \theta^2}\right)\right)\right] - \frac{1}{r}\tau_b^{\theta} + f\bar{u} = 0\,. \tag{2.65}$$

The shallow water equations are competent in the description of the characteristics of the tsunami waves throughout several flow regimes. George (2006) noted that attention should be paid to the additional computational costs by solving more computationally expensive systems, even if a more accurate numerical solution is achieved and the outcome justifies the time consumption.

2.1.5.3 Numerical codes

As a rule, numerical models are used to simulate the several physical processes that compose the lifespan of a tsunami. To achieve the proper functioning of a numerical hydrodynamic model, it is necessary to ensure that the model follows the law of conservation of mass. This means that the volume of water at the beginning and at the end of the simulation must be the same. It is also necessary to guarantee the convergence of the numerical model which, according to Thompson (1992), occurs when "a sequence of models solutions with increasingly refined solution domains approaches a fixed value". Therefore, the conservation of mass and convergence testing are fundamental hydrodynamic conditions when intending to use any numerical model.

Several operational codes are implementing the shallow water theory, such as TUNAMI-N2 (Imamura 1996; Shuto et al. 2014), MOST code by NOAA (Titov and Synolakis 1998; Shuto et al. 1997), COMCOT (Philip Liu Group 2014), TsunAWI (Behrens 2008) and GeoClaw (Clawpack Development Team 2014b), among others. The solution of the mathematical models based on the partial differential equations demands the application of certain approximations, simplifications and numerical schemes. Numerical methods are applied to solve the hyperbolic equations of the model. The discretisation of the equations is performed to transform the continuous differential equations into discrete differential equations.

For TUNAMI-N2, MOST and COMCOT codes, uniform and nested finite difference (FD) mesh discretisation of the SWE is performed (Behrens and Dias 2015). In the finite differences method, the resolution of the differential equations is based on the approximation of the derivatives by finite differences, with the approximation formula obtained from the Taylor's series of the derivative function. Finite differences numerical schemes have been by far the most commonly used numerical methods in tsunami simulation, due to its easy implementation.

TsunAWI (Behrens 2008) applies a discretisation based on finite elements (FE). Finite element methods find approximate solutions to boundary value problems for differential equations. With this numerical technique, it is possible to simplify a large system, dividing it into small finite elements, dealing more easily with complex geometries and boundaries.

A widely used numerical method is the finite volume (FV) method, where the computational domain is divided into volumes or cells. GeoClaw code applies a finite volume numerical scheme, that has been demonstrated to be robust and flexible, with adaptive mesh refinement (AMR). AMR is used to speed up the simulation and resolves the tsunami wave in specific areas of interest, flagged for refinement. Finite volumes have also shown to be very efficient and accurate in solving conservative equations with its shock-capturing ability. Recently, as explained by Shi et al. (2012b), hybrid models combining both finite difference and finite volume methods, designated as Total Variation Diminishing (TVD)-type schemes (Toro 2009), have been applied in

Boussinesq-type wave models. These methods have shown great performance and robustness of the shock-capturing mechanisms, especially in coastal inundation and wave breaking simulations (Erduran et al. 2005; Tonelli and Petti 2009; Roeber et al. 2010).

When the tsunami enters the coastal waters and the wave interacts with the structures, it is fundamental to understand the wave-structure interaction. For this stage, both Eulerian (grid based) formulations, such as in OpenCFD Limited (2019), and Lagrangian (particle based) formulations, such as in the three-dimensional smoothed particle hydrodynamics (SPH) models (St-Germain et al. 2013), have been widely used. Although most computational codes ignore tsunami dispersion, the dispersive effects are still investigated and are a topic of discussion in tsunami science (Glimsdal et al. 2013). Codes like FUNWAVE-TVD (Shi et al. 2012b; Kirby et al. 2013)—initially developed by Kirby et al. (1998)—and GlouBous (Løvholt et al. 2008; Løvholt et al. 2010) include the dispersion contribution, as they solve Boussinesq-like models.

2.1.6 Tsunami flow regimes and coastal interactions

2.1.6.1 From the deep ocean to the shoreline

The propagation of tsunamis evolves through diverse flow regimes, from the deep ocean to the intermediate and shallow waters, being subject to several transformations. Considering the tsunami wave propagation in deep waters, it is observed that the wavelength of a tsunami wave is very long—hundreds of kilometres—when compared with the water depth it is propagating in—few kilometres. In the shallow water approximation, a parameter υ is defined to be the ratio between the water depth h and the wavelength λ, which is small and therefore the flow's vertical variation is ignored. This implies that tsunami waves propagate a long way from the source, carrying its enormous energy until it is finally dissipated in the coast.

In deep water, the tsunami wave amplitude is relatively small—from tens of centimetres to a few metres—, making them difficult to be detected from the air or to be felt on board of a ship in the deep ocean. As tsunami waves enter shallower waters, the waves start to shoal. It is important to note that the bathymetric features of the ocean bottom are quite relevant in the tsunami propagation and its amplification effects (see for instance Geraghty 2006). As the tsunami approaches the coast, the speed decreases and the amplitude increases. The tsunami waves slow down and the waves' energy is compressed, piling up and striking with devastating force. The flow regime changes with the shoaling effect and afterwards with the turbulent and complex energy dissipation of the propagating waves, giving origin to breaking waves. Undular bores can also be observed as a result of the frequency dispersion.

Tsunami waves originate strong enhanced currents in the coastal harbours and ports, also transporting the debris resultant from the destruction due to the impact of the tsunamis waves on the coastal structures. Observations from the 2004 IOT and 2011 Tohoku tsunami showed that the strong currents are highly turbulent and sheared (Lynett et al. 2012; Dias et al. 2014). The physical processes involved are complex and difficult to emulate, which can easily lead to erroneous modelling. Therefore, models should be able to simulate the rotational flows and turbulent characteristics associated with the currents. Ultimately, the goal is to understand the damage that can occur in the harbours and ports struck by the tsunami waves. Behrens and Dias (2015) considered the importance of formulating guidelines to keep ships offshore and safe from tsunami induced currents. The authors also note the lack of knowledge about the interaction of tsunami with marine renewable energy farms.

The last flow regime is composed by the complex fluid flow interaction with the shoreline features, the coastal vegetation, the existing coastal structures, river courses and other existing streams, the complex inland propagation and inundation, and also by the transport of debris. In the long run, what is aimed from all the tsunami modelling process is to determine, as accurately

as possible, what happens in and along the coast, as the tsunami wave reaches land and its energy is dissipated.

2.1.6.2 Inundation and coastal interactions

Wave run-up and run-in

Wave run-up is a parameter widely used to evaluate the coastal impact of tsunami waves. It is defined as the vertical maximum rise reached by the tsunami incident wave (Figure 2.11, where the run-in R_i is the maximum inundation distance measured horizontally and β is the slope angle of the beach). The estimation of the run-up R parameter is a long-established challenge in hydrodynamic modelling, tackled to assess tsunami coastal impact. Wave run-up has been investigated and documented in several empirical, analytical and numerical research studies (Lima et al. 2010).

Numerical models compute tsunami inundation in terms of flow depth, run-in and run-up. The tsunami propagation over dry land is possible using a numerical algorithm, able to update the water depth along the shoreline grid cells. The trustworthy forecast of these parameters is highly dependent on the bathymetric and topographic information and detail, which are also influenced by the roughness data (Gayer et al. 2010).

Basic empirical approximations have been adopted to predict run-up heights. Using the non-linear shallow water theory, Carrier and Greenspan (1958) presented a method to solve the run-up problem. Mehauté et al. (1968) resumed the theories and works on the run-up of waves, pointing out the important contribution of the work by Carrier and Greenspan (1958). Pedersen and Gjevik (1983) investigated the run-up of long water waves using a Lagrangian Boussinesq model, with good agreement between the experimental run-up and numerical results. Synolakis (1987) presented the theory and asymptotic results on the run-up of non-breaking solitary waves on plane beaches. Using a Lagrangian finite element Boussinesq wave model, Zelt (1991) studied the non-breaking and breaking solitary waves run-up on plane impermeable beaches. Pelinovsky and Mazova (1992) reviewed research works on wave run-up on a slope and solving methods, starting from Carrier and Greenspan (1958); they presented their study of leading depression N-waves run-up and a linear formulation for the solution of wave run-up non-one-dimensional problems.

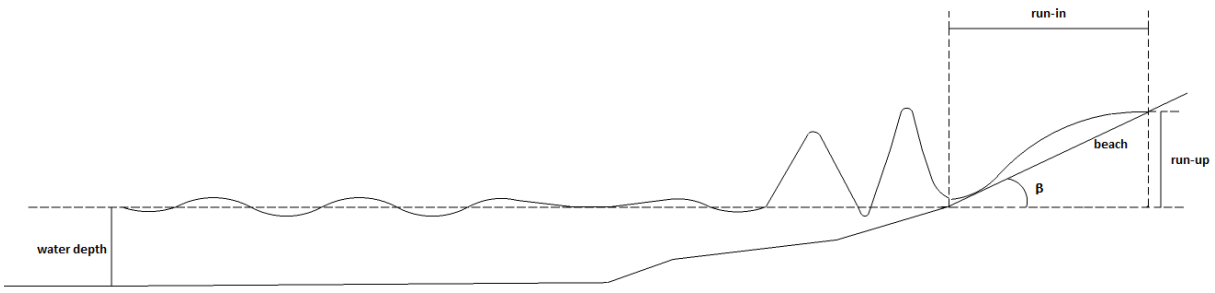

Figure 2.11: Scheme illustrating the fundamental concepts regarding the tsunami inundation stage: run-up R; run-in R_i; slope angle β.

Tadepalli and Synolakis (1994) applied the shallow water equations, with first order accuracy, to determine the wave run-up of different N-waves: the generalised N-wave, the isosceles N-wave and the double N-wave. They provided asymptotic results for both leading depression N-waves (LDN) and leading elevation N-waves (LEN) maximum wave run-up, as well as the validity limits for the proposed approximated theory. Tadepalli and Synolakis (1994) found LDN-waves to have higher run-up comparing with equivalent LEN and focus on the importance of determining the sign of the leading wave to find the direction of slip motion and better model the run-up of nearshore

tsunamis. Dias and Dutykh (2007) supported that the solitary wave model might not be suitable to predict the run-up upper limit of nearshore generated tsunamis, as the run-up of LDN-waves is higher than the run-up for LEN-waves (Tadepalli and Synolakis 1994).

Baldock and Holmes (1999) compared numerical results with analytical solutions of swash oscillations on a steep beach, with agreement on the shoreline displacement determination based on bore run-up theory. Li and Raichlen (2001) studied run-up of solitary waves, improving the accuracy of maximum run-up prediction with the presented nonlinear theory and a good agreement with experimental data for steep and smaller slopes. Li and Raichlen (2002) developed a model, based on the nonlinear shallow water equations and using a weighted essentially non-oscillatory (WENO) shock-capturing scheme from gas dynamics, to simulate wave breaking and run-up. The numerical scheme was found to predict reasonably well several aspects of the run-up process. Li and Raichlen (2003) investigated the impact on the run-up of a plunging breaking solitary waves' jet and the post-breaking bore formed. The authors also developed a simple empirical method, based on energy conservation principles, to estimate run-up of breaking solitary waves on a plane slope.

Didenkulova et al. (2006) demonstrated that a wave with increased steepness of the leading front travels longer distances inland comparing with a symmetric profile incident wave. Didenkulova et al. (2007) presented an analytical formula for the maximum height of run-up of a solitary wave on a beach, for variable geometry of the incident wave, especially for tsunami events. Okal and Synolakis (2004) established the Plafker's rule of thumb, which says that the ratio between the maximum run-up and the average slip on the fault plane cannot be much greater than 1 on a nearby beach with a smooth topography.

Chang et al. (2009) generated solitary waves in the super tank at the Tainan Hydraulics Laboratory (THL), with 300 m $\times$ 5 m $\times$ 5.2 m, and investigated the run-up flow and pressure of breaking solitary waves climbing up a slope. Baldock et al. (2009) collected data on run-up for different wave conditions and found a better correlation with a run-up semi-empirical formula than with Hunt's formula (Hunt 1959). Madsen and Schäffer (2010) presented analytical solutions of the nonlinear shallow water equations, for the run-up and run-down of single and LDN-waves.

Zhao et al. (2011) used a high-order Boussinesq model to study the generation, propagation and run-up of tsunamis, as well as the maximum run-ups of solitary and N-waves and validated run-up field data from the IOT. Using a Boussinesq-type model, Kim and Son (2019) investigated the run-up and wave evolution characteristics of idealised leading depression and leading elevation N-waves, with a special focus on the shelf geometry effects and wave breaking under the geophysical scale.

Klettner et al. (2012) generated depressed waves in the laboratory with a novel technique and performed beach run-up measurements. Using a pneumatic generator, Charvet et al. (2013) took the new retrieved data to find novel run-up expressions. The authors found consistency with previous studies, but suggest potential energy as a useful parameter to predict run-up. Drähne et al. (2015) compared both physical and numerical approaches with known analytical solutions for long wave run-up. McGovern et al. (2016) documented tests performed using a long wave generator and run-up results for very long period LDN-waves. In a 300 m wave flume, Sriram et al. (2016) generated long waves and compared run-up values of long-period pulses and standard soliton solutions. They support Madsen et al. (2008), stating that long waves such as tsunami should not be modelled by solitary waves.

2.1.6.3 Wave run-up formulations

The wave run-up, R, can be estimated directly from the trigonometric relation (Chang et al., 2009; Charvet et al., 2013):

$$R = R_{in} \cdot \tan\beta\,, \tag{2.66}$$

where R_{in} is the horizontal distance travelled by the wave on land (wave run-in) and β is the slope angle of the beach.

Baldock et al. (2009) compared the experimental results obtained with Hunt's formula (Hunt, 1959) for breaking waves

$$R = K \cdot \tan\beta \cdot \sqrt{H_0 \cdot L_0}\,, \tag{2.67}$$

where K is an empirical coefficient, H_0 is the offshore wave height and L_0 is the offshore deep water wavelength. The previous expression can be written in terms of the Iribarren number, Ir:

$$\frac{R}{H_0} = K \cdot \frac{\tan\beta}{\sqrt{H_0/L_0}} \tag{2.68}$$

with the Iribarren number Ir defined as:

$$\mathrm{Ir} = \frac{\tan\beta}{\sqrt{H_0/L_0}}\,. \tag{2.69}$$

The Iribarren number Ir is a dimensionless parameter that expresses several effects of surface gravity waves propagating over slopes and obstacles. Besides run-up, it is also used as a description parameter of the type of breaking waves on the beach.

Sriram et al. (2016) used the formula presented by Synolakis (1987) for the run-up of solitary waves, which is

$$R_{\mathrm{SW}} = 2.831 \cdot h \cdot \sqrt{\cot\beta} \cdot \left(\frac{H}{h}\right)^{5/4}\,, \tag{2.70}$$

where R_{SW} is the maximum run-up of solitary non-breaking waves, predicted by the linear and nonlinear theories, h is the water depth and H is the wave height.

For the N-waves, Synolakis et al. (2007) proposed the expression:

$$R_{\mathrm{NW}} = 3.86 \cdot h \cdot \sqrt{\cot\beta} \cdot \left(\frac{H}{h}\right)^{5/4} \tag{2.71}$$

and compared the run-up of the Boussinesq solitary wave, expression(2.70), with the run-up of an isosceles N-wave, establishing that $R_{\mathrm{NW}} = 1.364 \cdot R_{\mathrm{SW}}$.

In this thesis, additional expressions for the run-up are proposed, which simultaneously account for the water depth h and the wave height H. Both parameters are included in expressions of the type:

$$\frac{R}{d} = K \cdot \tan\beta \cdot \mathrm{St}^m, \tag{2.72}$$

where K and m are coefficients to be determined by the minimum square method and St is the Stokes parameter, which indicates the balance between the nonlinearity ϵ and the dispersion σ of long surface gravity waves:

$$\mathrm{St} = \frac{\epsilon}{\sigma^2}\,. \tag{2.73}$$

Amplitude dispersion of a long wave is quantified by the nonlinearity parameter ϵ, as the ratio between its height and the local depth, i.e.

$$\epsilon = \frac{H}{h}\,, \tag{2.74}$$

while the frequency dispersion is quantified by the shallowness or dispersion parameter σ, as a relation between the local depth and the wavelength, defined as

$$\sigma = \kappa \cdot h\,. \tag{2.75}$$

The following run-up expressions are also proposed:

$$\frac{R}{d} = K \cdot \left(\frac{\tan\beta}{\mathrm{St}} \right)^m , \tag{2.76}$$

and

$$\frac{R}{d} = K \cdot (\tan\beta \cdot \mathrm{St})^m . \tag{2.77}$$

However, we do not have run-up measurements obtained with different β angles and therefore it is difficult to determine the influence of the term $\tan\beta$.

2.1.6.4 Tsunami pressure forces

The coastal areas affected by tsunamis are subject to hydrodynamic forces due to the tsunami bore-like waves that reach the coast and/or debris carried in the water. To estimate all the forces involved remains still a great challenge in tsunami science. Palermo et al. (2009) review and decompose the tsunami-induced hydraulic bores into their component forces. In general, the existing studies on the tsunami hydrodynamic forces consider solitary waves, hydraulic bores and the dam break problem (Al-Faesly et al. 2012; Nouri et al. 2010). Coastal structures are barely prepared to outlive the tsunami forces involved. Please refer to Al-Faesly et al. (2012) for the damage description of the events of Chile 2010 and Tohoku 2011.

It is important to estimate the forces to which the structures can be subject during a worst case scenario, therefore giving us an insight about the improvements required in coastal planning and tsunami impact reduction on the human environment.

When the tsunami waves reach land, coastal structures are subject to hydrodynamic forces. These forces can be estimated for a steady flow as (see for instance Chang et al., 2009):

$$F_d = \frac{1}{2} \cdot \rho \cdot C_d \cdot B \cdot \left(h^* \cdot u^{*2} \right) , \tag{2.78}$$

where F_d is the resultant hydrodynamic force, ρ is the density of the fluid (including the sediment load), C_d is the drag coefficient, B is the width of the body where the forces are exerted (e.g. the dimension in the plane normal to the fluid direction). The term $h^* \cdot u^{*2}$ is the moment flux per unit mass per unit width occurring on the body. Dividing by $B \cdot h^*$, the frontal area normal to the run-up flow, the mean hydrodynamic pressure over the area is obtained as:

$$P_d = \frac{1}{2} \cdot \rho \cdot C_d \cdot u^{*2} . \tag{2.79}$$

Based on the proposal by FEMA P646 (2008) to estimate $h^* \cdot u^{*2}$ and further simplification, Al-Faesly et al. (2012) obtained the following expression for this term:

$$h^* \cdot u^{*2} = \frac{1}{8} \cdot g \cdot R^2 , \tag{2.80}$$

where R is the design run-up at the site.

For rectangular shaped structures, Al-Faesly et al. (2012) used $C_d = 2.0$ as suggested in FEMA 55 (2000).

Chapter 3

Computational modelling

3.1 Introduction

The most straightforward way to predict the outcome of a tsunami event is to reproduce the phenomenon through numerical modelling. In numerical modelling, sets of mathematical equations and models describe and emulate the physical conditions of the event to be simulated. In the case of tsunamis, the first stage of its lifespan concerns the generation of the tsunami, which can be a consequence of different triggering mechanisms. For earthquake triggered tsunamis, numerical models use the elastic dislocation model in an homogeneous half-space approach (Mansinha and Smylie 1971; Okada 1985), to determine the initial deformation of the ocean sea bottom, which translates towards the free surface as an initial condition. It is assumed water incompressibility and the initial deformation of the ocean surface is used, for the initial time instant, as the initial condition of the propagation model. The assumption that the bottom displacement corresponds to an instantaneous vertical displacement is performed for earthquake triggered tsunamis. The Okada's equations do not describe the physics of landslide motion, therefore for events such as landslide movements other assumptions are introduced to determine the initial motion. Please refer to the literature (Gisler 2008; Løvholt et al. 2015), as this is beyond the scope of this thesis.

To model the propagation phase of tsunamis the simplest and most used models are the shallow water equations (SWE)—also known as the Saint-Venant equations (section 2.1.5)—in its linear or nonlinear forms. The two-dimensional (2DH) SWE are widely used to model tsunamis (Synolakis et al. 2007), as these equations can model several physical aspects of the phenomenon and can reproduce many important features of the propagation, including the inundation and the run-up. It is considered in general that the linear shallow water equations (LSW) set of equations are satisfactory in modelling tsunami propagation in deep waters (Synolakis and Bernard 2006). The nonlinear shallow water equations (NLSW) are commonly used to describe the tsunami run-up (section 2.1.6) and there are several available models generally used, as TUNAMI-N2 (Imamura 1996; Shuto et al. 2014), MOST code by NOAA (Titov and Synolakis 1998; Shuto et al. 1997), GeoClaw (Clawpack Development Team 2014b), COMCOT (Philip Liu Group 2014), TsunAWI (Behrens 2008), NSWING (Miranda et al. 2014), among others. Different numerical techniques, such as the finite differences (FD), finite volumes (FV), finite elements (FE) and smoothed-particle hydrodynamics (SPH), are applied to solve the set of equations used to describe the tsunami and its phases, which also distinguishes the different codes.

Besides the shallow water models, Boussinesq long wave models, like FUNWAVE (Kennedy et al. 2000; Kirby et al. 1998; Wei et al. 1995), which evolved to FUNWAVE-TVD (Shi et al. 2012b; Kirby et al. 2013), GloBouss (Pedersen and Løvholt 2008; Løvholt et al. 2008; Løvholt et al. 2010) and COULWAVE (Lynett et al. 2002; Kim and Lynett 2011), are an alternative to model tsunami propagation and transformation. Boussinesq-type models account for frequency

dispersion, which is present even in shallow waters, and will behave better in case of wave fission (Løvholt et al. 2010). Pujiraharjo and Hosoyamada (2006) and Kazolea and Delis (2013) stated that Boussinesq models provide more accurate results for highly dispersive waves over increasing water depth. As Grilli et al. (2007) discussed, the importance of the dispersive effects on tsunami wave evolution has been shown by Kulikov (2005a), as well as its relevance in the tsunami hazard mitigation (Horrillo and Kowalik, 2006), which therefore supports the necessity of its inclusion in numerical long wave models, as in FUNWAVE-TVD. This comes into agreement with what has been earlier discussed by Ward (1980) and Okal (1982).

To model the interaction of tsunami waves with the nearshore environment, coastal vegetation and structures, turbulence models are necessary. Therefore, computational fluid dynamics (CFD) models are used for the two-dimensional and three-dimensional numerical modelling, such as the direct numerical simulation (DNS), large eddy simulation (LES) and Reynolds-Averaged Navier-Stokes (RANS) models. CFD models, such as OpenFOAM (OpenCFD Limited 2019), ANSYS® Fluent and ANSYS® CFX, are capable of modelling complex fluid flow problems. All of them include several approaches to model turbulence.

In this chapter, we will go through each numerical code used throughout this research work, from global to local tsunami modelling. The focus will be on the numerical modelling of tsunamis triggered by submarine earthquakes only. One by one, each code will be described, generally and in detail, in its governing equations and numerical methods. The benchmark testing of numerical tsunami modelling codes is mandatory. The presently accepted benchmarking standard adopted by the National Tsunami Hazard Mitigation Program (NTHMP) were taken from Synolakis et al. (2007, 2008). Results from the benchmark test cases are presented here to determine the performance characteristics of each code.

The numerical models used in this dissertation were (1) GeoClaw, a NLSW model for the generation and early propagation phases of a tsunami, (2) FUNWAVE-TVD, a fully nonlinear Boussinesq model for the nearshore water wave propagation and transformation, and (3) OpenFOAM, a CFD code used to model the nearshore processes in two- and three-dimensional domains and to determine the properties and characteristics of the tsunami interaction with the coastal structures and the surrounding areas. OpenFOAM is used with the olaFlow toolbox.

All the numerical codes used in this work are open-access and free and were installed and used in Linux operating system (from Ubuntu version 14.04 Trusty to 18.04 Bionic). Serial runs were performed with a portable computer with Intel® Core™ i5 CPU M 430 @ 2.27GHz x 4 Processor with 7.6GB RAM and a desktop computer with Intel® Core™ i7-4790 CPU @ 3.60GHz x 8 Processor with 15.6GB RAM. Parallel simulations were performed in clusters with Linux operating system: 1) bhuta, with CPU 2x Intel® Xeon E5649 @ 2.53GHz (2x6Cores) and 48GB RAM; 2) tornado, with CPU 2x Intel® Xeon X5560 @ 2.80GHz (2x4Cores) and 48GB RAM; 3) Grid FEUP (Avalanche cluster hardware details in `https://grid.fe.up.pt`).

3.2 GeoClaw

3.2.1 Introduction

In this thesis, GeoClaw was chosen to model the tsunami generation and part of the propagation of the triggering tsunami event. The capability of the code to generate and visualize the initial deformation/perturbation and to quickly monitor the propagation of the tsunami, with its easy implementation and high speed of performance, showed GeoClaw code to be the best option available for this stage. The code has also been used to model and validate data for tsunami events, with extensive studies of the 2011 Tohoku earthquake and tsunami (Melgar and Bock 2013; MacInnes et al. 2013b; Sraj et al. 2014; Sraj et al. 2017), achieving good numerical results in comparison

with the expected results (Arcos and LeVeque, 2015). GeoClaw, from Clawpack version 5.2.2, was then used to perform the numerical modelling.

The computational open source Clawpack is the "Conservation Laws Package", a set of related hyperbolic partial differential equations (PDEs) solvers, such as Classic, AMRClaw, GeoClaw and PyClaw solvers. The GeoClaw solver is designed to deal with geophysical problems and includes the block-structured adaptive mesh refinement (AMR) capability from AMRClaw (Berger et al. 2011). Originally, GeoClaw spawned from TsunamiClaw code developed by George (2006), as part of Clawpack. The GeoClaw numerical tsunami model (Clawpack Development Team, 2014b) then became an extension of Clawpack for geophysical flows, which solves the nonlinear shallow water equations (NSWE), a depth-averaged system of PDEs, by implementing high-resolution finite volume methods. The FV methods are based on dividing the computational domain into rectangular grid cells and storing cell averages of mass and momentum in each of the grid cells. The values are then updated in each time step by means of a high-resolution Godunov-type scheme (LeVeque, 2002), based on solving the Riemann problems at the interfaces of neighboring cells and applying nonlinear limiters to avoid non-physical oscillations (Arcos and LeVeque, 2015). These numerical methods are second order accurate in smooth regions of the flow but still can robustly handle strong shock waves and other discontinuous solutions.

The GeoClaw code presents the advantage of being capable of applying block-structured adaptive mesh refinement in time and space (George and LeVeque, 2006; LeVeque and George, 2007), by employing finer grid resolutions in regions of interest. Cells are flagged for refinement according to pre-established refinement criteria and multiple levels of patches can be used until a certain level of refinement is reached. Accordingly, the time step on the refined patches is reduced, such that the stability of the finite volume scheme is preserved.

3.2.2 Governing physics, numerical methods and adaptive mesh refinement

The governing model for the propagation of tsunami waves is based on the shallow water equations (SWE). The most general form of the SWE, which is a nonlinear system of hyperbolic conservation laws for depth and momentum, is solved in LeVeque et al. (2011), as they use shock-capturing methods that can converge to discontinuous weak solutions. The equations are presented in Chapter 2, expressions (2.52), (2.53), (2.54) in Cartesian coordinates and expressions (2.56), (2.57) and (2.58) in spherical coordinates.

For local scale problems, the GeoClaw equations can be set in Cartesian coordinates. For tsunami global scale modelling, as in the case of transoceanic propagation, latitude and longitude, i.e. geographical coordinates, are used. According to Shuto et al. (1990) (in Kirby et al. 2013), the sphericity and Coriolis effects are relevant for tsunami modelling in global scale distances and in fact the standard NSWE tsunami models typically contemplate these effects. In contrary, LeVeque et al. (2011) stated that, although the Coriolis terms are quite simple to include, the tests that LeVeque and co-authors have performed indicated that the terms are neglectable. This statement is also in agreement with Kowalik et al. (2005). For the reasons stated previously, the Coriolis terms f were not included in the GeoClaw simulations presented in this thesis. For simulations in the coastal vicinities, the drag term can be included in the momentum equation.

The description of the algorithms used in GeoClaw can be found in LeVeque (2002) and LeVeque et al. (2011). In Clawpack, a class of high-resolution finite volume methods is implemented, and each grid cell is viewed as a volume over which cell averages of the solution variables q are computed (Berger et al. 2011). Following Berger et al. (2011)'s explanation, "logically rectangular grids are used, where Q_{ij}^n denotes the cell average in cell (i, j) at time t_n. Cell averages are updated at each time step, by waves propagating into the grid cell from each cell edge. In Figure 3.1 (a) it is represented the propagation of a piecewise constant wave into the *i*th cell (designated as the increment wave, by LeVeque 1996); in (b) we can see the propagation of a piecewise linear

wave and in (c) the correction wave. The wave shown in (b) can be decomposed into the increment wave and the correction wave. In Figure 3.2 (a) the wave propagation interpretation of the upwind method with fluxes (equation 3.2 in LeVeque 1996) is represented and in (b) the wave propagation for the modified upwind method with fluxes corrected by equations (3.3) and (3.4) in LeVeque (1996). In (c) there is a representation of the new cell value, which can be equivalently computed as the weighted average of four cell values, overlapped by the shaded region. In Figure 3.3 it is represented part of the extended grid for imposing the boundary conditions, in which the heavy line is the physical boundary and two additional rows of cells are added in each direction. These are Godunov-type methods, in which the waves are computed by solving a "Riemann problem" at each cell edge. The Riemann problem is an initial value problem (IVP), that uses the SWE with piecewise constant data determined by the cell averages of the dependent variables and topography on each side of the interface. Godunov-type methods (Figure 3.4) provide a robust approach to solving problems with discontinuous solutions, particularly from shock waves that generally arise in the solution to nonlinear hyperbolic equations. In the SWE, shocks are "hydraulic jumps" or "bores", as often arise in practical flow problems. In Figure 3.4 there is a representation of waves, interface values, and flux differences for Godunov's method in a 1D grid with cell average q_i^n in the grid cell $[x_i, x_{i+1}]$ at time t_n. LeVeque (1997) explains that "the Godunov's method is obtained by constructing a solution over the time step as in the Figure. With piecewise constant (the upwind method) initial data Riemann problems can be solved at each interface and piece these together to get the global solution for a sufficiently small time step. Averaging this solution over the *i*th grid cell at time t_{n+1} gives the new cell average q_i^{n+1}."

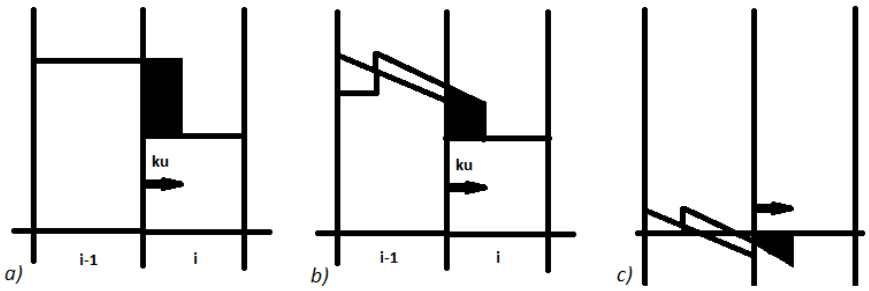

Figure 3.1: Propagation of a piecewise constant wave and the correction wave.

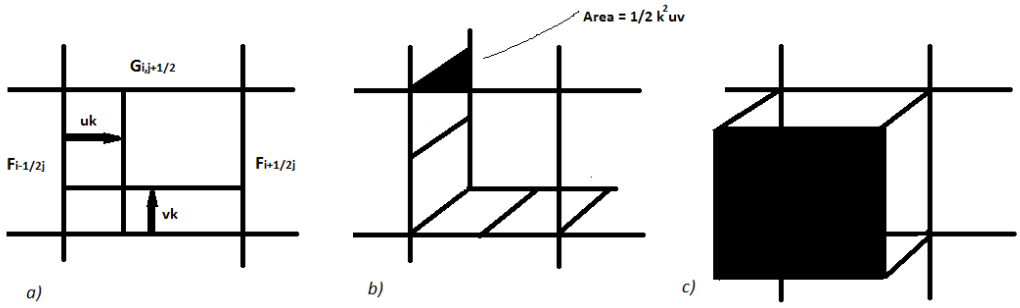

Figure 3.2: Wave propagation interpretation of the upwind method with fluxes and corrected version.

The Riemann problem defined at each cell interface allows for shock waves in each Riemann solution (Figure 3.5) and "approximate Riemann solvers" are used, that rapidly produce robust solutions as a building block for the numerical method. Correction terms are also incorporated to guarantee second-order accuracy in smooth regions of the fluid flow. In Figure 3.5 (adapted from

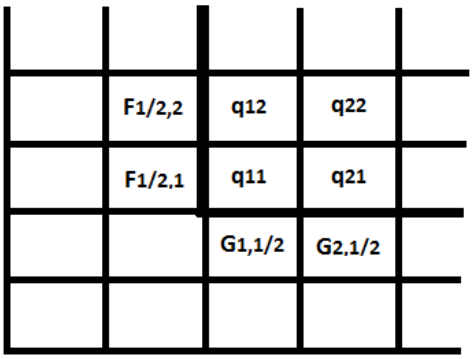

Figure 3.3: Portion of the extended grid used for imposing boundary conditions.

Figure 1 from LeVeque 2002), the structure of the all-shock Riemann solution for the 1D elastic wave equation for compressional waves is represented. The goal of LeVeque (2002) was to apply the high-resolution wave-propagation algorithms in LeVeque (1997) to the elasticity equations and to Clawpack (Clawpack Development Team 2014a), presented in the paper.

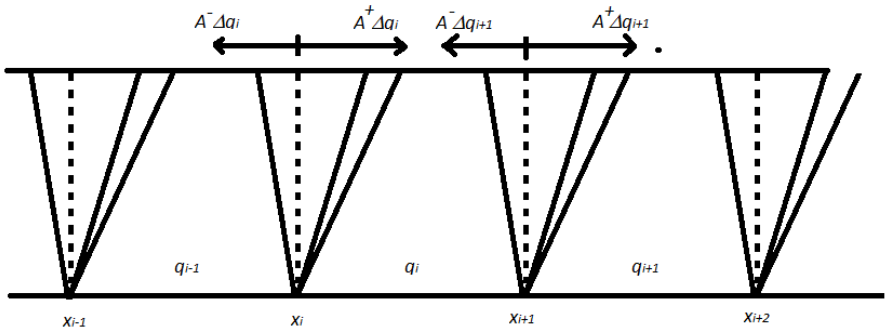

Figure 3.4: Waves, interface values, and flux differences for Godunov's method in a 1D grid with cell average q_i^n in the grid cell $[x_i, x_{i+1}]$ at time t_n.

GeoClaw employs a variant of the f-wave formulation—as described in George (2008)—, allowing the incorporation of the topography source terms directly into the Riemann problem. The f-wave formulation of the wave-propagation algorithms was originally presented for the SWE in Bale et al. (2003). Extended discussion and literature references on this topic can be found in Chapter 3 of Berger et al. (2011).

The capability of performing mesh refinement during the numerical simulations is contemplated in GeoClaw. The mesh refinement technique (Figure 3.6) is done in patches, to cover several orders of magnitude between the spatial scales of geophysical problems. From the ocean propagation to the coastal scales, multiple levels of patches have to be used to reach a satisfactory fine resolution (to the order of the tens of metres). The time step is chosen so that the stability of the explicit finite volume method is maintained, which in general requires refining in time by the same factor as in space, to keep the Courant number with the same value. The Courant number is a dimensionless number that expresses the Courant-Friedrichs-Levy (CFL) convergence condition. The CFL condition is necessary to assure the numerical convergence of the partial differential equations (PDE) systems (in general, hyperbolic PDE). In Figure 3.6 (a) there is a representation of a coarse grid for the one-dimensional example, shown in space-time, where values of q and

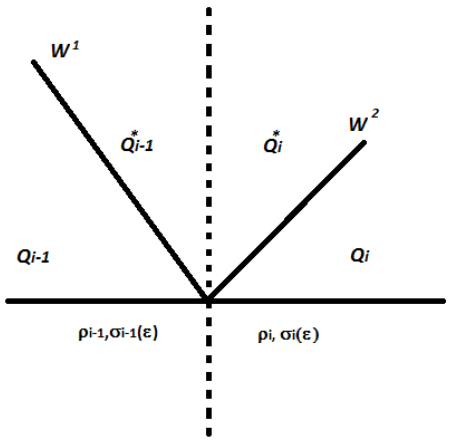

Figure 3.5: Structure of the all-shock Riemann solution for the 1D elastic wave equation for compressional waves.

fluxes F are indicated. In Figure 3.6 (b) it is shown a fine grid that is overlaid for and the grid interface, in which values of ^{q} on the fine grid are indicated. In (c) the flux values ^{F} needed on the fine grid are shown, where the ghost cells $m + 1$ and $q^m + 2$ are also indicated. As LeVeque (2002) explained, the computations are always performed on some finite set of grid cells covering a bounded domain and in the first and last cells the required neighboring information is not accessible. Instead, there will be some set of physically boundary conditions that must be used in updating these cell values. In general, the easiest solution is to extend the computational domain to include a few additional cells on either end, called ghost cells, whose values are set at the beginning of each time step in some manner that depends on the boundary conditions and perhaps the interior solution. The values of the ghost cells provide the neighboring-cell values needed in updating the cells near the physical domain. It is important to notice that these values are needed to compute the fine grid fluxes at the grid interface. The development of the adaptive mesh refinement technique is described in a series of papers by Marsha Berger, Joseph Oliger and Philip Colella (Berger and Colella 1989; Berger and Oliger 1984), that developed an algorithm for the dynamic griding. It is a dynamic programming technique, which allows the adaption of computational numerical precision to the specific requirements of a computation problem: specific areas of interest that need added precision and resolution are tagged to be refined, leaving other regions at lower levels of precision and resolution. This technique is of broad use in several scientific areas, with increased computational and storage savings of a dynamic griding scheme when compared to a static grid. Detailed description of the adaptive mesh refinement (AMR) technique in GeoClaw can be found in Berger and LeVeque (1998) (and subsequent papers) and in LeVeque et al. (2011).

For the tsunami modelling, the GeoClaw code also allows for the anisotropic refinement in time. This means that the factor of the refinement in time does not have to be equal to the factor of the refinement in space (e.g., the time step from one level to the next one can be done using different refinement factors). To perform the grid refinement, cells where the resolution is insufficient are flagged; these flagged cells are then clustered into refinement patches. Flagging can be done by two methods: firstly, with an error estimate that examines the gradients of the solution—Richardson extrapolation—, which will detect the location of the largest waves; secondly, by flagging cells where the surface elevation is perturbed from the sea level above a specified level, in the case of tsunami applications. It is also possible to specify rectangular shaped regions, where a certain level of resolution is required. Features in the solution which need refinement will move after few time steps, therefore the grid patches will also "move". This means that new grid patches

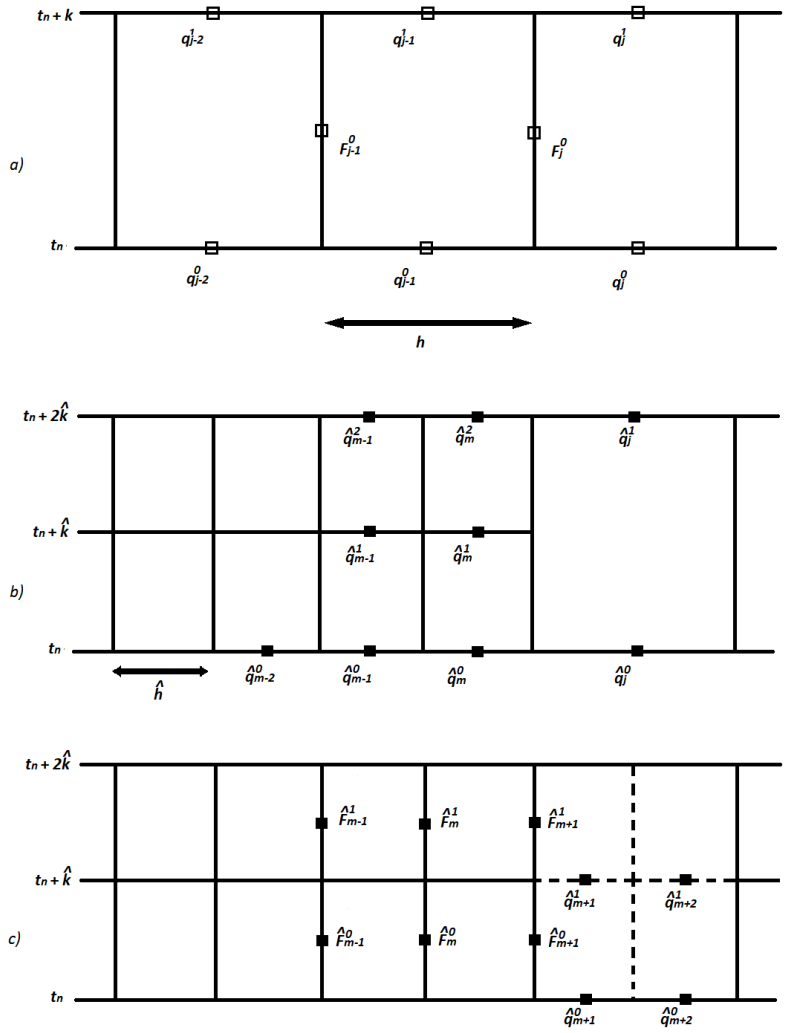

Figure 3.6: Coarse grid and fine grid for the one-dimensional example, shown in space-time and indication of the values of q and fluxes F.

are created, at discrete time, and its solution is interpolated from the finest previously existing grids, which are then removed (Berger et al. 2011). More details and further explanations can be found in Berger et al. (2011), from where the previous descriptions have been taken.

Additional descriptions considering GeoClaw can be found in Appendix A.1.

3.3 FUNWAVE-TVD

3.3.1 Introduction

In this thesis, FUNWAVE-TVD was chosen to model the propagation and transformation of tsunami events. The numerical schemes of the model are demanding when compared with the commonly used SWE models for tsunami modelling. FUNWAVE-TVD contemplates wave propagation and transformation, with a robust performance in the modelling of surf zones and retrieval of inundation extent mapping, with run-up, run-in and flow depth of nearshore coastal zones.

The fully nonlinear Boussinesq wave model FUNWAVE was initially developed by Kirby et al. (1998) for nearshore water wave propagation (Kirby 2003; Wei et al. 1995). Originally, it used an unstaggered finite difference formulation for space and a fourth-order Adams-Bashforth-Moulton (ABM) scheme for time (Wei and Kirby 1995), applied to the fully nonlinear model equations of Wei et al. (1995). A novel formulation for FUNWAVE was developed to solve weak instabilities to high wavenumbers near the grid Nyquist limit and overall grid based noise generation from several sources (Kirby et al. 2013). The novel model FUNWAVE-TVD is a fully nonlinear, phase-resolving, time stepping Boussinesq model, following the work of Chen (2006), extended to include the moving reference elevation, as in Kennedy et al. (2000). For the spatial discretisation, an hybrid finite volume–finite difference method is applied. Adaptive time stepping based on a third-order Strong Stability-Preserving (SPP) Runge-Kutta method was used. This upgraded version of FUNWAVE is capable of modelling tsunami waves and is formulated in both Cartesian and spherical coordinates. The Cartesian version for the description of the nearshore processes is documented in Shi et al. (2012b). The spherical version, suitable for the global scale modelling, is described in Kirby et al. (2013). Several improvements have been introduced from version to version: a more complete set of fully nonlinear Boussinesq equations; MUSCLE-TVD solver with finite volume scheme, together with adaptive Runge-Kutta time stepping; shock-capturing wave breaking scheme; code parallelization; wetting-drying scheme for shoreline movement modelling.

FUNWAVE-TVD has been used to model several tsunami events (as the 2011 Tohoku earthquake and tsunami, Grilli et al. 2013) and hypothetical scenarios of tsunami propagation along the Atlantic ocean and inundation along the coasts (Grilli et al. 2015), as well as tsunamis of volcanic origin (Grilli and Grilli 2013). It has also been widely used to model tsunamis triggered by submarine mass failure scenarios (Schnyder et al. 2016). It is important to notice that the generation of the tsunami triggered phenomena has to be done outside FUNWAVE-TVD, as the code has no internal feature to deal with the tsunami generation stage. This information can be introduced in the code through the files of surface elevation η and velocity, u and v, that describe the tsunami propagation after the tsunami generation stage.

3.3.2 Governing physics and numerical methods

The description of the model equations, in both Cartesian and spherical (latitude–longitude) coordinates, and numerical schemes implemented is performed (Shi et al. 2012c). The description of the Cartesian version can be found in Tehranirad et al. (2011), Shi et al. (2012c) and Shi et al. (2012b), while the description of the spherical-polar version of the code can be found in Shi et al. (2012a) and Kirby et al. (2013).

The Boussinesq equations were presented in Chapter 3, in Cartesian coordinates in expressions (2.59), (2.60) and (2.61) and in spherical coordinates in expressions (2.63), (2.64) and (2.65).

3.3.3 Numerical schemes

3.3.3.1 Spatial discretisation and time stepping

Spatial discretisation is performed using a combined finite volume and finite difference technique. For the flux terms and the first-order derivative terms, a high-order MUSCL–TVD scheme is implemented. The high-order MUSCL–TVD scheme can be written in compact form, including different orders of accuracy from the second- to the fourth-order, according to Erduran et al. (2005), who modified Yamamoto et al. (1998) fourth-order approach. For the detailed explanations and expressions please refer to Shi et al. (2012a). Higher derivative terms were discretised using a central difference scheme at the cell centroids, as in Wei et al. (1995). No discretisation of the dispersion terms at the cell interfaces is needed. The Surface Gradient Method (SGM), as in Zhou

et al. (2001), was used to eliminate unphysical oscillations.

For the time stepping, Shi et al. (2012a) adopted the third-order Strong Stability-Preserving (SPP) Runge-Kutta scheme. Due to the use of this scheme, the time stepping has to be calculated like this:

$$\begin{aligned}
\boldsymbol{\Psi}^{(1)} &= \boldsymbol{\Psi}^{n} + \Delta t\Big(-\nabla\cdot\boldsymbol{\Theta}(\boldsymbol{\Psi}^{n}) + \mathbf{S}^{(1)}\Big),\\
\boldsymbol{\Psi}^{(2)} &= \frac{3}{4}\boldsymbol{\Psi}^{n} + \frac{1}{4}\left[\boldsymbol{\Psi}^{(1)} + \Delta t\left(-\nabla\cdot\boldsymbol{\Theta}(\boldsymbol{\Psi}^{(1)}) + \mathbf{S}^{(2)}\right)\right],\\
\boldsymbol{\Psi}^{n+1} &= \frac{1}{3}\boldsymbol{\Psi}^{n} + \frac{2}{3}\left[\boldsymbol{\Psi}^{(2)} + \Delta t\left(-\nabla\cdot\boldsymbol{\Theta}(\boldsymbol{\Psi}^{(2)}) + \mathbf{S}^{n+1}\right)\right],
\end{aligned} \tag{3.1}$$

where $\boldsymbol{\Psi}^{n}$ denotes $\boldsymbol{\Psi}$ at time level n and $\boldsymbol{\Psi}^{(1)}$ and $\boldsymbol{\Psi}^{(2)}$ are values at intermediate stages in the Runge-Kutta integration. As $\boldsymbol{\Psi}$ is obtained at each intermediate step, the velocity (u, v) can be solved by a system of tridiagonal matrix equations, formed by expression (22) of Shi et al. (2012a). $\mathbf{S}$ needs to be updated using (u, v, η) at the corresponding time step and an iteration is needed to achieve convergence. An adaptive time step in chosen in accordance with the Courant-Friedrichs-Levy (CFL) criterion:

$$\Delta t = \mathrm{Cr}_{\min}\left(\min\frac{\Delta x}{|u_{i,j}| + \sqrt{g(h_{i,j}+\eta_{i,j})}}, \min\frac{\Delta y}{|v_{i,j}| + \sqrt{g(h_{i,j}+\eta_{i,j})}}\right), \tag{3.2}$$

where Cr is the Courant number.

3.3.3.2 Wave breaking and wetting-drying schemes for shallow water

The model implementation also includes the wave breaking and the wetting-drying schemes for shallow water, as described in Shi et al. (2012a). The wave breaking follows the approach by Tonelli and Petti (2009), who interestingly presented a numerical code for solving the extended Boussinesq equations with an hybrid scheme, which combined finite volume and finite differences methods. In their work, they switched from Boussinesq equations to NSWE, according to a pre-established threshold for the Froude number for a bore or a spilling breaker (Tonelli and Petti 2009). This is performed in FUNWAVE-TVD.

For the wetting-drying scheme a moving boundary is modelled. The normal flux $\mathbf{n}\cdot\mathbf{M}$ at the cell interface of a dry cell is set to zero. A mirror boundary condition is applied to the fourth-order MUSCL–TVD scheme and discretisation of dispersive terms in (ψ_x, ψ_y) at dry cells. It may be noted that the wave speeds of the Riemann solver, following expressions (37) and (38) in Shi et al. 2012a are

$$c_L = \min\Big(\mathbf{V}^{L}\cdot\mathbf{n} - \sqrt{g(h+\eta)^{L}}, u_s - \sqrt{\varphi_s}\Big), \tag{3.3}$$

$$c_R = \min\Big(\mathbf{V}^{R}\cdot\mathbf{n} + \sqrt{g(h+\eta)^{R}}, u_s + \sqrt{\varphi_s}\Big), \tag{3.4}$$

in which u_s and φ_s are estimated as

$$u_s = \frac{1}{2}\Big(\mathbf{V}^{L} + \mathbf{V}^{R}\Big)\cdot\mathbf{n} + \sqrt{g(\eta+h)^{L}} - \sqrt{g(\eta+h)^{R}}, \tag{3.5}$$

$$\sqrt{\varphi_s} = \frac{\sqrt{g(\eta+h)^{L}} + \sqrt{g(\eta+h)^{R}}}{2} + \frac{(\mathbf{V}^{L} - \mathbf{V}^{R})\cdot\mathbf{n}}{4} \tag{3.6}$$

and $\mathbf{n}$ is the normalized side vector for a cell face, for a dry cell are modified as:

$$\begin{aligned} c_L &= \mathbf{V}^L \cdot \mathbf{n} - \sqrt{g(h+\eta)^L}, \\ c_R &= \mathbf{V}^L \cdot \mathbf{n} + 2\sqrt{g(h+\eta)^L}, \end{aligned} \tag{3.7}$$

for the right dry cell and

$$\begin{aligned} c_L &= \mathbf{V}^R \cdot \mathbf{n} - \sqrt{g(h+\eta)^R}, \\ c_R &= \mathbf{V}^R \cdot \mathbf{n} + 2\sqrt{g(h+\eta)^R}, \end{aligned} \tag{3.8}$$

for the left dry cell.

3.3.3.3 Boundary conditions and wind effect

Various types of boundary conditions are implemented, as the wall boundary condition, the absorbing boundary condition (Kirby et al. 1998) and the periodic boundary condition (Chen et al. 2003). Wave-makers are also implemented, as internal wave-makers for regular and irregular waves (Wei and Kirby 1995). Wind effects are also modeled using the wind stress forcing proposed by Chen et al. (2004) as:

$$\mathbf{R}_w = \frac{\rho_a}{\rho} C_{dw} |\mathbf{U}_{10} - \mathbf{C}| (\mathbf{U}_{10} - \mathbf{C}), \tag{3.9}$$

where ρ_a and ρ represent air density and water density respectively, C_{dw} is the wind drag coefficient, $\mathbf{U}_{10}$ is the wind velocity vector, at a reference height of 10 m above the sea surface, and $\mathbf{C}$ is the wave celerity vector.

3.3.3.4 Numerical instabilities

In FUNWAVE-TVD Version 3.0, Shi et al. (2016) aimed with success at improving the numerical stability for large-scale and long time simulations. Nevertheless, they point out some aspects to be aware of when performing simulations with the code (Shi et al., 2016): avoiding large bathymetric slopes, as rapid changes in the bathymetry may cause numerical instabilities caused by $\nabla h > 1.0$ in the source term; limiting huge unrealistic velocities from occurring in extremely shallow waters, specifically at a wetting-drying boundary; adjust carefully the minimum depth for the wetting-drying threshold, as a small value may lead to numerical noises; use the default Courant number suggested of 0.5, as small values may cause instabilities; select preferably a lower-order spatial scheme (considering that second order is the lowest-order spatial scheme possible), as numerical instabilities increase with increasing higher-order numerical schemes.

3.3.3.5 The weakly nonlinear Boussinesq equations in spherical polar coordinates

Kirby et al. (2013) derived weakly nonlinear and dispersive model equations for the propagation of surface gravity waves in a shallow, homogeneous ocean of variable depth, on the surface of a rotating sphere. In the model equations (which follow exactly Shi et al. 2012a), dimensional forms are preserved, as well as references to the apparent $\mathcal{O}\left(\mu^2, \delta\right)$ ordering of terms with the implicit assumption that $\delta/\mu^2 = \mathcal{O}(1)$ (Shi et al. 2012a). Parameter μ characterizes the ratio between the water depth and wavelength (assumed to be small in classical Boussinesq theory) and parameter

δ, given by the ratio between the wave amplitude and the water depth, is termed the shallow water nonlinearity parameter.

Kirby et al. (2013) extensively described the model equations in spherical polar coordinates. The numerical implementation is based on the dimensional forms of the weakly nonlinear governing equations, augmented by bottom friction related terms. Direct generation of waves caused by bottom motion was neglected.

3.3.4 Tsunami modelling and grid nesting

FUNWAVE-TVD code does not have any internal feature to generate the initial sea level displacement, resultant from events such as earthquakes and landslides. Nevertheless, it is possible to perform the numerical modeling of a tsunami event with FUNWAVE-TVD by feeding that information into the program. To simulate an event such as a tsunami generated from an earthquake, the bottom deformation can be retrieved from another program—such as GeoClaw, NHWAVE, etc—or directly from the Okada model (Okada 1985), to generate this surface elevation data for FUNWAVE-TVD as an initial condition *. The initial bottom deformation originated by the earthquake triggers an equal rise of the water surface, with null initial velocity. Here we used GeoClaw to retrieve the free surface elevation η and velocities (u, v) of a tsunami generated from an earthquake, in its early propagation stage.

Afterwards, to start a FUNWAVE-TVD tsunami simulation, the user should use the initial uvz deformation facility within the code. This initial bottom deformation is provided, in the form of ASCII files, by means of three individual files, for an equal specific time instant: the free surface elevation η file and the velocities u and v files.

Since version 2.0, it is possible to perform grid nesting within the numerical simulations. Version 3.0 does not allow multilevel nesting. If the user desires to nest multiple grids, this has to be done one at a time, according to the intended nesting. The nesting capability allows the passage of the free surface elevation η and the velocities u and v, calculated in a large computational domain, to a nested small domain (grid) contained in the larger grid, through ghost cells at the nesting boundaries. Through several pre-established virtual gauges which are coincident in both grids (yet located at the inner grid boundaries), the data is passed between both grids.The structure of a one-way nesting case is represented in Figure A.5. Additional descriptions can be found in Appendix A.2.

3.4 Computational Fluid Dynamics (CFD) Code

3.4.1 Introduction

To model nearshore processes in two- and three-dimensional domains and to determine the properties and characteristics of tsunami interaction with coastal structures and surrounding areas, we used the open access numerical code OpenFOAM (OpenCFD Limited, 2019) and the olaFlow toolbox solver (Higuera, 2019).

OpenFOAM (Open source Field Operation And Manipulation) is a free and open source computational fluid dynamics (CFD) package code, released and maintained by OpenCFD since 2004, under the GNU General Public License. It is composed by several libraries, designated as applications, written in C++, an object-oriented programming language. These applications are divided into the so-called solvers—which are conceived to solve a specific kind of problem—and the utilities—which pre- and post-process the data. The package can deal with several types of fluid

*In the case of a dynamic bottom deformation, for a sequence of time steps (e.g. landslide), GeoClaw can be used as the code is prepared to model dynamic fault motions.

dynamics problems, allowing also the creation of new solvers for the resolution of specific problems and extension of the existing functionalities. It has a wide applicability in several distinct engineering research areas, such as automotive, biomedical, chemical, polymeric, coastal, among many others.

OpenFOAM uses the finite volume method to solve computational fluid dynamics problems and includes several approaches to tackle turbulence, such as Reynolds-Averaged Navier-Stokes (RANS): large scale turbulence models for compressible and incompressible fluids; Large Eddy Simulation (LES) method: isochoric and anisochoric LES turbulence models, LES deltas and LES filters; Detached Eddy Simulation (DES) method: hybrid method that combines RANS and LES approaches; Direct Numerical Simulation (DNS) method: Navier-Stokes (NS) equations solved without any turbulence model. The OpenFOAM package includes Lagrangian particle tracking, pre- and post-processing modules, dynamic meshes and parallel computing. It is very efficient as it can use all the available nodes to perform the parallel computing. In Mesquita (2013), a turbulence model, tailored for wave breaking modelling, was developed and integrated within OpenFOAM. Some recent publications with OpenFOAM include studies about wave-structure interaction (Higuera et al. 2018a), numerical wave tank (Windt et al. 2019), a sediment transport solver (Bonamy et al. 2017) and wave energy conversion (Deng et al. 2019).

The olaFlow solver package (Higuera, 2019) consists on a set of solvers for the simulation of wave dynamics, enabling the generation and absorption of waves at the boundaries and wave interaction with coastal structures. It descends from IHFOAM (Higuera et al., 2017), presented and validated in Higuera et al. (2013a,b, 2014a,b). It is very versatile, with high performance and improved two-phase flow through porous media (relevant for the modeling with structures) and includes a moving boundary-type wave generating mechanism, simulating a piston-like laboratory wave-maker.

The module features the dynamic mesh refinement and mesh motion for floating body simulation, as in OpenFOAM. olaFlow has been recently used to validate a novel methodology for breaking focused waves in CFD simulations (Stagonas et al., 2017). A recent study on swash flows with olaFlow was published in Higuera et al. (2018b).

In this research work, OpenFOAM and specially the olaFlow solver were used to model the interaction of the tsunami triggered waves with the coastal surroundings.

3.4.2 The olaFlow solver

The olaFlow solver (Higuera, 2019), included in OpenFOAM, was used in the framework of this project. It is based in `interFoam`, a solver adequate for the simulation of incompressible two-phase fluid flow with an interface. This means that it is suitable for the case of the incompressible flow of air and water, separated by a well defined interface: the free surface.

olaFlow solves the Volume Averaged Reynolds-Averaged Navier-Stokes (VARANS) equations for the two incompressible phases, applying the finite volume (FV) discretisation method for numerical integration, and the volume of fluid (VOF) method for phase definition.

As mentioned before, turbulence modelling in OpenFOAM can be performed by means of RANS, LES and DES approaches and several turbulence models are incorporated, such as the $\kappa-\varepsilon$ (Launder and Spalding 1974), the $\kappa-\omega$ SST (Menter 1994; Menter et al. 2003)—where SST stands for Menter's Shear Stress Transport—, RANS and Large Eddy Simulation (LES) [†]. The olaFlow solver is adequate to work with static meshes and it incorporates also the olaDyMFlow, suitable for dynamic meshes (with *DyM* standing for Dynamic Mesh). The existing boundary condition modules work equally for both solvers, together with the wave generation (with multiple wave theories available) and active wave absorption capabilities (Higuera, 2019).

[†] https://www.cfd-online.com/Wiki/Large_eddy_simulation_(LES)

The current solving algorithm applied in olaFlow is PIMPLE, which is a combination between the PISO (Jasak 1996; Kissling et al. 2010) and SIMPLE (Jasak 1996) algorithms. PISO stands for Pressure Implicit with Splitting of Operators and was the original solving algorithm within olaFlow; SIMPLE stands for Semi-Implicit Method for Pressure-Linked Equations. Higuera (2016) explains that the main structure of the PIMPLE algorithm is equal to that of the original PISO, allowing equation under-relaxation to ensure the convergence of all equations at each time step.

The continuous improvements to the olaFlow solver are documented periodically online in the website[‡].

The fundamental equations that describe mathematically the motion of a fluid flow are the Navier-Stokes equations. These and the RANS equations are presented in section 2.1.4.

3.4.3 Turbulence modelling

Turbulence is a characteristic of fluid flows, which often occurs in natural and mechanical systems. An accurate resolution of the turbulence problems requires very detailed meshes. For that reason, if not so relevant to the problem, the turbulence occurrence is neglected. When considered relevant, turbulence can be modelled at all scales or a parametrised model can be used.

There are many turbulence models and three common approaches are listed here. The first one is the Direct Numerical Simulation (DNS), which directly solves the Navier-Stokes equations, solving all the turbulence scales. This method is limited to low Reynolds number flows and small domains with simple geometries.

The second approach is the Large Eddy Simulation (LES). As the method separates the large-scale vortices and small-scale vortices—which are modelled via Sub-Grid Scale (SGS) turbulence models in the large-scale vortices—, the computational cost of the method increases for large domains with complex geometries.

The third approach to model turbulence is the Reynolds-Averaged Navier-Stokes (RANS), the most commonly used. The models based on Reynolds-Averaged Navier-Stokes equations result from a Reynolds decomposition of the governing equations in average and fluctuations fields. As all the turbulence scales are parametrised, the computational efforts are less than those required in the LES models.

The turbulence model used will be defined through the stress tensor $\mathbf{T}$ in equation (2.22). The olaFlow solver incorporates several turbulence models, such as the $\kappa - \varepsilon$, the $\kappa - \omega$ SST—where SST stands for Menter's Shear Stress Transport (Menter 1994; Menter et al. 2003)—, Large Eddy Simulation (LES). It includes libraries with modified versions of the $\kappa - \varepsilon$ and $\kappa - \omega$ turbulence models [‡]. The turbulence models (Devolder et al. 2017, 2018; Larsen and Fuhrman 2018) include the Multiphase $\kappa - \varepsilon$ model, the Multiphase $\kappa - \omega$ SST, the Buoyancy $k - \omega$ SST model and the Stable $\kappa - \omega$ SST model. Example of the turbulence model $\kappa - \omega$ SST coefficients, in log form from a simulation, can be found in Appendix A.3.3.1.

3.4.4 Free surface definition: the VOF method

The interface that separates two immiscible fluids, just like air and water, is designated as the free surface. The position of the free surface can be determined through the free surface boundary conditions, the kinematic and the dynamic conditions. Nowadays, there are several methods to determine the temporal evolution of the free surface, which can be divided in two distinct groups (Ferziger and Peric 2012): the surface methods or interface tracking methods—where the free surface is defined as a line composed by markers, and where the positions of the points are retrieved through piecewise polynomial interpolations—and the volume methods or interface

[‡] https://olaflow.github.io

capturing methods—, where the domain is marked with points without mass or by an indicatory function.

In OpenFOAM, the free surface is defined through a Volume Of Fluid (VOF) method, a volume or interface capturing method, originally proposed by Hirt and Nichols (1981). An equation describing the movement of the phases is necessary, therefore a transport equation of a scalar quantity α (also called phase function) is defined, where α is the fraction of volume (or quantity of water per unit of volume) occupied by a fluid (here defined as fluid 1) in the control volume (in each cell). When α is 1, the cell is occupied with water (fluid 1) and when α is 0 the cell has air, or another fluid if defined that way (fluid 2). Values of α between 0 and 1 indicate that the cell contains the interface. A symbolic representation of α can be:

$$\alpha = \frac{\text{volume of fluid 1}}{\text{volume of fluid 1 + volume of fluid 2}}.$$

As explained by Mesquita (2013), the main advantage of this method is that one can obtain the position of the free surface only by solving a single transport equation for a volume fraction α, given by:

$$\frac{\partial \alpha}{\partial t} + \nabla \cdot (\bar{\mathbf{u}}\alpha) = 0. \tag{3.10}$$

3.4.5 Wave generation, wave theories and wave absorption

In numerical modelling, the accuracy involved in the wave generation stage determines the quality of the output results and our evaluation of the outcome of the problem. In the literature there are several boundary conditions for the wave generation [§]. olaFlow wave generation boundary conditions include the active wave absorption and the emulation of both piston and flap laboratory wave-makers. It is possible to generate waves at the boundaries according to several wave theories (Figure 3.7, where H is the wave height and h is the water depth): Stokes I (Airy wave theory), Stokes II and Stokes V; cnoidal theory; streamfunction theory; Boussinesq solitary wave; irregular first and second order waves. It is also possible to perform a piston or flap wave-maker emulation, via time and displacement of the wave-maker (ts), via time and velocity of the wave-maker (tv), via time, displacement of the wave-maker and free surface elevation (txeta) and via time, velocity of the wave-maker and free surface elevation (tveta).

To emulate nature the most accurate way possible, wave absorption is used in laboratory experiences, to reduce the effect of the spurious reflected waves (generated by the physical domain boundaries) in the wave profile at the generation boundary. The same can be done in numerical modelling due to the computational domain influence. In olaFlow, the two-dimensions active absorption method is based in Schäffer and Klopman (2000). Following from the previously cited work, a quasi-three-dimensions absorption method, to absorb oblique waves, is presented (Higuera 2016). For three-dimensional cases, olaFlow has an original method applicable only to numerical models for three-dimensional absorption. Extended explanations about all the olaFlow absorption methods are presented in Higuera (2016).

[§] `https://openfoamwiki.net/index.php/Contrib/groovyBC` and Jacobsen et al. 2012.

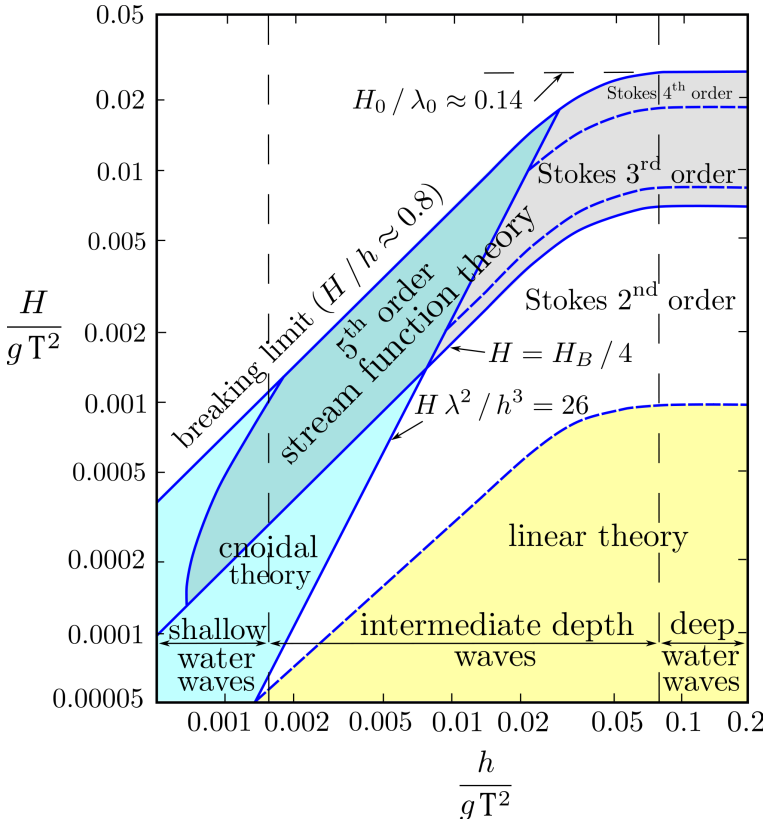

Figure 3.7: Range of applicability of the wave theories, according to Le Méhauté (1976) (adapted from Higuera 2016).

3.5 Applications

In the simulations performed for this thesis, the Coriolis forcing was not used. In principle, the Coriolis effect has reduced influence on the propagation of the tsunami, given that the source of the events studied are located close to the coast.

The quality of the numerical modelling results obtained in this section, applying each of the previously described numerical codes, is evaluated by means of the 3 metrics described next.

3.5.1 Metrics

The accuracy of the analytical, experimental and/or numerical wave profiles is measured using the most common metrics, over the first complete wave period: (1) the Pearson correlation coefficient, r, defined as

$$r = \frac{\mathrm{cov}(\eta^{\mathrm{TS}}, \eta^{\mathrm{wg1}})}{\sigma_{\eta^{\mathrm{TS}}} \cdot \sigma_{\eta^{\mathrm{wg1}}}}, \tag{3.11}$$

where $\mathrm{cov}(\cdot\,,\cdot)$ stands for the covariance function, $\sigma(\cdot)$ is the standard deviation, and η_{TS} and η_{wg1} are respectively the expected and the measured free surface elevations at wave gauge wg1 (the reference wave gauge); (2) the bias, given by

$$\mathrm{Bias} = \frac{1}{N} \sum_{i=1}^{N} \left(\eta_i^{\mathrm{wg1}} - \eta_i^{\mathrm{TS}} \right), \tag{3.12}$$

where N is the number of observations within the range t/T = 0.5–1.5; (3) the root-mean-square error as:

$$\mathrm{RMSE} = \sqrt{\frac{1}{N}\sum_{i=1}^{N}\left(\eta_i^{\mathrm{wg1}} - \eta_i^{\mathrm{TS}}\right)^2}. \tag{3.13}$$

3.5.2 Monai Valley Benchmark: Tsunami run-up onto a complex 3D beach (Liu et al. 2008)

The validation of GeoClaw and FUNWAVE-TVD is performed with a classical laboratory benchmark from *The third international workshop on long wave runup models* [¶] , focused on tsunami run-up onto a complex three-dimensional beach (Appendix A.1.2.1). As González et al. (2011) noted, this benchmark problem appears to be a good test for tsunami models, has been widely used and many models have been shown to give results that agree quite well with the laboratory measurements. Also, as pointed out by González et al. (2011), is it well documented, the data is fairly well specified and the wave tank geometry scales up to a reasonable physical tsunami problem, thus it appears to agree very well with the actual tsunami it was designed to model. As documented in González et al. (2011), some benchmark tests show that the quality of the bathymetry/topography computational grids and the accurate specification of the computational domain is essential.

The Monai Valley Benchmark is based on the 1993 tsunami that struck the Okushiri Island, in Japan. The computational solutions from the code are compared with data for the water surface elevations collected during the laboratory experiment. The 1/400 scale model that was built for the purpose is approximated to the region of Monai, in Japan, which suffered severe inundation from the 1993 Okushiri tsunami (Matsuyama and Tanaka, 2001). The laboratory experiments were performed in a tank with 200 m length, 3.4 m width and 6 m depth. The benchmark files of this case study used for the validation of GeoClaw version 5.2.2. are available at `https://github.com/vanialima/BP07`.

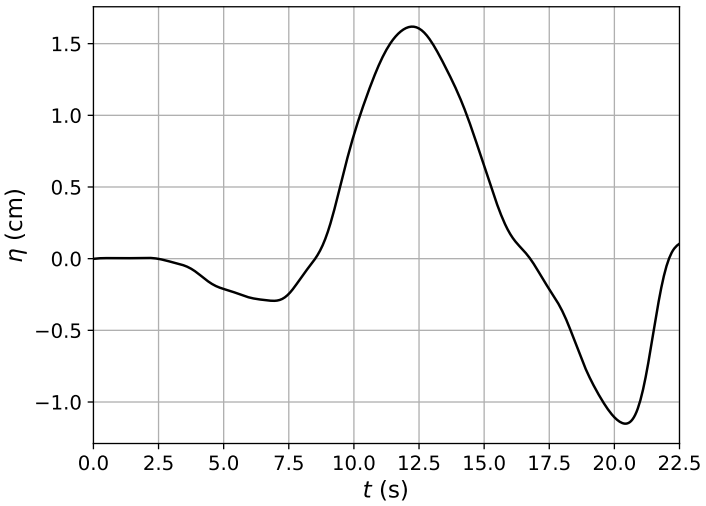

Figure 3.8: Profile of the incident N-wave of the Monai Valley study case.

[¶] http://isec.nacse.org/workshop/2004_cornell/background.html

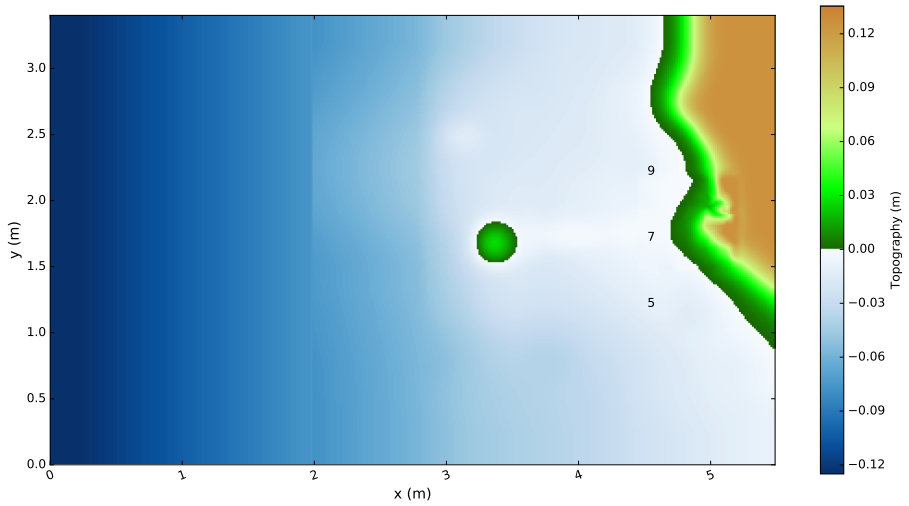

Figure 3.9: Topography setting of the Monai Valley study case and wave gauges 5, 7 and 9.

The given input wave profile of the incident wave used in the experimental case is plotted in Figure 3.8. The incident leading depression N-wave from offshore is at water depth h = 0.135 m. This N-wave profile was specified as boundary condition at the left boundary of the domain. Reflective walls were used at $y = 0$ m, $y = 3.5$ m and $x = 5.448$ m. The incoming wave data for the benchmark problem was provided for a total time of 22.5 s. The topography of the experimental setting can be seen in Figure 3.9. The computational domain is 5.488 m $\times$ 3.402 m, with 0.014 m grid sizes. The time step recommended and used is 0.05 s. The bathymetric setting of the Monai Valley experiment is pictured in Figure A.2.

Table 3.1: Location of the wave gauges for the Monai Valley experiment.

wave gauge	x (m)	y (m)
5	4.521	1.196
7	4.521	1.696
9	4.521	2.196

Computations of this benchmark were performed with GeoClaw, in Cartesian coordinates, and with FUNWAVE-TVD, in spherical coordinates. For FUNWAVE-TVD, the simulation was performed on a $\lambda_L = 1/4$ geometrical scale and $\lambda_T = 1/2$ temporal scale. The results from FUNWAVE-TVD were rescaled to $\lambda_L = 1/400$ and $\lambda_T = 1/20$, for visualization and comparison with other authors. The code FUNWAVE-TVD does not accept direct input wave profile in the form of a time series of water surface elevations, as provided for this benchmark. For this reason, the given time series of η is converted to an ASCII file with three columns with the wave components period, amplitude and phase. This is achieved through a MATLAB script provided with the FUNWAVE-TVD package. The resultant file is then prepared to be read by the code. In the conversion of the time series of η to the wave components, a sample frequency of 0.5 Hz was used, with 0.001 low cut-off frequency and 0.03333 high cut-off frequency. A comparison between the experimental N-wave profile and the computed waves retrieved from 5 virtual wave gauges located at the left boundary of the domain, at y = 1.701 m, starting at x = 0, evenly spaced and covering the generation zone, is presented in Figure 3.10.

Figure 3.11 shows the comparison between the experimental data for wave gauges 5, 7 and 9 (Table 3.1) respectively with results from GeoClaw. It was found that the second wave registered in all gauges is resultant from reflections at the beach and mountain, on the wall located on the

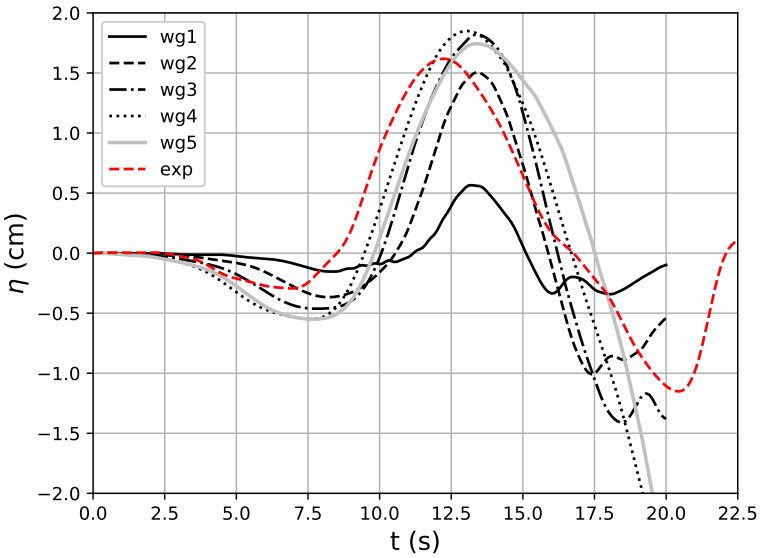

Figure 3.10: Comparison between the experimental N-wave time series (- -) and the wave profiles retrieved from 5 virtual gauges, covering the wave generation zone.

further end and also on the right side lateral wall ($y = 0$ m and $x = 5.488$ m), which can be observed in Figure 4 of LeVeque and George (2007). The results depend on the grid resolution applied.

The results of the simulation with FUNWAVE-TVD for the benchmark test of the Monai Valley case are also plotted in Figure 3.11. After the completion of the simulation, comparing the output wave profile results with the experimental data, for wave gauges 5, 7 and 9, we find that the results obtained for the first 25 sec of FUNWAVE-TVD's simulation are quite satisfactory.

The results from González et al. (2011) also, obtained with GeoClaw for a 423 $\times$ 243 grid, are presented in Figure 3.11. We see that the results are overall coincident with the results of our GeoClaw simulation. The slight differences observed could be related to the GeoClaw code versions used in each of the simulations.

Overall, the results obtained with both codes for this benchmark problem can be considered satisfactory. The computed metrics are presented in Table 3.2. Its analysis shows that a high linear correlation exists, with r close to or above 0.9, for both codes. The highest linear correlation values are obtained at wave gauges 7 and 9 for FUNWAVE-TVD code. At wave gauge 5, GeoClaw obtains a r of 0.886 and FUNWAVE-TVD obtains 0.874. Also bias is negative for both codes, though for FUNWAVE-TVD it is close to 0 and lower than what was obtained for GeoClaw. The root-mean-square error varies between 0.60 and 0.70 cm for GeoClaw and between 0.46 and 0.60 cm for FUNWAVE-TVD. The error metrics indicate that FUNWAVE-TVD produces better results than GeoClaw. Nevertheless, the dispersive model wave seems to lead to a smoother wave front when compared with the observations. The wave arrival time is similar for both codes.

In Figure 3.12, we can observe the first wave arriving to Okushiri island, simulation results for several time instants and the wave run-up over the area, which show good comparison with the video recorded for the laboratory experiment[‖]. The maximum run-up is observed around t = 16.67 s (Figure 3.12d), at x = 5.15 m and y = 1.85 m, corresponding to values between 0.06 and 0.09 m. This would correspond to run-up values between 24 and 36 m, which is in agreement with the experimental observations that the run-up would have reached 32 m.

[‖] http://isec.nacse.org/workshop/2004_cornell/data/benchmark2/overhead.avi

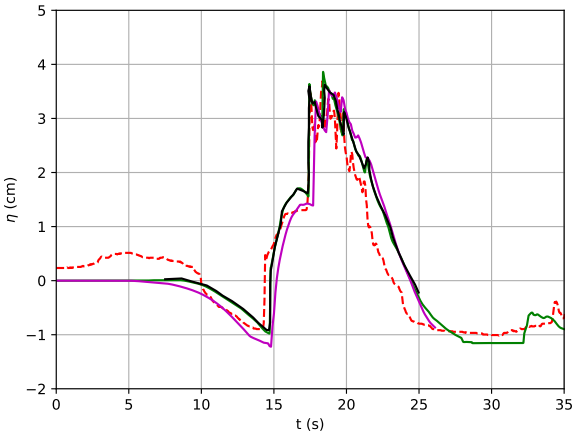

(a) wg5

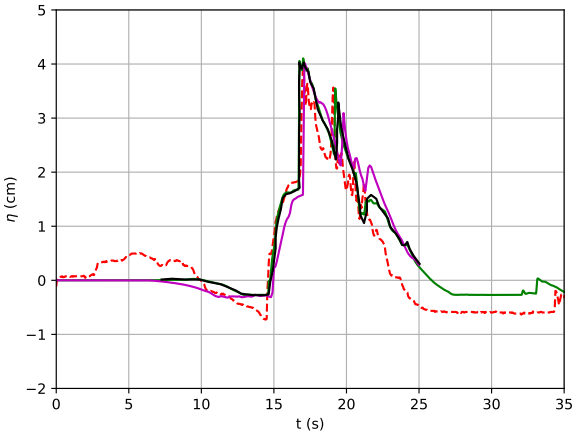

(b) wg7

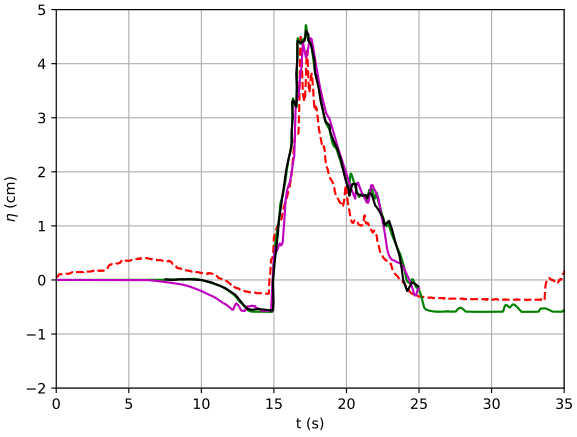

(c) wg9

Figure 3.11: Monai Valley: numerical simulation with GeoClaw (—) and with FUNWAVE-TVD (—), from González et al. (2011)(—) and experimental data (- -) recorded at wave gauges 5, 7 and 9.

Table 3.2: Error metrics for the Monai Valley study case.

Code	Wave gauge	r (—)	Bias (cm)	RMSE (cm)
GeoClaw	5	0.886	-0.1352	0.5906
	7	0.848	-0.1828	0.6377
	9	0.873	-0.1367	0.6852
FUNWAVE-TVD	5	0.874	0.0641	0.6043
	7	0.869	-0.0752	0.5663
	9	0.956	0.0099	0.4616

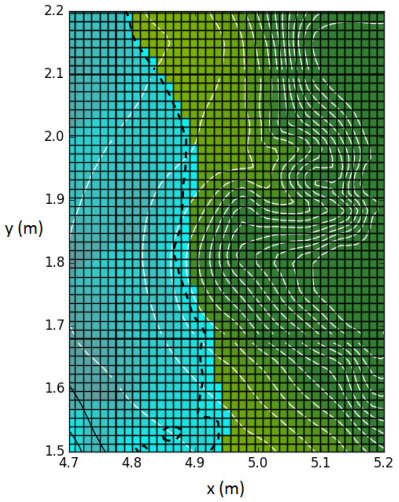

(a) t = 15.15 s

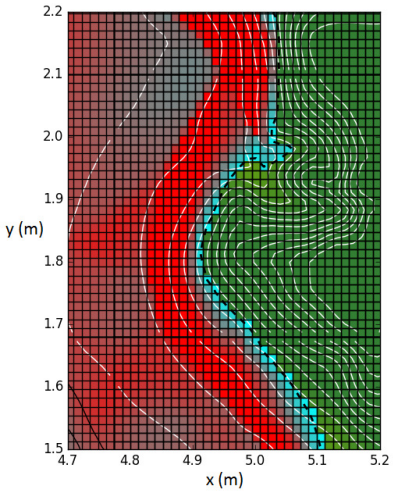

(b) t = 15.65 s

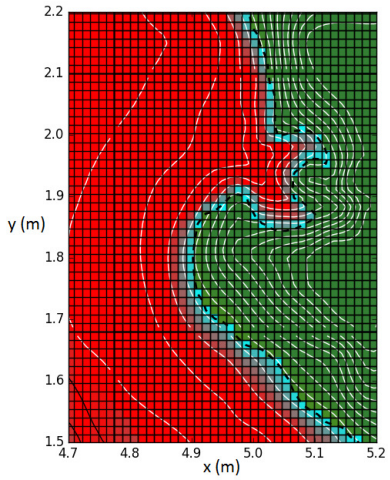

(c) t = 16.15 s

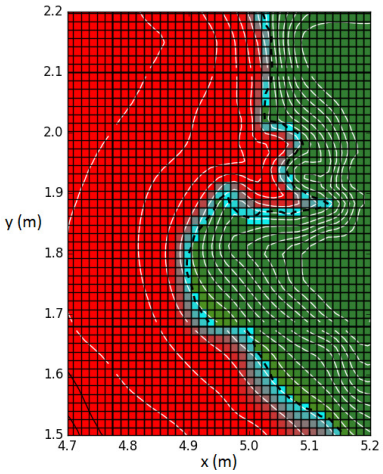

(d) t = 16.67 s

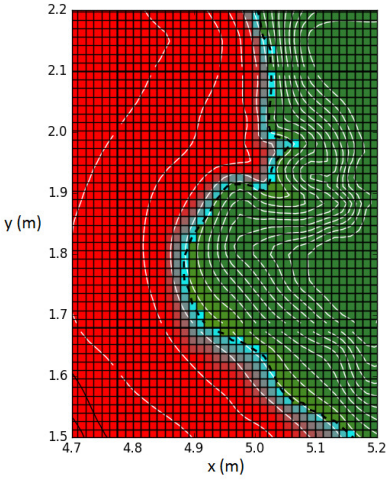

(e) t = 17.17 s

Figure 3.12: Monai Valley area: numerical results for GeoClaw for several time instants.

3.5.3 With GeoClaw

Benchmark tests and validation of GeoClaw has been performed by the authors of the code for versions of the code previous to version 5 (George 2006, LeVeque and George 2007, González et al. 2011). In this research work, GeoClaw version 5.2.2. was used and validated with the same established benchmarks. For that purpose, scripts available for code benchmarking (possibly written for version 4.6) were adapted and tested with GeoClaw version 5.2.2. Good results were obtained from the benchmark tests.

When relevant in the computations, the Manning coefficient n is taken as 0.025 s/$m^{1/3}$ (Te Chow 1959). The bathymetric grids used are referred to the mean sea level.

The objective of both tests is to show the performance of GeoClaw in the modeling of the generation and initial propagation of the generated tsunami, as well as the use of the adaptive mesh refinement of the model.

3.5.3.1 The Chile 2010 Earthquake

The magnitude $\mathrm{M_w}$ = 8.8 earthquake and tsunami offshore Maule, Chile, on the 27$^{\text{th}}$ February 2010 occurred at 6h34min11.5s UTC, with epicentre (35.826°S, 72.668°W). A very simple source model with a single fault plane and constant slip is used (available from an early inversion by the USGS – Clawpack Development Team 2014b) for the generation. The fault parameters used to simulate this event are shown in Table 3.3. A 361 × 361, 10 min ETOPO2 grid with dimensions 120°– 60°W and 60°– 0°S was used (Figure 3.13). The initial time step used was 0.2 s and the simulation had a total run time of 10 hours. Non-reflecting outflow boundary conditions are used at the domain boundaries.

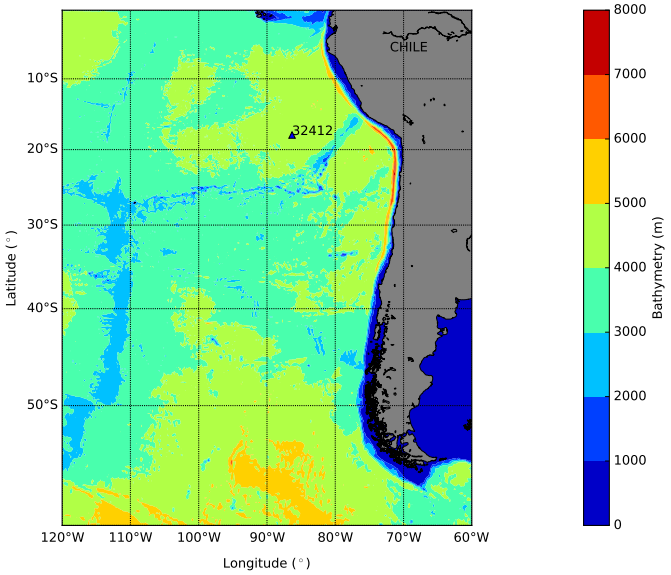

Figure 3.13: Bathymetric setting of Chile, with the location of studied DART 32412.

The initial deformation of the ocean sea bottom was determined from the elastic dislocation model in a homogeneous isotropic elastic half-space (Mansinha and Smylie 1971; Okada 1985). It is assumed that the static seabed displacement is instantaneous and translated towards the free surface as an initial condition, reproducing the elastic bottom deformation caused by the earthquake. It is assumed water incompressibility and the initial deformation of the ocean surface is used as the

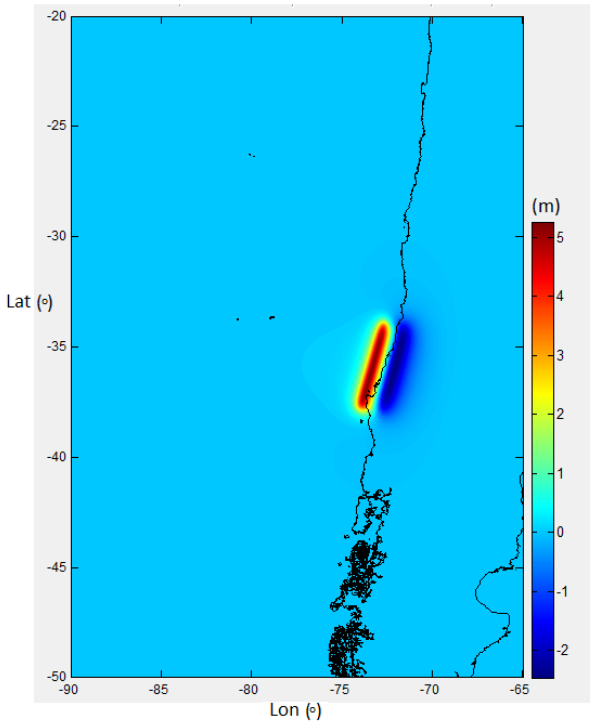

Figure 3.14: Initial deformation (in metres) of the Chile 2010 event.

initial condition of the propagation model, for the initial instant, and null velocity field. Through the maketopo.py script existent within the GeoClaw code, the seafloor deformation is generated using the Okada model (Okada 1985). The seafloor deformation of this event is represented in Figure 3.14. The focal mechanism, representing a shallow thrust fault, is plotted in Figure 3.15. Simulations were conducted for a total of 10 h with a time step of 0.2 s. The base resolution of the computational grid was 2°× 2°. Two simulations were carried out: a 3-level simulation with refinement factors of 4 (30 min × 30 min) and 3 (10 min × 10 min), so that the finest grid resolution matches the bathymetric resolution; a 4-level simulation with refinement factors of 4 (30 min × 30 min), 3 (10 min × 10 min), and 8 (1.25 min × 1.25 min), so that the finest grid resolution is 8 times finer than the bathymetric resolution. The uniform grid simulation was performed on a 361 × 361 grid, with 10 min grid resolution, which corresponded to the finest level of the 3-level simulation.

Table 3.3: Chile 2010 fault mechanism parameters, according to USGS.

Length (km)	Width (km)	Strike (°)	Dip (°)	Rake (°)	Slip (m)	Depth† (km)
450	100	16	14	104	15	35

†Top of the fault

At the time of the Maule 2010 event, there was only one operational Deep-ocean Assessment and Reporting of Tsunamis (DART) active in the area, namely DART 32412, located Southwest of Lima, Peru, which recorded this event. Thus, GeoClaw code was validated for Chile 2010 event using DART 32412 observation and comparing it with the results from the simulation. Using vast DART data, GeoClaw has been mainly used to validate other input fields rather than the surface elevation (Arcos and LeVeque 2015, MacInnes et al. 2013b, Sraj et al. 2014, Sraj et al.

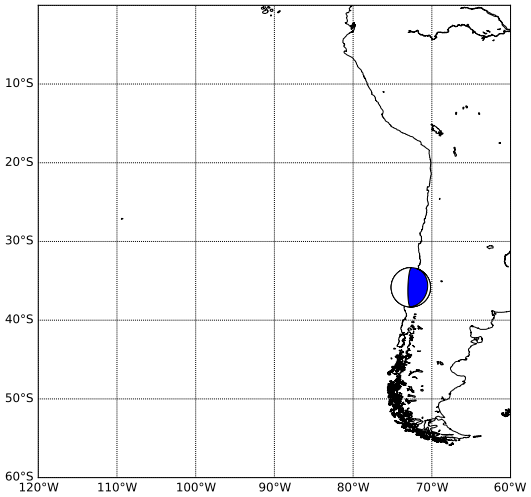

Figure 3.15: Focal mechanism of the Maule, Chile, 2010 event. The Centroid-Moment-Tensor (CMT) is provided by USGS and located at the epicentre.

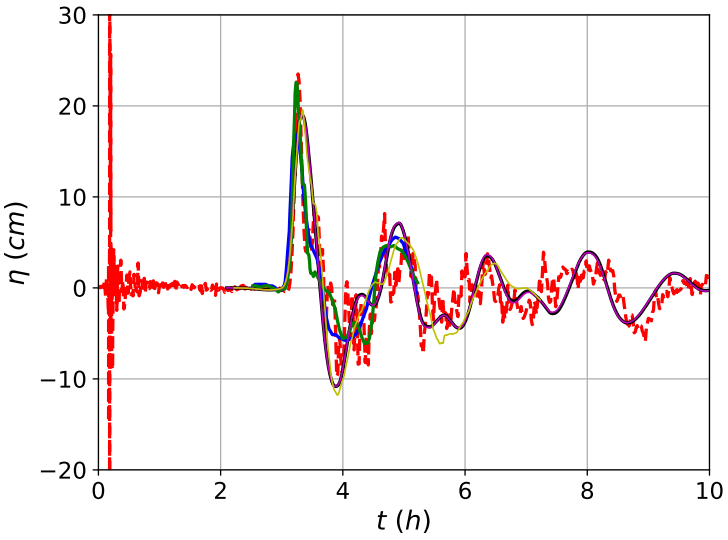

Figure 3.16: Chile 2010 comparison between observational data (- -), GeoClaw computed tsunami waveforms for DART 32412 from an uniform grid simulation (—), from a 3 level simulation (—) and 4 level simulation (—), Berger et al. (2011) with 3 level simulation (—) and 4 level simulation (—). Time of earthquake event corresponds to the beginning of the plot.

2017). The original DART data can be retrieved from the National Data Buoy Center. Data is provided at different sampling intervals, which causes repetition of data points, as well as some gaps and spikes. After their removal from the time series, data is detided: applying variable degree n polynomial fitting, we estimate the tidal signals and then remove these from the original records. Afterwards, the detided waveforms are used for comparison with our simulations results.

Comparing the observational data at DART 32412 with GeoClaw's results, we find that the first wave is well reproduced by the numerical model in terms of period but its amplitude is moderately

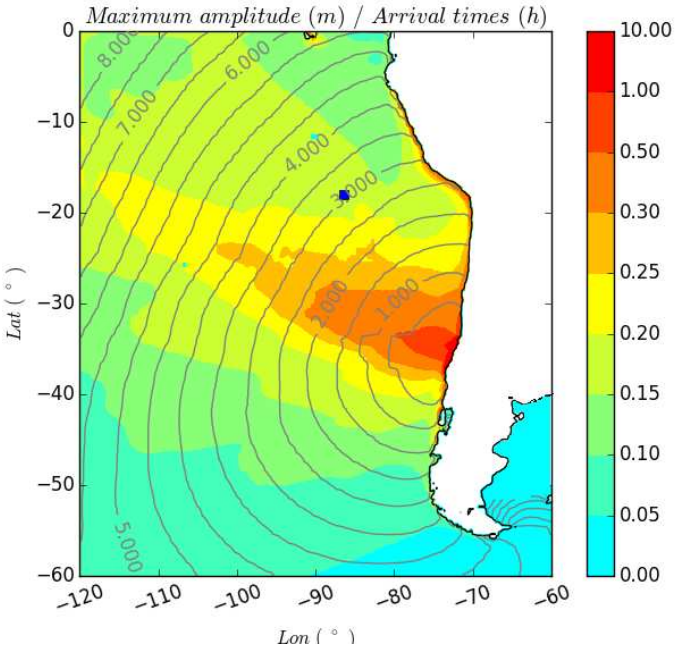

Figure 3.17: Maximum amplitude (in metres) and tsunami arrival times (in hours) for the Chile 2010 event. The blue square indicates the location of DART 32412.

underestimated (Figure 3.16). We found that there is a good match in the tsunami arrival times (Figure 3.17) between the observations retrieved from DART 32412 and the numerical results, for a virtual gauge located at the same position as DART 32412. The results are similar for both the 3-level and the 4-level simulations.

Berger et al. (2011) also performed two simulations (results shown in Figure 3.16) with the same bathymetric information and the same base resolution of the computational grid (2°× 2°). The sequence of refinement levels was somehow different from ours: a 3-level simulation with refinement factors of 2 (1°× 1°) and 6 (10 min × 10 min), so that the finest grid resolution matches the bathymetric resolution; a 4-level simulation with refinement factors of 2 (1°× 1°), 6 (10 min × 10 min), and 8 (1.25 min × 1.25 min), so that the finest grid resolution is 8 times finer than the bathymetric resolution.

From the analysis of Figure 3.16, we notice that Berger's 3-level simulation presents worse results than ours. Namely, their 3-level simulation underestimates both the first wave crest amplitude and the first trough amplitude. Their time of arrival is also slightly ahead of the observed one. Nevertheless, their 4-level simulation shows much better results in terms of first crest amplitude than our 4-level one, although still underestimating the first trough amplitude.

Due to the refinement sequence we used, our results should outperform those of Berger et al. (2011) both for the 3-level and the 4-level simulation. As that did not happen to the 4-level case, we tried to reproduce Berger's results using the same refinement sequence. We obtained results close to our 4-level simulation, which led us to speculate that Berger's 4-level simulation is based on better bathymetric information or on a more sophisticated source model.

Analyzing the computed metrics for the Chile 2010 event with GeoClaw (Table 3.4), a relatively high linear correlation exists, with r around 0.8, with a very small positive bias of 5 mm. The magnitude of the root-mean-square error is about 5 cm, which is at about 15% of the first wave height, which is 29.8 cm.

Table 3.4: Error metrics for Chile 2010 GeoClaw simulation.

Case	r (—)	Bias (m)	RMSE (m)
Chile 2010*	0.806	0.0047	0.0526

*For DART 32412 record from the Maule 2010 event.

3.5.3.2 Case study of a M_w 8 Earthquake at the Southwest Iberian Margin—The 1969 Portugal Earthquake and Tsunami (1969 PET)

The GeoClaw has been used to model several historic tsunami events (George 2006; Berger et al. 2011; MacInnes et al. 2013a; Arcos and LeVeque 2015). To test the global tsunami modelling capacity of GeoClaw, an earthquake with M_w = 8 located at the Southwest Iberian Margin (with location similar to the 1969 Portugal earthquake, event that caused a small tsunami) was selected to perform a tsunami test in GeoClaw version 5.2.2 . The 1969 event occurred at 2h40min30s UTC of 28th February 1969, with epicentre (36.010°N, 10.570°W)(Gjevik et al. 1997), the location we used in our study. The parameters of the selected fault are detailed in Table 3.5 and were taken from Grandin et al. (2007).

Table 3.5: Fault mechanism parameters (Grandin et al., 2007)

Scenario	Length (km)	Width (km)	Strike (°)	Dip (°)	Rake (°)	Slip (m)	Depth† (km)	μ (Pa)	M_0 (N·m)	M_w
A	85	20	231	47	54	5.29	20	4×10^{10}	3.6×10^{20}	7.8

†Top of the fault

In the numerical simulations, a 1245 $\times$ 1601 GEBCO grid with 0.0064°cell size ($\approx$ 700 m) was used. The seafloor deformation is generated using the Okada's equations (Okada 1985), through the maketopo.py script computed within the GeoClaw code. Figure 5.8 illustrates the initial sea surface displacement caused by the Okada deformation, computed with the parameters documented in Table 3.5. The correspondent source mechanism is plotted in Figure 3.19. Two levels of refinement were set with factors 2 and 6. The Sommerfeld or radiation condition was imposed at the boundaries of the domain.

We show the results of the simulation for this earthquake and tsunami. In Figure 3.20, four frames of the 3 level simulation are presented. In Figures 3.21 and 3.22, we show the free surface elevation comparison between observations and numerical results for two locations in the Portuguese coast: Cascais, near Lisbon, and Lagos, in the southern part of Portugal (locations in Table 3.6). The positions of the virtual gauges were chosen at grid points located the closest possible to the original position of the wave gauge at the time of the original event.

From the analysis of the results, it is possible to observe that there is a delay in the arrival time of the first wave, at both gauges. This could be due to the difference between the tide gauges location at the time of the event and the location in the computational grid, which are slightly different. When comparing the observation and the computation at Cascais, it is seen that the amplitude of the computed first wave at Cascais is smaller; also the subsequent observed waves are not simulated by the numerical code. At Lagos, the amplitude of the first wave is less than the observed one and its shape is more flattened. Analyzing the computed metrics for 1969 PET, shown in Table 3.7, the value of r is close to 0.50, the bias is negative and the magnitude of the root-mean-square error is about 11.5 cm.

The poor results obtained from this simulation are probably related to the fact that the refine-

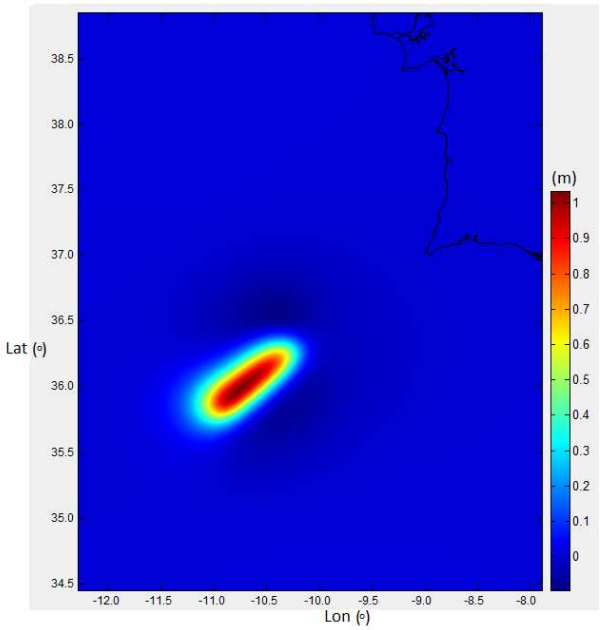

Figure 3.18: Initial deformation (in metres) of the 1969 PET event.

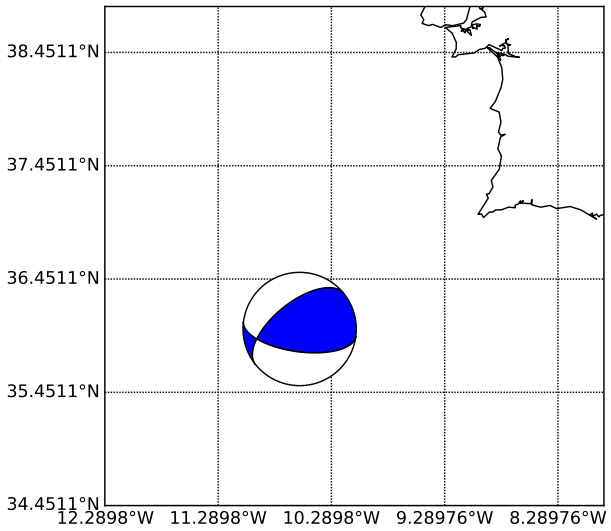

Figure 3.19: Focal mechanism of the 1969 PET event. The CMT is provided by Grandin et al. (2007) and located at the epicentre.

ment was applied only in the areas of location of the virtual tide gauges. The AMR capability of GeoClaw should have been applied also in the generation and propagation areas. Results of both refinements could be compared to evaluate the differences obtained in the simulations.

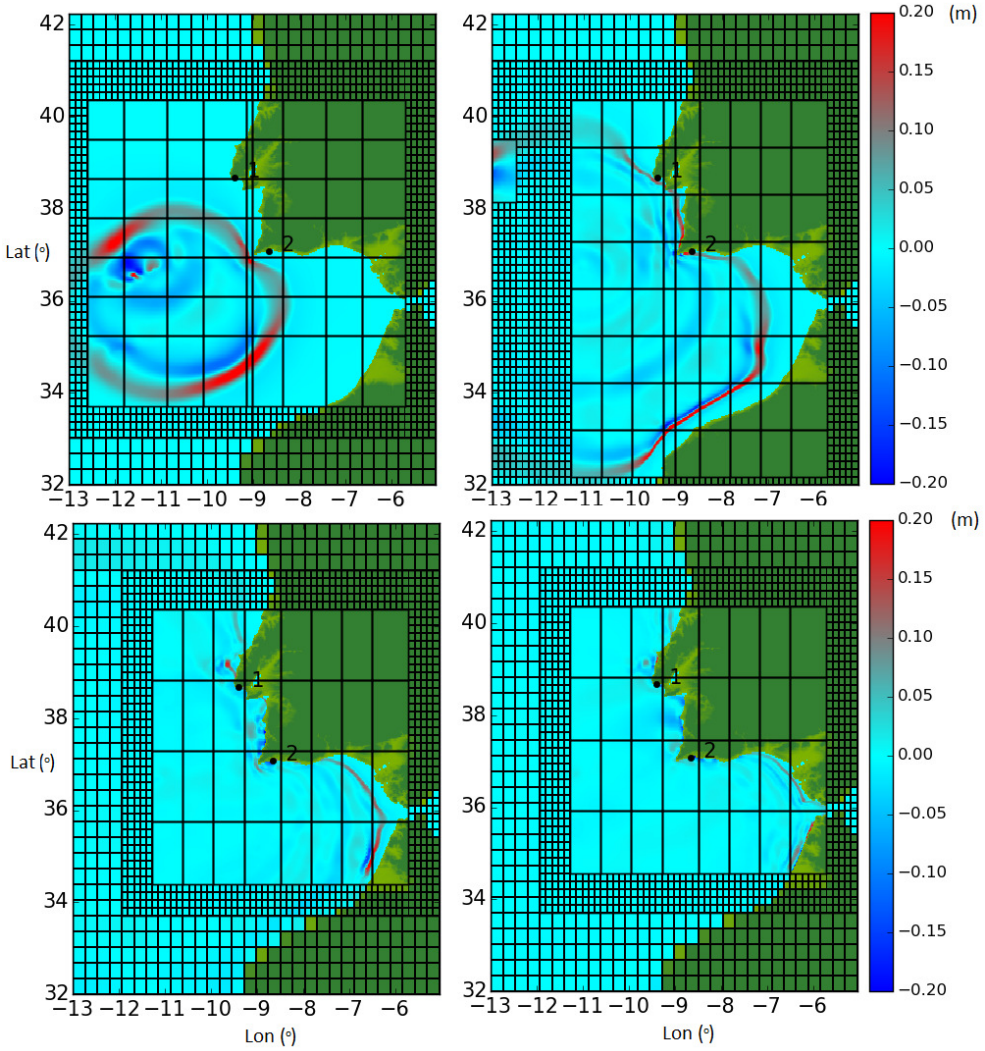

Figure 3.20: Four frames of the simulated surface elevations (in metres) from a level 3 simulation of the 28th February 1969 Portugal event. Time zero of the simulation corresponds to 2h40min30s UTC, the origin time of the event. The approximate location of the gauges used is marked with 1, which corresponds to Cascais, and 2, which corresponds to Lagos.

Table 3.6: Positions of the virtual gauges: Cascais and Lagos (locations 1 and 2, respectively, in Figure 3.20).

Station	Location		Depth[1]	Dist.[2]
	Lon	*Lat*		
	(°)	(°)	(m)	(km)
Cascais	-9.4112	38.6816	17.37	313.77
Lagos	-8.6688	37.0688	22.81	206.84

[1]Retrieved from the simulation mother grid

[2]Distance from tide station to source location, determined according to Vincenty (1975).

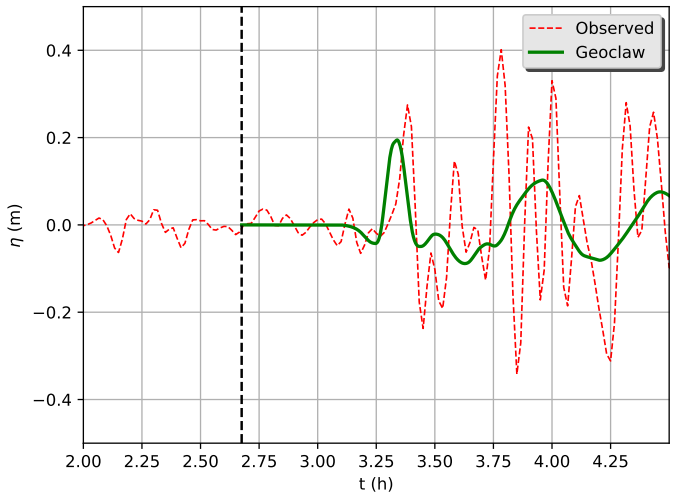

Figure 3.21: Cascais: comparison between the free surface elevation observations and simulations for the 1969 PET event.

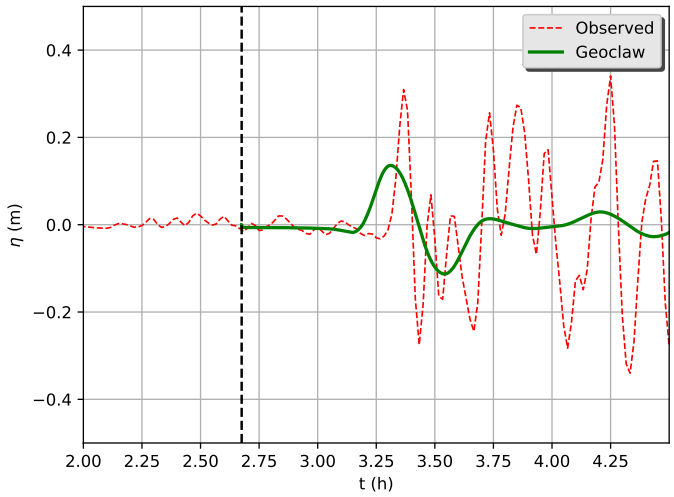

Figure 3.22: Lagos: comparison between the free surface elevation observations and simulations for the 1969 PET event.

Table 3.7: Error metrics for GeoClaw simulations.

Case	r (—)	Bias (m)	RMSE (m)
1969 PET[1]	0.487	-0.0347	0.1151

[1]For Cascais tide gauge record from the 1969 event.

3.5.4 With FUNWAVE-TVD

FUNWAVE-TVD has been benchmarked by the authors of the code, with the examples presented in the manual. The authors published the Cartesian version benchmarking in Tehranirad et al. (2011) and the spherical version benchmarking in Shi et al. (2012a). In this research work, FUNWAVE-TVD version 2.0 was used for the first simulations, being later substituted by FUNWAVE-TVD version 3.0. Yet, both versions were previously validated with state-of-the-art benchmarks. Recently, Kirby et al. (2017) presented the code benchmark testing performed with the 2015 National Tsunami Hazard Mitigation Programs Workshop on Modeling of Tsunami Currents. In the following application, the threshold value of the ratio of the wave height to the total water depth was defined as 0.8 (according to Tonelli and Petti 2009).

3.5.4.1 Solitary wave on a conical island

This case study is based on the laboratory experiments by Briggs et al. (1995a), in which the objective was to study the three-dimensional tsunami run-up on a conical island (Appendix A.1.2.2). The waves tested were solitary waves with H/h (where H is the wave height and h is the water depth) varying between 0.05 and 0.20 in two levels of water depths. A total of 27 wave gauges were used to measure surface elevation and transects. These large-scale laboratory experiments were motivated by the 1992 Flores tsunami, that struck the Babi Islands, Indonesia. The initial wave is defined as half wavelength ($\lambda/2$, i.e. gauges 1 to 4) away from the toe of the island (Synolakis et al. 2007).

Table 3.8: Location of the 4 monitored wave gauges.

wave gauge	Lon (°)	Lat (°)
6	0.01246	0.01745
9	0.01246	0.01848
16	0.01470	0.02068
22	0.01246	0.02298

The computational domain is composed by a 702 $\times$ 602 grid, with Δx = Δy $= 0.05$ m. The simulation has a total run time of 25 s, with a Δt $= 0.05$ s. We present results from the numerical modelling with FUNWAVE-TVD at the 4 wave gauges, for a water depth h = 32 cm. We compare them with the equivalent laboratory measurements taken at the four locations, which correspond to the front of the conical island at the toe (gauge 6) and to the three wave gauges 9, 16 and 22 located near the shoreline (Figure A.3c and Table 3.8). The results from the simulations for three different H/h relations are compared with the experimental results by Briggs et al. (1995a) in Figure 3.23. Gauges 6, 9, 16 and 22 are represented for three ratios of H/h (Table 3.9) and the plots are oriented downwards, with the first plot corresponding to wave gauge 6 and the fourth plot corresponding to wave gauge 22.

Table 3.9: Wave conditions tested for the 32 cm water depth experiments.

Case	H/h	h (cm)	H (m)
A	0.045	32	0.014
B	0.091	32	0.029
C	0.181	32	0.058

The computed metrics for the conical island case study are presented in Table 3.10. The analysis shows a very high linear correlation, with r above 0.9 and close to 1.0, for all the three

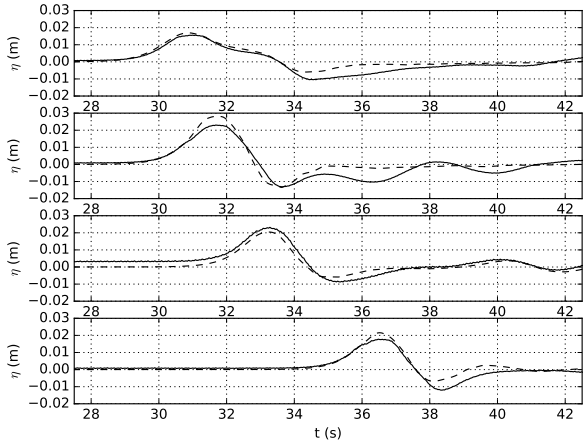

(a) $H/h = 0.045$

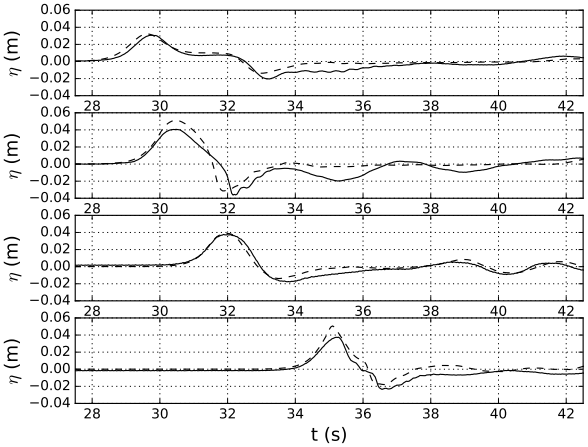

(b) $H/h = 0.091$

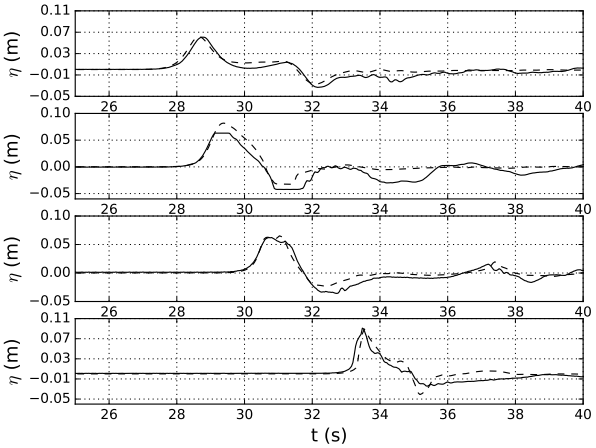

(c) $H/h = 0.181$

Figure 3.23: Conical island: FUNWAVE-TVD numerical simulation (—) results and experimental data (- -) recorded at wave gauges 6, 9, 16 and 22 (downward) for 3 different H/h solitary waves.

Table 3.10: Error metrics for FUNWAVE-TVD's simulations for wave gauge 6.

Case	r (—)	Bias (m)	RMSE (m)
A	0.974	-0.0005	0.0015
B	0.962	-0.0015	0.0030
C	0.955	-0.0021	0.0058

ratios of H/h, with negative bias. The magnitude of the root-mean-square error varies from 0.15 to 0.58 cm for the three cases. Comparing with the experimental measurements, the results obtained from FUNWAVE-TVD simulation are, as expected , very satisfactory for the 3 distinct solitary waves computed, as FUNWAVE-TVD is a dispersive Boussinesq model.

3.5.5 With the CFD code

OpenFOAM comes with several tutorial cases to test the various solvers existent within the CFD code. olaFlow also presents several tutorial cases that show the performance of the solver, to model wave simulation in channels and wave tanks.

In this research work, blockMesh was used for the meshing of simple geometric domains, as in the case of canals and tanks, with and without slopes and with and without simple geometric barriers or obstacles (such as breakwaters, walls, etc). For more complex geometric domains, such as ports and harbours, snappyHexMesh was used. The snappyHexMesh tool generates three-dimensional meshes, composed by hexaedra (hex) and split-hexahedra (split-hex) automatically from triangulated surface geometries in Stereolithography (STL) format. The mesh approximately conforms to the surface by iteratively refining a starting mesh and morphing the resulting split-hex mesh to the surface. Since the geometry has to be only surface data, the files need to be in Stereolithography (STL) or Wavefront Object (OBJ) formats [**]. In this research work, the STL format, a Computer-aided design (CAD) file format which defines only the surface geometry of 3D objects, was used. Originally, an ASCII file with the topography/bathymetry was available and a GNU Octave® script was used to perform its conversion to the STL format. After the conversion, it is advisable to check the integrity of the STL file, which can be done with the open source softwares Blender version 2.7.9 [††] and/or Gmsh version 4.02 [‡‡] and freeCad version 0.14 [§§]. These softwares allow for some pre-processing of the STL file just before using it for the CFD simulations. Within OpenFOAM, the user can also use checkMesh to track the quality of the mesh created after blockMesh and/or snappyHexMesh tools have been used. This allows the user to improve the quality of the produced mesh, which is crucial for the quality of the simulations results. In this thesis, OpenFOAM version 1606+ was used in the serial simulations and OpenFOAM version 1712 was used for parallel simulations.

Next, the results for some benchmark test cases performed with olaFlow are documented, which include solitary and N-wave profiles input and propagation over channels and tanks and its validation with experimental available data. Both the wave theories capability and wave-maker emulation within olaFlow are tested.

[**] https://www.openfoam.com/documentation/user-guide/snappyHexMesh.php
[††] https://www.blender.org
[‡‡] http://gmsh.info
[§§] https://www.freecadweb.org

3.5.5.1 Beji and Battjes (1993) Case A — Wave propagation over a flat channel

We benchmark the code with the experiment by Beji and Battjes (1993), which considers the wave propagation over a trapezoidal submerged bar. Here we only consider the flat zone of the bathymetric setting, just before the bar. The wave case simulated is Case A, in which the wave height is H = 0.02 m and the period is T = 2.02 s, for a water depth h = 0.4 m. Waves are generated at the inlet boundary, x = 0 m, applying the Airy linear wave theory (Dean and Dalrymple 1991), and absorbed at x = 10 m. In this case study the wave parameters and theory are specified inside olaFlow's waveDict file. The objective of this case study was to show the generation ability of the olaFlow code, with the wave theories embedded in the code, and the possibility to use any wave theory, from the ones available, to simulate and propagate a wave over a 2DV channel.

Table 3.11: Location of the wave gauges along a flat channel.

wave gauge	x (m)	y (m)
1	2.0	0.01
2	4.0	0.01
3	5.2	0.01

This case study was based on the olaFlow *baseWaveFlume* example. A 2D model is used and the computational domain is set into 1 block specified inside blockMeshDict. The 2DV numerical channel has a width of one element, length of 10 m and height of 0.7 m. The cell resolutions are Δx $= 0.02$ m, Δy $= 0.02$ m and Δz $= 0.01$ m. The total run time is 40 s and the Δt $= 0.001$ s. Results are presented for the first 3 virtual wave gauges located along the flat part of the channel (Table 3.11). A very good agreement was found between the numerical results, by applying the Airy linear wave theory, and the experimental measurements for the 3 wave gauges used (Figure 3.24).

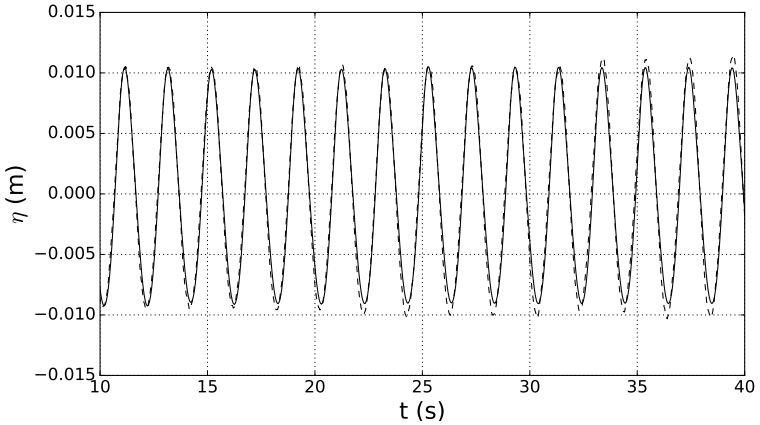

(a) station 1 ($x = 2$ m)

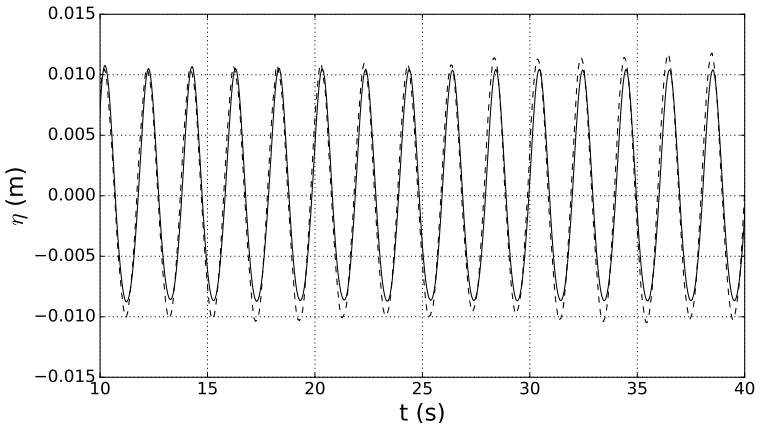

(b) station 2 ($x = 4$ m)

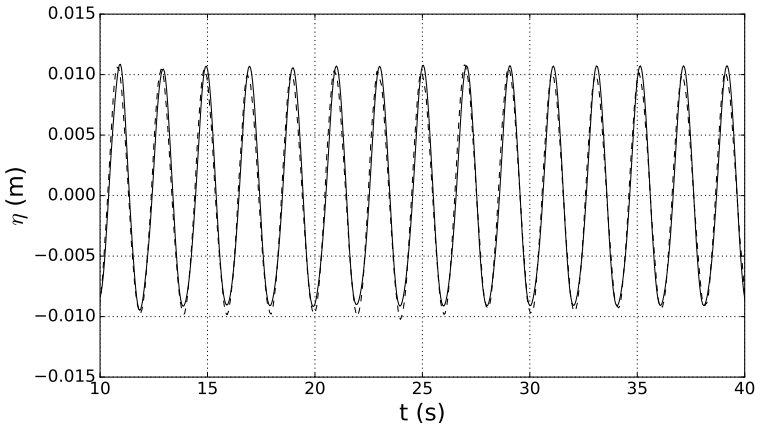

(c) station 3 ($x = 5.2$ m)

Figure 3.24: Wave propagation over a flat channel: numerical simulation results (—) and experimental data (- -) recorded at wave gauges 1, 2 and 3.

3.5.5.2 With piston wave-maker generation

In this section, the waves are generated within a wave flume by means of a piston wave-maker. Flap wave-maker generation option also exists but it will not be described here. A file with the wave-maker trajectory can be created by means of a Python (van Rossum 1995) script included in the package, which generates the displacement of the paddle according to the linear theory. Another method is to provide the wave-maker time series displacement, determined according to the theories described in Goring (1978), Goring and Raichlen (1980) and Lima et al. (2019), considering the generation of solitary and N-waves and taking the expressions deducted for the piston trajectory for each type of wave. The time series file structure has to be written according to the file format expected by the code.

Case 1: Waves generated in a wave flume In this case study a Boussinesq like solitary wave (Lee et al. 1982) is generated at x = 0 m, with wave height H = 0.10 m and the wave period T = 3.0 s, for water depth h = 0.4 m, and absorbed at x = 10 m. A 2D model is used and the computational domain is set into 3 blocks specified inside blockMeshDict. The 2DV channel has a width of one element, length of 10 m and height of 0.7 m. The cell resolutions are $\Delta \mathrm{x} = 0.02$ m, $\Delta \mathrm{y} = 0.02$ m and $\Delta \mathrm{z} = 0.01$ m. The total run time is 60 s and the $\Delta \mathrm{t} = 0.001$ s. In this case study the wave parameters and theory are specified inside olaFlow's waveDict file. The objective of this case study was to show the generation ability of the olaFlow code, which include the Boussinesq theory, among others, as used in this case.

The wave propagation is shown in Figure 3.25 for several time instants. The variable shown in the figure, fraction of water α, indicates that the cell is occupied with water when its value is α = 1; when α = 0, the cell is filled with air. We observe the wave propagating from the inlet boundary to the right side of the domain, to the outlet. The feature of introducing an external time series into the code has shown a good performance.

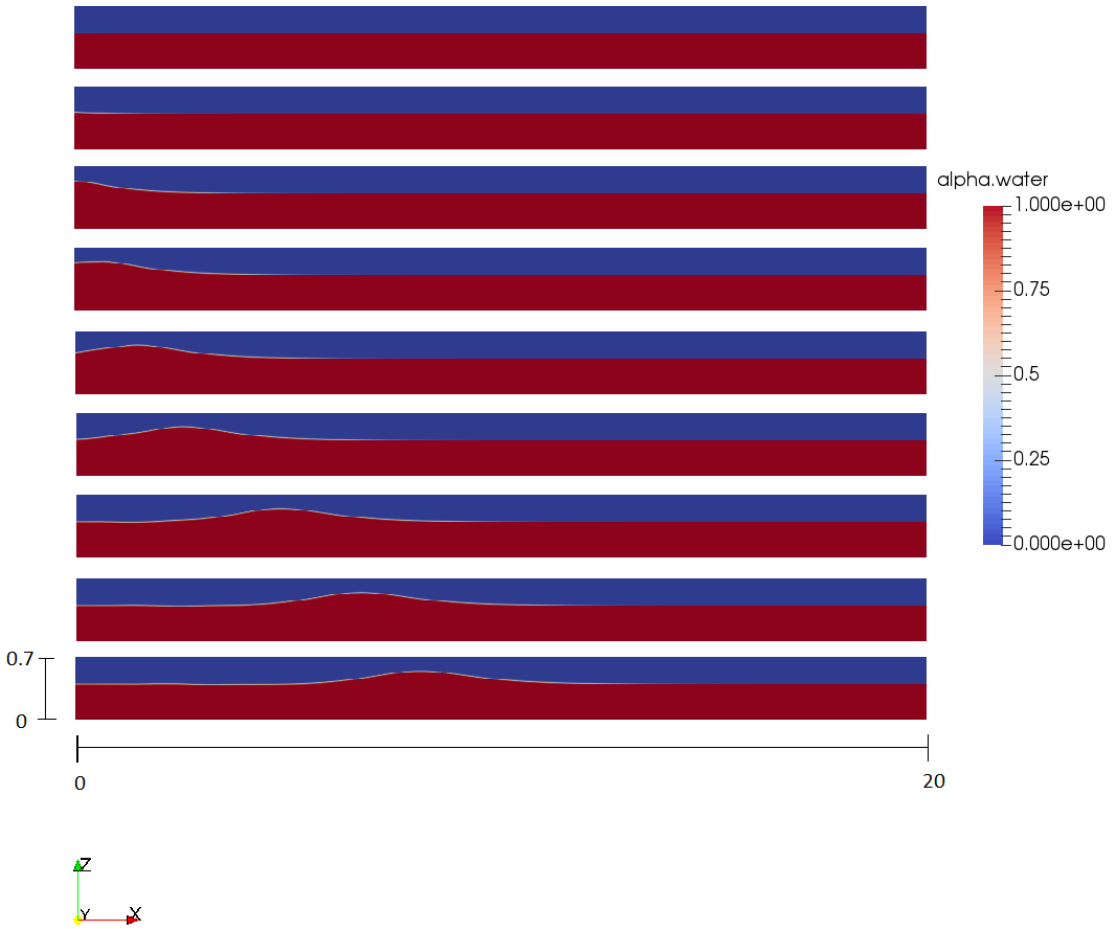

Figure 3.25: Wave propagation along a flat flume, using the wave-maker option. Scales in metres. H = 0.01 m, T = 3.0 s, h = 0.4 m. Simulation time steps (from top to bottom): 0.75 s, 1.25 s, 1.75 s, 2.00 s, 2.25 s, 2.50 s, 3.00 s, 3.40 s, 3.70 s.

Case 2: Solitary and N-waves generated at the wave basin in FEUP We now compare the results from the olaFlow code, for each virtual wave gauge, with the preliminary laboratory test measurements performed at the wave basin in FEUP. The objetive of this case study was to compare the laboratory measurements with the results from the olaFlow simulations, where the boundary condition at x = 0 m corresponds to the free surface elevation and velocity of the theoretical profile used to generate the solitary waves and the N-waves in the laboratory. In this case study the wave parameters are specified by means of the wavemakerMovementDict in olaFlow. No turbulence is used in this simulation. A 2D model is used and the computational domain is set into 1 block, specified inside blockMeshDict. The 2DV channel has a width of one element, length of 16.25 m, width of 1.5 m and height of 0.7 m. The cell resolutions are Δx $= 0.0325$ m, Δy $= 1.5$ m and Δz $= 0.01$ m. The total run time is 10 s and the Δt $= 0.05$ s. The wave gauge setting is shown in Figure 3.26 and the location of the wave gauges is detailed in Table 3.12.

In Figures 3.27 and 3.28, we show the comparison between the numerical results and the experimental measurements for the solitary wave C6, with wave height H = 0.155 m and T = 1.31 s, for water depth h = 0.26 m. In Figures 3.29 and 3.30 experimental and olaFlow numerical results are shown for C13, a leading depression N-wave (LDN-wave), with wave height H = 0.085 m and T = 6.05 s, for water depth h = 0.26 m.

A good match is generally found when comparing the observed experimental wave profile

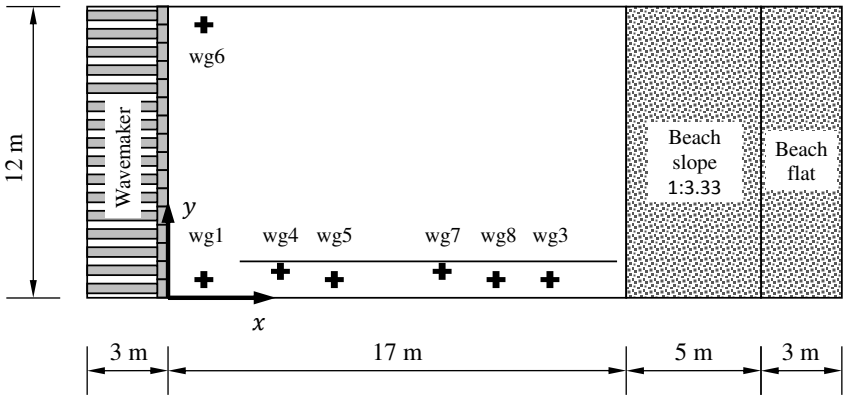

Figure 3.26: Wave basin and wave gauges positioning.

Table 3.12: Location of the wave gauges.

wave gauge	x (m)	y (m)
wg1	1.32	0.75
wg6	1.32	11.25
wg4	4.16	1.10
wg5	6.16	0.75
wg7	10.16	1.10
wg8	12.16	0.75
wg3	14.16	0.75

with the olaFlow wave profile for the same wave gauge, for both solitary wave C6 and leading depression N-wave C13.

Nevertheless, for the solitary wave case, C6, at wave gauge 1 the numerical wave, with an amplitude close to 17 cm (larger than the intended one), is larger than the experimental wave, which has an amplitude close to 13 cm (lower than the intended one). As the wave propagates along the canal, the amplitude of the numerical wave decreases and its shape becomes close to the shape of the experimental wave (cf. 3.27c at station 5). After this point, the experimental wave is slightly larger than the numerical one, while this last one seems to be producing a dispersive tail. This might result from the non-existence of an equilibrium between the convective and the dispersive effects for the initial numerical profile. Another reason might be related to the fact that there is not enough resolution in the z-direction, which might have provoked some excessive energy dissipation. Until the end of the experiment, the experimental wave keeps a profile close to the SW profile, specifically of a 0.12 m-high SW with period close to the intended period, T = 1.31 s.

On the other hand, the behaviour for the N-wave case, C13, is very different. At gauge 1, the experimental wave has a N-wave profile, but its wave height is close to 0.06 m, thus smaller than the expected wave height of 0.085 m. Its period is close to the desired period of 6.05 s. At the same gauge, the numerical wave has the profile of a N-wave with a wave height close to the intended one, but with a period around 2 – 4 s, thus much shorter than the target period of 6.05 s. As the wave propagates down the canal, the experimental wave tends to the target wave profile, although with a dispersive tail, while the numerical wave tends to a solitary wave profile with the expected wave height, shorter period, and a dispersive tail.

For the olaFlow case studies of Beji and Battjes (1993), Case A, and the case studies of solitary

Table 3.13: Error metrics for olaFlow simulations.

Case	r (—)	Bias (m)	RMSE (m)
Beji and Battjes Case A	0.996	0.0025	0.0026
Case 2 SW (lab FEUP)	0.985	-0.0044	0.0097
Case 2 NW (lab FEUP)	0.465	-0.0011	0.0179

and N-waves generated at the wave basin in FEUP, the computed metrics are shown in Table 3.13. The analysis of the error metrics shows a very high linear correlation, with r greater than 0.95 and close to 1.0 respectively for the Beji and Battjes case study and for the solitary wave case simulated at the Laboratory of Hydraulics at FEUP. For the N-wave, r is close to 0.50, showing low linear correlation. For the waves generated at the Laboratory of Hydraulics at FEUP, the bias is negative. For the Beji and Battjes case, the bias is positive and the root-mean-square error is about 0.26 cm. For the experimental solitary wave, the RMSE is about 1 cm and for the N-wave is around 2 cm. The difference in the results obtained for the solitary waves and N-waves are most probably related to the fact that the waves generated in the laboratory were very high. As pointed out by Goring (1978), and later by Grilli (1997), a first-order long wave generation method for waves of permanent form is accurate for a wave height-to-depth ratio below 20%.

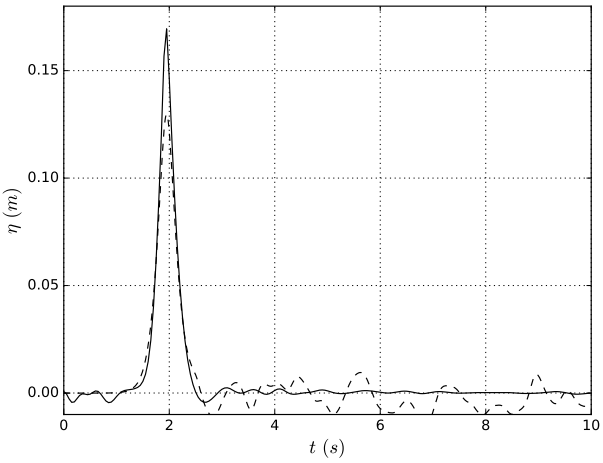

(a) station 1 ($x = 1.32$ m)

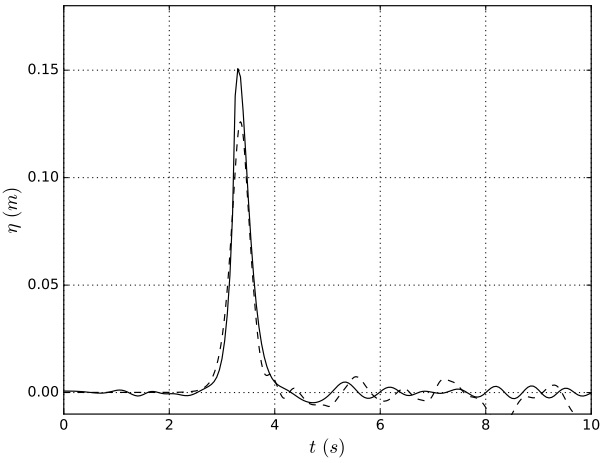

(b) station 4 ($x = 4.16$ m)

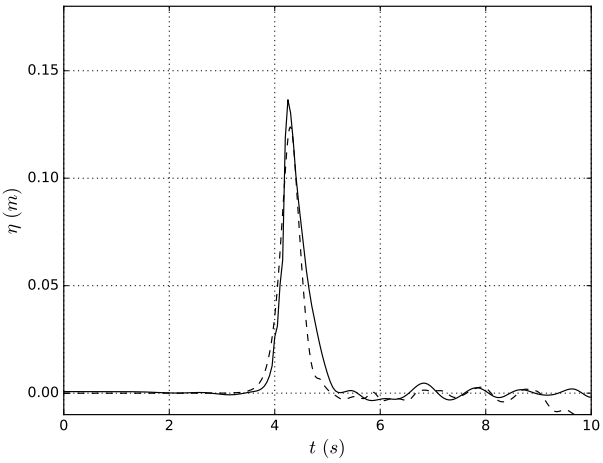

(c) station 5 ($x = 6.16$ m)

Figure 3.27: Numerical wave profile (—) and experimental wave profiles (- -) for SW case 6.

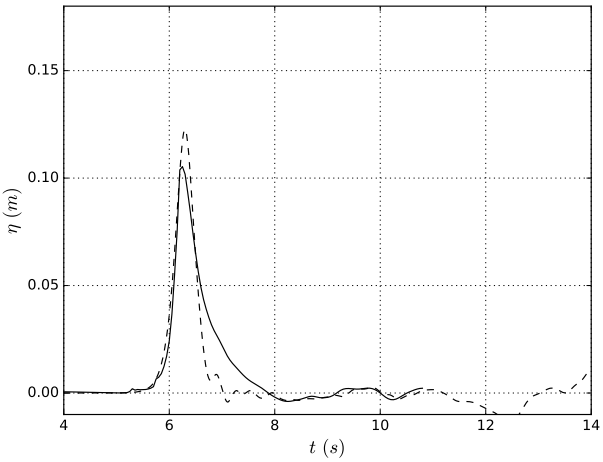

(a) station 7 ($x = 10.16$ m)

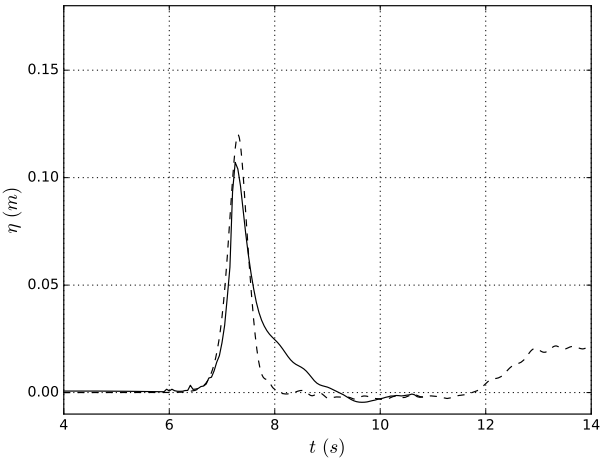

(b) station 8 ($x = 12.16$ m)

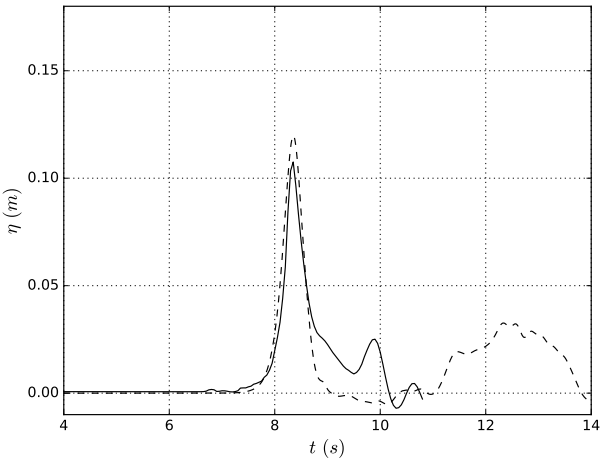

(c) station 3 ($x = 14.16$ m)

Figure 3.28: Numerical wave profile (—) and experimental wave profiles (- -) for SW case 6.

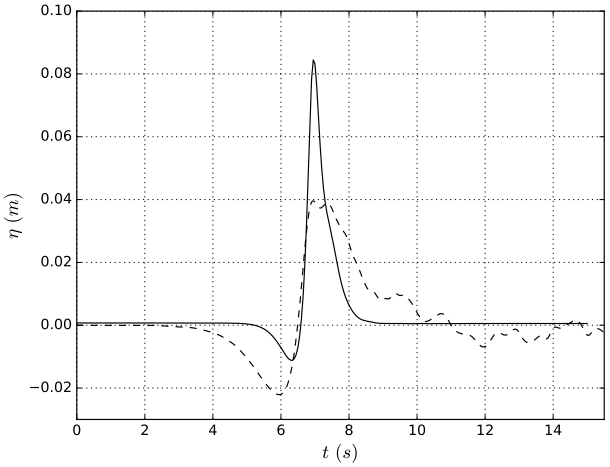

(a) station 1 ($x = 1.32$ m)

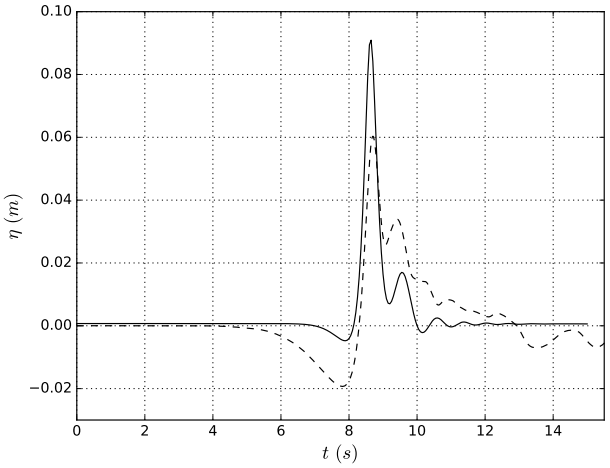

(b) station 4 ($x = 4.16$ m)

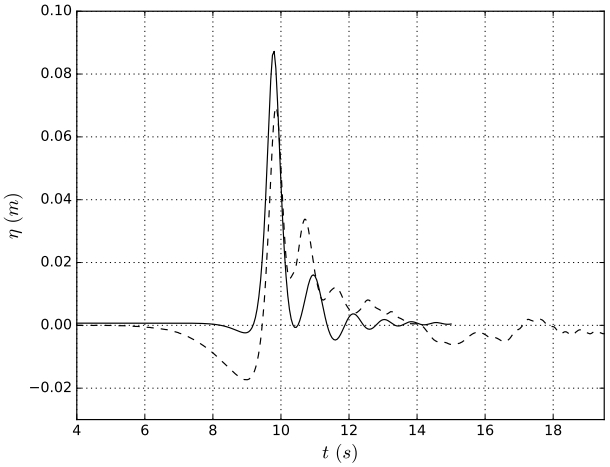

(c) station 5 ($x = 6.16$ m)

Figure 3.29: Numerical wave profile (—) and experimental wave profiles (- -) for LDN-wave case 13.

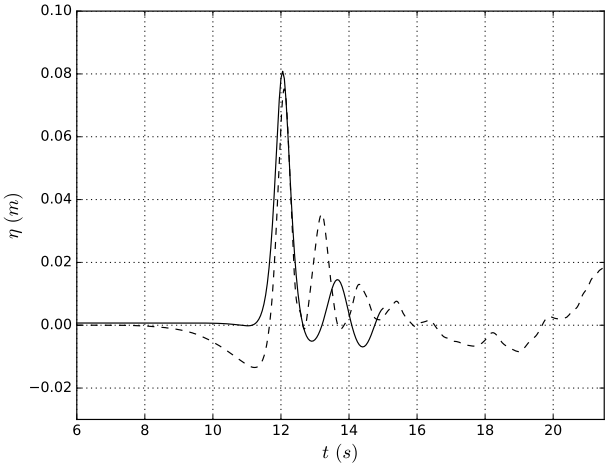

(a) station 7 ($x = 10.16$ m)

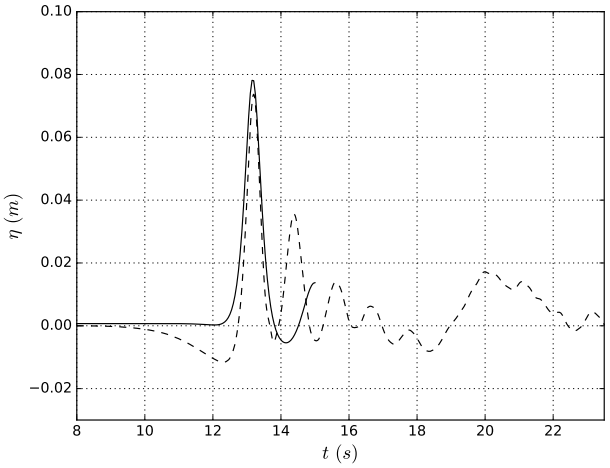

(b) station 8 ($x = 12.16$ m)

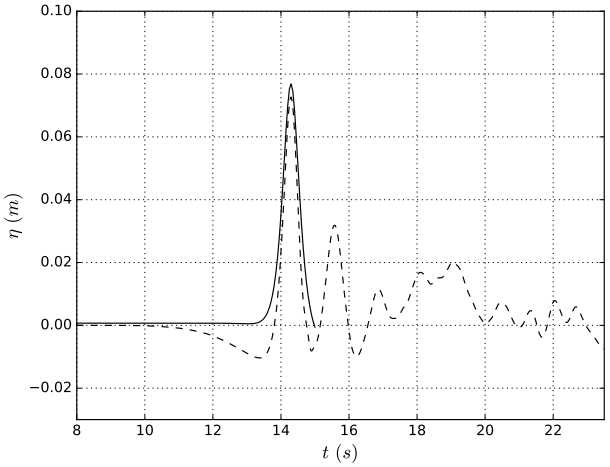

(c) station 3 ($x = 14.16$ m)

Figure 3.30: Numerical wave profile (—) and experimental wave profiles (- -) for LDN-wave case 13.

Wave propagation in a wave tank This case study is generally similar to the previous one, except that now 10 wave paddles are used to generate the waves in the numerical wave tank. A multi-piston wave-maker system is available, which makes it possible to generate oblique waves. The objective of this case study was to perform a 3D simulation in a tank with olaFlow, using its wavemaker facility, and to show the capabilities of the code and how it is necessary to run such a simple example as this one in a cluster, in parallel. In fact, this benchmark runs in parallel using the olaDyMFlow solver. The wave is generated at x = 0 m, with wave height H = 0.01 m and wave period T = 3.0 s, for a water depth h = 0.4 m. A wavemakerMovement.txt file is generated through the wavemakerMovementDict. No turbulence is included. Waves are absorbed on the outlet patch.

This case study was based on the olaFlow *wavemakerTank* example. A 3D model is used and the computational domain is set into 2 blocks specified inside blockMeshDict. The 3D numerical channel has length and width of 10 m and height of 0.7 m. The cell resolutions are $\Delta \mathrm{x} = 0.05$ m, $\Delta \mathrm{y} = 0.05$ m and $\Delta \mathrm{z} = 0.02$ m. The total run time is 30 s and the $\Delta \mathrm{t} = 0.05$ s.

Table 3.14: Location of the virtual wave gauges along a wave tank.

wave gauge	x (m)	y (m)
1	0.50	2.50
2	1.00	2.50
3	1.75	2.50
4	2.75	2.50
5	3.50	2.50

Several snapshots of the wave propagation over the tank are shown in Figure 3.31. The wave profiles at several virtual wave gauges, placed along the wave tank (locations in Table 3.14), are represented in Figures 3.32 and 3.33. A 3D perspective of the wave propagation over the wave tank is represented in Figure 3.34.

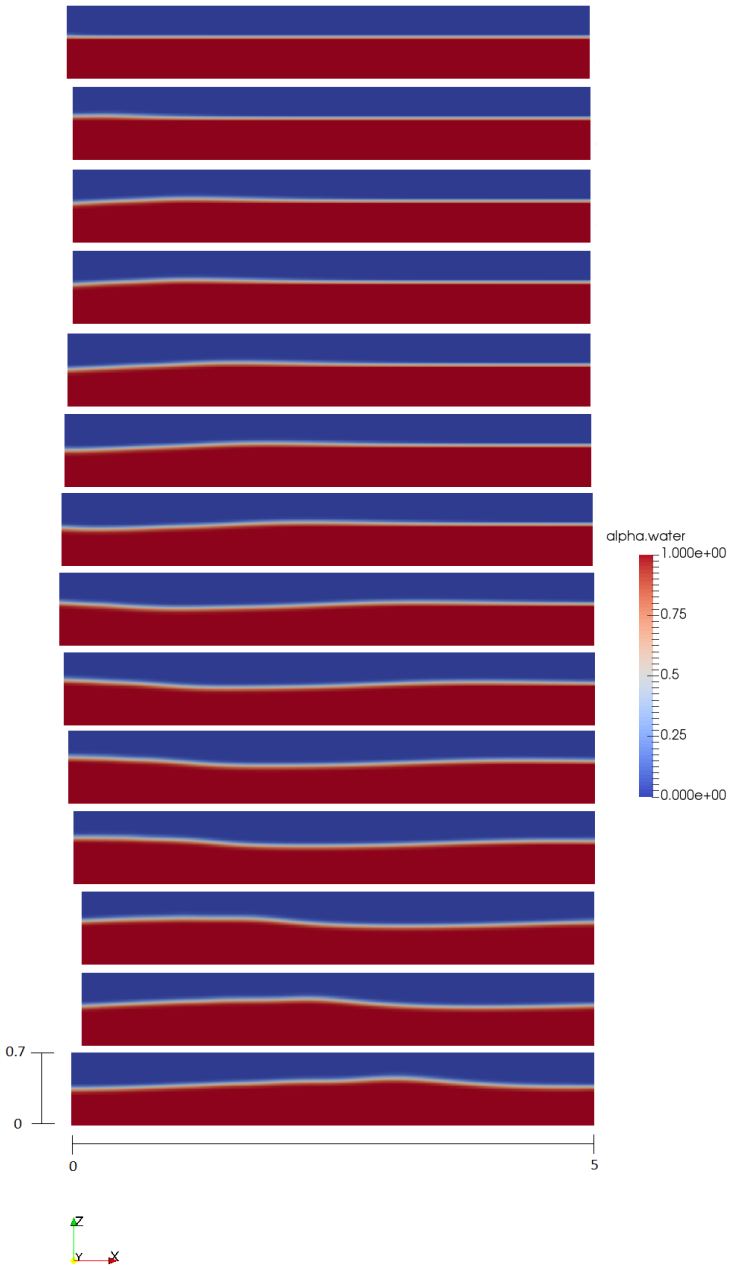

Figure 3.31: Wave propagation over the tank, using the wave-maker option. Scales in metres. H = 0.01 m, T = 3.0 s, h = 0.4 m . Simulation time steps (from top to bottom): 0.15 s, 0.70 s, 1.25 s, 1.50 s, 1.65 s, 1.85 s, 2.40 s, 2.70 s, 2.90 s, 3.10 s, 3.60 s, 4.00 s and 4.50 s.

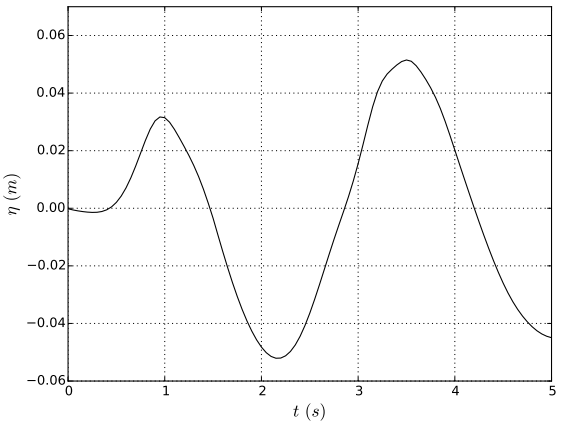

(a) station 1 ($x = 0.50$ m)

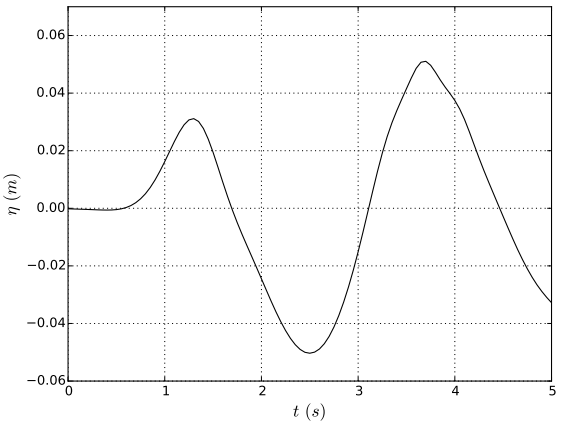

(b) station 2 ($x = 1.00$ m)

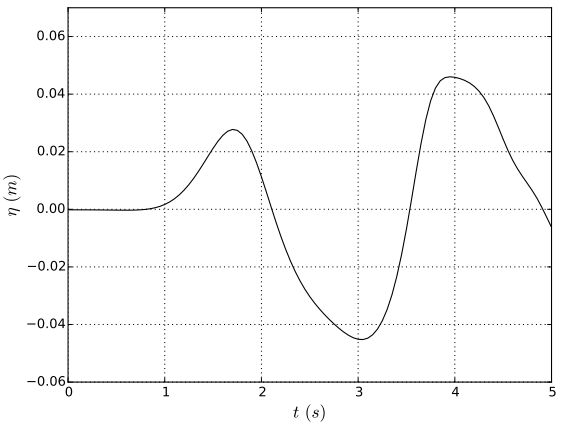

(c) station 3 ($x = 1.75$ m)

Figure 3.32: Wave profiles at virtual wave gauges 1 to 3.

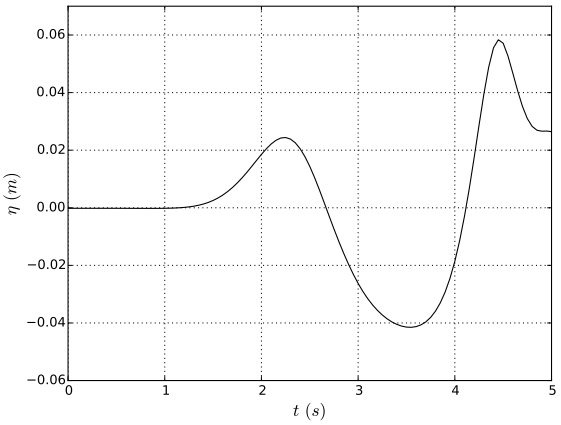

(a) station 4 ($x = 2.75$ m)

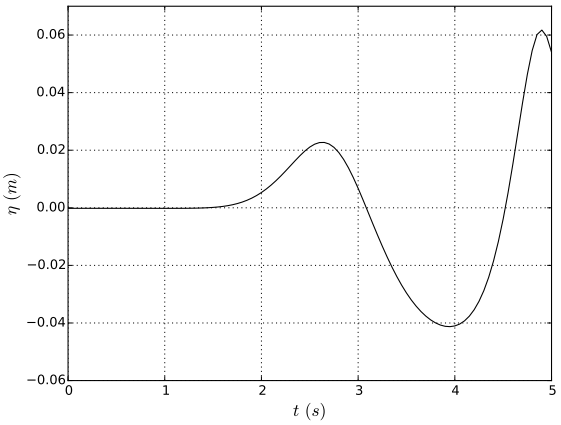

(b) station 5 ($x = 3.50$ m)

Figure 3.33: Wave profiles at virtual wave gauges 4 and 5.

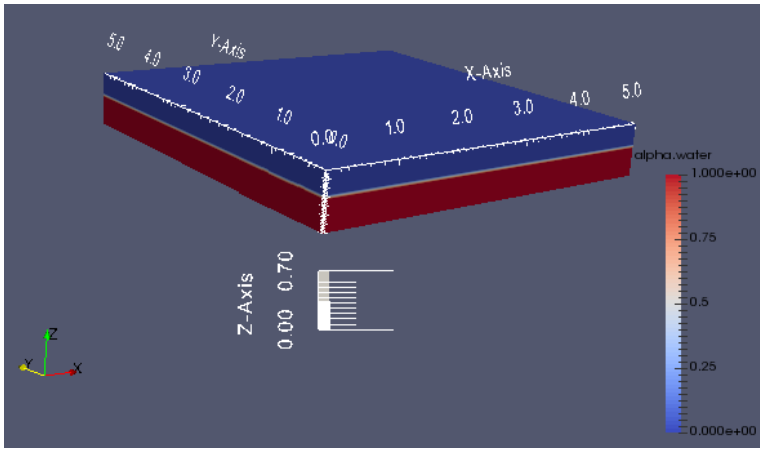

(a)

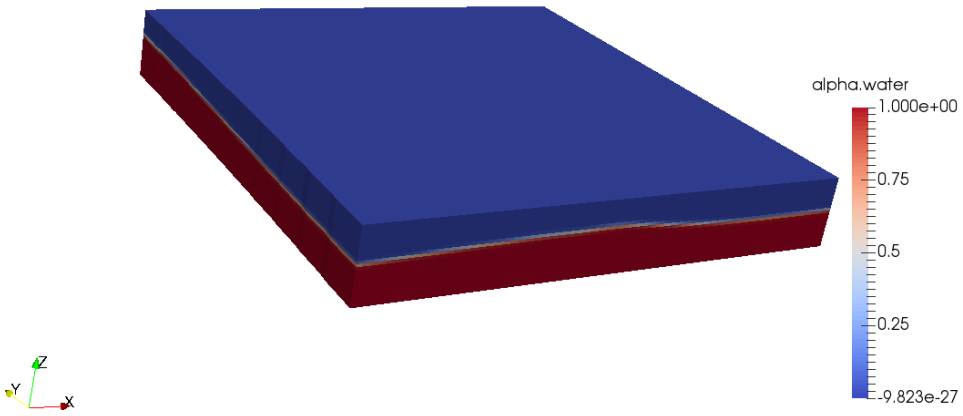

(b)

Figure 3.34: (a) Wave tank dimensions. Scales in metres. (b) 3D view of the wave propagation over the tank, using the wave-maker option. H = 0.01 m, T = 3.0 s, h = 0.4 m.

Chapter 4

Experiments of Solitary and N-waves

4.1 Introduction

When no field data is available or when a more conceptual analysis is envisaged, it is a common approach to model tsunamis as solitary waves, both in experimental and numerical studies (Synolakis 1987, Liu et al. 1995). However, Madsen et al. (2008) stated that in general tsunamis do not generate solitary-like waves (SW) in the ocean or on the continental shelf. Pelinovsky and Mazova (1992) presented a study on the run-up of leading depression N-waves, that at the time they called pulse perturbations. The concept of N-wave (NW) was formalized afterwards by Tadepalli and Synolakis (1994). The authors suggested that N-type waves, previously discussed in gas dynamics (Whitham, 1974), are more adequate to describe the main tsunami wave, which is often observed with a leading depression (where the wave crest is preceded by a trough). In Tadepalli and Synolakis (1994), the authors proposed three classes of N-waves to study the run-up of nearshore tsunamis.

The study of the laboratory generation of long waves traces back to the 19^{th} century (Scott Russell, 1845) and several methods have been proposed. From the general approach of applying moving partitions to a certain amount of water (Havelock, 1929; Kennard, 1949), Biésel and Suquet (1951) developed the linear wave-maker theory, later validated through laboratory experiments by Ursell et al. (1960). The horizontal movement of a water volume by means of a vertical plate, powered up by a piston-type wave-maker, is by far the most common method applied (see for instance Hughes 1993).

The most used method for the generation of solitary waves in a laboratory is based on the first-order wave-maker theory of Goring (1978) and Goring and Raichlen (1980) for a piston-type wave-maker. This method is limited to waves with a low height-to-depth ratio. Synolakis (1990) pointed out a flaw in Goring's theoretical considerations: the change of variable from (x, t) to θ performed during the generation phase, since at that stage the wave is still evolving and cannot be considered of permanent form. Thus, Synolakis (1990) presented a wave-maker theory of finite amplitude long wave generation by means of a piston wave-maker, achieving a very detailed description of single waves at arbitrary lengths from the wave-maker. His method was used to generate solitary waves with a piston wave-maker and to study the two- and three-dimensional long wave run-up in a wave canal and in a wave tank (Briggs et al., 1995b).

Goring's procedure is based on the Boussinesq first-order solitary wave solution. Following a similar reasoning, Katell and Eric (2002) presented a novel piston wave-maker theory, based on Rayleigh's solitary wave solution. They analysed the evolution of the wave during the generation stage and attested an increased accuracy and a more stable wave form. Jensen et al. (2003) extended Goring's method for higher amplitude solitary waves, using a fully nonlinear and fully dispersive wave solution (Tanaka, 1986). These authors studied the kinematics of strongly nonlin-

ear waves and related run-up on a steep beach, with special focus on bore run-up. Later, the same procedure was used for an experimental and numerical study on on-shore breaking solitary waves (Jensen et al., 2005).

Due to all this research work, solitary waves generated by piston wave-makers are now quite accurate in terms of wave characteristics and can be generated at short distances from the wave-maker. Such waves have been extensively used both in experimental and in numerical research work (Baldock et al., 2009; Chang et al., 2009; Hsu et al., 2012; Oliveira et al., 2017). In fact, it became the preferred generation method, due to its wide diffusion among the scientific community.

In this work, the generation of solitary waves and N-waves in laboratory by means a piston wave-maker mechanism is performed. The novel theoretical first-order formulation for the generation of N-waves in laboratory, by means of a piston-type wave-maker, is presented and detailed in Lima et al. (2019) presented and included here as appendix B.1. The formulations for the generation of N-waves, presented next, are adapted from the theory developed by Goring (1978), for the wave generation of long waves propagating with constant form. No report or scientific publication of laboratory experiments of N-waves with characteristics similar to those described in Lima et al. (2019) were found in the literature. It is expected that this research work might contribute to a better understanding and definition of the theoretical principles behind the generation of N-waves in laboratory. Nevertheless, this formulation suffers of the same shortcoming of the original work of Goring, namely the limitation to waves to low height-to-depth ratio.

In this chapter, several preliminary laboratory tests, adopted definitions and advanced laboratory experiments are described. The laboratory experiments were performed at the Laboratory of Hydraulics of the Faculty of Engineering of the University of Porto (LH-FEUP). 76 wave cases of propagation of SW and NW along a canal with constant section, with and without a beach assembled, are presented. The results and observations are presented, as well as the discussion of the results of the overall laboratory work. Results from numerical simulations are presented and compared with the laboratory measurements of both solitary waves and LDN-waves (leading depression N-waves), in terms of free surface elevation, run-in and pressure. Additionaly, expressions for the run-in, run-up and pressure of solitary waves and LDN-waves are proposed. Flaws and improvements are pointed out and future work and applications are suggested.

4.2 Physical tests (first stage)

The physical experiments were carried out at the LH-FEUP wave basin, which is 28 m long and 12 m wide, with a maximum water depth of 1.20 m. The basin floor and walls are made of concrete and the side walls have glass windows for flow observation.

The wave basin is equipped with a multi-element piston-type wave-maker by HR Wallingford (HRW), which allows the generation of regular and irregular multi-directional waves. It is composed by 16 piston paddles, which are moved horizontally by electrical motors. The maximum piston stroke is 1.08 m. The trajectory of the paddle must be provided as a time series to the wave generation system.

The instrumentation used throughout all the physical experiments is detailed in Table 4.1. Several resistance wave gauges (wgi), long and short, were used to acquire surface elevation time series. Every day, before data acquisition, the instrumentation used is calibrated. The wave gauges were connected to two wave probe monitors, which in turn were linked to a computer with a HRW software program for data acquisition, conversion and analysis (HRW DAQ Suite version 1.24.0.0). The pressure transducers (pti) were connected to the MCC DAQ software and InstaCal version 6.26 was used for the installation, calibration and testing of the pressure transducers. The calibration line for the pressure transducers can be found by measuring the voltage at three different water depth points. TracerDAQ version 2.2.0.0 was used for the monitoring, acquisition and

recording of the pressure transducers measurements.

Table 4.1: Available instrumentation and data type acquired.

Device	Type	Measured variable[a]	Calibration interval (cm)
wg1	long wave gauge	surface elevation	6
wg3	long wave gauge	surface elevation	4
wg4	long wave gauge	surface elevation	6
wg5	long wave gauge	surface elevation	6
wg6	long wave gauge	surface elevation	6
wg7	long wave gauge	surface elevation	6
wg8	long wave gauge	surface elevation	6
wg11	long wave gauge	surface elevation	4
wg12	short wave gauge	surface elevation	4
wg13	short wave gauge	surface elevation	4
wg14	short wave gauge	surface elevation	4
pt0	pressure transducer	pressure	4
pt1	pressure transducer	pressure	4
pt2	pressure transducer	pressure	4
pt3	pressure transducer	pressure	4
cam1[b]	camera	video, run-in, run-up	-

[a] direct and/or indirect measurement
[b] variable position depending on recorded variable

4.2.1 The wave velocity formulation

At the very beginning of the laboratory studies, several wave velocity formulations for the generation of the solitary waves and N-waves profiles were considered, according to the water wave theory (Dean and Dalrymple, 1991). For solitary waves, the wave velocity was assumed to be given by Rayleigh's solitary wave solution:

$$c = \sqrt{g \cdot (d + H)}\,, \tag{4.1}$$

where g is the gravity acceleration. The N-wave velocity, being unknown, was initially assumed to be given by the linearised long wave solution:

$$c = \sqrt{g \cdot d}\,. \tag{4.2}$$

For the N-waves, we observed a mismatch between the analytical time series and the observed time series at wave gauge 1 (Lima et al. 2019). We reasoned that the assumption that the N-waves velocity is given by expression (4.2) might not be the most correct. We proposed a further thorough investigation on the formulation of the wave velocity of the N-waves, aiming at a time-dependent wave velocity formulation, as suggested by Malek-Mohammadi and Testik (2010). This type of formulation might lead to an increased accuracy in the obtained N-wave profile.

In the meantime, we performed various solitary wave and N-wave propagation numerical studies for the second stage of the laboratory studies, adopting several different wave velocity formulations for each type of generated wave (SW and NW). This numerical study is briefly described in section 4.2.4.

For the solitary waves, the following wave formulations were considered:

- the wave speed in shallow waters is given by the linear shallow water formulation. In these conditions the wave celerity is
$$c = \sqrt{g \cdot d}\,; \tag{4.3}$$
- the wave celerity for the Rayleigh's solitary wave solution
$$c = \sqrt{g \cdot (d + H)}\,; \tag{4.4}$$
- the wave celerity for the Korteweg-de Vries (KdV), Regularized Long Wave (RLW), Improved Long Wave (ILW) solitary wave solutions (see for instance Dingemans 1997)
$$c = \left(1 + \frac{1}{2} \cdot \epsilon\right) \cdot \sqrt{g \cdot d}\,, \tag{4.5}$$
where $\epsilon = H/d$;
- Boussinesq approximate solution by Yates (1995)
$$c = \sqrt{1 + \epsilon} \cdot \sqrt{g \cdot d}\,; \tag{4.6}$$
- Boussinesq exact solution by Teng and Wu (1992)
$$c = \sqrt{\frac{6 \cdot (1 + \epsilon)^2}{\epsilon^2 \cdot (3 + 2 \cdot \epsilon)} \cdot \left[(1 + \epsilon) \cdot \ln(1 + \epsilon) - \epsilon\right]} \cdot \sqrt{g \cdot d}\,; \tag{4.7}$$
- Euler approximations
  - Laitone (1960), 2nd order
$$c = \left(1 + \frac{\epsilon}{2} - \frac{3}{20} \cdot \epsilon^2\right) \cdot \sqrt{g \cdot d}\,; \tag{4.8}$$
  - Grimshaw (1970), 3rd order
$$c = \left(1 + \frac{\epsilon}{2} - \frac{3}{20} \cdot \epsilon^2 + \frac{3}{56} \cdot \epsilon^3\right) \cdot \sqrt{g \cdot d}\,; \tag{4.9}$$
  - Fenton (1972), 9th order
$$\begin{aligned} c = \Bigg(1 + \epsilon - 0.05 \cdot \epsilon^2 - 0.0428571 \cdot \epsilon^3 - 0.0342857 \cdot \epsilon^4 \\ -0.0315195 \cdot \epsilon^5 - 0.0292784 \cdot \epsilon^6 - 0.0268451 \cdot \epsilon^7 \\ -0.0302634 \cdot \epsilon^8 - 0.0219347 \cdot \epsilon^9\Bigg) \cdot \sqrt{g \cdot d}\,. \end{aligned} \tag{4.10}$$

For the wave celerity of the N-waves, we considered the wave celerity expressions for cnoidal waves:

- KdV, RLW, ILW equations (see for instance Dingemans 1997)
$$c = \left[1 - \frac{1}{2} \cdot \epsilon + \frac{1}{m} \cdot \epsilon \cdot \left(1 - \frac{3}{2} \frac{E(m)}{K(m)}\right)\right] \cdot \sqrt{g \cdot d}, \tag{4.11}$$
where $\epsilon = H/d$, m is the elliptic parameter, $K(m)$ is the complete elliptic integral of the first kind and $E(m)$ is the complete elliptic integral of the second kind.

- Boussinesq approximate solution

  The KdV-RLW-ILW solitary wave velocity expression is a second-order approximation of the Boussinesq's Yate solitary wave expression:

$$\sqrt{1+\epsilon} = 1 + \frac{1}{2}\cdot\epsilon + \mathcal{O}(\epsilon^2). \tag{4.12}$$

  There might exist a solution for a cnoidal Boussinesq wave with the same kind of result.

  Let us assume that

$$c_{cnB} = \sqrt{1-\epsilon+\frac{2}{m}\cdot\epsilon\cdot\left(1-\frac{3}{2}\frac{E(m)}{K(m)}\right)}\cdot\sqrt{g.d}\,. \tag{4.13}$$

  It can be shown that

$$\sqrt{1-\epsilon+\frac{2}{m}\cdot\epsilon\cdot\left(1-\frac{3}{2}\frac{E(m)}{K(m)}\right)} = 1-\frac{1}{2}\cdot\epsilon+\frac{1}{m}\cdot\epsilon\cdot\left(1-\frac{3}{2}\cdot\frac{E(m)}{K(m)}\right)+\mathcal{O}(\epsilon^2). \tag{4.14}$$

  This equation was considered as a possible expression for the cnoidal wave velocity.

For the wave celerity of the N-waves, we also considered expression (4.3) and the following expression:

$$c = \sqrt{g\cdot(d+a^+)}, \tag{4.15}$$

where a^+ is the amplitude of the wave crest of the N-wave.

All these wave formulations expressions were considered as possible alternatives to be adopted for the following physical tests. The wave formulations were tested numerically (section 4.2.4) using the SWASH code (Zijlema et al. 2011) (Appendix B.2). The objective of this analysis was to determine if—for our wave generating model—any of these formulations would lead to a constant shaped wave, i.e. a wave that would propagate keeping its shape. Several authors do not mention the wave celerity formulations adopted in their physical studies (Baldock et al. 2009; Rossetto et al. 2011).

4.2.2 Physical tests 1

The tests described in Lima et al. (2019) (Appendix B.1) were part of the first physical tests, performed to study the generation of solitary waves and N-type waves. A set of five positive solitary waves and six leading depression N-waves (LDN)—with ratio $a^-/a^+ = 0.5$—were generated for a water depth of 26 cm. A 1.50 m wide canal was set-up close to the right-hand side wall of the tank. Six wave gauges were placed along the canal and an additional wave gauge was installed for control purposes (Table 2 and Figure 6 in Lima et al. 2019). The experimental free surface elevations of the generated wave profiles were recorded at the installed wave gauges. The characteristics of the five generated solitary waves are detailed in Table 4.2. The piston trajectories for the generation of the solitary waves are plotted in Figure 4.1. For the tested N-wave cases, please refer to Table 3 from Lima et al. (2019). Wave parameters of the generated N-waves are presented in Table 4.3, where δ is the eccentricity parameter, λ is the apparent wavelength and ε is the scale

Table 4.2: Wave conditions and wave-maker parameters for the 5 generated solitary waves.

Wave	d (m)	H (m)	λ (m)	T (s)	S (m)	τ (s)	ϵ (—)	σ (—)	St (—)
C6	0.26	0.155	2.640	1.31	0.50	2.87	0.60	0.62	1.56
C7	0.26	0.070	5.845	3.25	0.50	6.78	0.27	0.28	3.45
C8	0.26	0.050	4.302	2.47	0.26	5.09	0.19	0.38	1.33
C9	0.26	0.125	2.721	1.40	0.42	3.02	0.48	0.60	1.33
C10	0.26	0.175	2.299	1.11	0.49	2.47	0.67	0.71	1.33

factor. Piston trajectories for the generation of the N-waves are plotted in Figure 7 in Lima et al. (2019).

The generation and results for the 5 leading depression N-waves are described in Lima et al. (2019). Please refer to Goring (1978) and Goring and Raichlen (1980) for the principles of the generation of the solitary waves. Wave velocity formulations (4.4) and (4.3) were adopted for the solitary waves and N-waves respectively.

Table 4.3: Parameters used to generate N-waves time series.

δ/λ	ε
0.04254	-1.079

The analytical time series (TS) for solitary wave profiles and experimental wave profiles recorded at wave gauge wg1 are represented in Figure 4.2, for C6, C7 and C8, and in Figure 4.3 for C9 and C10.

For the solitary waves tests, it was observed at wave gauge 1 (wg1, placed right after the wave-maker) that the wave height was 17% less than the wave height of the expected wave height provided to the wave-maker. This difference increased with increasing distance from the wave-maker.

For the N-waves tests (Lima et al. 2019), we observed a mismatch between the generated N-wave profile and the provided N-wave time series at wg1. In the following wave gauges, the wave started assuming the shape of a solitary wave, with an increasing wave crest amplitude and a decreasing wave trough amplitude. In the beginning, we hypothesized that the mismatch could be due to the fact that: (1) the equation used to described the N-wave profile was not a good solution for this wave; (2) the bottom friction effects were relevant for this water depth. At a later stage, we proposed that the possible explanations for the obtained results might be due to the fact that the used wave celerity was not correct. We also considered that the wave amplitude in our experiments was too high, meeting Goring's observations for the solitary waves, that stated that the relation between the amplitude and the water depth should not exceed 0.1.

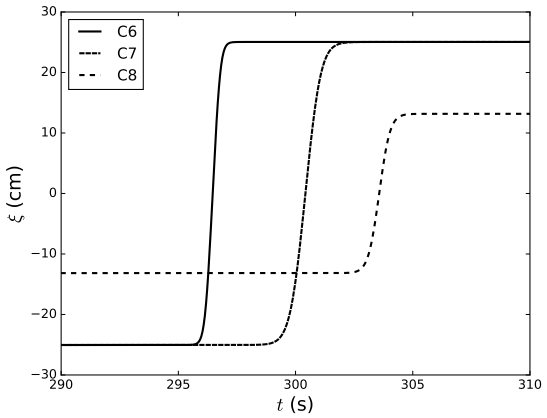

(a) C6, C7, C8

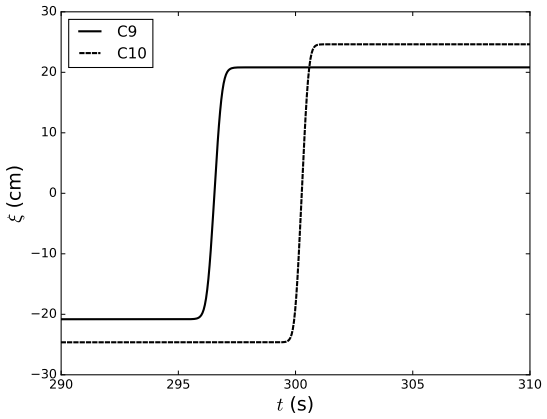

(b) C9, C10

Figure 4.1: Piston trajectories for the generation of the solitary waves.

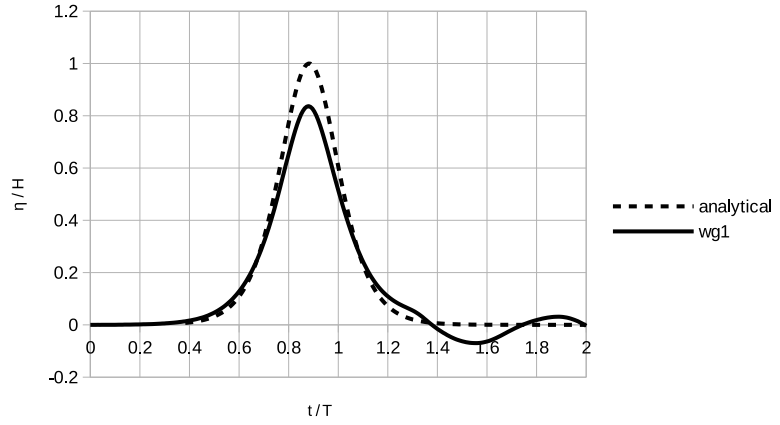

(a) C6

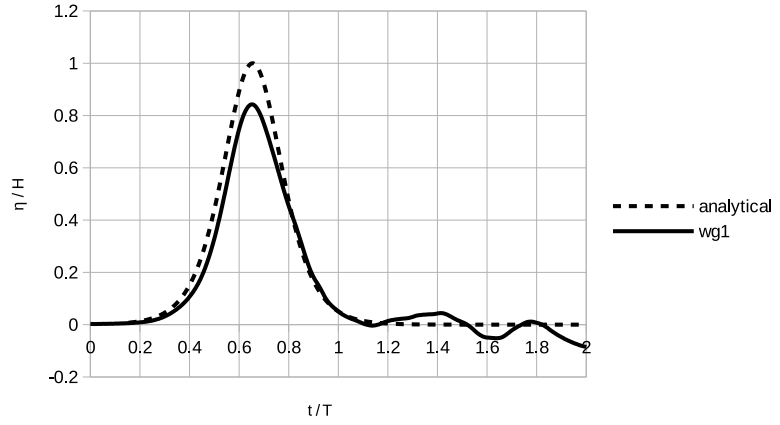

(b) C7

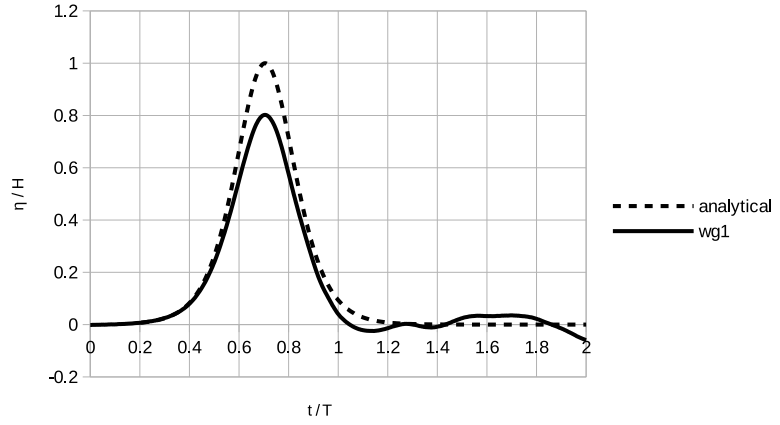

(c) C8

Figure 4.2: Analytical TS for solitary wave profiles and experimental wave profiles recorded at wave gauge wg1.

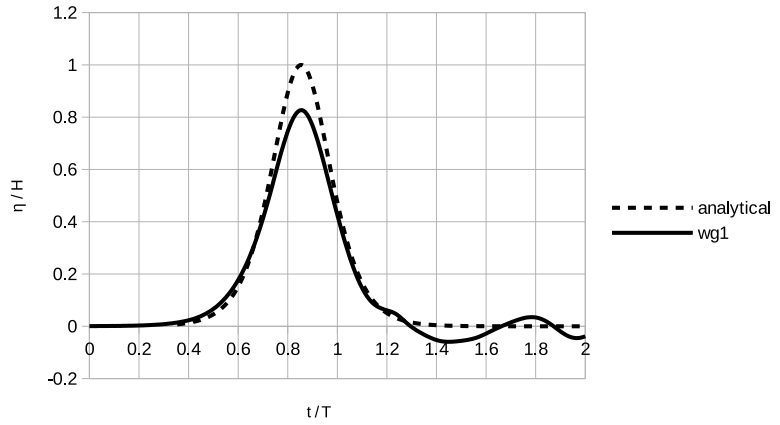

(a) C9

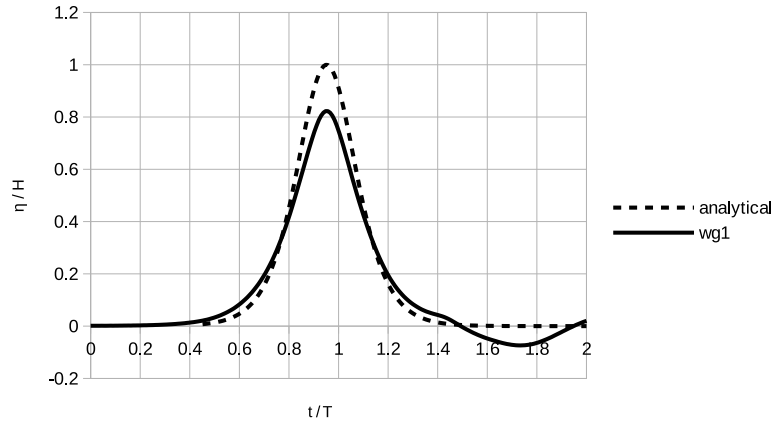

(b) C10

Figure 4.3: Analytical TS for solitary wave profiles and experimental wave profiles recorded at wave gauge wg1.

4.2.3 Physical tests 2

A second set of tests was performed in a canal 75 cm wide and 10 m long, for 25 cm water depth. Four gauges were placed within the first 4 m of canal length (Table 4.4) and the free surface elevation was retrieved for each wave gauge. Five solitary waves with wave heights between 6 and 15.5 cm and four N-waves with wave heights between 6 and 12 cm were generated. The characteristics of the generated waves are detailed in Table 4.5.

Table 4.4: Wave gauge positions for physical tests 2.

wave gauges (wg)	x (m)	y (m)
4	1.030	0.375
5	1.680	0.375
7	2.835	0.375
8	3.980	0.375

Table 4.5: Wave conditions and wave-maker parameters for the generated solitary and N-waves.

Wave	d (m)	H (m)	λ (m)	T (s)	S (m)	τ (s)	ϵ (—)	σ (—)	St (—)
C6	0.25	0.155	2.534	1.27	0.50	2.794	0.62	0.62	1.613
C201	0.25	0.060	6.545	3.75	0.50	7.796	0.24	0.24	4.167
C202	0.25	0.090	4.363	2.39	0.50	5.054	0.36	0.36	2.778
C203	0.25	0.120	3.272	1.63	0.50	3.700	0.48	0.48	2.083
C204	0.25	0.150	2.618	1.25	0.50	2.897	0.60	0.60	1.667
C13	0.25	0.085	9.628	6.03	0.50	6.340	0.34	0.16	12.772
C301	0.25	0.060	11.223	6.62	0.50	9.128	0.24	0.14	12.253
C302	0.25	0.090	7.482	4.26	0.50	5.969	0.36	0.21	8.168
C303	0.25	0.120	5.612	3.09	0.50	4.401	0.48	0.28	6.126

Table 4.6: Parameters used to generate the N-waves time series.

δ/λ	ε
0.05629	-1.05245

The parameters used to generate the N-waves are listed in Table 4.6, where δ is the eccentricity parameter, λ is the apparent wavelength and ε is the scale factor.

Analyzing the results obtained for both solitary and N-wave tests (which are not plotted in the thesis), we observed that the wave height at wg1 was lower and differed more than 25% from the original wave height intended. The difference increased with the increase of the wg distance from the wave-maker. This was frequent for most of the wave tests. We concluded that this could be a consequence of the theoretical formulation found for the generation of the N-waves using a piston-type wavemaker (Lima et al. 2019), which is limited by the fact that, as pointed out by Synolakis (1990), during the generation phase the wave is not of permanent form, as it is still evolving. Also, Goring's method is limited to waves with a low height-to-depth ratio. Additionally, the canal width used in the tests was too small for the aimed wave conditions, with contributions of the frictional effects of the walls, that became dominant in the fluid flow, therefore contaminating the retrieved measurements.

4.2.4 Computational tests using SWASH

To overcome the problems and mismatches detected in the physical tests of the generation of solitary waves and leading depression N-waves, mainly in terms of wave heights and wave shape generated, several computational tests using different wave velocity formulations were performed, separately for both solitary and N-waves respectively. The SWASH code (Appendix B.2) by Zijlema et al. (2011) was used for this purpose. Physical tests 1 were simulated with SWASH for two wave cases: solitary wave C6 and N-wave C13 (Lima et al. 2019). The generated solitary waves were positive shaped. The N-waves generated were leading depression (LDN) type and several a^-/a^+ ratios were tried with SWASH. The best results were obtained with the ratio $a^-/a^+ = 0.4$, which means that $H = 1.4 \times a^+$, which was adopted for the N-waves. A numerical domain with 60 m length, grid size of 0.1 m and time step of 0.01 s were used. The velocity time series determined from equation (13) from Lima et al. (2019) was used as input condition to the code. It was determined in accordance with the wave type tested and velocity formulations selected. The Sommerfeld or radiation condition was imposed at the eastern boundary of the domain.

Several computational tests were performed with SWASH, using different wave velocity formulations, separately for both solitary and N-waves respectively. For the generation of the solitary waves, numerical simulations applying respectively the wave velocity formulations (4.6), (4.7) and (4.10) were performed. For the propagation of N-waves, computation of wave profiles using wave velocity formulations (4.3), (4.11) and (4.15), proposed in the literature for solitary, cnoidal and N-waves, were analysed.

As a result from this wave velocity formulation study, we found that the computational results which best fitted the analytical profiles were achieved applying wave velocity expression (4.6) for the solitary waves velocity (Figure 4.4) and expression (4.15) for the N-waves (Figure 4.5). We found these formulations to better preserve the simulated wave shape during the simulation, when comparing with tests performed using the other mentioned wave velocity formulations.

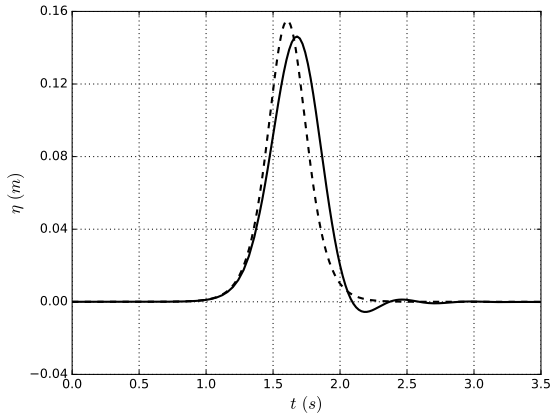

(a)

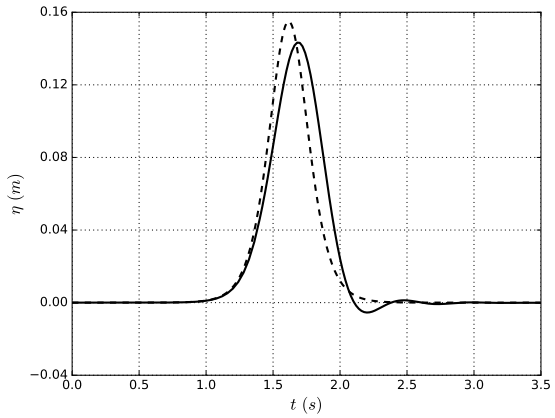

(b)

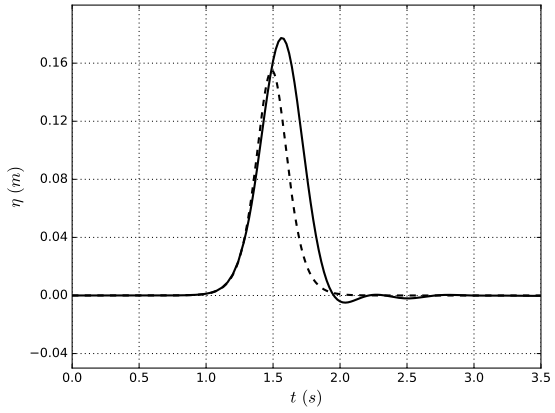

(c)

Figure 4.4: Analytical TS (- -) and computational time series (—) at the wave-maker for solitary wave C6, applying wave velocity formulation (a) expression (4.6), (b) expression (4.7) and (c) expression (4.10).

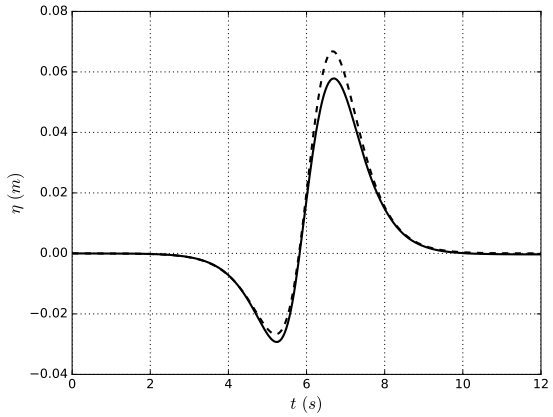

(a)

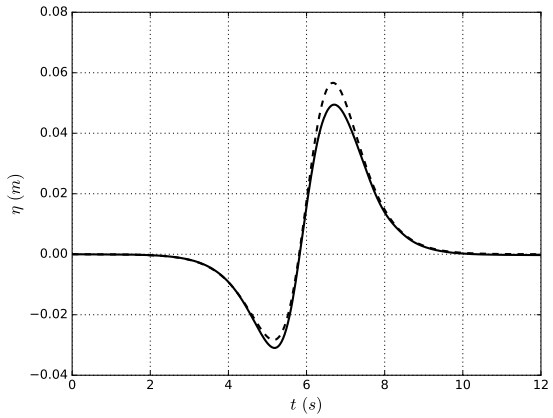

(b)

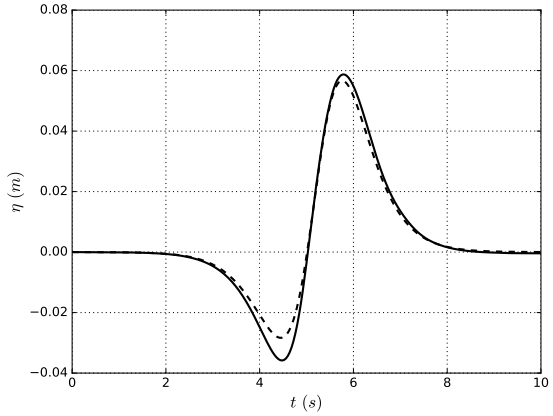

(c)

Figure 4.5: Analytical TS (- -) and computational time series (—) at the wave-maker for N-wave C13, applying wave velocity formulation (a) expression (4.11), (b) expression (4.13) and (c) expression (4.15).

4.3 Physical tests (second stage)

Propagation and transformation of solitary and N-waves

4.3.1 Physical experiments without canal (Set A)

For the experiments with constant water depths of 25 and 50 cm, the 16 paddles of the wave generation system were activated. Let us define this set of experiments without canal and without beach as set A. The experiments with 25 cm water depth are refered as subset A25 and the experiments with 50 cm water depth are refered as subset A50.

A set of four wave gauges (Table 4.7) were installed on tripods and fixed on the basin floor (Figures 4.6, 4.7 and 4.8). We placed three wave gauges 1.30 m away from the wave-maker, 5.25 m apart from each other. A fourth wave gauge wg6 was placed behind wg1/wg5, distanced 1.20 m from it, for control purposes.

The wave cases listed in Table 4.10 were generated for 25 and 50 cm water depths. The measurements time series were acquired and recorded by the HRW software program. Data sets retrieved for wave gauge 5 presented variable quality. The connection of this wave gauge to the board was found to acquire data with a rather large amount of noise, which affected the overall quality of some data sets measurements. Nevertheless, the data sets for wave gauge 5 are presented in this study.

Table 4.7: Location of the instrumentation within the wave basin, for the set A experiments.

Device[1]	x (m)	y (m)
wg1/wg5[2]	1.30	0.75
wg3	1.30	11.25
wg4	1.30	6.00
wg6	2.50	0.75

[1] wg: wave gauge

[2] Problems were detected in wg5, which was later replaced by wg1, at the exact same location.

Figure 4.6: Wave basin at the LH-FEUP. Setting of the wave gauges used in the set A experiments.

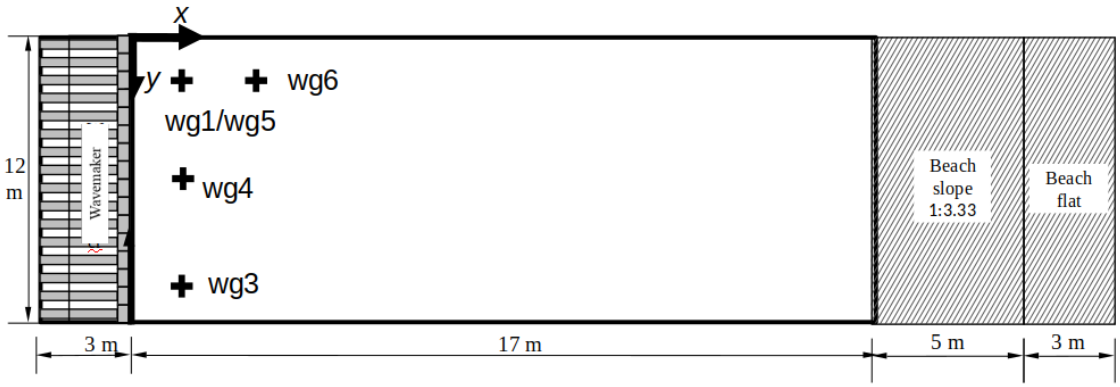

Figure 4.7: Scheme of the wave basin and wave gauges positioning (+: wave gauges) for the set A experiments.

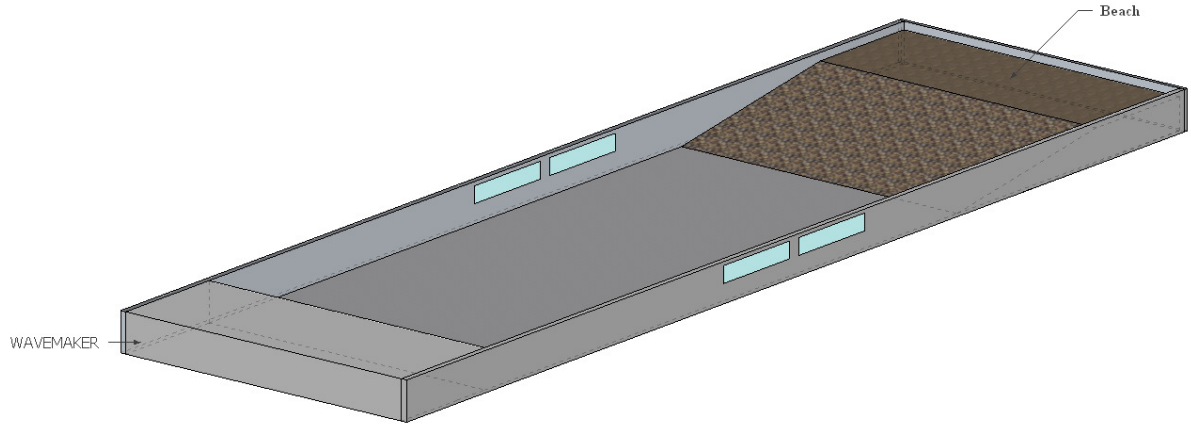

Figure 4.8: Scheme of the LH-FEUP wave basin, 28 m long (working length), 12 m wide and with a maximum water depth of 1.20 m.

4.3.2 Plane slope physical experiments (with beach) (Set B)

A canal with 1.5 m width was built inside the wave basin, limited on one side by a perspex wall along the tank and by its side wall (Figures 4.9 and 4.10). A beach composed by two slopes with 1:15 and 1:30 respectively was assembled along the canal (Figure 4.10). This beach is composed by one flat 5 m long section, starting right after the wave-maker, followed by a 1:15 plane slope (angle β_1 = 3.81°) with 3.75 m of length and a second plane slope (angle β_2 = 1.91°) with 7.5 m of length and 1:30 plane slope. For the experiments inside the canal, only 2 wave-maker paddles were activated. The limiting plexiglass wall was extended up to the paddles. Let us define this set of experiments with canal and with beach as set B. The experiments with 25 cm water depth are refered as subset B25 and the experiments with 50 cm water depth are refered as subset B50.

Several sets of experiments (76) were performed for the two water depth levels of 25 cm (Figures 4.11 and 4.12, Table 4.8) and 50 cm (Figures 4.13 and 4.14, Table 4.9). The wave cases, detailed in Table 4.10, were generated and the time series measurements were acquired and recorded.

For the 50 cm water depth experiments, an obstacle was installed at the end of the second slope, with dimensions 1.5 m wide, 0.5 m high and 8 mm thick.

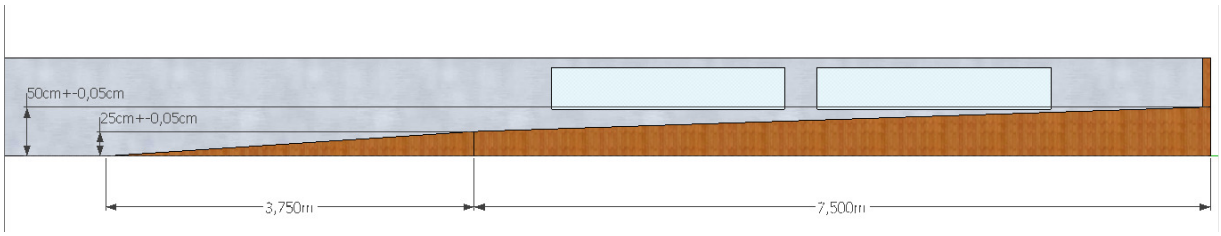

Figure 4.9: 25 cm and 50 cm water depth levels used in set B experiments, corresponding to the end of each slope.

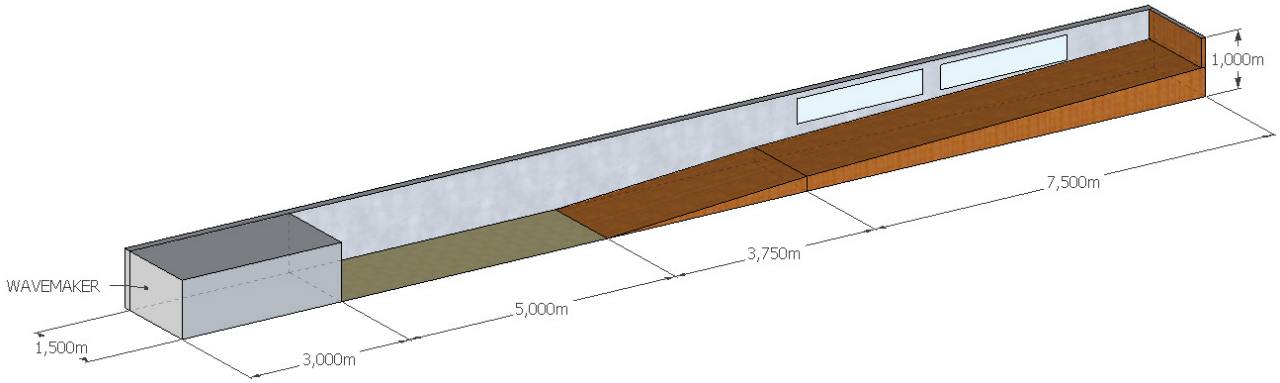

Figure 4.10: Scheme of the beach profile assembled inside the wave basin, in a canal 1.5 m wide, composed by a flat 5 m section and 2 slopes with slopes 1:15 and 1:30 respectively.

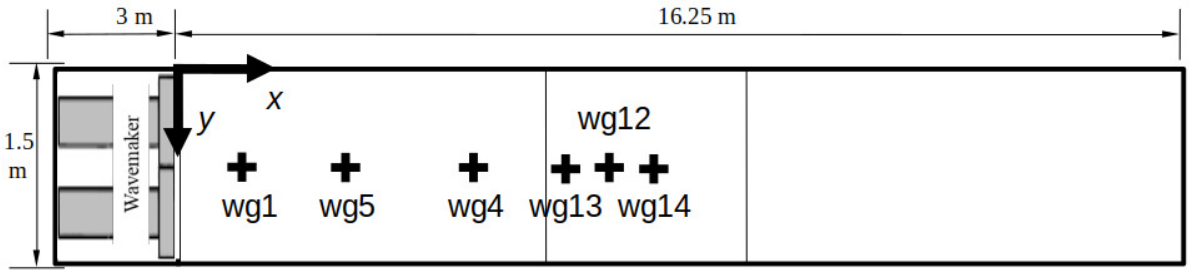

Figure 4.11: Scheme of the wave gauges positioning inside the 1.5 m wide canal, for the subset B25 experiments (+: wave gauges).

Table 4.8: Location of the instrumentation used, positioned along the assembled beach (subset B25 experiments).

Device	x (m)	y (m)
wg1	1.30	0.75
wg5	2.60	0.75
wg4	4.30	0.75
wg13	5.37	0.75
wg12	6.00	0.75
wg14	6.24	0.75

Figure 4.12: Wave gauges setting for the subset B25 experiments.

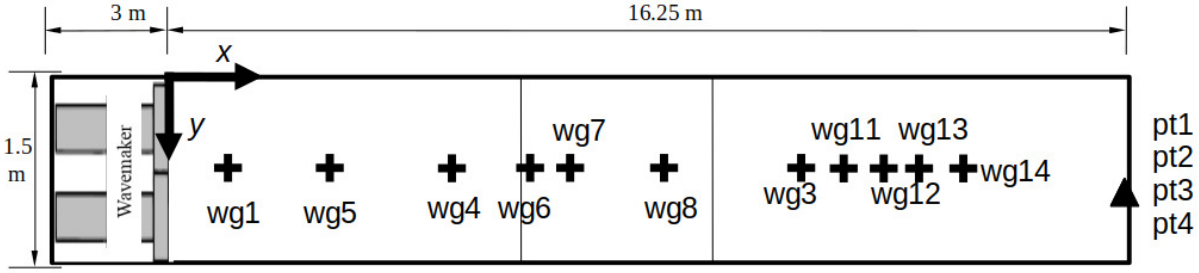

Figure 4.13: Scheme of the instrumentation positioning inside the 1.5 m width canal, for the subset B50 experiments (+: wave gauges; Δ: pressure transducers).

Table 4.9: Location of the instrumentation used, positioned along the assembled beach (subset B50 experiments).

Device [1]	x (m)	y (m)	z^2 (cm)	Δz^3 (cm)
wg1	1.30	0.75	14.00	—
wg5	2.50	0.75	14.00	—
wg4	4.30	0.75	11.00	—
wg6	5.10	0.75	—	17.01
wg7	5.95	0.75	—	14.06
wg8	7.20	0.75	—	13.15
wg3	9.90	0.75	—	38.83
wg11	10.95	0.75	—	35.83
wg12	11.30	0.75	—	32.33
wg13	11.60	0.75	—	33.33
wg14	11.95	0.75	—	33.33
pt0	16.25	0.75	—	52.00
pt1	16.25	0.75	—	55.00
pt2	16.25	0.75	—	58.00
pt3	16.25	0.75	—	61.00

[1]wg: wave gauge; pt: pressure transducer.
[2]Measured from the wave basin floor to the zero calibration position of the wg.
[3]Measured from the beginning of the first slope and along the slope to the zero calibration position, in the case of the wg, and to the pressure transducer position, in the case of the pt.

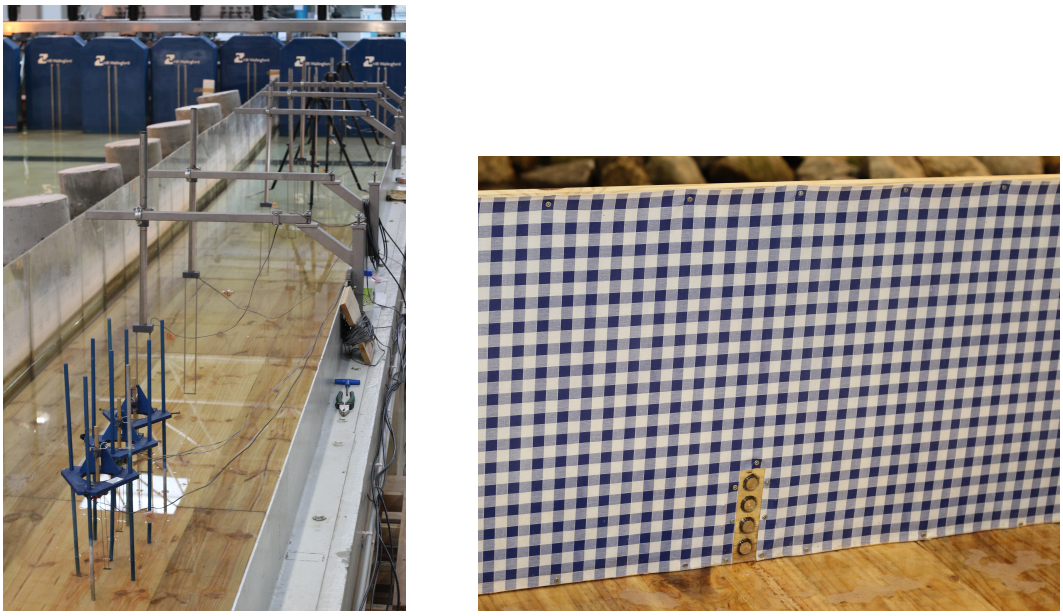

(a) (b)

Figure 4.14: Subset B50 experiments: (a) Wave gauges setting along the canal. (b) Pressure transducers in the rectangular obstacle. From bottom to top: pt0, pt1, pt2, pt3.

For set B experiments, a maximum of eight long wave gauges were installed on fixed arms and mounted on the side wall of the wave basin. Three short wave gauges were installed on small tripods, to measure data in reduced water depth (Figures 4.13 and 4.14). During the experiments, it was visually observed that the short wave gauges were slightly moved away from their original

position, specifically for waves with wave heights equal or larger than 15 cm. We were aware that this aspect could affect the acquired measurements; to account for spurious effects in the wave gauges measurements, wave gauges 11 and 13 were installed. Experiments for which run-in, R_{in}, and run-up, R_{up}, measurements were considered to be relevant were video recorded, with a Canon EOS 600D camera. Nevertheless, due to the lack of disk space, only a maximum of two trials were recorded for each wave case experiment.

Taking advantage of a measuring system appended to the bottom surfaces of the slopes (Figure 4.14), we used the camera to record the run-in distances reached by each generated wave. These measurements were taken for the experiments performed for a water depth of 25 cm (subset B25).

For subset B50 experiments, we used four HRW water gauge pressure transducers, with 0 to 2 m (0 to 20kPa) operating range, attached to an obstacle located at the end of the beach (cf. Figures 4.13 and 4.14, with locations in Table 4.9). The goal was to measure the pressure impact of the generated waves on the obstacle. The pressure transducers were connected to a unit linked to a computer with the software program for data acquisition. The pressure measurements were visualized live, by means of a continuous plot. As the experiments occurred, the measurements were treated and registered by the Tracer DAQ software. Additionally, a camera was installed and mounted on the side walls, with variable positioning, to record the run-up of the generated waves on the obstacle.

4.3.3 Definition of wave conditions

We defined a set of solitary waves and N-waves—specifically leading depression N-waves—, to be generated in the laboratory. The wave heights varied between 6 and 24 cm, for water depths of 25 cm and 50 cm and for piston strokes between 0.25 m and 1.00 m. Wave characteristics and wave-maker parameters are presented in Table 4.10. For each wave case and several bathymetric settings defined (Tables 4.7, 4.8 and 4.9) three or more trials were performed and data was acquired and recorded. To guarantee initial still water conditions—which was checked through visual observation—, the trials were separated by 10 to 15 min, depending on the water depths and/or generated wave heights.

The generated solitary waves were positive shaped. The generated N-waves were leading depression (LDN) type, with ratio $a^-/a^+ = 0.4$, which means that $H = 1.4 \times a^+$ (section 4.2.4). This ratio was found to present the best fitting results both in the preliminary experimental tests and the numerical tests.

For the solitary wave velocity formulation, we used the definition by Yates (1995), expression (4.6). We assumed the N-wave velocity to be given by expression (4.15). In the previous expressions g, which is the local acceleration due to gravity, was considered to be equal to 9.803 m/s^2 (calculated locally).

We represent the time series of the piston wave-maker trajectories for waves C6 and C13 in Figure 4.15, for waves C203 in Figure 4.16 and for waves C303 in Figure 4.17.

Table 4.10: Wave conditions used in the experiments and wave-maker control parameters.

Wave	Type	H (m)	d (m)	c (m/s)	λ (m)	T (s)	S (m)	ϵ (–)	σ (–)	St (–)
C6a	SW*	0.155	0.25	1.99	2.534	1.27	0.50	0.62	0.62	1.61
C6b	SW	0.155	0.50	2.53	5.067	2.00	0.50	0.31	0.62	0.81
C201a	SW	0.060	0.25	1.74	6.545	3.75	0.50	0.24	0.24	4.17
C201b	SW	0.060	0.25	1.74	9.817	5.63	0.75	0.24	0.16	9.38

*solitary wave

C201c	SW	0.060	0.25	1.74	13.09	7.51	1.00	0.24	0.12	16.67
C201d	SW	0.060	0.50	2.34	13.09	5.59	0.50	0.12	0.24	2.08
C201e	SW	0.060	0.50	2.34	19.64	8.38	0.75	0.12	0.16	4.69
C201f	SW	0.060	0.50	2.34	26.18	11.17	1.00	0.12	0.12	8.33
C202a	SW	0.090	0.25	1.83	4.363	2.39	0.50	0.36	0.36	2.78
C202b	SW	0.090	0.25	1.83	6.545	3.59	0.75	0.36	0.24	6.25
C202c	SW	0.090	0.25	1.83	8.727	4.78	1.00	0.36	0.18	11.11
C202d	SW	0.090	0.50	2.40	8.727	3.63	0.50	0.18	0.36	1.39
C202e	SW	0.090	0.50	2.40	13.090	5.44	0.75	0.18	0.24	3.13
C202f	SW	0.090	0.50	2.40	17.453	7.26	1.00	0.18	0.18	5.56
C203a	SW	0.120	0.25	1.90	3.272	1.72	0.50	0.48	0.48	2.08
C203b	SW	0.120	0.25	1.90	4.909	2.58	0.75	0.48	0.32	4.69
C203c	SW	0.120	0.25	1.90	6.545	3.44	1.00	0.48	0.24	8.33
C203d	SW	0.120	0.50	2.47	6.545	2.65	0.50	0.24	0.48	1.04
C203e	SW	0.120	0.50	2.47	9.817	3.98	0.75	0.24	0.32	2.34
C203f	SW	0.120	0.50	2.47	13.090	5.31	1.00	0.24	0.24	4.17
C204a	SW	0.150	0.25	1.98	3.927	1.98	0.75	0.60	0.40	3.75
C204b	SW	0.150	0.25	1.98	5.236	2.64	1.00	0.60	0.30	6.67
C204c	SW	0.150	0.50	2.52	7.854	3.11	0.75	0.30	0.40	1.88
C204d	SW	0.150	0.50	2.52	10.472	4.15	1.00	0.30	0.40	3.33
C205a	SW	0.180	0.25	2.05	3.272	1.59	0.75	0.72	0.48	3.13
C205b	SW	0.180	0.25	2.05	4.363	2.13	1.00	0.72	0.36	5.56
C205c	SW	0.180	0.50	2.58	6.545	2.54	0.75	0.36	0.48	1.56
C205d	SW	0.180	0.50	2.58	8.727	3.38	1.00	0.36	0.36	2.78
C206a	SW	0.210	0.25	2.12	2.805	1.32	0.75	0.84	0.56	2.68
C206b	SW	0.210	0.25	2.12	3.740	1.76	1.00	0.84	0.42	4.76
C206c	SW	0.210	0.50	2.64	5.610	2.13	0.75	0.42	0.56	1.34
C206d	SW	0.210	0.50	2.64	7.480	2.84	1.00	0.42	0.56	2.38
C207a	SW	0.240	0.25	2.19	2.454	1.12	0.75	0.96	0.64	2.34
C207b	SW	0.240	0.25	2.19	3.272	1.49	1.00	0.96	0.48	4.17
C207c	SW	0.240	0.50	2.69	4.909	1.82	0.75	0.48	0.64	1.17
C207d	SW	0.240	0.50	2.69	6.545	2.43	1.00	0.48	0.48	2.08
C13a	NW[†]	0.085	0.25	1.81	7.923	4.37	0.50	0.34	0.20	8.65
C13b	NW	0.085	0.50	2.34	15.846	6.76	0.50	0.17	0.20	4.33
C301a	NW	0.060	0.25	1.74	5.612	3.22	0.25	0.24	0.28	3.06
C301b	NW	0.060	0.25	1.74	11.224	6.44	0.50	0.24	0.14	12.25
C301c	NW	0.060	0.50	2.31	11.224	4.87	0.25	0.12	0.28	1.53
C301d	NW	0.060	0.50	2.31	22.449	9.73	0.25	0.12	0.14	6.13
C302a	NW	0.090	0.25	1.83	3.741	2.05	0.25	0.36	0.42	2.04
C302b	NW	0.090	0.25	1.83	7.483	4.10	0.50	0.36	0.21	8.17
C302c	NW	0.090	0.25	1.83	11.224	6.15	0.75	0.36	0.14	18.38
C302d	NW	0.090	0.25	1.83	14.966	8.20	1.00	0.36	0.10	32.68
C302e	NW	0.090	0.50	2.35	7.483	3.18	0.25	0.18	0.42	1.02
C302f	NW	0.090	0.50	2.35	14.966	6.36	0.50	0.18	0.21	4.08
C302g	NW	0.090	0.50	2.35	22.449	9.54	0.75	0.18	0.14	9.19
C302h	NW	0.090	0.50	2.35	29.932	12.73	1.00	0.18	0.10	16.339
C303a	NW	0.120	0.25	1.90	5.612	2.95	0.50	0.48	0.28	6.13
C303b	NW	0.120	0.25	1.90	8.418	4.42	0.75	0.48	0.19	13.79

[†]N-wave

C303c	NW	0.120	0.25	1.90	11.224	5.89	1.00	0.48	0.14	24.51
C303d	NW	0.120	0.50	2.40	11.224	4.68	0.50	0.24	0.28	3.06
C303e	NW	0.120	0.50	2.40	16.836	7.03	0.75	0.24	0.19	6.893
C303f	NW	0.120	0.50	2.40	22.449	9.37	1.00	0.24	0.14	12.25
C304a	NW	0.150	0.25	1.98	4.490	2.27	0.50	0.60	0.35	4.90
C304b	NW	0.150	0.25	1.98	6.735	3.40	0.75	0.60	0.23	11.03
C304c	NW	0.150	0.25	1.98	8.979	4.53	1.00	0.60	0.17	19.61
C304d	NW	0.150	0.50	2.44	8.979	3.68	0.50	0.30	0.35	2.45
C304e	NW	0.150	0.50	2.44	13.469	5.52	0.75	0.30	0.23	5.51
C304f	NW	0.150	0.50	2.44	17.959	7.36	1.00	0.30	0.17	9.80
C305a	NW	0.180	0.25	2.05	3.741	1.82	0.50	0.72	0.42	4.08
C305b	NW	0.180	0.25	2.05	5.612	2.73	0.75	0.72	0.28	9.19
C305c	NW	0.180	0.25	2.05	7.483	3.64	1.00	0.72	0.21	16.34
C305d	NW	0.180	0.50	2.48	7.483	3.01	0.50	0.36	0.42	2.04
C305e	NW	0.180	0.50	2.48	11.224	4.52	0.75	0.36	0.28	4.60
C305f	NW	0.180	0.50	2.48	14.966	6.03	1.00	0.36	0.21	8.17
C306a	NW	0.210	0.25	2.12	4.810	2.27	0.75	0.84	0.33	7.88
C306b	NW	0.210	0.25	2.12	6.414	3.02	1.00	0.84	0.24	14.01
C306c	NW	0.210	0.50	2.52	9.621	3.81	0.75	0.42	0.33	3.94
C306d	NW	0.210	0.50	2.52	12.828	5.08	1.00	0.42	0.24	7.00
C307a	NW	0.240	0.25	2.19	4.209	1.92	0.75	0.96	0.37	6.89
C307b	NW	0.240	0.25	2.19	5.612	2.56	1.00	0.96	0.28	12.25
C307c	NW	0.240	0.50	2.57	8.418	3.28	0.75	0.48	0.37	3.45
C307d	NW	0.240	0.50	2.57	11.224	4.38	1.00	0.48	0.28	6.13

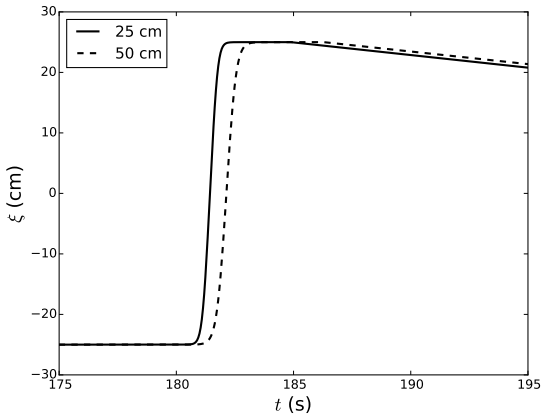

(a) C6

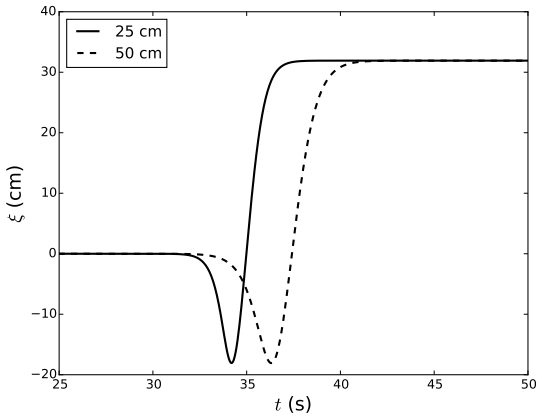

(b) C13

Figure 4.15: Piston trajectories for the generation of solitary wave C6 (a) and LDN-wave C13 (b), with a 0.50 m stroke, for water depths of 25 and 50 cm.

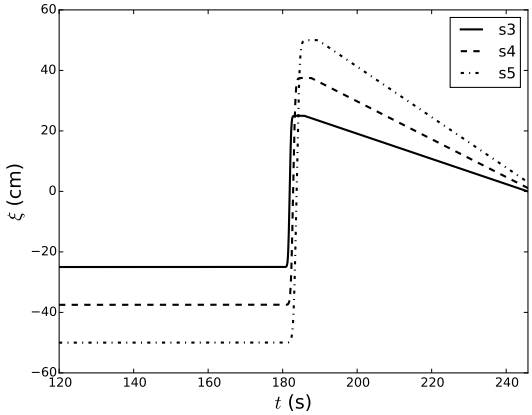

(a) d = 25 cm

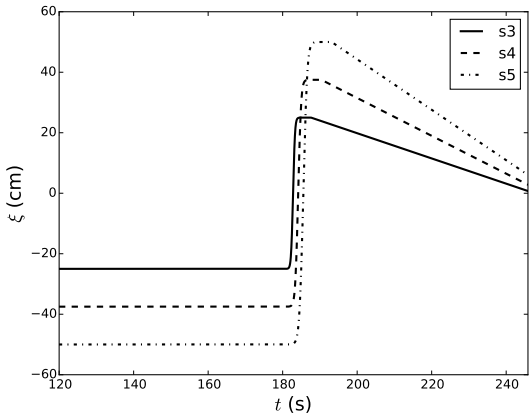

(b) d = 50 cm

Figure 4.16: Piston trajectories for the generation of solitary wave C203, for strokes of 0.50 m (s3), 0.75 m (s4) and 1.00 m (s5).

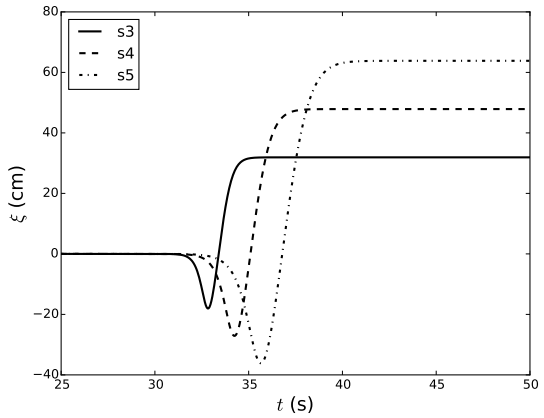

(a) d = 25 cm

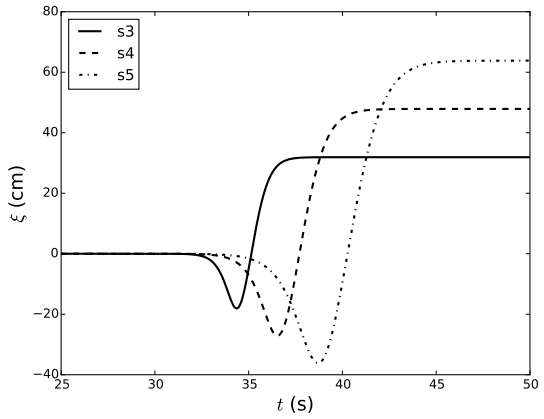

(b) d = 50 cm

Figure 4.17: Piston trajectories for the generation of LDN-wave C303, for strokes of 0.50 m (s3), 0.75 m (s4) and 1.00 m (s5).

4.3.4 Computational experiments using olaFlow

The computational domain for the olaFlow numerical tests is a replication of the laboratory wave canal (Figures 4.9 and 4.10). A 2DV model is used and the computational domain is set into 3 blocks specified inside a blockMeshDict file. The first block corresponds to the first 5 m of the canal (which is flat); the second block corresponds to the first slope, which, for the simulations of the 25 cm water depth experiments, is covered with water; the third block corresponds to the second slope, that has no water (totally dry). For the simulations of the 50 cm water depth experiments, both slopes, and therefore the simulation blocks, are covered with water.

An additional geometric feature was set, in STL format, at the end of the second slope, representing the vertical obstacle assembled at the end of the beach (Figures 4.9 and 4.10). The dimensions of the STL are equal to those of the vertical obstacle (section 4.3.2).

The number of cells in the x direction is 200 and 50 in the z direction. The applied boundary condition uses the wave type wavemaker with the wavemakerMovementDict dictionary; for that purpose, a wavemakerMovement.txt file (Appendix A.3.2.2) is created beforehand and used in the simulations. The file is composed by a time series with the data for the several paddle positions and the free surface elevation at each paddle position (see wave theory txeta in Chapter 3, section 3.4.5). The blockMeshDict definition is detailed in Table 4.11 and the boundary conditions are listed in Table 4.12. The RANS modelling computations are performed for a total run time of 15 s and a time step of 0.001 s, which takes about a total run time of 20 min for a serial computation.

To numerically simulate phenomena such as the wave breaking and the wave structure impact of the generated waves, turbulence was turned on in the numerical simulations performed with olaFlow. OpenFOAM does not provide by default incompressible turbulence models for multiphase systems—i.e. models that take into account the density variation between the air and water phases (Higuera 2019)—which, as the simulation progresses, often causes excessive wave height damping (due to the increasing *nut*, which is the turbulent viscosity, ν_t, field), caused by the turbulence build-up (Higuera 2019).

The olaFlow library with the modified $\kappa - \varepsilon$ and $\kappa - \omega$ turbulence models enables the code to more accurately simulate multiphase systems. Additionally, there is a modified $\kappa - \omega$ turbulence model, based on the work by Devolder et al. (2017), to more correctly model surface waves, featuring an additional buoyancy term to eliminate spurious turbulence generation at the waves free surface. Devolder et al. (2017) explained that the $\kappa - \varepsilon$ and $\kappa - \omega$ turbulence models caused more wave damping over the wave flume length and therefore implemented a modified turbulence model, the $\kappa - \omega$ SST model, in OpenFOAM. Thus, this was the turbulence model selected to use in the simulations.

Table 4.11: Definition of blockMeshDict (bMD).

boundaryField	bMD
inlet	patch
outlet	wall
frontAndBack	empty
bottom	wall
atmosphere	patch

Table 4.12: Boundary conditions for the olaFlow simulations (0.org folder).

boundaryField	alpha.water	prgh	U
inlet	zeroGradient	fixedFluxPressure	movingWallVelocity
outlet	zeroGradient	fixedFluxPressure	waveAbsorption2DVelocity
obstaculo	zeroGradient	fixedFluxPressure	fixedValue
bottom	zeroGradient	fixedFluxPressure	fixedValue
atmosphere	inletOutlet	totalPressure	pressureInletOutletVelocity

4.4 Results and Discussion

We consider the solitary waves and leading depression N-waves experiments performed in the LH-FEUP wave tank (Figure 4.7), with the physical model of a beach composed by two slopes, respectively with 1:15 and 1:30 (Figures 4.8 and 4.9) (Set B), for 2 water levels of 25 and 50 cm (subset B25 and B50 respectively).

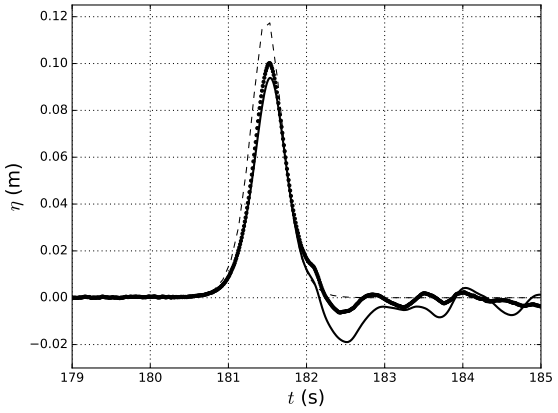

(a)

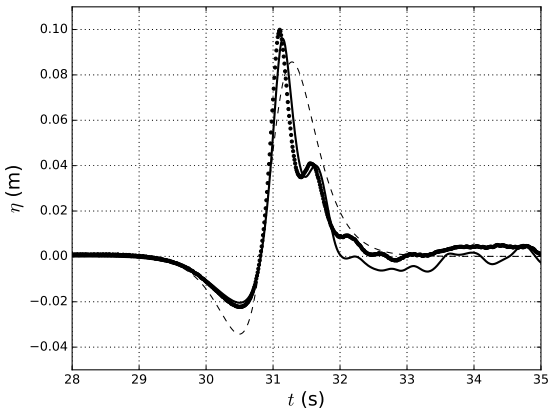

(b)

Figure 4.18: Comparing results at wg1/wg5 for experimental (a) SW C203 (b) NW C303 (stroke 50 cm), for set A (—), set B (○) and analytical TS (- -) (25 cm water depth).

For set A experiments (Figure 4.7 and Table 4.7), comparison for the same wave gauge is

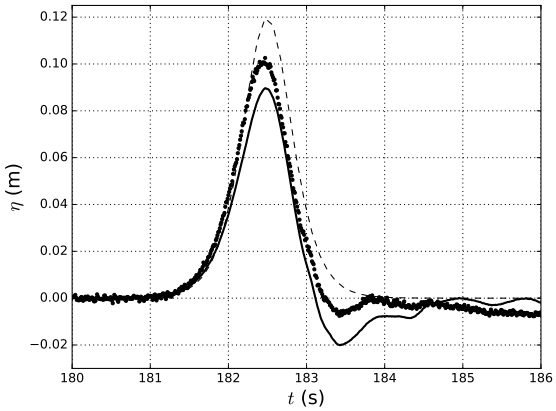

(a)

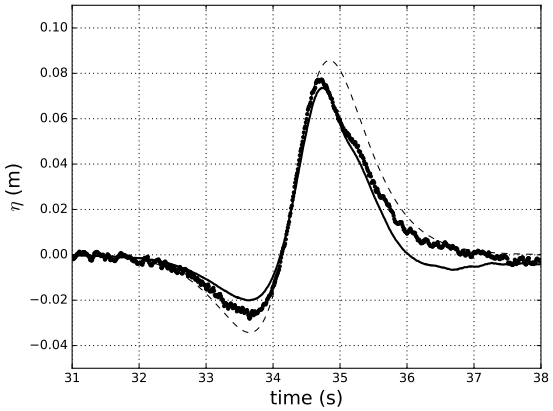

(b)

Figure 4.19: Comparing results at wg1/wg5 for experimental (a) SW C203 (b) NW C303 (stroke 50 cm), for set A (—), set B (○) and analytical TS (- -) (50 cm water depth).

presented, for wave cases C203 and C303 (solitary and N-wave with H = 12 cm respectively) in Figure 4.18 and Figure 4.19 respectively, plotting also the theoretical time series (TS). It was found that there is a more pronounced difference for the SW at 50 cm water depth. Noise at wg5 was predominant in these measurements, with a distinct shift between wave profiles (Figure 4.19). When comparing the results from set A experiments with the results from set B experiments, we found that the measured wave height from set B is greater.

We determined the Stokes number St for each wave case experimented (Table 4.10). The expression for the Stokes number is:

$$\mathrm{St} = \frac{\epsilon}{\sigma^2}\,. \tag{4.16}$$

The Stokes number St relates the waves nonlinearity and dispersion (Lima et al., 2019) and classifies the wave cases according to their characteristics and behaviour. The limits on this classification scale are flexible and we defined three increasing intervals for St : $\mathrm{St} < 3$ correspond to short Boussinesq waves; $3 < \mathrm{St} < 10$ correspond to a mixed behaviour, and $\mathrm{St} > 10$ correspond to long non-Boussinesq waves (Lima et al. 2019). In Figure 4.20, we observe that, for a water depth of 50 cm, most SW show a behaviour closer to short Boussinesq waves or a mixed behaviour and

most N-waves show a mixed behaviour. For a water depth of 25 cm, both SW and N-waves tend to show a mixed behaviour or a long non-Boussinesq waves behaviour.

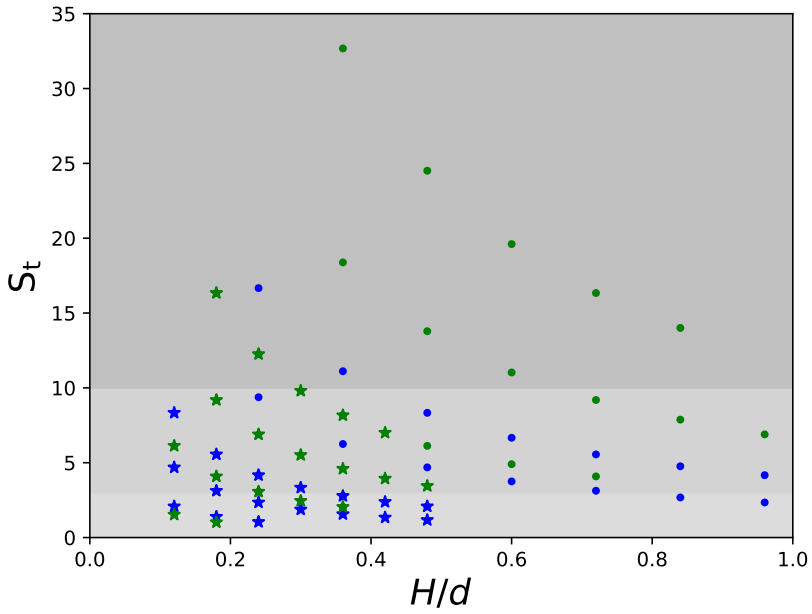

Figure 4.20: St versus H/d for SW (blue) and NW (green), for 25 cm ($\circ$) and 50 cm ($*$) water depths. Grey scale intensity increases from short Boussinesq waves to long non-Boussinesq waves.

For set B experiments, it is important to recall that in the subset B25 experiments there is a slope transition between wave gauges wg4 and wg13 (Figures 4.21 and 4.22). For subset B50 experiments, there are two slope transitions, the first one between wg4 and wg6, and the second one between wg8 and wg3 (Figures 4.23 and 4.24). From the wave celerity evolution plots, we can clearly distinguish the slope transitions and its effects on the wave propagation and wave celerity.

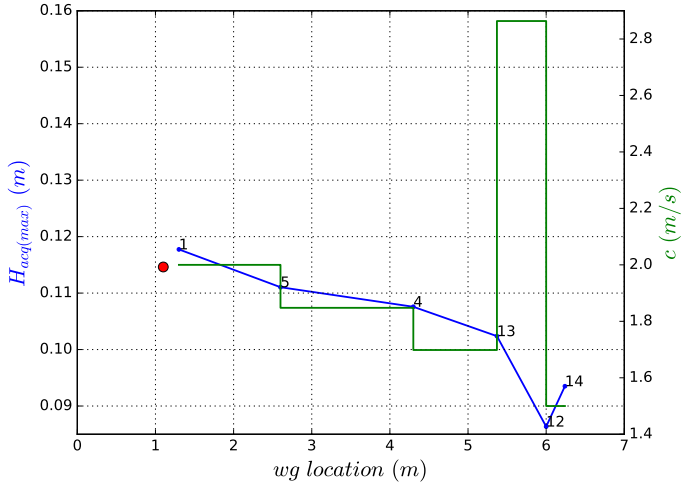

(a)

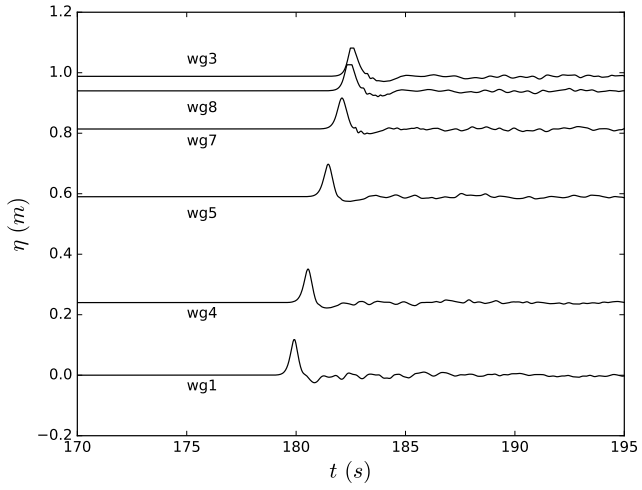

(b)

Figure 4.21: Case 6a: (a) Maximum wave height H and average celerity c evolution at each wave gauge. Red dot corresponds to SW wave celerity determined from expression (4.6). (b) Recorded SW traces at each wave gauge.

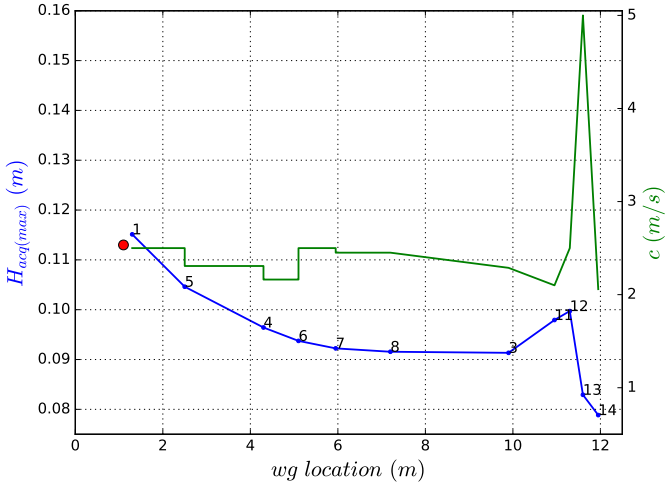

(a)

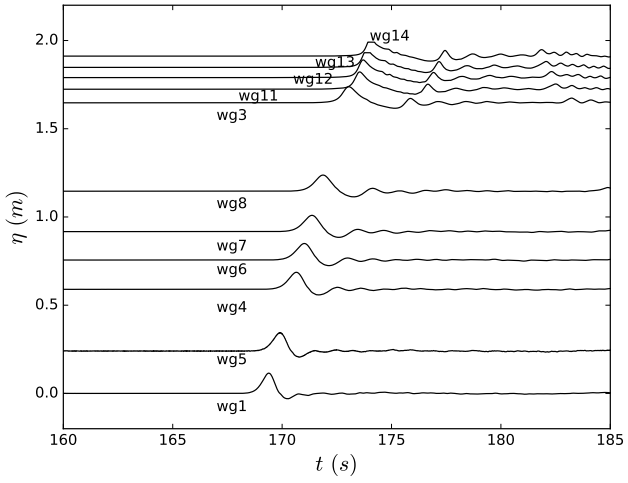

(b)

Figure 4.22: Case 6b: (a) Maximum wave height H and average celerity c evolution at each wave gauge. Red dot corresponds to SW wave celerity determined from expression (4.6). (b) Recorded SW traces at each wave gauge.

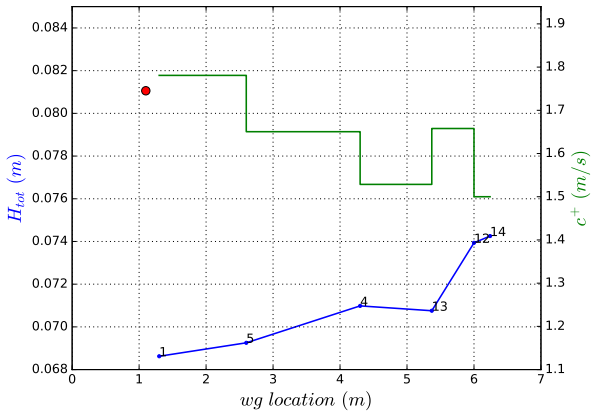

(a)

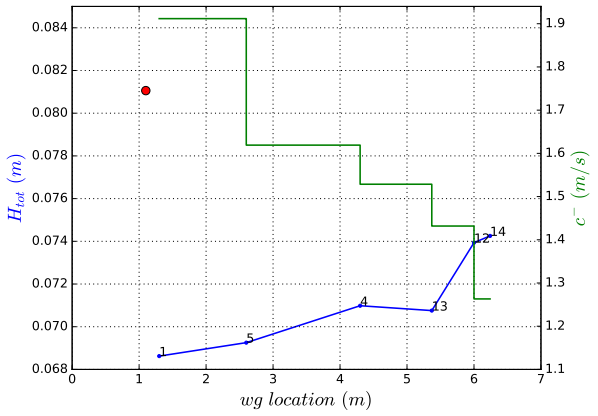

(b)

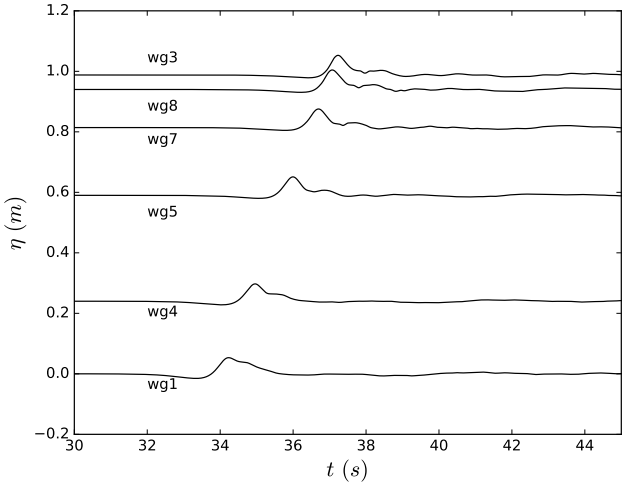

(c)

Figure 4.23: Case 13a: (a) and (b) Maximum wave height H and average celerity c^+ and c^- evolution at each wave gauge. Red dot corresponds to SW wave celerity determined from expression (4.15). (c) Recorded LDN-waves traces at each wave gauge.

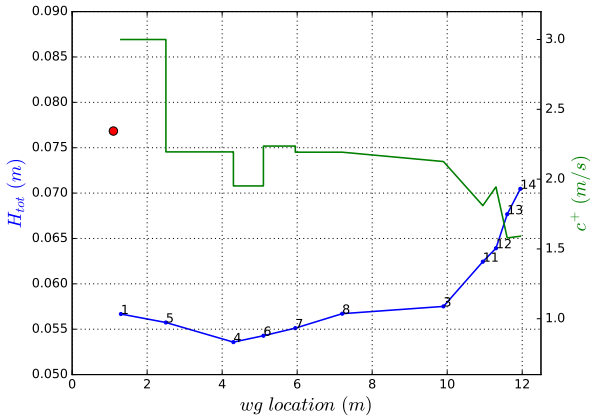

(a)

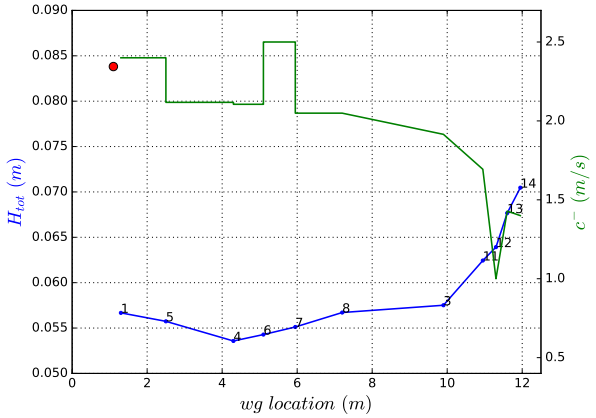

(b)

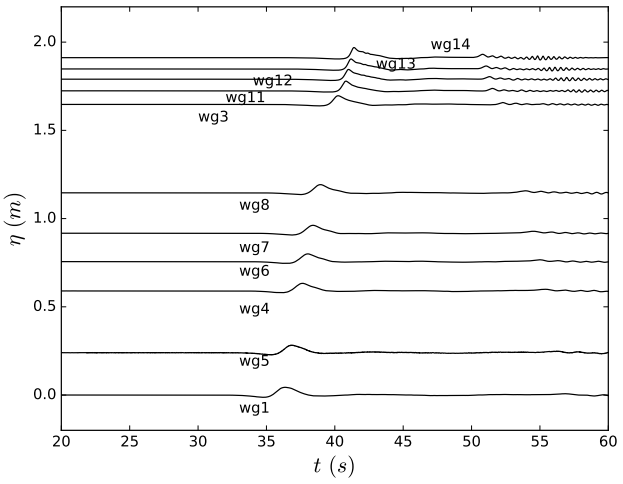

(c)

Figure 4.24: Case 13b: (a) and (b) Maximum wave height H and average celerity c^+ and c^- evolution at each wave gauge. Red dot corresponds to SW wave celerity determined from expression (4.15). (c) Recorded LDN-waves traces at each wave gauge.

4.4.0.1 Wave heights and wave velocities

In Figures 4.21 and 4.22, for the solitary wave Case 6, C6 (H = 15 cm), the maximum wave height at each wave gauge, the average celerity c evolution at each wave gauge and the recorded traces at each wave gauge are plotted, respectively for waves C6a and C6b (where C6a corresponds to the 25 cm water depth experiments, subset B25 experiments, and C6b corresponds to the 50 cm water depth experiments, subset B50 experiments). From the traces of the solitary waves, it is possible to see that there is a preservation of their shape with a continuous decrease of wave height and an increase of the back wave trough, as observed in Figure 4.21b. From wave gauge 8 onwards, a series of increasing trailing waves are detected. There is a jump in the value of the average wave celerity, c, between wave gauges 13 and 14 (Figure 4.22). The wave celerity jump and its quantitative difference is caused by the water depth difference at the wave gauges location. The slope modification influences the speed at which the wave celerity changes. The higher the slope, the faster the speed variation. Another aspect that most probably affected the measurements is related to the difficulty encountered in having the smaller wave gauges remaining static, due to the light weight of these small wave gauges and the high wave height H = 15 cm generated. In Figure 4.22, it was observed that the wave height decreased progressively, although an increase was registered around wave gauges 11 and 12, which could probably be related to the shoaling effect. Around this location, the wave celerity spiked to a value more than two times the previous registered wave celerity value registered. Looking to the traces, it is observed that the wave celerity is not constant between wave gauge 11 and 12, with a large difference between the wave crests. Between wg3 and wg14, it is observed what seems to be trailing waves, but are most certainly reflected waves from the obstacle (Figures 4.9 and 4.10).

For the LDN-wave Case 13, C13 (H = 8.5 cm), Figures 4.23 and 4.24 show the maximum wave height at each wave gauge, the average wave celerities c^- (leading wave trough wave velocity) and c^+ (leading wave crest wave velocity) evolution at each wave gauge and the recorded traces at each wave gauge, for subset B25 experiments (Case 13a, C13a) and subset B50 experiments (Case 13b, C13b). In Figure 4.23, it was observed an increase of the wave height, as the N-wave lost its original shape and turned into a solitary-type wave. The wave celerity c^+ decreased along the gauges, with a sudden increase between wave gauges 13 and 12. On the other hand, the wave celerity c^- decreased smoothly with no other changes to register. For subset B50 experiments (Figure 4.24), the wave height decreased until the first slope transition, starting to increase afterwards. Wave celerities decreased except between the slope transitions, with small jumps in its value.

4.4.0.2 Run-in

The run-in was measured in subset B25 experiments. In Figure 4.25, it is observed that there is a break in the values of run-in with the increase of H, for $H/d > 0.6$ ($H > 0.15$ m), for the N-waves. This can be a consequence of the occurrence of early wave breaking during the experiments which, for some of the waves generated, was visually observed right after the wave-maker and/or at the flat zone of the beach.

Run-in calibration models are proposed for both solitary and N-waves respectively. For the solitary waves, the linear calibration model was adjusted:

$$\frac{R_{in}}{d} = 8.35\,\frac{H}{d} + 0.86, \tag{4.17}$$

with R^2 = 0.86, and is represented in Figure 4.25. The linear function reaches the maximum run-in R_{in} around 8 m, this value then becomes constant and the linear function tends to be horizontal. For this reason, the last two measurements of the solitary waves run-in were disregarded (red dots

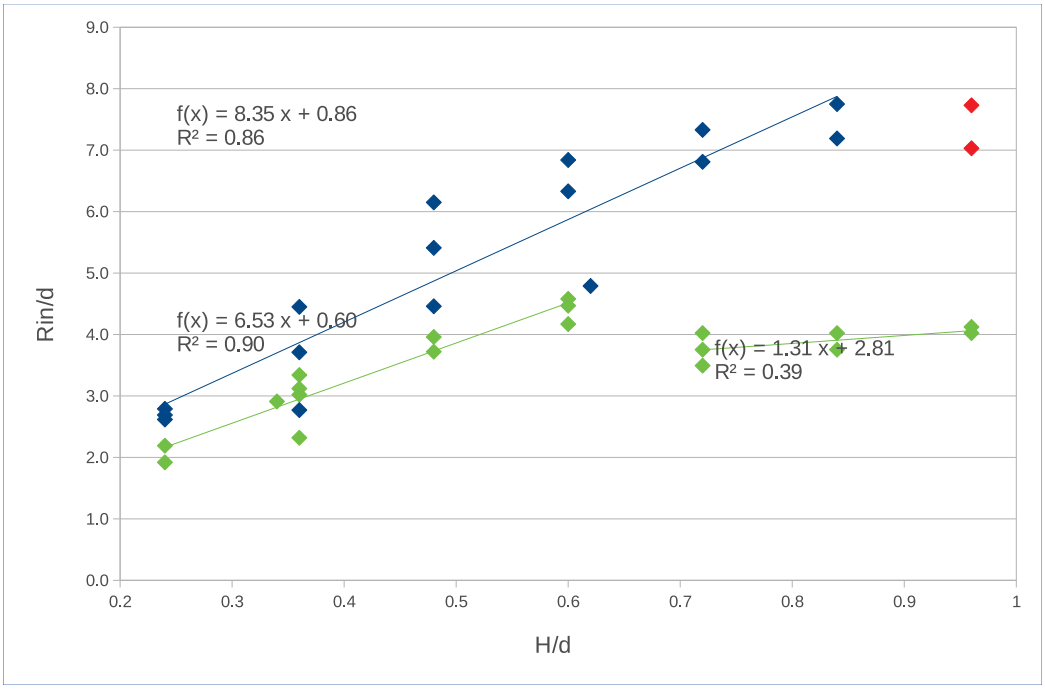

Figure 4.25: Subset B25 experiments: Experimental run-in R_{in}/d versus H/d : (x) SW (x) NW. Calibration model fit to the SW (blue linear line) and NW (yellow and green linear lines) run-in measurements. Red diamonds were measurements excluded from the SW run-in calibration model.

in Figure 4.25). Wave breaking seems to be occurring and consequent energy dissipation, which limits the maximum run-in value reached.

Two separated linear functions are proposed for the N-waves run-in R_{in}:

$$\frac{R_{in}}{d} = 6.53\,\frac{H}{d} + 0.60, \tag{4.18}$$

with R^2 = 0.90, and

$$\frac{R_{in}}{d} = 1.31\,\frac{H}{d} + 2.81, \tag{4.19}$$

with R^2 = 0.39. In the first function, a maximum run-in R_{in} of 4.5 m is measured and in the second function the maximum run-in measured diminishes. It looks like a great amount of energy is consumed in the N-wave propagation and wave breaking, which translates into two distinct run-in evolutions.

4.4.0.3 Run-up

We measured the run-up for subset B50 experiments (Figure 4.26). Calibration models are proposed for both solitary and N-waves respectively. For the solitary waves, the linear calibration model was adjusted to:

$$\frac{R_{up}}{d} = 2.15\,\frac{H}{d} + 0.07, \tag{4.20}$$

with R^2 = 0.84. A linear function is proposed for the N-waves run-up R_{up} :

$$\frac{R_{up}}{d} = 1.82\,\frac{H}{d} - 0.10, \tag{4.21}$$

with R^2 = 0.91. Both SW and NW linear functions are represented in Figure 4.26, which is the plot of experimental R/d vs H/d, for all the waves generated in the laboratory. For the solitary waves, the maximum ratio R/d is approximately 1.00 for H/d = 0.425, which means that the maximum SW run-up R_{up} value measured was 0.50 m. In the N-waves experiments, for $H/d <$ 0.15, the ratio R/d = 0.19 and R_{up} = 0.10 m. For $H/d >$ 0.15, the maximum ratio R/d is around 0.84, which means that the maximum NW run-up R_{up} value measured was 0.42 m.

Following the run-up expressions (2.76) and (2.77) proposed in Chapter 2 (section 2.1.6.3), and the results obtained from our physical experiments, we propose two run-up laws, one for the solitary waves and another one for the N-waves. Considering a slope angle β_2, the proposed run-up formula for the solitary waves is:

$$\frac{R_{upSW}}{d} = 0.22 \cdot (\tan\beta_2 \cdot \mathrm{St})^{-0.39}, \tag{4.22}$$

represented in Figure 4.27 (blue line). For the N-waves, the following run-up law is proposed:

$$\frac{R_{upNW}}{d} = 0.37 \cdot (\tan\beta_2 \cdot \mathrm{St})^{0.02}, \tag{4.23}$$

which is represented in Figure 4.28 (green line).

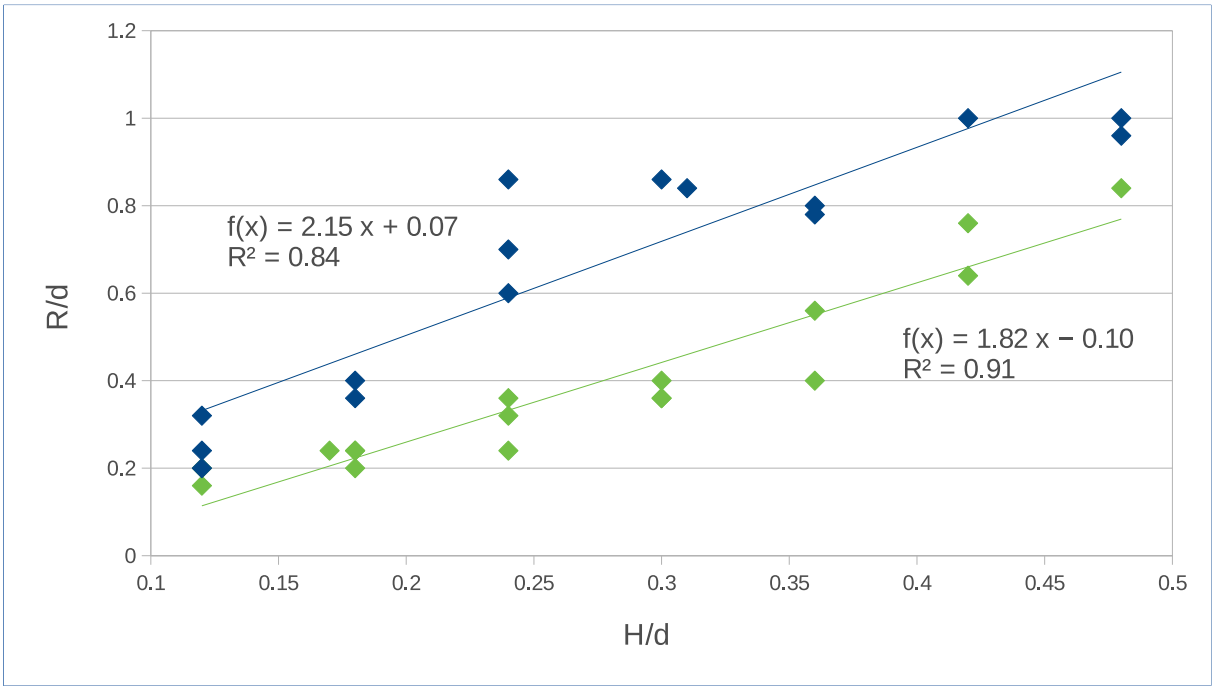

Figure 4.26: Subset B50 experiments: Experimental run-up R_{up}/d versus H/d: (**blue**) SW (**green**) NW. Calibration model fit to the SW (blue linear line) and NW (green linear line) run-up measurements.

4.4.0.4 Numerical simulations

Numerical simulations were performed and compared with the physical experiments. Simulations for waves cases C6 and C13 (for 25 cm and 50 cm water depth) hereby presented apply the $\kappa -$

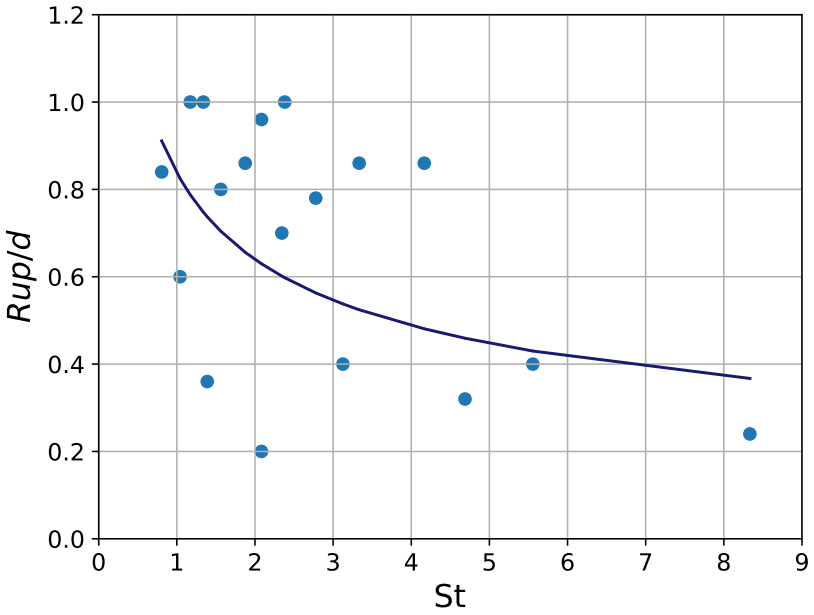

Figure 4.27: SW subset B50 experiments: R_{up}/d versus St for experimental run-up (**blue circles**) and run-up calculated from power-law (**blue line**).

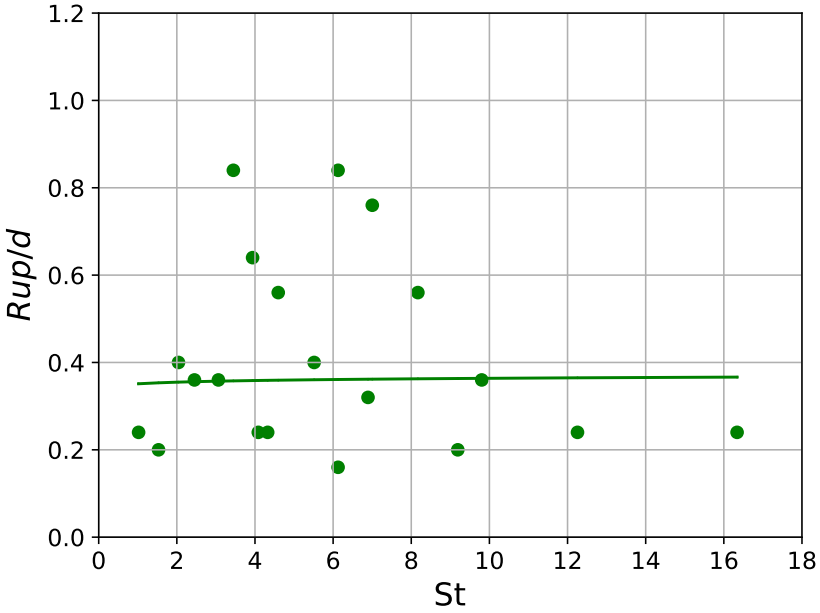

Figure 4.28: NW subset B50 experiments: R_{up}/d versus St for experimental run-up (**green circles**) and run-up calculated from power-law (**green line**).

ω SST turbulence model. Figures 4.29 to 4.30 show the comparison between the experimental and numerical SW propagation between wg1 and wg14 for subset B25 experiments. Although the numerical wave height is 25% less than the laboratory measurement, the shape is similar to what was obtained experimentally. The wave displays a step-like shape and becomes unstable at

Table 4.13: Experimental and numerical run-in R_{in} values observed for C6 and C13, for the $\kappa-\omega$ SST turbulence model, in 25 cm water depth.

R_{in} (m)	exp	num	dif (%)
C6a	13.54	13.10	3.2
C13a	11.66	10.10	13.4

wg12, after 4 s of propagation. Experimentally, a series of smaller waves are observed before the generated solitary wave, which are most probably a consequence of lateral wall reflections.

Figures 4.31 to 4.32 plot the comparison between the experimental and the numerical leading N-wave propagation between wg1 and wg14 for subset B25 experiment. In wg1, it is observed that the N-wave crest is already in fission and its trough is larger than expected. The fission originates the division of the wave crest in two. Several trailing waves are observed in the next wave gauges, as well as an increase of the wave height of the crest.

To study the run-in with olaFlow, several virtual wave gauges where displaced along the numerical computational domain (canal), to find out where the wave stopped: the maximum horizontal coordinate point reached by the generated wave was determined. This limit was established to be less than 0.009 m. The turbulence model $\kappa-\omega$ SST was applied and the run-in results for solitary wave C6a and N-wave C13a are shown in Table 4.13. The numerical results from olaFlow are good, although the computational run-in measured is systematically smaller than the experimental run-in. The computational run-in R_{in} results are 3% less for the SW and 13% less for the LDN, when compared with the experimental measurement values. Eventually, this can mean that more energy dissipation occurs numerically, before reaching the maximum value verified experimentally. It was also attempted to study the run-in of solitary waves with the SWASH code, with the turbulence turned on, but without success. The code is not able to "follow" the wave until it dissipates, outputting on average a constant maximum run-in R_{in} of about 8.62 m.

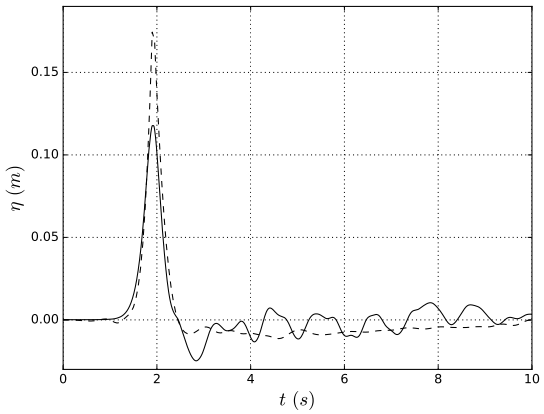

(a) gauge 1 (x = 1.30 m)

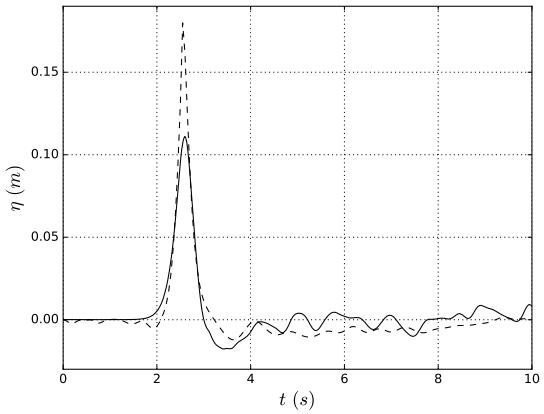

(b) gauge 5 (x = 2.60 m)

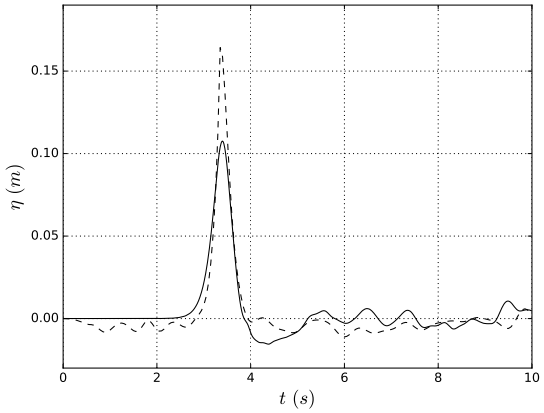

(c) gauge 4 (x = 4.30 m)

Figure 4.29: Wave propagation over the canal for solitary wave C6 for a water depth of 25 cm (C6a): Numerical simulation wave profiles (—) for the $\kappa - \omega$ SST turbulence model and subset B25 experimental wave profiles (- -) recorded at wave gauges 1, 5 and 4.

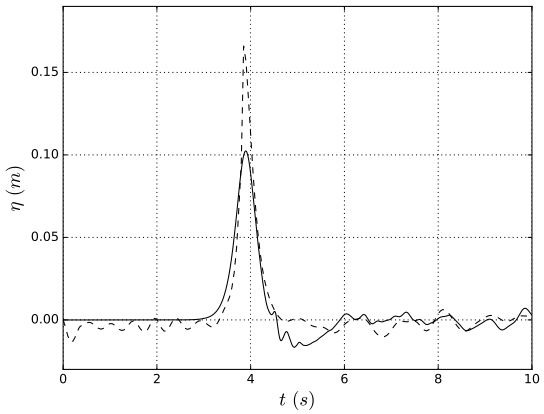

(a) gauge 13 (x = 5.37 m)

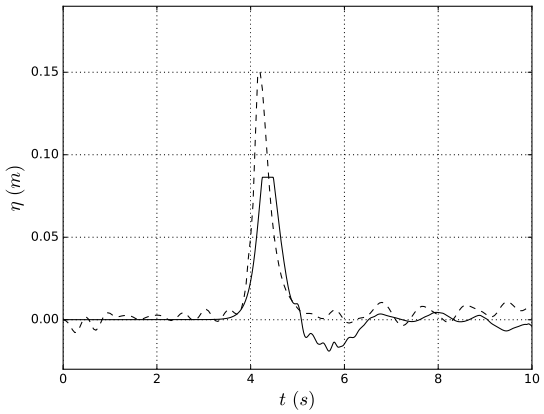

(b) gauge 12 (x = 6.00 m)

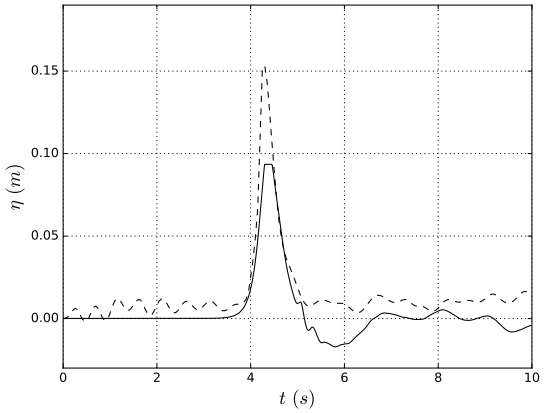

(c) gauge 14 (x = 6.24 m)

Figure 4.30: Wave propagation over the canal for solitary wave C6 for a water depth of 25 cm (C6a): Numerical simulation wave profiles (—) for the $\kappa - \omega$ SST turbulence model and subset B25 experimental wave profiles (- -) recorded at wave gauges 13, 12 and 14.

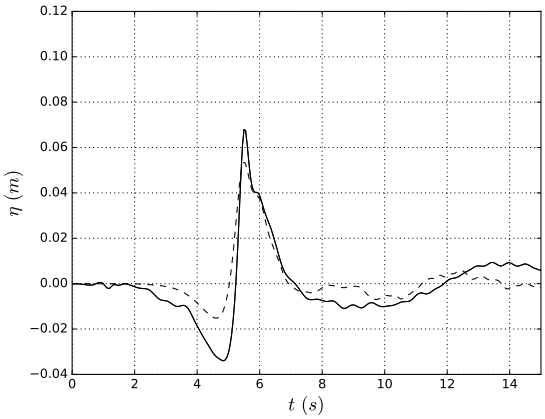

(a) gauge 1 (x = 1.30 m)

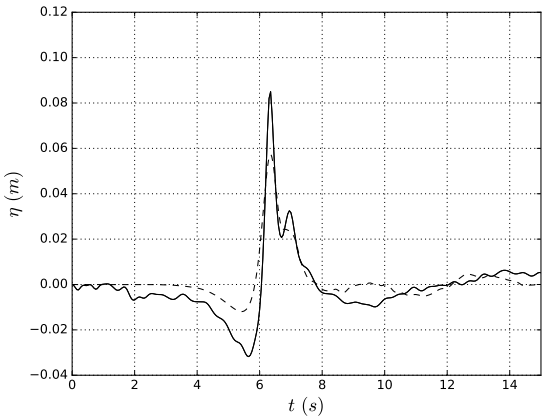

(b) gauge 5 (x = 2.60 m)

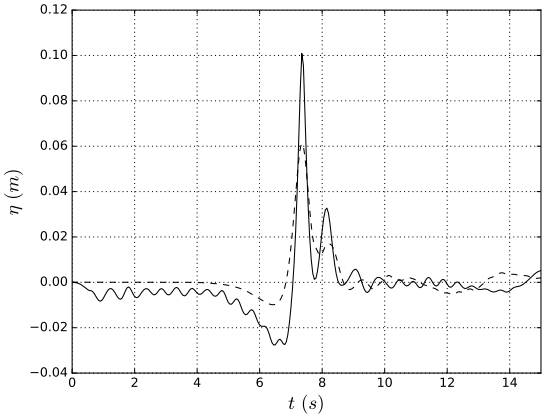

(c) gauge 4 (x = 4.30 m)

Figure 4.31: Wave propagation over the canal for LDN-wave C13 for a water depth of 25 cm (C13a): Numerical simulation wave profiles (—) for the $\kappa - \omega$ SST turbulence model and subset B25 experimental wave profiles (- -) recorded at wave gauges 1, 5 and 4.

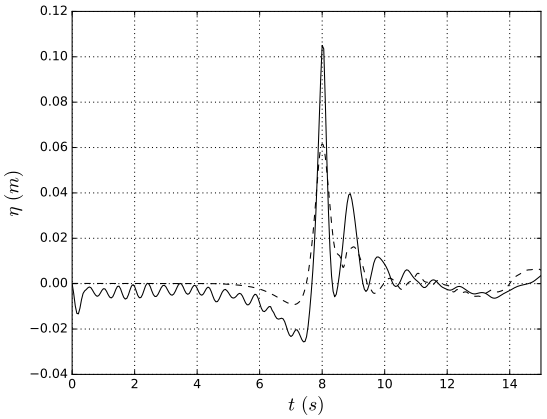

(a) gauge 13 (x = 5.37 m)

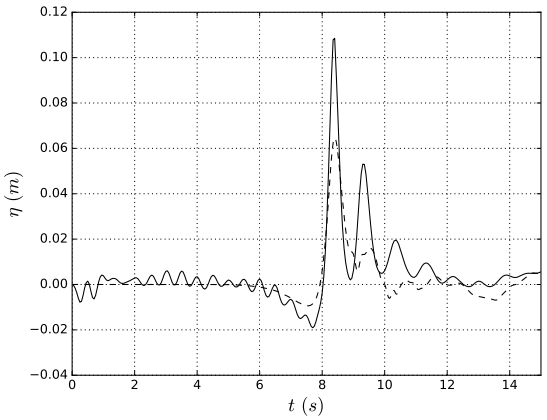

(b) gauge 12 (x = 6.00 m)

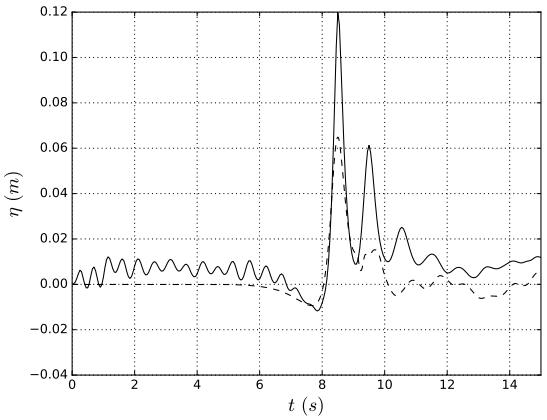

(c) gauge 14 (x = 6.24 m)

Figure 4.32: Wave propagation over the canal for LDN-wave C13 for a water depth of 25 cm (C13a): Numerical simulation wave profiles (—) for the $\kappa - \omega$ SST turbulence model and subset B25 experimental wave profiles (- -) recorded at wave gauges 13, 12 and 14.

For the subset B50 experiments (Figures 4.33 to 4.36), the SW numerical wave height is 15% less than the laboratory measurement but the wave shapes are similar. A larger trough is observed following the solitary wave. At wg12, although following what is observed from the experiments, the wave starts to rumble losing its shape. The wave crest assumes a step-like shape from wg13 onwards.

We notice that for the solitary wave C6, both for subset B25 experiments (wave gauges 12 and 14 in Figure 4.30) and for subset B50 experiments (wave gauges 13 and 14 in Figure 4.36) the experimental wave profiles recorded show a step-like shape. This can be due to the effect of white capping at the wave crest or a problem related to the calibration interval of 4 cm we used, limited by the dimension of the wave gauges and the water depth. Also, as mentioned previously, for larger waves the short wave gauges (wg12, wg13, wg14) were subject to small movements, consequently moving from their original position. This measurement problem could be an additional reason to justify this feature observed in the wave profiles recorded.

Comparing the 50 cm N-wave physical experiments with the numerical simulations results (Figures 4.37 to 4.40), it is observed that the N-wave generated with the numerical wave-maker is closer to the experimental LDN-wave. From wg5 onwards, the wave trough starts displaying several smaller waves, with increase of the wave crest tending to a solitary wave shape. As the experimental wave progressively decreases in height, the wave height is continuously increasing in the numerical simulation, being larger between wg8 and wg3 due to shoaling and showing a decrease only after wg13. The continuous wave height increase could be related to the fact that bottom friction was not contemplated in the numerical simulations, which should have been accounted for.

4.4.0.5 Pressure

For the subset B50 experiments, the four pressure transducers located at the obstacle (pt0, pt1, pt2, pt3) measured the pressure variations caused by the generated waves (Figure 4.41). It was observed that the pressure decreased from the bottom to the top pressure transducer. The maximum experimental pressure was measured by the pressure transducer located at the bottom of the obstacle (pt0). The maximum experimental pressure is calculated as the average of the maximum pressure values, at the pressure transducer, measured over two consecutive trials ($P_{exp.aver}$).

Calibration models for the maximum experimental pressure are proposed for both solitary and N-waves. For the solitary waves, the linear calibration model was adjusted to:

$$\frac{P_{atm} + P_{exp.aver}}{P_{atm}} = 36.82\,\frac{H}{d} + 0.90, \tag{4.24}$$

with R^2 = 0.79. A linear function is proposed for the N-waves experimental pressure:

$$\frac{P_{atm} + P_{exp.aver}}{P_{atm}} = 29.54\,\frac{H}{d} - 2.07, \tag{4.25}$$

with R^2 = 0.97. Both SW and NW linear functions are represented in Figure 4.42. For solitary waves, the maximum experimental pressure is 1800 Pa for H = 0.21 m. For the N-waves, the maximum experimental pressure is around 1260 Pa for H = 0.24 m.

There are notorious differences observed when comparing the experimental pressure measurements at the obstacle with the olaFlow simulations results (Figures 4.41, 4.43 and 4.44). One possibility is related to the fact that in the physical experiments there were some small irregularities between the slopes, as these were two individual structures (constructed specifically for these experiments) that were attached together. These irregularities caused energy dissipation and are not reproduced in the numerical model, as the transition between the slopes is regular in the computational domain.

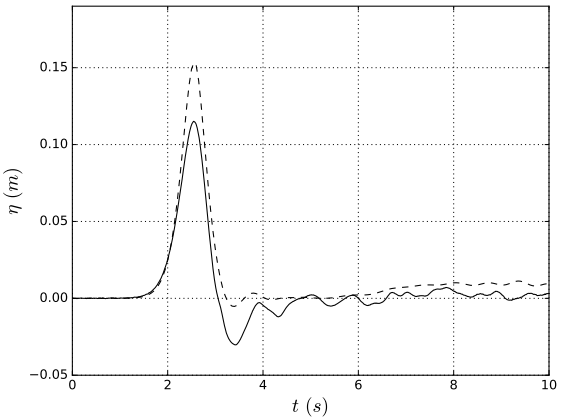

(a) gauge 1 (x = 1.30 m)

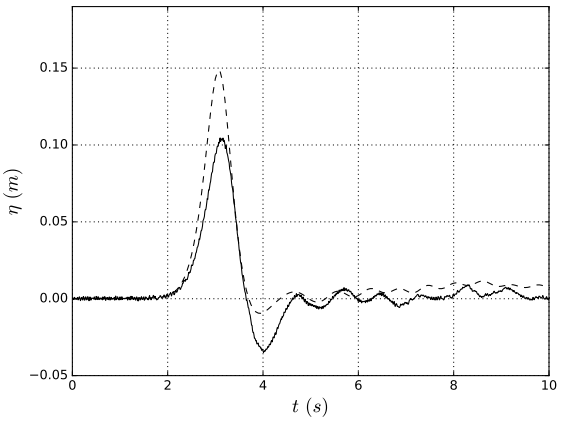

(b) gauge 5 (x = 2.50 m)

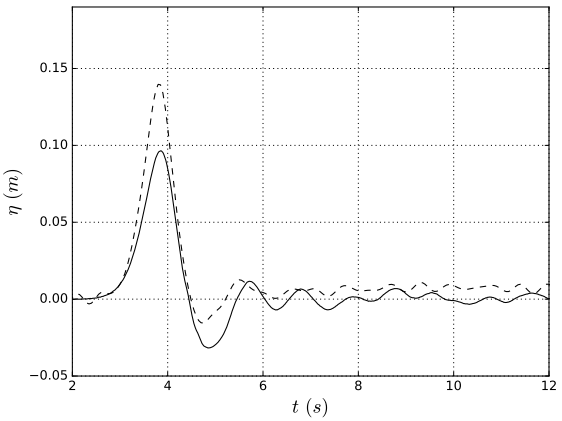

(c) gauge 4 (x = 4.30 m)

Figure 4.33: Wave propagation over the canal for solitary wave C6 for a water depth of 50 cm (C6b): Numerical simulation wave profiles (—) for the $\kappa - \omega$ SST turbulence model and subset B50 experimental wave profiles (- -) recorded at wave gauges 1, 5 and 4.

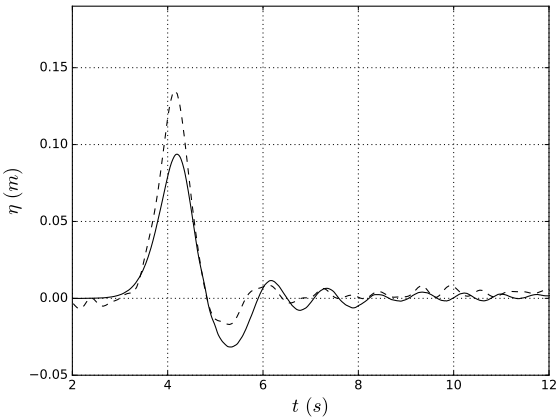

(a) gauge 6 (x = 5.10 m)

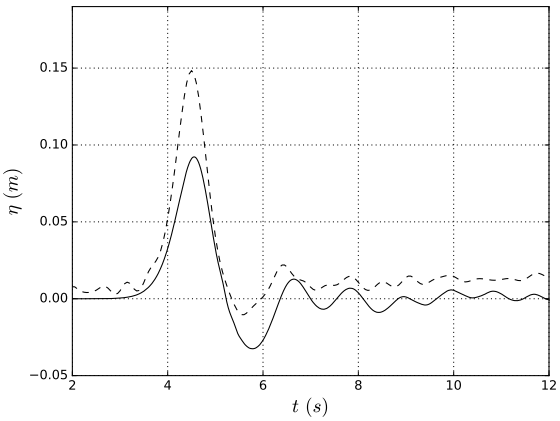

(b) gauge 7 (x = 5.95 m)

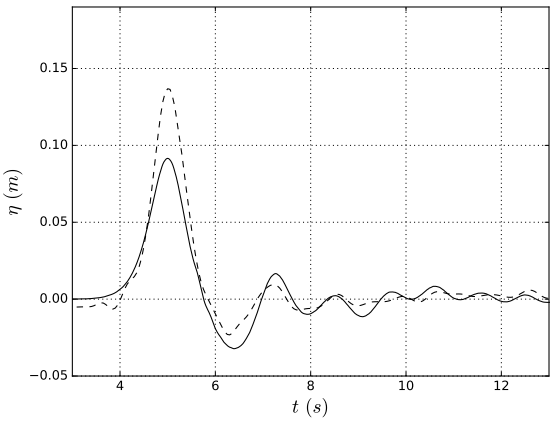

(c) gauge 8 (x = 7.20 m)

Figure 4.34: Wave propagation over the canal for solitary wave C6 for a water depth of 50 cm (C6b): Numerical simulation wave profiles (—) for the $\kappa - \omega$ SST turbulence model and subset B50 experimental wave profiles (- -) recorded at wave gauges 6, 7 and 8.

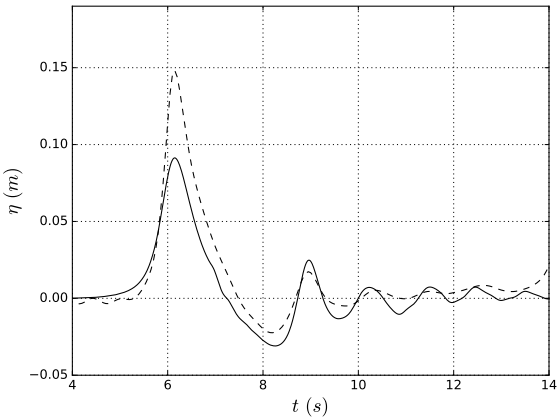

(a) gauge 3 (x = 9.90 m)

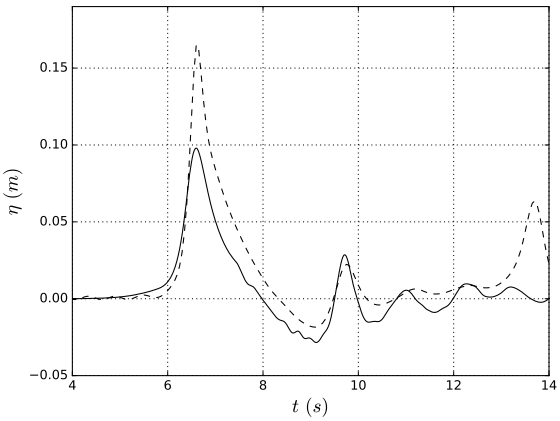

(b) gauge 11 (x = 10.95 m)

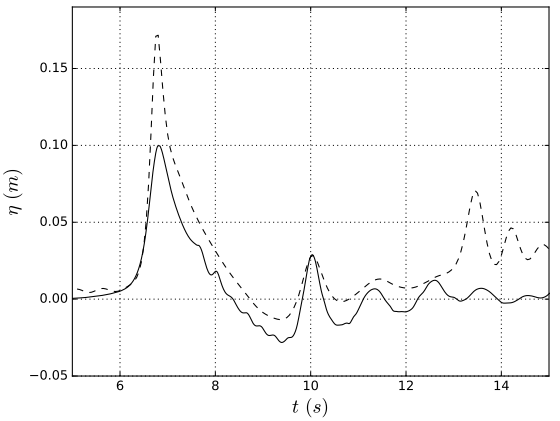

(c) gauge 12 (x = 11.30 m)

Figure 4.35: Wave propagation over the canal for solitary wave C6 for a water depth of 50 cm (C6b): Numerical simulation wave profiles (—) for the $\kappa - \omega$ SST turbulence model and subset B50 experimental wave profiles (- -) recorded at wave gauges 3, 11 and 12.

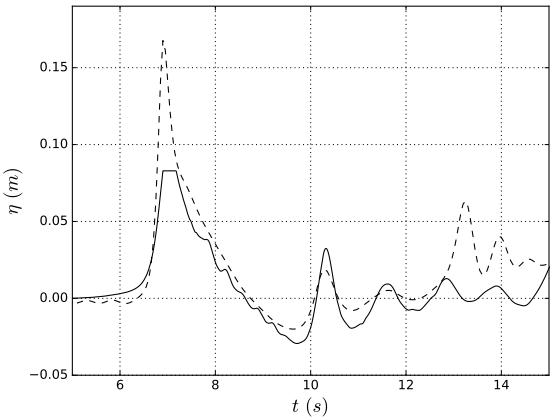

(a) gauge 13 (x = 11.60 m)

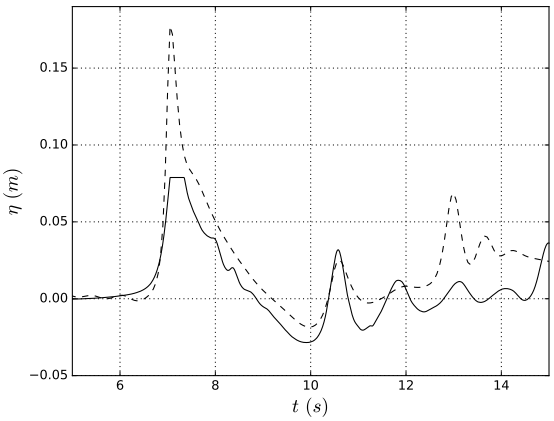

(b) gauge 14 (x = 11.95 m)

Figure 4.36: Wave propagation over the canal for solitary wave C6 for a water depth of 50 cm (C6b): Numerical simulation wave profiles (—) for the $\kappa - \omega$ SST turbulence model and subset B50 experimental wave profiles (- -) recorded at wave gauges 13 and 14.

The large negative peaks recorded in the numerical simulation may be due to a phenomenon of numerical implosion. One possibility is that the cell size does not adjust to what goes on in the physical experiment, resulting in these unexpected negative spikes.

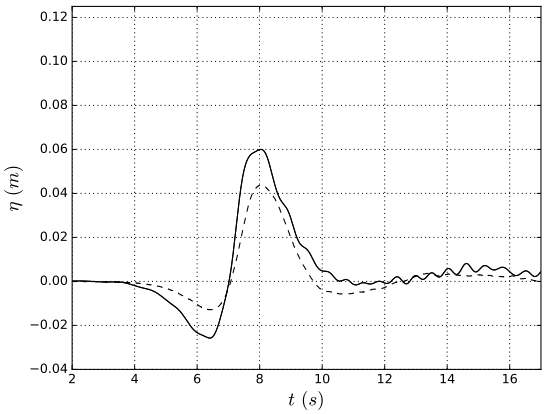

(a) gauge 1 (x = 1.30 m)

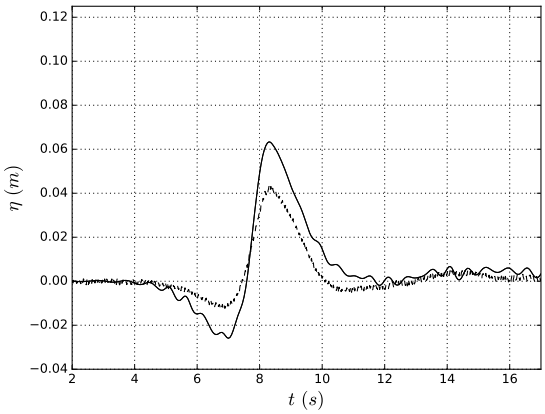

(b) gauge 5 (x = 2.50 m)

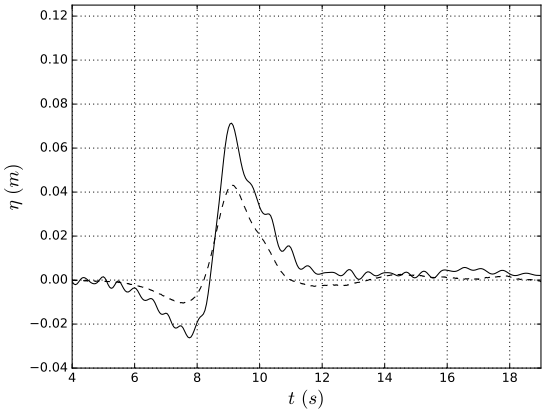

(c) gauge 4 (x = 4.30 m)

Figure 4.37: Wave propagation over the canal for LDN-wave C13 for a water depth of 50 cm (C13b): Numerical simulation wave profiles (—) for the $\kappa - \omega$ SST turbulence model and subset B50 experimental wave profiles (- -) recorded at wave gauges 1, 5 and 4.

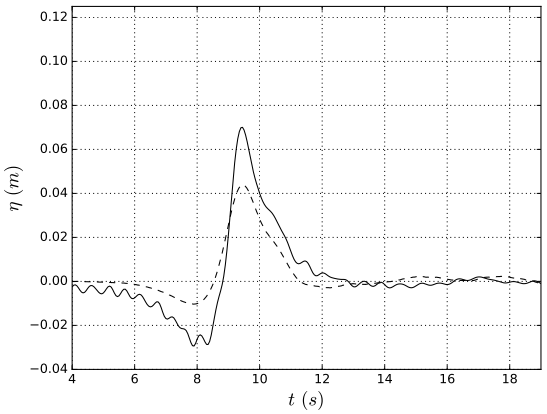

(a) gauge 6 (x = 5.10 m)

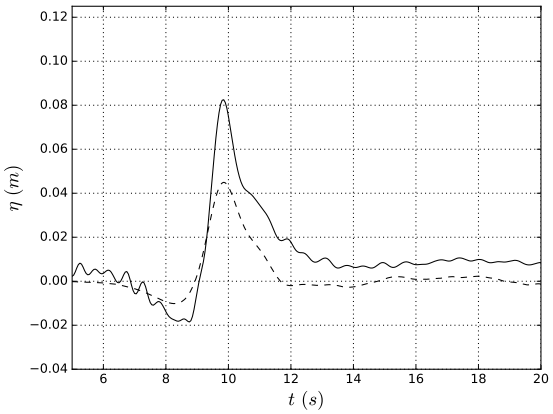

(b) gauge 7 (x = 5.95 m)

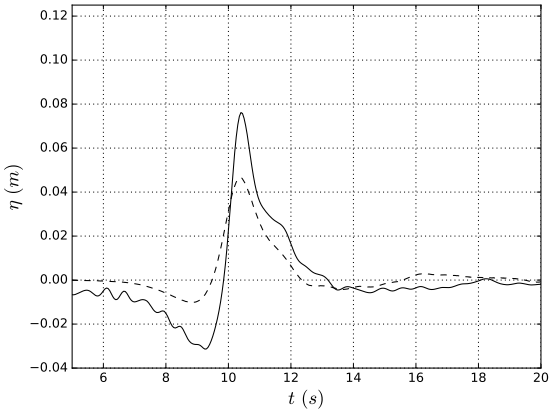

(c) gauge 8 (x = 7.20 m)

Figure 4.38: Wave propagation over the canal for LDN-wave C13 for a water depth of 50 cm (C13b): Numerical simulation wave profiles (—) for the $\kappa - \omega$ SST turbulence model and subset B50 experimental wave profiles (- -) recorded at wave gauges 6, 7 and 8.

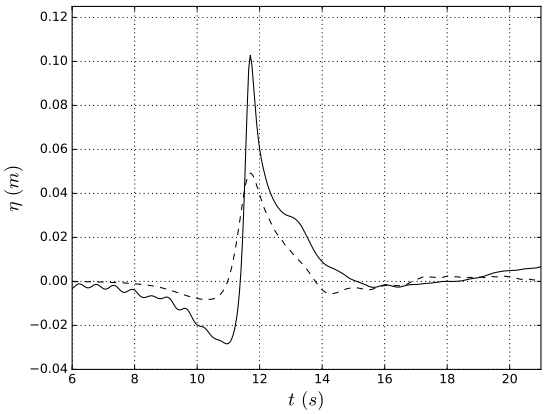

(a) gauge 3 (x = 9.90 m)

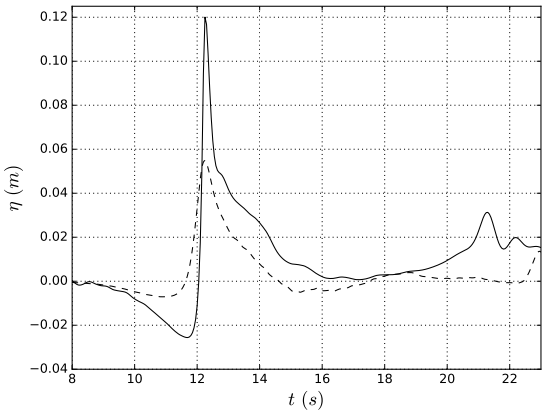

(b) gauge 11 (x = 10.95 m)

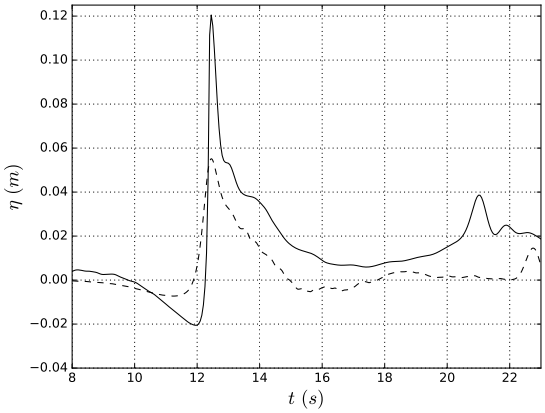

(c) gauge 12 (x = 11.30 m)

Figure 4.39: Wave propagation over the canal for LDN-wave C13 for a water depth of 50 cm (C13b): Numerical simulation wave profiles (—) for the $\kappa - \omega$ SST turbulence model and subset B50 experimental wave profiles (- -) recorded at wave gauges 3, 11 and 12.

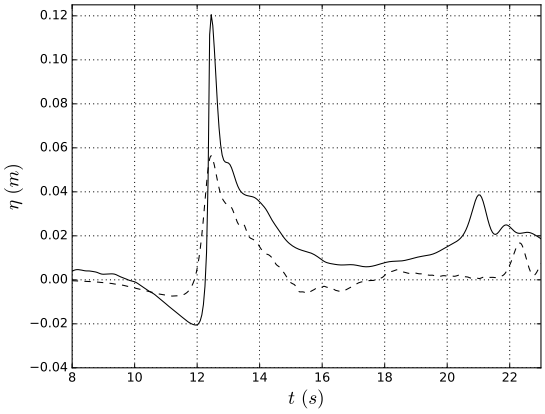

(a) gauge 13 (x = 11.60 m)

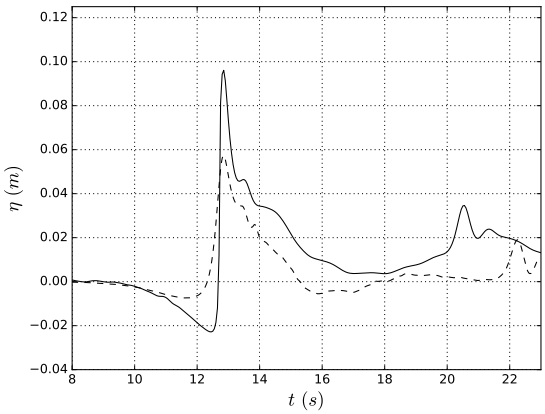

(b) gauge 14 (x = 11.95 m)

Figure 4.40: Wave propagation over the canal for LDN-wave C13 for a water depth of 50 cm (C13b): Numerical simulation wave profiles (—) for the $\kappa - \omega$ SST turbulence model and subset B50 experimental wave profiles (- -) recorded at wave gauges 13 and 14.

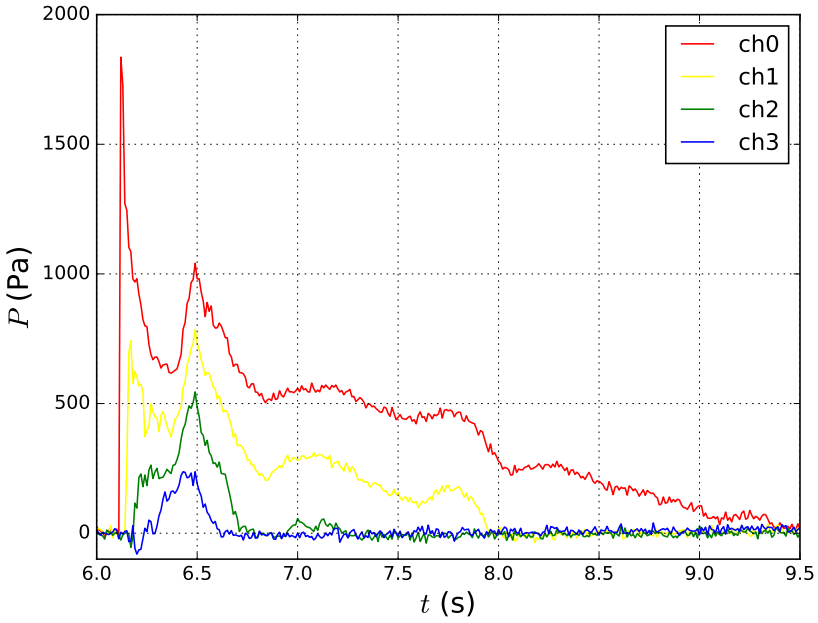

(a) C6b

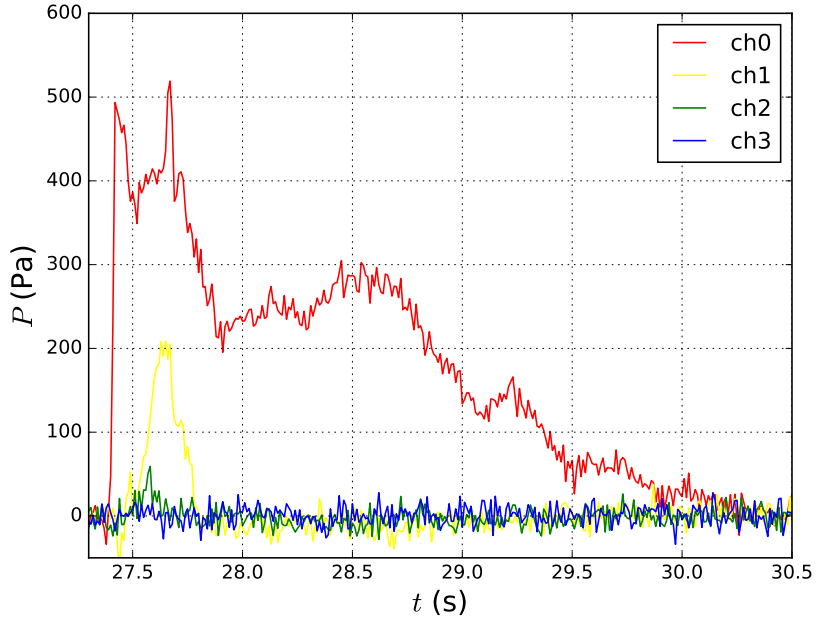

(b) C13b

Figure 4.41: Subset B50 physical experiments: Pressure exerted on a rectangular obstacle, located at the end of the second slope for (a) Case 6b (b) Case 13b. (—) pt0 (—) pt1 (—) pt2 (—) pt3 (ch $\equiv$ channel of the pressure transducer).

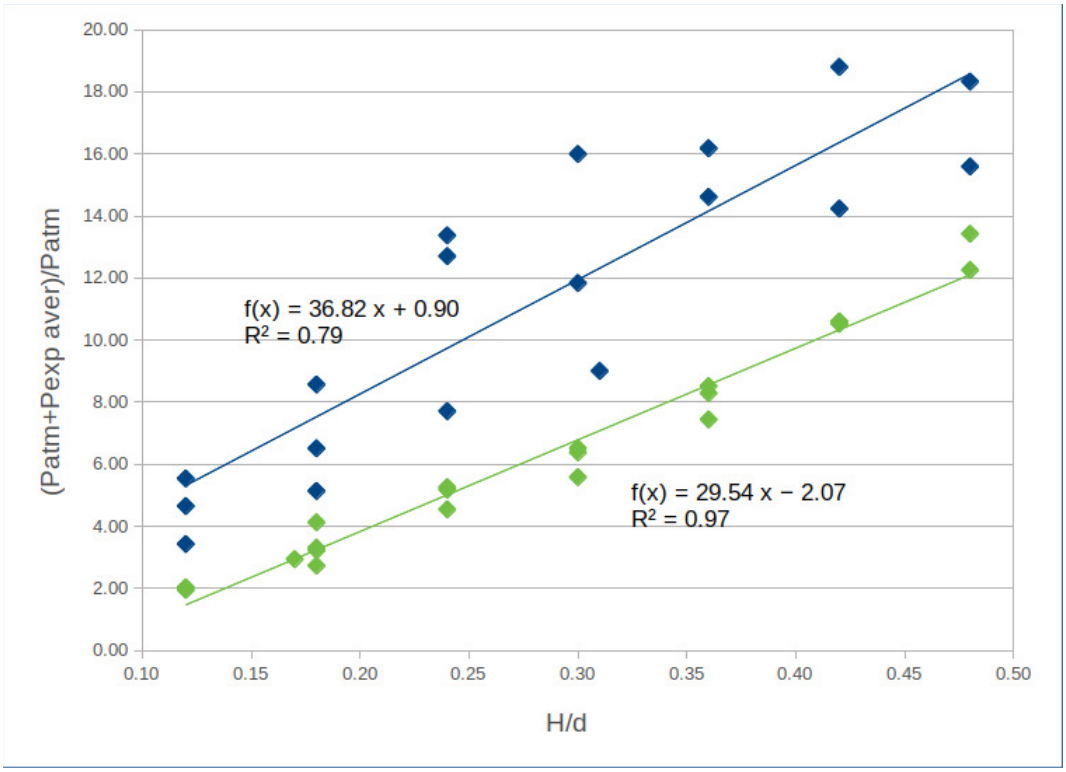

Figure 4.42: Subset B50 physical experiments: $(Patm + P_{exp.aver})/Patm$ (Patm is the atmospheric pressure and $P_{exp.aver}$ is the average maximum experimental pressure, measured at the pressure transducer pt0, located at the bottom of the obstacle) versus H/d. (**blue**) Solitary wave (**green**) N-wave. Calibration model fit to the SW (**blue linear line**) and NW (**green linear line**) pressure measurements. Red triangles were excluded from the N-wave pressure calibration model.

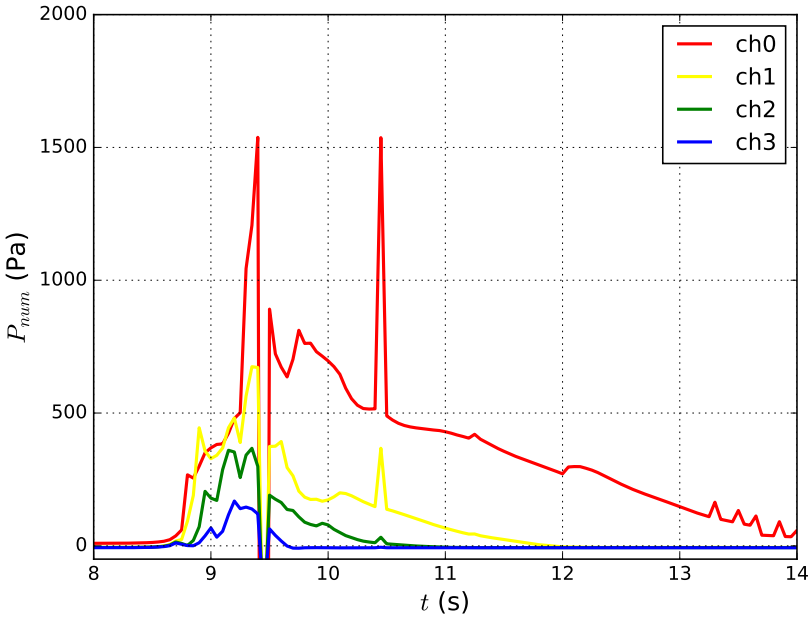

(a) C6b

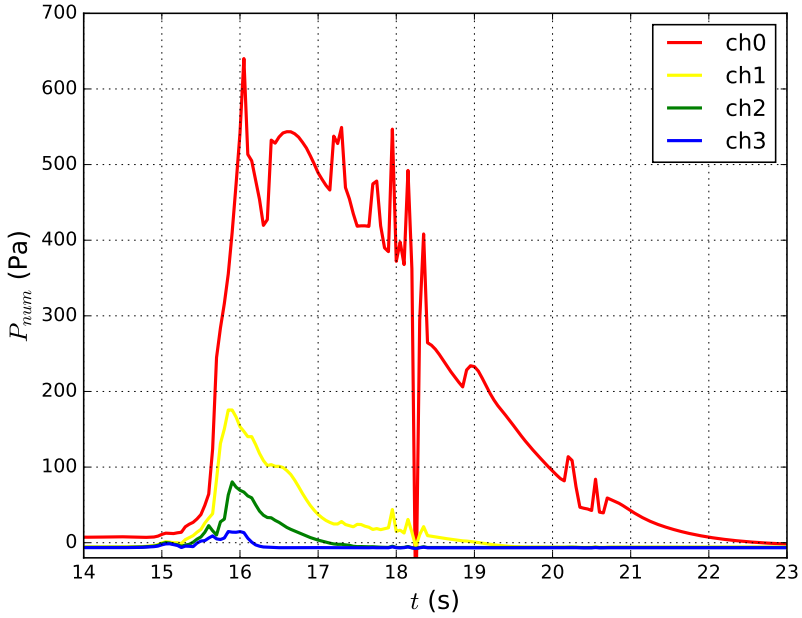

(b) C13b

Figure 4.43: Subset B50 numerical simulations: $\kappa - \omega$ SST model: numerical pressure exerted on a rectangular obstacle, located at the end of the second slope for (a) Case 6b (b) Case 13b. (—) pt0 (—) pt1 (—) pt2 (—) pt3.

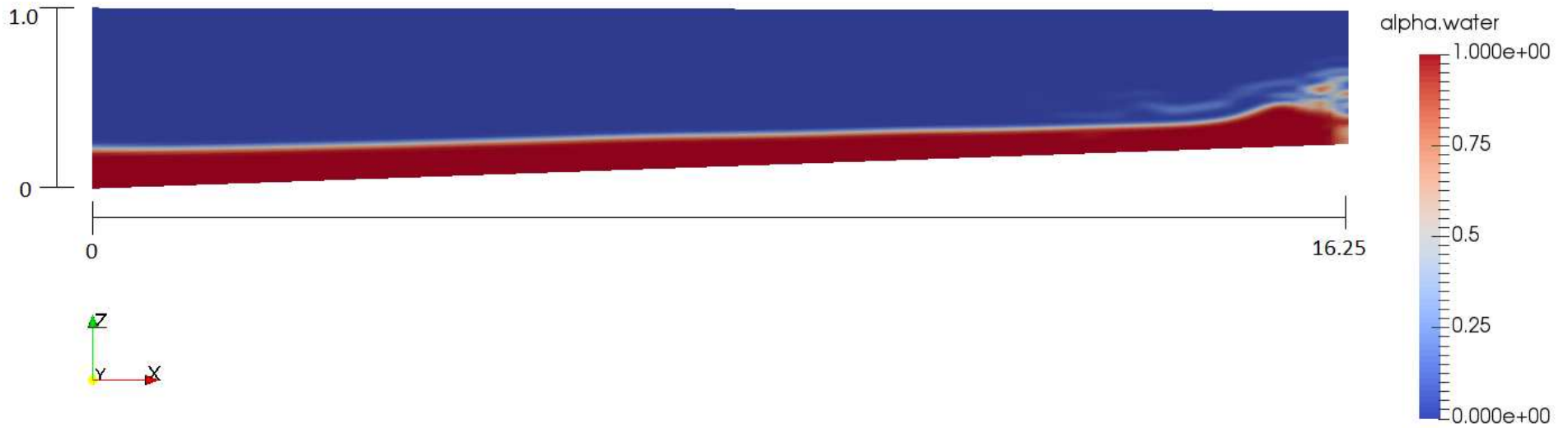

(a) C6b

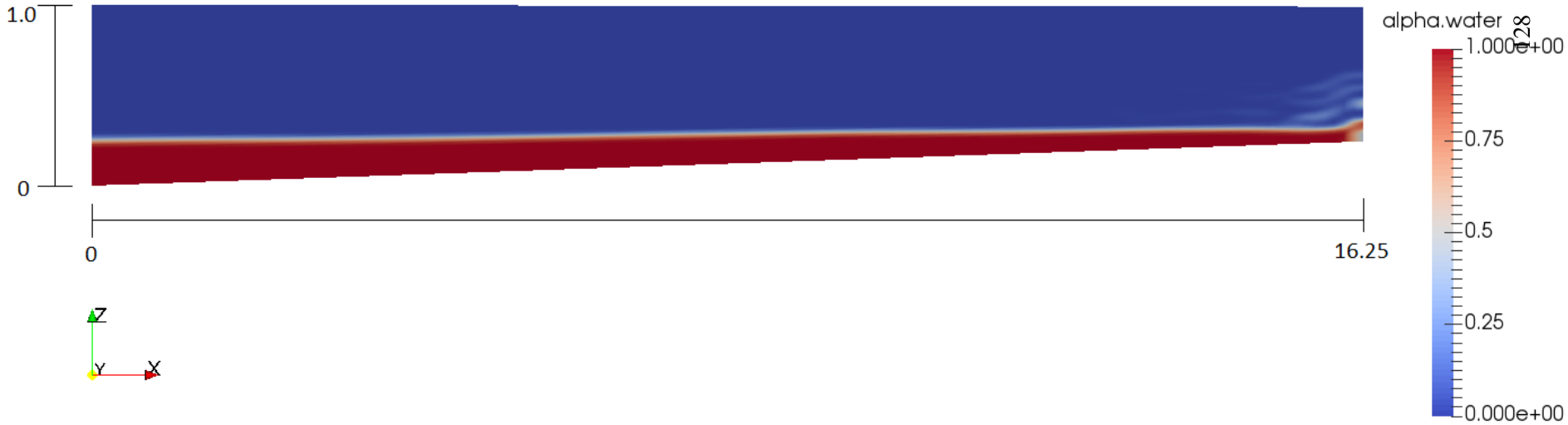

(b) C13b

Figure 4.44: Subset B50 numerical simulations with $\kappa - \omega$ SST model: propagation over the canal and impacting on the vertical rectangular obstacle, located at the end of the second slope for (a) Case 6b (b) Case 13b.

4.5 Concluding remarks

Several wave celerity formulations for solitary, cnoidal and N-waves are presented. For several laboratory experiments performed, different wave celerity formulations were adopted. In the framework of the preliminary laboratory tests performed at LH-FEUP, the wave celerity formulations adopted for the solitary waves and for the N-waves were respectively equations (4.4) and (4.3). Afterwards, a large number of computational tests were performed with the SWASH code, to evaluate the most adequate wave celerity formulations to adopt in the solitary and N-waves experimental tests. It was found that the computational results presented the best fit with the analytical profiles when applying expression (4.6) for the solitary waves velocity, and expression (4.15) for the N-waves velocity. We found these formulations to better preserve the simulated wave shape during the simulation, when comparing with tests performed using the other tested wave formulations. Therefore, the later wave celerity formulations, expression (4.6) for solitary waves and expression (4.15) for the N-waves, were adopted in the final full laboratory experiments.

Afterwards, the laboratory experiments of solitary and LDN-waves, on the wave basin and on a beach with two different slopes, were described. Measurements of the water surface elevation, run-up, run-in and pressure exerted on an obstacle were retrieved from the physical experiments.

We found that, for both solitary and LDN-waves, the measured wave height H is systematically less than what was initially expected, when comparing with the theory and with the numerical simulations, using the theoretical wave profile as input. The wave celerity formulations adopted for the solitary and N-waves seem to be adequate, when comparing measurements and simulations with olaFlow results.

We defined the Stokes number St and used it to classify the characteristics and behaviour of the experimented wave cases. From this classification, we found that, for a water depth of 50 cm, most SW show a behaviour closer to short Boussinesq waves or a mixed behaviour and most N-waves show a mixed behaviour. For a water depth of 25 cm, both SW and N-waves tend to show a mixed behaviour or a long non-Boussinesq waves behaviour

Experimental run-in measurements were retrieved for both solitary waves and N-waves (subset B25 experiments). For the solitary waves, the maximum run-in R_{in} value was approximately 8 m for $(H/d)_{max}$ = 0.85. For the N-waves, the maximum run-in R_{in} is 4.5 m for $H/d < 0.6$. For $H/d > 0.6$, the wave breaking causes a great loss of energy and the run-in is limited to 4 m.

The run-up measurements were also retrieved from the physical experiments with solitary and N-waves (subset B50 experiments). The maximum run-up R_{up} measured for the solitary waves was 0.50 m; for the LDN-waves, for $H/d < 0.15$, the maximum run-up R_{up} measured was 0.10 m; for $H/d > 0.15$, the maximum run-up R_{up} was 0.42 m. Based on our physical experiments, we propose run-up laws for solitary waves and N-waves respectively.

Calibration models with linear fit were proposed both for the run-in and for the run-up measurements. It should be kept in mind that the experimental measurements were retrieved for a beach with two different slopes, which is a special case distinct from what is usually presented in the literature (single slope).

The comparison of the experimental and the olaFlow simulations results show overall good agreement for both solitary and N-wave, although there is an underestimation of the numerical wave height. The run-in obtained from the simulation was also shorter than what was measured experimentally. Considering the pressure measurements, a clear disparity is verified between the laboratory measurements and the simulations results, which should be further investigated.

As future work, the following tasks are proposed:

- considering Synolakis 1990's arguments on Goring's theoretical considerations on the generation of solitary waves in the laboratory, the first-order formulation for the generation of

N-wave in laboratory, presented in Lima et al. (2019), should be reformulated following Synolakis's method (Synolakis 1990);

- perform numerical tests with time-dependent wave celerity formulations, as it might lead to an increased accuracy in the obtained N-wave profile;
- perform the analysis of the results obtained with turbulence models $\kappa - \varepsilon$ and compare them with the results obtained with $\kappa - \omega$ SST turbulence model;
- perform additional simulations with olaFlow for 25 cm and 50 cm water depths respectively, using another turbulence model, such as the RNG $\kappa - \omega$ turbulence model developed by Mesquita (2013), to check and understand the possible differences in the results (run-in, run-up and pressure exerted) from applying different turbulence models;
- determine a metric, such as that presented in Lima et al. (2019), to evaluate the results obtained from case 6 and case 13 simulations, for water depths of 25 and 50 cm;
- vertically locate several virtual gauges along the obstacle, to find out which is the highest vertical point reached by the generated wave, and therefore infer the value of the experimental run-up.

Chapter 5

Coupling of Numerical Models

5.1 Introduction

Combined models bring together the advantages of the individual models into a single model, enabling increased accuracy, efficiency and regime of validity. Existing combined tsunami models are usually not fully available, as they are still under development and/or can only be applied to some specific phases of the tsunami lifecycle. Watts et al. (2003) presented and validated GEOWAVE, a combined simulation model, which couples the tsunami generation model TOPICS with the fully nonlinear and dispersive model FUNWAVE. Those authors showed that nonlinear and dispersive wave models are best suited to model landslide generated tsunamis. Sitanggang and Lynett (2009) developed a hybrid wave model for wave propagation from deep to shallow waters and shoreline, which combines an irrotational 1DH Boussinesq model and a 2DV Reynolds-Averaged Navier-Stokes (RANS) model. Their model was tested with good comparisons with idealized cases and experimental data. Choi et al. (2011) proposed a combined shallow water numerical model for tsunami generation and propagation and an analytical 1DV long wave run-up theory. Løvholt et al. (2010) presented a combined model approach contemplating the Boussinesq model GloBouss, to simulate the long distance tsunami propagation, and the ComMIT/MOST model for the shallow water propagation and the study of coastal impact and run-up. This combination revealed satisfactory results. Also Narayanaswamy et al. (2010) presented the hybrid model SPHunwave, which coupled the known fully nonlinear Boussinesq model FUNWAVE, for wave propagation, with the Smoothed-Particle Hydrodynamics (SPH) model SPHysics, for breaking and post-breaking processes. Satisfactory results were obtained for a solitary wave in a constant depth tank and the code has been further tested with several case studies (Gomez-Gesteira et al. 2012a,b). Simulating the Hokkaido-Nansei-Oki event, they found good agreement between the estimates of the run-up heights and the observations, demonstrating their approach to be a more reasonable and rapid method of forecasting than the coastal inundation models. There are other proposals of coupled models such as Løvholt et al. (2008), which coupled a multi-material model, for the wave generation, with a Boussinesq propagation model, and Løvholt et al. (2010), which combined a model focused on dispersive tsunami propagation. Similarly, Abadie et al. (2012) coupled the Navier-Stokes/VOF model Thetis with FUNWAVE-TVD, for landslide generated tsunamis. Also the coupling of TSUNAMI3D and NEOWAVE is described in Horrillo et al. (2010), where averaged field variables along the water column from TSUNAMI3D are set as initial condition for the 2DH depth-integrated model NEOWAVE, which simulates tsunami propagation and inundation of the study area. The last model was improved by López-Venegas et al. (2015), with a 3D-2DH coupled model for submarine landslide studies. Zhang et al. (2016) introduced a 3D unstructured-grid hydrodynamic model for tsunami currents. Recently Kim et al. (2017) published a model extension of the GeoClaw code with Boussinesq characteristics.

In this chapter, we will describe the methodologies selected to achieve the coupling between the numerical codes used in this research work. In section 5.2, we detail the coupling between GeoClaw and FUNWAVE-TVD codes, which is named as Combined Model 1 (CM1). The coupling approach is validated with a Gaussian hump test case and with the event of the 16th September 2015 Illapel tsunami, in Chile. The nesting facility within CM1 is explored and results for the Portugal Earthquake and Tsunami of the 28th February 1969 (hereby, referred to as 1969 PET) are presented. In section 5.3, we describe the methodology used to combine CM1, via FUNWAVE-TVD, with the CFD code OpenFOAM, via olaFlow, obtaining the combined model CM2. In section 5.3, the coupling between models, which resulted in the combined model CM2, is validated against the laboratory data from the Monai Valley benchmark.

5.2 Combined Model 1 (CM1)

The Combined Model 1 (CM1) is a combination of a shallow water generation and propagation model with a Boussinesq model for propagation, transformation, dispersion and breaking. The used models, GeoClaw and FUNWAVE-TVD, are both open source codes.

The CM1 is validated with the 2015 Illapel earthquake, in Chile. This is a well documented earthquake and tsunami event, which has been widely studied (Melgar et al. 2016, Tang et al. 2016, Calisto et al. 2017). We use the water level observations recorded at 3 DARTs (Deep-ocean Assessment and Reporting of Tsunamis) to evaluate the performance of the proposed combined model. Spectral and wavelet analysis of the surface elevation records and of the model results are performed. Using the 1969 PET event, we show the usefulness and efficiency of the nesting capability within the proposed combined model CM1.

5.2.1 Coupling methodology

To improve the description of the tsunami waves propagation and transformation, we propose to combine GeoClaw (Clawpack Development Team 2014b), a 2DH nonlinear shallow water equations (NSWE) model, for the tsunami generation and adaptive mesh refinement, with FUNWAVE-TVD (Shi et al. 2012b), a fully nonlinear and dispersive Boussinesq model, for the wave propagation, transformation and inundation. Both GeoClaw and FUNWAVE-TVD have presented good agreement when subject to the National Tsunami Hazard Mitigation Program (NTHMP) established benchmark tests (Synolakis et al. 2007).

The tsunami generation capability inside the 2DH NSWE model GeoClaw—the Okada model—is used to provide the initial seafloor deformation to FUNWAVE-TVD, also taking advantage of the adaptive mesh refinement capability within the GeoClaw model. The free surface deformation and velocities are then input as initial conditions to the Boussinesq model, which will afterwards compute the wave propagation and transformation.

To achieve the combined model between GeoClaw and FUNWAVE-TVD, several approaches have been tested. The first approach was to use the output data from GeoClaw computation and, after several data manipulations, to input it directly into FUNWAVE-TVD. To have a fine output data of the free surface elevation η and velocities u and v extracted from GeoClaw, the simulation costs would be high: computational simulation times would increase and the amount of output data to be converted would be very large. For these reasons, this approach was abandoned.

A second approach was tested: use the output information extracted from a very fine grid of numerical gauges within the 2DH NSWE model simulation. After careful manipulation of the data, water kinematic (u,v) and free surface (η) fields were transferred to the fully nonlinear Boussinesq model. This data corresponded to some minutes of simulation with the NSWE model. In general, we used the data corresponding to the first 5 to 10 min of simulation with GeoClaw. As

the tsunami waves propagate quite rapidly, we consider that at this stage, within this 5 min time interval, the tsunami generated waves are fully developed and that the propagation is no longer subject to source area influence. The time instant was selected visually from the simulation plots. The best instant can depend on the magnitude and depth of the event, although further studies have not been done to calibrate this time interval. Yet, this calibration should be done according to the mentioned earthquake parameters, as the considered time interval is dependent on the simulated case study.

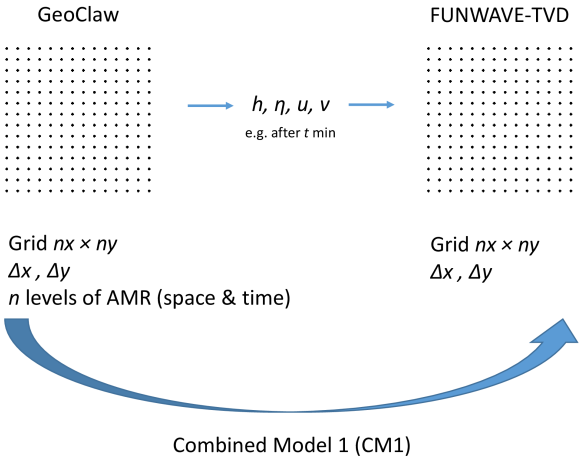

Figure 5.1: Scheme of the selected coupling approach between GeoClaw and FUNWAVE-TVD, the refined covered gauge domain approach, in order to achieve CM1.

For the CM1 simulation, the computational domain should be large enough, so that the generated waves do not leave the domain boundaries right after the simulation starts. It is crucial that the source is fully included in the domain and it cannot be too close to the boundaries. This is also due to the fact that the Boussinesq model applies sponge layers, which are used at the open boundaries, so these layers should not overlap the source. These sponge layers are used to reduce reflection effects in the boundaries of the domain. Therefore, the distance between source and boundaries has to be large enough to contain the sponge layers.

The second approach, described before, was the one selected for the coupling of the two models. Henceforth, Combined Model I (CM1) refers to the ensemble GeoClaw + FUNWAVE-TVD (Figure 5.1).

In both codes, the file format of the input (propagation) files is ASCII. For the combined model approach, the GeoClaw code was modified and additional manipulation scripts have been written to enable the coupling of the models. The programming language used herein is Python (van Rossum 1995).

It should be noted that there is no continuous exchange of information/data between both models at any time during the simulations. The computations performed by each model are independent, which means that the first numerical simulation of the event to be studied is performed with GeoClaw; then GeoClaw's data output is manipulated and saved into individual ASCII files; these files, which concern surface elevation η, velocities u, v and depth h data, will be directly

input into FUNWAVE-TVD. Thus, there is no direct and/or continuous exchange of data between the two models during the computations and therefore there is no need for overlapping information between both models.

To evaluate the performance of the CM1 selected coupling approach, several test cases and simulations have been performed, which will be presented further ahead in this Chapter. Some of the test cases were also presented and described previously in Lima et al. (2016).

In this PhD thesis, Clawpack version 5.2.2 was used and FUNWAVE-TVD versions 2.0 and 3.0 were both tested. The final version of CM1 is a combination of Clawpack 5.2.2 and FUNWAVE-TVD 2.0.

5.2.2 Verification and testing: Gaussian hump simulation test

As a preliminary test case to investigate and evaluate the performance of the coupling methodology adopted, we simulate tsunami waves in a parabolic shaped ocean. Waves in a parabolic bowl (Figure 5.2a) are generated at the the centre of the domain by a Gaussian hump of water (Figure 5.2b).

The water surface disturbance propagates equally in all directions and should remain circularly symmetric. The Gaussian hump is defined as:

$$\eta = 40 \cdot e^{-\frac{x^2+y^2}{10}}. \tag{5.1}$$

Consider a domain of 200 by 200 m, where both x and y vary between -100 and 100 m, with $\Delta x = \Delta y = 1$ m. The depth of the bowl is 80 m and a time step of 0.016 s is used. To achieve the CM1, the adaptive mesh refinement in GeoClaw is applied to the virtual gauge covered area and in this case study it is done for the entire domain, in space and time. Here, three levels of refinement were set with factors (2,4,4). This means that at level 4 the grid resolution will be 0.03 m. The Sommerfeld or radiation condition was imposed at the boundaries of the domain.

The complete simulation in GeoClaw takes 8 s (see Figures 5.3 and 5.4). After 0.333 s of GeoClaw simulation, data is extracted and provided to the FUNWAVE-TVD simulation (Figures 5.5 and 5.6). The wave evolves as expected (Figure 5.7) and similarly as in the GeoClaw simulation (Figure 5.4). We can state that data from GeoClaw is being provided correctly as input data to FUNWAVE-TVD.

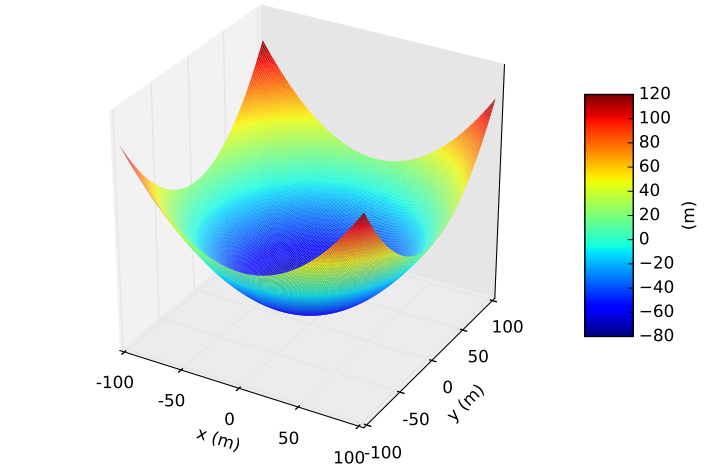

(a)

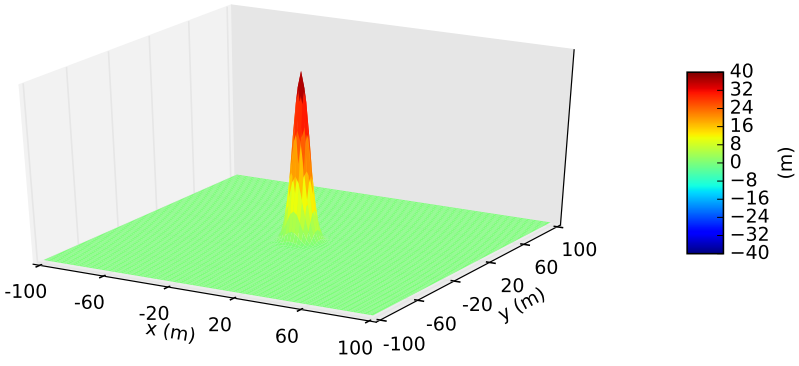

(b)

Figure 5.2: (a) Parabolic bowl. (b) Gaussian hump.

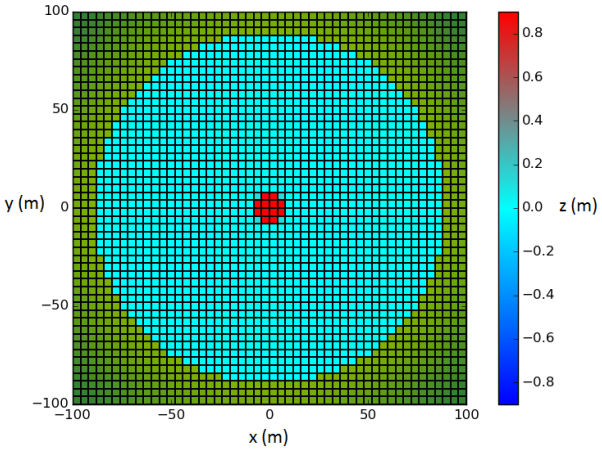

(a) t = 0.000 s

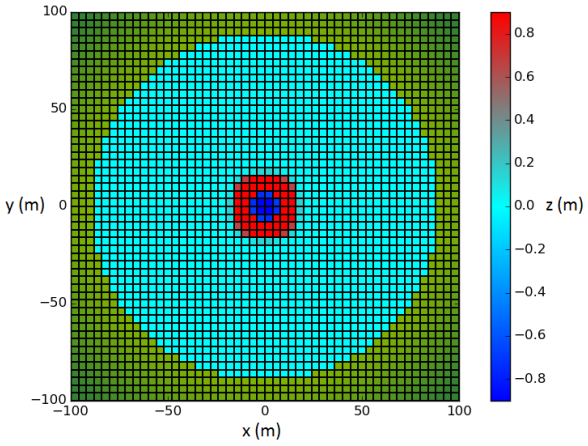

(b) t = 0.333 s

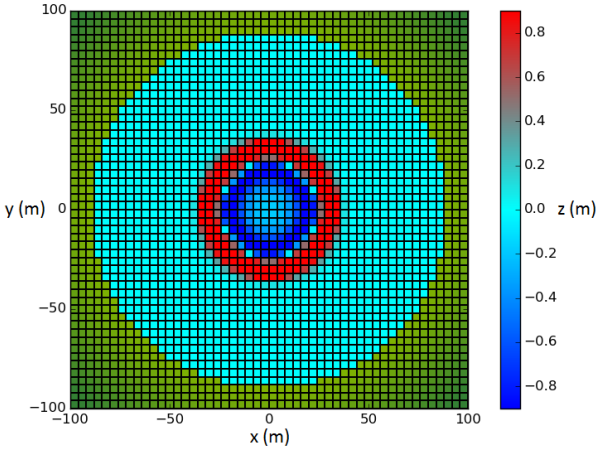

(c) t = 1.000 s

Figure 5.3: GeoClaw computation of the initial deformation at t = 0.000 s and propagation at t = 0.333 s and t = 1.000 s.

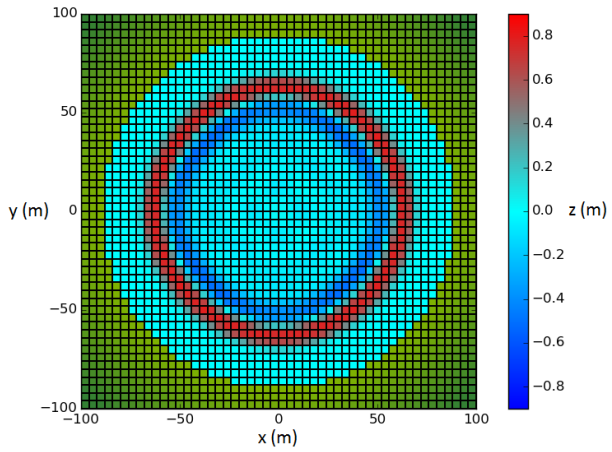

(a) t = 2.333 s

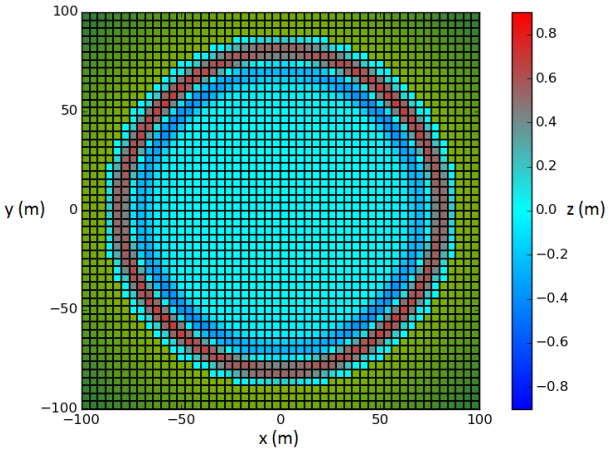

(b) t = 3.333 s

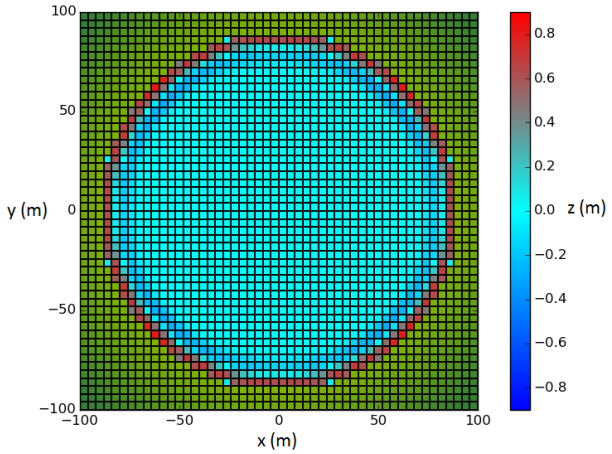

(c) t = 4.000 s

Figure 5.4: GeoClaw computation of propagation at t = 2.333 s, t = 3.333 s and t = 4.000 s.

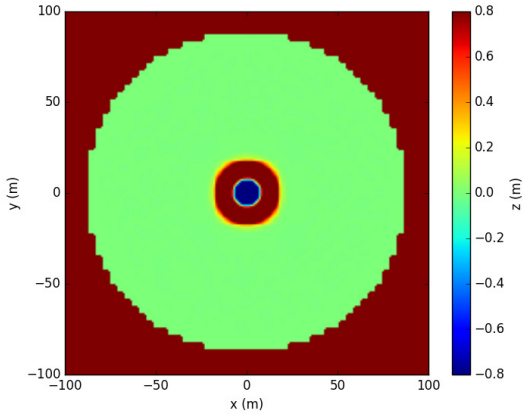

(a) t = 0.666 s

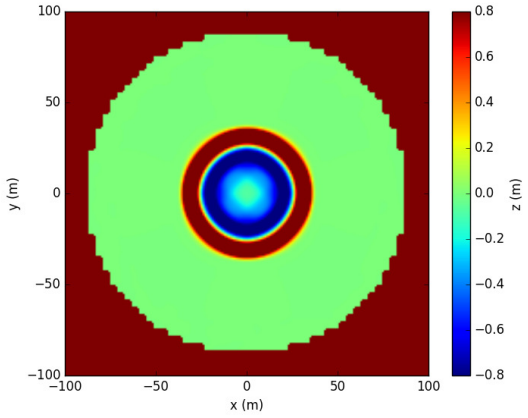

(b) t = 1.000 s

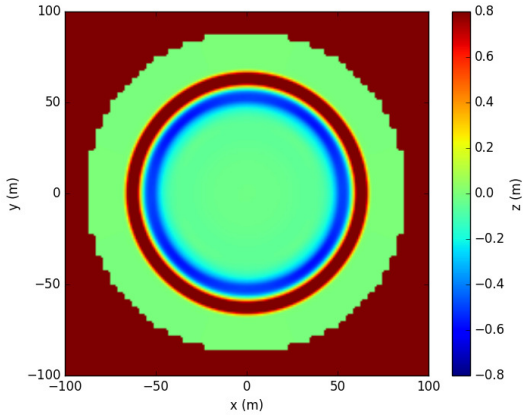

(c) t = 1.333 s

Figure 5.5: CM1 computation of the initial deformation at t = 0.666 s and propagation at t = 1.000 s and t = 1.333 s.

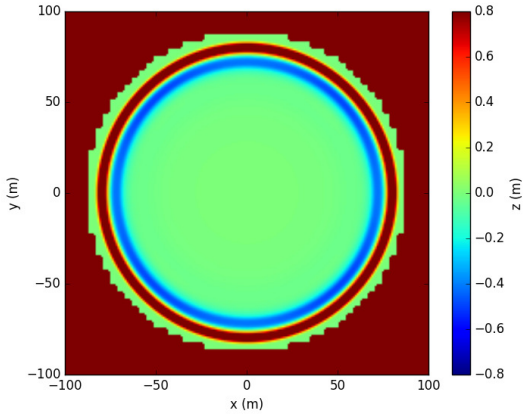

(a) t = 3.333 s

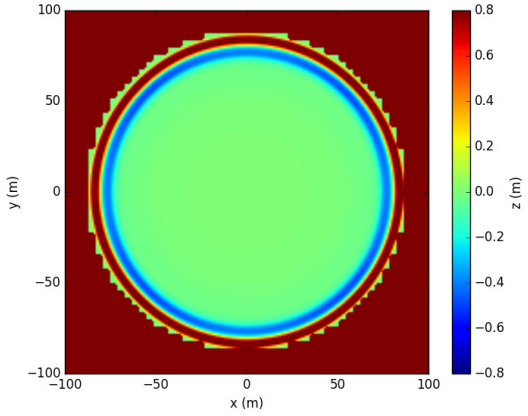

(b) t = 3.666 s

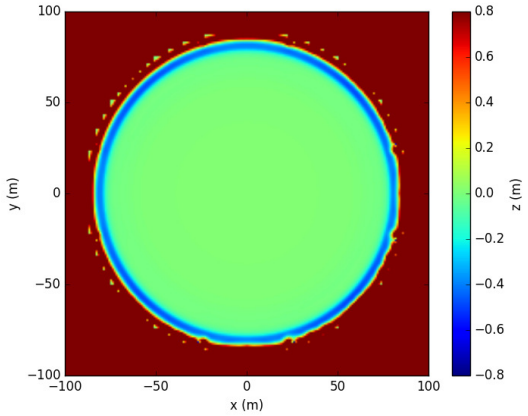

(c) t = 4.000 s

Figure 5.6: CM1 computation of propagation at t = 3.333 s, t = 3.666 s and t = 4.000 s.

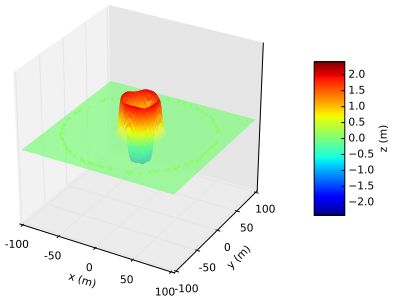

(a) t = 0.666 s

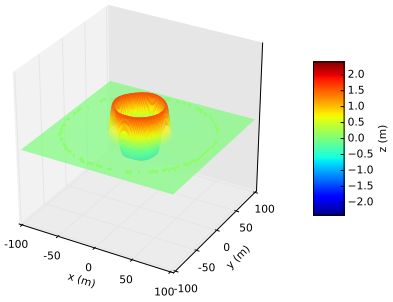

(b) t = 1.000 s

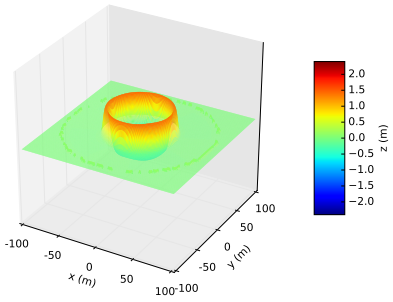

(c) t = 1.333 s

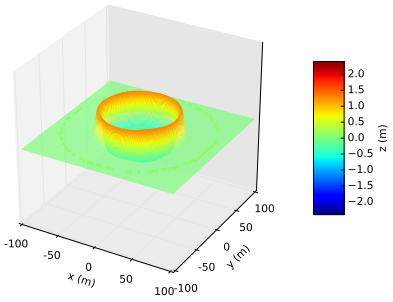

(d) t = 1.666 s

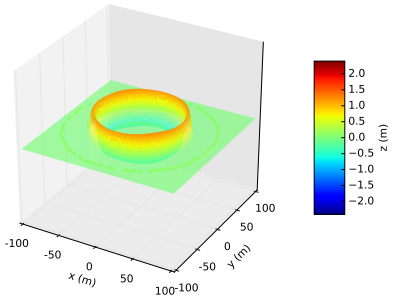

(e) t = 2.000 s

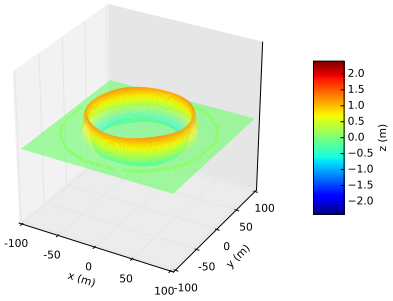

(f) t = 2.333 s

Figure 5.7: 3D visualization of CM1 computation of propagation at t = 0.666 s, t = 1.000 s, t = 1.333 s, t = 1.666 s, t = 2.000 s and t = 2.333 s.

5.2.3 Nesting capability: Case study of a M_w 8 Earthquake at the Southwest Iberian Margin—The 1969 Portugal Earthquake and Tsunami (1969 PET)

5.2.3.1 CM1 1st level grid simulations

We verify the performance of the nesting capability within CM1, using an earthquake event with M_w = 8, located at the Southwest Iberian Margin. It is an event similar to the 1969 Portugal Earthquake and Tsunami (1969 PET) event, with magnitude M_w = 7.7 – 7.8, that occurred at 2h40min30s UTC of the 28th February 1969, with epicentre (36.010°N, 10.570°W).

Table 5.1: 1969 PET fault mechanism parameters (Grandin et al., 2007).

Scenario	Length (km)	Width (km)	Strike (°)	Dip (°)	Rake (°)	Slip (m)	Depth† (km)	μ (Pa)	M_0 (N · m)	M_w
A	85	20	231	47	54	5.29	20	4×10^{10}	3.6×10^{20}	7.8

†Top of the fault

This event has been studied by Gjevik et al. (1997) and used by Clain et al. (2016) to check the performance of a finite volume shallow water code.

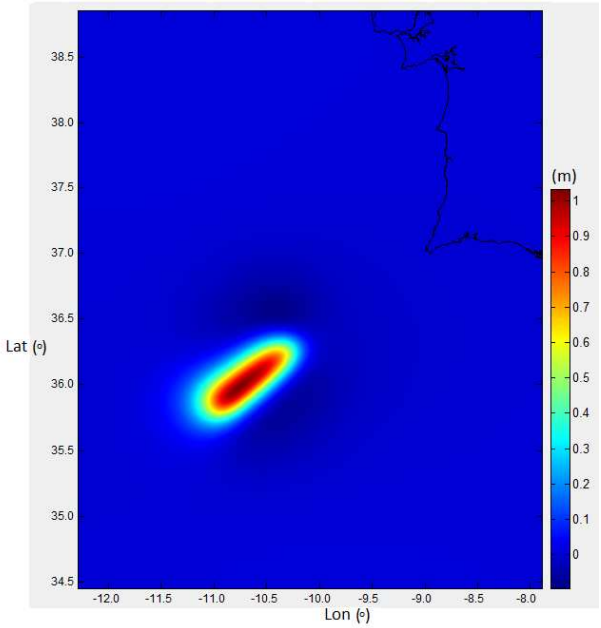

Figure 5.8: Initial deformation (in metres) of the 1969 PET event.

Two sets of grids were used in this study: grid set A (GA) with bathymetry from GEBCO — General Bathymetric Chart of the Oceans (Sandwell et al. 2002) and grid set B (GB) (Baptista 2017). Layer 01, the mother grid from grid set A, is a 1245×1601 grid with 700 m grid resolution. Layer 01, the coarsest grid from grid set B, is a 2951×2951 grid with 163 m grid resolution. Tsunami simulations were performed separately with both grid sets. The bathymetry is referred to the mean sea level. In GeoClaw, two levels of refinement were set with factors (2,6). The initial time step used is 0.2 s. The Sommerfeld or radiation condition was imposed at the boundaries of the domain.

The fault parameters used to simulate this event were taken from Grandin et al. (2007) and are listed in Table 5.1. The initial seafloor deformation is represented in Figure 5.8 and the focal

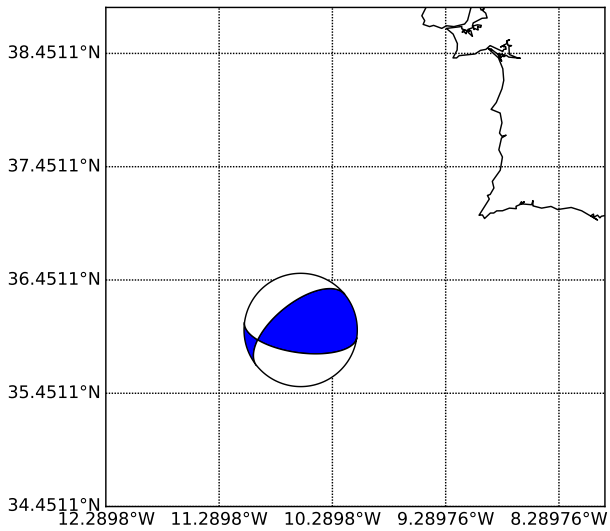

Figure 5.9: Focal mechanism of the 1969 PET event. The CMT is provided by Grandin et al. (2007) and located at the epicentre.

mechanism is plotted in Figure 5.9. The seafloor deformation was determined from the elastic dislocation model in a homogeneous isotropic elastic half-space (Mansinha and Smylie 1971; Okada 1985). It assumes an instantaneous static seabed displacement, translated towards the free surface as an initial condition, reproducing the elastic bottom deformation caused by the earthquake. In the GeoClaw code, the Okada equations are implemented in the `maketopo.py` routine.

The initial data, necessary to run the Boussinesq model, was retrieved from GeoClaw output results, as explained before in section 5.2. The data was written in four separated ASCII files, concerning the water depth h, the water surface elevation η, the velocity u and the velocity v. This initial information corresponds to 300 s after the generation of the earthquake and tsunami. From the visual analysis of simulation plots, we selected this time instant and we considered that at this stage the tsunami generated waves are fully developed and that the propagation is no longer subject to the source area influence. Starting 300 s after the generation of the earthquake, the snapshots of the tsunami propagation with CM1 are shown in Figure 5.10.

Computations were performed with both sets of grids A and B. Results are shown in Table 5.2. Free surface elevation plots for Cascais, Lagos and Faro are respectively presented in Figures 5.11, 5.12 and 5.13 and compared with some of the available wave records from the 1969 event.

For Faro, in Figure 5.13, we only show results for grid set A (GA). From the plot analysis, there seems to be a significative lag between the simulations time series of water surface displacement and the observations at the Faro tide gauge.

Table 5.2: Virtual gauges used to study the 1969 PET event. Characteristics and respective computational results with layer 01 from GA and layer 01 from GB.

Station	Location [1]		Depth[1]	Dist.[2]	H_{obs} [3]	H_{Geo} [4]		H_{CM1} [5]		TTT diff [6]	
	Lon	Lat				GA[7]	GB[8]	GA	GB	GA	GB
	(°)	(°)	(m)	(km)	(cm)	(cm)	(cm)	(cm)	(cm)	(min)	(min)
Cascais	-9.4112	38.6816	17.37	313.77	51.2	28.3	35.5	41.4	47.5	2.0	0.5
Lagos	-8.6688	37.0688	22.81	206.84	58.4	24.9	16.1	33.5	24.6	3.9	2.6
Faro	-7.8688	36.9728	8.74	264.33	23.5	24.9	– [9]	18.4	–[9]	6.5	–[9]

[1]Retrieved from layer 01 of grid set A (GA).
[2]Distance from station to source location, determined according to Vincenty (1975).
[3]Observed maximum trough-to-crest wave height (first wave arrival).
[4]GeoClaw maximum trough-to-crest wave height (first wave arrival).
[5]CM1 maximum trough-to-crest wave height (first wave arrival).
[6]Tsunami Travel Time difference between observations and CM1.
[7]Grid set A.
[8]Grid set B.
[9]Not available.

5.2.3.2 Nested grid simulations

The simulation of the tsunami propagation of the 1969 PET was performed in a series of nested grids of increasing resolution, using a one-way coupling method.

Two sets of three series of nested grids of increasing resolution were applied in the computation of the 1969 PET event (Figure 5.10): grid set A (Table 5.3 and Figure 5.14) and grid set B with finer resolutions (Table 5.4 and Figure 5.16).

Grids 01, 21 and 31 from grid set A use bathymetry from GEBCO, with the water depth referred to the mean sea level. Grid 41 was obtained by combining two data sets: the digital elevation model with topographic data from the Cascais City Council and a set of bathymetric data from the Hydrographic Institute, Portugal. Grids 01, 21 and 31 from grid set B use bathymetry provided by Baptista 2017.

The time series of surface elevation and depth-averaged velocity were computed for a vast number of synthetic wave gauges (please refer to Table 5.5 for the exact number of synthetic wave gauges, which correspond to the boundary points, used along each boundary), defined in the coarser grid along the mutual boundary with the finer grid used in the next level of nesting. To agilize this nesting step between the several couples of grids, a script was written to generate the virtual gauges locations.

Table 5.3: Characteristics of grid set A (GA) for the 1969 PET.

grid	nx[1]	ny[2]	cell size		X0Lon	Y0Lat
			(°)	(m)	(°)	(°)
01	1001	1001	0.0064	700	-12.2890	34.4519
21	404	336	0.0016	175	-9.7976	38.4808
31	752	528	0.0004	44	-9.5678	38.6050

[1]Number of grid columns.
[2]Number of grid rows.

The computations are fully performed (complete simulation run time) in the coarser layer;

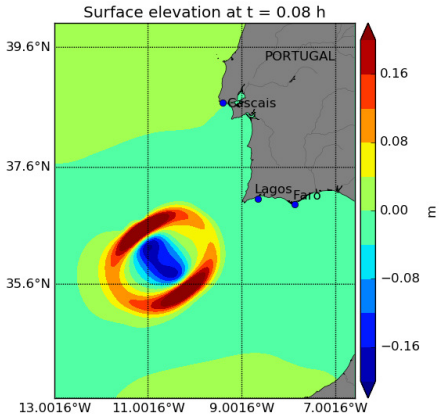

(a) t = 0.08 h

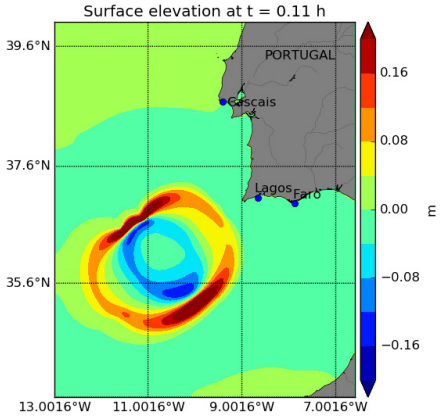

(b) t = 0.11 h

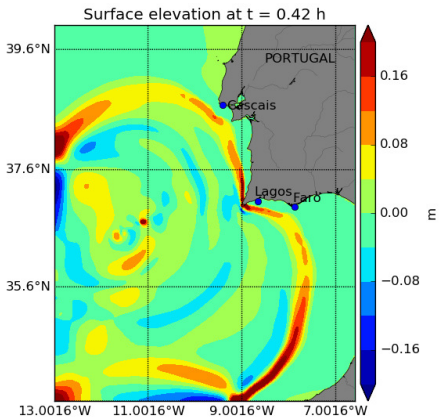

(c) t = 0.42 h

Figure 5.10: Snapshots from CM1 results at t = 0.08 h, t = 0.11 h and t = 0.42 h, with initial deformation data retrieved from GeoClaw (corresponding to t = 0.08 h), using the source described in Grandin et al. (2007) and layer 01 (with 700 m resolution) from grid set A.

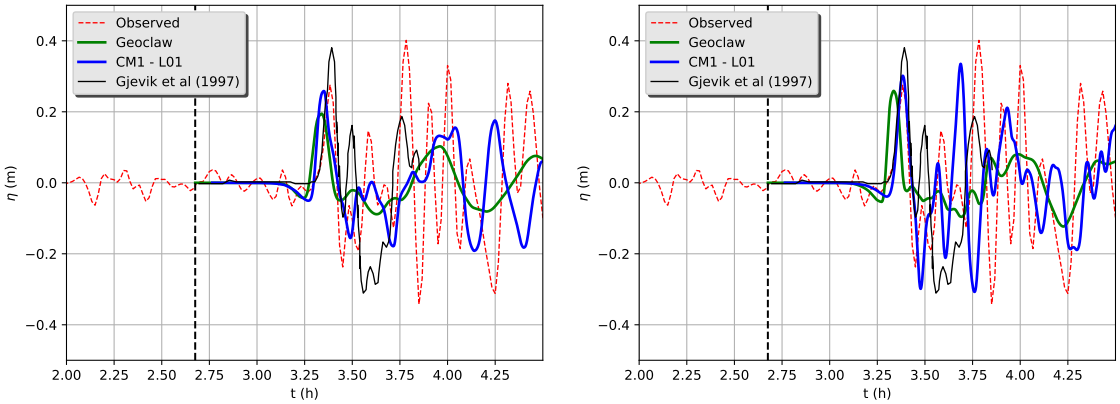

(a) (b)

Figure 5.11: Cascais: Comparison of the synthetic tsunami time series of water surface displacement and the observations from the 1969 event for (a) 700 m grid A (GA) and (b) 163 m grid B (GB). Earthquake origin time is indicated by the vertical dashed line.

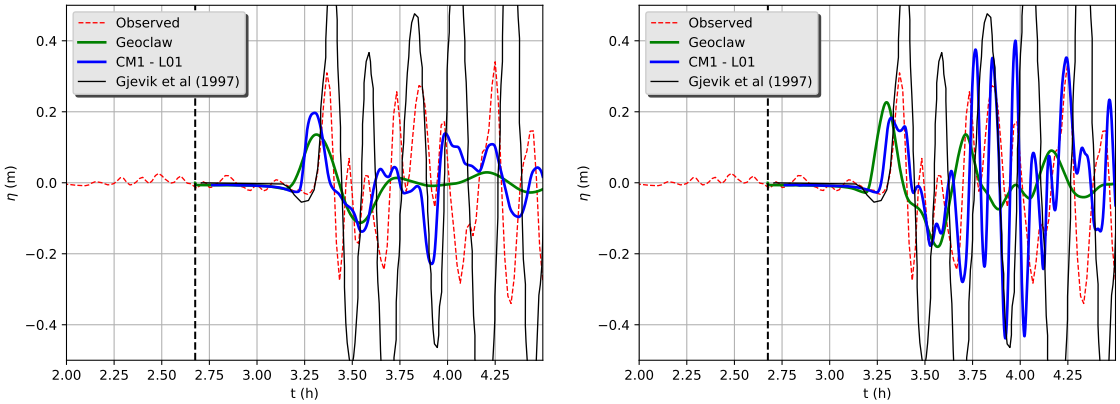

(a) (b)

Figure 5.12: Lagos: Comparison of the synthetic tsunami time series of water surface displacement and the observations from the 1969 event for (a) 700 m grid A and (b) 163 m grid B. Earthquake origin time is indicated by the vertical dashed line.

Table 5.4: Characteristics of grid set B (GB) for the 1969 PET.

grid	nx	ny	cell size		X0Lon	Y0Lat
			(°)	(m)	(°)	(°)
01	2951	2951	0.001493	163	-12.2890	34.4519
21	840	640	0.000373	41	-9.4573	38.4884
31	1228	1068	0.000093	10	-9.4358	38.6245

after completion, and using the code coupling capability, the computations are restarted in the finer layer, using virtual wave gauges time series as boundary conditions. A constant nesting ratio of 4 was used between layers at all the nesting levels. Boundary sponge layers are applied in the computations to reduce reflection effects in the boundaries. The sponge layers are 50 km wide and

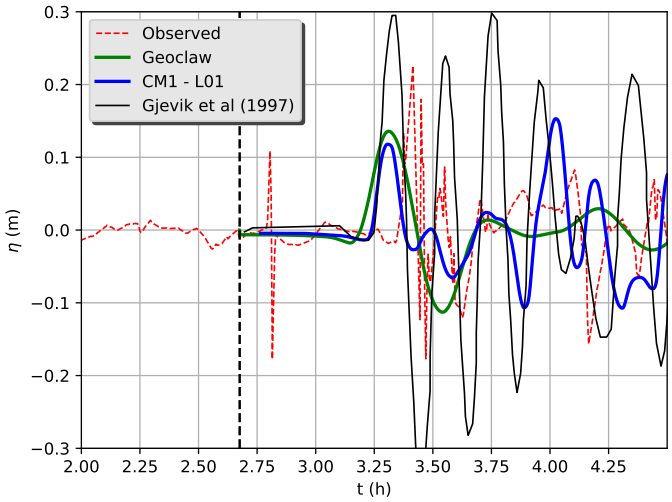

Figure 5.13: Faro: Comparison of the synthetic tsunami time series of water surface displacement and the observations from the 1969 event (700 m grid set A; Faro not available for 163 m grid set B). Earthquake origin time is indicated by the vertical dashed line.

Table 5.5: 1969 PET: Number of boundary points (synthetic gauges) between layers, used in the nested simulations, for grid set A (GA) and for grid set B (GB).

boundary	L01–L21		L21–L31	
	GA	GB	GA	GB
North (N)	102	211	189	307
South (S)	102	211	189	307
West (W)	85	161	133	159
East (E)	0	0	0	0
total no points	289	583	511	881

were applied in all the boundaries of the layer 01 simulation. In GeoClaw, the Manning coefficient n is taken as 0.025 s/$m^{1/3}$ (Te Chow 1959). In FUNWAVE-TVD, the bottom friction coefficient $Cd = 0.0025$ is used in the simulations, equivalent to n = 0.025 s/$m^{1/3}$.

We analysed the results obtained at the virtual gauges, placed at the approximate locations of the Cascais tide gauge in 1969 (Figures 5.15 and 5.17). These results are compared with the observations recorded at the time of the event, for the mentioned tide gauge locations (Table 5.2).

The very first stage of the nesting grid simulations is to verify that the data between the nested grids would get across correctly. We then started by comparing the computed water surface elevations, at each boundary grid point, between nested grids. It is very important to verify that this step is thoroughly done.

Table 5.6 contains a summary of the nesting results obtained using grid set A and grid set B. The term of comparison is the 1969 PET tide record at Cascais (Table 5.2).

The nesting tests presented served to evaluate the nesting capability within the code and to show its usefulness and efficiency. These tests also showed the performance of the proposed combined model CM1, supporting its validation process.

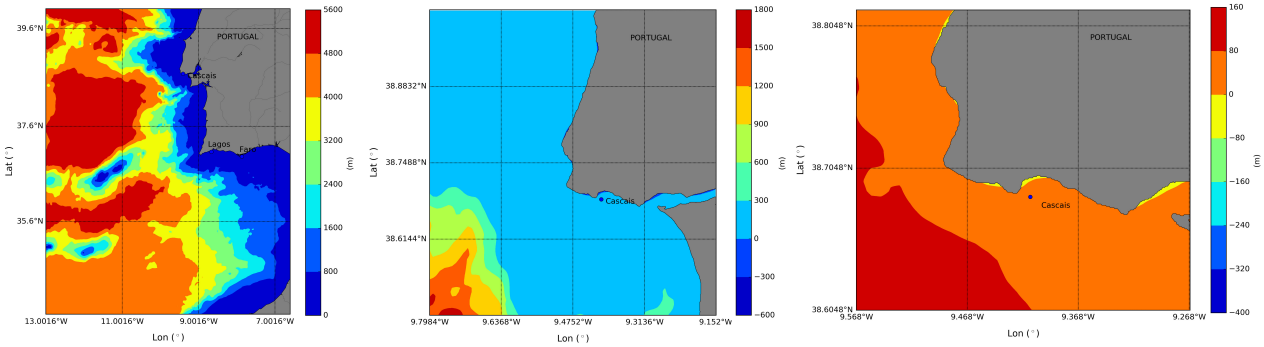

Figure 5.14: Grid set A: Layers 01, 21 and 31 comprising respectively 1) Portugal and part of the Atlantic Ocean, 2) the Cascais area, and 3) a detailed area of Cascais.

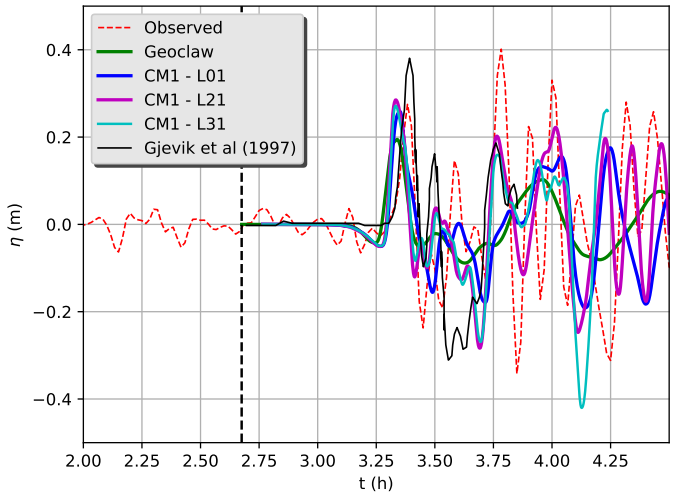

Figure 5.15: Grid set A: Comparing the computational results for a virtual tide gauge at Cascais and the time series recorded during the 1969 PET at the Cascais tide gauge. Two levels of nesting were used in the computation with CM1 (layers 01, 21 and 31). Earthquake origin time is indicated by the vertical dashed line.

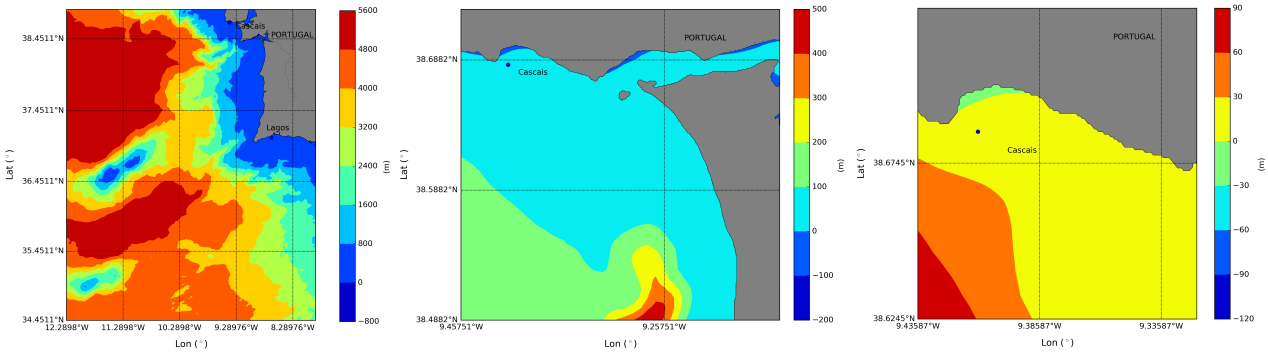

Figure 5.16: Grid set B: Layers 01, 21 and 31 comprising respectively 1) Portugal and part of the Atlantic Ocean, 2) the Cascais area and Costa da Caparica, and 3) Cascais.

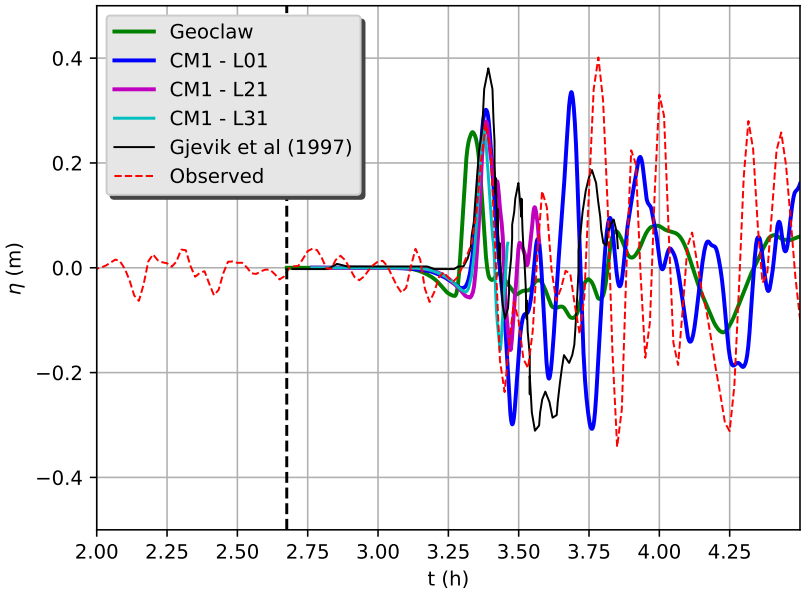

Figure 5.17: Grid set B: Comparing the computational results for a virtual tide gauge at Cascais and the time series recorded during the 1969 PET at the Cascais tide gauge. Two levels of nesting were used in the computation with CM1 (layers 01, 21 and 31). Earthquake origin time is indicated by the vertical dashed line.

Table 5.6: Cascais: Computed maximum trough-to-crest wave height for CM1 $\left(H_{CM1}\right)$ and the tsunami travel time (TTT) difference of the first wave arrival from the original tide records, for grid set A and for grid set B.

grid set	A		B	
grid	H_{CM1} (cm)	TTT diff (min)	H_{CM1} (cm)	TTT diff (min)
01	41.4	2.0	47.5	0.5
21	40.6	3.0	43.6	0.0
31	35.5	3.1	30.8	0.5

5.2.3.3 Data set deviations

We quantify the deviations of the computational data sets, comparing the wave records from the event, retrieved at the Cascais tide gauge, with the results from the numerical codes, retrieved at a virtual tide gauge located close to the real Cascais tide gauge. Deviations are found when comparing observations with the numerical results. Two metrics were used:

- the relative amplitude deviation, defined by:

$$L_{amp} = \sum_{i=1}^{N} \frac{|\eta_{i_{obs}} - \eta_{i_{num}}|}{N}; \tag{5.2}$$

- the L2-norm, calculated as:

$$L_{2_{obs-num}} = \sqrt{\sum_{i=1}^{N} \frac{(\eta_{i_{obs}} - \eta_{i_{num}})^2}{N}}. \tag{5.3}$$

Table 5.7: Quantification of the data set deviations for Cascais (Grid set B).

	L_{amp} (cm)	L_2-norm (cm)
Observed – GeoClaw	4.25	8.70
Observed – CM1 L01	0.97	1.92
Observed – CM1 L21	1.47	3.31
Observed – CM1 L31	1.33	2.93
Observed – Gjevik et al. (1997)	1.67	4.06

Results are discussed in the next section.

5.2.3.4 Discussion of Results

At the beginning of the time series of the observations for the three tide gauges, Cascais, Lagos and Faro, some oscillations in the water levels are observed before the earthquake occurs and the tsunami arrives. These are short period oscillations (when compared with the tidal periods) of small amplitude, less than 10 cm. This happens because the tide gauges, unlike the DARTs, are located in sheltered waters, and some oscillations due to resonance are present in the records. Looking at the 1969 PET simulation results from GeoClaw and CM1, at Cascais and Lagos, and comparing with the event observations at these locations, we can state that the CM1 computational results using grid set B (GB) are quite satisfactory. The results show a better fit with the observational data, when comparing with the results obtained with grid set A (GA), as the layers from grid set B (GB) have finer resolutions than grid set A layers. Considering the first wave arrival, the trough-to-crest wave height obtained with GB is closer to the observed one; also, the tsunami travel time difference (TTT diff) is smaller than for GA: around 30 s for Cascais, quite close to the observations, and around 150 s for Lagos. For GA, the difference is 2 min for Cascais and 4 min for Lagos. However, from the metrics we see that the errors increase as the cell size decreases, that is to say that the errors increase with the nesting between finer layers. The nesting seems to originate wave dissipation and wave arrival delayal. In the nesting the values from the free surface elevation and the velocities are input at the boundary. Model equations [1]–[8] in Shi et al. (2012c) include the velocity term $\mathbf{u_2}$, which is dependent of the velocity gradient. The information on the velocity gradient, which is necessary to the correct definition of the model, is lost in the boundary conditions of the nested layers, causing an error increase as the cell size decreases.

The computational results from the CM1, using grid set B, are also better than those obtained by Gjevik et al. (1997) (Figure 5.17 and Table 5.7), which used a Boussinesq model. Gjevik et al. (1997) overestimated the wave amplitude of the first wave arrival, whereas CM1 computational results, with the several GB nested layers used, show wave amplitudes similar to the first and second wave arrival of the Cascais tide gauge event record. The wave profile results, from the simulations using grid set B, are closer to the observations. The tsunami travel time differences are 0 to 30 s, whereas with GA these vary between 2 and 3 min. Maximum trough-to-crest wave height is also closer to the tide record observations at Cascais.

As expected from the two separated nesting simulations, with GA and GB, it is clear that the grid resolution of the coarse/mother layer is of crucial importance and influence on the quality of the nesting simulations results, as well as the child layers resolution. For both grid sets A and B,

the grid extensions and the bathymetries are different and the cell size of the mother layer is 4 times the cell size of the child layer.

5.2.4 Benchmark case study: 2015 Illapel Earthquake and Tsunami

5.2.4.1 CM1 results

The 2015 Illapel earthquake occurred on the 16th of September at 22h54min33s UTC, offshore from Illapel, Chile, with a moment magnitude M_w = 8.3. According to the USGS *, the earthquake epicentre was (31.577°S, 71.652°W), with a focal depth of 25 km. A GEBCO (General Bathymetric Chart of the Oceans) grid, 7200 × 7200, with resolution of 30 arc seconds (≈ 1 km) and dimensions 120°– 60°W and 60°– 0°S was used (Figure 5.18). The bathymetry is referred to the mean sea level.

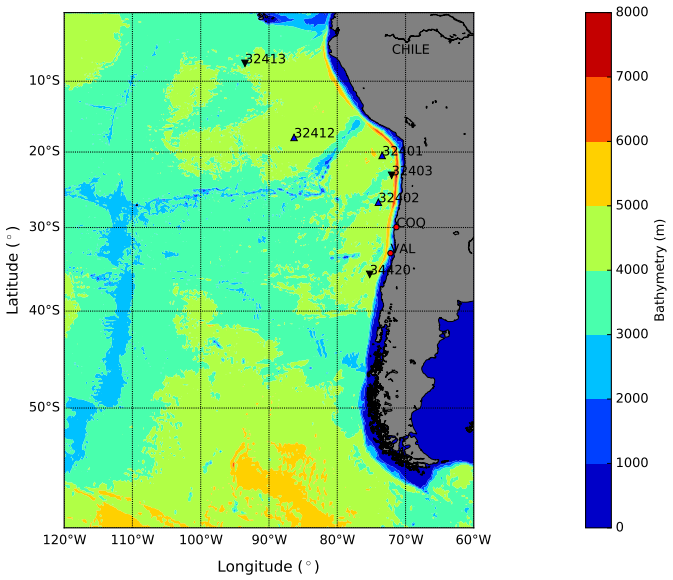

Figure 5.18: Bathymetric setting of Chile with the location of the nearest DARTs (triangles) and tide gauge stations (○). △ : observations available. ▽ : no observations available.

The initial seafloor deformation used to simulate this event was provided by Diego Melgar and his team. It is based on the work described in Melgar et al. (2016), where the authors described the detailed study of the source kinematics. First they resolved a kinematic source model by jointly inverting several regional geophysical observables, as high-rate GPS records, strong motion records, satellite interferograms and tide gauges. For slip inversion, the authors used the MudPy open source inversion code (Melgar and Bock 2015), the Centro Sismologico Nacional (CSN) hypocentre and the Slab 1.0 model (Hayes et al. 2012) to define the fault and discretised it to 225 subfaults. They also computed the elastodynamic Green's functions (GFs) for every subfault/station pair using the frequency wavenumber integration technique. The potential sources were gridded at 5 km spacing at the hypocentral depth (19 km) within the latitude range (-34.23°) to (-28.87°) and longitude range (-74.49°) to (-70.29°) (600 km by 400 km). For other informations, please consult the supplementary documents and figures in `https://agupubs.onlinelibrary.wiley.com/doi/full/10.1002/2015GL067369`.

*`https://earthquake.usgs.gov/earthquakes/eventpage/us20003k7a/origin/detail`

Melgar et al. (2016) further validated the kinematic source inversion, by using it to forward calculate a local tsunami propagation model and by comparing the model predictions to the run-ups measured at 28 locations. They produced slip inversions that use the local tide gauges, as well as the seismic and geodetic data and validated their model.

Using the authors' research findings on the source of this event, we performed the tsunami simulation with GeoClaw using the referred 7200 $\times$ 7200 GEBCO bathymetric grid with resolution of 30 arc seconds ($\approx$ 1 km) (Figure 5.18). The initial sea surface propagation is plotted in Figure 5.19. The CMT provided by the USGS is plotted in Figure 5.20.

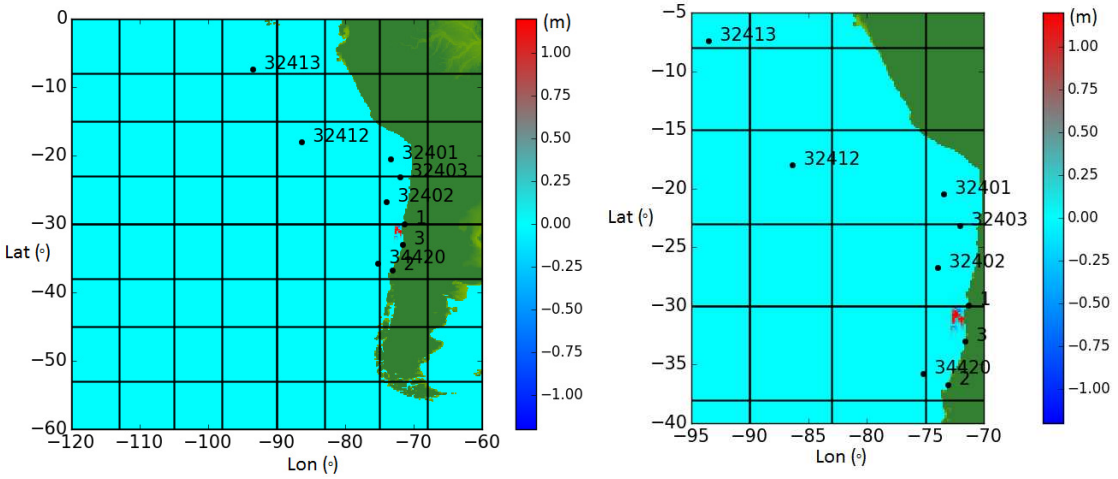

(a) (b)

Figure 5.19: (a) Initial sea surface propagation (in metres) of the Chile 2015 event (Melgar et al. 2016). (b) Zoom of Figure (a).

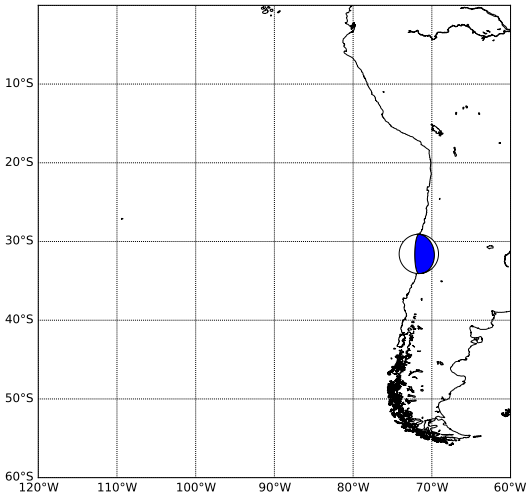

Figure 5.20: Focal mechanism of the 2015 Chile event. The CMT is provided by USGS and located at the epicentre.

The propagation of the tsunami was performed with the GeoClaw code (Figure 5.19); afterwards, the data from GeoClaw, after 420 s of computation, was provided as an input to the

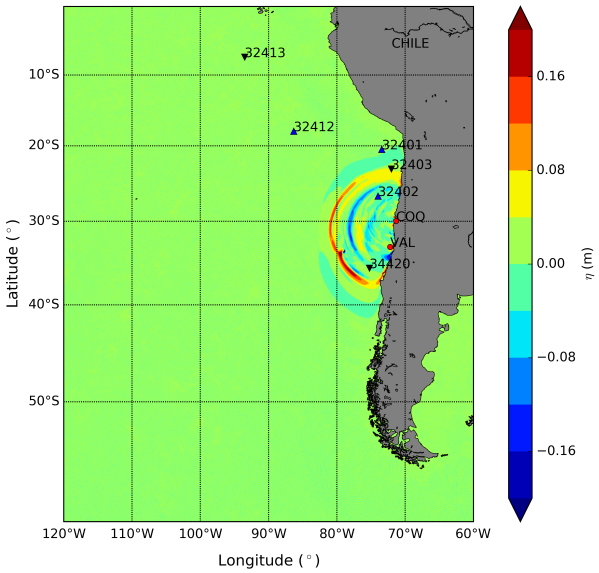

Figure 5.21: Tsunami propagation with CM1 after 420 s.

Table 5.8: Details about the tide gauges used to study the Illapel 2015 event.

Tide station	Station name	Location		Depth[1]	Dist.[2]	H_{Geo} [3]	H_{CM1} [4]
		Lon (°)	*Lat* (°)	(m)	(km)	(cm)	(cm)
COQ	Coquimbo, CHL[5]	-71.38	-29.95	104	182.2	88.9	311.4
VAL	Valparaiso, CHL	-71.70	-33.02	127	160.1	37.9	35.1

[1]Retrieved from the simulation mother grid.
[2]Distance from tide station to source location, determined according to Vincenty (1975).
[3]GeoClaw maximum trough-to-crest wave height (first wave arrival).
[4]CM1 maximum trough-to-crest wave height (first wave arrival).
[5]Chile

FUNWAVE-TVD code. We selected this time instant from the visual analysis of the simulation plots, as we considered that at this stage the tsunami generated waves are fully developed and that the propagation is no longer subject to the source area influence. Tsunami propagation computed with CM1 at a later stage is plotted in Figure 5.21.

For all the simulations with GeoClaw and CM1, computed tsunami waveforms at two distinct coastal locations in Chile (Figure 5.18) are presented and analysed (Figure 5.22 and Table 5.8).

Computed tsunami waveforms at the location of each DART station (Figure 5.18) were retrieved and compared with the DART observations available. The original DART data was retrieved from the National Data Buoy Center [†]. Overall, we aimed to use 6 DART locations to study the event, although the wave height records from the event were only available for 3 of the listed DARTs (Table 5.9): DART 32401, DART 32402 and DART 32412. The data from the DARTs is provided at different sampling intervals, which causes repetition of the data points, as well as some gaps and spikes. After its removal from the time series, data is de-tided: applying variable degree *n* polynomial fitting (with *polyfit* function from GNU Octave—Eaton et al. 2014),

[†]`https://www.ndbc.noaa.gov/dart.shtml` (last consulted in October 2016).

Table 5.9: DART stations used to study the Illapel 2015 event. Characteristics and respective computational results.

DART station	Station name	Location		Depth[1]	Dist.[2]	H_{obs} [3]	H_{Geo} [4]	H_{CM1} [5]	TTT [6] diff
		Lon (°)	Lat (°)	(m)	(km)	(cm)	(cm)	(cm)	(min)
32401	SW Arica, CHL[7]	-73.429	-20.473	4797	1242.9	7.9	7.0	8.0	0.2
32402	W Caldera, CHL	-73.983	-26.743	4070	581.8	19.4	11.5	18.7	4.3
32403	W Antofagasta, CHL	-72.037	-23.163	–[8]	933.1	–[8]	10.0	10.8	–[8]
32412	SW Lima, PER[9]	-86.330	-17.980	4387	2110.2	9.1	11.4	13.8	5.1
32413	NW Lima, PER	-93.517	-7.406	4018	3509.2	–[8]	4.1	5.8	–[8]
34420	NW Concepcion, CHL	-75.243	-35.758	–[8]	570.8	–[8]	13.5	18.1	–[8]

[1]Retrieved from the simulation mother grid.
[2]Distance from DART to source location, determined according to Vincenty (1975).
[3]Observed maximum trough-to-crest wave height (first wave arrival).
[4]GeoClaw maximum trough-to-crest wave height (first wave arrival).
[5]CM1 maximum trough-to-crest wave height (first wave arrival).
[6]Tsunami Travel Time difference between observations and CM1.
[7]Chile.
[8]Not available.
[9]Peru.

we estimated the tidal signals and then removed these from the original records (Figure 5.23). Afterwards, the de-tided waveforms were used to compare with our simulations results (Figures 5.24). We also compare our results with the results by Heidarzadeh et al. (2016).

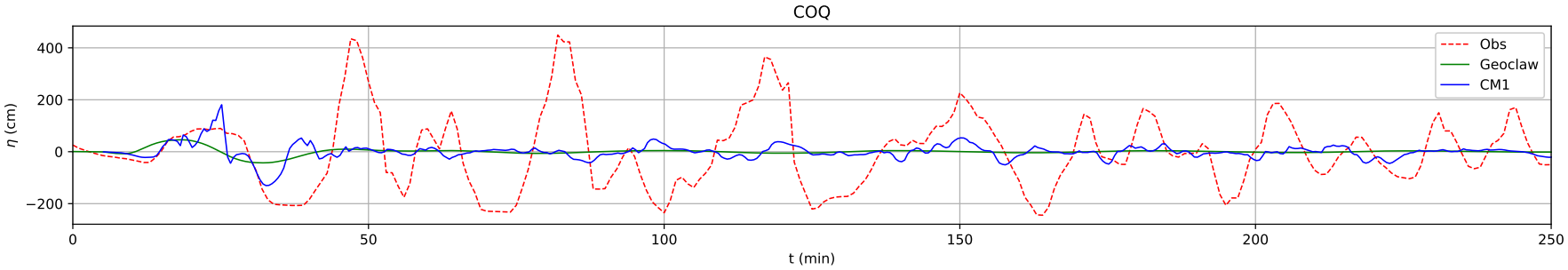

(a) Coquimbo

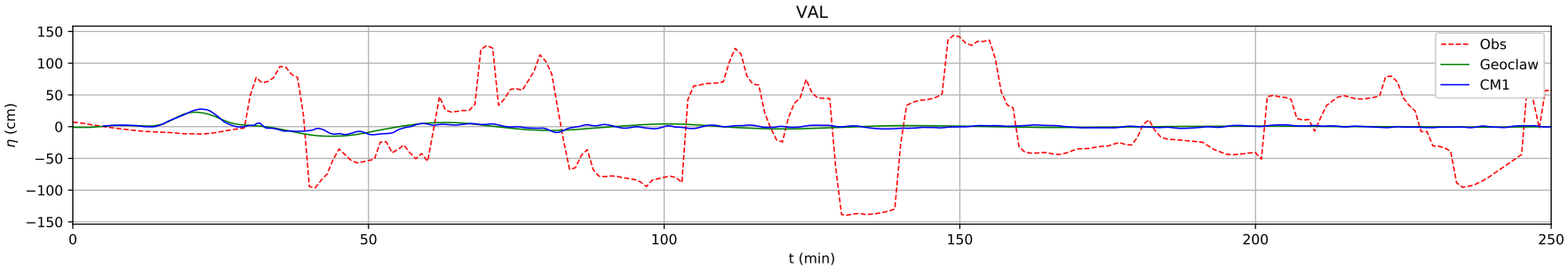

(b) Valparaiso

Figure 5.22: 2015 Illapel event:: Comparison between the observed data (red) and the computed tsunami waveforms from GeoClaw (green) and CM1 (blue), for two Chile tide gauges.

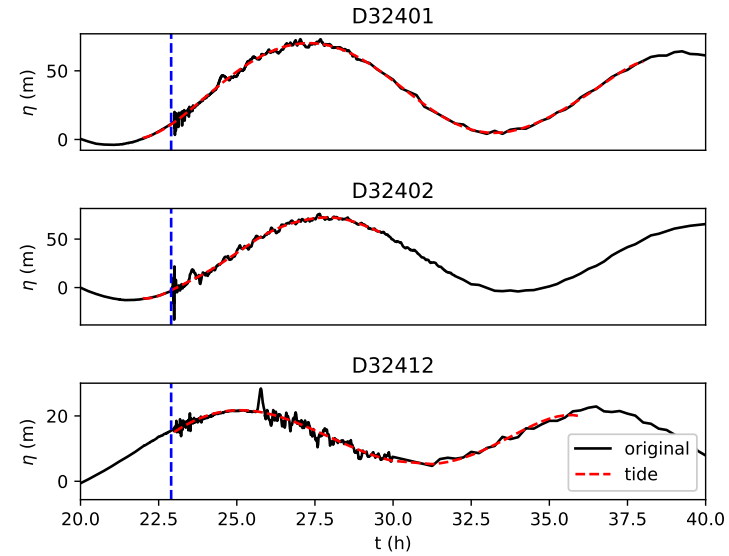

(a)

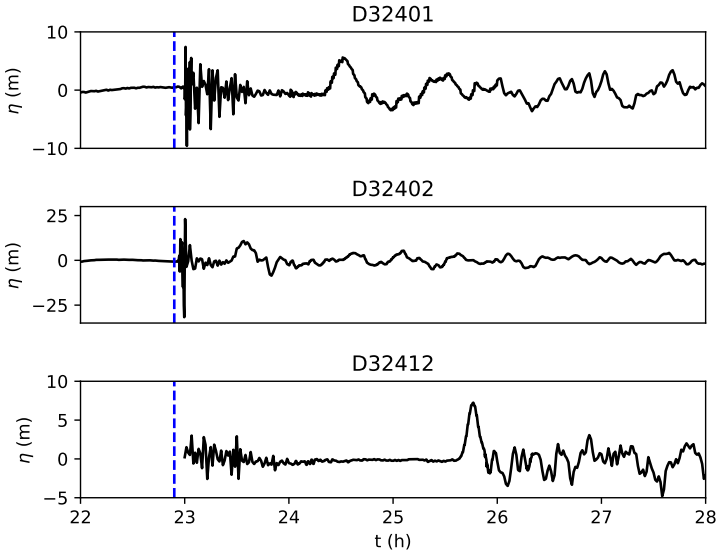

(b)

Figure 5.23: 2015 Illapel event: DART 32401, 32402 and 32412 (a) original records and (b) detided waveforms using polynomial fit. Earthquake origin time is indicated by the vertical dashed line.

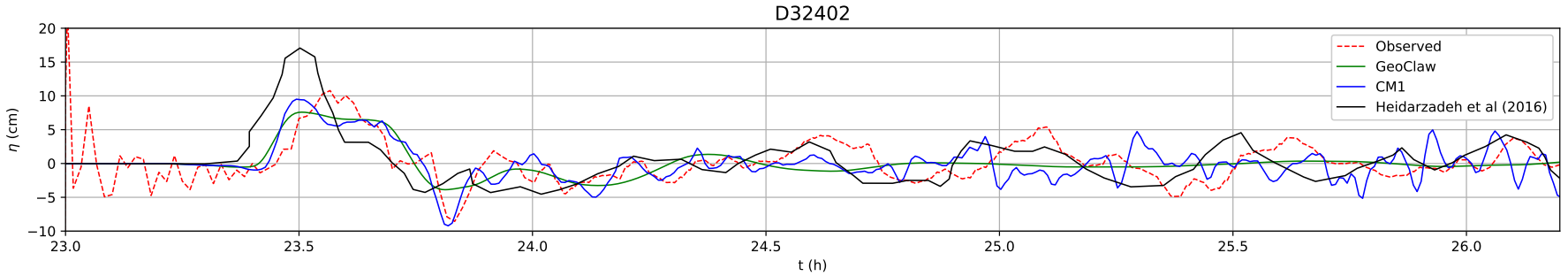

(a) 32402

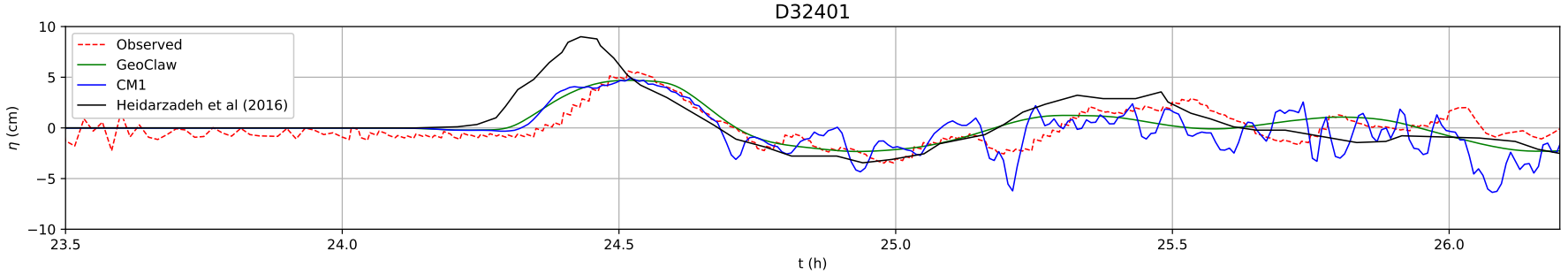

(b) 32401

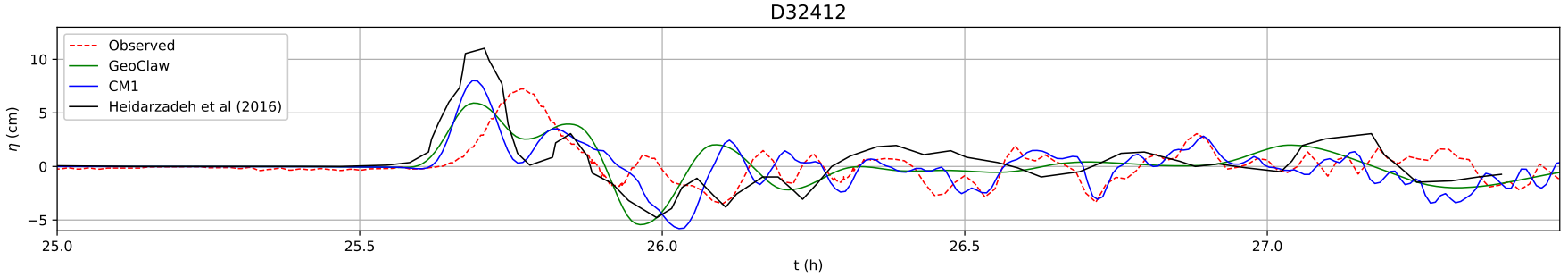

(c) 32412

Figure 5.24: 2015 Illapel event: Comparison between the DARTs observed data (red), GeoClaw (green) and CM1 (blue) computed tsunami waveforms, and the simulation results of Heidarzadeh et al. (2016) (black). Earthquake origin time: 22h54min33s UTC.

5.2.4.2 Data set deviations

We quantified the computational data sets deviations comparing them with the wave records retrieved from DART 32401, DART 32402 and DART 32412. The metrics used herein are described in section 5.2.3.3.

Table 5.10: Quantification of data set deviations.

DART		L_{amp} (cm)	L_2-norm (cm)
32401	Observed – GeoClaw	1.54	1.24
	Observed – CM1	3.44	1.85
32402	Observed – GeoClaw	1.91	2.37
	Observed – CM1	2.41	2.98
32412	Observed – GeoClaw	1.08	1.72
	Observed – CM1	0.92	1.66

The discussion of the results is presented further ahead in this section.

5.2.4.3 Fourier and wavelet analysis

We performed the spectral analysis of the wave records for DARTs 32401, 32402 and 32412. Using Python (van Rossum 1995), we applied the fast Fourier transform (FFT) method. For the Fourier analysis, we used 2 h 45 min of the tsunami waveforms.

As stated by Heidarzadeh et al. (2015), in general DARTs are free from local and/or regional bathymetric effects; nevertheless, these effects cannot be excluded due to the existence of submarine topography, as ridges, sea-mount chains, and islands.

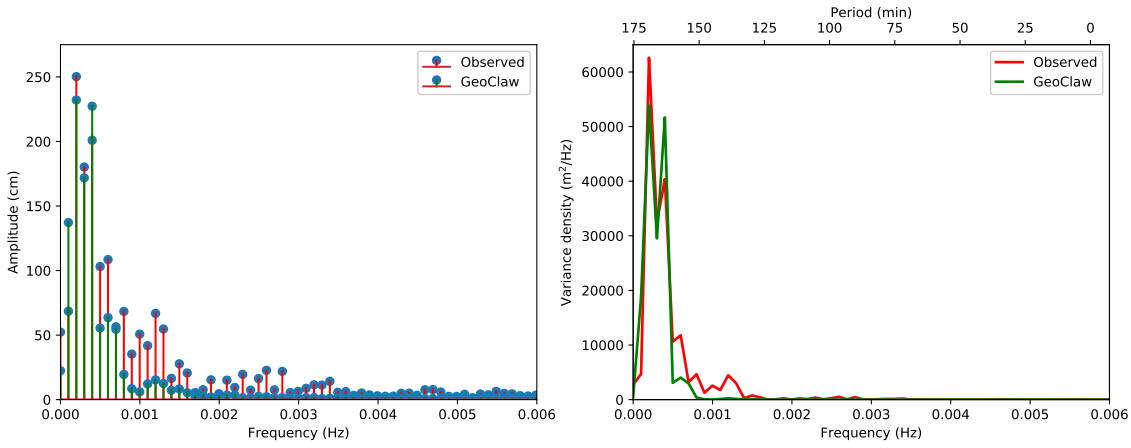

(a) (b)

Figure 5.25: 2015 Illapel event: (a) Amplitude of the harmonic components for the observed wave record at DART 32401 and for the computed virtual DART in GeoClaw. (b) Variance spectrum for the observed time series at DART 32401 and the computed results for the virtual gauge in GeoClaw.

Wavelet analysis was also performed, as this type of analysis details the tsunami waveforms both in the domain of time and frequency. We followed the practical guide for wavelet analysis by Torrence and Compo (1998). The Morlet wavelet basis function was used. The wavelet scale used was 0.1 and frequency used was 6. Python language was used for this purpose.

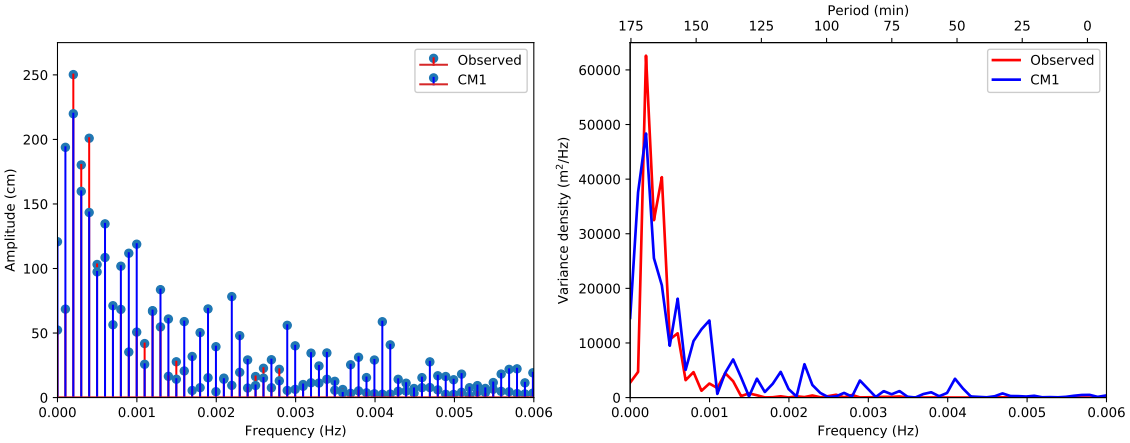

(a) (b)

Figure 5.26: 2015 Illapel event: (a) Amplitude of the harmonic components for the observed wave record at DART 32401 and for the computed virtual DART in CM1. (b) Variance spectrum for the observed time series at DART 32401 and the computed results for the virtual gauge in CM1.

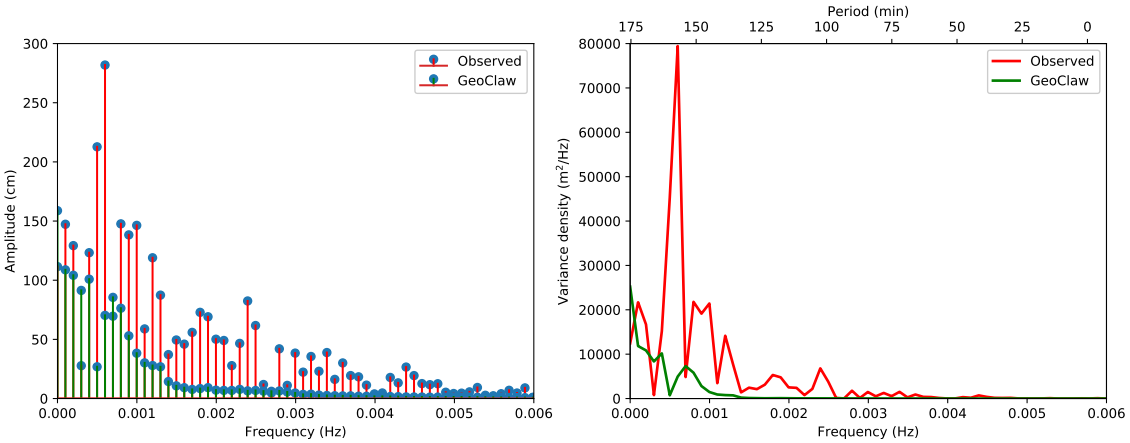

(a) (b)

Figure 5.27: 2015 Illapel event: (a) Amplitude of the harmonic components for the observed wave record at DART 32402 and for the computed virtual DART in GeoClaw. (b) Variance spectrum for the observed time series at DART 32402 and the computed results for the virtual gauge in GeoClaw.

Table 5.11: Total energy spectrum for each time series.

DART	32401	32402	32412
Time Series	Energy (m^2/Hz)		
Observed	38.0×10^4	64.4×10^4	28.7×10^4
GeoClaw	33.1×10^4	13.6×10^4	28.8×10^4
CM1	53.4×10^4	58.2×10^4	32.2×10^4

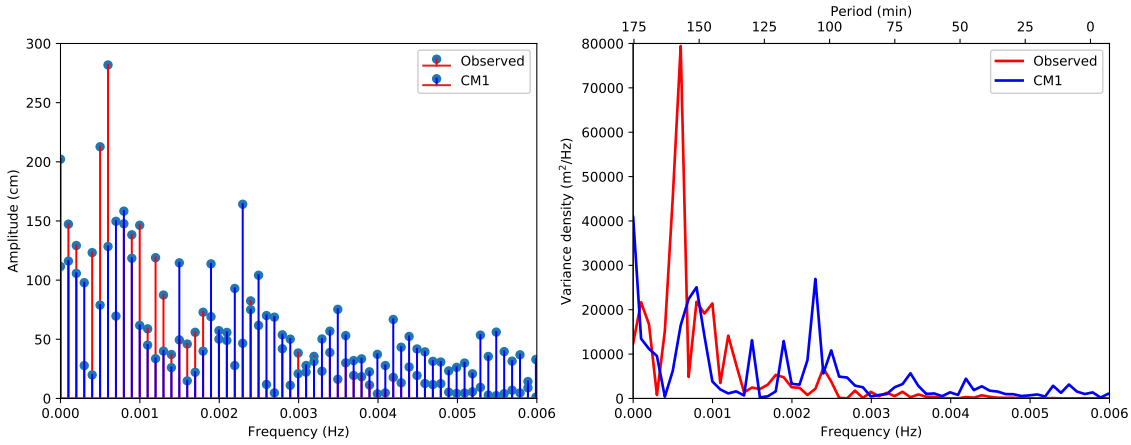

(a) (b)

Figure 5.28: 2015 Illapel event: (a) Amplitude of the harmonic components for the observed wave record at DART 32402 and for the computed virtual DART in CM1. (b) Variance spectrum for the observed time series at DART 32402 and the computed results for the virtual gauge in CM1.

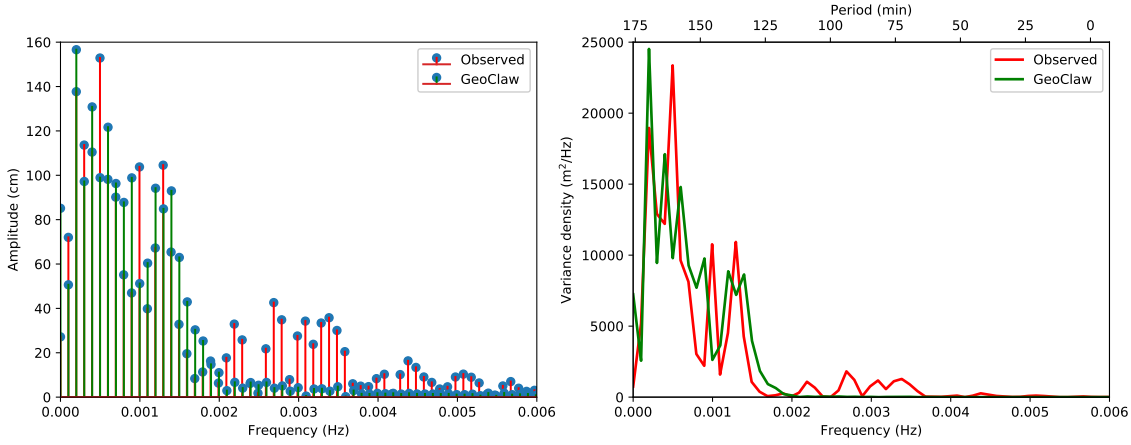

(a) (b)

Figure 5.29: 2015 Illapel event: (a) Amplitude of the harmonic components for the observed wave record at DART 32412 and for the computed virtual DART in GeoClaw. (b) Variance spectrum for the observed time series at DART 32412 and the computed results for the virtual gauge in GeoClaw.

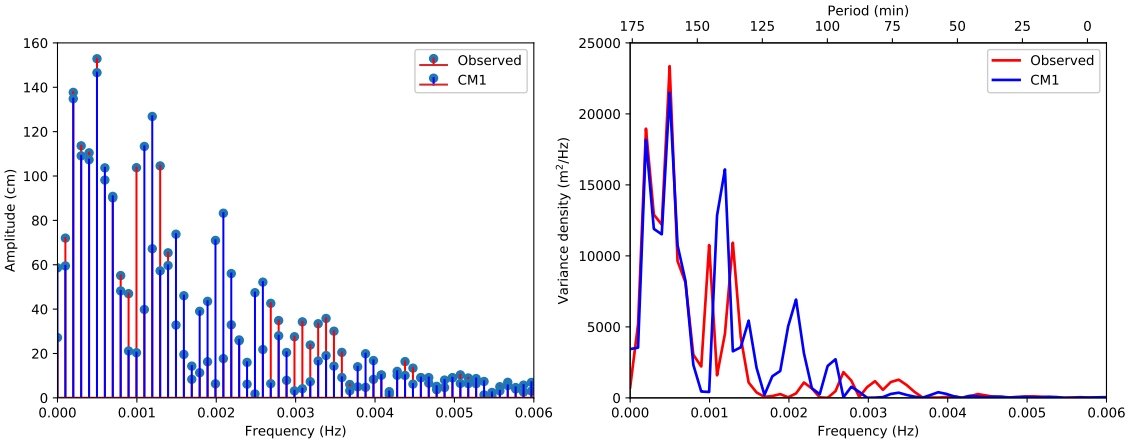

(a) (b)

Figure 5.30: 2015 Illapel event: (a) Amplitude of the harmonic components for the observed wave record at DART 32412 and for the computed virtual DART in CM1. (b) Variance spectrum for the observed time series at DART 32412 and the computed results for the virtual gauge in CM1.

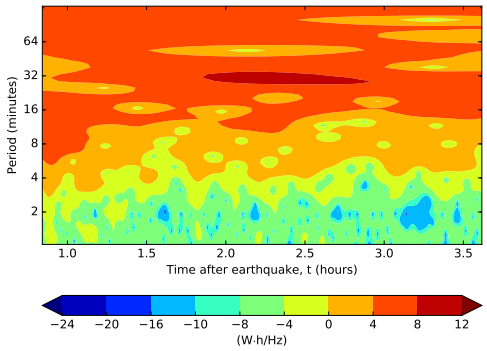

(a) DART 32402

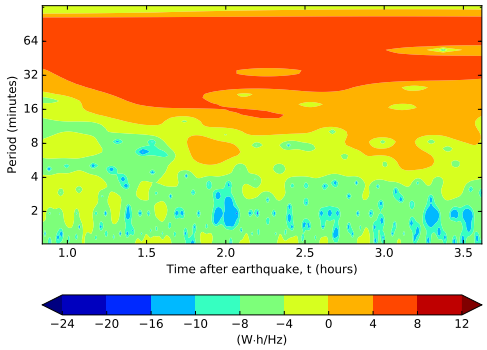

(b) DART 32401

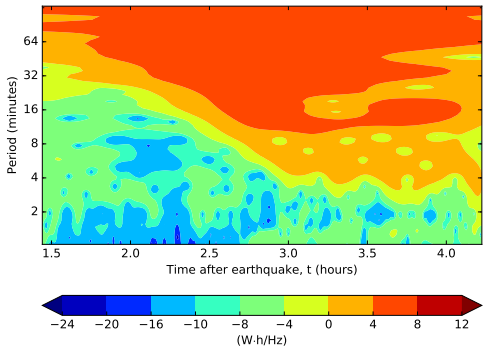

(c) DART 32412

Figure 5.31: 2015 Illapel event: Wavelet analysis of the DART records during the 2015 Illapel event.

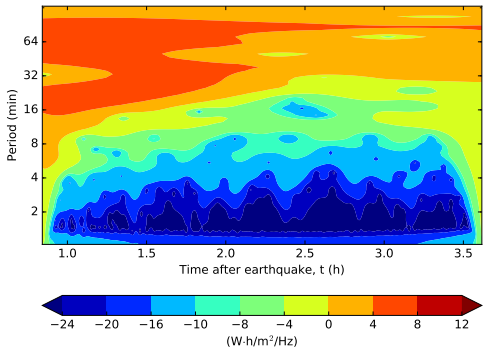

(a) DART 32402

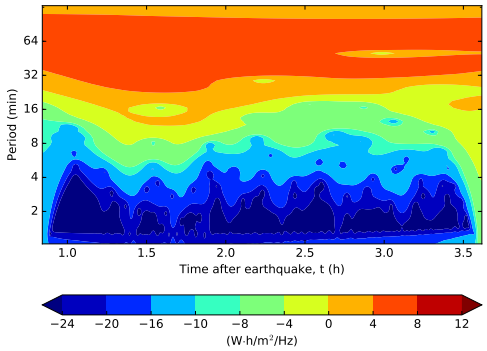

(b) DART 32401

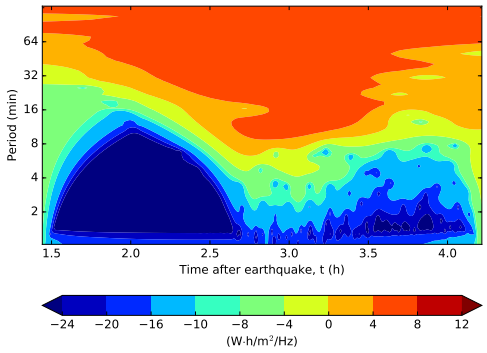

(c) DART 32412

Figure 5.32: 2015 Illapel event: Wavelet analysis of the GeoClaw results at each studied DART location.

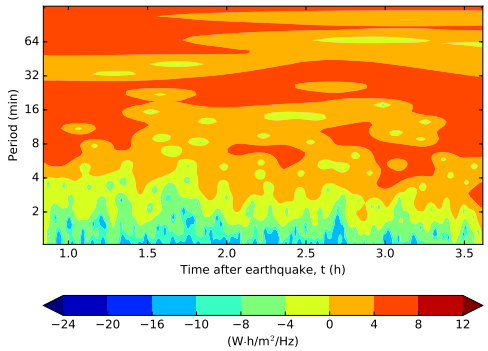

(a) DART 32402

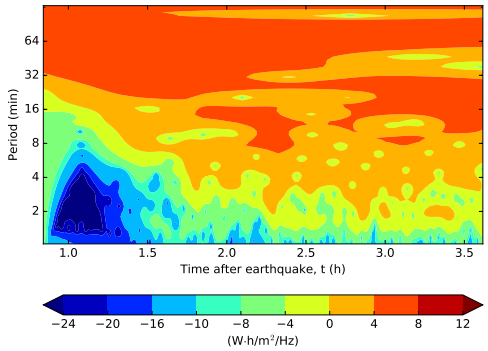

(b) DART 32401

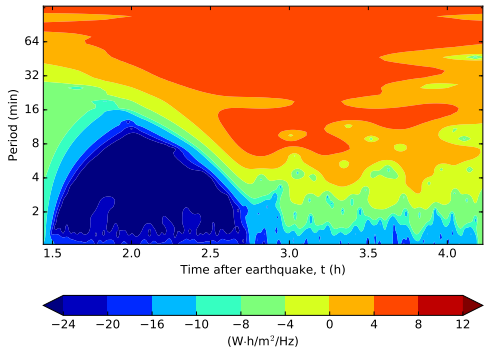

(c) DART 32412

Figure 5.33: 2015 Illapel event: Wavelet analysis of the combined model CM1 results at each studied DART location.

5.2.5 Discussion of Results

We compare the observations of the Illapel 2015 event with the simulation results, for both GeoClaw and CM1 models, using the source model by Melgar et al. (2016).

The computational results from GeoClaw and CM1 retrieved from the virtual tide gauges, located close to the Coquimbo and Valparaiso tide gauges, are plotted in Figure 5.22 and presented in Table 5.8. Figure 5.22 also shows the observations retrieved from the tide gauges at the time of the event. From the plots, we see that there is a very large difference between the observational data and the computational results both at Coquimbo and Valparaiso. This contrast between the time series plots is most probably a consequence of the tide gauges locations, which are very close to the earthquake source limits (Calisto et al. 2017). The tide gauges are affected by minor modifications of the seafloor caused by subsidence and/or uplift, causing large changes in the tide gauges plots. These problems detected in the tide gauges are also documented by authors such as Omira et al. (2016) and Calisto et al. (2017) and are a consequence of the coseismic stress and onshore effect and consequent surface displacement. The differences between the computational models results are minimal, with a difference of 2.8 cm at Valparaiso. A large difference between the maximum trough-to-crest wave heights, from the computations with GeoClaw and with CM1 at Coquimbo, is obtained. This difference can be related to the models capability to model the nearshore processes, with better results being obtained with the CM1.

Both models computed quite well the first arrivals of the DARTs (Figure 5.24): GeoClaw smooths the solution and CM1 mimics satisfactorily the dispersive components of the tsunami waves, which lack from GeoClaw, as it is a non-dispersive model. The results from CM1 at DART 32402 are better for the main wave, first trough and second wave, mimicking correctly the wave amplitudes. Geoclaw, on the other hand, is very dissipative and the waves are smoothed during propagation. At DART 32401, the wave amplitude computed with the CM1 is similar to the observated one and afterwards the wave profile behaviour resembles the observed one. However, the real observed wave at the DART seems to be more dissipative. On the other hand, CM1, which is not so dissipative, is possibly introducing more harmonic components, maybe generated at shallow water depths, which reflect on the coast. At DART 32412, the computational results from CM1 are similar to the event records, although there is a time shift in the first wave arrival.

Tsunami waves arrive first at DART 32402, then DART 32401 and finally DART 32412. For DART 32401 the first wave arrival time difference between the observations and the computational results was of 1 min, 4 min for DART 32402 and 5 min for DART 32412 (Table 5.9).

From Figure 5.18, we see that DART 32402 and DART 32401 are quite near the coast—approximately 290 km and 357 km, respectively. The source of the event (Figure 5.19), located south of the mentioned DARTs, is very close to the coast. For this reason, coastal interactions are a very important factor for this event and therefore in the computations, which can contribute with reflections and intensification of other nearshore effects, such as diffraction and refraction. From the CM1 simulation results, comparing the events records at the DARTs with the CM1 simulations results, we see that CM1 performs well at DART 32402 and DART 32401. At DART 32412 the CM1 and the observed wave profiles are similar, although in the model the waves arrive earlier; again, the nearshore effects are quite important and present in these DARTs. The arrival time differences between the observed wave records and simulations, both from GeoClaw and CM1, could be associated with an error in the source location: however, if that was the case, the arrival time differences would be the same for the DARTs, which is not what is observed from Figure 5.24 and Table 5.9. In fact, with the CM1 the obtained tsunami travel times at the studied DARTs 32401, 32402 and 32412 are closer to the observed tsunami travel times, with minimum and maximum travel time differences of 1 and 5 min respectively. The largest tsunami travel time difference of 5 min, registered for the most distant DART 32412, is probably caused by its larger distance from the source.

Comparing with Heidarzadeh et al. (2016), our results for the DARTs are more ajusted to the observations and we show better tsunami travel times estimations. Heidarzadeh et al. (2016) also overestimate the wave amplitude at the DARTS, with a smoother wave solution. All the models, including Heidarzadeh et al. (2016)'s, anticipate the arrival of the crest of the first wave. The wave arrival advance observed in the computational time series relatively to the observations can be a consequence of the bathymetric grid resolution.

We analysed the computational data sets deviations. Comparing the observed data sets and the simulated data sets (Table 5.10), from GeoClaw computation and from the simulation with CM1, we found that the best results for CM1 are found at DART 32412, with $L_{amp} < 1$. In relative terms, the results are better for GeoClaw in DART 32401, better for CM1 for DART 32412 and similar between GeoClaw and CM1 at DART 32402, with L_2-norm values ranging between 2 and 3. We found both approaches to be suitable measures for the data sets deviations.

The maximum trough-to-crest tsunami height, corresponding to the first wave arrival, was recorded at DART station 32402 with 19.4 cm. The results from CM1 are close to these observations (18.7 cm), with 8 cm difference obtained using GeoClaw code. For DART 32401, the CM1 differs in 0.1 cm from the observations (7.9 cm observed and 8.0 cm from CM1). For DART 32412, the maximum trough-to-crest tsunami height for CM1 results and the observations from the event differ in 2 cm. Comparing the maximum trough-to-crest tsunami height for CM1 results and the resuts from GeoClaw, the difference is 5 cm.

The spectra for each observed and computed waveforms—GeoClaw and CM1—at each DART are shown in Figures 5.25 to 5.30 and the energy spectrum is detailed in Table 5.11. In general, the spectra show two main peaks between 160 to 180 min. One should note that these stations are considerably close to the tsunami source (582 to 2110 km), specially DART 32402 (582 km distant). It is interesting to see that the observed peak at 160 min is not reproduced in the computations, which is not the case for DART 32401 and DART 32412. This could be due to the strong coastal interaction effects at DART 32402.

Considering the wavelet analysis for the DART records, it is observed that the longer wave components with periods greater than 32 min arrive earlier at the 3 DARTs. This is probably due to the frequency dispersion phenomena. We can see that the tsunami energy is mainly concentrated in the period band between 16 to 64 min (Figure 5.31). At DART 32402, the wave components with periods from 6 to 64 min arrive earlier also. The greatest concentration of energy is at 32 min. In fact, this DART has a great concentration of energy during the whole period of time of the 3.5 h considered for the wavelet analysis. In DART 32412, the energy is more scattered in time, which might be due to dispersion, as it is the DART which is most far from the source. At this DART, there is also low tsunami source influence. Between DART 32401 and DART 32412 (which are considerably close), there seems to be some energy transfer from the longer to the shorter wave periods. The wavelet analysis for the DART results of the simulations with GeoClaw (Figure 5.32) and CM1 (Figure 5.33) show that the tsunami energy is mainly concentrated in the period bands between 0 to 8 min and 16 to 64 min. For GeoClaw, there is great concentration of tsunami energy at DART 32401, 32402 and 32412, and for CM1 the concentration of tsunami energy is greater at DART 32401 and 32412. The wavelet analysis for DART 32402, for the simulation with CM1, shows a tsunami energy distribution similar to that obtained from the observed DART 32402 record. The wavelet analysis of the simulations show greater tsunami energy comparing with the wavelet anaysis of the DART records of the event.

Overall, the CM1 results are very satisfactory, with good tsunami waves arrival times, waveform observations (wave amplitudes) and frequency content. The model shows better results than the models presented by Gjevik et al. (1997) and Heidarzadeh et al. (2016), for the modelling of the tsunami events of the 1969 PET and the 2015 Illapel, respectively.

In conclusion, the Combined Model 1, CM1, achieved good results in the simulation of both

the 1969 PET and the Illapel 2015 events and it is a competent model, which satisfies the purpose of the present (and future) case studies.

5.3 Combined Model 2 (CM2)

The proposed Combined Model 2 (CM2) is a combination of the CM1, via the FUNWAVE-TVD, and OpenFOAM (OF), via the olaFlow module. FUNWAVE-TVD is a Boussinesq model for wave propagation, transformation, dispersion and breaking. olaFlow is a module of the CFD code OpenFOAM, which is best suited for the modelling of the complex interaction of the tsunami waves with the nearshore environment, coastal vegetation and structures.

The main event used for the validation of CM2 is the Monai Valley benchmark (Liu et al. 2008). Numerical results retrieved at the three wave gauges, located behind the Okushiri island, are compared with the laboratory free surface elevation data measurements available.

5.3.1 olaFlow format structures

Due to the structure of olaFlow, the input of the boundary conditions of the problem has to follow one of the specific format structures that the code accepts. For the wave generation in olaFlow, the boundary conditions are imposed through the dictionary files waveDict or wavemakerMovementDict (located in the constant folder). These dictionary files have different structures: waveDict is composed by several parameters, including the waveType and the waveTheory. The second one refers to a text file wavemakerMovement.txt (Appendix A.3.2.1), composed by a header with a couple of parameters, including the specification of the wavemakerType (piston or flap) and time series structured data, according to the type of time series used as input (Appendix A.3.2.2).

The first setting in olaFlow dictionary files concerns the type of the waves. For the coupling methodology, the waveType wavemaker (W) will be used, which is the replication of a custom-made wave-maker with constant velocity profile. The second setting is the waveTheory, in which the type of waves to be generated is controlled. Diverse formats of data are possible to input with the wavemaker waveTheory: tx, tv, txeta, tveta. The t stands for time series (in s), as all of these formats are time series. The x stands for the wave-maker displacement or paddle position (in m), v for the paddle velocity (in m/s) and eta for the free surface elevation at the wave paddle (in m). The time series t does not have to be provided with a constant fixed interval, because the variables values will be linearly interpolated between the given times. It is also possible to emulate the movement of several independent paddles, up to a maximum of 10 (like in a directional wave basin). This is only possible to simulate in the wavemakerTank case (Higuera 2016), with several moving paddles.

In short, the piston or flap wave-maker emulation is possible with (a) time (t) and displacement (x) of the wave-maker (tx), (b) time and velocity of the wave-maker (tv), (c) time, displacement of the wave-maker and free surface elevation (txeta) and (d) time, velocity of the wave-maker and free surface elevation (tveta). For example, for a water wave problem in which a time series of the initial input boundary wave condition is given, one should simulate the problem in olaFlow via the tveta format. When the problem to be simulated involves a laboratory experiment, one can use the txeta or the tveta formats. In any case, the user should convert the original data into the format expected by olaFlow. Yet, it is rather important to note that it is also possible in olaFlow to provide a specific time series of the surface elevation (time t, in seconds, and η, in metres), without the displacement of the wave-maker, using directly the waveType wavemaker. In this option, the user needs to provide a time series of the horizontal velocity and η (the free surface elevation around the still water depth). From now on, this will be referred to as the timeSeries

condition. The format is as shown in Figure 5.34.

```
/*-------------------------------------------------------------------------*
| =========                 |
| \\      /  F ield         | OpenFOAM: The Open Source CFD Toolbox
|  \\    /   O peration     | Version:  1.3
|   \\  /    A nd           | Web:      http://www.openfoam.org
|    \\/     M anipulation  |
\*-------------------------------------------------------------------------*
FoamFile
{
    version     2.0;
    format      ascii;
    class       dictionary;
    location    "constant";
    object      waveDict;
}
// * * * * * * * * * * * * * * * * * * * * * * * * * * * * * * * * * * * * * /

waveType   wavemaker;

waveTheory         tveta;

genAbs          1;

absDir          0.0;

nPaddles          1;
```

Figure 5.34: Header and initial parameters of a waveDict file in olaFlow, applying the wavemaker waveType and tveta waveTheory.

5.3.2 Coupling methodology

The fully nonlinear Boussinesq model FUNWAVE-TVD, for wave transformation, propagation and inundation, is coupled with the computational fluid dynamics (CFD) code OpenFoam, via the olaFlow module (previously known as olaFoam). Both codes have been benchmarked with the NTHMP benchmark tests and are being subject to continuous improvements, with new versions being released. FUNWAVE-TVD version 3.0, OpenFOAM version 1712 and olaFlow version 2018 are used in this work.

The Boussinesq model FUNWAVE-TVD is used to provide the input conditions on the tsunami waves—as these are approaching the coast and being subject to the several nearshore processes (which are contemplated by the fully nonlinear Boussinesq model)—into the CFD code. The free surface elevation η and velocities u and v are then used as boundary conditions to start the CFD code, more specifically the olaFlow package (Higuera, 2019). olaFlow consists on a set of solvers for the simulation of wave dynamics, enabling the generation and absorption of waves at the boundaries and wave interaction with coastal structures. It is very versatile, with high performance in two-phase flow through porous media and with moving-boundary wave generation, just like in

the laboratory wave-makers. olaFlow also features other capabilities from OpenFOAM, such as the dynamic mesh refinement and the mesh motion for floating body emulation.

In any simulation in FUNWAVE-TVD, the user can retrieve time series at several pre-specified locations/points of the computational grid. For these locations, in a specific study area, it is possible to obtain the time series (for a specific total run time) of the free surface elevation η (in m) and velocities u and v (in m/s). Several station files are generated, one for each location of the computational grid, specified inside a station.txt file in the format (Longitude, Latitude), for geographical coordinates, or (x, y), for Cartesian coordinates.

To achieve the combined model between FUNWAVE-TVD and olaFlow (CM2), several approaches were studied. Due to several characteristics of the olaFlow toolbox, which were described before, it was found that the most simple way to combine both codes was to take the time series output from FUNWAVE-TVD and, after careful conversion between codes, input it into the olaFlow. The most important step would be the construction of the waveDict file in a data format accepted by olaFlow. The waveDict file is composed by a standard OpenFOAM header, followed by the specification of the waveType wavemaker and the waveTheory tveta or other. The structure of the file is similar to that which is presented in Figure 5.34. The parameter genAbs is a boolean variable that acts as a switch that controls wave absorption (0 means that it is turned off and 1 means that it is turned on). The parameter absDir turns on the quasi-3D absorption, setting the direction in which the correction velocity will be applied in the quasi-3D absorption. The parameter nPaddles indicates the number of paddles used, which is generally 1, except when using the wavemakerTank case example (OpenCFD Limited 2019), with a maximum possible of 10 paddles. Afterwards, the file is composed by the information of the timeSeries, the paddleVelocity and the paddleEta data. Another variable called tuningFactor can be introduced for this wave type. It is a factor by which the velocities and free surface elevation are multiplied, and can be used as a tuning factor to match the expected laboratory results. The reason for including it is that, as the numerical boundary does not move, a calibration factor may be needed; by default it takes the value 1.

As previously mentioned, the olaFlow feature that allows a maximum of 10 wave paddles with the waveType wavemaker is limited to the wavemakerTank case, which at the moment is not applicable to the combination of waveType – waveTheory necessary to achieve the combination of the two models, CM2. This would be the best suited coupling approach, as it would include a more complete set of data. Yet, the coupling of the codes is only possible to perform at one single location. For that reason, the information from the simulation in FUNWAVE-TVD at one single location is passed to one single wave paddle in olaFlow, using the combination of waveType – waveTheory. The waveDict file is constructed after formatting the data from FUNWAVE-TVD.

The computational grid has to be converted separately from the FUNWAVE-TVD format (ASCII format) to a format accepted by olaFlow. There are different options depending on the shape of the computational domain of the problem. When the domain is simple, one can define it by blocks with the elementary tool blockMesh, that generates a simple structure mesh with hexahedral cells. When the domain of the problem presents more complex geometric features, it is possible to use the snappyHexMesh tool within OpenFOAM. This tool adapts the geometry of the domain to a structured mesh and removes unnecessary pieces of the mesh. There are some specific file formats that can be read by OpenFOAM, such as the stereolithography (STL) format. It was found that a good option for the case of a digital elevation model (DEM) or a digital terrain model (DTM) was to convert the ASCII file into the STL format, which snappyHexMesh can deal with. This file format is then convert into a mesh, within the code, by snappyHexMesh. In this case, due to the complexity of the computational domain, the ASCII file of the domain, which is a cloud of points with x, y and z data, is converted to the STL format. The `stlwrite`

script (written in GNU Octave®)[‡] is used to load the ASCII file, characteristic parameters of the grid are input and the cell spacing is specified. The grid is then converted from its original ASCII format to the STL format. A generic scheme of the coupling of the CM1 and the module olaFlow is represented in Figure 5.35.

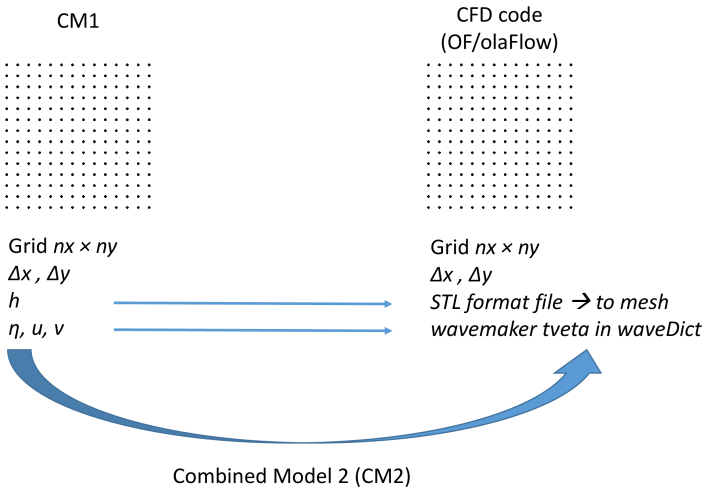

Figure 5.35: Scheme of the coupling approach between CM1 and the CFD code, necessary to achieve CM2.

5.3.3 The Monai Valley benchmark. Discussion of results.

The benchmark used to validate the combined model is the Monai Valley benchmark. In this benchmark test case, a leading depression N-wave (LDN-wave) is initially input into the domain through the western boundary (Figure 5.36). The computational domain is 12.474 m $\times$ 3.402 m $\times$ 0.25 m. The grid spacing in x and y is 0.014 m and data is converted from the original ASCII file into a STL file (Figures 5.37 and 5.38).

Beforehand, the case study is simulated with olaFlow only: an initial N-wave profile (Figure 5.36) is fed into the code through waveDict, with waveType wavemaker and waveTheory tveta. The time series of the N-wave is passed to the waveDict, with the wave propagating for a total time of 22.5 s with a $\Delta t = 0.05$ s and the corresponding free surface elevation η. Velocity is previously calculated assuming:

$$\bar{u} = \frac{c \cdot \eta}{h + \eta}\,, \tag{5.4}$$

where h is the water depth, which is equal to 0.135 m, and c is given by:

$$c_2 = \sqrt{g \cdot (h + a^{+})}, \tag{5.5}$$

where a^{+} is the amplitude of the wave crest. The corresponding waveDict, to be used in the simulation, is presented in Appendix A.3.2.3. A similar simulation was performed, with the wave

[‡]available at https://github.com/vanialima/

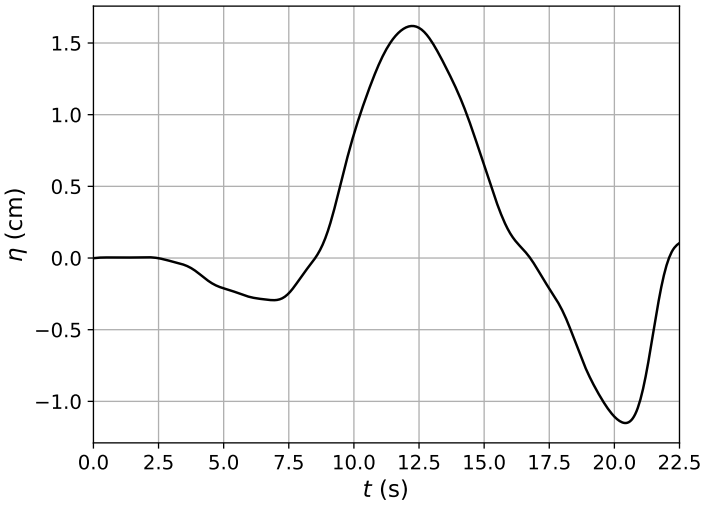

Figure 5.36: Profile of the incident N-wave of the Monai Valley study case.

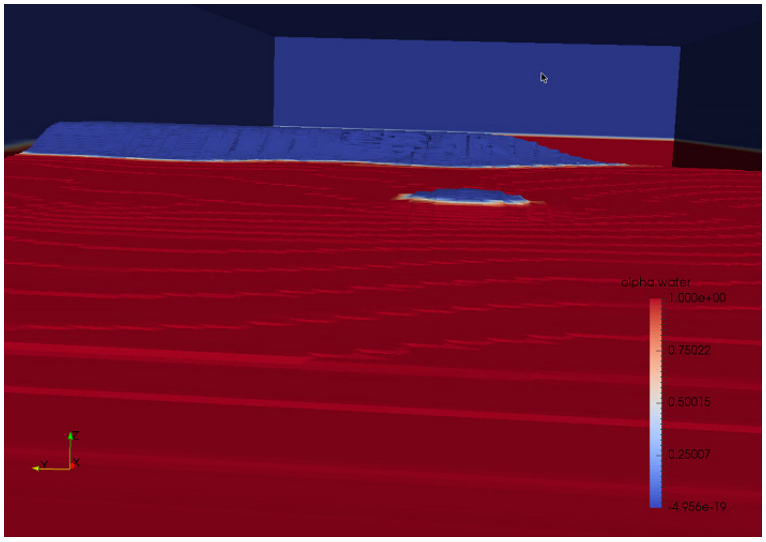

Figure 5.37: 3D view of the Okushiri Island and Monai Valley.

celerity c given by:

$$c_1 = \sqrt{g \cdot h}. \tag{5.6}$$

Parameters for the physical properties used in the simulations and mesh characteristics are detailed in Tables 5.12 and 5.13. The initial cell size varied between 0.02 m and 0.2 m and up to 3 levels of refinement were selected. During the first OpenFOAM simulations, several computational problems were found. There was a pressing need to optimize all the usage of OpenFOAM computational needs with the available resources, which was not straightforward in the beginning. All the simulations ran in parallel, using the simple decompositionMethod, for 16 processors, dealing with 75000 mesh cells each (Table 5.14). Bottom friction is set with the nutWallFunction and it includes the lateral walls and bottom of the computational domain. Turbulence model $\kappa - \varepsilon$ was used. A 3D model is used and the computational domain is set into 1 block specified inside blockMeshDict. The 3D numerical domain has cell resolutions of Δx =

0.04 m, Δy = 0.2 m Δz = 0.02 m The comparison between wave celerities expression (5.6) and expression (5.5) is plotted in Figure 5.39, where c_1 corresponds to the wave celerity (5.6) and c_2 corresponds to the wave celerity (5.5).

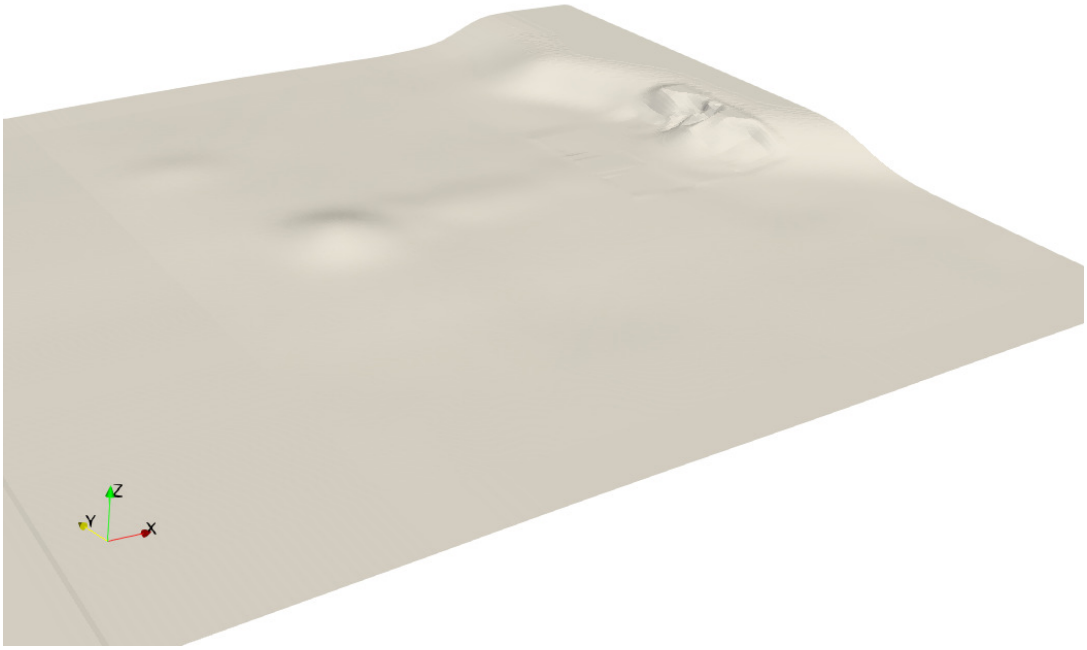

(a)

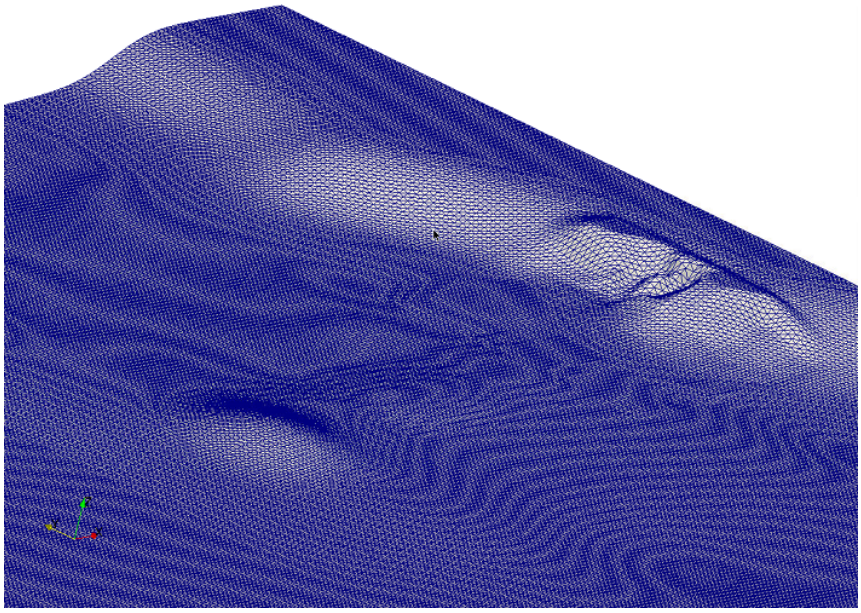

(b)

Figure 5.38: (a) 3D representation of the Monai Valley area and Okushiri Island, in Japan. (b) Simulation area mesh, obtained with the snappyHexMesh tool.

Boundary conditions for the simulations are presented in Table 5.15.

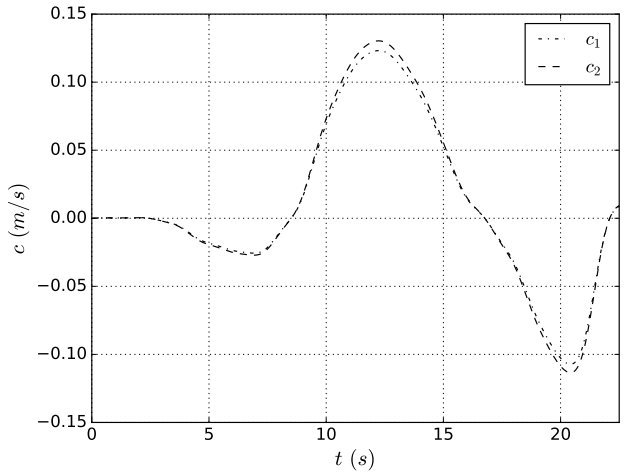

Figure 5.39: Wave celerity formulations c_1 (-.-) and c_2 (- -).

Table 5.12: Physical properties used in the simulations.

Physical property	Value used				
g (m/s^2)	ρ_{water} (kg/m^3)	ρ_{air} (kg/m^3)	μ_{water} (Pa·s)	μ_{air} (Pa·s)	γ (N/m)
9.81	1000	1.2	1×10^{-3}	1.8×10^{-5}	0.07[†]

[†]Nayar et al. (2014)

Table 5.13: Mesh characteristics. Wave and simulation parameters.

Cell size			Mesh size	Time step	Computational time / resources
Δx	Δy	Δz	number	Δt	16 CPU[†] cores[*]
(m)	(m)	(m)	of cells	(s)	(h)
0.04	0.2	0.02	1.2×10^6	0.05	20

[†]Central processing unit

[*]The olaFlow's `simple decompositionMethod` was used.

Table 5.14: Options and parameters defined in olaFlow's dictionaries.

dictionary		
fvSchemes	ddtSchemes	Euler
	gradSchemes	Gauss linear
decomposeParDict[1]	method	simple
	no of processors/cores	16

[1]In OpenFOAM, the parallel computing method used is designated as the domain decomposition method.

The free surface elevation is retrieved at three locations in the domain, corresponding to the three wave gauges published data locations (Figure 3.9 and Table 3.1). The comparison between the numerical results and the laboratory published data are shown in Figure 5.40. A first low

Table 5.15: Boundary conditions (BC) for the Monai Valley benchmark simulations with olaFlow and CM2 (0.org folder).

boundaryField	block boundary type	alpha.water.org	prgh	U
inlet	patch	waveAlpha	fixedFluxPressure	waveVelocity
outlet	patch	zeroGradient	fixedFluxPressure	waveAbsorption2DVelocity
bottom	wall	zeroGradient	fixedFluxPressure	fixedValue
monai	—	zeroGradient	fixedFluxPressure	fixedValue
atmosphere	patch	inletOutlet	totalPressure	pressureInletOutletVelocity
wall1	wall	zeroGradient	fixedFluxPressure	fixedValue
wall2	wall	zeroGradient	fixedFluxPressure	fixedValue

amplitude wave, with less than 1 cm, is observed, corresponding to a wave also observed in the experimental results. These oscillations do not occur in the 2DH simulations performed with FUNWAVE-TVD (see Figure 3.11). The main numerical wave arrives slightly before the physical wave. This can be originated by small errors in the wave gauges positioning, the domain that is slightly larger or a timing error. Another possibility might be related to an incorrect boundary condition. In this case, the velocity had to be calculated assuming a specific formulation for the wave celerity, which affects the boundary condition.

The exact same input time series, as given within the benchmark case package, was used. The time discretisation of the input time series in waveDict is equal to 0.05 s, for a total run time of 22.5 s. An aspect to be taken into account is that the input N-wave signal is smooth and the results obtained follow the initial smooth signal. Using the shallow water wave celerity formulation—expression (5.6)—, the results did not change significantly. The high-period oscillations observed could be caused by wave breaking. Another possibility considered was that the waves could be breaking at the input boundary. Looking at the sequence of the waves propagating in the domain, no breaking was observed at the input boundary. If wave breaking is happening, the current mesh probably is too coarse in the vertical direction to solve it properly, as it has 10 cells/wave height and the oscillations that we are trying to capture are much smaller.

Afterwards, boundary conditions from FUNWAVE-TVD for the Monai Valley case study are fed into olaFlow. The output results retrieved from a virtual wave gauge, at half width of the computational domain and located approximately 10 cm away from the western Monai Valley computational boundary, are used as the boundary condition to olaFlow. This boundary wave profile, retrieved from an intermediate location of the western Monai Valley computational boundary, is input to the problem domain at the same location where it was retrieved from in FUNWAVE-TVD. The waveDict, with waveType wavemaker and waveTheory tveta (timeSeries condition), is used, where time t, free surface elevation η and velocity u compose the waveDict time series (Appendix A.3.2.4). In this specific benchmark, only the velocity (retrieved from FUNWAVE-TVD), in the direction of propagation, is used and the tangential component is disregarded.

Results for the published three virtual wave gauges were analysed and are presented in Figure 5.41. The simulations from the combined model show that CM2 captures the general wave shape, which is in agreement with the results obtained solely with olaFlow. It is firm to state that the models combination was efficiently and correctly achieved.

To evaluate the results obtained with CM2, a series of metrics are applied to the simulations results. Please refer to section 3.5.1 for the metrics description. The simulations error metrics are presented in Table 5.16. The analysis of the error metrics show a high linear correlation between the laboratory data and the computational results, which is highest for olaFlow, with an r between 0.811 and 0.928, and an r between 0.793 and 0.920 for CM2. Bias is negative and root-mean-

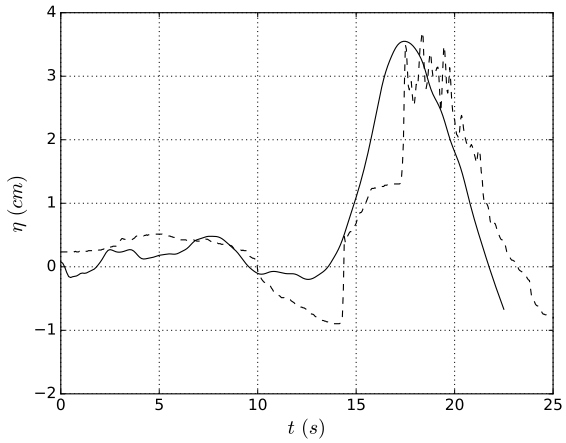

(a) wg5

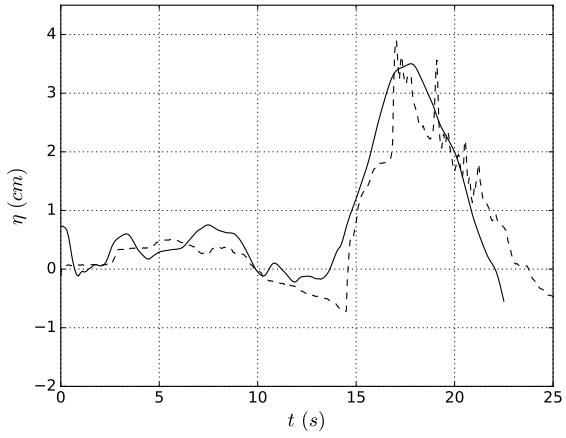

(b) wg7

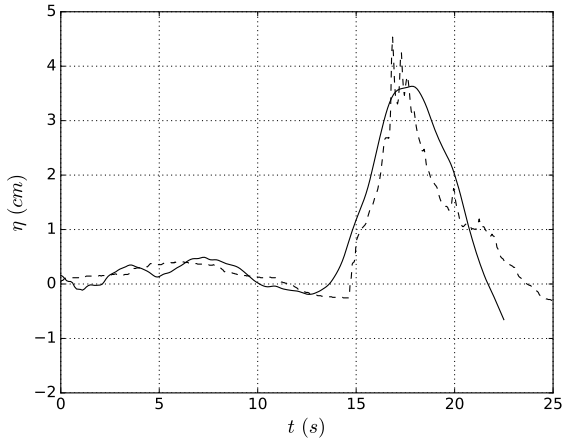

(c) wg9

Figure 5.40: Monai Valley: numerical simulation with olaFlow (–) and experimental data (- -) recorded at wave gauges 5, 7 and 9.

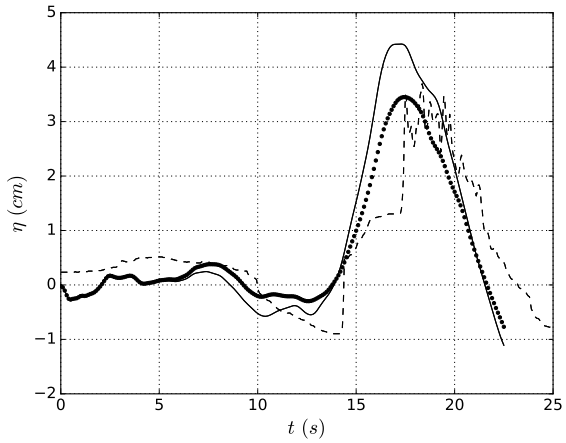

(a) wg5

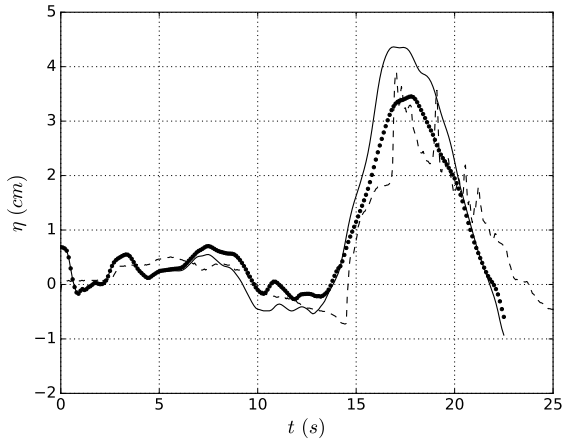

(b) wg7

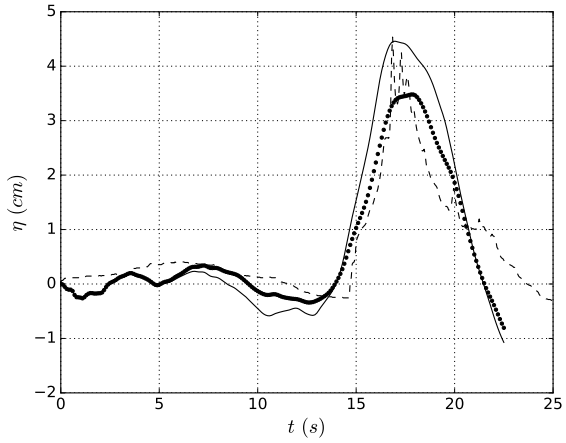

(c) wg9

Figure 5.41: Monai Valley: numerical simulation with CM2 (–), olaFlow ($\cdots$) and experimental data (- -) recorded at wave gauges 5, 7 and 9.

square error varies between 0.80 and 1.61 cm for olaFlow and between 0.94 and 1.10 cm for CM2.

Table 5.16: Error metrics to evaluate the performances of the OF/olaFlow and the CM2, for the Monai Valley benchmark.

Code	wave gauge	r (—)	Bias (cm)	RMSE (cm)
OF/olaFlow	5	0.811	-0.4176	0.8032
	7	0.910	-0.5525	0.7167
	9	0.928	-0.3896	1.6141
CM2	5	0.793	-0.5419	1.1028
	7	0.901	-0.6562	0.9790
	9	0.920	-0.5174	0.9372

5.4 Concluding remarks

In the first task, we combined two individual models, the 2DH nonlinear shallow water equations (NSWE) model GeoClaw, with FUNWAVE-TVD, a fully nonlinear Boussinesq model for the wave propagation, transformation and inundation, into one combined model (CM1).

We explained the methodology adopted to combine both models, as well as the verification and testing performed to the chosen methodology. We presented the case study results of the 2015 Illapel Earthquake and Tsunami, to show the quality of the performance of the CM1, evaluating data set deviations, complemented by Fourier and wavelet analysis. Additionally, we presented the CM1 results for the 1969 Portugal Earthquake and Tsunami (1969 PET) event, taking advantage of the nesting capability existent within the combined model. We concluded that the combined model 1, CM1, results are very satisfactory, with good tsunami waves arrival times, waveform observations (wave amplitudes) and frequency content. The CM1 achieved good results in the simulation of both the 1969 PET and the Illapel 2015 events and it is a competent model, which satisfies the purpose of the case studies presented.

In the second task, we established a methodology to combine the CM1, via FUNWAVE-TVD, with OpenFOAM, via the olaFlow module. The combined model methodology applied the timeSeries condition, which was used to simulate the Monai Valley benchmark. This methodology resulted in the Combined Model 2 (CM2). The CM2 showed good computational performance, capturing the general wave shape, with a good match achieved when comparing the results from the simulation with olaFlow and the results from the simulation with the CM2. Thus, the models combination was efficiently and correctly achieved.

In this Chapter, we have successfully achieved the coupling of the CM1 and the CM2, which resulted in the final combined model, CM. The simulation results obtained using the final combined model CM are presented in the next chapter.

Chapter 6

Final Combined Model

6.1 Introduction

In this chapter, the necessary preparation and settings for using the fully combined tsunami model CM is shown and described. The final combined model is tested in terms of its performance with the case study of a mega earthquake and tsunami hitting the coast of Portugal. A brief summary on the tectonics of the region is presented. Afterwards, the work methodology applied in this case study and all the numerical modelling description are presented. A discussion on the modelling uncertainties, the limitations of the applied numerical models and the (computational) challenges of the fully combined tsunami model proposed are described and some solutions are proposed.

6.2 Case study: $\mathrm{M_w}$ 8.5 Earthquake and Tsunami hitting the Portuguese coast

6.2.1 Brief tectonic context of the region

The western segment of the Eurasia-Nubia plate boundary extends between the Azores and the western Mediterranean. Along the Azores, the interplate domain is rather complex as consequence of the small spreading velocity, though it generates spreading along the Terceira axis. In the area defined between 24°W and 19°W it is supposed to follow a prominent morphological feature, the Gloria Fault, in an almost pure transcorrent way. To the east of 19°W, the interplate domain is morphologically complex and characterized by a series of huge ridges and seamounts—as the Gorringe Bank, the Coral Patch and Ampere seamounts (Argus et al. 1989; Zitellini et al. 2009). These features morphologically delimitate depressions such as the Horseshoe and Tagus abyssal plains and integrate the complex Southwestern Iberian Transpressive zone.

The SW Iberian margin is characterized by a very complex tectonic setting, with registers of moderate magnitude earthquakes and tsunamigenic earthquakes, such as the 1755 and 1969 earthquakes and tsunamis (Baptista and Miranda 2009; Baptista et al. 1996; Gjevik et al. 1997). All known catastrophic tsunamis in SW Iberia were triggered by earthquakes even if landslides are also a common phenomenon, mainly concerning smaller or local events (Baptista and Miranda 2009). In this sense, we must consider as probable sources the main active faults in the SW Iberian domain, whose dimensions are compatible with the generation of at least an $\mathrm{M_w}$ 8 earthquake.

The search for active faults in the Gulf of Cádiz able to generate large earthquakes and tsunamis has been actively conducted by a number of teams, mainly based on the intensive use of multi-channel seismic and high-resolution swath bathymetry surveys (see Zitellini et al. 2009 and references herein). It cannot be considered a closed question, in particular because none of the well established faults is able to generate alone the large 1755 event, correctly reproducing all

known historical data. To simulate the effects of a large tsunami in the Gulf of Cádiz one must, nevertheless, rely on the best available geological knowledge and consider the potential effect of all relevant candidate sources. In Lima et al. (2010), five candidate sources were selected and used to model the tsunami impact of a 1755-like tsunami event in Huelva, Spain. The candidate sources were fixed using simplified geometries, as depicted in Table 1 and sketched in Figure 3 in the paper. All the candidate sources corresponded to thrusts, positively identified on multi-channel seismic profiles (cf. Figure 3 from Lima et al. 2010), with Quaternary activity, and longer than 50 km. The strike and length of each source was obtained from multichannel seismic research (Zitellini et al. 2009). The width and average slip were fixed using scaling relationships (see Manighetti et al. 2007 and references herein) and geological constrains for the thickness of the seismogenic zone. Most of the sources considered in the study are pure thrusts. The five candidate sources considered in Lima et al. (2010) (cf. Table 1 from Lima et al. 2010) are now described: the first one corresponds to the northern flank of the Gorringe Bank, a large stratigraphic discontinuity and an area of widespread seismicity; the second one, identified by Zitellini et al. 2009, is the Horseshoe Fault, a reverse fault oriented perpendicular to the present day kinematic displacement of Nubia with respect to Iberia; the third one is the Marquês de Pombal fault, an active compressive tectonic structure located 100 km offshore SW Cape San Vicente, with a pronounced drag fold on the fault hanging-wall and the height of the escarpment is taller in the north, where it reaches 1.2 km and where we considered in its maximum possible length; the fourth one is the Portimão Bank Fault, which follows the southern flank of the Guadalquivir and Portimão Banks; the fifth one, the Cádiz Wedge Fault, corresponds to the interpretation made by Gutscher et al. (2006) that the Alboran lithospheric slab could act as a potential seismogenic and tsunamigenic generator. For modeling purposes, all these sources are geometrically simplified as described in Table 1 in Lima et al. (2010).

Custódio et al. (2016) developed a joint focal mechanism and hypocentre clustering approach, which allowed the identification of dominant faulting patterns and of faulting localization. The joint clustering analysis was applied to earthquakes located on the Azores–western Mediterranean region. The authors identified major known regions of active faulting identified, that included the mid-Atlantic ridge, the Terceira rift, the Trans-Alboran shear zone and the northern coast of Algeria. Custódio et al. (2016) also found found normal faulting in the northern Iberia, normal faulting in the Granada basin and oblique reverse faulting in the SW Betics, and showed that strike–slip faulting prevails in the region—with reverse faulting limited to its south and normal faulting limited to its north—and confirmed slip partitioning offshore SW Iberia.

The 1969 main shock had its epicentre located SW of the Saint Vincent Cape, at the plate boundary between the Eurasia and Africa, with the transition between an oceanic well defined plate boundary to the west and a continental more diffuse limit to the east (Buforn et al. 2019). With its epicentre located at the Horseshoe Abyssal Plain (Fukao 1973), south of the Gorringe Bank, the 28th February 1969 earthquake (frequently referred as the 1969 Horseshoe Abyssal Plain earthquake) is characterized as a tsunamigenic event, which generated a small tsunami, which was recorded at tide gauges located in Portugal, Spain, Morocco, Azores and Canary Islands (Gjevik et al. 1997).

Recently, it has been suggested by Duarte et al. (2019) that the Horseshoe Abyssal Plain may be the start of a subduction zone. From their research work, they have shown evidence of possible peeling occurring at the bottom of the tectonic plate, lying off the coast of Portugal. Thus, Duarte et al. (2019) propose that the earthquakes registered in this area were the consequence of the birth process of a new subduction zone.

6.2.2 Work methodology for the application of the fully combined tsunami model (CM)

The objective of the case study of an earthquake event triggering a tsunami near the coast of Portugal aims to show the overall performance of the final combined model and finally the complex three-dimensional interaction of the tsunami waves with the Cascais Marina (Cascais, Portugal) and surrounding coastal area.

A step-by-step description of the necessary procedures to run the simulation of this event with the final combined model is done.

The methodology involves GeoClaw and FUNWAVE-TVD codes and OpenFOAM (OF) code and the olaFlow module. The description follows:

- Characterization of the earthquake source, with earthquake parameters of the case study event provided by/retrieved from the USGS, peer reviewed articles, etc.
- Initial seafloor deformation (in metres) is determined from the elastic dislocation model in a homogeneous isotropic elastic half-space (Mansinha and Smylie 1971; Okada 1985). It is assumed instantaneous static seabed displacement, translated towards the free surface as an initial condition, reproducing the elastic bottom deformation caused by the earthquake. The Okada equations are implemented in the `maketopo.py` routine in GeoClaw. Depth is assumed top of the fault.
- GeoClaw computation with application of adaptive mesh refinement (AMR). Parameters η, u, v and h are written in the fort.gauge file. Results are retrieved after t min, in general 5 – 10 min after the beggining of the event. We consider that at this stage the tsunami generated waves are fully developed, the propagation is no longer subject to the source area influence and that no more waves are originating from the source area. This time interval depends on the characteristics of the earthquake event.
- Manipulation of the fort.gauge data from GeoClaw, for t min, and conversion to individual ASCII η, u, v and h files, with $nx \times ny$ dimensions, for the FUNWAVE-TVD computation.
- FUNWAVE-TVD computation with specification of the input conditions as initial deformation uvz. Application of nesting capability to n layers, with preparation of the nesting data, specification of the nesting boundary(ies) and of the coupling data.
- Manipulation of the output results from FUNWAVE-TVD computation, specifically the η, u and v files, to the adequate dictionary file waveDict, which will contain the boundary conditions to start olaFlow simulation.
- Manipulation and conversion of the h file of the computational domain to the Stereolithography (STL) format, via the `stlwrite.m` GNU Octave® script.
- OF/olaFlow computation. At this stage the STL file is converted to a mesh by the snappyHexMesh tool. The emulation of a piston wave-maker is performed, via time, velocity of the wave-maker and free surface elevation (timeSeries condition via waveType wavemaker and waveTheory tveta), for one single paddle.

For the GeoClaw model, the earthquake parameters are prescribed from the USGS, the literature or other source. The initial conditions for the FUNWAVE-TVD code are then prescribed from GeoClaw simulations and olaFlow uses as boundary conditions the results from the FUNWAVE-TVD/CM1 simulation.

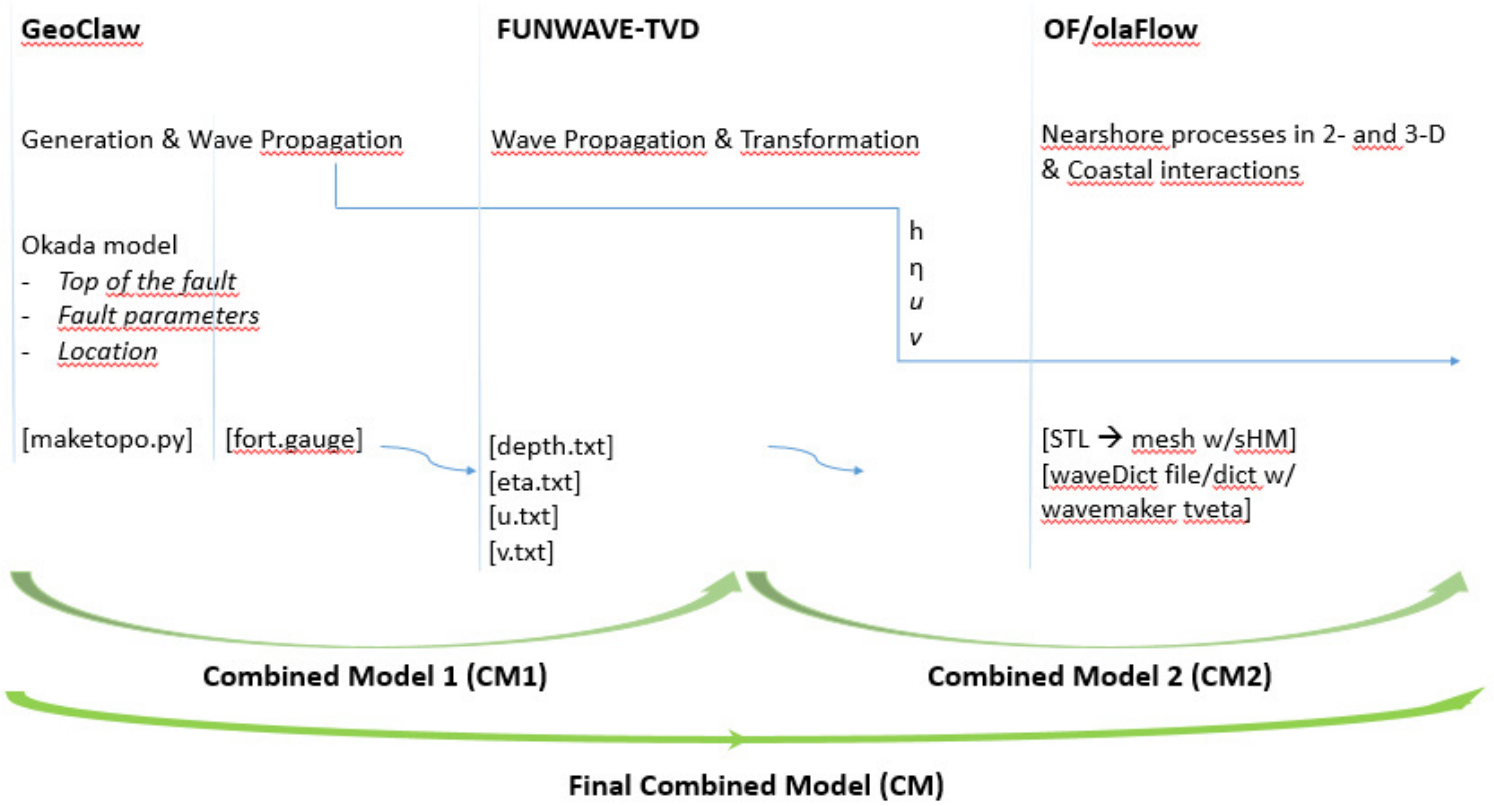

Figure 6.1: Flowchart illustrating the application methodology of the full combined tsunami model.

6.2.3 Numerical simulation with the fully combined tsunami model, CM. Discussion of results.

To simulate a complete combined model case, adequate steps within each code have to be taken. The first simulation is performed with GeoClaw. An earthquake event with $M_w = 8.5$, located at the Southwest Iberian Margin, with epicentre (36.010°N, 10.570°W)—same epicentre as the Portugal Earthquake and Tsunami of 1969 (Gjevik et al., 1997)—, was selected. The fault parameters used to generate this event are listed in Table 6.1. The mother grid used is a 1001×1001 grid (Figure 6.2) with 700 m cell size (0.0064°). The seafloor deformation was determined from the elastic dislocation model in a homogeneous isotropic elastic half-space (Mansinha and Smylie 1971; Okada 1985), assuming an instantaneous static seabed displacement, translated towards the free surface as an initial condition, which reproduces the elastic bottom deformation caused by the earthquake (fault mechanism parameters in Table 6.1). The Okada model is available within the GeoClaw code and the initial deformation is generated with a simple straighforward code. The initial deformation caused by the earthquake is plotted in Figure 6.3. The bathymetries used are referred to the mean sea level.

Grid set A is a set of grids with successive mesh refinements with a ratio of 4. This was the grid set selected (section 5.2.3) because it is the only grid set that includes a layer with a cell size of 11 m (layer 41), whose cells correspond to the division by 4 of the cells of the previous layer. Grids 01, 21 and 31 were obtained from GEBCO. The construction of the digital elevation model of grid 41 was obtained by combining two data sets: the topographic data from the Cascais Municipal Chamber and a set of bathymetric data from the Hydrographic Institute (Baptista and Omira, 2014). More details are described in the previously cited report.

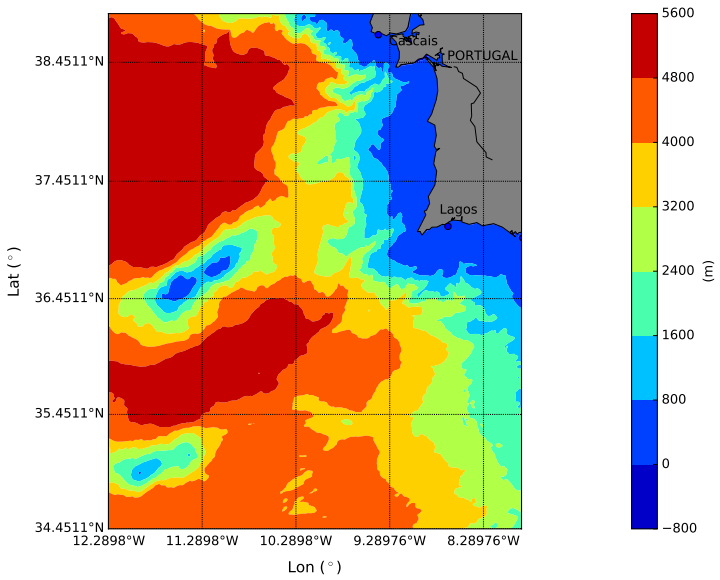

Figure 6.2: First level grid 01 used in the first global scale tsunami simulation of the M_w 8.5 Earthquake near the coast of Portugal.

The initial data necessary to run the Boussinesq model FUNWAVE-TVD was retrieved from GeoClaw output results, as explained before in section 5.2 (the combined model 1, CM1). This initial information corresponds closely to 2 min of GeoClaw's simulation, right after the generation of the earthquake and tsunami. This time interval is shorter than that previously established, due to the fact that this is a very large event, located close to the coast and above all with a wide

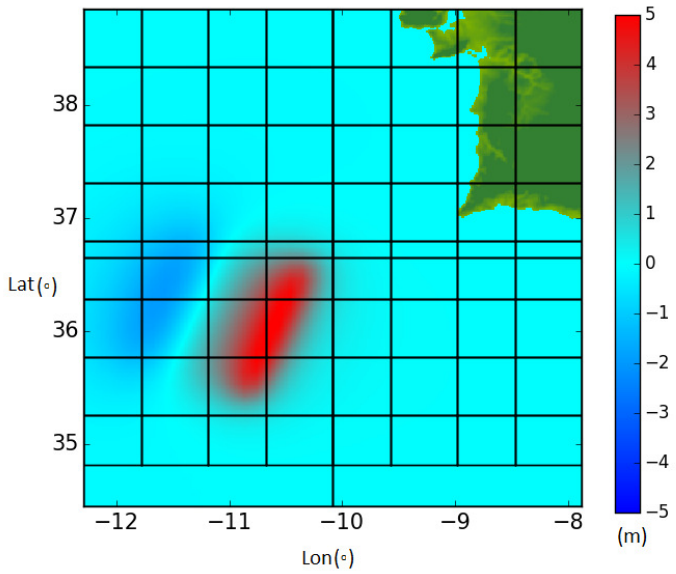

Figure 6.3: Initial sea floor deformation (in metres) of the M_w 8.5 earthquake near the Portuguese Coast.

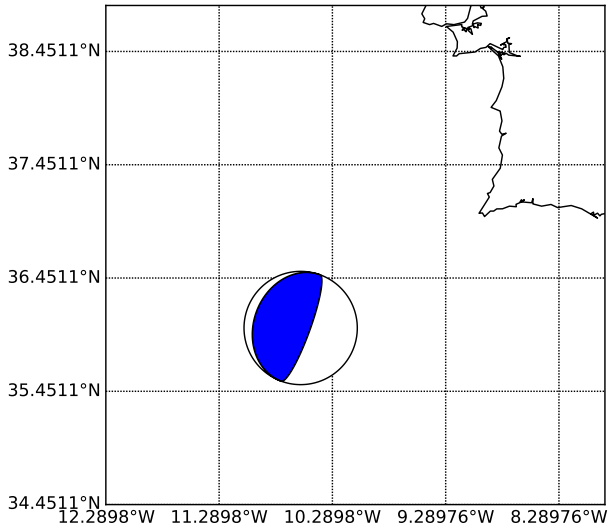

Figure 6.4: Representation of the source mechanism of the M_w 8.5 Earthquake event, near the coast of Portugal, located at the epicentre of the event.

Table 6.1: M_w 8.5 Earthquake fault mechanism parameters.

Length (km)	Width (km)	Strike (°)	Dip (°)	Rake (°)	Slip (m)	Depth† (km)	μ (Pa)	M_0 (N·m)	M_w
140	90	200	15	90	13	20	4×10^{10}	6.56×10^{21}	8.5

†Top of the fault

influence area. The data was written into four separated ASCII files, concerning depth h, water surface elevation η, velocity u and velocity v, with 1001 $\times$ 1001 cells and cell size 0.0064°, such as the mother grid.

Computations with FUNWAVE-TVD were performed for a total run time of 2 h and grid spacing ($\delta\phi$, $\delta\theta$) equal to 0.0064°. Boundary sponge layers with 50 km were applied in all the boundaries, of the layer 01 simulation, to avoid reflections in the simulation and contamination of the results. Three additional grids were used in the simulations, applying the nesting capability of FUNWAVE-TVD. The characteristics of each grid are indicated in Table 6.2.

Table 6.2: Characteristics of the layers used in the simulations, with indication of the codes and features applied.

grid	nx[1]	ny[2]	cell size		XoLon	YoLat	Code
			(°)	(m)			
L01	1001	1001	0.0064	700	-12.2890	34.4519	GeoClaw + FUN-TVD (CM1)
L21	404	336	0.0016	175	-9.7976	38.4808	FUN-TVD (nesting)
L31	752	528	0.0004	44	-9.5678	38.6050	FUN-TVD (nesting)
L41	1704	632	0.0001	11	-9.5185	38.6533	FUN-TVD + OF/olaFlow (CM2)

[1]Number of grid columns.
[2]Number of grid rows.

Sponge layers were used in all the simulations and its dimensions are detailed in Table 6.3.

Table 6.3: Width of the sponge layers used in the nested simulations. Absence of sponge layer is represented by a width equal to zero.

grid	North (N) (km)	South (S) (km)	West (W) (km)	East (E) (km)
L01	50	50	50	0
L21	25	25	25	0
L31	5	5	5	0
L41	1	1	1	0

In between the CM1 simulations using layers 01, 21, 31 and 41 (Figures 6.5, 6.6 and 6.7) the output of the results at the boundary points (located at the common boundaries) were used. Table 6.4 lists the number of boundary points used in the nesting process, in between the layers, and the respective boundary locations.

Table 6.4: Number of mutual boundary points between the layers used in the nested simulations.

boundary	L01–L21	L21–L31	L31–L41
North (N)	102	189	0
South (S)	102	189	426
West (W)	85	133	159
East (E)	0	0	0
total no points	289	511	585

In Figure 6.8, the red box refers to the area of interest for the CFD simulation. This area of

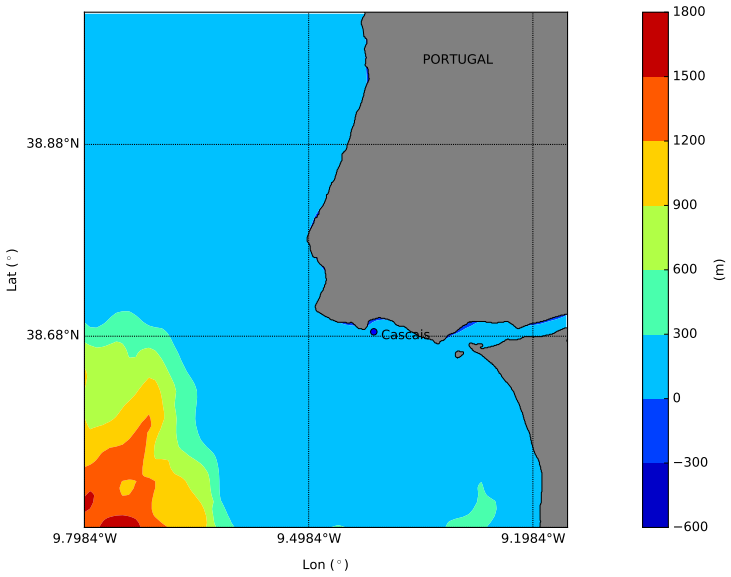

Figure 6.5: Grid 21 (nested in grid 01) for the simulation of the M_w 8.5 Earthquake near the coast of Portugal.

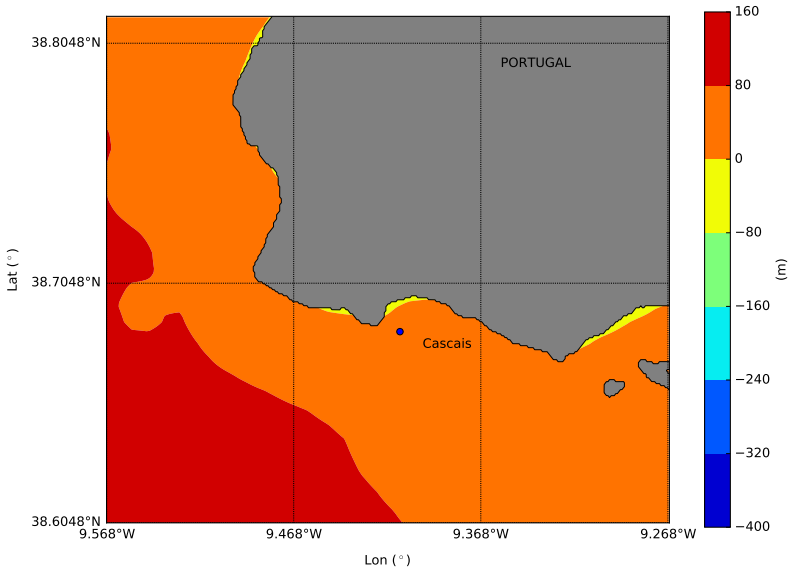

Figure 6.6: Grid 31 (nested in grid 21) for the simulation of the M_w 8.5 Earthquake near the coast of Portugal.

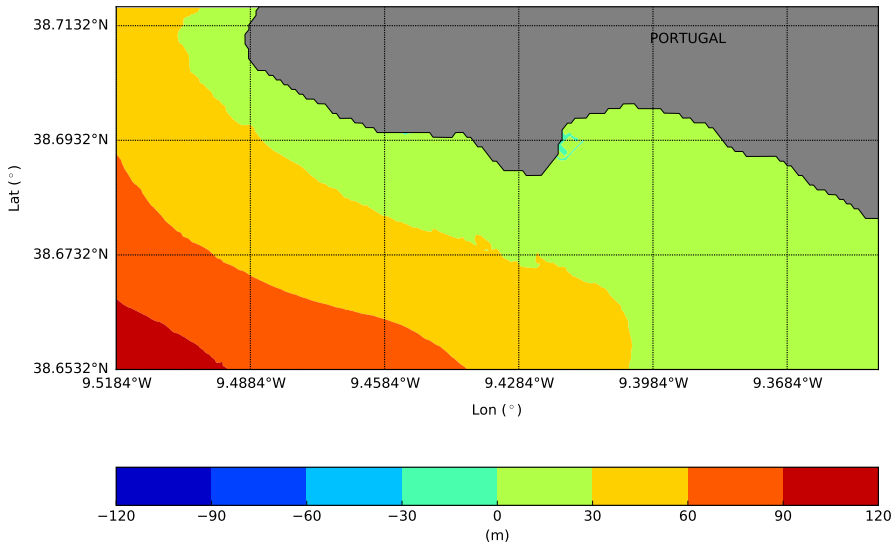

Figure 6.7: Grid 41 (nested in grid 31) for the simulation of the M_w 8.5 Earthquake near the coast of Portugal.

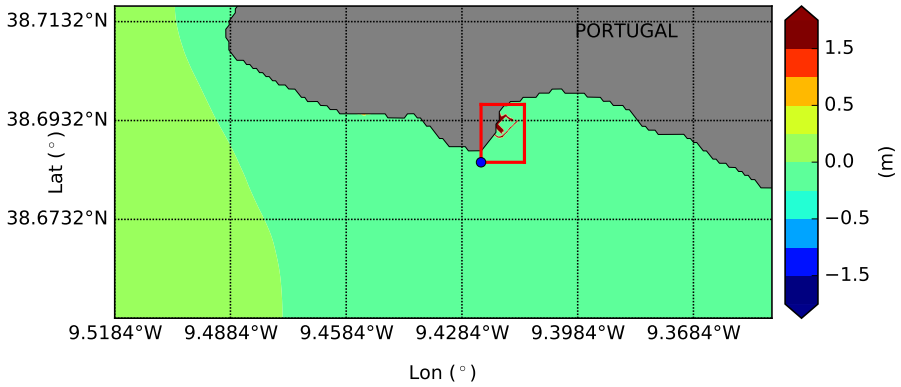

Figure 6.8: Computation of the free surface elevation in grid 41, 35 minutes after the beggining of the M_w 8.5 Earthquake near the coast of Portugal. The red contour defines the CFD simulation area, which includes the Cascais marina.

interest, represented in Figure 6.9, has approximate dimensions of 1000 m in x direction by 1000 m in y direction and 40 m in z direction.

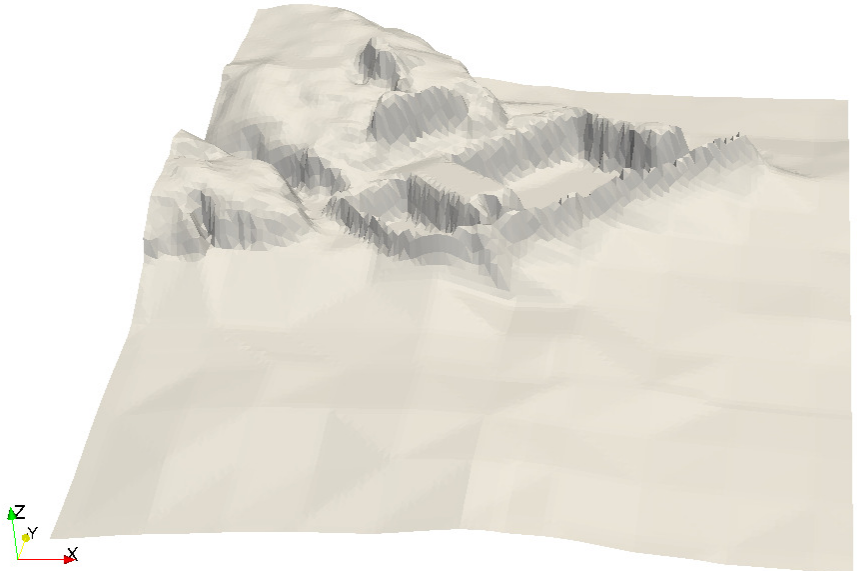

(a)

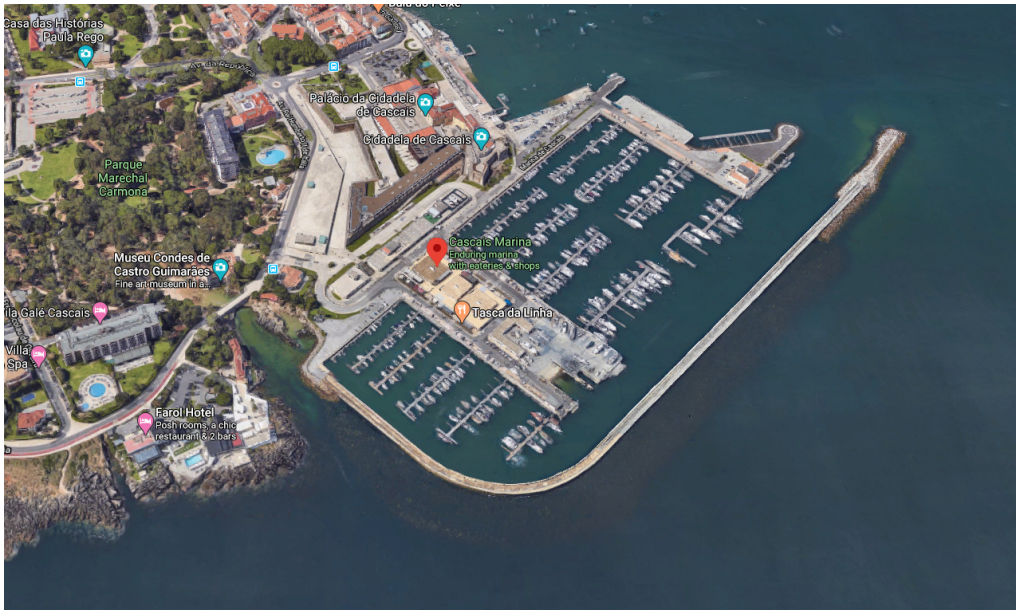

(b)

Figure 6.9: (a) 3D representation of the coastal zone to be studied. (b) Real view, including the Cascais marina.

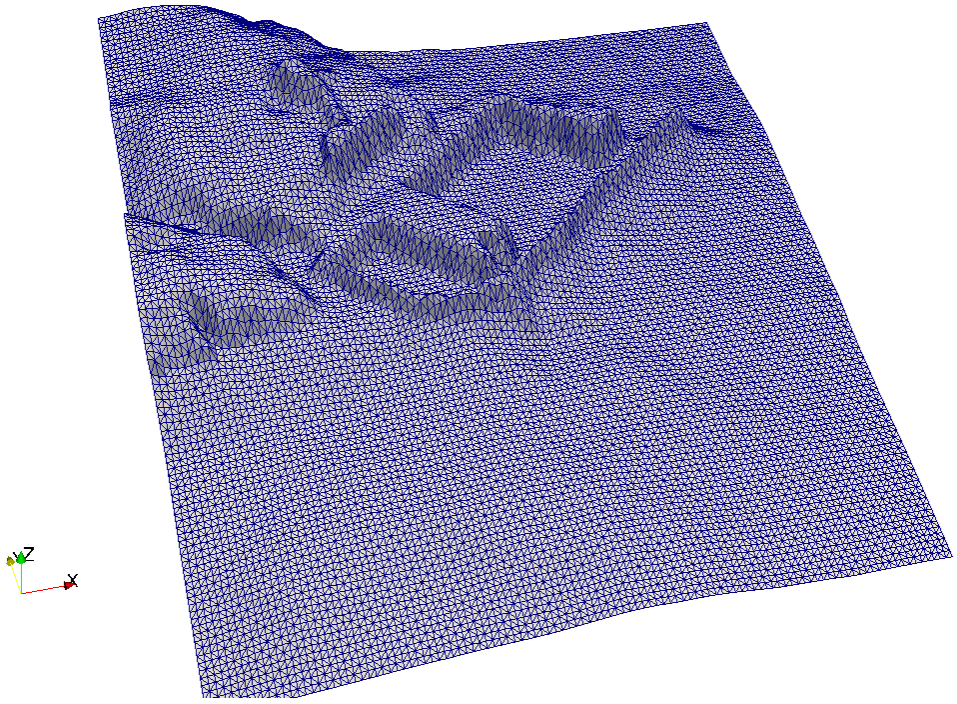

(a)

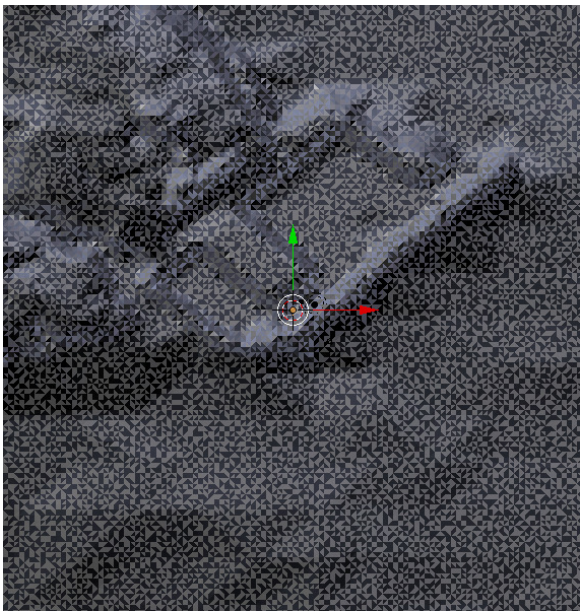

(b)

Figure 6.10: (a) Mesh of the simulation area, concerning Cascais and its marina, obtained with the snappyHexMesh tool. (b) Top view of the coastal zone (STL file).

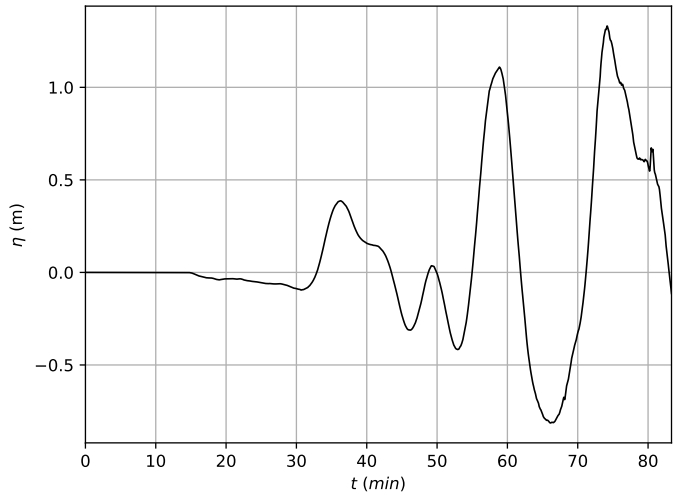

Figure 6.11: Time series of the surface wave elevation retrieved at the most southwestern boundary point [(38.685°, -9.423°), h = 16.0 m] of the Cascais marina area.

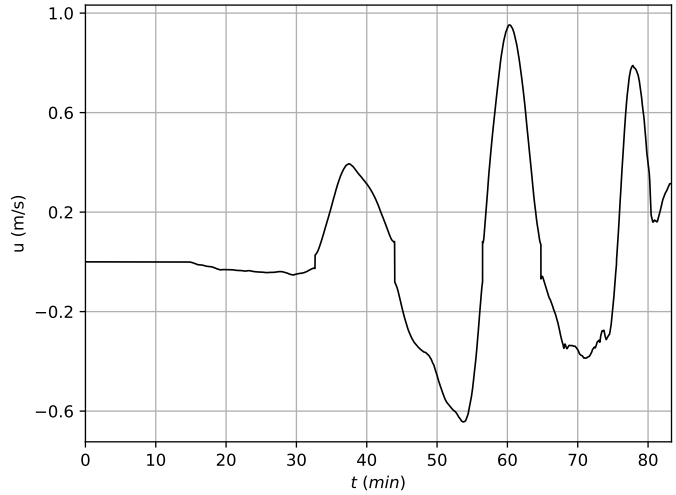

Figure 6.12: Time series of the velocity retrieved at the most southwestern boundary point [(38.685°, -9.423°), h = 16.0 m] of the Cascais marina area.

The CFD code is applied in the study of the tsunami event fluid-flow interaction with the Cascais marina coastal surroundings. As a first approach, the 3D simulation was attempted. The finest layer available containing the digital terrain model (DTM)—also called DEM (digital elevation model)—of the coastal area of interest, located near the marina of Cascais, was used in the computations. For this purpose, we used the CM1 nested simulation results applying layer 41 (Figure 6.8). The output results were used in the CFD simulation, concerning a zoomed area of layer 41. In these 3D simulations there was the necessity of applying a reduced area of layer 41, due to the limited cluster resources availability, the large amount of time required for simulations total runtime, the large size occupied by the output simulation results and thus the pos-processing.

In the first stage, when the 3D simulations were considered and simulations were trialed, some

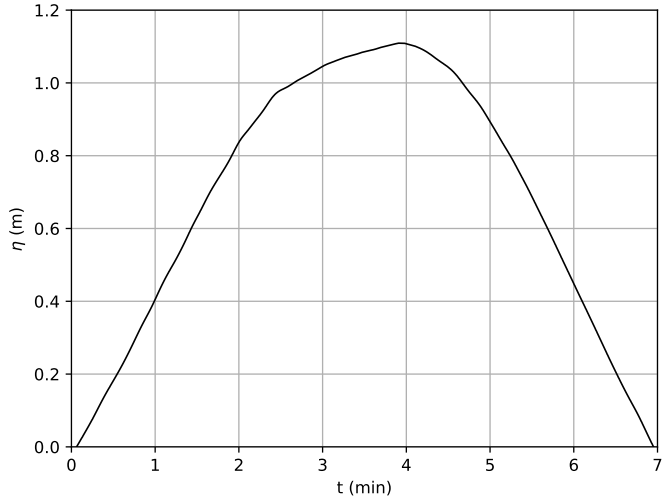

Figure 6.13: Surface wave elevation time series of the second wave, extracted from η profile, at the most southwestern boundary point [(38.685°, -9.423°), h = 16.0 m] of the Cascais marina area.

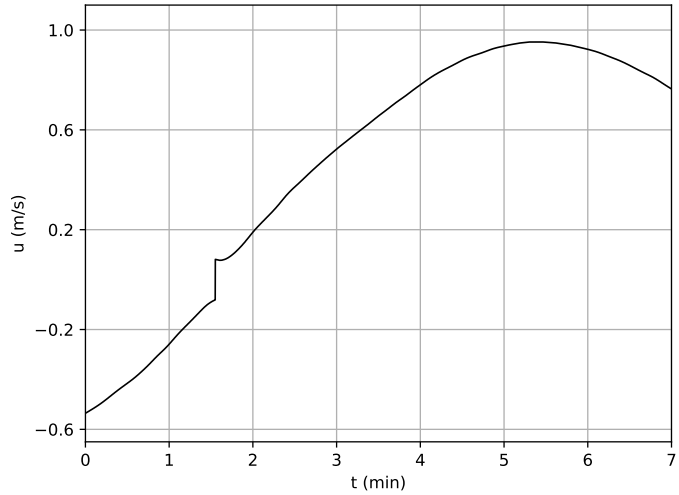

Figure 6.14: Velocity time series of the second wave, extracted from $\mathbf{u}$ profile, at the most southwestern boundary point [(38.685°, -9.423°), h = 16.0 m] of the Cascais marina area.

problems were detected. The first problem was that some format manipulation had to be performed, to have a file format that could be read by the CFD code and that could be converted to a mesh for the numerical simulation. It was found that layer 41 data, in ASCII format, needs to be processed to the STL format that, through the snappyHexMesh (sHM) tool within OpenFOAM, will enable for the creation of the mesh necessary to run the simulations (Figure 6.10). The terrainBlockMesher tool * cannot be used in this case, as it does not work for sharp edges, which means that it is not adequate for urban flows, such as the case we aim to model at this stage.

The second problem was related to the input time series used in the CFD code. The time series of the free surface elevation η (Figure 6.11) and of the total velocity $\mathbf{u}$ (Figure 6.12) were

*Available at http://openfoamwiki.net/index.php/Sig_WindE/Getting_Processing_Terrain_Data.

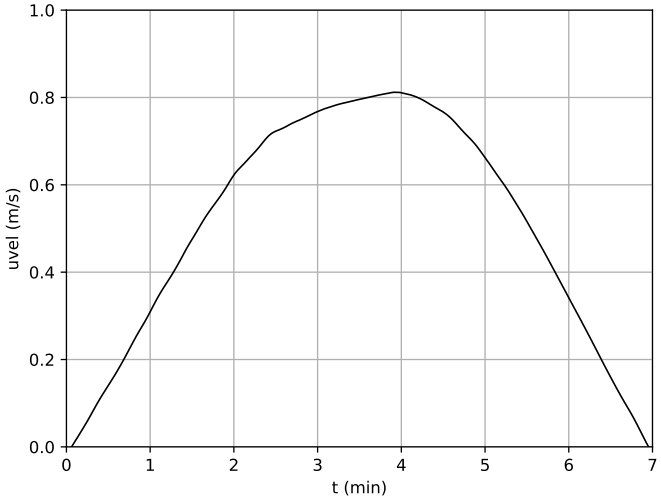

Figure 6.15: Calculated velocity time series of the second wave.

retrieved from the CM1, via a virtual wave gauge located at the southwestern point (38.685°, -9.423°) (blue dot in Figure 6.8). This point location was chosen because it was found to be the most representative of the incoming tsunami wave directivity. The water depth h at this location is approximately 16 m. This information on the free surface elevation η and total velocity $\mathbf{u}$ is then converted to the wave-maker tveta condition, as part of the waveDict file, containing the initial conditions to start olaFlow code. For olaFlow, the wave generation takes place at the southern boundary area, limited by coordinates (38.68475°, -9.42345°) and (38.68475°, -9.41225°).

As a consequence of the existing computational limitations and for which exactly the reasons are unknown (possibilities will be discussed later in this chapter), a part of the original time series, contemplating the second wave, has been extracted for use in the simulation (Figure 6.13). This part of the time series was chosen because it was the second highest wave registered in the time series, thus we used it as representative of a worst case tsunami wave profile. From the simulations results it was verified that the input free surface time series was modified when entering the domain. As a consequence of the lag between the free surface elevation and velocity profiles (Figures 6.11 and 6.12), the velocity profile of the extracted free surface elevation time series started at a negative velocity value (Figure 6.14). As it is not possible to correct this shift, it is necessary to calculate the respective wave speed profile separately from the free surface elevation profile, with the wave direction being given by the respective wave (Figure 6.15). The particle velocity is calculated from expression (5.4), with d = 16 m and assuming shallow water wave celerity (expression (5.6)). This velocity wave profile has to be adopted to obtain the correct input free surface elevation. The trial tests performed in a 2DV waveflume showed that the free surface elevation is now correctly input into the domain problem.

Table 6.5: Time schemes options.

dictionary		
fvSchemes	ddtSchemes	Euler
	gradSchemes	Gauss linear

Due to the limited cluster resources availability, the large amount of time required for sim-

Table 6.6: Boundary conditions for the CM2 simulations (0.org folder).

boundaryField	block boundary type laminar / turbulent	alpha.water.org	prgh	U
inlet	patch	waveAlpha	fixedFluxPressure	waveVelocity
outlet	patch	zeroGradient	fixedFluxPressure	waveAbsorption2DVelocity
bottom	wall	zeroGradient	fixedFluxPressure	fixedValue
quebramar	—	zeroGradient	fixedFluxPressure	fixedValue
talude	—	zeroGradient	fixedFluxPressure	fixedValue
paredão	—	zeroGradient	fixedFluxPressure	fixedValue
atmosphere	patch	inletOutlet	totalPressure	pressureInletOutletVelocity

ulations total runtime, the large size occupied by the output simulation results and thus the post-processing, it was chosen to perform the simulations in 2DV, as not being sure about the advantages of the 3D simulation at this point.

6.2.4 Simulations in two dimensions

The 2DV simulations that are presented in this section reflect the best possible the bathymetric configuration of a transect with the direction southwest–northeast, extracted from the boundary point where the original free surface elevation and velocity time series where retrieved from in the FUNWAVE-TVD/CM1 simulation (blue dot in Figure 6.8) and the first meters of the technical pier wall. The 2DV domain contemplates an initial long slope, after which there is a small slope. Afterwards, there is the marina of Cascais breakwater, the interior part of the marina and finally the technical pier wall (Figure 6.16). A cross profile of the Cascais breakwater is shown in Figure 6.17 (Teixeira (2012)).

For the simulations we consider a 2DV channel with the width of one element, length of 830 m and height of 30 m. The time step of the numerical simulations is 1 s and the water depth is 16 m. The cell resolutions varies for each zone of the 2DV computational domain. In the breakwater zone it is used a Δx = 1 m, otherwise Δx = 5 m is used (Table 6.7). Refinement is performed around the flat area, the breakwater and the area between the breakwater and the technical pier wall. Details of the mesh can be seen in Figure 6.18.

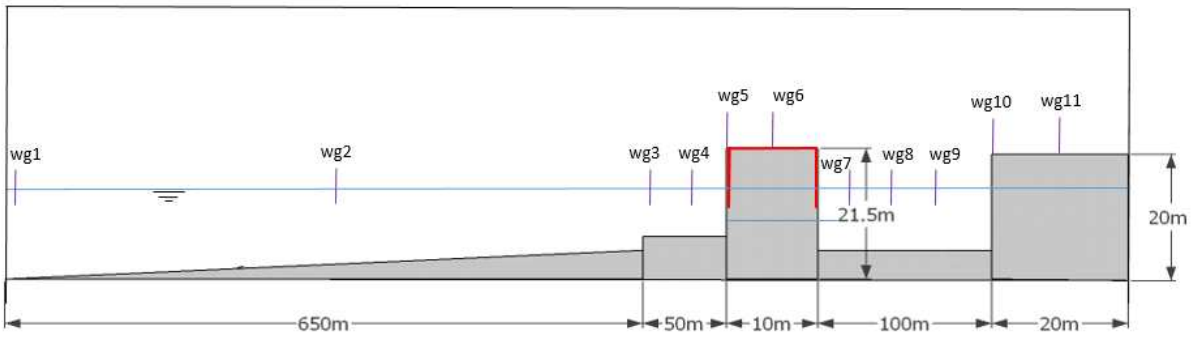

Figure 6.16: Configuration of the domain of the Cascais marina used in the 2DV simulations (not to scale).

The buoyancy-modified $\kappa - \omega$ SST turbulence model is used in the simulations. No porosity is considered in the simulation. Virtual water level gauges are deployed along the domain and free

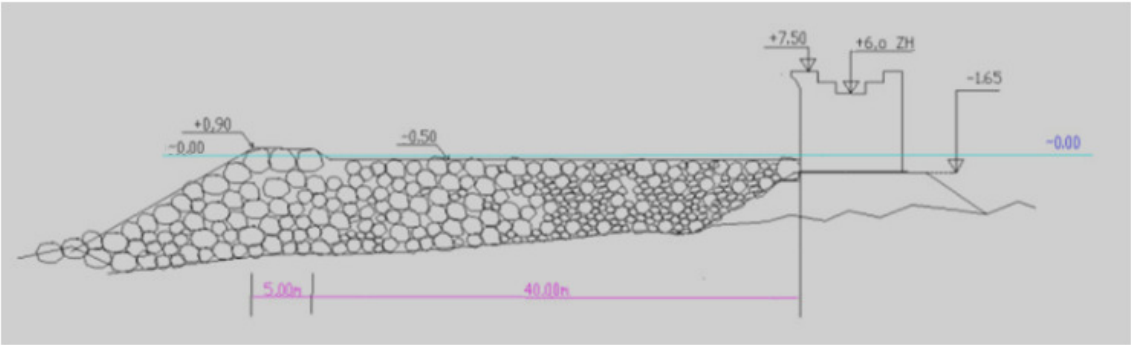

Figure 6.17: Cross profile of the marina of Cascais breakwater (Teixeira, 2012).

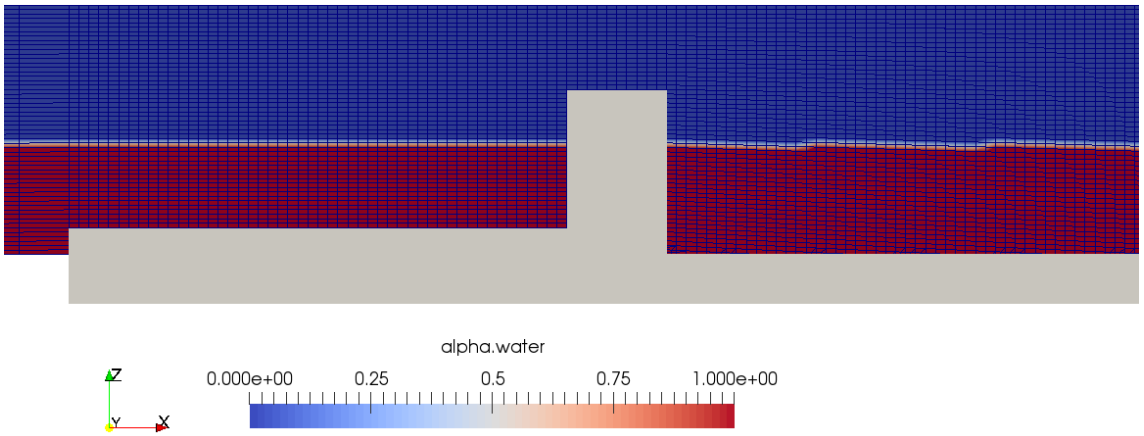

Figure 6.18: Details of the mesh used in the 2DV simulation of the Cascais marina.

Table 6.7: Computational domain and mesh characteristics.

Zone	long slope	flat area	breakwater	flat zone	technical pier wall
Lx (m)	650	50	10	100	20
Ly (m)	10	10	10	10	10
Lz (m)	10	13.5	21.5	11	20
Δx (m)	5	1	1	1	5
Δy (m)	10	10	10	10	10
Δz (m)	0.5	0.5	0.5	0.5	0.5

surface elevation at each location is retrieved (Table 6.8). Pressure is measured on the breakwater and at each one of its sides (Table 6.9). Pressure gauges 1 to 10 are located on the seaward side of the breakwater, pressure gauges 12 to 20 are located at the breakwater crest and pressure gauges 21 to 30 are located on the leeward side of the breakwater.

The physical conditions used in the simulations are documented in Table 5.12. The time scheme options used olaFlow are listed in Table 6.5. The boundary conditions for each boundary field in olaFlow are documented in Table 6.6. In the simulations herein presented, the contribution of turbulence is presented. The files relevant for the application of the $\kappa - \varepsilon$ SST turbulence model are detailed in Appendix A.3.4.

The simulations for 3 wave cases are presented next. First, a constant bore-like wave with

Table 6.8: Location of the virtual wave gauges along the domain.

wave gauge	x (m)	y (m)
1	5.0	5.0
2	325.0	5.0
3	655.0	5.0
4	678.0	5.0
5	700.0	5.0
6	705.0	5.0
7	720.0	5.0
8	750.0	5.0
9	780.0	5.0
10	810.0	5.0
11	820.0	5.0

Table 6.9: Location of the pressure gauges along the domain.

pressure gauge	x (m)	y (m)	z (m)
1	700.0	5.00	12.00
2	700.0	5.00	13.00
3	700.0	5.00	14.00
4	700.0	5.00	15.00
5	700.0	5.00	16.00
6	700.0	5.00	17.00
7	700.0	5.00	18.00
8	700.0	5.00	19.00
9	700.0	5.00	20.00
10	700.0	5.00	21.00
12	702.0	5.00	21.50
13	703.0	5.00	21.50
14	704.0	5.00	21.50
15	705.0	5.00	21.50
16	706.0	5.00	21.50
17	707.0	5.00	21.50
18	708.0	5.00	21.50
19	709.0	5.00	21.50
20	710.0	5.00	21.50
21	710.0	5.00	21.00
22	710.0	5.00	20.00
23	710.0	5.00	19.00
24	710.0	5.00	18.00
25	710.0	5.00	17.00
26	710.0	5.00	16.00
27	710.0	5.00	15.00
28	710.0	5.00	14.00
29	710.0	5.00	13.00
30	710.0	5.00	12.00

H = 1.1 m, the same wave height as the wave retrieved from the wave series in Figure 6.13, is simulated. The second wave is a constant bore-like wave 4 times higher than the previous one, with H = 4.4 m. The constant bore-like wave cases are used to simulated the peak of the flooding, in which the wave is shorter and arrives faster, and its effect and impact on the studied structures can be perceived more quickly. The third case simulated is the main N-wave of the time series from Figure 6.11.

With these 2DV simulations we aim to investigate what happens to the tsunami waves, when reaching the marina of Cascais, considering that the direction of the tsunami waves propagation did not change.

6.2.4.1 Propagation of a H = 1.1 m constant tsunami like wave

A constant tsunami-like wave with H = 1.1 m (Figures 6.19 and 6.20) was generated into the domain of the marina of Cascais in a 2DV simulation (Figure 6.21). The total run time was 311 s and Δt = 1 s. Its shape starts transforming right after the generation, with the propagation over the slope, with the increase of the wave height. In the propagation the wave reaches 2.5 m. Around 30 s after the beggining of the simulation, it is possible to observe the wave generated propagating against the breakwater and waves reflecting back (Figures 6.22 and 6.23). The wave rises between 30 s and 1 min 30 s after its generation into the domain, dissipating after a while. With this H = 1.1 m constant tsunami like wave there is no overtopping of the breakwater, with the impact of the wave been absorbed by the breakwater. The pressures registered against the breakwater wall vary between 4 and 20 kPa (Figures 6.24 and 6.25).

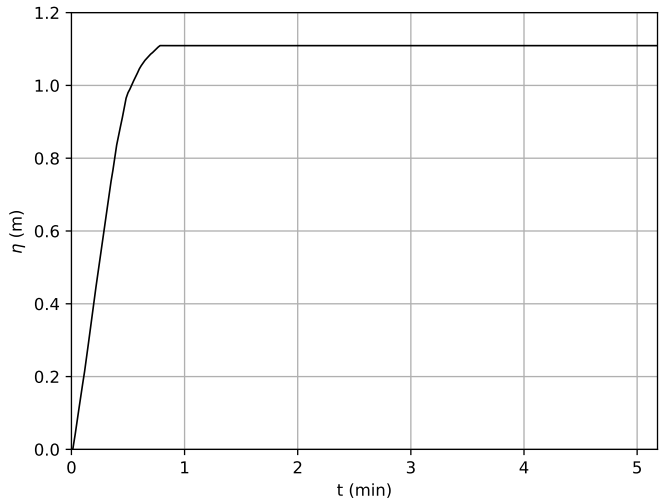

Figure 6.19: Surface wave elevation time series of a H = 1.1 m constant tsunami like wave.

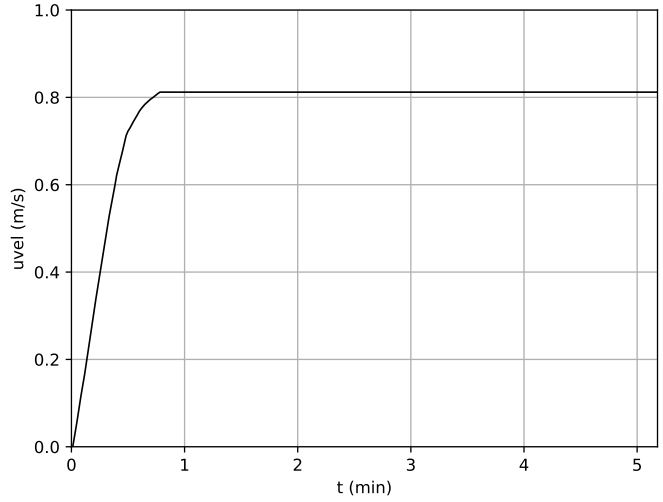

Figure 6.20: Velocity time series of a H = 1.1 m constant tsunami like wave.

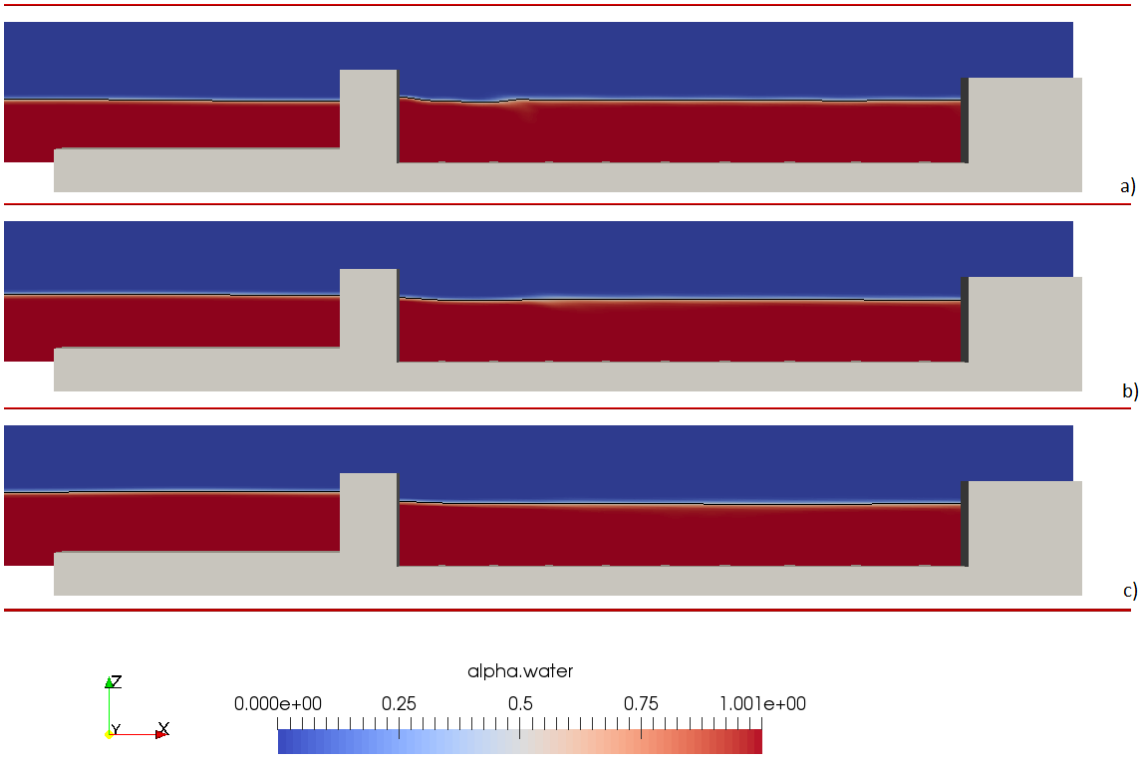

Figure 6.21: Spatial evolution of the wave propagation of a H = 1.1 m constant tsunami like wave over the marina of Cascais, at time instants a) 47 s, b) 1 min and 10 s and c) 1 min and 30 s.

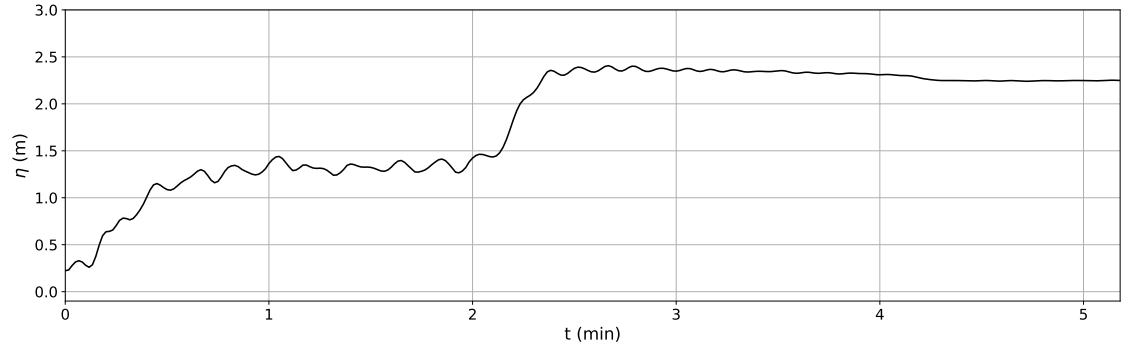

(a) wave gauge 1 (x = 5 m)

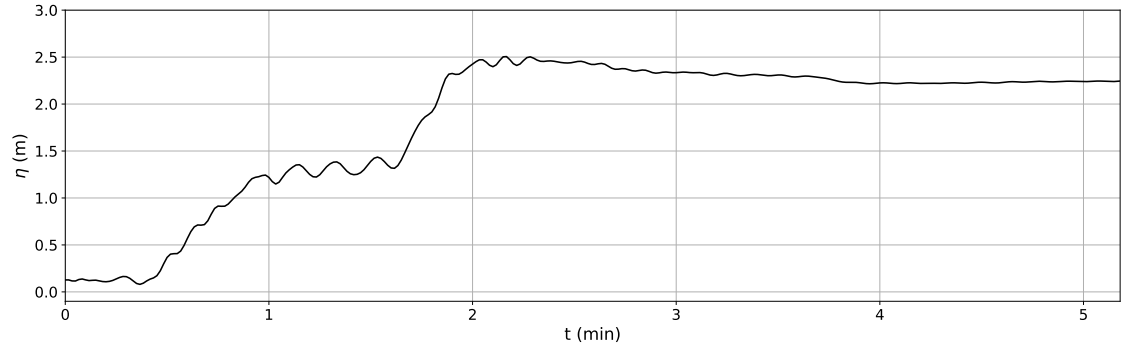

(b) wave gauge 2 (x = 325 m)

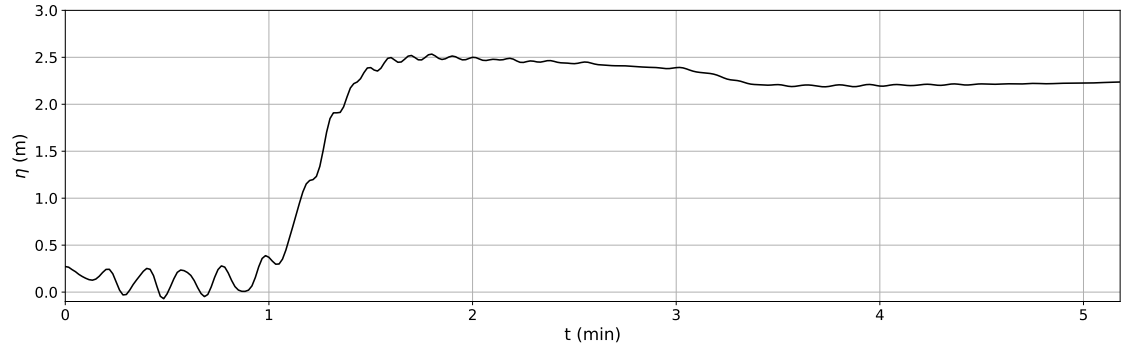

(c) wave gauge 3 (x = 655 m)

Figure 6.22: Temporal evolution of the wave propagation of a H = 1.1 m constant tsunami like wave over the marina of Cascais

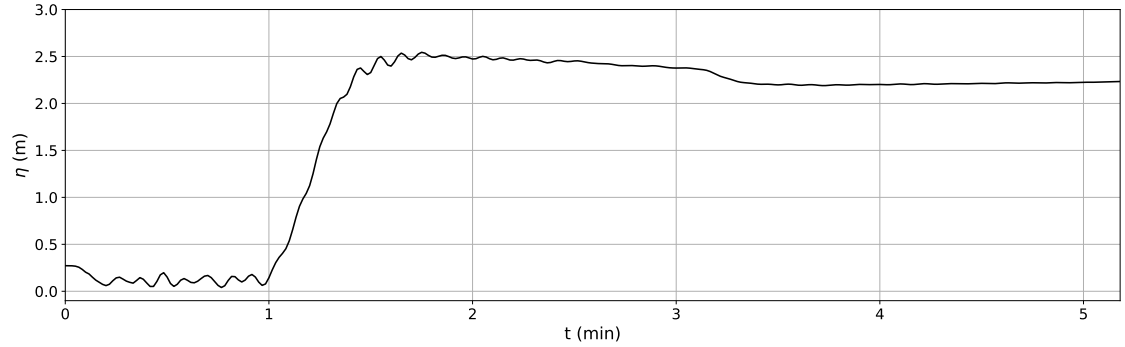

(a) wave gauge 4 (x = 678 m)

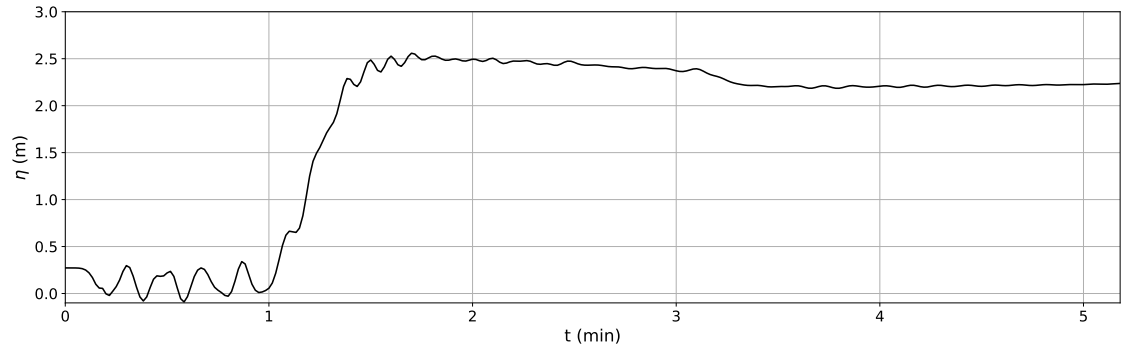

(b) wave gauge 5 (x = 700 m)

Figure 6.23: Temporal evolution of the wave propagation of a H = 1.1 m constant tsunami like wave over the marina of Cascais

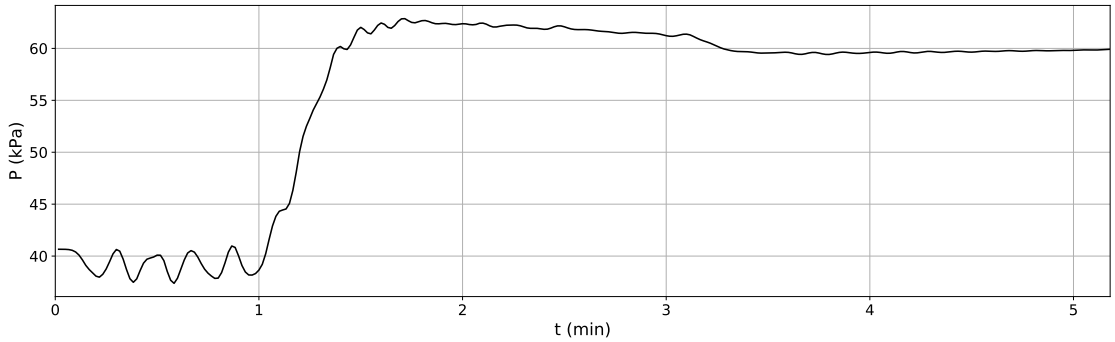

(a) pressure gauge 1

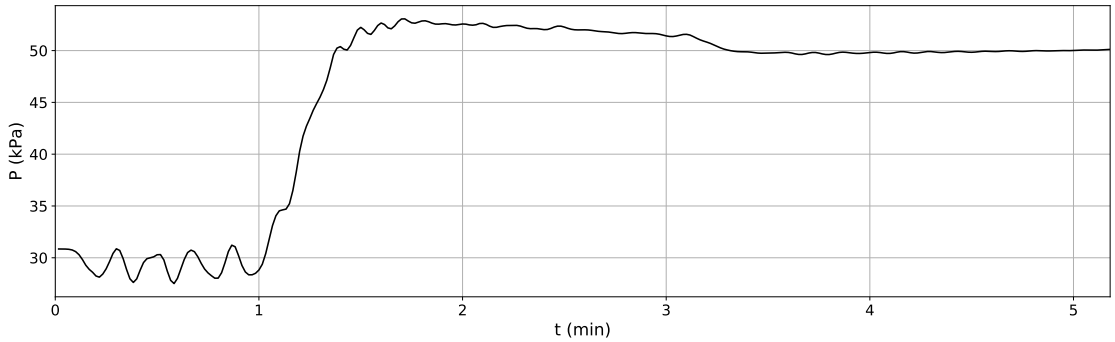

(b) pressure gauge 2

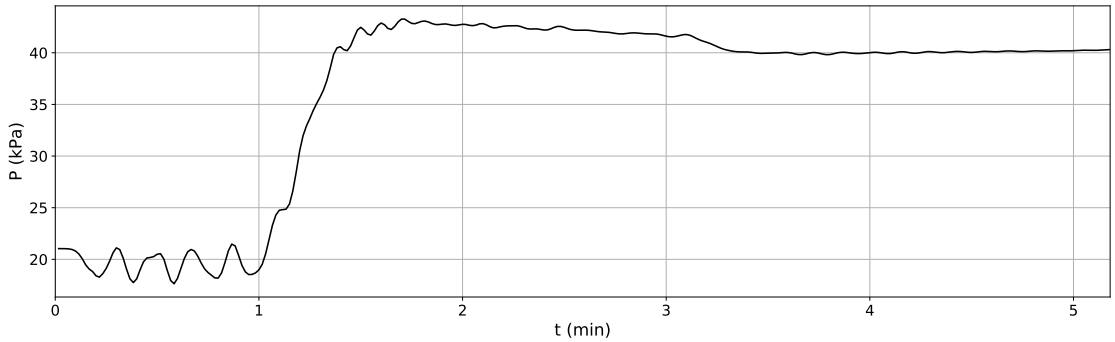

(c) pressure gauge 3

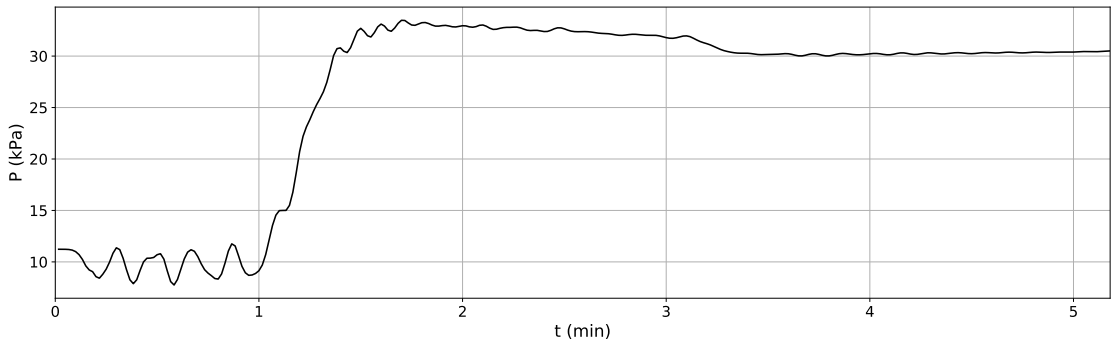

(d) pressure gauge 4

Figure 6.24: Temporal evolution of the pressure of a H = 1.1 m constant tsunami like wave over the marina of Cascais.

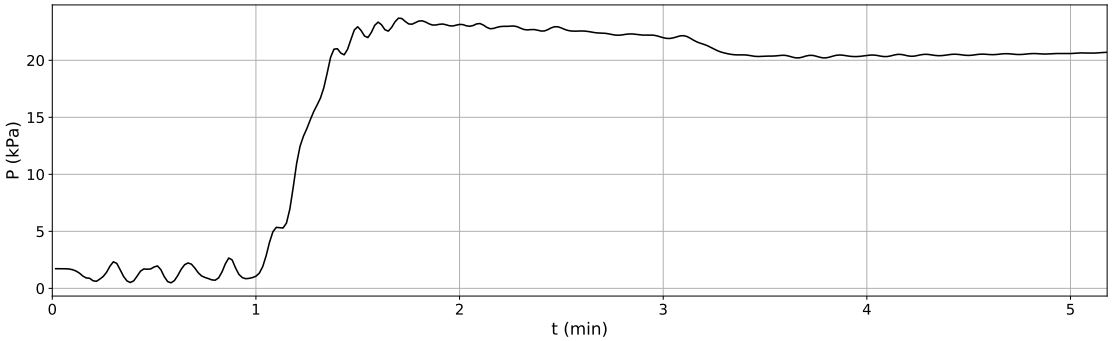

(a) pressure gauge 5

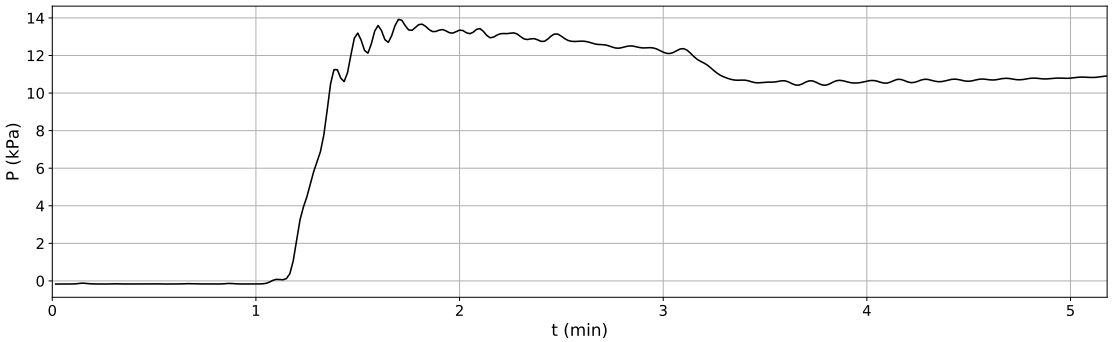

(b) pressure gauge 6

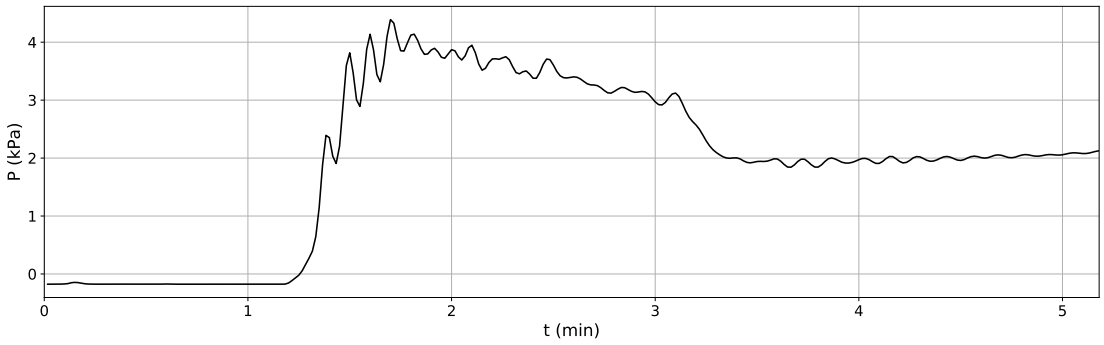

(c) pressure gauge 7

Figure 6.25: Temporal evolution of the pressure of a H = 1.1 m constant tsunami like wave over the marina of Cascais.

6.2.4.2 Propagation of a H = 4.4 m constant tsunami like wave

We took the same wave from the previous case study and increased its wave height by 4 times. We now have a constant tsunami like wave with H = 4.4 m (Figures 6.26 and 6.27), which was generated into the domain of the marina of Cascais. The total run time was 311 s and Δt = 1 s.

From Figures 6.28 to 6.30 we observe the wave height increasing in the first meters of the domain, with reflected waves appearing in the free surface time series, stabilizing in the small slope at gauge 3, with about 8 m. Looking to wave gauge 6 and wave gauge 7 we see that on the breakwater crest the wave reaches around 2 m and 6 m just right after the breakwater. The tsunami waves reach the technical pier wall, flooding the area with about 2 to 3 m height (wave gauge 11). It is possible to observe from Figure 6.31 the tsunami wave arriving around 1 min after the beggining of the simulation, and starting to overtop the breakwater less than 10 s later. In Figure 6.32 we see that the continuous tsunami like wave is filling the area between the breakwater and the technical pier wall. Velocity magnitude is higher in the leeward side of the breakwater wall, starting to increase to increase around 72 s after the beginning of the simulation (Figures 6.34 to 6.35).

Numerical pressure gauges were placed along the breakwater walls and crest (Figure 6.16). The analysis of the instantaneous pressure distribution along the breakwater showed that the pressures vary between a minimum of around 20 KPa on the breakwater crest, 40 kPa on the leeward side of the breakwater, with the maximum pressure reaching 50 kPa at the seaward side of the breakwater (Figure 6.40). This pressure implies the possible occurrence of a big impulsion on the breakwater, which could be sufficient to move or even to take down parts of the structure. The time frame of biggest overturning for the structure can be considered occurring after 1 minute of computation of the tsunami wave. In the time interval when we observed that the velocity magnitude was higher in the leeward side of the breakwater, we also observed negative pressure values on the leeward side of the breakwater. These pressure values are most critical to the structure, as the breakwater is subject to strain forces, which should be further analysed. The streamlines are shown in Figures 6.37 to 6.39. We can observe the vortex shape on the slope and high velocity magnitudes on the leeward side of the breakwater.

The pressure field distribution along the sides of the breakwater, for t = 1.6 min, is shown in Figure 6.41. We see that the pressure in the walls of the breakwater (seaward side, leeward side, breakwater crest) has a hydrostatic distribution.

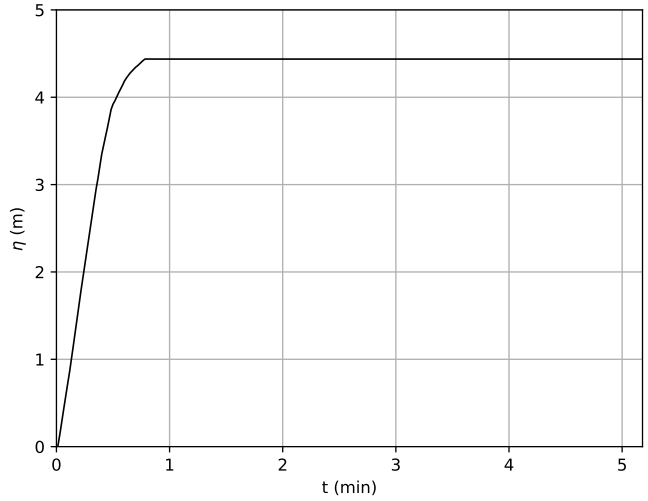

Figure 6.26: Surface wave elevation time series of a H = 4.4 m constant tsunami like wave.

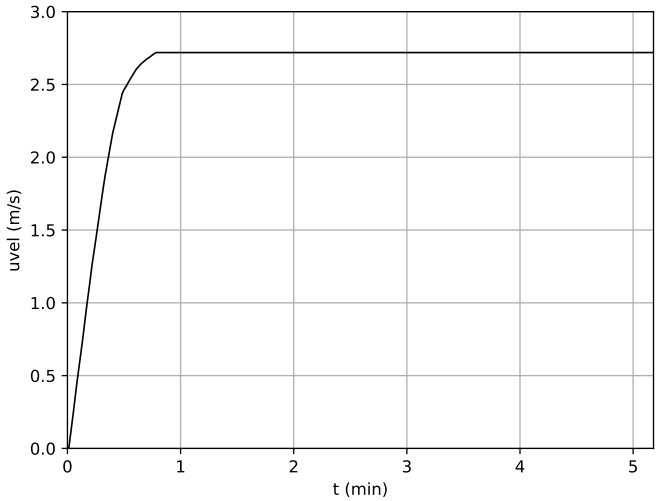

Figure 6.27: Velocity time series of a H = 4.4 m constant tsunami like wave.

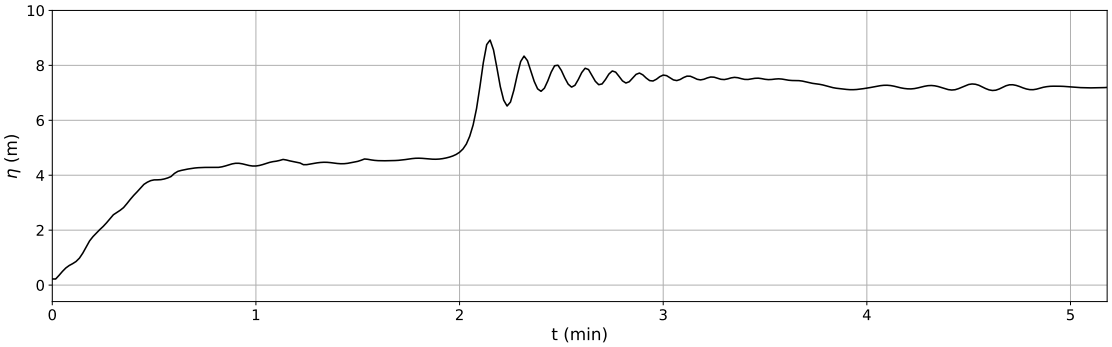

(a) wave gauge 1 (x = 5 m)

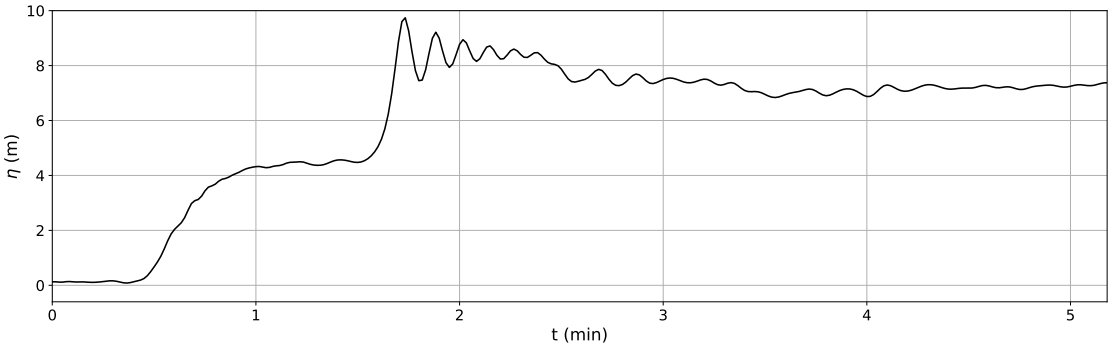

(b) wave gauge 2 (x = 325 m)

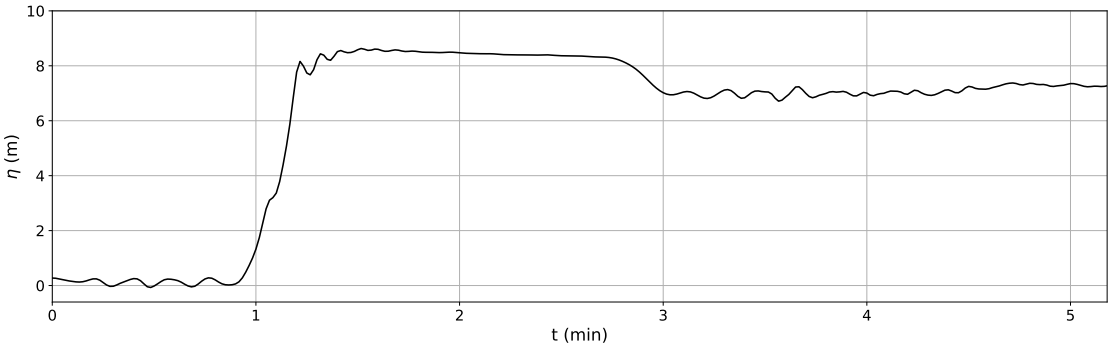

(c) wave gauge 3 (x = 655 m)

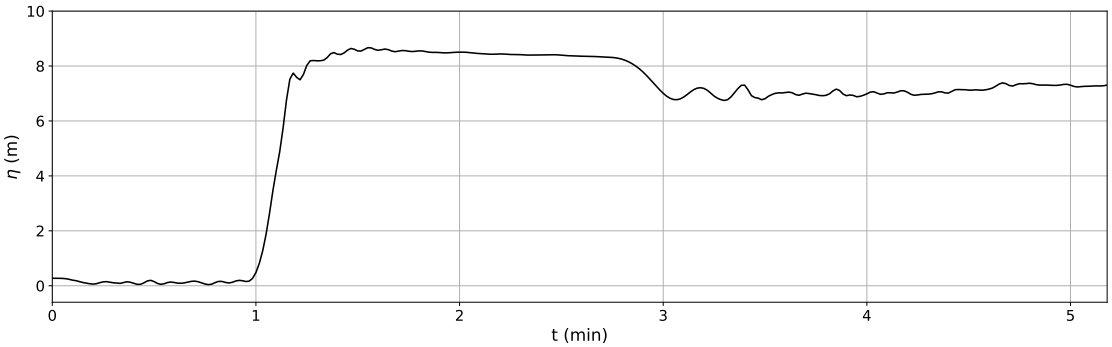

(d) wave gauge 4 (x = 678 m)

Figure 6.28: Temporal evolution of the wave propagation of a H = 4.4 m constant tsunami like wave over the marina of Cascais.

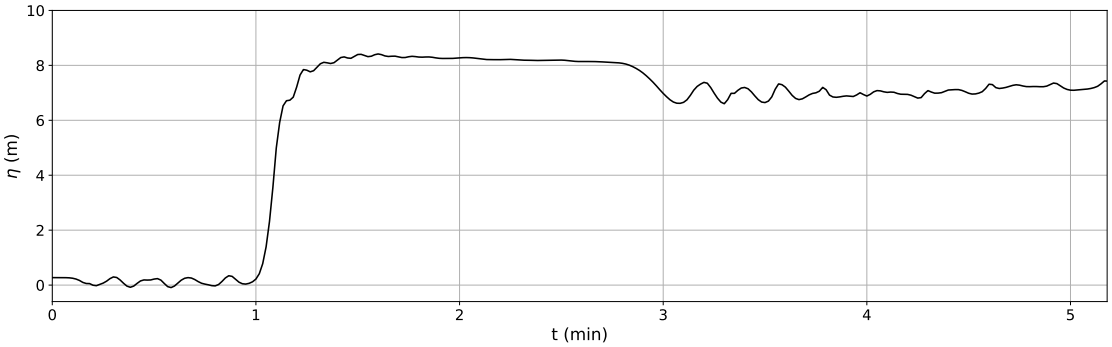

(a) wave gauge 5 (x = 700 m)

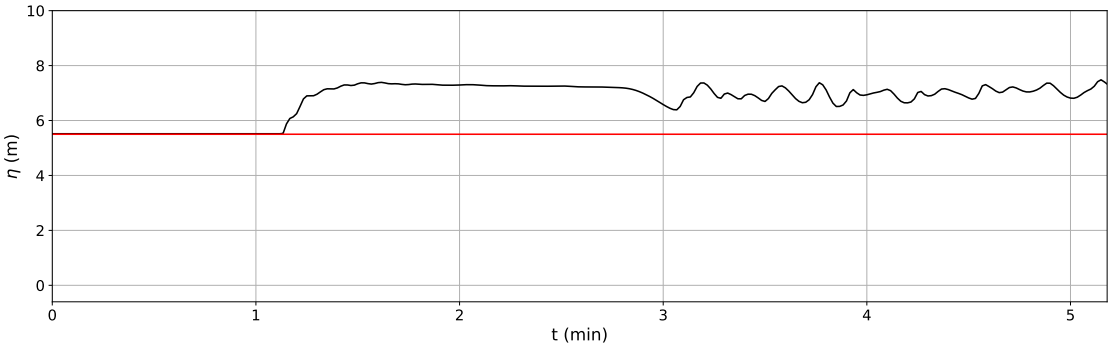

(b) wave gauge 6 (x = 705 m) — located on the breakwater crest

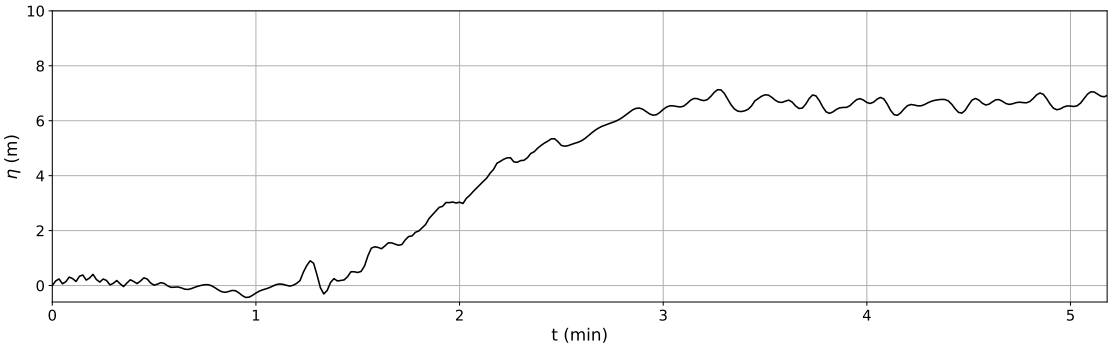

(c) wave gauge 7 (x = 720 m)

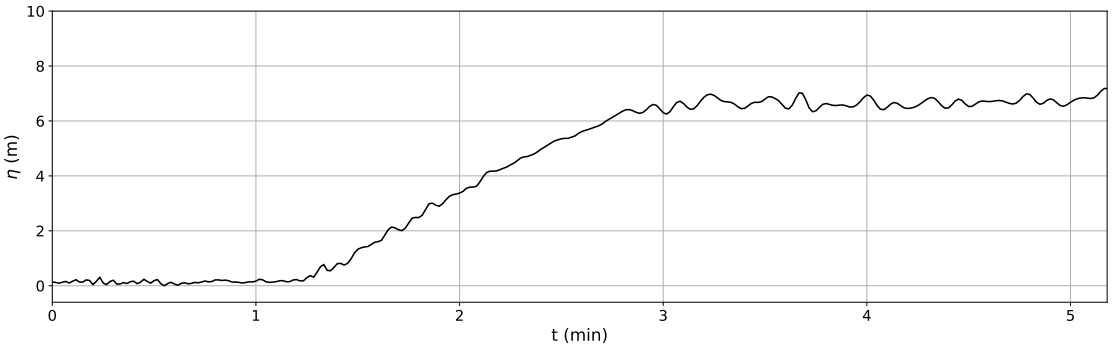

(d) wave gauge 8 (x = 750 m)

Figure 6.29: Temporal evolution of the wave propagation of a H = 4.4 m constant tsunami like wave over the marina of Cascais. Breakwater crest level (—).

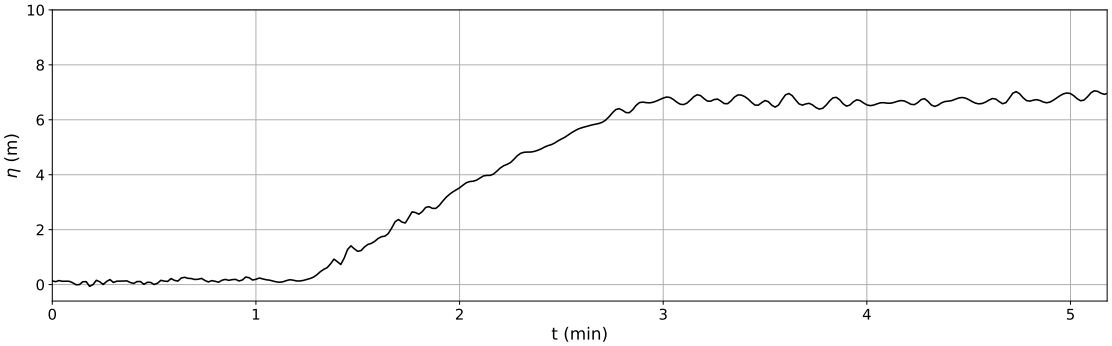

(a) wave gauge 9 (x = 780 m)

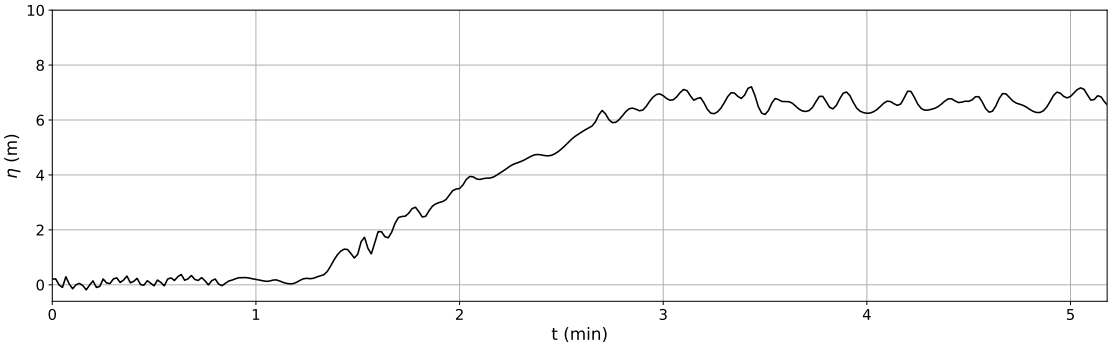

(b) wave gauge 10 (x = 810 m)

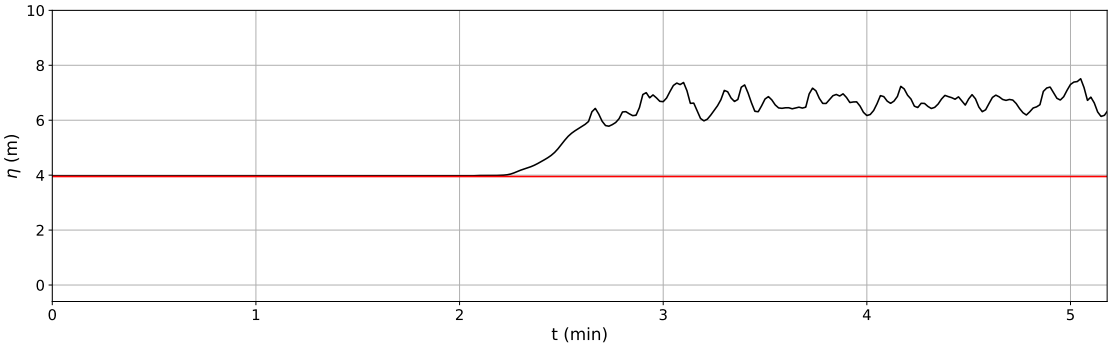

(c) wave gauge 11 (x = 820 m) — located on the top of the technical pier

Figure 6.30: Temporal evolution of the wave propagation of a H = 4.4 m constant tsunami like wave over the marina of Cascais. Technical pier top level (—).

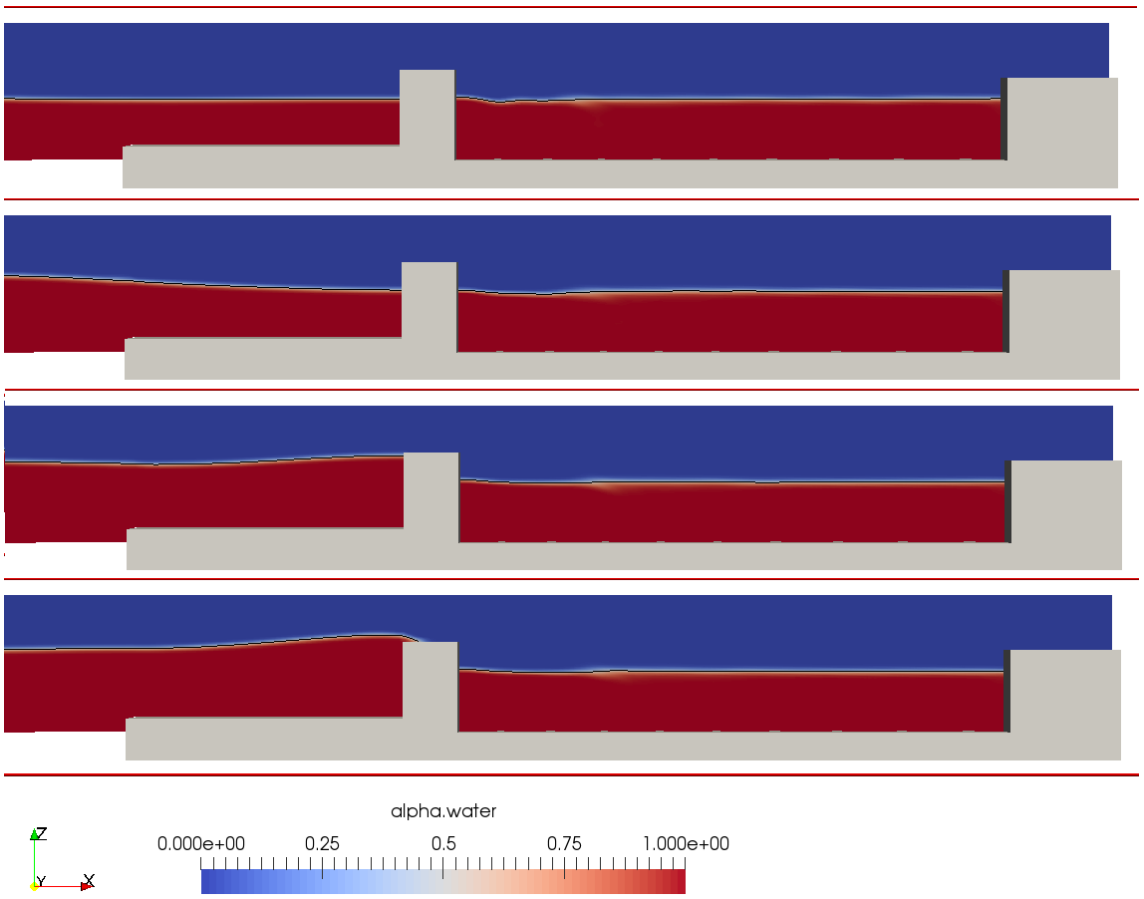

Figure 6.31: Spatial evolution of the wave propagation of a H = 4.4 m constant tsunami like wave over the marina of Cascais, at time instants (top to bottom): 55 s, 61 s, 66 s and 68 s.

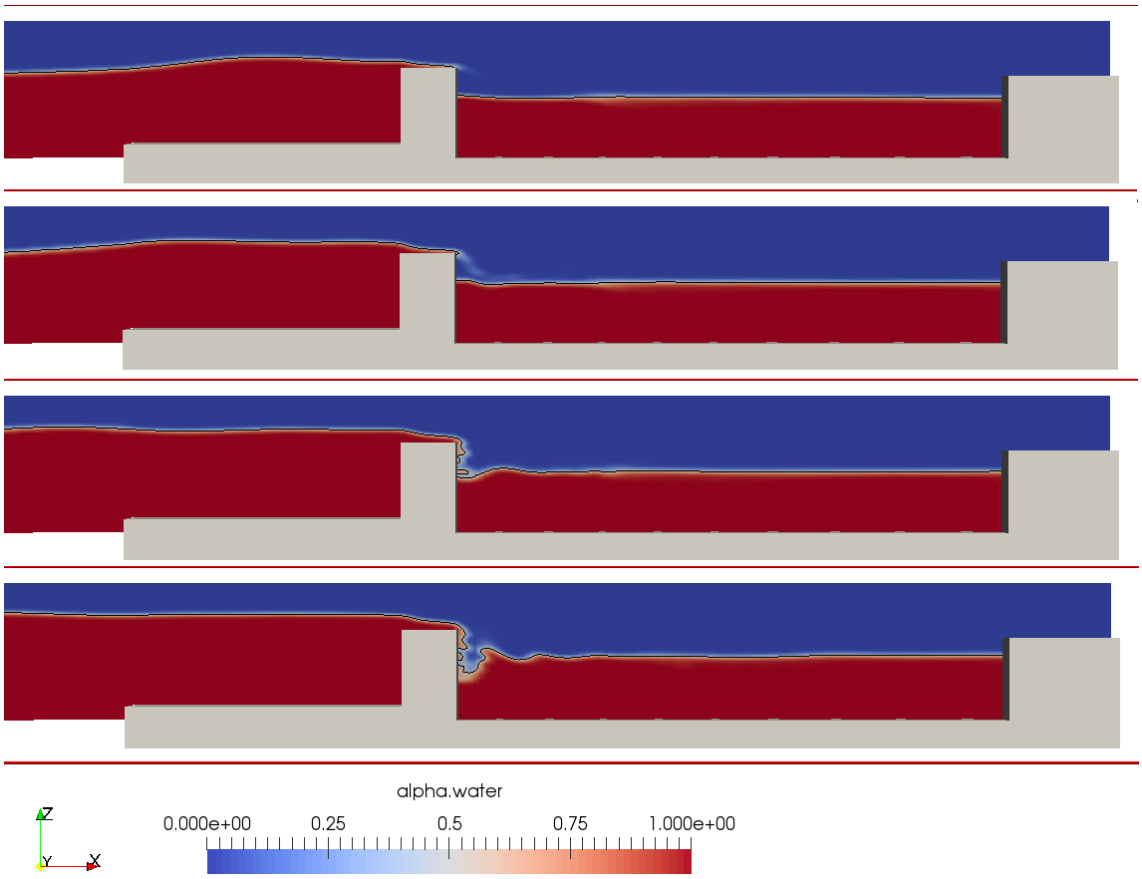

Figure 6.32: Spatial evolution of the wave propagation of a H = 4.4 m constant tsunami like wave over the marina of Cascais, at time instants (top to bottom): 70 s, 72 s, 75 s and 83 s.

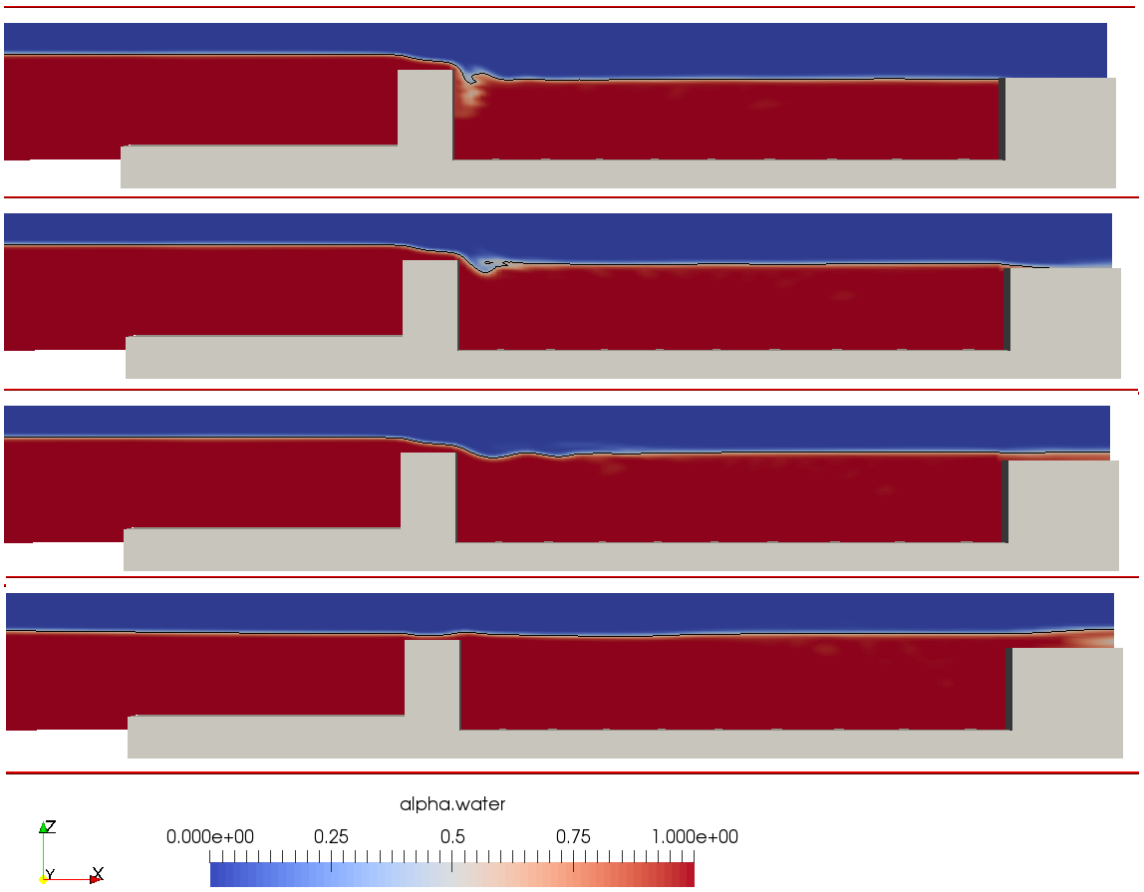

Figure 6.33: Spatial evolution of the wave propagation of a H = 4.4 m constant tsunami like wave over the marina of Cascais, at time instants (top to bottom): 126 s, 142 s, 155 s and 183 s.

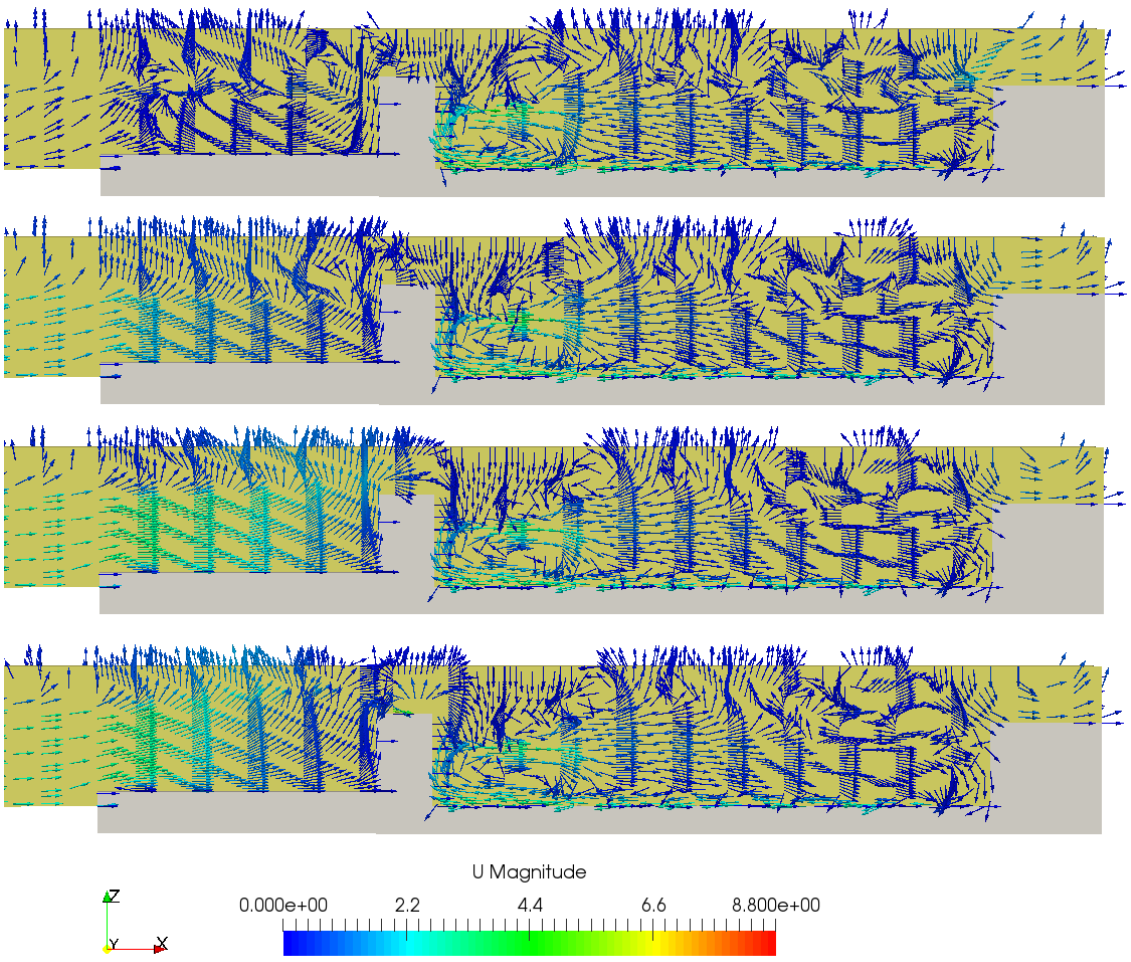

Figure 6.34: Velocity vectors (m/s) of the wave propagation of a H = 4.4 m constant tsunami like wave over the marina of Cascais, at time instants (top to bottom): 54 s, 61 s, 66 s and 68 s.

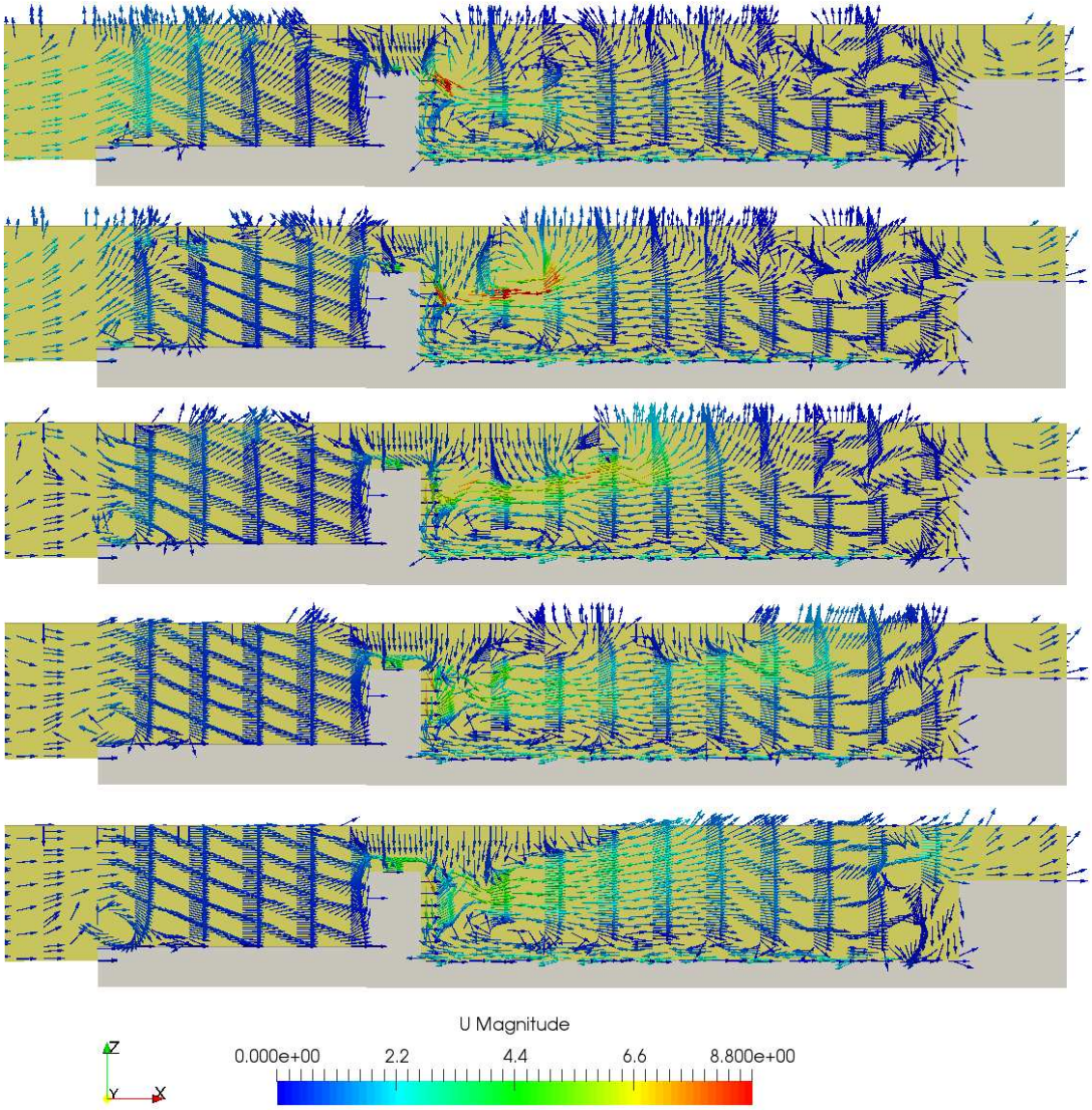

Figure 6.35: Velocity vectors (m/s) of the wave propagation of a H = 4.4 m constant tsunami like wave over the marina of Cascais, at time instants (top to bottom): 70 s, 72 s, 75 s, 83 s and 98 s.

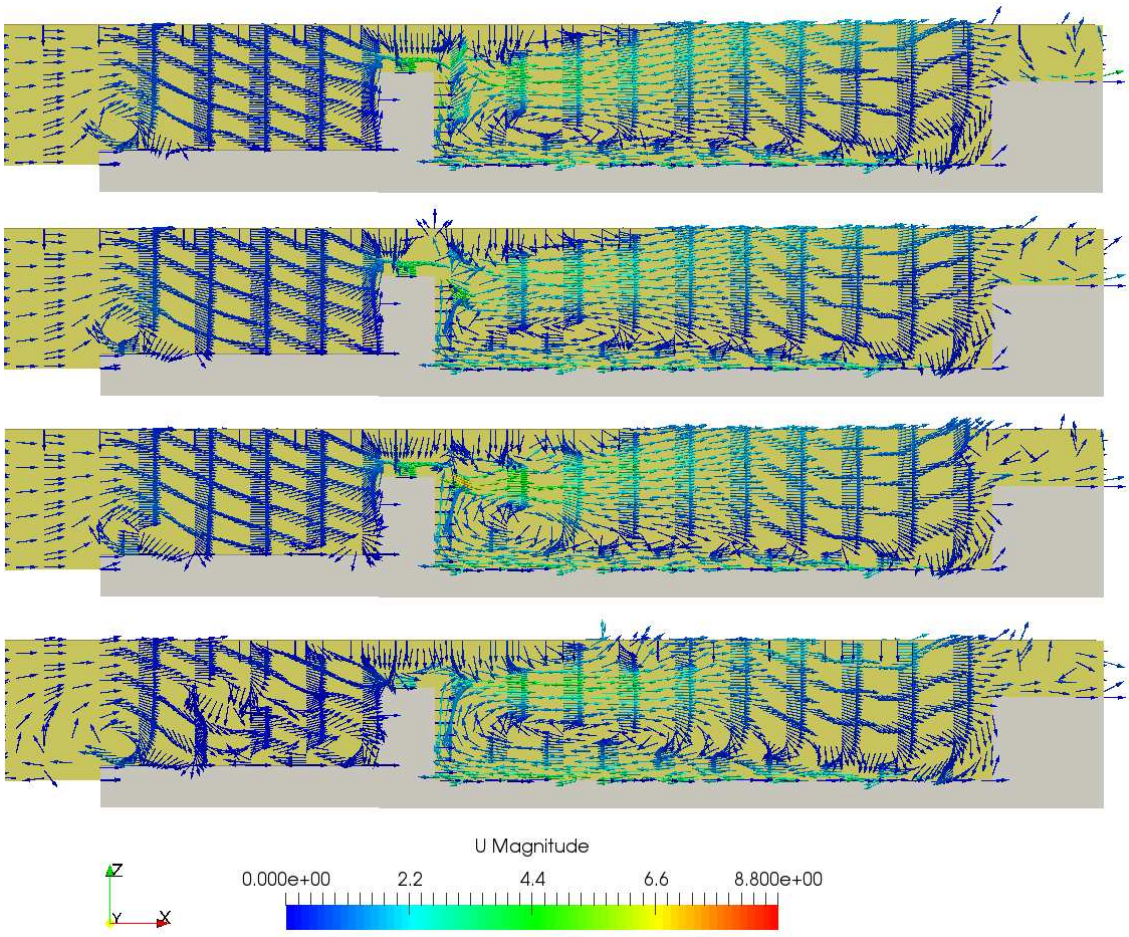

Figure 6.36: Velocity vectors (m/s) of the wave propagation of a H = 4.4 m constant tsunami like wave over the marina of Cascais, at time instants (top to bottom): 126 s, 142 s, 155 s and 183 s.

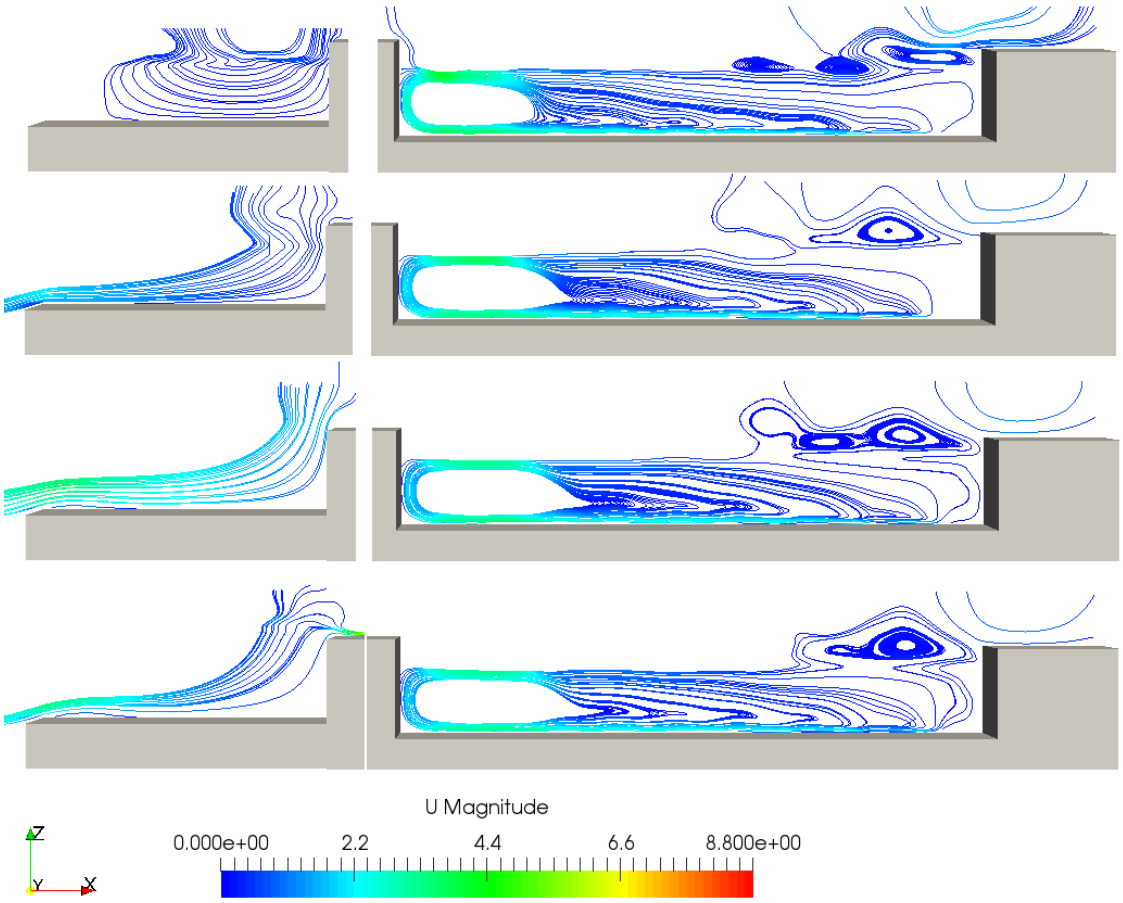

Figure 6.37: Streamlines (m/s) of a H = 4.4 m constant tsunami like wave over the marina of Cascais. Time instants (top to bottom): 54 s, 61 s, 66 s, 68 s.

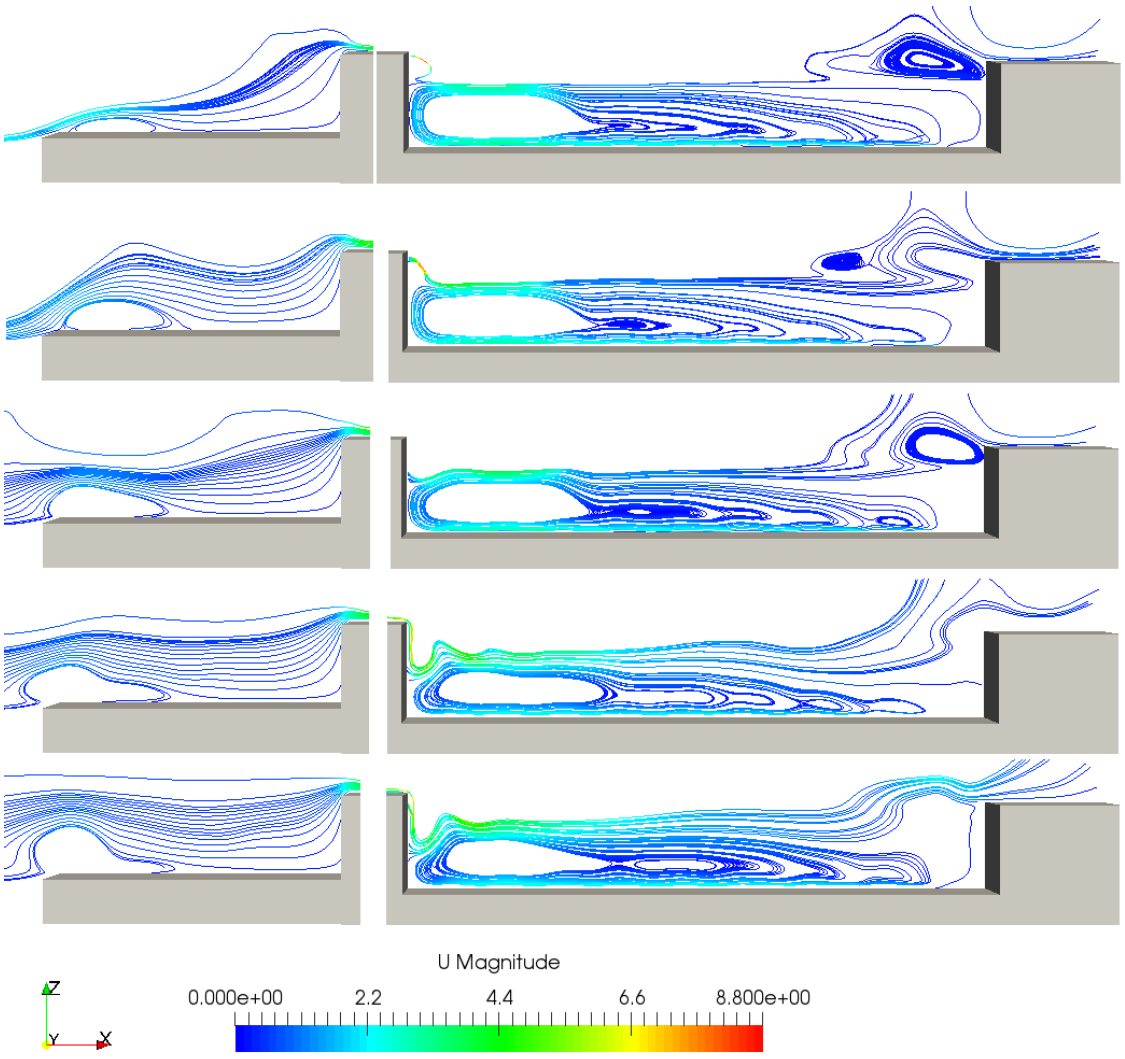

Figure 6.38: Streamlines (m/s) of a H = 4.4 m constant tsunami like wave over the marina of Cascais. Time instants (top to bottom): 70 s, 72 s, 75 s, 83 s, 98 s.

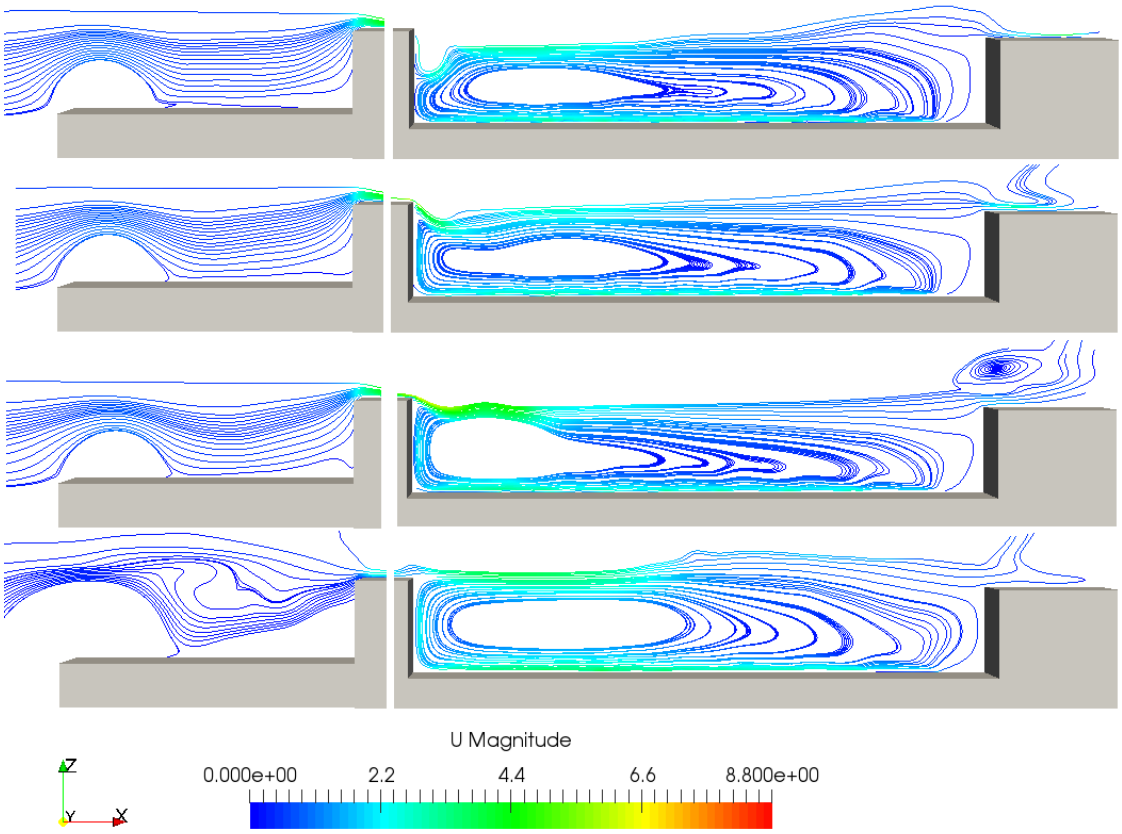

Figure 6.39: Streamlines (m/s) of a H = 4.4 m constant tsunami like wave over the marina of Cascais. Time instants (top to bottom): 126 s, 142 s, 155 s, 183 s.

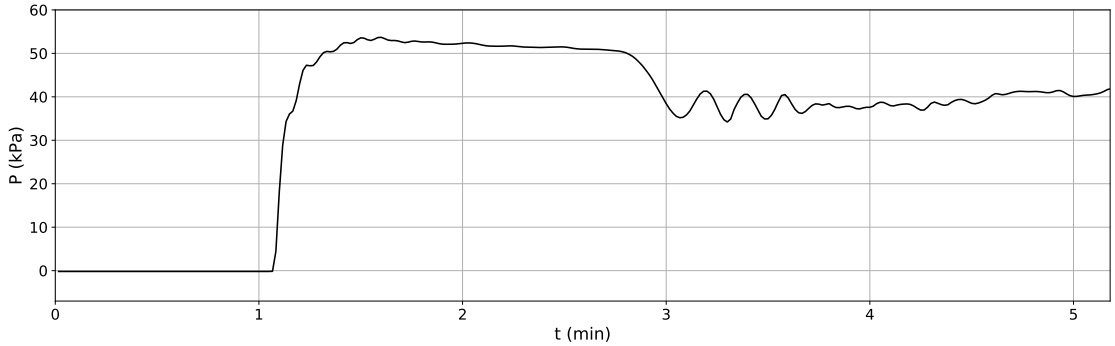

(a) Seaward side (pressure gauge 8)

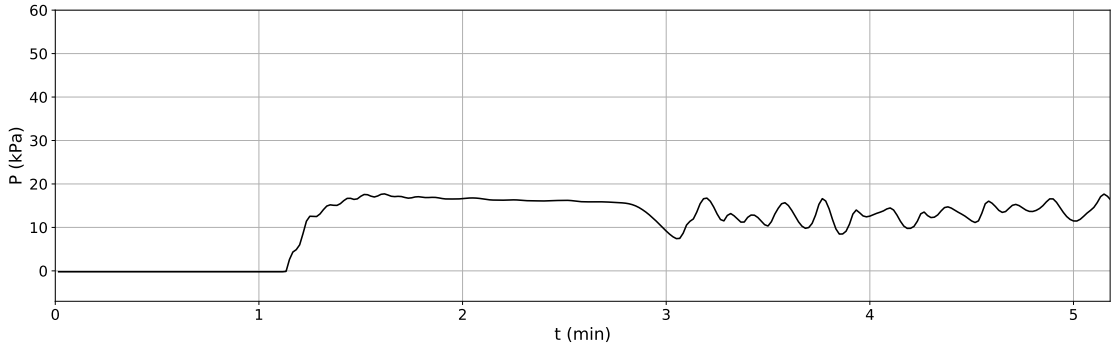

(b) Breakwater crest (pressure gauge 15)

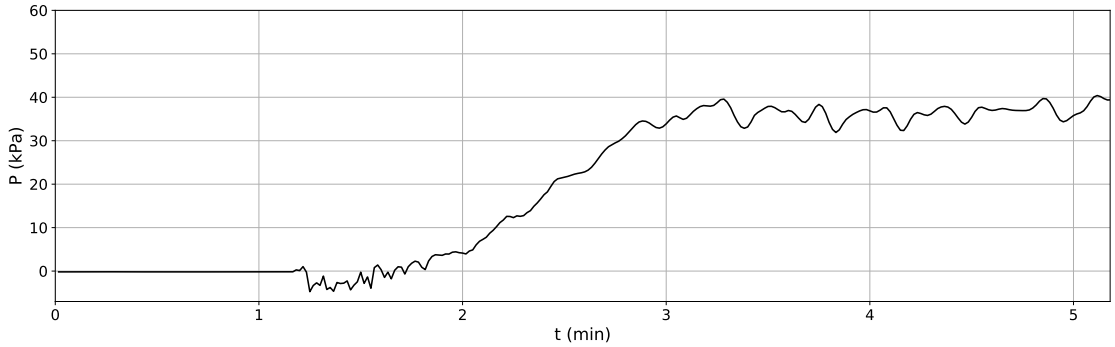

(c) Leeward side (pressure gauge 23)

Figure 6.40: Temporal evolution of the pressure at three locations of the breakwater (seaward side, breakwater crest, leeward side) of a H = 4.4 m constant tsunami like wave.

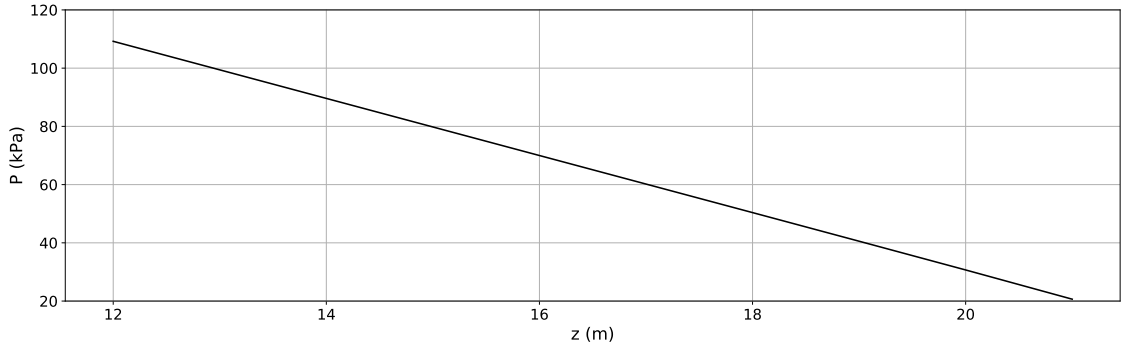

(a) Seaward side

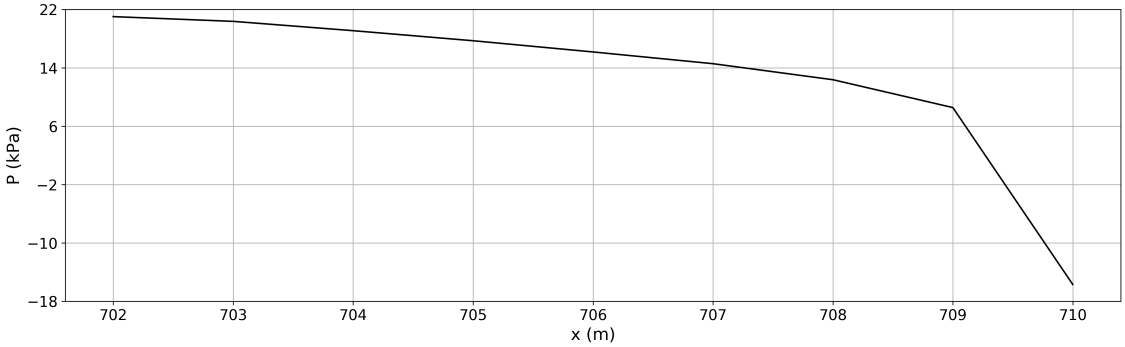

(b) Breakwater crest

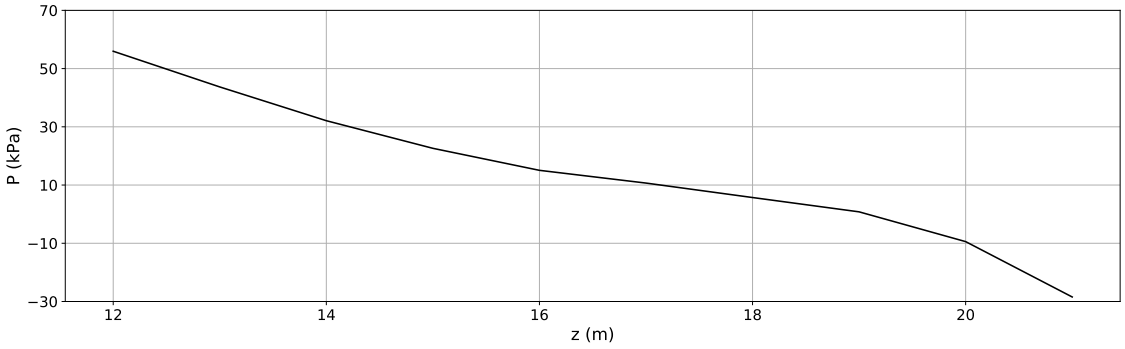

(c) Leeward side

Figure 6.41: Pressure distribution on the breakwater (seaward side, breakwater crest, leeward side) of a H = 4.4 m constant tsunami like wave, for t = 1.6 min.

6.2.4.3 Propagation of a leading depression N-wave

To further understand the effects of tsunami waves in the marina of Cascais area, we took a part of the time series in Figure 6.11, from the simulation described in the beggining of this Chapter, and extracted the time series corresponding to the time interval between 48 and 63 minutes. This wave profile corresponds to a leading depression wave (LDN) with a wave height of about 1.5 m. As in the previous case study, we increased the wave height by 4 times (H = 6 m). The free surface elevation and velocity time series are plotted in Figures 6.42 and 6.43. The total run time was 715 s and Δt = 1 s.

The wave height increases in the first meters of its propagation, and the wave crest amplitude becomes larger than 8 m. Trough to crest, the wave height becomes close to 10 m. For the next 700 m of propagation, the wave crest elevation becomes almost constant, while the wave trough amplitude increases by about 0.5 m (see Figure 6.44). The wave crest becomes flatter as well. The quick change of the free surface elevation profile in the first 5 meters (with a wave height increase greater than 20%) is probably a readjustment of the solution, so that the free surface elevation and the velocity are compatible, since the velocity introduced is not a physical velocity. In fact, the formulation used assumes constant velocity from the bottom to the water surface. When this compatibility between the free surface elevation and the velocity is reached, the wave has already adapted and the wave height remains constant, as observed until the 700 m. Looking at wave gauges 6 and 7, we notice that the wave overtops the breakwater with a water blade about 1 m deep. When this blade reaches the marina basin, it becomes a 5 m high wave (see Figure 6.45). The marina technical pier is inundated, and the water reaches a depth of 1 m on top of it (see Figure 6.46). The tsunami reaches the breakwater crest around 7 min 15 s after the beggining of the simulation (Figure 6.47). The tsunami overtops the breakwater and fills the area between the breakwater and the technical pier wall. Velocity magnitude is higher in the leeward side of the breakwater wall, starting to increase around 7 min 15 s after the beginning of the simulation (Figures 6.50 and 6.51). After 10 min the wave reaches the technical pier wall, overtopping and flooding the pier. The streamlines are shown in Figures 6.53 to 6.55. A vortex is clearly identifiable over the seaward side berm of the breakwater. A second vortex is observed on the leeward side of the breakwater.

Numerical pressure gauges were placed along the breakwater walls and crest (as shown in Figure 6.16). Analysis of the instantaneous pressure distribution along these surfaces showed that the pressures on the crest decrease from the seaward to the leeward side, becoming negative, i.e. below atmospheric pressure, at the inner end of the crest and at the upper end of the leeward wall of the breakwater (cf. Figure 6.57). The vortices and recirculation effects observed on both sides of the breakwater point to the possible occurrence of scouring, sand suspension and erosion, and consequent deballasting of the structure. This, together with the large positive pressure on the seaward side of the breakwater and the negative pressure recorded on the leeward side of the breakwater, may induce the collapse of the structure.

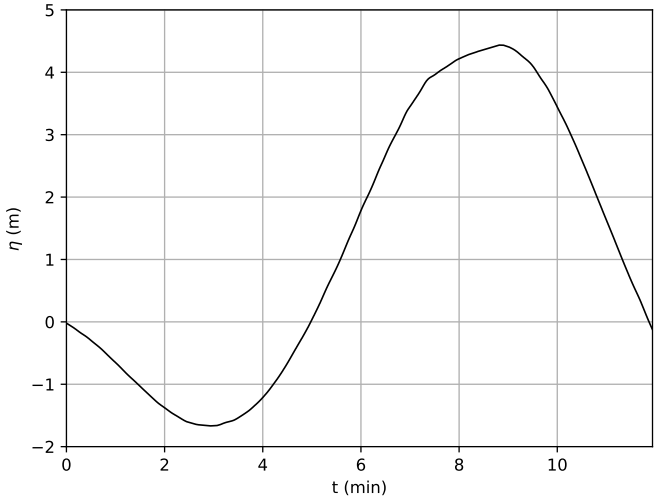

Figure 6.42: Surface wave elevation time series of a H = 6 m leading depression N-wave.

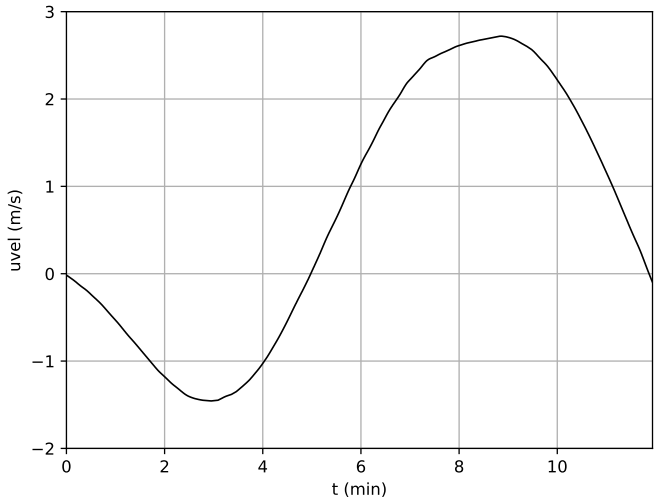

Figure 6.43: Velocity time series of a H = 6 m leading depression N-wave.

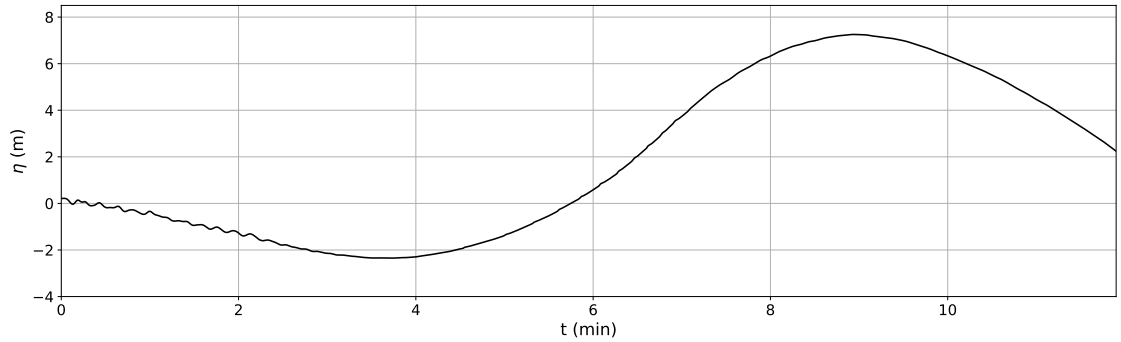

(a) wave gauge 1 (x = 5 m)

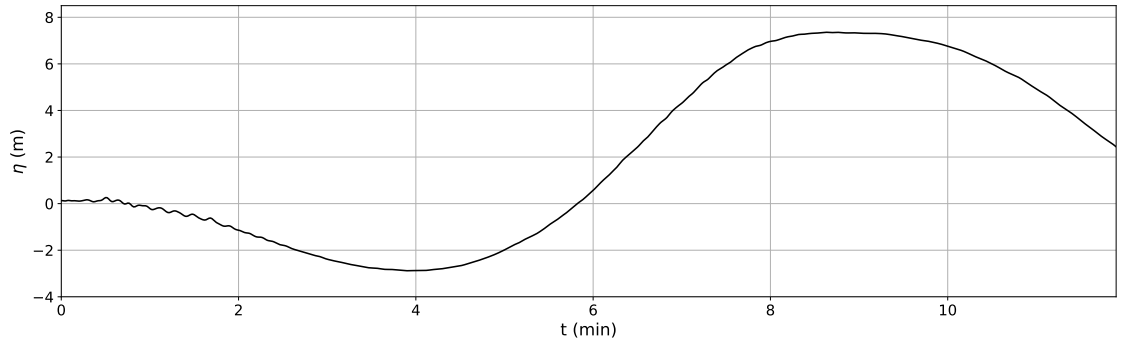

(b) wave gauge 2 (x = 325 m)

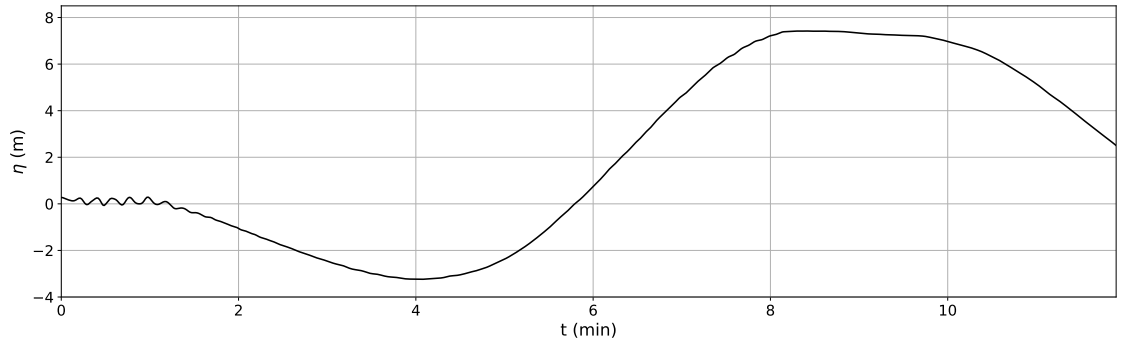

(c) wave gauge 3 (x = 655 m)

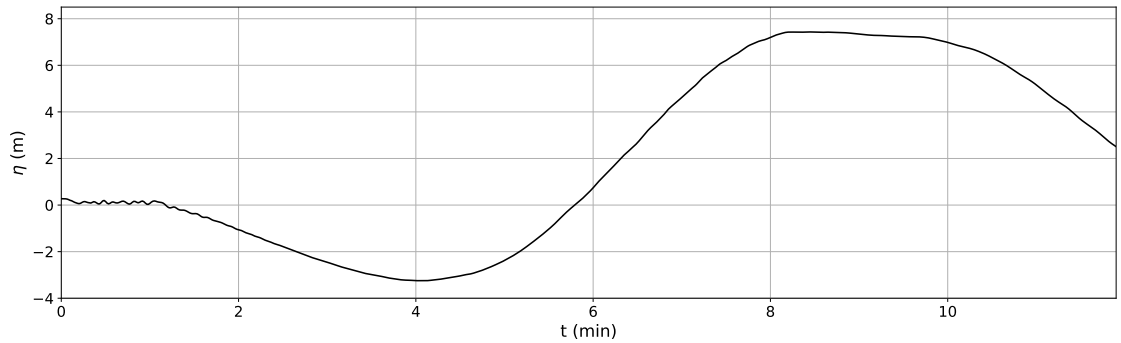

(d) wave gauge 4 (x = 678 m)

Figure 6.44: Temporal evolution of the wave propagation of a leading depression N-wave over the marina of Cascais.

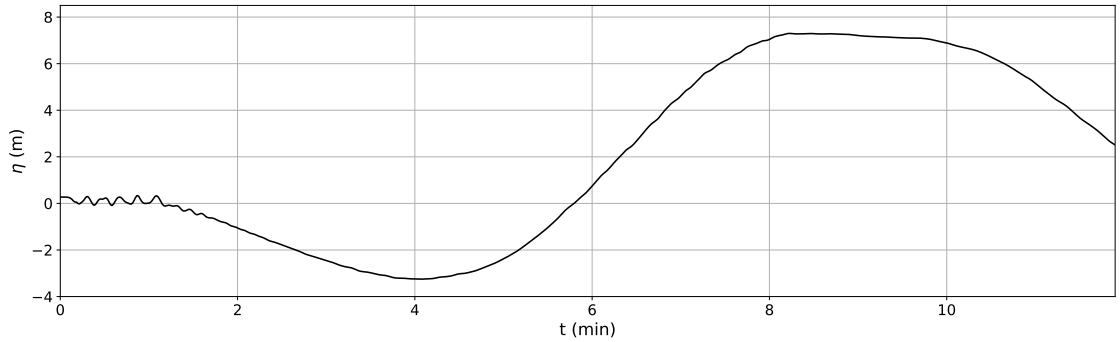

(a) wave gauge 5 (x = 700 m)

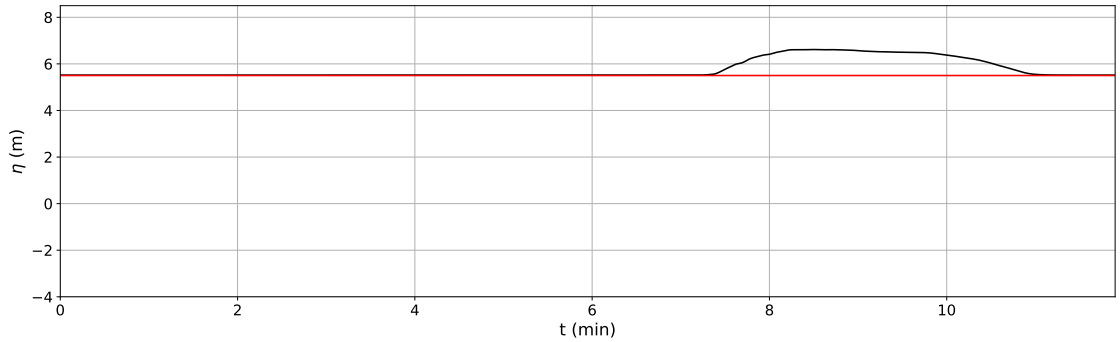

(b) wave gauge 6 (x = 705 m) — located on the breakwater crest

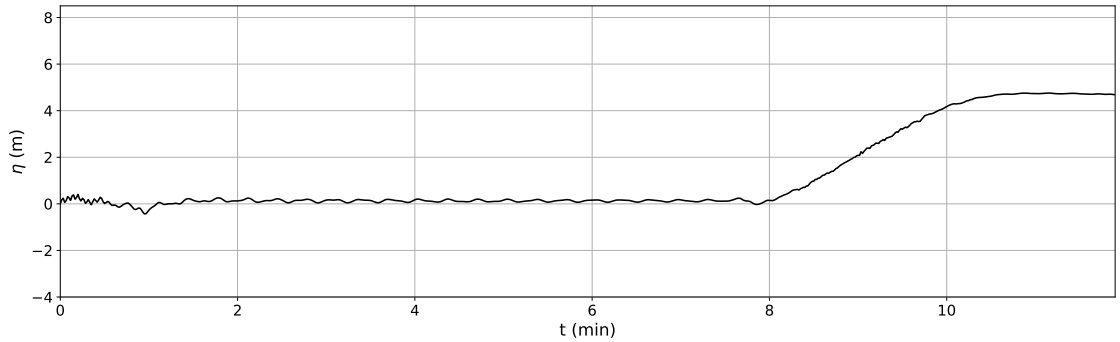

(c) wave gauge 7 (x = 720 m)

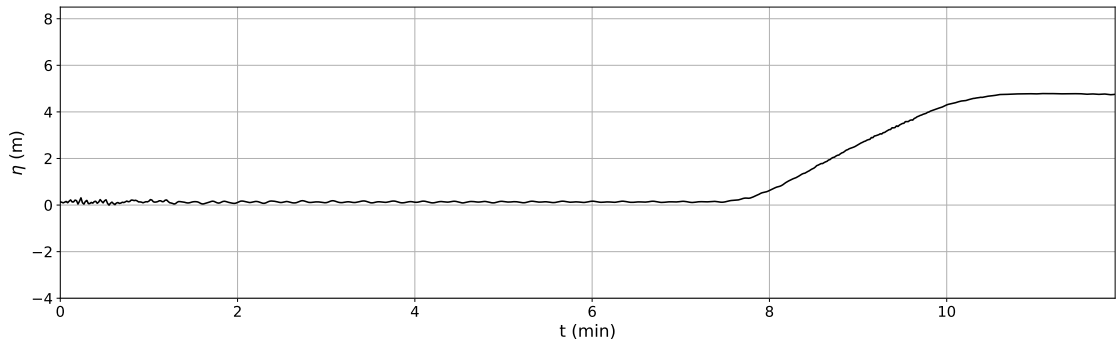

(d) wave gauge 8 (x = 750 m)

Figure 6.45: Temporal evolution of the wave propagation of a leading depression N-wave over the marina of Cascais. Breakwater crest level (—).

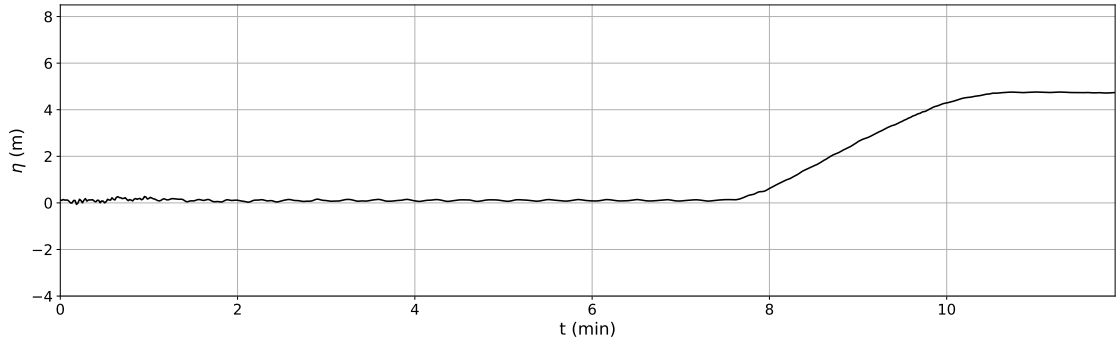

(a) wave gauge 9 (x = 780 m)

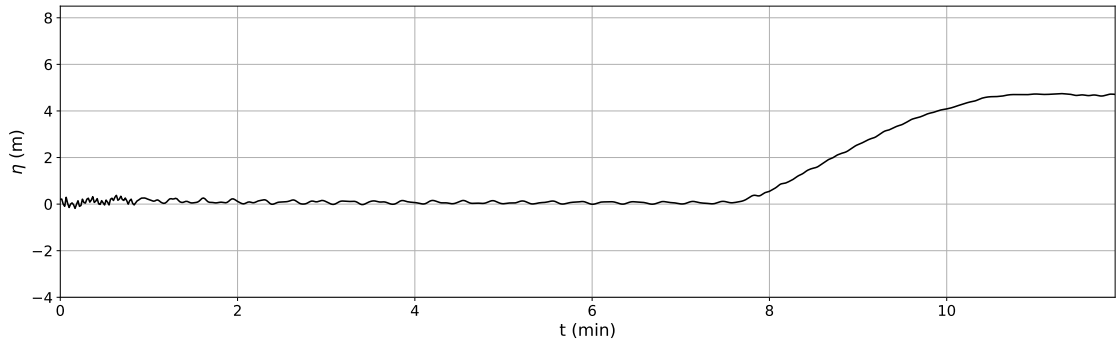

(b) wave gauge 10 (x = 810 m)

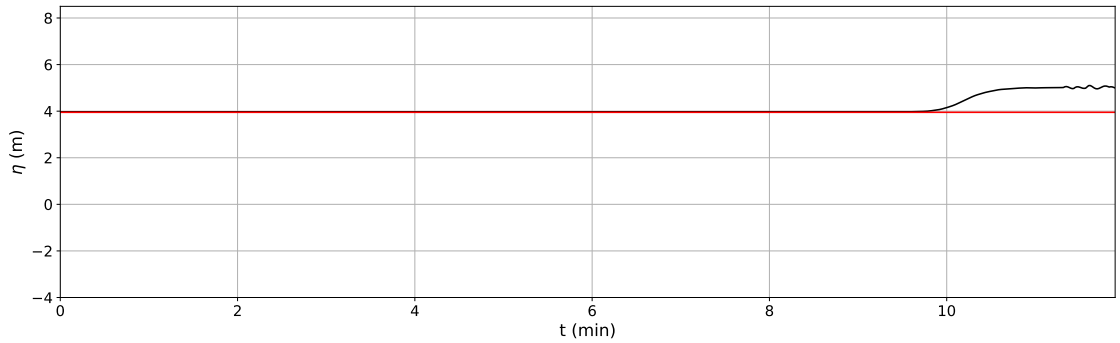

(c) wave gauge 11 (x = 820 m) — located on the top of the technical pier

Figure 6.46: Temporal evolution of the wave propagation of a leading depression N-wave over the marina of Cascais. Technical pier top level (—).

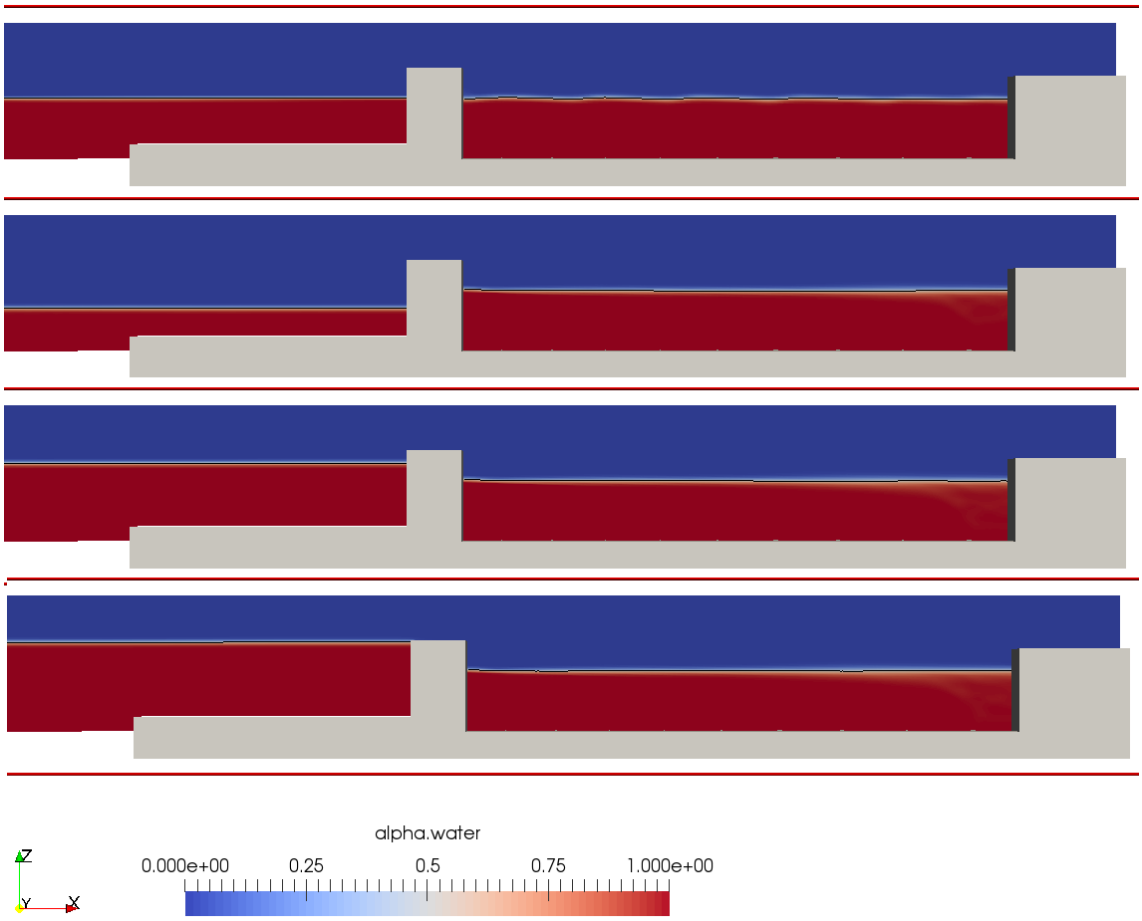

Figure 6.47: Spatial evolution of the wave propagation of a H = 6 m over the marina of Cascais, at time instants (top to bottom): 5 s, 220 s, 400 s and 434 s.

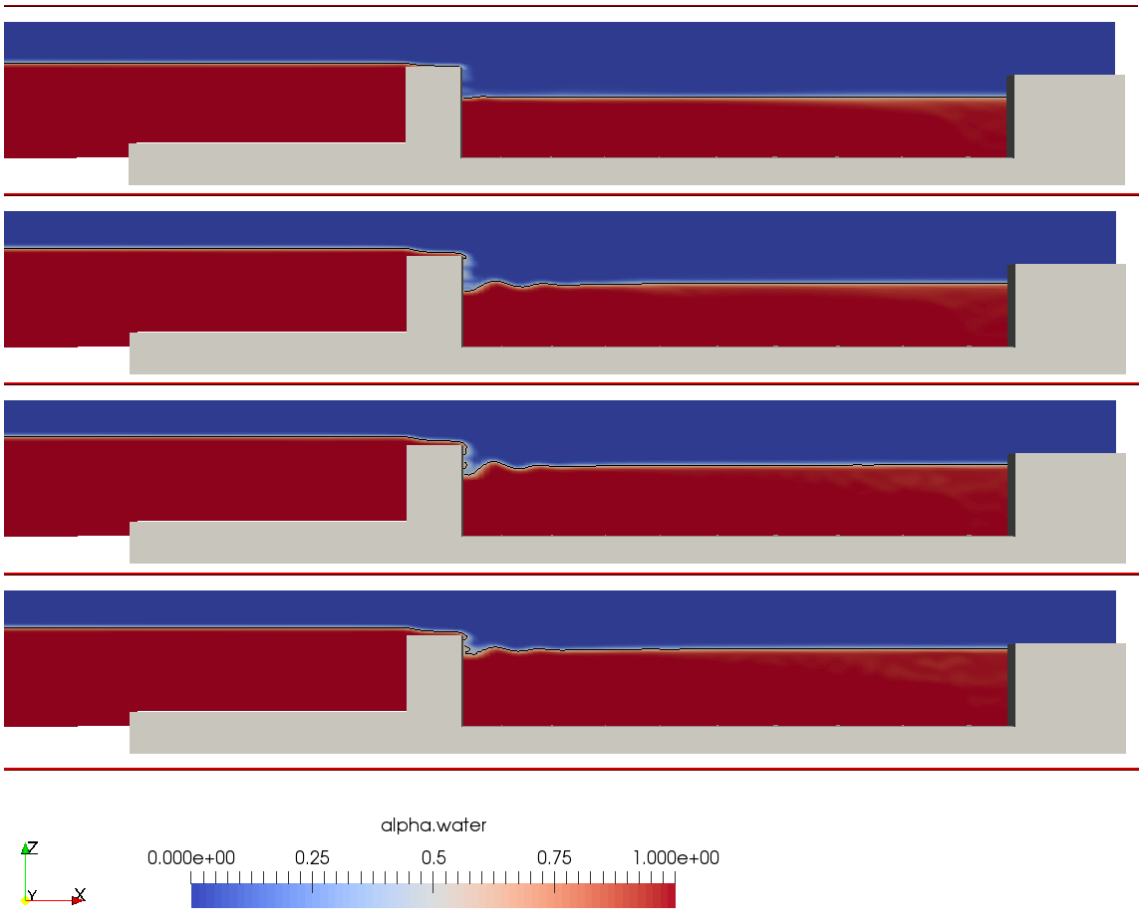

Figure 6.48: Spatial evolution of the wave propagation of a H = 6 m over the marina of Cascais, at time instants (top to bottom): 457 s, 482 s, 524 s and 562 s.

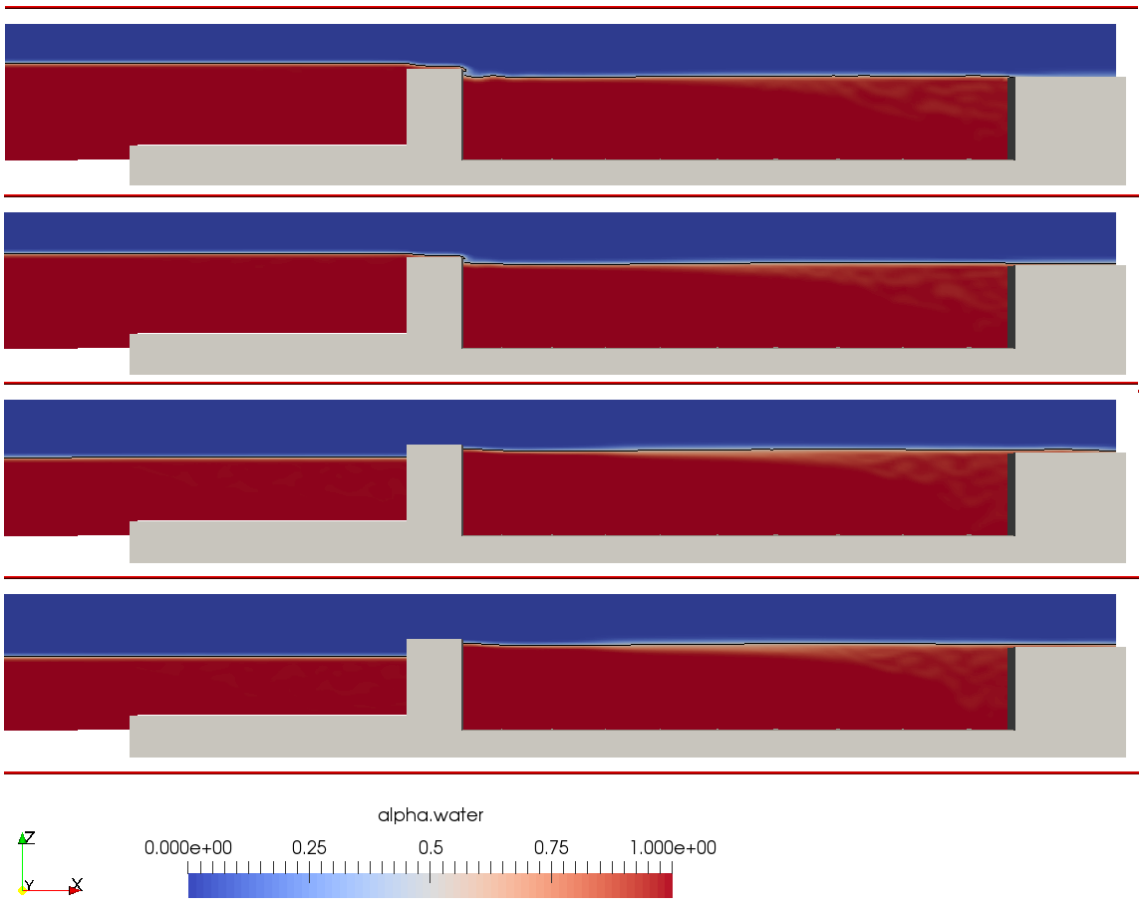

Figure 6.49: Spatial evolution of the wave propagation of a H = 6 m over the marina of Cascais, at time instants (top to bottom): 608 s, 625 s, 696 s and 714 s.

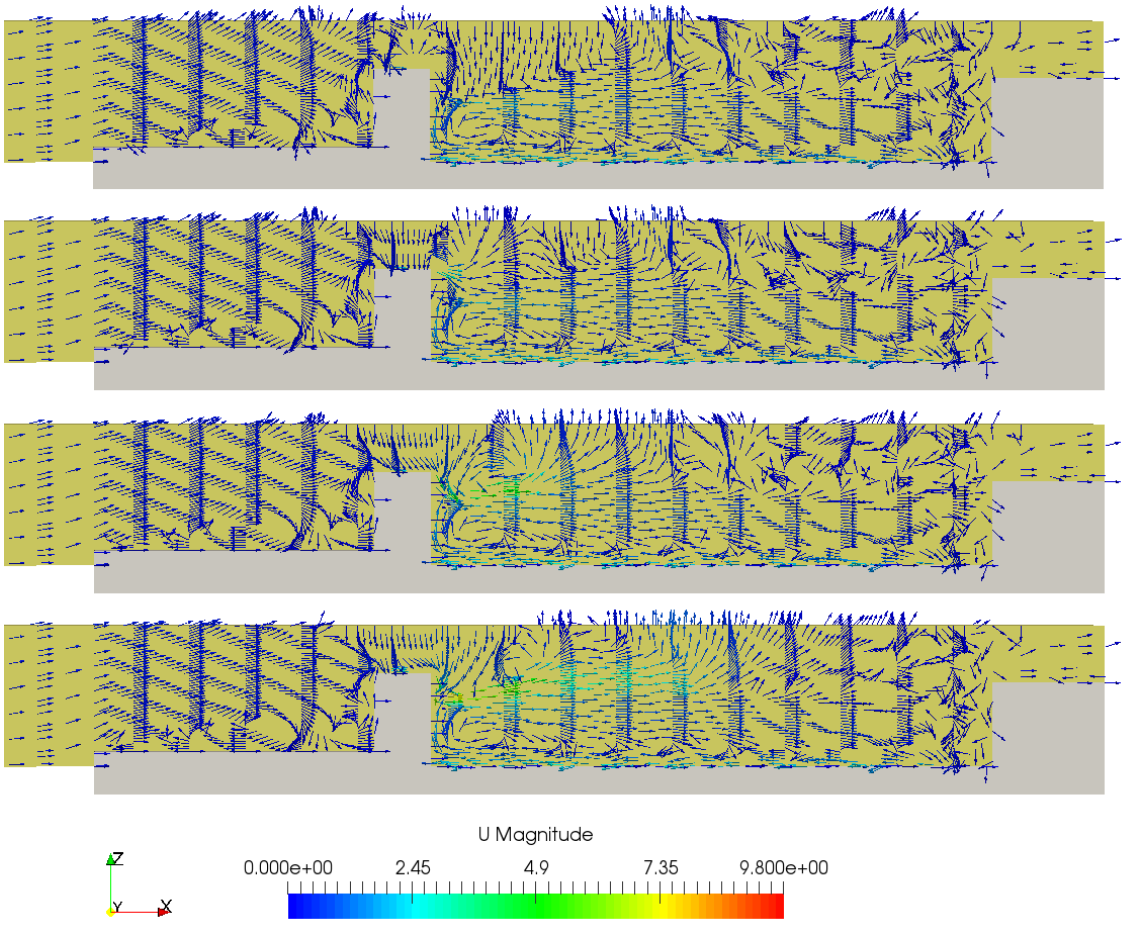

Figure 6.50: Velocity vectors (m/s) of the wave propagation of a H = 6 m over the marina of Cascais, at time instants (top to bottom): 431 s, 435 s, 440 s and 450 s.

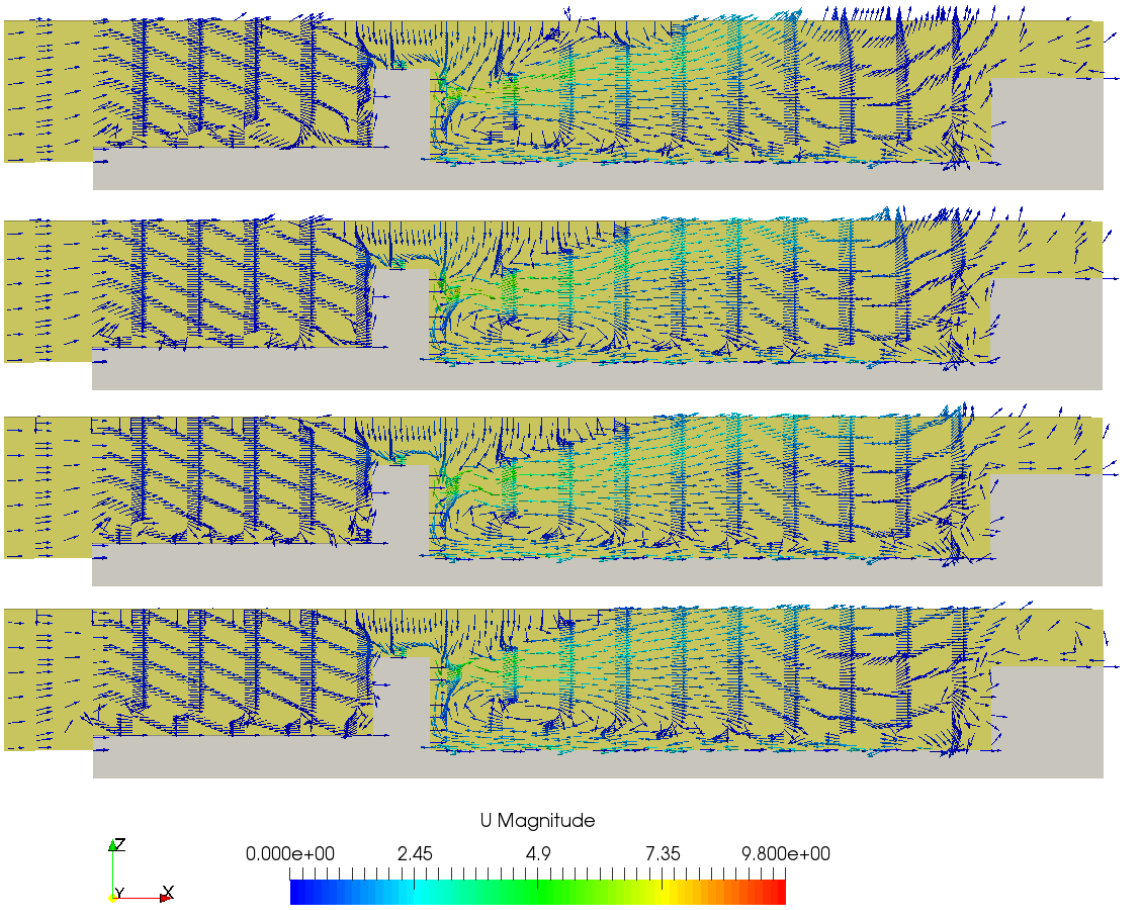

Figure 6.51: Velocity vectors (m/s) of the wave propagation of a H = 6 m over the marina of Cascais, at time instants (top to bottom): 466 s, 485 s, 500 s and 545 s.

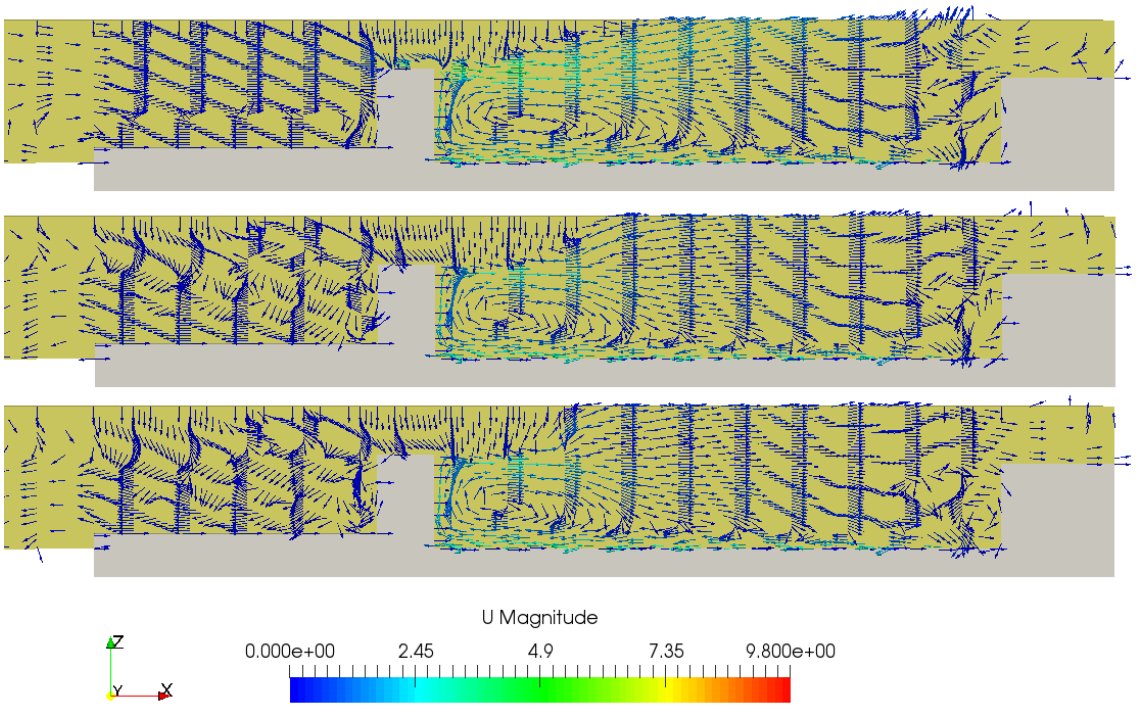

Figure 6.52: Velocity vectors (m/s) of the wave propagation of a H = 6 m over the marina of Cascais, at time instants (top to bottom): 615 s, 690 s and 715 s.

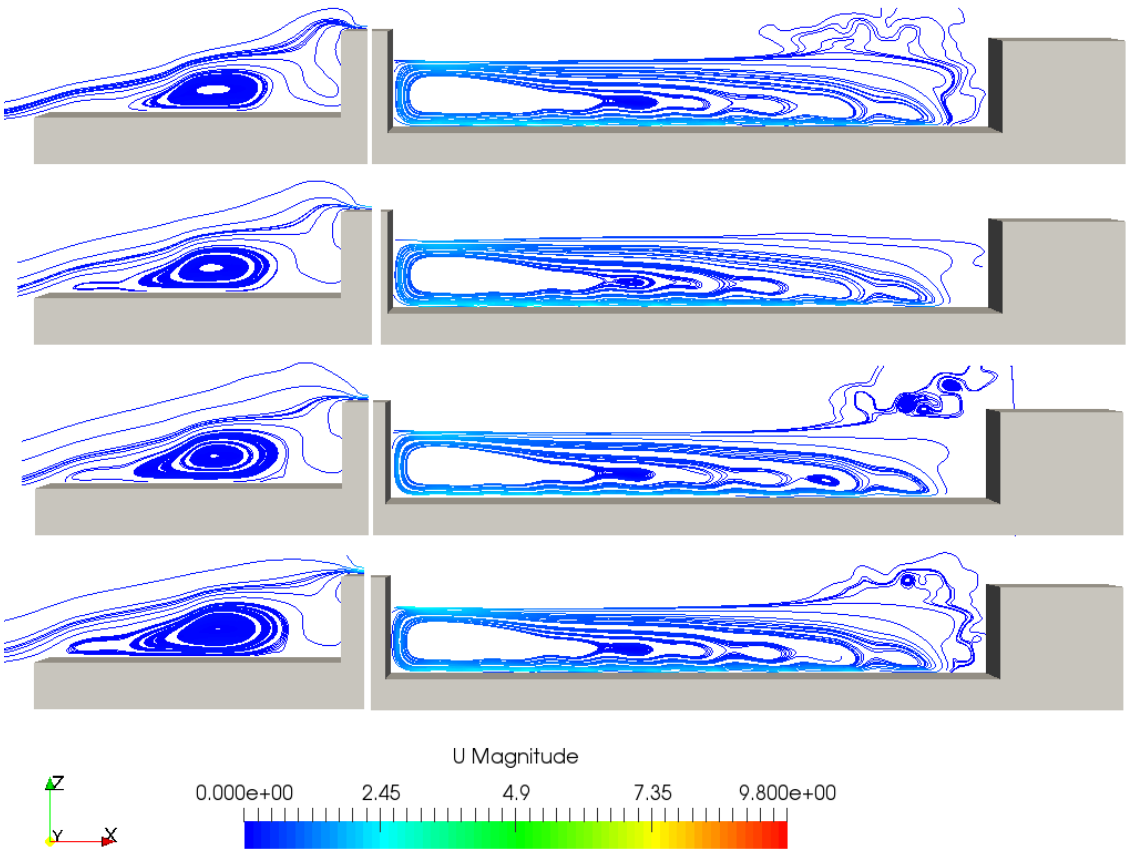

Figure 6.53: Streamlines (m/s) of a leading depression N-wave over the marina of Cascais. Time instants (top to bottom): 431 s, 435 s, 440 s, 450 s.

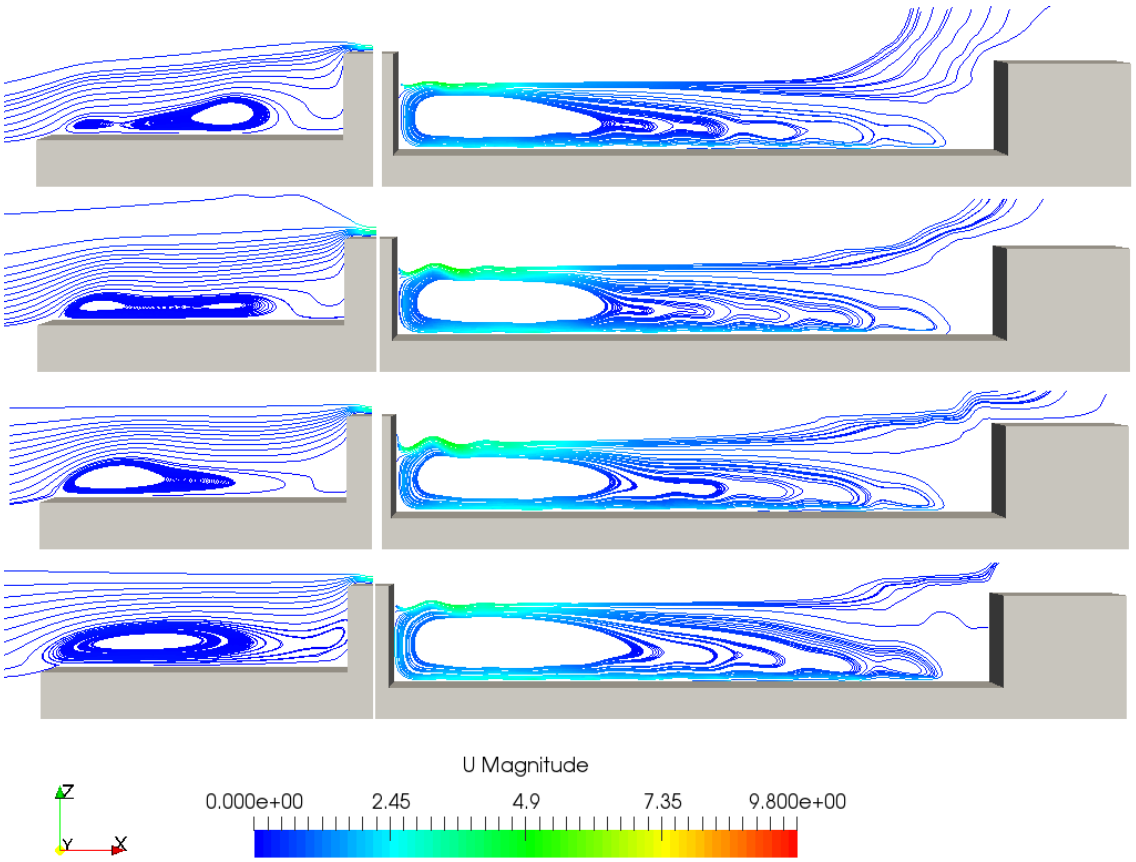

Figure 6.54: Streamlines (m/s) of a leading depression N-wave over the marina of Cascais. Time instants (top to bottom): 466 s, 485 s, 500 s, 545 s.

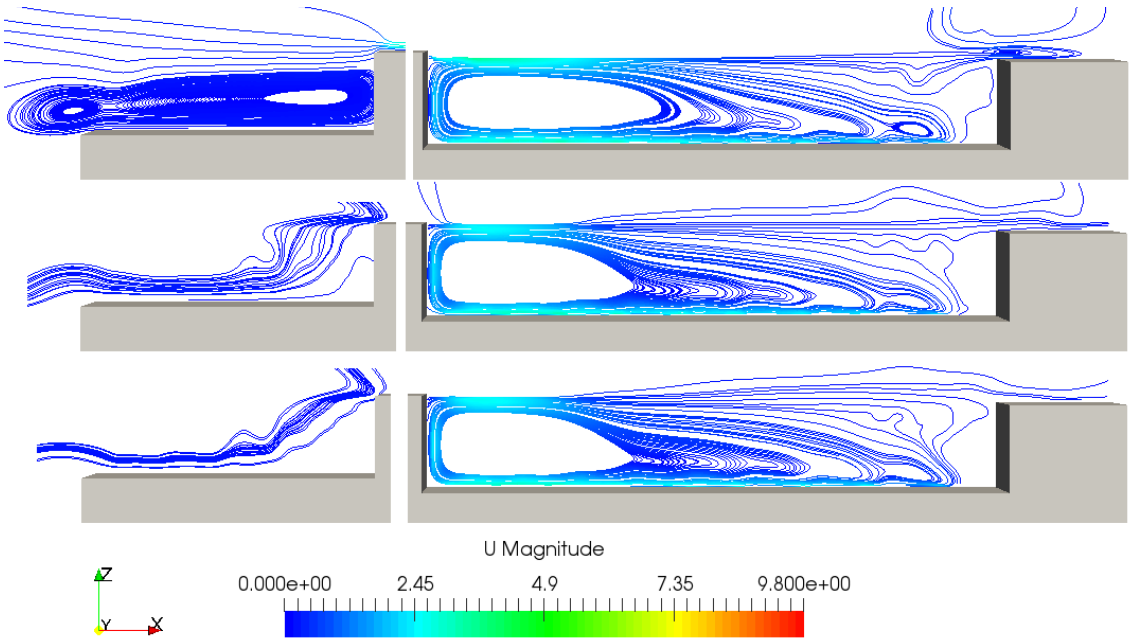

Figure 6.55: Streamlines (m/s) of a leading depression N-wave over the marina of Cascais. Time instants (top to bottom): 615 s, 690 s, 715 s.

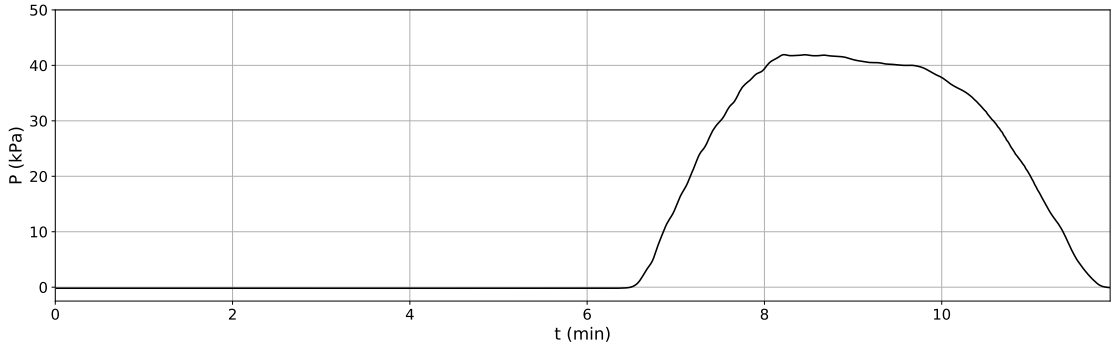

(a) Seaward side (pressure gauge 8)

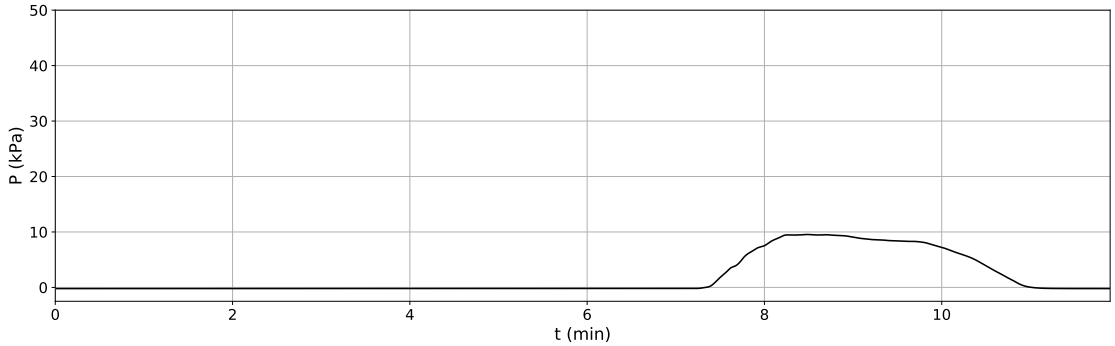

(b) Breakwater crest (pressure gauge 15)

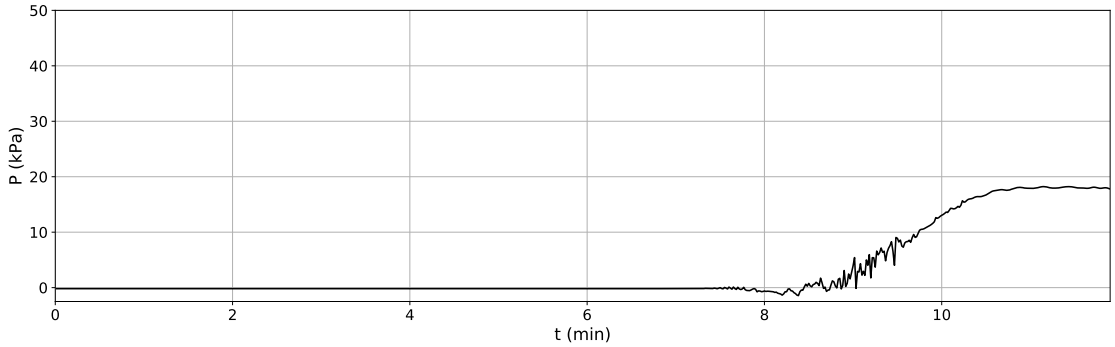

(c) Leeward side (pressure gauge 23)

Figure 6.56: Temporal evolution of the pressure at three locations of the breakwater (seaward side, breakwater crest, leeward side) of a leading depression N-wave.

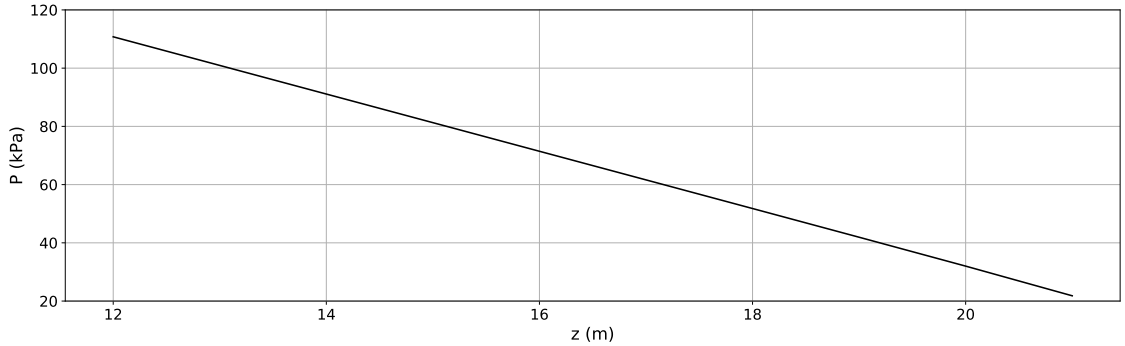

(a) Seaward side

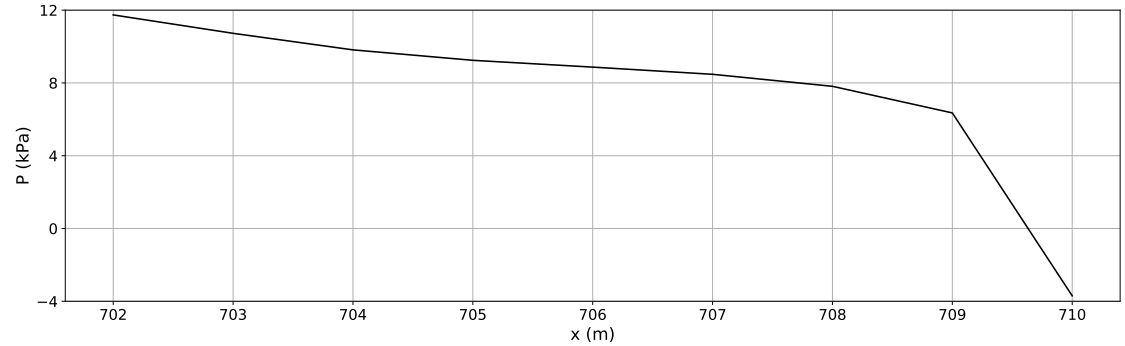

(b) Breakwater crest

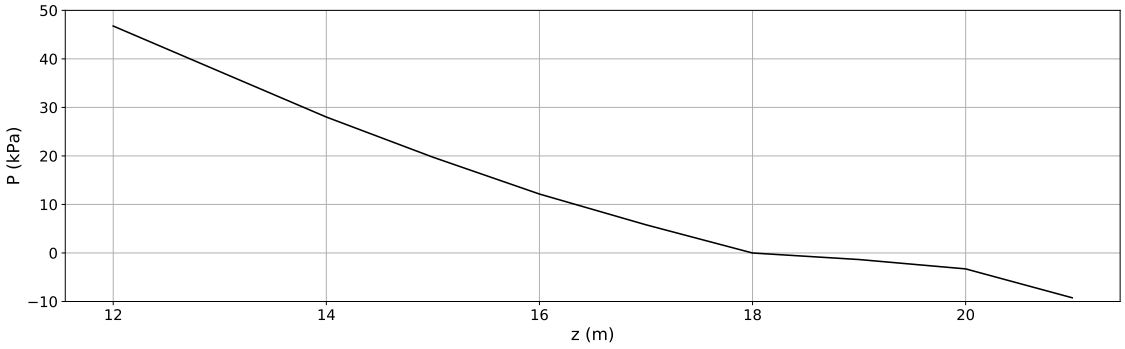

(c) Leeward side

Figure 6.57: Pressure distribution on the breakwater (seaward side, breakwater crest, leeward side) of a leading depression N-wave, for t = 8.2 min.

6.3 Discussion

6.3.1 Simulations in 2DV

In these 2DV simulations we aim to investigate what happens for three tsunami-like wave scenarios, using the combined model CM and specifically the CFD code OpenFOAM and olaFlow module, considering that the direction of the tsunami waves propagation does not change.

The simulation include the propagation of the tsunami waves over a 650 m-long slope and the 50-m wide breakwater berm, and the impact on the breakwater of the marina of Cascais, its overtopping and the subsequent flooding of the marina basin and of the technical pier.

Two of the scenarios feature a tsunami-like wave with a constant wave height, which is based on the peak of a tsunami wave with a large wavelength. The objective of these scenarios was to investigate and learn what happens at the peak of the flooding of the tsunami wave, disregarding the higher frequency oscillations and focusing on the first order interactions of the tsunami wave with the surrounding areas and structures.

In scenario 1 (section 6.2.4.1), the tsunami wave has H = 1.1 m and in scenario 2 we have a larger wave with H = 4.4 m (section 6.2.4.2). In both scenarios, a very steep tsunami wave with a very long wavelength was considered. The third case study, scenario 3, features a leading depression N-wave with H = 6 m (section 6.2.4.3), 4 times higher than the original wave (Figure 6.11).

The large continuous tsunami wave with H = 4.4 m proved to be the most destructive tsunami wave of the three cases tested. In both scenarios 2 and 3, the tsunami waves overtop the breakwater, and the technical pier area is flooded. In both scenarios two large vortices are present, one in the seaward side of the breakwater and the other vortex on its leeward side. On both cases, negative pressures were recorded on the leeward side of the breakwater. These negative pressures are higher in scenario 2.

These negative pressures associated with the presence of the vortices, which might cause the occurrence of scouring, sand suspension and erosion of the breakwater foundation, may undermine the stability of the breakwater and lead to its possible failure. The maximum recorded pressure is about 50 kPa, registered on the seaward side of the breakwater. These high-pressure values are largest during the very first wave impact on the breakwater, lasting for about 4 min for both scenarios 2 and 3.

On this 2DV simulation there is no way for the water to leave the marina basin after entering it. Under these conditions, in the scenarios where there is an overtopping of the breakwater by the tsunami wave, the water level in the marina basin does not return to the pre-tsunami level. For an investigation of the duration of flooding time, a full 3D simulation is needed.

This kind of analysis is possible to perform with the CFD code used, but not possible with the Boussinesq model used in this work. The Boussinesq model accurately simulates wave breaking and flooding but cannot detail the full overtopping features of the tsunami waves, namely the pressure distribution on the breakwater, nor the turbulence features of the fluid flow.

The 2DV simulations will ignore some 3D effects, such as currents generated along the breakwaters and the 3D patterns of the vortices that may lead to asymmetric erosion along the breakwater walls. In addition, flooding of the marina basin will also occur due to the overtopping of the southeast breakwater. Finally, the effect of the northeast marina entrance is also overlooked. However, we believe that this 2DV analysis, although limited, can prove quite useful on a breakwater stability analysis of the breakwaters in the event of a tsunami impact.

The results here presented can be used to study the potential causes and impacts of tsunami waves on breakwater structures, such as the Cascais breakwater and other breakwaters in Portugal. We show that this can be done in 2DV, more quickly than in 3D, where it takes too long to run. The scale of the problem is observable both in 2DV and 3D. The study of the breakwater failures

can be extended after this work.

6.3.2 Tsunami modelling uncertainties and the applied numerical models

Here are presented a series of factors that affect the modeling of tsunamis, factors that are generally and specifically related to the work developed in this thesis and to the research work that has been presented here.

- Every numerical model applied in the tsunami modelling has its strengths and flaws. The numerical model GeoClaw, used in the first part of the combined model in this PhD thesis for the generation and propagation of tsunamis, models tsunamis using the shallow water equations. The SWE are only an approximation of the three-dimensional water dynamics, found to be accurate enough to model the tsunami lifecycle stages. The choice of applying FUNWAVE-TVD, a Boussinesq model, afterwards had its strength in its ability to model the dispersive nature of the tsunami wave propagation. The modelling of the 3D tsunami waves interaction with the coast was chosen to be performed by OpenFOAM, as it is a well established CFD model, widely used in the scientific community. The great challenge was to model real tsunami waves, for a real coastal domain. However, the application of the CFD code to a real tsunami event, and the preparation of the essential elements necessary to perform the CFD simulation, were not as straighforward as in the other models applied to achieve the final combined model. Yet, the aspect offered by the CFD code in terms of the three-dimensional modelling, including turbulence and wave-structure interaction, was the strength of this option.

- The first step in the tsunami modelling of an earthquake event is of course related to the generation phase, which is dependent on the seismic source definition and its characteristics (Dias et al. 2014). It is defined by some as the major source of uncertainty in the tsunami modelling results (Adams et al. 2020). Although it is out of the scope of this thesis, this has to be referred to here, as it is an important factor that affects the numerical modeling results and its analysis.

- Although it is a standard practice in tsunami modelling to assume the mean sea level tide level stage, it would have been interesting to perform and show results for this same study with other tide levels and for larger tide levels that can occassionally occur. The influence of the several tide stages in the tsunami modelling output results is important for the coastal impact analysis.

- The final objective of the combined model was to model the complex interaction of the tsunami waves with the coastal vegetation and existing structures. With the CFD code and a bathymetric and topographic grid of the Cascais area, we managed to understand the range of heights, tsunami velocities and pressure impact in the Cascais marina area. Even so, it would be a major improvement to this research work to perform the CFD modelling with a grid which would consider the existent in situ buildings and structures. This was attempted for at an early stage of the CFD modelling task, but did not advance.

- A factor that is not taken into account in tsunami modelling, as it is extremely complex and random, is the consequent modification of both the bathymetry and the topography (Adams et al. 2020). The amount of natural and/or artificial material can reduce the tsunami energy and the fluid flow patterns, changing the final coastal impact.

6.3.3 The challenges of the fully tsunami combined model

Several types of challenges were found in the development of the combined model concept. First of all, there are the existing limitations of each individual model used. When possible, the recognised limitations were easily and directly overcome (e.g., FUNWAVE-TVD's absence of an inner code tsunami generation mechanism). Other problems were not readily or easily identified (e.g., CFD simulations that advanced and ended without recording any errors), so their determination and understanding ended up limiting the time scope of the study in question.

Next, we will summarize the obstacles, difficulties and flaws encountered in each phase and, when possible, what approach was followed to overcome the aspects described.

6.3.3.1 Combined Model 1 (CM1)

Combined model 1 is obtained through the coupling of GeoClaw with FUNWAVE-TVD. The direct passage of data between models is performed for a certain output time instant from the GeoClaw's simulation. The time instant was chosen from an interval ranging from 5 to 10 minutes after the beginning of the tsunami wave propagation. It was assumed that as the tsunami waves propagate quite rapidly, within this 5 min time interval, the tsunami generated waves are fully developed and that the propagation is no longer subject to source area influence after this time interval.

The time instant is selected visually from the simulation plots, for each individual simulation. Nevertheless, this time instant should be chosen through a more weighted approach. A calibration of the time interval should be done, according to the magnitude, fault parameters and depth of the earthquake event.

Yet, another aspect should be attended to: the earthquake proximity to the coastal zones. As seen in the $\mathrm{M_w}$ 8.5 earthquake and tsunami event hitting the Portuguese coast (section 6.2.3), for very large earthquakes with such proximity, another method has to be adopted for the time instant selection for the data passage between GeoClaw and FUNWAVE-TVD. In the event studied, a time instant of 2 min was chosen to account for the short earthquake source–coast distance. This very short distance event was chosen to spare computational time and resources in the CM1 part. On the other hand, it has shown that the CM1 has room for improvement.

In resume, from the simulations and results obtained we consider the 5 to 10 minutes time interval as an acceptable interval to pass data from GeoClaw to FUNWAVE-TVD. The choice of 2 minutes to pass data between models, for the case of a very large earthquake with short earthquake source–coast distance, was an arguable option. Thus, this aspect of the CM1 has margin for improvement.

6.3.3.2 Combined Model 2 (CM2)

In the coupling and data passage between CM1, via FUNWAVE-TVD, and the CFD code, the coupling methodology of CM2 applies the olaFlow's wave generating system, with the emulation of a piston wave-maker. Thus, the boundary conditions are input using this wave generation capability of the OF module. However, this code capability presents a flaw: it is only possible to pass the boundary conditions retrieved from one single boundary point location in the domain. This means that the initial wave profile retrieve from CM1, via FUNWAVE-TVD, has to be retrieved from one single boundary point and then input and assumed constant at the inlet boundary, as a consequence of the functioning of the `waveType wavemaker` (W). It is a limitation of the module capability. Ideally, the best would be to input the time series through the `waveType wavemaker`, from the olaFlow module, using the tveta (timeSeries condition), retrieved from several or all the boundary points at the input boundary, as it would be more representative of the tsunami wave profile.

The grid reorientation should be considered, when necessary. In the case of the simulation of the M_w 8.5 earthquake and tsunami event hitting the Portuguese coast (section 6.2.3), the grid extracted from layer 41, to perform the numerical simulation with the CFD code, is plotted in Figure 6.10. As verified from the computation of the free surface, in Figure 6.8, the incoming tsunami comes from the southwest. In this case, it would be more representative of the incoming tsunami wave pattern if the computational domain (grid extracted) had an orientation coincident with the incoming tsunami. Thus, the boundary points could coincide with the tsunami waves trajectory, which would require the rotation of the computational grid in accordance to the trajectory.

Multi input boundaries would be another possibility but the `waveType wavemaker` feature described disabled the possibility of choosing several inlets, which would improve the definition of the input data. For the reasons presented, the free surface elevation and velocity were retrieved from the most southwestern point, as this point is considered to be representative of the incoming tsunami wave due to wave directivity.

6.3.3.3 OpenFOAM and the olaFlow module related

There are several different aspects from the OpenFOAM (OF) code that present some time-consuming challenges, which can unfortunately pose continuous difficulties, not so simple to solve.

When compared to the other models used in this combined model, OF was the code that presented a great number of adversities and most time was spent in solving the problems associated with its proper functioning. For that reason, we extend the discussion on the tackling of some of the problems faced with the code and also on how these problems were dealt with and overcome during this research work.

6.3.3.3.1 Mesh generation and conversion

In general, for simple geometry problems, the use of the `blockMesh` to generate simple meshes of blocks of hexahedral cells is almost straightforward. The only aspect that needs to be paid more attention to are the specifications in the `blockMeshDict` file, concerning all the parameters of the blocks, specially the definition of the boundaries. For applications with bigger geometries, a simple block assembling script should be used, in order to avoid errors in the specifications of the parameters.

In some computational problems, it is necessary to use the `snappyHexMesh` tool, so difficulties can arise, especially for non-symmetric geometries. The `snappyHexMesh` tool generates complex meshes of hexahedral and split-hexahedral cells, automatically from triangulated surface geometries.

When the computational domain is complex, it is necessary to make its correct conversion, in order to obtain an adequate computational mesh to perform the numerical simulation. There are some mesh conversion utilities that generate meshes using other packages and convert them into the format that OpenFOAM uses. Please refer to the manual to check the more popular mesh converters available.

In the case of the work developed in this PhD, the computational domains to be used in the CFD simulations were in ASCII file format. It concerned the bathymetric and topographic data and also the data from the digital terrain or elevation model (DTM or DEM). For the information to be recognized by the OpenFOAM code, the terrain data has to be processed into the STL format, as this format is required to work with the `snappyHexMesh` for the mesh creation. This conversion process is not supported by any OF mesh converters available.

A relevant aspect that should be noted is that it is possible to have the `checkMesh` tool reporting great quality mesh results and the surface of the computational mesh looking visibly

wrong, e.g. with "bridges" between distinct edges. It is possible that the mesh refinement performed is not enough. To obtain a high quality and most exact surface in the computational mesh, when compared to the original STL file, it is necessary to have high cell and/or high surface resolution, and also to provide enough refinement levels when using `snappyHexMesh`. Besides `snappyHexMesh`, it is also important to check `surfaceFeatureExtract`. After this process, the STL file is always verified in Blender software (version 2.7.9[†]) in terms of dimensions and orientation, to guarantee correct vertices specifications in the`blockMeshDict` dictionary.

6.3.3.3.2 Wave generation

Comparing with the time series duration of several benchmark case studies, e.g. the Monai Valley benchmark, the challenge arised with the input time series to simulate the real case event, as the M_w 8.5 Earthquake and Tsunami hitting the Portuguese coast (this chapter). The time series is input through the `waveType wavemaker` from the olaFlow module and the tveta (timeSeries condition) is used. As we are modelling real incoming tsunami waves in a real bathymetric/topographic layer, with Δt = 0.05 s, the input time series, provided by CM1, is quite long. Looking to the time series in Figure 6.11, we see that the first wave lasts around 30 minutes, the second wave around 16 minutes and the third wave around 12 minutes. Using the complete time series as an input condition to the CFD code revealed to be a problem, as the program became idle after some hours and/or days, without writing any output results. We suppose that the extent of the time series, longer than the expected or usual time series size, combined with the large complex computational domain, clashed with the available cache memory, inactivating the program after some time of numerical simulation.

6.3.3.3.3 Computational limitations of the CFD numerical simulations

As a sort of a wrap-up, a short-list of the computational limitations found in OpenFOAM are presented next, complemented by some ideas worth exploring:

- The definition of the computational domain size for the computational fluid dynamics study, its initial file format and the mesh conversion are important steps, that require a preliminary study. It can take some time and several tests, so the starting point should be to perform short simulations with smaller domains, to tackle the problems step by step; only afterwards, after every problem has been overcome, should the user increase the level of difficulty of the problem to solve.

- If the grid where our numerical problem has to be solved is very big, that means that we will have to deal with a very big computational domain. The size of the grid has to be well evaluated, due to the time-consuming and resources necessity that such a condition demands. In this research work, this aspect caused long delays during the CFD modelling stage. The computational domain used for the simulation had to be continuously changed/reduced and redefined several times, as its size was overwhelming for the CFD code.

- A large total number of cells results in a good grid resolution. Nevertheless, the greater the number of cells, the longer the simulation takes and a greater volume of output results is obtained. This can be very hard to deal with also in terms of the pos-processing stage (reconstruct the results, sampling of variables, visualization of results with Paraview, etc).

- The size of the initial time series was found to influence the computational response of the CFD code. At first, a very large time series of the free surface elevation was used in the

[†] https://www.blender.org

simulations (Figure 6.11) and this would cause out of memory problems after some days of simulation, without writing any output results from the simulation. Therefore, after several simulation attempts it was chosen to reduce the input time series to 1/5 of its original size, which was found to make the numerical simulation advance. For future reference, it would be interesting to determine the simulation feasibility of an input time series composed by the first N-wave and second wave observed (extracted from the original input time series).

- An important aspect that must be taken into account is the correct definition of the background mesh. It is possible for the simulation to appear to run normally, even if the background mesh is not well defined. The simulation ends without any error and the only sign that something is wrong is that no output results have been written.

- When the computational domain is large and a small output time interval is required, the volume of output results can be quite big. For instance, for a total simulation time of 20 s and a domain with more than one million cells, with a time interval of 0.5 s for the output results and a parallel simulation, the volume of output results, in compressed format, can reach around 300 Gb. In terms of post-processing, this aspect can be quite demanding in terms of time, disk capacity and of course graphics card, which may crash often, specially in the OpenFOAM post-processing with ParaView.

- The determination of the inundation extent, the flow depths, the run-in and the run-up caused by the tsunami, in the reduced layer 41 simulation, was not retrieved due to the several computational problems encountered. This kind of procedure was computationally very demanding, due to the large area mapped and correspondent retrieval of results. This procedure was attempted but did not succeed, as we could not recover complete results for the whole simulation area. This methodology has to be further looked into, developed and/or improved.

- Both turbulence and porosity modelling could not be considered in the simulation presented in this chapter, due to high computational resources requirement related to the (still) large computational domain. It caused a highly variable simulation speed. Although the Cascais marina would justify the inclusion of porosity, it was chosen to disregard it from the beggining of the study onwards and apply it at a later stage and/or as future work, as long as more computational resources are available for this purpose.

Chapter 7

Final considerations, conclusions and future work

It was proposed in this thesis to develop a fully combined tsunami model, that would be able to simulate the several tsunami stages, from the generation phase to the tsunami coastal interaction.

With the combined model developed, which is composed by GeoClaw, FUNWAVE-TVD and OpenFOAM/olaFlow, it was possible to simulate both laboratorial and real case type tsunami events.

The new combined model developed in this work allows for: the generation, propagation and simulation of earthquake triggered tsunamis using in a first stage the nonlinear shallow water model GeoClaw; the tsunami propagation, transformation, dispersion and breaking using the dispersive Boussinesq type model FUNWAVE-TVD; and finally the OpenFOAM CFD code, via the olaFlow module, for the modelling of the complex interaction of tsunami waves with the nearshore coastal area.

The development of the combined model was divided in two main phases: the development of the combined model 1 (CM1), composed by GeoClaw and FUNWAVE-TVD, and the development of the combined model 2 (CM2), composed by CM1 and the OpenFOAM CFD code, via the olaFlow module, which resulted in the final combined tsunami model (CM). Firstly, all the numerical codes were individually benchmarked. The benchmarking of the applied numerical codes was performed with both numerical and physical test cases (Chapter 3). In this work, several physical experiments were carried out at the LH-FEUP (Laboratory of Hydraulics of the Faculty of Engineering of the University of Porto), in order to generate both solitary and N-waves.

The most used method for the generation of solitary waves in a laboratory is based on the first-order wave-maker theory of Goring (1978) and Goring and Raichlen (1980) for a piston-type wave-maker. For the generation of N-waves in a wave flume, by means of a piston wave-maker, a novel first-order theoretical formulation had to be developped in this thesis and was presented. The expressions for the piston trajectory, velocity and acceleration were derived, as well as the expressions for the paddle stroke, the stroke period, and the maximum paddle velocities. Limits for the initial paddle velocity and acceleration were established. LDN-waves with relative wave heights between 0.19 and 0.60 were generated in the laboratory and classified into three groups, according to their Stokes parameter. The generated longer waves presented the best results when compared with the expected Tadepalli–Synolakis N-wave profiles.

From the large-scale physical experiments, we found that for both solitary and LDN-waves the measured wave height H was systematically less than what was initially expected, when comparing with the theory and with the numerical simulations using the theoretical wave profile as input. The wave celerity formulations adopted for the solitary and N-waves proved to be adequate, when comparing measurements and simulations with olaFlow. Applying the Stokes number, it

was found that most waves seemed to have a mixed behaviour, between short Boussinesq waves and long-non Boussinesq waves. Part of the solitary waves showed a behaviour closer to short Boussinesq waves and part of the N-waves showed a long non-Boussinesq waves behaviour.

Experimental run-in and run-up measurements were retrieved for both solitary waves and N-waves. Maximum run-in values were established for different intervals of H/d. For $H/d > 0.6$, the wave breaking causes a great loss of energy in the N-waves generated and we found that, for these experimental conditions, the run-in was limited to 4 m. Based on our physical experiments, we proposed run-in and run-up laws for solitary waves and N-waves respectively. It should be kept in mind that the experimental measurements were retrieved for a beach with two different slopes, which is a special case and distinct from what is usually presented in the literature (single slope). The comparison between the experimental measurements and the results of the simulations showed overall good agreement for both solitary and N-wave studied, although there is an underestimation of the numerical wave height and run-in. Disparity was verified between the pressure laboratory measurements and the simulations results, which should be further investigated.

In the first part of the combined model 1 development (Chapter 5), a coupling methodology between the individual models was developed, based on the output information extracted from a refined covered gauge domain from the 2DH NSWE model simulation. After manipulation of the data, water kinematic (u,v) and free surface (η) fields were transferred to the fully nonlinear Boussinesq model. Verification and testing of the adopted coupling methodology were performed, with good fitting results.

In the second part, the 2015 Illapel Earthquake and Tsunami event was used to benchmark the CM1. The model computed quite well the first arrivals at the DART gauges, simulating satisfactorily the dispersive components of the tsunami waves, the waveform observations and tsunami travel times. From the methods used to evaluate the quality of the results obtained and from the Fourier and wavelet analysis performed, this benchmark case study showed the good performance quality of the CM1. The nesting capability existent within the combined model was presented for the 1969 Portugal Earthquake and Tsunami (1969 PET).

In the first part of the combined model 2 development, a coupling methodology to combine the CM1 (via the FUNWAVE-TVD model) with OpenFOAM (via the olaFlow module) was presented. It was found that the most simple way to couple both codes was to take and convert the time series output from FUNWAVE-TVD/CM1 and apply it in olaFlow, using the timeSeries condition available within olaFlow. The construction of the waveDict file has to follow a data format accepted by olaFlow, where it is mandatory the specification of the waveType wavemaker and the waveTheory tveta or other. The combined model methodology applied the timeSeries condition, used to simulate the Monai valley benchmark. This methodology resulted in the Combined Model 2 (CM2).

The coupling of the CM1 and CM2 models resulted in the final combined tsunami model, CM. The simulation results obtained using the CM were presented in Chapter 6 for a $\mathrm{M_w}$ 8.5 Earthquake and Tsunami hitting the Portuguese coast. We show that with a 2DV CFD simulation focused on the Marina of Cascais bathymetric and topographic profile it was possible to understand the consequence of three diferent tsunami waves scenarios and to observe the vortices behind the breakwater. The capacity of the combined model to cover the tsunami stages was shown. It was possible to retrieve the free surface elevation of the tsunami waves registered, velocities and to perform a pressure analysis.

The final combined tsunami model gathered some interesting features from each numerical code used, tackling some of the existing problems and challenges of tsunami science. Using the GeoClaw code, it was possible to use the tsunami generation module within the code and more importantly to take advantage of GeoClaw's capability of applying block-structured adaptive mesh refinement in time and space (George and LeVeque, 2006; LeVeque and George, 2007), by em-

ploying finer grid resolutions in regions of interest. This was used for the coupling methodology between GeoClaw and FUNWAVE-TVD to obtain the CM1. The frequency dispersion in long distance tsunami propagation was dealt with the fully nonlinear Boussinesq model FUNWAVE-TVD. To tackle the modelling of the nearshore processes in two-dimensional domains and determine the tsunami interaction with coastal structures and surrounding areas, we used the OpenFOAM code and the olaFlow solver.

The fully combined tsunami model achieved in this work is a novelty, since it is composed by a sequence of distinct numerical models, and can be extended to include the three-dimensional component granted by the CFD code. With this combined model, it is possible to perform the simulation of real case tsunami events and hypothetical scenarios, applying real or synthetic tsunami-type wave profiles, studying and researching the impact and tsunami interaction with coastal areas, such as in a coastal city as Cascais.

As future work, the following tasks are suggested:

- perform the final case study in three dimensions, as one of the gains from the 3D simulation is that the flow around the breakwater can be analysed;
- perform simulations for more scenarios with larger tsunami waves and extent the vortices analysis around the breakwater, also testing with different turbulence models;
- apply the final combined tsunami model using several separated patches of the original time series from the CM1 in the CFD code part, to understand the possible different results obtained with distinct tsunami wave profiles. This analysis can be used to extend the observations and conclusions presented in Chapter 6 for the Cascais coastal area, complementing the information collected in this case study;
- apply the final combined tsunami model with turbulent regime, for a reduced part of the Cascais domain, using the $\kappa - \omega$ SST turbulence model and the $\kappa - \varepsilon$ turbulence model for comparison of results;
- implement the computational study taking into account the existing buildings and its characteristcs, determining forces applied and possibly the expected resulting damage;
- extend the final combined model to be able to retrieve wave inundation, run-in and run-up estimates. It would be also useful to determine how the tsunami water inlet/surges affects the coastal and urban areas and river courses, and the complex patterns of the on land propagation and fluid flow interactions with the structures and vegetation;
- development of an user interface for the final combined tsunami model, based on the individual settings of the combined numerical codes applied and computational simulations, to streamline all the processes necessary to perform the simulations and obtain the final combined tsunami model results;
- considering the physical experiments performed and the development of the first-order theoretical formulation for the generation of N-waves in a wave flume, by means of a piston wave-maker, further research should be performed for the N-waves with smaller relative heights and larger Stokes parameters, as these are a better model for real tsunami waves. Whenever possible, longer trajectories should be also tested. The formulation of time-dependent wave velocity should be investigated, as it might lead to an increased accuracy in the obtained N-wave profile.

  Regarding the latter laboratorial component of the work presented, more suggestions for future work, which should also be considered, are presented by the end of Chapter 4.

Appendix A

Appendix to Chapter 3

A.1 GeoClaw

A.1.1 Description and input data files

Clawpack is composed by a set of Fortran based packages and simulation conditions are specified mainly through Python scripts. Fortran is a structured, imperative, generic programming language, classically used in numerical and scientific computing, which has evolved through successive versions. Python (van Rossum 1995) is a high-level, object-oriented, interpreted and iterative scripting programming language. It is a very dynamic language, with simple syntax, easy to read and of straightforward use, with vast internal libraries and user-developed modules.

There are specific prerequisites for the installation of Clawpack*. For this thesis, the Clawpack 5.2.2 version was installed and tested with some initial basic tests. After debugging the code, several examples included within the package and tutorials were tested, to better understand the code functioning and the set up of the case studies. Tutorial cases for the GeoClaw module, such as the 27$^{\text{th}}$ February 2010 Chile tsunami, sloshing water in a parabolic bowl and a tsunami in a parabolic bowl shaped ocean, were tested. In general, the proper functioning of a numerical code is guaranteed by the correct input of the initial data. As input information, the GeoClaw code needs a topography file—which refers to both bathymetry and topography data—containing data concerning the domain of study, and the deformation file refering to the initial disturbance which occurs inside that specific domain. This data should be ordered from the northernmost point to the east, and north to south. The topographic data (the so-called topo files) can be defined in ASCII and netCDF formats. Three possible configurations of ASCII files can be used, which are distinguished by its topotype number 1 to 3. Rectangular grids with uniform grid spacing are mandatory. These files can be generated by the user or downloaded from specific sources: for instance, one can obtain topography data from the National Oceanic and Atmospheric Administration (NOAA) from the U.S. Department of Commerce website † and deformation files from the United States Geological Survey (USGS) website ‡. As mentioned, in GeoClaw $H < 0$ corresponds to the bathymetry and $H > 0$ corresponds to the topography, above the sea level, so the topo files should be converted accordingly. The elevation of the topography H at each point with coordinates (x, y) is stored in the topo file of the rectangular grid. If several overlapping grids with different resolutions are used, a piecewise-bilinear function is applied in GeoClaw to retrieve the best available data to construct the resultant rectangular topo grid. This function is then integrated over computational grid cells, to obtain the single topo value in each grid cell needed when solving depth-averaged

*www.clawpack.org/

†https://www.noaa.gov//

‡https://www.usgs.gov/

equations such as the SWE with these finite volume methods [§]. For tsunami modelling, it is generally assumed that the sea level is 0. Nevertheless, sea level can be specified and also tide gauges locations.

The deformation or displacement file (dtopo files), with two supported formats, dtopotype 1 and 3, can be given or created by the `maketopo.py` script. The dtopo file is created, corresponding to the deformation of the seafloor due to an earthquake event. The location and parameters of the fault are indicated inside the script and the deformation is generated using the Okada model. In the Okada model, an isotropic half-space with uniform elastic moduli is assumed. The Poisson ratio ν is taken as equal to 0.25 and the rigidity or shear modulus G is constant and often equal to 4×10^{11} dyne$/cm^2 = 40$ GPa. In the case studies presented in this thesis, the depth indicated concerns the top of the fault and is specified as *top center* in the `maketopo.py` script. Although not common, there are numerical models which are able to use a dynamic fault input, with the information of a deformation variable in time. It can also be applied for the case of a landslide generated tsunami. This is the case of GeoClaw, where in the generation stage one can feed a variable initial deformation of the ocean sea bottom, with a dtopo file corresponding to the dynamic fault motion, where time-dependent displacements dz are considered. Also a perturbation to the depth, momentum, or surface elevation of the initial data, via `qinit` data files, is possible. A scheme explaining the structure of GeoClaw functioning, case study files and scripts is presented in Figure A.1.

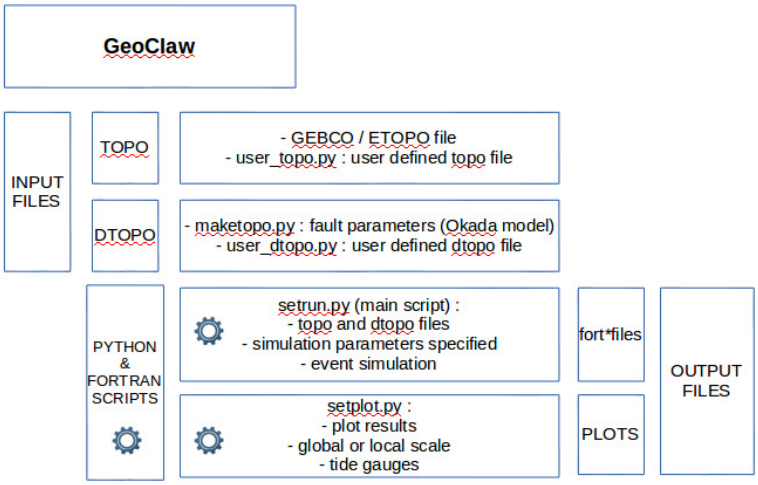

Figure A.1: Structure of a case study simulation in GeoClaw.

The simulation parameters are set in the `setrun.py` script, afterwards the program is compiled and the results can then be plotted. GeoClaw models tsunamis with the SWE applying well balanced conservative methods and in the nearshore inundation is modelled with shock-capturing methods. George and Mandli (2012) pointed out the need for 10 meter resolution coastal grids within 160 km resolution global-scale simulation domain in some tsunami inundation studies.

[§] `http://www.clawpack.org/tsunamidata.html`

A.1.2 Benchmark test cases

A.1.2.1 Monai Valley Benchmark: Tsunami run-up onto a complex 3D beach

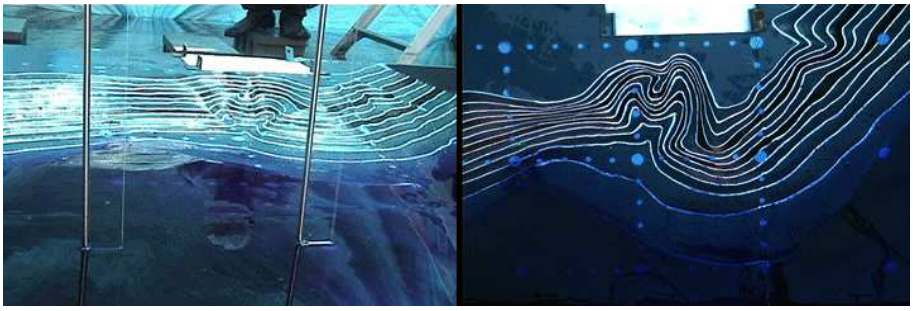

Figure A.2: Bathymetric setting for the Monai Valley experiment (Adapted from Figure A24 from Synolakis et al. 2007). It corresponds to the detailed area of Monai Valley, right after gauges 5, 7 and 9 in Figure 3.9 of this document.

A.1.2.2 Solitary wave on a conical island

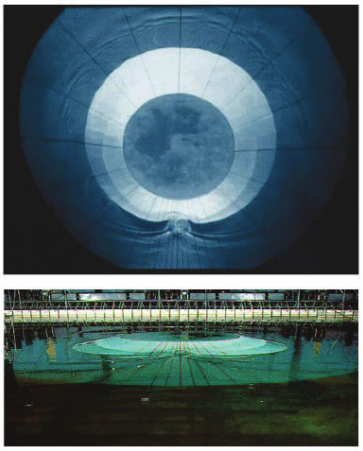

(a)

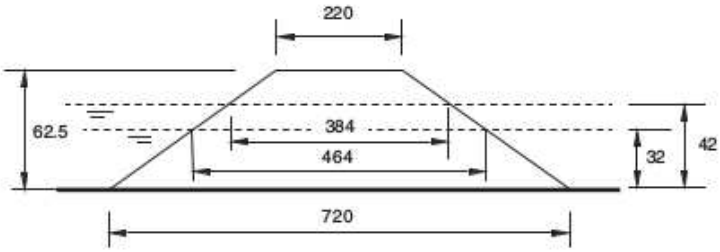

(b)

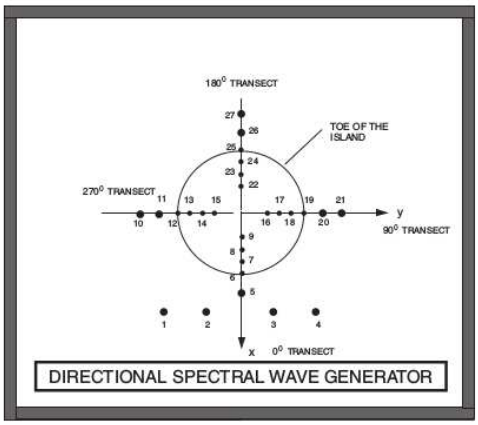

(c)

Figure A.3: (a) Top and bottom views of the conical island (Adapted from Figure A16 from Synolakis et al. 2007). (b) Conical island sketch. Not to scale. (Adapted from Figure A17 from Synolakis et al. 2007). (c) Scheme with the locations of the wave gauges. Not to scale. (Adapted from Figure A18 from Synolakis et al. 2007).

A.2 FUNWAVE-TVD

A.2.1 Description and input data files. Parallelization of the code.

FUNWAVE-TVD Version 2.0 comes in a simple package, composed by Fortran script files, which can be extracted anywhere in the computer. The files are compiled accordingly depending on the tasks set to be executed, choosing for instance if the simulation is in serial or parallel. The code has no dependencies on other programs in order to fully function, which makes it almost ready to start using. It can be used in both Cartesian coordinates (x, y), in metres, for nearshore wave simulations, and/or spherical coordinates (latitude and longitude), in decimal degrees, for ocean basin scale problems. Both Cartesian and spherical versions of the code have been benchmarked (the tests are described in Tehranirad et al. 2011 and Shi et al. 2012a, respectively), using PMEL-135 benchmarks, provided by Synolakis et al. (2007) (see also Synolakis et al. 2008). The input data files are in ASCII format and the parameters for the simulation are specified in the file `input.txt`: the user has to specify the water depth data (and make it available by means of a text file, if that is the case), the grid characteristics, the simulation specifications (such as the total run time and plot time), and the initial wave profile (time series, wave-maker or other). The depth file `depth.txt` has dimensions $M_{glob} \times N_{glob}$, where the first point corresponds to the south-west corner of the domain. Data from virtual stations located within the computation domain can be specified inside a `station.txt` file. For specific locations in the grid, the user can retrieve the time series of the free surface elevation and the velocities, which are saved in individual `stanumber` files. For more details, please refer to the user manual (Shi et al., 2016, 2012c). A scheme explaining the structure of a FUNWAVE-TVD case study is represented in Figure A.4.

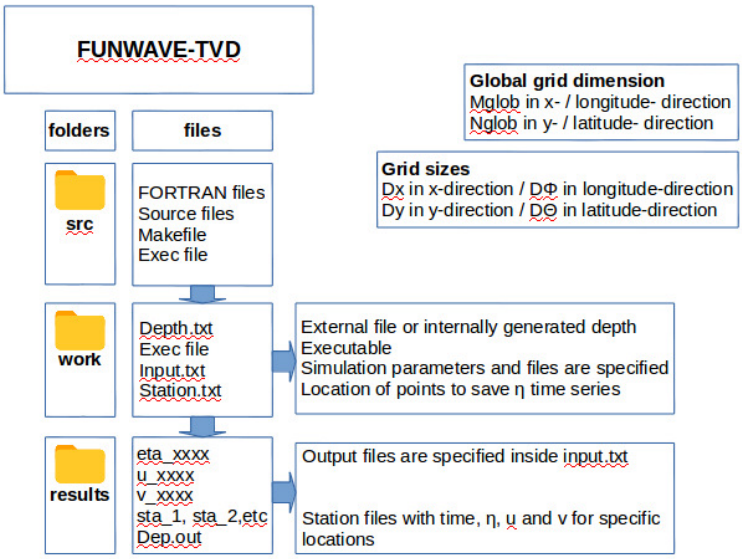

Figure A.4: Structure of the simulation of a case study in FUNWAVE-TVD.

In this research work, we started by using FUNWAVE-TVD Version 2.0, which later on was updated to FUNWAVE-TVD Version 3.0 (Shi et al., 2016). Both versions of the code were tested by running some of the examples suggested in the manual (several examples are available with the software package). FUNWAVE-TVD Version 3.0 was then used throughout all the work presented in this dissertation. Parallelization of the computational model is possible. The parallel option can be set in the `Makefile` of the code, defined by the flag *-Dparallel*. Shi et al. (2012c) used the domain decomposition technique to subdivide the domain of the problem into multiple regions, assigning each subdomain to a separate processor core. The subdomain regions contain

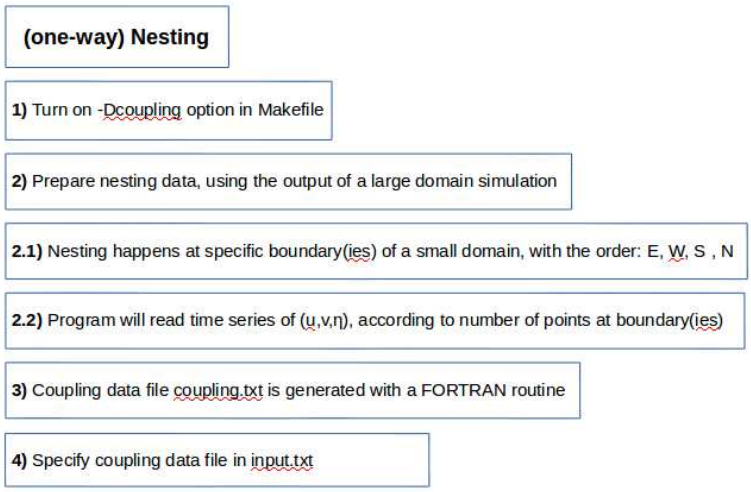

Figure A.5: One-way nesting functioning structure in FUNWAVE-TVD.

an overlapping ghost cell area, three rows deep, according to the MUSCL-TVD scheme (Kirby et al. 2013). The Message Passing Interface (MPI) with non-blocking communication allows the exchange of data in the overlapping region between neighboring processors.

A.3 olaFlow

A.3.1 Meshing

The generation of the model mesh is a very delicate and critical stage. The quality of the generated mesh will determine the quality of the results obtained from the simulation. Within OpenFOAM there are two available tools (utilities), allowing for the generation of the problem mesh: the blockMesh and the snappyHexMesh tools.

blockMesh is a tool for the generation of high-quality structured meshes, composed by simple blocks of hexahedral cells, where the block edges can be defined as straight lines, arcs or splines. The mesh is defined by the number of cells and its expansion rate in each block direction. For simple geometry problems, it is a very simple and competent tool. However, for the case of a problem with complex geometry features, an unstructured mesh is required and snappyHexMesh should be used.

snappyHexMesh generates three-dimensional meshes, composed by hexahedrons. It requires the existence of a background mesh, which can be previously generated with blockMesh. snappyHexMesh is a complex and powerful tool, that can be run in parallel, and involves three steps: the castellation, which deletes the cells located beyond a predefined region; the snapping, which allows the reconstruction of the cells to the boundary region; the layering, which creates additional layers in the boundary region.

There are other additional external meshing tools, such as ANSYS GAMBIT® [¶], Salome [‖] and cfMesh [**], that require environments other than OpenFOAM.

[¶] https://www.ansys.com/
[‖] https://www.salome-platform.org/
[**] https://cfmesh.com/

A.3.2 Examples of dictionaries

A.3.2.1 wavemakerMovementDict file example - Case 6, h = 25 cm (C6a)

```
/*--------------------------------------------------------------------------*
| =========                 |
| \\      /  F ield         | OpenFOAM: The Open Source CFD Toolbox
|  \\    /   O peration     | Version:  1.3
|   \\  /    A nd           | Web:      http://www.openfoam.org
|    \\/     M anipulation  |
\*--------------------------------------------------------------------------*
FoamFile
{
    version     2.0;
    format      ascii;
    class       dictionary;
    location    "constant";
    object      wavemakerMovementDict;
}
// * * * * * * * * * * * * * * * * * * * * * * * * * * * * * * * * * * * * * /

// Change to true to re-read this dictionary upon restart.
reread          false;

#include "wavemakerMovement.txt"
```

A.3.2.2 wavemakerMovement.txt file file example - Case 6, h = 25 cm (C6a)

```
wavemakerType   Piston;
tSmooth         1.5;
genAbs          0;

timeSeries 371(
0.0
0.01
0.02
0.03
.
.
.
3.67
3.68
3.69
3.7
);

paddlePosition 1(
371(
  0.00000000e+00   1.18292147e-07   2.60620972e-07   4.13747677e-07
  .
  .
```

```
  .
  4.99996111e-01   4.99996263e-01   4.99996377e-01   4.99996508e-01
)
);

paddleEta 1(
371(
  5.20879534e-14   6.31134374e-14   7.64726913e-14   9.26597054e-14
  .
  .
  .
  1.10565290e-18   9.12502930e-19   7.53094936e-19   6.21534423e-19
)
);
```

A.3.2.3 waveDict file example (timeSeries condition) - Monai Valley benchmark w/ olaFlow

```
/*--------------------------------------------------------------------------*
| =========                 |
| \\      /  F ield         | OpenFOAM: The Open Source CFD Toolbox
|  \\    /   O peration     | Version:  1.3
|   \\  /    A nd           | Web:      http://www.openfoam.org
|    \\/     M anipulation  |
\*--------------------------------------------------------------------------*
FoamFile
{
    version     2.0;
    format      ascii;
    class       dictionary;
    location    "constant";
    object      waveDict;
}
// * * * * * * * * * * * * * * * * * * * * * * * * * * * * * * * * * * * * * * * * * * * * /

waveType   wavemaker;

waveTheory         tveta;

genAbs          1;

absDir          0.0;

nPaddles          1;

timeSeries 451(
0.0
0.05
0.1
0.15
```

```
.
.
.
22.35
22.4
22.45
22.5
);

paddleVelocity
451(
 -1.07320e-04  -1.70547e-05   6.66646e-05   1.41562e-04   2.05569e-04
  .
  .
  .
  6.39228e-03   7.35879e-03   8.15295e-03   8.80744e-03   9.35201e-03
);

paddleEta
451(
 -1.19000e-05  -1.89122e-06   7.39300e-06   1.57000e-05   2.28000e-05
  .
  .
  .
  7.12600e-04   8.21000e-04   9.10200e-04   9.83800e-04   1.04510e-03
);
```

A.3.2.4 waveDict file example (timeSeries condition) - Monai Valley benchmark w/ CM2

```
/*--------------------------------------------------------------------------*
| =========                 |
| \\      /  F ield         | OpenFOAM: The Open Source CFD Toolbox
|  \\    /   O peration     | Version:  1.3
|   \\  /    A nd           | Web:      http://www.openfoam.org
|    \\/     M anipulation  |
\*--------------------------------------------------------------------------*
FoamFile
{
    version     2.0;
    format      ascii;
    class       dictionary;
    location    "constant";
    object      waveDict;
}
// * * * * * * * * * * * * * * * * * * * * * * * * * * * * * * * * * * * * * * * * * * * * /

waveType   wavemaker;

waveTheory         tveta;
```

```
genAbs          1;

absDir          0.0;

nPaddles          1;

timeSeries 2268(
0.0
0.0061
0.0182
0.0243
0.0365
.
.
.
22.6239
22.6339
22.6439
22.6539
22.6639
);

paddleVelocity
2268(
  6.74000e-10   3.38000e-09   2.03000e-08   3.73000e-08   9.54000e-08
  .
  .
  .
  3.77000e-02   4.16000e-02   4.57000e-02   5.02000e-02   5.47000e-02
);

paddleEta
2268(
 -3.10000e-08  -9.34000e-08  -3.13000e-07  -4.72000e-07  -8.84000e-07
  .
  .
  .
  2.13000e-01   2.09000e-01   2.04000e-01   1.98000e-01   1.92000e-01
);
```

A.3.2.5 fvSchemes file example - Case 6, h = 25 cm (C6a)

```
/*---------------------------------*- C++ -*----------------------------------*
| =========                 |
| \\      /  F ield         | OpenFOAM: The Open Source CFD Toolbox
|  \\    /   O peration     | Version:  2.3.0
|   \\  /    A nd           | Web:      www.OpenFOAM.org
|    \\/     M anipulation  |
```

```
\*---------------------------------------------------------------------------*
FoamFile
{
    version     2.0;
    format      ascii;
    class       dictionary;
    location    "system";
    object      fvSchemes;
}
// * * * * * * * * * * * * * * * * * * * * * * * * * * * * * * * * * * * * * * * * * * * * * * * * * /

ddtSchemes
{
    default         Euler;
}

gradSchemes
{
    default         Gauss linear;
}

divSchemes
{
    div(rhoPhi,U)  Gauss limitedLinearV 1;
    div(U)  Gauss linear;
    div((rhoPhi|interpolate(porosity)),U)  Gauss limitedLinearV 1;
    div(rhoPhiPor,UPor)  Gauss limitedLinearV 1;
    div(rhoPhi,UPor)  Gauss limitedLinearV 1;
    div(rhoPhiPor,U)   Gauss limitedLinearV 1;
    div(phi,alpha)  Gauss vanLeer;
    div(phirb,alpha) Gauss interfaceCompression;
    div((muEff*dev(T(grad(U))))) Gauss linear;
    div(phi,k)      Gauss upwind;
    div(phi,epsilon) Gauss upwind;
    div((phi|interpolate(porosity)),k)      Gauss upwind;
    div((phi*interpolate(rho)),k)      Gauss upwind;
    div((phi|interpolate(porosity)),epsilon) Gauss upwind;
    div(phi,omega) Gauss upwind;
    div((phi|interpolate(porosity)),omega) Gauss upwind;
    div((phi*interpolate(rho)),omega) Gauss upwind;
    div((phi*interpolate(rho)),epsilon) Gauss upwind;
}

laplacianSchemes
{
    default         Gauss linear corrected;
}

interpolationSchemes
```

```
{
    default         linear;
}

snGradSchemes
{
    default         corrected;
}

fluxRequired
{
    default         no;
    p_rgh;
    pcorr;
    alpha.water;
}

wallDist
{
    method meshWave;
}


// ************************************************************************* //
```

A.3.2.6 fvSolution file example - Case 6, h = 25 cm (C6a)

```
/*--------------------------------*- C++ -*----------------------------------*
| =========                 |
| \\      /  F ield         | OpenFOAM: The Open Source CFD Toolbox
|  \\    /   O peration     | Version:  2.3.0
|   \\  /    A nd           | Web:      www.OpenFOAM.org
|    \\/     M anipulation  |
\*---------------------------------------------------------------------------*/
FoamFile
{
    version     2.0;
    format      ascii;
    class       dictionary;
    location    "system";
    object      fvSolution;
}
// * * * * * * * * * * * * * * * * * * * * * * * * * * * * * * * * * * * * * //

solvers
{
    "alpha.water.*"
    {
        nAlphaCorr      1;
        nAlphaSubCycles 2;
```

```
    alphaOuterCorrectors yes;
    cAlpha          1;

    MULESCorr       no;
    nLimiterIter    3;

    solver          smoothSolver;
    smoother        symGaussSeidel;
    tolerance       1e-8;
    relTol          0;
}

"pcorr.*"
{
    solver          PCG;
    preconditioner  DIC;
    tolerance       1e-5;
    relTol          0;
}

p_rgh
{
    solver          PCG;
    preconditioner  DIC;
    tolerance       1e-07;
    relTol          0.05;
}

p_rghFinal
{
    $p_rgh;
    relTol          0;
}

U
{
    solver          smoothSolver;
    smoother        symGaussSeidel;
    tolerance       1e-06;
    relTol          0;
}

cellDisplacement
{
    solver          GAMG;
    tolerance       1e-5;
    relTol          0;
    smoother        GaussSeidel;
    cacheAgglomeration false;
```

```
        nCellsInCoarsestLevel 10;
        agglomerator    faceAreaPair;
        mergeLevels     1;
    }

    cellDisplacementFinal
    {
        $cellDisplacement;
        relTol          0;
    }

    "(k|epsilon|omega|B|nuTilda).*"
    {
        solver          smoothSolver;
        smoother        symGaussSeidel;
        tolerance       1e-08;
        relTol          0;
    }
}

PIMPLE
{
    momentumPredictor   no;
    nOuterCorrectors    1;
    nCorrectors         3;
    nNonOrthogonalCorrectors 0;
}

relaxationFactors
{
    fields
    {
    }
    equations
    {
        ".*" 1;
    }
}


// ************************************************************************* //
```

A.3.3 Examples of olaflow.log

A.3.3.1 Turbulence model $\kappa - \omega$ SST coefficients - Case 6, h = 50 cm (C6b)

```
/*---------------------------------------------------------------------------*
| =========                 |
| \\      /  F ield         | OpenFOAM: The Open Source CFD Toolbox
|  \\    /   O peration     | Version:  v1606+
```

```
|   \\  /    A nd           | Web:      www.OpenFOAM.com
|    \\/     M anipulation  |
\*---------------------------------------------------------------------------*
Build  : v1606+
Exec   : olaDyMFlow
Date   : Oct 05 2019
Time   : 18:17:44
Host   : "859973156ad5"
PID    : 24594
Case   : /home/user/OpenFOAM/user-v1606+/run/tutorials/olaFlow_supplementary/t
nProcs : 1
sigFpe : Enabling floating point exception trapping (FOAM_SIGFPE).
fileModificationChecking : Monitoring run-time modified files using timeStampM
allowSystemOperations : Allowing user-supplied system call operations

// * * * * * * * * * * * * * * * * * * * * * * * * * * * * * * * * * * * * * /
Create time

Create mesh for time = 0

Selecting dynamicFvMesh dynamicMotionSolverFvMesh
Selecting motion solver: displacementLaplacian
Selecting motion diffusion: inversePointDistance

PIMPLE: Operating solver in PISO mode

Reading field porosityIndex

Porosity NOT activated

Reading field p_rgh

Reading field U

Reading/calculating face flux field phi

Reading transportProperties

Selecting incompressible transport model Newtonian
Selecting incompressible transport model Newtonian
Selecting turbulence model type RAS
Selecting RAS turbulence model kOmegaSST
Selecting patchDistMethod meshWave
kOmegaSSTCoeffs
{
    alphaK1         0.85;
    alphaK2         1;
    alphaOmega1     0.5;
    alphaOmega2     0.856;
```

```
    gamma1          0.555556;
    gamma2          0.44;
    beta1           0.075;
    beta2           0.0828;
    betaStar        0.09;
    a1              0.31;
    b1              1;
    c1              10;
    F3              false;
}


...
```

A.3.4 Files for turbulence modelling application

A.3.4.1 volScalarField k

```
/*--------------------------------*- C++ -*----------------------------------*
| =========                 |
| \\      /  F ield         | OpenFOAM: The Open Source CFD Toolbox
|  \\    /   O peration     | Version:  1.7.1
|   \\  /    A nd           | Web:      www.OpenFOAM.com
|    \\/     M anipulation  |
\*---------------------------------------------------------------------------*
FoamFile
{
    version     2.0;
    format      ascii;
    class       volScalarField;
    location    "0";
    object      k;
}
// * * * * * * * * * * * * * * * * * * * * * * * * * * * * * * * * * * * * * * * * * * * * /

dimensions      [0 2 -2 0 0 0 0];

internalField   uniform 0.00000001;

boundaryField
{
    inlet
    {
        type            inletOutlet;
        inletValue      uniform 0.00000001;
        value           uniform 0.00000001;
    }
    outlet
    {
        type            inletOutlet;
```

```
        inletValue      uniform 0.00000001;
        value           uniform 0.00000001;
    }
    bottom
    {
        type            kqRWallFunction;
        value           uniform 0.00000001;
    }
    atmosphere
    {
        type            inletOutlet;
        inletValue      uniform 0.00000001;
        value           uniform 0.00000001;
    }
    marina
    {
        type            kqRWallFunction;
        value           uniform 0.00000001;
    }
    patch1
    {
        type            inletOutlet;
        inletValue      uniform 0.00000001;
        value           uniform 0.00000001;
    }
    patch2
    {
        type            inletOutlet;
        inletValue      uniform 0.00000001;
        value           uniform 0.00000001;
    }
}


// ************************************************************************* //
```

A.3.4.2 volScalarField omega

```
/*--------------------------------*- C++ -*----------------------------------*
| =========                 |
| \\      /  F ield         | OpenFOAM: The Open Source CFD Toolbox
|  \\    /   O peration     | Version:  1.7.1
|   \\  /    A nd           | Web:      www.OpenFOAM.com
|    \\/     M anipulation  |
\*---------------------------------------------------------------------------*/
FoamFile
{
    version     2.0;
    format      ascii;
    class       volScalarField;
```

```
    object      omega;
}
// * * * * * * * * * * * * * * * * * * * * * * * * * * * * * * * * * * * * * * * * * * * * /

dimensions      [0 0 -1 0 0 0 0];

internalField   uniform 0.001;

boundaryField
{
    inlet
    {
        type            inletOutlet;
        inletValue uniform 0.001;
        value           uniform 0.001;
    }
    outlet
    {
        type            inletOutlet;
        inletValue uniform 0.001;
        value           uniform 0.001;
    }
    bottom
    {
        type            omegaWallFunction;
        value           uniform 0.001;
    }
    atmosphere
    {
        type            inletOutlet;
        inletValue uniform 0.001;
        value           uniform 0.001;
    }
    marina
    {
        type            omegaWallFunction;
        value           uniform 0.001;
    }
    patch1
    {
        type            omegaWallFunction;
        value           uniform 0.001;
    }
    patch2
    {
        type            omegaWallFunction;
        value           uniform 0.001;
    }
}
```

```
// ************************************************************************* //
```

A.3.4.3 volScalarField nut

```
/*--------------------------------*- C++ -*----------------------------------*
| =========                 |                                                 |
| \\      /  F ield         | OpenFOAM: The Open Source CFD Toolbox           |
|  \\    /   O peration     | Version:  3.0.0                                 |
|   \\  /    A nd           | Web:      www.OpenFOAM.org                      |
|    \\/     M anipulation  |                                                 |
\*---------------------------------------------------------------------------*/
FoamFile
{
    version     2.0;
    format      ascii;
    class       volScalarField;
    location    "0";
    object      nut;
}
// * * * * * * * * * * * * * * * * * * * * * * * * * * * * * * * * * * * * * //

dimensions      [0 2 -1 0 0 0 0];

internalField   uniform 0;

boundaryField
{
    inlet
    {
        type            calculated;
        value           uniform 0;
    }
    outlet
    {
        type            calculated;
        value           uniform 0;
    }
    bottom
    {
        type            nutkWallFunction;
        Cmu             0.09;
        kappa           0.41;
        E               9.8;
        value           uniform 0;
    }
    atmosphere
    {
        type            calculated;
```

```
        value           uniform 0;
    }
    marina
    {
        type            nutkWallFunction;
        Cmu             0.09;
        kappa           0.41;
        E               9.8;
        value           uniform 0;
    }
    patch1
    {
        type            nutkWallFunction;
        Cmu             0.09;
        kappa           0.41;
        E               9.8;
        value           uniform 0;
    }
    patch2
    {
        type            nutkWallFunction;
        Cmu             0.09;
        kappa           0.41;
        E               9.8;
        value           uniform 0;
    }
}


// ************************************************************************* /
```

Appendix B

Appendix to Chapter 4

B.1 Wave basin experiments (article *Generation of N-waves in laboratory*, Coastal Engineering, 2019)

Coastal Engineering 148 (2019) 1–18

Contents lists available at ScienceDirect

Coastal Engineering

journal homepage: www.elsevier.com/locate/coastaleng

Generation of N-waves in laboratory

Vânia Veloso Lima[a,c,*], Paulo Avilez-Valente[b,c], Maria Ana Viana Baptista[a,d], Jorge Miguel Miranda[a,e]

[a] Instituto Dom Luiz, Faculdade de Ciências da Universidade de Lisboa, Campo Grande, Edifício C1 — Piso 1, 1749-016 Lisboa, Portugal
[b] Faculdade de Engenharia, Universidade do Porto, Rua Dr. Roberto Frias s/n, 4200-465 Porto, Portugal
[c] Centro Interdisciplinar de Investigação Marinha e Ambiental, Universidade do Porto, Terminal de Cruzeiros de Leixões, Av. General Norton de Matos s/n, 4450-208 Matosinhos, Portugal
[d] Instituto Superior de Engenharia de Lisboa, Rua Conselheiro Emídio Navarro 1, 1959-007 Lisboa, Portugal
[e] Instituto Português do Mar e da Atmosfera, Rua C do Aeroporto, 1749-077 Lisboa, Portugal

ARTICLE INFO

Keywords:
N-Wave
Wave basin
Wave generation
Tsunami-like wave
Stokes parameter

ABSTRACT

In this research work, a novel theoretical first-order formulation for the generation of N-waves in laboratory, by means of a piston-type wave-maker, is presented. The plate's trajectory, velocity and acceleration equations for the generation of tsunami N-waves in a wave flume are deduced. A set of laboratory experiments performed for the generation of leading depression N-waves in a wave basin is described.

A Tadepalli–Synolakis N-wave profile is assumed and the equations for the paddle's trajectory, velocity, and acceleration and for the piston stroke and stroke period are derived and discussed in detail. Limits for the initial paddle velocity and acceleration are established.

A set of experiments, devised and performed in the 28 m long wave basin of the Laboratory of Hydraulics, at the Faculty of Engineering of the University of Porto, is described. Six leading depression N-waves were selected and classified into three categories, according to their Stokes parameter. The results show that the shorter waves undergo a strong transformation, tending to a solitary wave-like pulse, followed by a trough. The longer waves show a distinct behaviour, tending to a bore-like wave exhibiting a leading trough. The generated longer waves presented the best results when compared with the expected Tadepalli–Synolakis N-wave profiles. Further investigation on the formulation of the wave velocity of the N-waves and on the behaviour of waves with higher order Stokes parameter is necessary.

1. Introduction

Tsunami are gravity waves resulting from sudden changes in the water equilibrium position, which cause the displacement of a large volume of water. The triggering mechanism of these large waves can be of seismic origin, volcanic activity, landslides or any vertical disturbance of a water body. Tsunami waves are very long waves, that propagate over the continental shelf at a relatively low depth, and thus are also highly non-linear. When no field data is available or when a conceptual analysis is envisaged, it is a common approach to model tsunamis as solitary waves, both in experimental and numerical studies (Camfield and Street, 1969b; Hammack and Segur, 1974; Synolakis, 1987; Liu et al., 1995; Briggs et al., 1995a, 1995b). On the other hand, Madsen et al. (2008) stated that in general tsunamis do not generate solitary-like waves in the ocean or on the continental shelf.

The N-wave concept was introduced by Tadepalli and Synolakis (1994), who suggested that N-type waves, previously discussed in gas dynamics (Whitham, 1974), are more suitable to describe the main tsunami wave, often observed with a leading depression (where the wave crest is preceded by the wave trough). Those authors proposed three classes of N-waves to study the run-up of near-shore tsunamis. Before them, Pelinovsky and Mazova (1992) presented an analytical study of the run-up of leading depression N-waves, modelling the wave as the initial perturbation of a Lorenz form. Later, Madsen and Schäffer (2010) described N-waves as two single waves, one positive solitary wave and one negative solitary wave, with wavelengths set to fit the tsunami wave data. Building on that idea, Chan and Liu (2012) proposed to model the tsunami wave as a combination of three solitary waves.

Taking into account the available field data, it is now generally accepted that the first tsunami waves approach the coast as leading depression (LDN) or leading elevation (LEN) N-waves. However,

* Corresponding author. Instituto Dom Luiz, Faculdade de Ciências da Universidade de Lisboa, Campo Grande, Edifício C1 — Piso 1, 1749-016 Lisboa, Portugal.
E-mail address: vcvalima@gmail.com (V. Veloso Lima).

https://doi.org/10.1016/j.coastaleng.2019.02.012
Received 28 April 2018; Received in revised form 17 January 2019; Accepted 21 February 2019
Available online 27 February 2019
0378-3839/

Notation

a^+	amplitude of the wave crest
a^+_{obs}	observed amplitude of the wave crest
a^+_{TS}	expected amplitude of the wave crest
a^-	amplitude of the wave trough
a^-_{obs}	observed amplitude of the wave trough
a^-_{TS}	expected amplitude of the wave trough
c	wave velocity
c_0	leading ascending zero wave velocity
c^+	leading wave crest wave velocity
c^-	leading wave trough wave velocity
$\bar{c}$	weighted averaged wave velocity
$\bar{c}^*$	weighted averaged wave velocity without wg8–wg7 run
$\bar{c}_{1-4}$	average wave velocity between gauges 1 and 4
$\bar{c}_{4-5}$	average wave velocity between gauges 4 and 5
$\bar{c}_{5-7}$	average wave velocity between gauges 5 and 7
$\bar{c}_{7-8}$	average wave velocity between gauges 7 and 8
$\bar{c}_{8-3}$	average wave velocity between gauges 8 and 3
d	undisturbed water depth
g	gravity acceleration
t	time
$t_{Arrival}$	time of arrival of the reflected wave at wave gauge wg3
u	particle velocity in front of the wave-maker
$\bar{u}$	depth-averaged particle velocity
x	horizontal coordinate
x_1	horizontal coordinate for the location of the wave crest of a solitary wave at $t = 0$
x_2	horizontal coordinate for the location of the inflexion point of an N-wave at $t = 0$
D	total displacement of the paddle
F	integration function
H	wave height
H_{obs}	observed wave height
H_{TS}	expected wave height
	non-linear mass flux
S	paddle stroke
St	Stokes parameter
T	apparent wave period
U_c	current speed
Ur	Ursell number
δ	eccentricity parameter
ε	scale factor
ϵ	non-linearity parameter
η	free surface elevation
θ	argument
κ	generalized wavenumber
λ	apparent wavelength
ξ	paddle trajectory of the wave-maker
ξ_f	final paddle position of the wave-maker
ξ_{max}	maximum space travelled by the paddle
ξ_{min}	minimum space travelled by the paddle
$\dot{\xi}$	paddle velocity of the wave-maker
$\dot{\xi}_{max}$	maximum paddle velocity of the wave-maker
$\dot{\xi}_{min}$	minimum paddle velocity of the wave-maker
$\ddot{\xi}$	paddle acceleration of the wave-maker
σ	dispersion parameter
τ	stroke period
φ	integration variable
ϕ	integration variable
Δt	total excursion time, back and forth, from wg3 to the beach

solitary waves were used in most early tsunami experimental studies, and McGovern et al. (2016) pointed out the lack of relevant experimental data for tsunami-like N-waves. One of the reasons is that, until recently, no fully described technique existed for the generation of N-waves in a wave flume.

The study of the laboratory generation of long waves traces back to the 19th century (Scott Russell, 1845) and several methods have been proposed. From the general approach of applying moving partitions to a certain amount of water (Havelock, 1929; Kennard, 1949), Biésel and Suquet (1951) developed the linear wave-maker theory, later validated through laboratory experiments by Ursell et al. (1960). The horizontal movement of a water volume by means of a vertical plate, powered up by a piston-type wave-maker, is by far the most common method applied (see for instance Hughes, 1993). For the generation of relatively long waves by a piston-type wave-maker, Madsen (1971) extended the linear wave-maker theory to second order accuracy, achieving the reduction of generated spurious harmonics. That author showed that secondary waves were related to the existence of a free second harmonic wave. Later, Madsen (1970) found substantial differences between observed and expected wave heights, which he attributed to leakage around the paddle.

Scott Russell (1845) was able to generate solitary waves by throwing a solid mass into a water tank. Daily and Stephan (1952), cited by Katell and Eric (2002), obtained solitary waves through the displacement of a mass of water by means of a piston travelling vertically from the bottom of a tank. According to Malek-Mohammadi and Testik (2010), Hall and Watts (1953) were the first to generate solitary waves in a laboratory, by means of a piston wave-maker composed by a vertical paddle, moved mechanically in the horizontal direction. Later, Camfield and Street (1969a) linked a computer to the mechanical system, which allowed for the control of the paddle movement.

The most used method for the generation of solitary in a laboratory is based on the first order wave-maker theory of Goring (1978) and Goring and Raichlen (1980) for a piston-type wave-maker. This method is limited to waves with a low height-to-depth ratio. Synolakis (1990) pointed out a flaw in Goring's theoretical considerations: the change of variable from (x, t) to θ performed during the generation phase, since at that stage the wave is still evolving and cannot be considered of permanent form. Thus, Synolakis (1990) presented a wave-maker theory of finite-amplitude long wave generation by means of a piston wave-maker, achieving a very detailed description of single waves at arbitrary lengths from the wave-maker. His method was used to generate solitary waves with a piston wave-maker and study the two- and three-dimensional long wave run-up in a wave channel and in a wave tank (Briggs et al., 1995b).

Goring's procedure is based on the Boussinesq first order solitary wave solution. Following a similar reasoning, Katell and Eric (2002) presented a novel piston wave-maker theory, based on Rayleigh's solitary wave solution. They analysed the evolution of the wave during the generation stage and attested an increased accuracy and a more stable wave form. Jensen et al. (2003) extended Goring's method for higher amplitude solitary waves, using a fully non-linear and fully dispersive wave solution (Tanaka, 1986). These authors studied the kinematics of strongly non linear waves and related run-up on a steep beach, with special focus on bore run-up. Later, the same procedure was used for an experimental and numerical study on on-shore breaking solitary waves (Jensen et al., 2005).

Malek-Mohammadi and Testik (2010) presented a new wave-maker theory for the generation of solitary waves. Addressing the concerns expressed in Synolakis (1990) towards Goring's method, they considered the time evolution of the wave, proposing the use of a time-dependent wave velocity during the generation process. Their

procedure seemed to lead to an increased accuracy for both Boussinesq and Rayleigh wave forms.

Due to all this research work, solitary waves generated by piston wave-makers are now quite accurate in terms of wave characteristics and can be generated at short distances from the wave-maker. Such waves have been extensively used both in experimental and in numerical research work (Baldock et al., 2009; Chang et al., 2009; Hsu et al., 2012; Oliveira et al., 2017). In fact, it became the preferred generation method, due to its wide diffusion among the scientific community.

For the generation of tsunami-like waves in large scale laboratory flumes, there are several other types of wave generation mechanisms (a review can be found in Goseberg et al., 2013). Pneumatic generators were used by Rossetto et al. (2011), Charvet et al. (2013) and McGovern et al. (2016), while Drähne et al. (2016) applied a pump-driven wave-maker. In Klettner et al. (2012) an adapted wave-maker was used to generate depression waves. Work with a bottom-tilting wave-maker is documented in Lu et al. (2017).

The pump wave-maker method is considered easy to implement (Goseberg et al., 2013), with increased accuracy of the wave characteristics being achieved. Pneumatic generators are capable of producing very long waves of large amplitude and waves of very large periods (Rossetto et al., 2011; McGovern et al., 2016).

One main drawback of both pump-driven and pneumatic wave generators is the fact that, as part of the generation process (air/gas–liquid compression), there are additional turbulence and pressure disturbances at the surface in the generated water waves. In the case of pneumatic generators, discontinuities were found in the surface elevation time series (Goseberg et al., 2013). McGovern et al. (2016) pointed out the limitations on the generation of wave heights at larger water depths, for the pump-driven wave-maker. Contrary to those generation techniques, there are reduced turbulence and minimal spurious effects resulting from piston wave-makers, because of the reduced distance travelled by the plate.

In the framework of this research work, one established task was to generate tsunami like waves in the laboratory. The main objective was to retrieve several datasets of free surface elevation, velocities, run-up, run in and pressure, to further validate the tsunami numerical models in development. A detailed literature review showed vast research work concerning the generation of solitary waves. However, it revealed a considerable lack of work on the process of N-wave generation in a wave flume, by means of a piston wave-maker. Applying solitary wave theory, Schmidt-Koppenhagen et al. (2006) used a piston-type wave-maker to generate tsunami waves, with both positive and negative wave segments, resembling leading depression N-waves. Recently, Schimmels and co-workers (Schimmels et al., 2014, 2016; Sriram et al., 2016) used a piston wave-maker in a large scale wave flume to successfully generate N-waves, using two methods: (1) a combination of solitary waves, as proposed by Chan and Liu (2012), and (2) a self-correcting method, first proposed by Daemrich and co-workers (Daemrich et al., 1980; Daemrich and Götschenberg, 1988), for regular and random wave generation.

In the present work, the authors propose a novel formulation for the generation of N-waves with piston wave-makers, by extending Goring's method (Goring, 1978; Goring and Raichlen, 1980) for the Boussinesq solitary wave to the general N-wave expression introduced by Tadepalli and Synolakis (1994, 1996a). Firstly, the wave formulation of N-type waves and the theory of the generation of N-waves by a piston wave-maker are detailed. The paddle's trajectory, velocity and acceleration are derived and presented, as well as the expressions for the piston stroke and for the stroke period. Secondly, the results of a set of six leading depression N-waves generated at the wave basin of the Laboratory of Hydraulics of the Faculty of Engineering of the University of Porto (LH-FEUP), Portugal, are presented. The experimental wave profiles are analysed and compared to the expected Tadepalli–Synolakis N-wave profiles.

2. Tsunami N-waves

2.1. Description

Whitham (1974) introduced the N-wave concept within a gas-dynamics framework, naming it after the shape of its profile, derived from a shock wave as a construction of its characteristic curves. Reports of tsunamis as leading depression waves followed by a steep wave front were traditionally devalued, as the solitary wave had become an ingrained model for earthquake-triggered tsunami waves and associated run-up estimation. Based on the observations retrieved from several events like the 1992 Flores, the 1993 Nicaragua, and the 1993 south-west-off Hokkaido earthquakes and tsunamis (Synolakis et al., 2007), Tadepalli and Synolakis (1994) borrowed Whitman's N-wave concept and introduced it into tsunami science. The dipolar characteristic of these waves is related to the seabed deformation pattern caused by the earthquake at the tsunami's source, as a combination of vertical uplift and ground subsidence. The authors used the N-waves (sometimes referred to as multilobe waves) to describe simple solutions to the canonical problem, classifying them into three types: the generalized N-wave, the isosceles N-wave, and the double N-wave. Isosceles N-waves have equal amplitude trough and crest; double N-waves are a series of N-waves. In their research, they also found that leading depression N-waves (LDN) run-up higher than leading elevation N-waves (LEN). In Tadepalli and Synolakis (1996a), the authors proposed a model for the leading wave of tsunamis and stated that most of the N-wave character is preserved even after transoceanic propagation and that locally generated tsunamis are generally N-wave like. They proposed the generalized N-wave as a general function for local and far-field tsunamis.

Geist and Yoshioka (1996) estimated the run-up of tsunamis along the Cascadia margin, applying the generalized leading depression N-wave run-up law presented in Tadepalli and Synolakis (1994). They concluded that it provided good estimations when parametrised accordingly to fit local recorded tsunami wave forms.

Borerro et al. (1997) documented the field survey to Tenacatita Bay, a location severely flooded after the 1995 Manzanillo earthquake and tsunami, in central Mexico. Statements from witnesses described the recession of the sea after the earthquake, in accordance with the concept of a leading depression N-wave proposed by Tadepalli and Synolakis (1994). The report was supported by a photograph of the sea surface recession at Tenacatita Bay, believed to be the first photographic record ever, before the 2004 Sumatra earthquake and tsunami.

As a follow-up to their previous work, Tadepalli and Synolakis (1996b) modelled N-waves in the far-field with the KdV equation and used the shallow water theory in the near-shore to evaluate the run-up of non breaking waves. They elaborated on the geometric parameters of the fault, modelling the 1992 Nicaragua tsunami.

Titov and Synolakis (1997) modelled the 1993 Hokkaido-Nansei-Oki earthquake and tsunami, comparing results with the recorded field data. Experiments based on this event, using an input leading depression N-wave, were performed at the Central Research Institute for Electric Power Industry in Abiko, Japan (Matsuyama and Tanaka, 2001).

Geist et al. (1998) established a relationship between the earthquake source parameters and the tsunami generation. Applying the run-up laws by Tadepalli and Synolakis (1994), the effect of the source parameters on the local run-up was studied.

Carrier et al. (2003) improved the tsunami run-up and draw-back motions onto an uniformly sloping beach, for initial wave conditions such as LDN-waves and submarine landslide waveforms.

Madsen et al. (2008) presented a very interesting discussion about the solitary wave paradigm and how it failed to represent tsunamis, in geophysical time and length scales. Madsen and Schäffer (2010) derived analytical solutions to the non-linear shallow water equations for the run-up and draw-back of single waves, extending it to the leading depression N-waves.

Fritz et al. (2011) documented the field survey for the 2010 Chile tsunami, reporting eyewitnesses' observations on the initial sea surface recession after the earthquake. Before, Fritz et al. (2007) also reported the LDN-wave pattern for the 17 July 2006 Java tsunami, along the affected area. Wei et al. (2008) observed LEN-waves for far-field tsunami measurements of the 2007 Peru earthquake and tsunami, in contrast with reports of LDN-waves in the near field, as noted before by Tadepalli and Synolakis (1996a) and Fritz et al. (2007).

Numerical modelling using N-waves has been done in Liang et al. (2013), Siva and Behera (2016) and Gao et al. (2017). Kânoğlu et al. (2013) and Aydin and Kânoğlu (2017) solved both linear and non-linear shallow water equations as an initial boundary value problem using N-waves; in the former, the authors showed the focusing effect in the direction of depression and discussed its relevance on extreme run-up field observations.

Zhao et al. (2009) verified the generation of N-waves due to an earthquake event with numerical modelling and in Zhao et al. (2010) the authors found N-wave signature in different tsunami wave patterns near the source, for different earthquake magnitudes, meeting other observations by Tadepalli and Synolakis (1996a).

Proposed analytical and laboratory benchmarks included N-waves as initial wave profile (Synolakis et al., 2007), but have been mainly focused on solitary waves. More recently research work concerning generation of N-waves in laboratory has been performed. Schmidt-Koppenhagen et al. (2006) applied solitary wave theory and a piston-type wave-maker to generate what they designated by composed tsunami waves, with both positive and negative wave segments. These waves resembled leading depression N-waves; however, its generation corresponded to the plate trajectory of one negative solitary wave plus the plate trajectory of a positive solitary wave (as also suggested by Madsen and Schäffer, 2010). After this work, N-waves have been generated by several authors (Rossetto et al., 2011; Klettner et al., 2012; Charvet et al., 2013; Goseberg et al., 2013; Schimmels et al., 2014; Bağcı and Kabdaşlı, 2015; Drähne et al., 2016; McGovern et al., 2016; Sriram et al., 2016). Yet, a theoretical formulation for the generation of Tadepalli–Synolakis generalized N-waves with a piston-like wave-maker is still missing, although the combination of elongated solitary waves, as proposed by Schimmels and co-workers (Schimmels et al., 2014, 2016; Sriram et al., 2016), can be used to fit the generalized N-wave profile.

2.2. Solitary wave

A solitary wave can be described by:

$$\eta(x, t) = H \cdot \mathrm{sech}^2\theta \tag{1}$$

where η is the surface elevation, x is the horizontal coordinate, t is the time, the argument θ is

$$\theta = \kappa \cdot (x - c \cdot t - x_1) \tag{2}$$

c is the wave velocity, H is the wave height, κ is a generalized wavenumber, and $x = x_1$ is the wave crest position at $t = 0$. An apparent wavelength can be defined as

$$\lambda = \frac{2 \cdot \pi}{\kappa} , \tag{3}$$

and an apparent wave period as

$$T = \frac{\lambda}{c} . \tag{4}$$

For expression (1) to be a first order permanent solution of the Boussinesq equations (Peregrine, 1967), the generalized wavenumber should be such that

$$\kappa = \sqrt{\frac{3}{4} \cdot \frac{H}{d^3}} , \tag{5}$$

where d is the undisturbed water depth, and its wave velocity is

$$c = \sqrt{g \cdot (d + H)} , \tag{6}$$

where g is the gravity acceleration.

2.3. Amplitude and frequency dispersion of tsunami waves

Amplitude dispersion of a long wave is quantified by the non-linearity parameter ϵ, as the ratio between its height and the local depth, i.e.

$$\epsilon = \frac{H}{d} , \tag{7}$$

while the frequency dispersion is quantified by the shallowness or dispersion parameter σ, as a relation between the local depth and the wavelength, defined as

$$\sigma = \kappa \cdot d . \tag{8}$$

The relation between these two phenomena is measured by the Stokes parameter, St, which gives an indication about the balance between non-linearity and dispersion of long surface gravity waves:

$$\mathrm{St} = \frac{\epsilon}{\sigma^2} . \tag{9}$$

In equation (9), the normalisation due to Stokes (1847), who first introduced this parameter, is used.[1] It can be shown that permanent long wave solutions in shallow water are only possible when amplitude dispersion (non-linearity) and frequency dispersion are in balance, i.e. when $\mathrm{St} \sim 1$ (see for instance Dingemans, 1997, page 183).

The Boussinesq solitary wave solution, with the wavenumber defined by equation (5), is a permanent form wave, with $\mathrm{St} = 4/3$. On the other hand, for real tsunami waves the Stokes parameter is several orders of magnitude larger. The near-shore tsunami trace of the Indian Ocean event in 2004, recorded by the Belgian yacht *Mercator*, located 1.6 km off the coast of South Phuket, over the continental shelf, at a depth of 14 m, showed a leading wave height of 6.6 m and a period of approximately 20 min (Grilli et al., 2007; Madsen and Fuhrman, 2008). Such a wave would have a length about 14 km and a Stokes parameter $\mathrm{St} \sim 10^4$. It is therefore evident that tsunami waves have independent wave heights and lengths and their forms will be unstable but, as stated by Madsen et al. (2008), this is a natural process that can be observed in nature.

2.4. Tadepalli–Synolakis N-wave

Real tsunami leading waves are usually described as an N-shaped wave with a leading trough, a leading depression N-wave (LDN-wave), or with a leading crest, a leading elevation N-wave (LEN-wave). Such N-waves were described by Tadepalli and Synolakis (1994, 1996a) as

$$\eta(x, t) = \varepsilon \cdot (\theta - \kappa \cdot \delta) \cdot H \cdot \mathrm{sech}^2\theta , \tag{10}$$

where ε is a scale factor necessary to define the wave height as H, $\delta = x_2 - x_1$ is an eccentricity parameter, defined as the distance between $x = x_2$, the location of the inflexion point of the wave profile at $t = 0$, thus $\eta(x_2, 0) = 0$, and $x = x_1$, the location at $t = 0$ of the crest of a solitary wave of the same height H and length λ (cf. Fig. 1).

The wave height H of an N-wave is obtained as $H = a^+ + a^-$, where a^+ is the amplitude of the wave crest, and a^- is the amplitude of the wave trough. The magnitude of the scale factor ε and the ratio a^-/a^+

[1] Ursell (1953), who further elaborated on the meaning of this parameter, used a different normalisation commonly known in the engineering community as the Ursell number, $\mathrm{Ur} = (H/d) \cdot (\lambda/d)^2$. This parameter is more sensitive to the definition of the wavelength. For the Boussinesq solitary wave, and depending on the wavelength definition, the Ursell number varies from $\mathcal{O}(10)$ to $\mathcal{O}(10^2)$, while the Stokes parameter remains $\mathcal{O}(1)$.

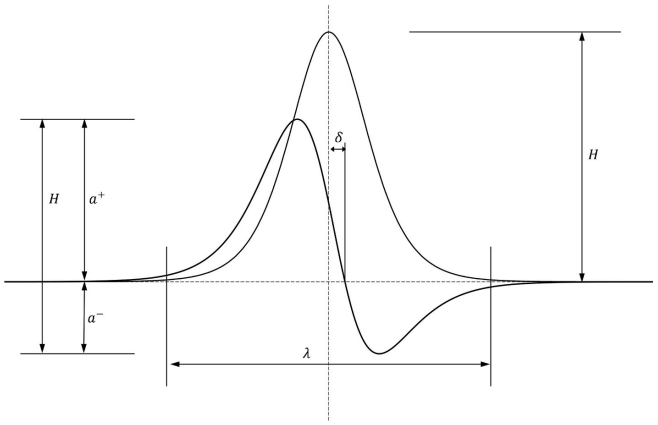

Fig. 1. N-wave profile and corresponding solitary wave of the same height H and length λ..

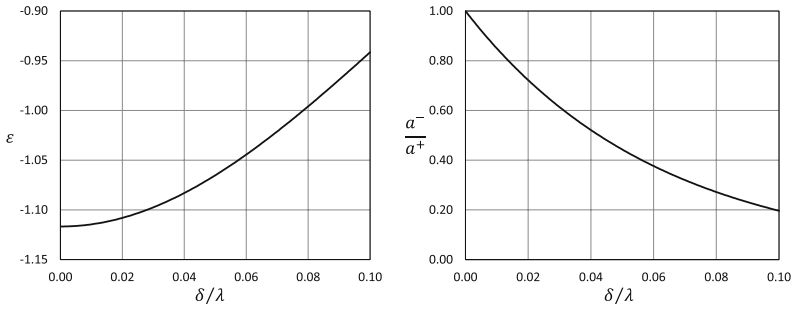

(a) LDN-wave.

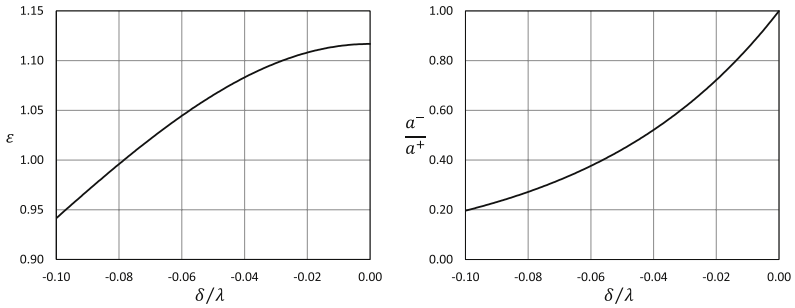

(b) LEN-wave.

Fig. 2. ε and a^-/a^+ as functions of δ/λ for an N-wave.

depend on the shifting ratio δ/λ (cf. Fig. 2). For $\varepsilon < 0$, an LDN-wave is obtained, while for $\varepsilon > 0$, an LEN-wave is defined. On the other hand, for $\delta = 0$ we have that $a^-/a^+ = 1$ and an isosceles N-wave is obtained, while for an LDN-wave, $\delta > 0$ leads to $a^- < a^+$, and $\delta < 0$ to $a^- > a^+$. For an LEN-wave, $\delta > 0$ leads to $a^- > a^+$, and $\delta < 0$ to $a^- < a^+$ (cf. Table 1).

3. N-wave generation by a piston wave-maker

In this section the theory of the generation of N-waves by a piston wave-maker is detailed: the paddle's trajectory, velocity and acceleration are derived and presented, as well as the expressions for the piston stroke and for the stroke period and initial velocity and initial acceleration.

3.1. Paddle trajectory

Let us assume that an N-wave is a wave of permanent form with wave velocity c, and closely following the reasoning of Goring and Raichlen (1980). For a wave of a permanent form (Svendsen and Justesen, 1984):

$$\int_{-d}^{\eta} u\, dz = c{\cdot}\eta + Q_s + U_c{\cdot}d\,, \tag{11}$$

where u is the particle velocity immediately in front of the wave-maker, is the non-linear mass flux averaged over a wave period, and U_c is the speed of the current defined as the averaged particle velocity below wave trough level. For an infinitely long wave, the right-hand side of (11) reduces to $c{\cdot}\eta$ (Grilli and Svendsen, 1990). Since the piston motion creates a depth uniform horizontal velocity $u = \bar{u}(t)$, equation (11) reduces to:

$$\bar{u}{\cdot}(d+\eta) = c{\cdot}\eta\,, \tag{12}$$

and thus the particle velocity is given by

$$\bar{u} = \frac{c{\cdot}\eta}{d+\eta}\,, \tag{13}$$

or in terms of the wave-maker's paddle velocity:

$$\dot{\xi} = \frac{c{\cdot}\eta}{d+\eta}\,, \tag{14}$$

where $\dot{\xi} = d\xi/dt$, and $\xi(t)$ is the paddle trajectory, which can be obtained through integration of equation (14).

Let us also assume that the wave has the form:

$$\eta(\xi, t) = \varepsilon{\cdot}H{\cdot}F(\theta)\,, \tag{15}$$

where

$$\theta = \kappa{\cdot}(\xi - c{\cdot}t - x_1)\,. \tag{16}$$

For a flat bottom, the total derivative of equation (16) is:

$$\frac{d\theta}{dt} = \kappa{\cdot}(\dot{\xi} - c)\,, \tag{17}$$

and thus

$$\dot{\xi} = \frac{d\xi}{dt} = \frac{d\xi}{d\theta}\cdot\frac{d\theta}{dt} = \frac{d\xi}{d\theta}{\cdot}\kappa{\cdot}(\dot{\xi} - c)\,. \tag{18}$$

Substituting equation (14) into equation (18), one obtains

$$\frac{d\xi}{d\theta} = \frac{\dot{\xi}}{\kappa{\cdot}(\dot{\xi} - c)} = -\frac{\eta}{\kappa{\cdot}d}\,, \tag{19}$$

which, after substituting equation (15) into it, becomes

$$\frac{d\xi}{d\theta} = -\frac{\varepsilon{\cdot}H}{\kappa{\cdot}d}{\cdot}F(\theta)\,, \tag{20}$$

and considering that $\theta \to +\infty$ when $t \to -\infty$, integrates as

$$\xi(t) = \lim_{t\to-\infty}\xi(t) + \frac{\varepsilon{\cdot}H}{\kappa{\cdot}d}\cdot\int_{\theta(t)}^{+\infty} F(\varphi)\, d\varphi\,. \tag{21}$$

Now, for an N-wave

$$F(\theta) = (\theta - \kappa{\cdot}\delta){\cdot}\mathrm{sech}^2\theta\,, \tag{22}$$

and therefore

$$\int_{\theta(t)}^{+\infty} F(\varphi)\, d\varphi = \int_{\theta(t)}^{+\infty} \varphi{\cdot}\mathrm{sech}^2\varphi\, d\varphi - \kappa{\cdot}\delta{\cdot}\int_{\theta(t)}^{+\infty}\mathrm{sech}^2\varphi\, d\varphi. \tag{23}$$

Integrating by parts the first integral in the right-hand side of equation (23), we get

$$\begin{aligned}\int_{\theta(t)}^{+\infty} \varphi{\cdot}\mathrm{sech}^2\varphi\, d\varphi &= \int_{\theta(t)}^{+\infty} \tfrac{d}{d\varphi}(\varphi{\cdot}\tanh\varphi)\, d\varphi - \int_{\theta(t)}^{+\infty}\tanh\varphi\, d\varphi\\ &= [\varphi{\cdot}\tanh\varphi - \ln(\cosh\varphi)]_{\theta(t)}^{+\infty}\,,\end{aligned} \tag{24}$$

while the second integral is

$$\int_{\theta(t)}^{+\infty}\mathrm{sech}^2\varphi\, d\varphi = [\tanh\varphi]_{\theta(t)}^{+\infty}\,. \tag{25}$$

Thus

$$\int_{\theta(t)}^{+\infty} F(\varphi)\, d\varphi = \ln(\cosh\theta) - (\theta - \kappa{\cdot}\delta){\cdot}\tanh\theta + \ln 2 - \kappa{\cdot}\delta\,. \tag{26}$$

Finally, assuming that $\lim_{t\to-\infty}\xi = 0$, the piston trajectory for the generation of an N-wave becomes

$$\xi(t) = -\frac{\varepsilon{\cdot}H}{\kappa{\cdot}d}{\cdot}[(\theta - \kappa{\cdot}\delta){\cdot}\tanh\theta - \ln(2{\cdot}\cosh\theta) + \kappa{\cdot}\delta]\,. \tag{27}$$

As θ is a function of ξ, equation (27) is implicit in ξ, and an iterative solution shall be sought.

3.2. Piston's velocity and acceleration

From equation (14), an expression for the piston velocity can be obtained as:

$$\dot{\xi} = \frac{\varepsilon{\cdot}H{\cdot}(\theta - \kappa{\cdot}\delta){\cdot}c}{\varepsilon{\cdot}H{\cdot}(\theta - \kappa{\cdot}\delta) + d{\cdot}\cosh^2\theta}\,. \tag{28}$$

The maximum positive and the maximum negative velocities correspond to $d\dot{\xi}/dt = 0$, which is equivalent to

$$\frac{d\dot{\xi}}{d\eta} = 0 \vee \frac{d\eta}{dt} = 0\,. \tag{29}$$

As

$$\frac{d\dot{\xi}}{d\eta} = \frac{c{\cdot}d}{(d+\eta)^2}\,, \tag{30}$$

and thus definite positive, the maximum velocities of the piston coincide with $d\eta/dt = 0$, i.e. with the crest and the trough of the N-wave. So for $\eta = a^+$,

$$\dot{\xi}_{\max} = \frac{c{\cdot}a^+}{d+a^+}\,, \tag{31}$$

and for $\eta = -a^-$,

$$\dot{\xi}_{\min} = -\frac{c{\cdot}a^-}{d-a^-}, \tag{32}$$

An expression for the acceleration of the piston, $\ddot{\xi}$, can be obtained from:

Table 1
N-wave profiles as a function of δ.

	Wave type	$\delta < 0$	$\delta = 0$	$\delta > 0$
$\varepsilon < 0$	LDN-wave	$a^-/a^+ > 1$	$a^-/a^+ = 1$	$a^-/a^+ < 1$
$\varepsilon > 0$	LEN-wave	$a^-/a^+ < 1$	$a^-/a^+ = 1$	$a^-/a^+ > 1$

$$\ddot{\xi} = \frac{d\dot{\xi}}{d\eta}\cdot\frac{d\eta}{d\theta}\cdot\frac{d\theta}{dt}\,, \tag{33}$$

where $d\dot{\xi}/d\eta$ is given by expression (30), $d\theta/dt$ is given by equation (17) and $d\eta/d\theta$ is:

$$\frac{d\eta}{d\theta} = \varepsilon\cdot H\cdot\mathrm{sech}^2\theta\cdot[1 - 2\cdot(\theta - \kappa\cdot\delta)\cdot\tanh\theta]\,. \tag{34}$$

Finally,

$$\ddot{\xi}(t) = c^2\cdot\kappa\cdot d\cdot\varepsilon\cdot H\cdot\mathrm{sech}^2\theta\cdot\frac{1 - 2\cdot(\theta-\kappa\cdot\delta)\cdot\tanh\theta}{[d + \varepsilon\cdot H\cdot(\theta-\kappa\cdot\delta)\cdot\mathrm{sech}^2\theta]^2} \cdot\left[\frac{\varepsilon\cdot H\cdot(\theta-\kappa\cdot\delta)\cdot\mathrm{sech}^2\theta}{d + \varepsilon\cdot H\cdot(\theta-\kappa\cdot\delta)\cdot\mathrm{sech}^2\theta} - 1\right]. \tag{35}$$

3.3. Piston stroke

The paddle trajectory for an N-wave generation consists of two consecutive movements, a backward one and a forward one, for an LDN-wave, and vice-versa for an LEN-wave. Hence, it is necessary to distinguish between the total displacement of the paddle, D, defined as

$$D = \lim_{t\to+\infty}\xi(t) - \lim_{t\to-\infty}\xi(t)\,, \tag{36}$$

and given by

$$D = -2\cdot\varepsilon\cdot\delta\cdot\frac{H}{d} = -4\pi\cdot\frac{\delta}{\lambda}\cdot\frac{\varepsilon\cdot H}{\kappa\cdot d}\,, \tag{37}$$

and the paddle stroke, S, defined as the total amplitude of the paddle trajectory, which for an LDN-wave, with $a^-/a^+ < 1$, is

$$S = D - \xi_{\min}\,, \tag{38}$$

and for an LEN-wave is

$$S = \xi_{\max} - D\,. \tag{39}$$

As a local minimum (or a maximum) of $\xi(t)$ exists for t such that $d\xi/d\theta = 0$, which happens when $\theta = \kappa\cdot\delta$, it is easy to conclude that

$$\xi_{\min} = \xi_{\max} = -\frac{\varepsilon\cdot H}{\kappa\cdot d}\cdot[\kappa\cdot\delta - \ln(2\cdot\cosh(\kappa\cdot\delta))]\,, \tag{40}$$

from where, for an LDN-wave,

$$S = -\frac{\varepsilon\cdot H}{\kappa\cdot d}\cdot[\kappa\cdot\delta + \ln(2\cdot\cosh(\kappa\cdot\delta))]\,, \tag{41}$$

and for an LEN-wave,

$$S = \frac{\varepsilon\cdot H}{\kappa\cdot d}\cdot[\kappa\cdot\delta + \ln(2\cdot\cosh(\kappa\cdot\delta))]\,. \tag{42}$$

3.4. Stroke period

As for a solitary wave, the leading and trailing edges of an N-wave occur at $t = -\infty$ and $t = +\infty$. However, and for practical purposes, one shall assume that they are two wave periods apart and that the wave is centred at the crest of the associated solitary wave of the same height and length. The stroke period, τ, i.e. the duration of the paddle motion, is defined as the time period between the instants at which the leading and trailing edge characteristics intersect the paddle trajectory, thus:

$$\tau = 2\cdot T + \frac{D}{c}\,, \tag{43}$$

which can be expanded as

$$\tau = \frac{4\cdot\pi}{\kappa\cdot c}\cdot\left(1 - \varepsilon\cdot\frac{H}{d}\cdot\frac{\delta}{\lambda}\right). \tag{44}$$

The phase planes for the paddle trajectories, for both LDN- and LEN-waves, are shown in Fig. 3. It is evident that when the crest amplitude is larger than the trough amplitude, $a^-/a^+ < 1$, the paddle motion is longer than twice the apparent wave period, while for waves with crest amplitude smaller than the trough amplitude, $a^-/a^+ > 1$, the paddle motion is shorter than twice the apparent wave period.

A family of normalized paddle trajectories is shown in Fig. 4, for an LDN-wave with fixed $\delta/\lambda = 0.06$ and wave height-to-depth ratios $H/d = 0.1 - 0.5$.

A family of normalized paddle trajectories is shown in Fig. 5, for an LDN-wave with fixed wave height-to-depth ratio $H/d = 0.1$ and for shifting ratios $\delta/\lambda = 0 - 0.10$.

3.5. Initial velocity and acceleration

Assuming that the leading and trailing edges of the N-wave are two periods or two wavelengths apart, and that the wave is centred at the crest of the associated solitary wave (see Fig. 1), this corresponds to considering that $x_1 = -\lambda$. As the scale factor is such that $|\varepsilon| \sim 1$ (see Fig. 2), and for a shifting ratio $\delta/\lambda \sim 0.05$, this corresponds to a wave with a free surface elevation reduction at both edges of $|\eta| < 10^{-4}H$. Furthermore, under these conditions, the initial velocity and acceleration of the piston can be shown to be, respectively:

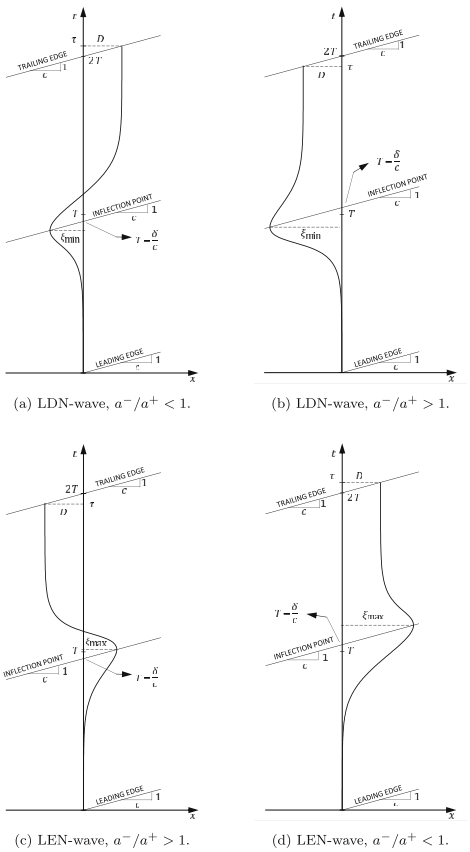

(a) LDN-wave, $a^-/a^+ < 1$. (b) LDN-wave, $a^-/a^+ > 1$.

(c) LEN-wave, $a^-/a^+ > 1$. (d) LEN-wave, $a^-/a^+ < 1$.

Fig. 3. Phase planes for paddle trajectories.

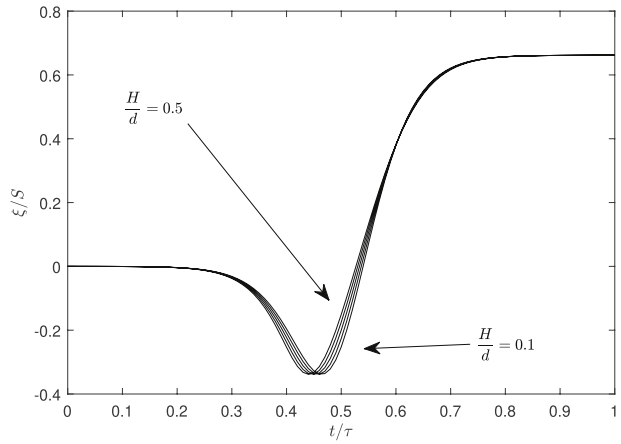

Fig. 4. Normalized paddle trajectories for LDN-waves with fixed $\delta/\lambda = 0.06$ shifting ratio, and wave height-to-depth ratios $H/d = 0.1 - 0.5$.

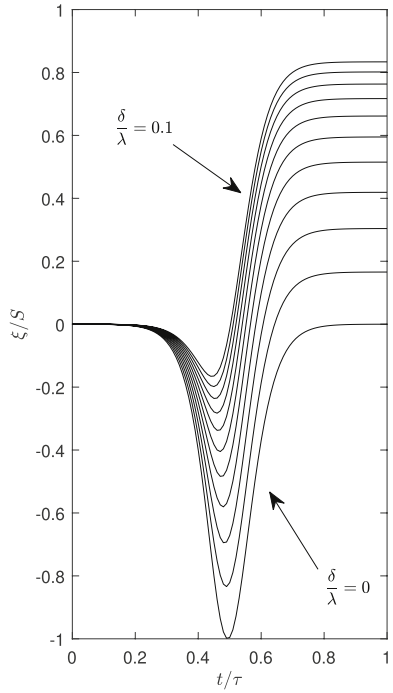

Fig. 5. Normalized paddle trajectories for LDN-waves with wave height-to-depth ratio $H/d = 0.1$, and variable $\delta/\lambda = 0 - 0.10$ ratio.

Table 2
Location of wave gauges.

Wave gauge	x (m)	y (m)
wg1	1.32	0.75
wg6	1.32	11.25
wg4	4.16	1.10
wg5	6.16	0.75
wg7	10.16	1.10
wg8	12.16	0.75
wg3	14.16	0.75

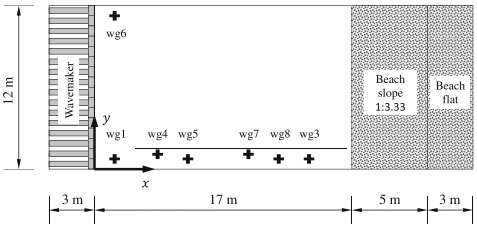

Fig. 6. Wave basin and wave gauges' positioning.

$$|\dot{\xi}(0)| < 10^{-4} \cdot \frac{H}{d} \cdot \sqrt{g \cdot d} \tag{45}$$

and

$$|\ddot{\xi}(0)| < 2 \times 10^{-4} \cdot \kappa \cdot H \cdot g \ . \tag{46}$$

These values are small enough to guarantee a smooth start and end of the paddle motion.

4. Wave basin experiments

4.1. Experimental setup

The LH-FEUP (Laboratory of Hydraulics of the Faculty of

Table 3
Wave conditions and wave-maker parameters.

Case	d	H	λ	T	δ/λ	ε	S	τ	ϵ	σ	St
	(m)	(m)	(m)	(s)	(−)	(−)	(m)	(s)	(−)	(−)	(−)
C12	0.26	0.150	5.47	3.43	0.04254	−1.079	0.54	7.04	0.58	0.30	6.47
C13	0.26	0.085	9.66	6.05	0.04254	−1.079	0.54	12.28	0.33	0.17	11.43
C14	0.26	0.065	12.63	7.91	0.04254	−1.079	0.54	16.01	0.25	0.13	14.94
C16	0.26	0.155	2.65	1.66	0.04254	−1.079	0.27	3.41	0.60	0.62	1.57
C17	0.26	0.070	5.86	3.67	0.04254	−1.079	0.27	7.44	0.27	0.28	3.46
C18	0.26	0.050	4.26	2.67	0.04254	−1.079	0.14	5.38	0.19	0.38	1.31

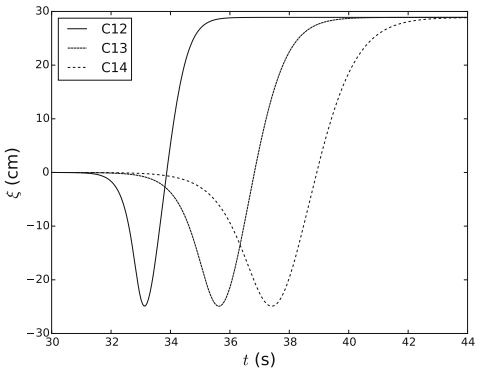

(a) C12, C13, C14

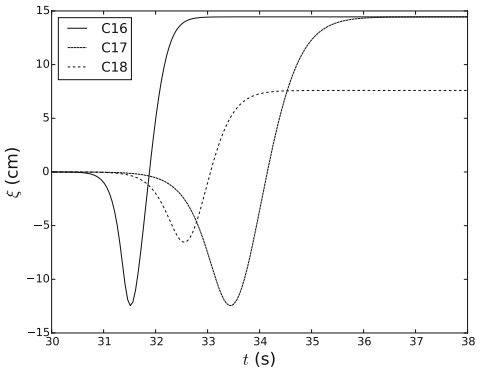

(b) C16, C17, C18

Fig. 7. Piston trajectories for the generation of the LDN-waves.

Engineering of the University of Porto) wave basin is 28 m long and 12 m wide, with a maximum water depth of 1.20 m. The floor and walls of the basin are made of concrete. The side walls of the basin have glass windows for flow observation. The wave-maker system occupies the first 3 m of the wave tank and the last 8 m are occupied by an absorbing beach with a 1:3.33 slope.

Table 4
Wave parameters recorded at wave gauge wg1.

Case	H	a^-	a^+	a^-/a^+
	(m)	(m)	(m)	(−)
C12	0.145	0.033	0.112	0.29
C13	0.062	0.022	0.040	0.55
C14	0.048	0.017	0.031	0.55
C16	0.106	0.018	0.088	0.20
C17	0.060	0.016	0.044	0.36
C18	0.043	0.010	0.033	0.30

The wave generator system is a multi-element piston wave-maker manufactured by HR Wallingford, which allows the generation of regular and irregular multi directional waves. It consists of 16 piston paddles, which are moved horizontally by electric motors. The maximum piston stroke is 1.08 m, the maximum velocity is 0.87 m/s and the maximum force is 1.5 kN. The paddle trajectory must be provided as a time series to the wave generator system.

Seven resistance wave gauges were used to acquire the surface elevation time series. The wave gauges were connected to two wave probe monitors, which in turn were connected to a computer with an HR Wallingford software program for data acquisition, conversion and analysis. A 1.5 m wide canal was set-up close to the southern wall of the tank. Six wave gauges were positioned along the length of the canal, while the seventh gauge was placed close to the northern wall of the tank, for control purposes (see Table 2 and Fig. 6).

4.2. Wave conditions

Six tsunami LDN-waves with wave heights ranging from 5 cm to 15.5 cm were generated, for a constant water depth of 26 cm and ratio $a^-/a^+ = 0.5$. The waves' characteristics and wave-maker parameters are shown in Table 3. The H/d ratios for the generated waves varied between 0.19 (small relative wave heights, $H/d < 0.3$) for C18 and 0.60 (large relative wave heights, $H/d > 0.3$) for C16.

The generated waves are classified into three groups, according to its Stokes parameter: C16 and C18 are shorter quasi-Boussinesq complying waves (St $\sim 4/3$), for which non-linearity and dispersion are close to equilibrium; C13 and C14 are longer non-linear waves, for which St>10; and an intermediate wavelength group for C12 and C17 ($3 <$ St < 10).

Trials were performed 5–10 min apart from each other to guarantee initial still water conditions, which was checked through visual observation. The real N-wave velocity, being unknown, was assumed to be given by the shallow water linear solution:

$$c = \sqrt{g \cdot d}\ , \tag{47}$$

where $g = 9.803$ m/s^2 is the local acceleration due to gravity, and thus $c = 1.60$ m/s.

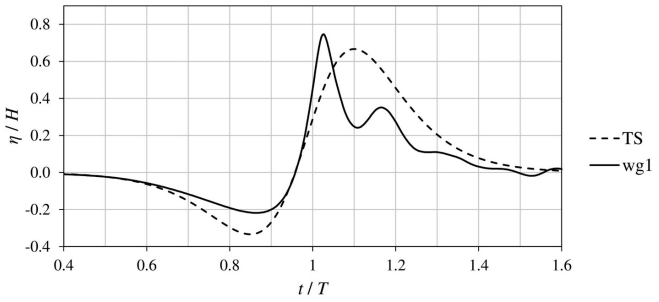

(a) C12

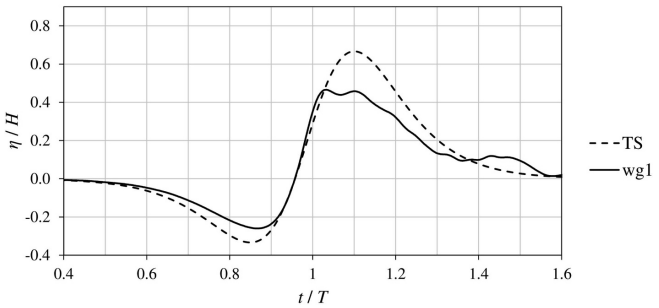

(b) C13

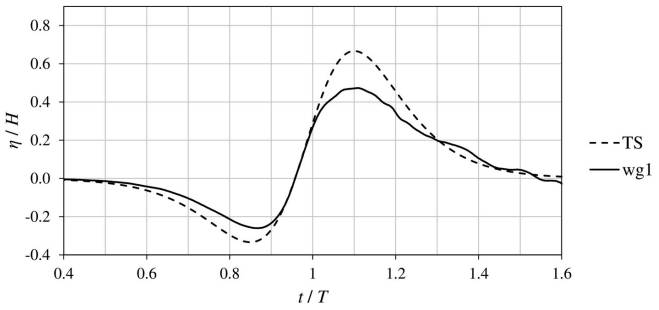

(c) C14

Fig. 8. Analytical TS LDN-wave profiles and experimental wave profiles recorded at wave gauge wg1.

4.3. Results and discussion

The piston trajectories were computed using equation (27) and the MATLAB® R2016b function *fsolve* for the iterative procedure. The corresponding time series are shown in Fig. 7. Experimental free surface elevation time series were registered at the seven wave gauges. The wave parameters recorded at wave gauge wg1 are listed in Table 4. Wave gauge wg6 was used for control purposes, therefore no results are

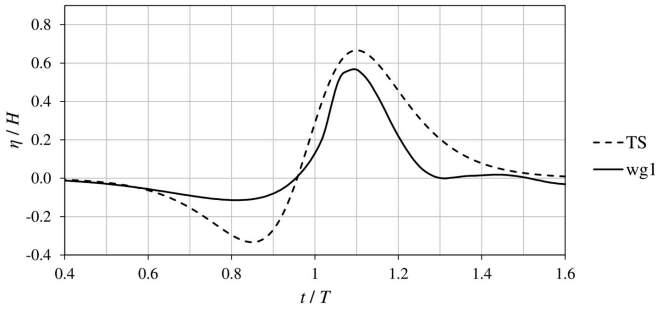

(a) C16

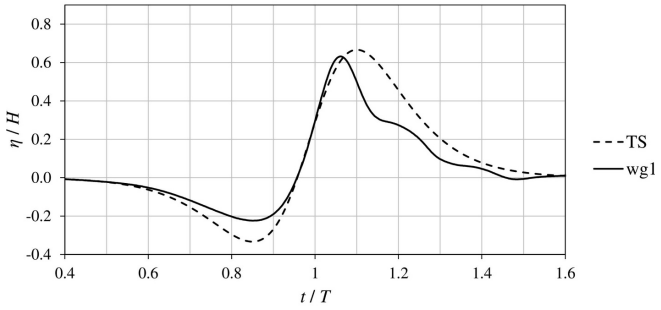

(b) C17

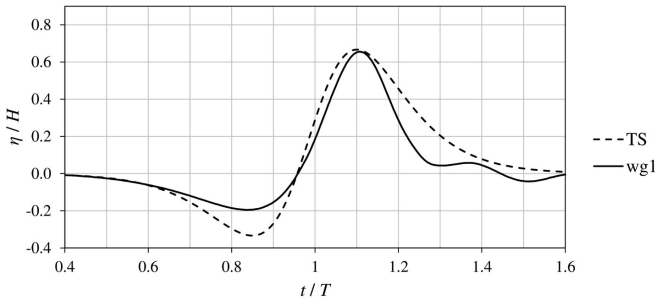

(c) C18

Fig. 9. Analytical TS LDN-wave profiles and experimental wave profiles recorded at wave gauge wg1.

presented for it. The expected TS (Tadepalli–Synolakis formulation) tsunami wave profile, as given by expression (10), and the actual wave profile recorded at wave gauge wg1 are compared in Figs. 8 and 9, where profiles are aligned by the leading ascending zero. In Figs. 10 and 11, the leading trough aligned profiles are shown for all wave gauges.

The accuracy of the experimental wave profiles is measured using the most common metrics, over the first complete wave period: (1) the Pearson correlation coefficient, r, defined as

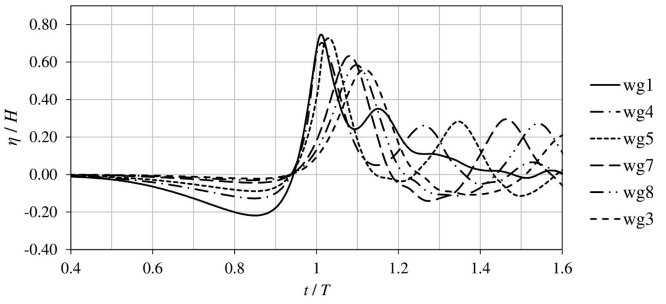

(a) C12

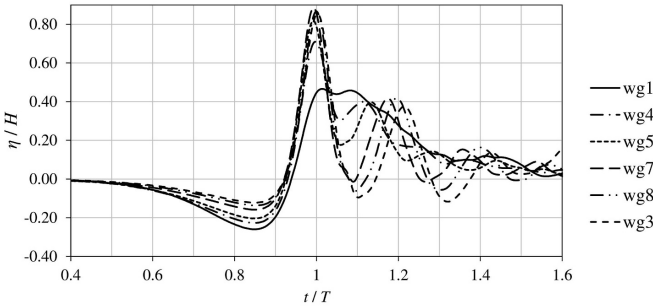

(b) C13

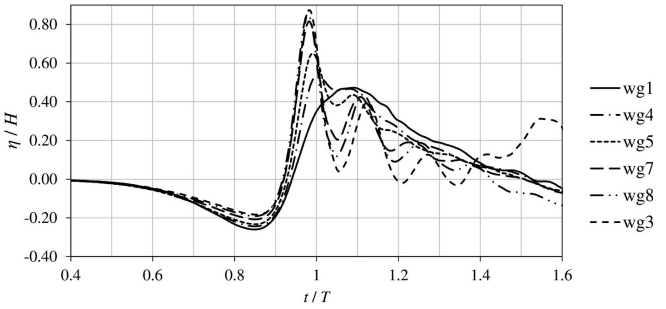

(c) C14

Fig. 10. Experimental wave profiles.

$$r = \frac{\mathrm{cov}(\eta^{\mathrm{TS}}, \eta^{\mathrm{wg1}})}{\sigma_{\eta^{\mathrm{TS}}} \cdot \sigma_{\eta^{\mathrm{wg1}}}}, \tag{48}$$

where $\mathrm{cov}(\cdot,\cdot)$ stands for the covariance function, $\sigma(\cdot)$ is the standard deviation, and η_{TS} and η_{wg1} are respectively the expected and the measured free surface elevations at wave gauge wg1; (2) the bias, given by

$$\mathrm{Bias} = \frac{1}{N}\sum_{i=1}^{N}\left(\eta_i^{\mathrm{wg1}} - \eta_i^{\mathrm{TS}}\right), \tag{49}$$

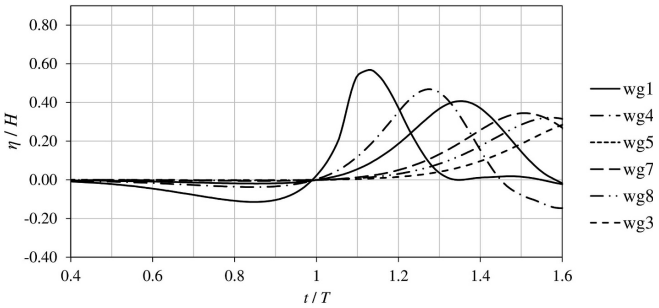

(a) C16

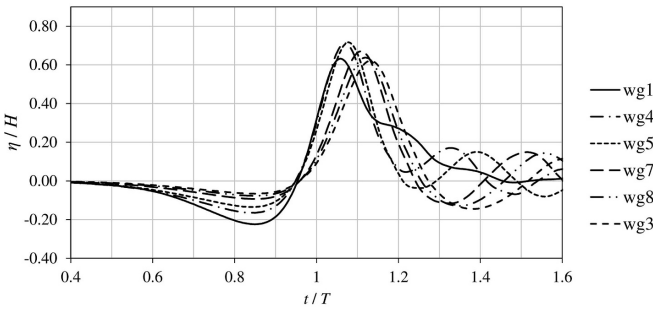

(b) C17

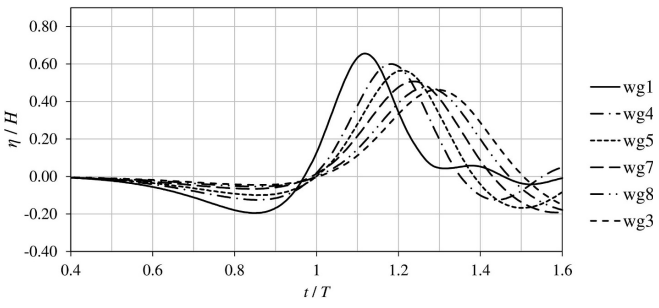

(c) C18

Fig. 11. Experimental wave profiles.

Table 5
Error metrics for wave gauge wg1.

Case	St	ϵ	r	Bias	RMSE
	(−)	(−)	(−)	(m)	(m)
C12	6.47	0.58	0.892	−0.0229	0.1194
C13	11.43	0.33	0.981	−0.0163	0.0912
C14	14.94	0.25	0.993	−0.0116	0.0796
C16	1.57	0.60	0.927	−0.0308	0.1407
C17	3.46	0.27	0.964	−0.0267	0.1026
C18	1.31	0.19	0.964	−0.0251	0.0959

Table 6
Measured wave velocities.

Case		$\bar{c}_{1-4}$	$\bar{c}_{4-5}$	$\bar{c}_{5-7}$	$\bar{c}_{7-8}$	$\bar{c}_{8-3}$	$\bar{c}$	$\bar{c}^*$
		(m/s)	(m/s)	(m/s)	(m/s)	(m/s)	(m/s)	(m/s)
C12	c^-	1.69	1.79	1.85	1.77	1.87	1.80	1.80
	c_0	1.71	1.80	1.85	1.78	1.87	1.80	1.81
	c^+	1.69	1.69	1.71	1.69	1.75	1.71	1.71
C13	c^-	1.50	1.57	1.67	1.67	1.71	1.62	1.61
	c_0	1.55	1.60	1.69	1.64	1.73	1.64	1.64
	c^+	1.60	1.61	1.66	1.61	1.68	1.63	1.64
C14	c^-	1.49	1.50	1.59	1.55	1.69	1.56	1.57
	c_0	1.54	1.56	1.62	1.58	1.67	1.59	1.60
	c^+	2.39	1.61	1.63	1.57	1.65	1.79	1.83
C16	c^-	1.80	1.83	1.90	1.79	1.96	1.86	1.87
	c_0	1.79	1.81	1.88	1.83	1.92	1.85	1.85
	c^+	1.56	1.65	1.69	1.63	1.71	1.65	1.65
C17	c^-	1.57	1.63	1.71	1.63	1.71	1.65	1.66
	c_0	1.59	1.63	1.68	1.63	1.71	1.65	1.65
	c^+	1.54	1.59	1.63	1.57	1.64	1.60	1.60
C18	c^-	1.64	1.64	1.64	1.64	1.69	1.65	1.65
	c_0	1.59	1.61	1.66	1.59	1.68	1.63	1.64
	c^+	1.49	1.54	1.59	1.53	1.60	1.55	1.56

where N is the number of observations within the range $t/T = 0.5$–1.5; (3) the root-mean-square error as:

$$\mathrm{RMSE} = \sqrt{\frac{1}{N}\sum_{i=1}^{N}\left(\eta_i^{\mathrm{wg1}} - \eta_i^{\mathrm{TS}}\right)^2}\ . \tag{50}$$

The computed metrics are presented in Table 5. Its analysis shows that a high linear correlation exists, with r close to or above 0.9, for all waves. For the two longer waves, C13 and C14, r is close to unity. Nevertheless, in all cases the bias is negative and for all cases, but the longer waves, its magnitude is larger than 2 cm, which corresponds to lower crest amplitudes and/or shorter crests. The magnitude of the root-mean-square error is about 10 cm for all waves, though slightly better for the longer waves and worse for the C16 case.

The mismatch between the analytical time series and the observed time series measured at wave gauge wg1 (see Figs. 8 and 9) is larger for the C12 and the C16 waves. For both waves the non-linearity parameter, ϵ, is above 0.50. As pointed out by Goring (1978), and later by Grilli (1997), a first-order long wave generation method for waves of permanent form is accurate for a wave height-to-depth ratio below 20%. One might expect that waves with a lower relative height perform better. On the other hand, the assumption that the N-waves have a propagation velocity given by expression (47) might not be the most correct and, as for the solitary wave case, the wave velocity might depend on the wave non-linearity.

The average wave velocities, measured between gauges, are shown in Table 6. Results are presented for velocities measured for the leading wave trough, c^-, for the leading ascending zero, c_0, and for the leading wave crest, c^+. Weighted average velocities, $\bar{c}$, were computed for the whole wave excursions from wg1 to wg3. Analysis of these velocities show a decrease of the wave velocities between gauges wg7 and wg8, $\bar{c}_{7-8}$, for all wave cases. The most probable reason is an error in the measured distance between wg8 and wg7. The average velocities were recomputed ignoring the wg8–wg7 run, and the results are presented as $\bar{c}^*$. Nevertheless, differences between $\bar{c}$ and $\bar{c}^*$ are very small (cf. Table 6).

Analysis of Fig. 8b, 8c, 10b and 10c show that waves C13 and C14, for which St>10, clearly display a bore like behaviour, exhibiting a steeper shorter wave front and a fission process that gives rise to two more waves trailing behind the main wave. Analysis of the measured wave velocities (see Table 6) show that these longer waves display $c^- \approx c_0 < c^+$, which leads to a decreasing distance between trough and crest.

On the other hand, the shorter quasi-Boussinesq waves C16 and C18, for which St $\sim 4/3$, seem to tend to a one-crested wave profile, keeping a wavelength close to the designed one at the first wave gauge (see Fig. 9a and 9c), with a small amplitude dispersive tail (cf. Fig. 11a and 11c). Besides that, these waves and also the intermediate wavelength waves, C17 and C12, display $c^- \approx c_0 > c^+$ (cf. Table 6), leading in this case to an increased distance between trough and crest.

The different behaviours are also evident in the evolution of the amplitude of the waves along the channel (cf. Fig. 12). The two shorter waves, C16 and C18, show a continuous decrease in all amplitudes, H, a^+ and a^-. The ratio $H_{\mathrm{obs}}/H_{\mathrm{TS}}$, where obs stands for observed and TS stands for the Tadepalli–Synolakis formulation, is always below unity with a monotonous decrease along the channel. In fact, all the observed to TS amplitude ratios display that pattern, for both waves. This leads to $(a^-/a^+)_{\mathrm{obs}}$ lower than the expected value of 0.5 at the first gauge, and close to 0.1 for $x/\lambda \approx 2$ (cf. Fig. 12d and 12f).

The longer waves, C13 and C14, display all observed to expected amplitude ratios close to $0.7 - 0.8$ at gauge wg1, but while $H_{\mathrm{obs}}/H_{\mathrm{TS}}$ increases towards 1.0 as x/λ approaches 1.0, $a^+_{\mathrm{obs}}/a^+_{\mathrm{TS}}$ has a faster rate of increase and reaches 1.4 at the same point, and thus $a^-_{\mathrm{obs}}/a^-_{\mathrm{TS}}$ seems to monotonously decrease along the channel, being close to 0.5 for $x/\lambda = 1$ (cf. Fig. 12b and 12c).

The waves in the third set, C12 and C17, display a mixed behaviour. Wave C12 behaves as the shorter waves (cf. Fig. 12a), while wave C17 shows a behaviour closer to that of the longer waves (cf. Fig. 12e), as expected from the differences in their Stokes parameters (see Table 3).

The traces of the generated LDN-waves at each wave gauge are represented in Fig. 13 for the shorter waves C13 and C14, in Fig. 14 for the longer waves C16 and C18, and in Fig. 15 for the intermediate length waves C12 and C17. It is clear that the shorter quasi-Boussinesq complying waves C16 and C18 suffer a strong transformation, tending towards a solitary wave type shape followed by a trough. Such a transformation does not seem to occur for the longer waves, i.e. larger Stokes parameter wave pair, C16 and C18. Nevertheless, the ratio between propagation time and wave period, or between propagation distance and wavelength, is much shorter for these longer waves, and further research must be done for longer trajectories.

The distance between wave gauge wg3 and the absorbing beach at the back end of the basin is very short, thus some interaction between the generated and the reflected waves might show up in the records. Wave reflection is expected to occur when the leading wave trough reaches the still water shoreline. For 26 cm water depth the still water shoreline is located 3.71 m away from wave gauge wg3. For the longest waves generated, C13 and C14, the highest measured wave velocities for the wg8–wg3 run were the trough defined ones, $c^- = 1.71$ m/s and $c^- = 1.69$ m/s respectively (cf. Table 6). Under these conditions, the total excursion time, back and forth from wg3 to the beach, would be $\Delta t = 4.33$ s for C13 and $\Delta t = 4.39$ s for C14, corresponding respectively to $\Delta t/T = 0.72$ and $\Delta t/T = 0.55$. In Figs. 10 and 11, the wave profiles are leading trough aligned at $t/T = 0.85$, thus the reflected wave is expected to show up in the wave record at $t/T = 1.57$ for wave C13 and at $t/T = 1.40$ for wave C14. Analysis of wg3 wave record for wave C14 (cf. Fig. 10c) clearly shows the arrival of the reflected wave and its interaction with the generated wave for $t/T > 1.40$. For wave C13 the

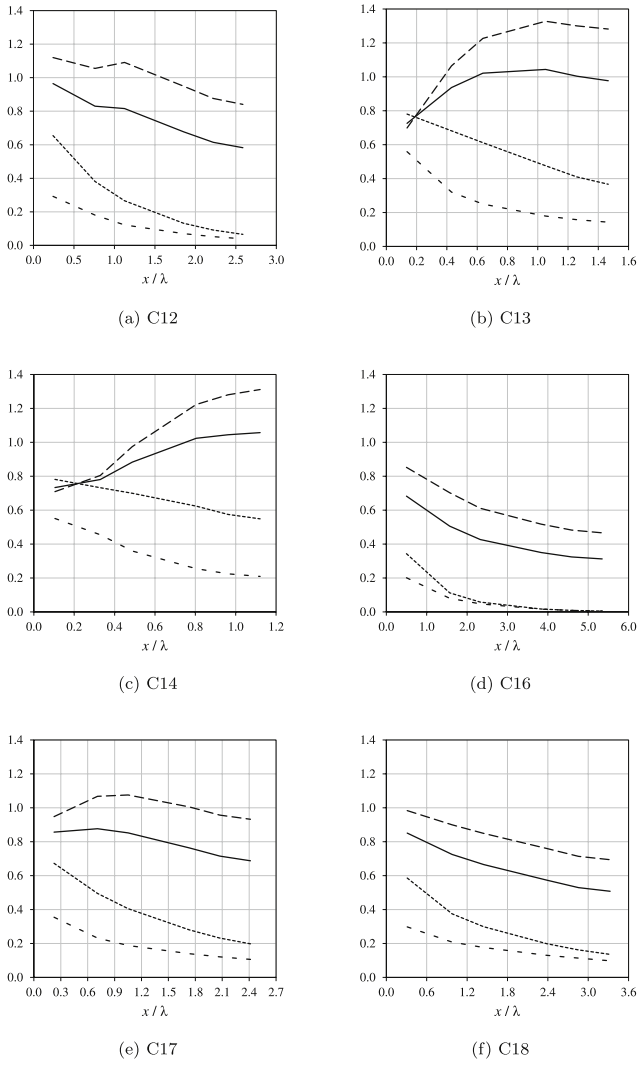

Fig. 12. Variation of wave amplitudes along the channel. H_{obs}/H_{TS} (−); a^{+}_{obs}/a^{+}_{TS} (– –); a^{-}_{obs}/a^{-}_{TS} (- - -); $(a^{-}/a^{+})_{obs}$ (– · –).

interaction at wave gauge wg3 occurs for $t/T > 1.57$, although not evident in the reproduced wave record, as the plot ends at $t/T = 1.60$ (cf. Fig. 10b). For all other wave gauges and wave cases the interaction between the generated and the reflected wave occurs for $t/T > 1.60$, not shown in the wave records in Figs. 10 and 11, therefore not affecting the previous discussion of results. The reflected waves' relative time of arrival at wave gauge wg3 is presented in Table 7, for all wave cases.

5. Summary and concluding remarks

In this study, the generation of N-waves in a wave flume is described. A novel first-order theoretical formulation, necessary to generate this type of waves experimentally, by means of a piston wave generating system, is detailed. The expressions for the piston's trajectory, velocity and acceleration were derived, as well as the expressions for the paddle stroke, the stroke period, and the maximum paddle velocities. Limits for the initial paddle velocity and acceleration were

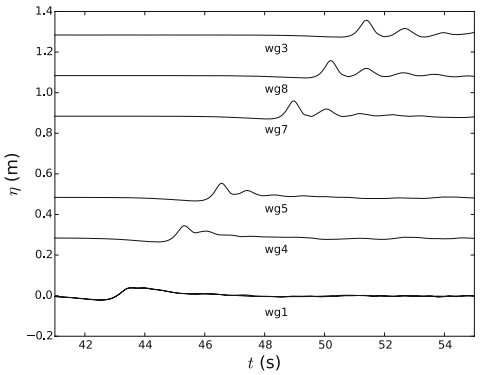

(a) C13

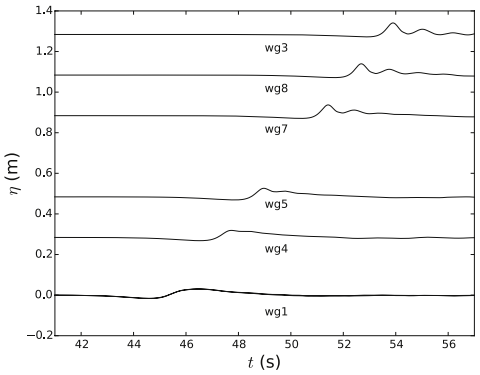

(b) C14

Fig. 13. Recorded LDN-wave traces for the shorter waves (St ∼ 4/3).

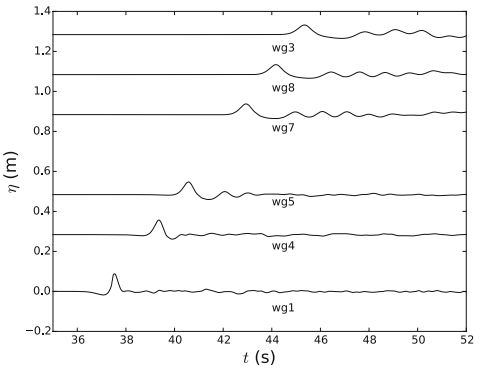

(a) C16

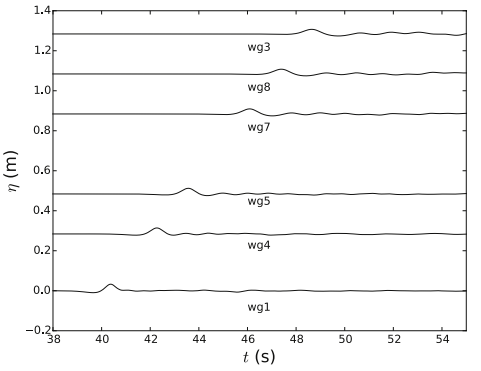

(b) C18

Fig. 14. Recorded LDN-wave traces for the longer waves (St>10).

established.

Six LDN-waves with relative wave heights between 0.19 and 0.60 were generated in the laboratory. The generated waves were classified into three groups, according to their Stokes parameters: shorter quasi-Boussinesq complying waves, with St ∼ 4/3; longer waves, with St>10; mixed behaviour waves, with $3 < St < 10$. The obtained results were presented and compared with the intended theoretical Tadepalli–Synolakis N-wave profiles. From that analysis, it was concluded that the shorter quasi-Boussinesq complying waves endure a strong transformation, tending to a solitary wave-type shape, followed by a trough. On the other hand, this behaviour was not observed for the longer waves, St>10, which seemed to tend to a leading trough bore-shaped wave. The generated longer waves presented the best results when compared with the expected Tadepalli–Synolakis N-wave profiles.

The discrepancies found between the analytical and the experimental wave time histories might be a consequence of the large height-to-depth ratio of the generated waves. Other authors reported that for solitary waves the height-to-depth ratio shall not exceed 20%, when a first-order generation method is used.

Further research shall be done for N-waves with smaller relative heights and larger Stokes parameters, as these are a better model for real tsunami waves. Whenever possible, longer trajectories shall be tested. The formulation of time-dependent wave velocity, as proposed by other researchers, shall be investigated, as it might lead to an increased accuracy in the obtained N-wave profile.

This research work presents a novel first-order theoretical formulation for the generation of N-waves in a wave flume, by means of a piston wave-maker. Moreover, the authors did not find any report of laboratory experiments of N-waves with characteristics similar to those described herein, and for a wave tank with similar dimensions. The authors expect that the present research work might contribute to a better understanding and definition of the theoretical principles behind the generation of N-waves in laboratory.

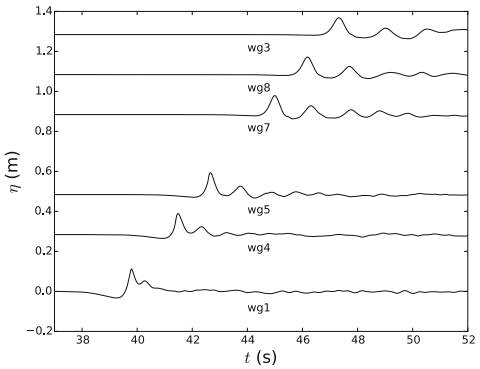

(a) C12

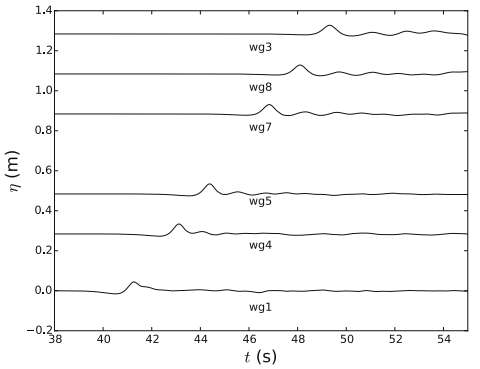

(b) C17

Fig. 15. Recorded LDN-wave traces for the mixed behaviour waves ($3 < \mathrm{St} < 10$).

Table 7
Time of arrival of the reflected wave at wg3.

Case	T	$\bar{c}$	Δt	$\Delta t/T$	t_{Arrival}/T
	(s)	(m/s)	(s)	(−)	(−)
C12	3.43	1.87	3.96	1.16	2.00
C13	6.05	1.71	4.33	0.72	1.57
C14	7.91	1.69	4.39	0.55	1.40
C16	1.66	1.96	3.78	2.28	3.13
C17	3.67	1.71	4.33	1.18	2.03
C18	2.67	1.69	4.39	1.69	2.49

Acknowledgements

This research was partially supported by the Research Line ECOSERVICES, integrated in the Structured Program of R&D&I INNOVMAR: Innovation and Sustainability in the Management and Exploitation of Marine Resources (NORTE-01-0145-FEDER-000035), funded by the Northern Regional Operational Programme (NORTE 2020) through the European Regional Development Fund. The first author was supported by FCT grant SFRH/BD/96725/2013. The authors would like to thank LH-FEUP for access to the laboratory facilities, support and assistance provided during the lab research work, and Dr. Paulo Rosa-Santos for his help and support with the HR Wallingford wave-maker and software. The authors would also like to thank the anonymous referee for the constructive comments, that very much helped to improve this research paper, and the journal editor for his comments.

Appendix A. Supplementary data

Supplementary data to this article can be found online at https://doi.org/10.1016/j.coastaleng.2019.02.012.

References

Aydin, B., Kânoğlu, U., 2017. New analytical solution for nonlinear shallow water-wave equations. Pure Appl. Geophys. 174 (8), 3209–3218.
Baldock, T.E., Cox, D., Maddux, T., Killian, J., Fayler, L., 2009. Kinematics of breaking tsunami wavefronts: a data set from large scale laboratory experiments. Coast. Eng. 56 (5), 506–516.
Bağcı, T., Kabdaşlı, M.S., 2015. Experimental investigation of effects of coastal morphology on N-waves. Int. J. Electron. Gov. 2 (2), 56–62.
Biésel, F., Suquet, F., 1951. Les appareils générateurs de houle en laboratoire. La Houille Blanche 5, 723–737.
Borerro, J., Ortiz, M., Titov, V.V., Synolakis, C.E., 1997. Field survey of Mexican tsunami produces new data, unusual photos. Eos, Trans. Am. Geophys. Union 78 (8), 85–88.
Briggs, J.M., Synolakis, C.E., Harkins, G.S., Green, D.R., 1995a. Laboratory experiments of tsunami run-up on a circular island. Pure Appl. Geophys. 144, 569–599.
Briggs, J.M., Synolakis, C.E., Harkins, G.S., Hughes, S.T., 1995b. Large scale three-dimensional laboratory measurements of tsunami inundation. In: In: Tsuchiya, Y., Shuto, N. (Eds.), Tsunami: Progress in Prediction, Disaster Prevention and Warning, Vol. 4 of Advances in Natural and Technological Hazards Research Springer, Dordrecht, pp. 129–149.
Camfield, F.E., Street, R.L., 1969a. Shoaling of solitary waves on small slopes. J. Waterw. Harb. Div. 95 (1), 1–22.
Camfield, F.E., Street, R.L., 1969b. The effects of bottom configuration on the deformation, breaking and run-up of solitary waves. In: O'Brien, M.P. (Ed.), Proceedings of 11th Conference on Coastal Engineering. ASCE, London, United Kingdom, pp. 173–189 1968.
Carrier, G.F., Wu, T.T., Yeh, H., 2003. Tsunami run-up and draw-down on a plane beach. J. Fluid Mech. 475, 79–99.
Chan, I.-C., Liu, P.L.-F., 2012. On the runup of long waves on a plane beach. J. Geophys. Res.: Oceans 117, C08006.
Chang, Y.-H., Hwang, K.-S., Hwung, H.-H., 2009. Large-scale laboratory measurements of solitary wave inundation on a 1:20 slope. Coast. Eng. 56 (10), 1022–1034.
Charvet, I., Eames, I., Rossetto, T., 2013. New tsunami runup relationships based on long wave experiments. Ocean Model. 69, 79–92.
Daemrich, K.F., Götschenberg, A., 1988. Wave generation and analysis in channels of the SFB 205. In: Proceedings of the 2nd International Symposium on Wave Research and Coastal Engineering. Hannover, Leibnizhaus, Germany.
Daemrich, K.F., Eggert, W.D., Kohlhase, S., 1980. Investigations on irregular waves in hydraulic models. In: Edge, B.L. (Ed.), Proceedings of 17th Conference on Coastal Engineering. ASCE, Sydney, Australia, pp. 186–203 1980.
Daily, J.W., Stephan Jr., S.C., 1952. The Solitary Wave: its Celerity, Profile, Internal Velocities and Amplitude Attenuation, Tech. Rep. 8. Massachusetts Institute of Technology, Hydrodynamics Laboratory, Department of Civil and Sanitary Engineering.
Dingemans, M.W., 1997. Water Wave Propagation over Uneven Bottoms (In 2 Parts), Vol. 13 of Advanced Series on Ocean Engineering World Scientific.
Drähne, U., Goseberg, N., Vater, S., Beisiegel, N., Behrens, J., 2016. An experimental and numerical study of long wave run-up on a plane beach. J. Mar. Sci. Eng. 4 (1), 1.
Fritz, H.M., Kongko, W., Moore, A., McAdoo, B., Goff, J., Harbitz, C., Uslu, B., Kalligeris, N., Suteja, D., Kalsum, K., Titov, V.V., 2007. Extreme runup from the 17 july 2006 Java tsunami. Geophys. Res. Lett. 34 (12), L12602.
Fritz, H.M., Petroff, C.M., Catalán, P.A., Cienfuegos, R., Winckler, P., Kalligeris, N., Weiss, R., Barrientos, S.E., Meneses, G., Valderas-Bermejo, C., Ebeling, C., 2011. Field survey of the 27 February 2010 Chile tsunami. Pure Appl. Geophys. 168 (11), 1989–2010.
Gao, J., Ji, C., Gaidai, O., Liu, Y., Ma, X., 2017. Numerical investigation of transient harbor oscillations induced by N-waves. Coast. Eng. 125, 119–131.
Geist, E., Yoshioka, S., 1996. Source parameters controlling the generation and propagation of potential local tsunamis along the Cascadia margin. Nat. Hazards 13 (2), 151–177.
Geist, E.L., 1998. Local tsunamis and earthquake source parameters. In: In: Dmowska, R., Saltzman, B. (Eds.), Tsunamigenic Earthquakes and Their Consequences, Vol. 39 of Advances in Geophysics Elsevier, pp. 117–209.
Goring, D.G., 1978. Tsunamis—The Propagation of Long Waves onto a Shelf. Ph.D.

thesis. California Institute of Technology report No. KH-R-38.
Goring, D., Raichlen, F., 1980. The generation of long waves in the laboratory. In: Edge, B.L. (Ed.), Proceedings of 17th Conference on Coastal Engineering. ASCE, Sydney, Australia, pp. 763–783 1980.
Goseberg, N., Wurpts, A., Schlurmann, T., 2013. Laboratory-scale generation of tsunami and long waves. Coast. Eng. 79, 57–74.
Grilli, S., Svendsen, I.A., 1990. Computation of nonlinear wave kinematics during propagation and runup on a slope. In: Tørum, A., Gudmestad, O.T. (Eds.), Water Wave Kinematics, NATO ASI Series E178. Kluwer Academic Publishers, The Netherlands, pp. 387–412.
Grilli, S., 1997. Fully nonlinear potential flow models used for long wave runup prediction. In: Yeh, H., Liu, P., Synolakis, C. (Eds.), Long-Wave Runup Models. World Scientific, pp. 116–180.
Grilli, S.T., Ioualalen, M., Asavanant, J., Shi, F.Y., Kirby, J.T., Watts, P., 2007. Source constraints and model simulation of the December 26, 2004, Indian ocean tsunami. J. Waterw. Port, Coast. Ocean Eng. 133 (6), 414–428.
Hall Jr., J.V., Watts, G.M., 1953. Laboratory Investigation of the Vertical Rise of Solitary Waves on Impermeable Slopes, Technical Memorandum 33, Beach Erosion Board. Army Coastal Engineering Research Center, Washington DC.
Hammack, J.L., Segur, H., 1974. The Korteweg-de Vries equation and water waves. Part 2. Comparison with experiments. J. Fluid Mech. 65 (2), 289–314.
Havelock, T.H., 1929. LIX. Forced surface-waves on water. The London, Edinburgh, and Dublin Philosophical Magazine and Journal of Science 8 (51), 569–576.
Hsu, H.-C., Chen, Y.-Y., Lin, C.-Y., Cheng, C.-Y., 2012. Experimental study of the velocity field in solitary water waves. J. Nonlinear Math. Phys. 19 (Suppl. 01), 1240003.
Hughes, S.A., 1993. Physical Models and Laboratory Techniques in Coastal Engineering, Vol. 7 of Advanced Series on Ocean Engineering World Scientific.
Jensen, A., Pedersen, G.K., Wood, D.J., 2003. An experimental study of wave run-up at a steep beach. J. Fluid Mech. 486, 161–188.
Jensen, A., Mayer, S., Pedersen, G.K., 2005. Experiments and computation of onshore breaking solitary waves. Meas. Sci. Technol. 16 (10), 1913–1920.
Kânoğlu, U., Titov, V.V., Aydın, B., Moore, C., Stefanakis, T.S., Zhou, H., Spillane, M., Synolakis, C.E., 2013. Focusing of long waves with finite crest over constant depth. Proceedings of the Royal Society A 469 (2153), 20130015.
Katell, G., Eric, B., 2002. Accuracy of solitary wave generation by a piston wave maker. J. Hydraul. Res. 40 (3), 321–331.
Kennard, E.H., 1949. Generation of surface waves by a moving partition. Q. Appl. Math. 7 (3), 303–312.
Klettner, C., Balasubramanian, S., Hunt, J., Fernando, H., Voropayev, S., Eames, I., 2012. Draw-down and run-up of tsunami waves on sloping beaches. Proceedings of the Institution of Civil Engineers – Engineering and Computational Mechanics 165 (2), 119–129.
Liang, D., Gotoh, H., Khayyer, A., Chen, J.M., 2013. Boussinesq modelling of solitary wave and N-wave runup on coast. Appl. Ocean Res. 42, 144–154.
Liu, P.L.-F., Cho, Y.-S., Briggs, M.J., Kânoğlu, U., Synolakis, C.E., 1995. Runup of solitary waves on a circular island. J. Fluid Mech. 302, 259–285.
Lu, H., Park, Y.S., Cho, Y.-S., 2017. Modelling of long waves generated by bottom-tilting wave maker. Coast. Eng. 122, 1–9.
Madsen, O.S., 1971. On the generation of long waves. J. Geophys. Res. 76 (36), 8672–8683.
Madsen, P.A., Fuhrman, D.R., 2008. Run-up of tsunamis and long waves in terms of surf-similarity. Coast. Eng. 55 (3), 209–223.
Madsen, O.S., 1970. Waves generated by a piston-type wavemaker. In: Johnson, J.W. (Ed.), Proceedings of 12th Conference on Coastal Engineering. ASCE, Washington, D.C., pp. 589–607 1970.
Madsen, P.A., Schäffer, H.A., 2010. Analytical solutions for tsunami runup on a plane beach: single waves, N-waves and transient waves. J. Fluid Mech. 645, 27–57.
Madsen, P.A., Fuhrman, D.R., Schäffer, H.A., 2008. On the solitary wave paradigm for tsunamis. J. Geophys. Res.: Oceans 113 (C12), 1–22.
Malek-Mohammadi, S., Testik, F.Y., 2010. New methodology for laboratory generation of solitary waves. J. Waterw. Port, Coast. Ocean Eng. 136 (5), 286–294.
Matsuyama, M., Tanaka, H., 2001. An experimental study of the highest run-up height in 1993 Hokkaido-Nansei-Oki earthquake tsunami. In: International Tsunami Symposium; Seattle, USA, August 7–10, 2001.
McGovern, D.J., Chandler, I., Rossetto, T., 2016. Experimental study of the runup of tsunami waves on a smooth sloping beach. In: Proceedings of the 6th International Conference on Application of Physical Modelling to Port and Coastal Protection. Coastlab16.
Oliveira, T.C.A., Sanchez-Arcilla, A., Gironella, X., Madsen, O.S., 2017. On the generation of regular long waves in numerical wave flumes based on the particle finite element method. J. Hydraul. Res. 55 (4), 538–556.
Pelinovsky, E.N., Mazova, R. Kh, 1992. Exact analytical solutions of nonlinear problems of tsunami wave run-up on slopes with different profiles. Nat. Hazards 6 (3), 227–249.
Peregrine, D.H., 1967. Long waves on a beach. J. Fluid Mech. 27 (4), 815–827.
Rossetto, T., Allsop, W., Charvet, I., Robinson, D.I., 2011. Physical modelling of tsunami using a new pneumatic wave generator. Coast. Eng. 58 (6), 517–527.
Schimmels, S., Sriram, V., Didenkulova, I., Fernández, H., 2014. On the generation of tsunami in a large scale wave flume. In: Lynett, P. (Ed.), Proceedings of 34th Conference on Coastal Engineering. Coastal Engineering Research Council, Seoul, Korea currents.14, 2014.
Schimmels, S., Sriram, V., Didenkulova, I., 2016. Tsunami generation in a large scale experimental facility. Coast. Eng. 110, 32–41.
Schmidt-Koppenhagen, R., Grüne, J., Oumeraci, H., 2006. Tsunami wave decay in near- and onshore areas. In: Smith, J.M. (Ed.), Proceedings of 30th Conference on Coastal Engineering. World Scientific, San Diego, California, pp. 1664–1676 2007.
Scott Russell, J., 1845. Report on waves. In: Report of the Fourteenth Meeting of the British Association for the Advancement of Science, York, John Murray, London, pp. 311–390.
Siva, M., Behera, M.R., 2016. Effect of continental slope on N-wave type tsunami run-up. The International Journal of Ocean and Climate Systems 7 (2), 47–54.
Sriram, V., Didenkulova, I., Sergeeva, A., Schimmels, S., 2016. Tsunami evolution and run-up in a large scale experimental facility. Coast. Eng. 111, 1–12.
Stokes, G.G., 1847. On the theory of oscillatory waves. Transactions of the Cambridge Philosophical Society 8, 441–455.
Svendsen, I.A., Justesen, P., 1984. Forces on slender cylinders from very high and spilling breakers. In: Proceedings of the Symposium on Description and Modelling of Directional Seas, Paper D-7-1. Technical University of Denmark 16 pp.
Synolakis, C.E., 1987. The runup of solitary waves. J. Fluid Mech. 185, 523–545.
Synolakis, C.E., 1990. Generation of long waves in laboratory. J. Waterw. Port, Coast. Ocean Eng. 116 (2), 252–266.
Synolakis, C.E., Bernard, E.N., Titov, V.V., Kânoğlu, U., González, F.I., 2007. Standards, Criteria, and Procedures for NOAA Evaluation of Tsunami Numerical Models, Technical Memorandum OAR PMEL-135 NOAA, Seattle, Washington.
Tadepalli, S., Synolakis, C.E., 1994. The run-up of N-waves on sloping beaches. Proc. Roy. Soc. Lond.: Mathematical and Physical Sciences A445, 99–112.
Tadepalli, S., Synolakis, C.E., 1996a. Model for the leading waves of tsunamis. Phys. Rev. Lett. 77, 2141–2144.
Tadepalli, S., Synolakis, C.E., 1996b. A realistic model for the 1992-96 tidal waves. In: Edge, B.L. (Ed.), Proceedings of 25th Conference on Coastal Engineering. ASCE, Orlando, Florida, pp. 1478–1490 1997.
Tanaka, M., 1986. The stability of solitary waves. Phys. Fluid. 29, 650–655.
Titov, V.V., Synolakis, C.E., 1997. Extreme inundation flows during the Hokkaido-Nansei-Oki tsunami. Geophys. Res. Lett. 24 (11), 1315–1318.
Ursell, F., 1953. The long wave paradox in the theory of gravity waves. Proc. Camb. Phil. Soc. 49, 685–694.
Ursell, F., Dean, R.G., Yu, Y.S., 1960. Forced small-amplitude water waves: a comparison of theory and experiment. J. Fluid Mech. 7 (1), 33–52.
Wei, Y., Bernard, E.N., Tang, L., Weiss, R., Titov, V.V., Moore, C., Spillane, M., Hopkins, M., Kânoğlu, U., 2008. Real-time experimental forecast of the Peruvian tsunami of August 2007 for US coastlines. Geophys. Res. Lett. 35 (4), L04609.
Whitham, G.B., 1974. Linear and Nonlinear Waves. John Wiley & Sons.
Zhao, X., Wang, B., Liu, H., 2009. Modelling the submarine mass failure induced tsunamis by Boussinesq equations. J. Asian Earth Sci. 36 (1), 47–55.
Zhao, X., Wang, B., Liu, H., 2010. Propagation and runup of tsunami waves with Boussinesq model. In: Smith, J.M., Lynett, P. (Eds.), Proceedings of 32nd Conference on Coastal Engineering, Shanghai, China. Coastal Engineering Research Council currents.9, 2011.

B.2 SWASH code

B.2.1 Introduction

The open access numerical code SWASH (Simulating WAves till SHore) by Zijlema et al. (2011) is suitable to model the nearshore processes in two-dimensional domains. It is a numerical model for simulating the wave propagation, transformation and nearshore phenomena from the offshore to the coastal zones.

B.2.2 Description, language and structure. Governing physics and numerical scheme

SWASH numerical model has been developed at TU Delft, with the main objective of modelling the nearshore processes of the coastal zones. It is based on the nonlinear shallow water equations, which describe the depth-averaged, non-hydrostatic, free surface flow. The SWE are presented in Chapter 2, expressions (2.52), (2.53), (2.54) in Cartesian coordinates and expressions (2.56), (2.57) and (2.58) in spherical coordinates. The bottom friction terms,τ_b, are different than zero.

The finite difference method is applied for the spatial discretisation of the equations and an explicit leapfrog scheme is used for time integration. A dynamically adjusted time step is implemented, which is controlled by the Courant number. The code has been validated with some of the classical benchmarks cases (Zijlema et al. 2011). For more details about the code, refer to Zijlema and Stelling (2005), Zijlema and Stelling (2008), Zijlema et al. (2011).

B.2.3 Benchmark test cases

B.2.3.1 Standing waves (seiches) in a basin

A standing or stationary wave is a wave oscillating in time, which remains in the same position; therefore, no motion is transmitted from one particle to the next one. Different particles have different amplitudes, with the minimum value at the nodes and the maximum value at the anti-nodes. Different particles throughout the wave oscillate in phase.

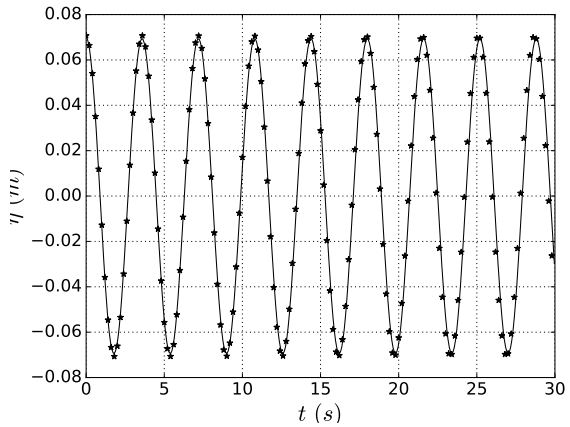

Figure B.1: Standing waves: (—) Exact solution. (* *) Numerical result, for $kh = 0.55\pi$ and depth-averaged mode.

Standing waves can be the result of the medium moving in the opposite direction of the wave or due to the interference of two waves traveling in opposite directions in a stationary medium. It is commonly a consequence of resonance within the medium.

Consider a standing wave resultant from the combination of an incident wave with a reflected wave. An harmonic wave traveling to the right along the x-axis can be described by the equation:

$$y_r(x,t) = A \cdot sin\left(\frac{2\pi x}{\lambda} - \omega t\right), \tag{B.1}$$

where A is the amplitude of the wave, x is the coordinate along x-axis, t is the time, λ is the wavelength, ω is the angular frequency and equal to $2\pi f$, where f is the frequency.

An identical harmonic wave traveling in the opposite direction to the latter can be described as follows:

$$y_l(x,t) = A \cdot sin\left(\frac{2\pi x}{\lambda} + \omega t\right). \tag{B.2}$$

Considering interference between both waves (Figure B.1), the resultant wave can be described by the equation:

$$y(x,t) = 2A \cdot sin\left(\frac{2\pi x}{\lambda}\right) cos(-\omega t). \tag{B.3}$$

B.2.3.2 Progressive waves in a basin

A progressive wave is a wave whose front is moving through the medium and traveling in time away from the source, on the sea surface or at an intermediate depth, referring to the specific coordinate system of the medium. It is a type of wave in which the energy transported is distributed from the source point to the surrounding areas. Energy is moved by means of the particles or fields vibrations. There are two types of progressive waves: transverse and longitudinal. In transverse waves, the particles vibrations are perpendicular to the wave motion. For horizontal motion, the particles will travel up and down (as in water and light). In longitudinal waves, the particles vibrations are parallel to the wave motion. For horizontal motion, the particles will be compressed or expanded as they travel (as sound waves and S-waves, the secondary or shear earthquake waves).

A progressive wave can be described by the equation:

$$y(x,t) = A \cdot sin\left(\frac{2\pi x}{\lambda} - \omega t\right), \tag{B.4}$$

where A is the amplitude of the wave, x is the coordinate along x-axis, t is the time, λ is the wavelength, ω is the angular frequency and equal to $2\pi f$, where f is the frequency. T is the wave period.

In this case study, a linear progressive wave in a wave flume is simulated for increasing values of κh and number of layers (Figure B.2).

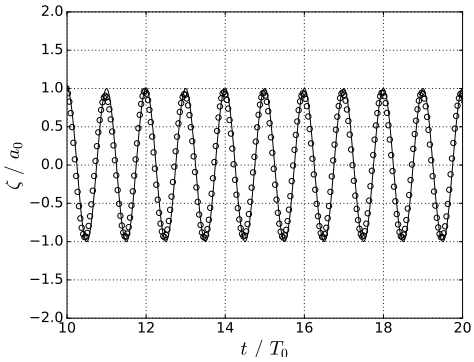

(a) $kh = \pi$; 2 $equidistant\ layers$

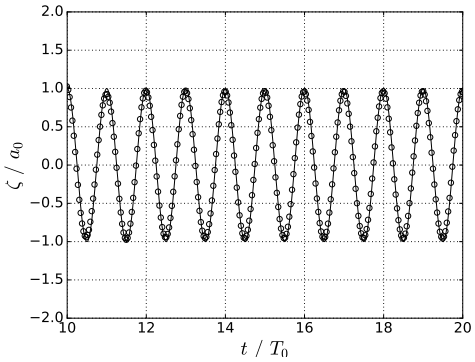

(b) $kh = 2\pi$; 3 $layers$: 10%, 20%, 70%

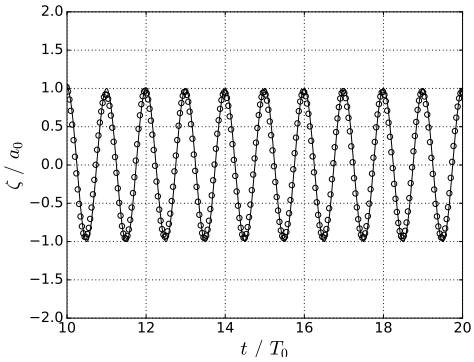

(c) $kh = 3\pi$; 3 $layers$: 10%, 20%, 70%

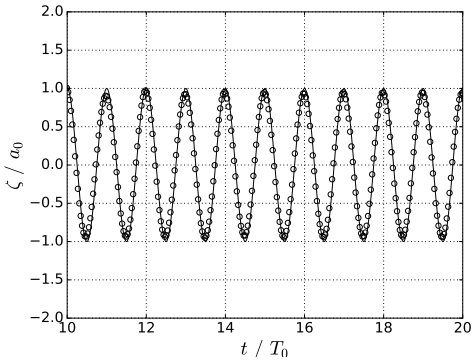

(d) $kh = 4\pi$; 3 $layers$: 10%, 20%, 70%

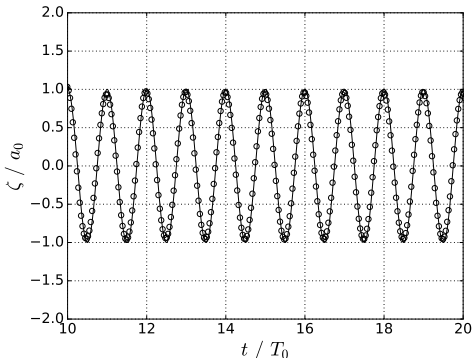

(e) $kh = 5\pi$; 3 $layers$: 5%, 15%, 80%

Figure B.2: Progressive waves: (—) Exact solution. (○ ○ ○) Numerical result, for multi-layered mode.

B.2.3.3 Wave propagation over a submerged bar

We study the experiment by Beji and Battjes (1993), considering the wave propagation over a trapezoidal submerged bar. The wave case simulated is Case A, in which the wave height is $H = 0.02$ m and the period is $T = 2.02$ s, for a water depth of 0.4 m. Results are presented in Figure B.3, for 8 virtual wave gauges located along the channel.

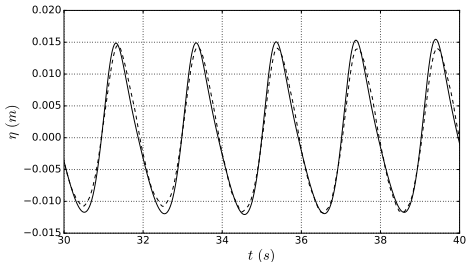

(a) *station* 4 ($x = 10.5\ m$)

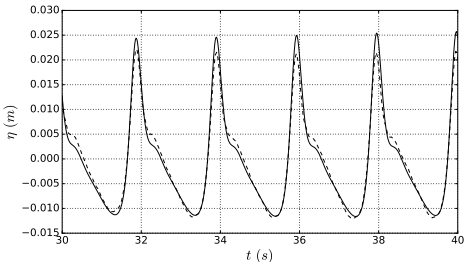

(b) *station* 5 ($x = 12.5\ m$)

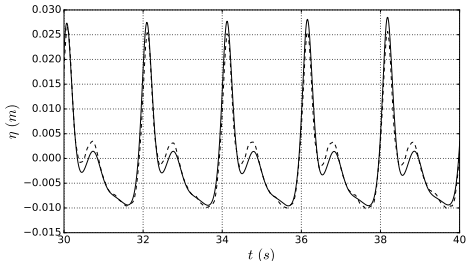

(c) *station* 6 ($x = 13.5\ m$)

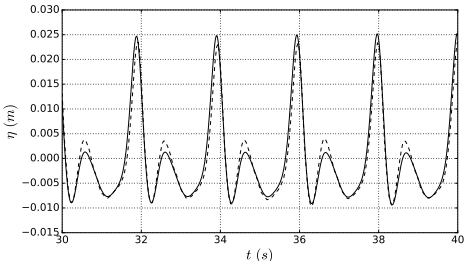

(d) *station* 7 ($x = 14.5\ m$)

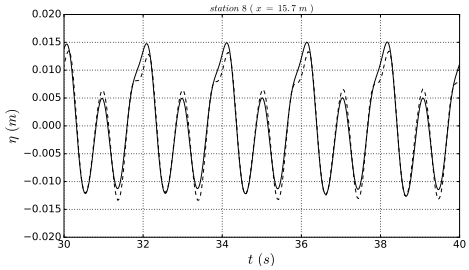

(e) *station* 8 ($x = 15.7\ m$)

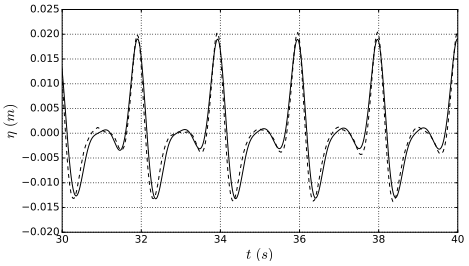

(f) *station* 9 ($x = 17.3\ m$)

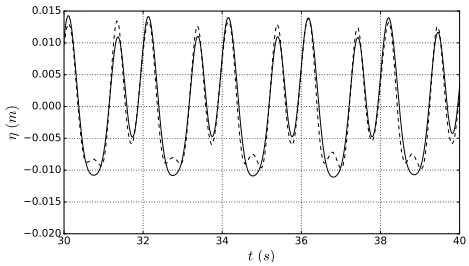

(g) *station* 10 ($x = 19.0\ m$)

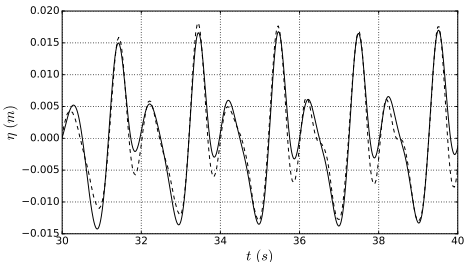

(h) *station* 11 ($x = 21.0\ m$)

Figure B.3: Wave propagation over a submerged bar: Experimental results (- -) comparing with SWASH results (—) for free surface elevation at every wave gauge.

Bibliography

Abadie S., Harris J., Grilli S. and Fabre R. (2012). Numerical modeling of tsunami waves generated by the flank collapse of the Cumbre Vieja Volcano (La Palma, Canary Islands): tsunami source and near field effects. *Journal of Geophysical Research: Oceans*, 117(C5).

Adams L., González F. and LeVeque R. (2020). *Modeling Study of a Proposed Vertical Evacuation Structure Site for the Shoalwater Bay Tribe*. Final Project Report.

Aki K. (1966). Generation and propagation of G-waves from the Niigata Earthquake of June 16, 1964. Part 2. Estimation of earthquake moment, released energy, and stress-strain drop from the G-wave spectrum. *Bulletin of Earthquake Research Institute, Tokyo University*, 44:73–88.

Al-Faesly T., Palermo D., Nistor I. and Cornett A. (2012). Experimental modeling of extreme hydrodynamic forces on structural models. *International Journal of Protective Structures*, 3(4):477–505.

Alonso M. and Finn E. (1972). *Física: Um Curso Universitário*, volume I—Mecânica. Editora Edgard Blücher Ltda.

Arcos M. and LeVeque R. (2015). Validating Velocities in the GeoClaw Tsunami Model using Observations Near Hawaii from the 2011 Tohoku Tsunami. *Pure and Applied Geophysics*, 172:849–867.

Argus D.F., Gordon R.G., DeMets C. and Stein S. (1989). Closure of the Africa-Eurasia-North America plate motion circuit and tectonics of the Gloria fault. *Journal of Geophysical Research: Solid Earth*, 94(B5):5585–5602.

Avilez-Valente P. (2000). *Métodos de Elementos Finitos para a Modelação a Uma e a Duas Dimensões Horizontais da Propagação de Ondas de Gravidade em Engenharia Costeira*. PhD Thesis, Faculdade de Ciências e Tecnologia da Universidade de Coimbra.

Baldock T., Cox D., Maddux T., Killian J. and Fayler L. (2009). Kinematics of breaking tsunami wavefronts: A data set from large scale laboratory experiments. *Coastal Engineering*, 56(5):506–516.

Baldock T. and Holmes P. (1999). Simulation and prediction of swash oscillations on a steep beach. *Coastal Engineering*, 36(3):219–242.

Bale D.S., LeVeque R.J., Mitran S. and Rossmanith J.A. (2003). A wave propagation method for conservation laws and balance laws with spatially varying flux functions. *SIAM Journal on Scientific Computing*, 24(3):955–978.

Baptista M. and Omira R. (2014). *Avaliação do risco de tsunami no concelho de Cascais*. Relatório Final, Instituto Dom Luiz.

Baptista M.A. (2017). Personal Communication.

Baptista M.A. and Miranda J.M. (2009). Revision of the Portuguese catalog of tsunamis. *Natural Hazards & Earth System Sciences*, 9(1):25–42.

Baptista M.A., Miranda P., Miranda J.M. and Victor L.M. (1996). Rupture extent of the 1755 Lisbon earthquake inferred from numerical modeling of tsunami data. *Physics and Chemistry of the Earth*, 21(1–2):65–70.

Behrens J. (2008). TsunNAWI—Unstructured mesh finite element model for the computation of tsunami scenarios with inundation. In *NAFEMS CFD Seminar: Simulation Komplexer Strömungsvorgänge (CFD)—Anwendungen und Trends*.

Behrens J. and Dias F. (2015). New computational methods in tsunami science. *Philosophical Transactions of the Royal Society A: Mathematical, Physical and Engineering Sciences*, 373(2053):20140382.

Beji S. and Battjes J. (1993). Experimental investigation of wave propagation over a bar. *Coastal Engineering*, 19(1-2):151–162.

Berger M., George D., LeVeque R. and Mandli K. (2011). The GeoClaw software for depth-averaged flows with adaptive refinement. *Advances in Water Resources*, 34(9):1195–1206.

Berger M.J. and Colella P. (1989). Local adaptive mesh refinement for shock hydrodynamics. *Journal of Computational Physics*, 82(1):64–84.

Berger M.J. and LeVeque R.J. (1998). Adaptive mesh refinement using wave-propagation algorithms for hyperbolic systems. *SIAM Journal on Numerical Analysis*, 35(6):2298–2316.

Berger M.J. and Oliger J. (1984). Adaptive mesh refinement for hyperbolic partial differential equations. *Journal of computational Physics*, 53(3):484–512.

Biésel F. and Suquet F. (1951). Les appareils générateurs de houle en laboratoire. *La Houille Blanche*, 5:723–737.

Bonamy C., Chauchat J., Cheng Z., Nagel T. and Hsu T.J. (2017). sedFoam, a OpenFOAM solver for sediment transport. In *12th OpenFoam Workshop*.

Boussinesq J. (1872). Théorie des ondes et des remous qui se propagent le long d'un canal rectangulaire horizontal, en communiquant au liquide contenu dans ce canal des vitesses sensiblement pareilles de la surface au fond. *Journal de Mathématiques Pures et Appliquées*, 17(2):55–108.

Boussinesq J. (1877). Théorie de l'écoulement tourbillant. *Mémoires presentés a L'Institut des Sciences, Lettres et Arts, par divers savants et lus dans ses assemblées: Sciences, Mathématiques et Physiques*, 23:46–50.

Briggs J., Synolakis C., Harkins G. and Green D. (1995a). Laboratory Experiments of Tsunami Run-up on a Circular Island. *Pure and Applied Geophysics*, 144:569–599.

Briggs J.M., Synolakis C.E., Harkins G.S. and Hughes S.T. (1995b). Large scale three-dimensional laboratory measurements of tsunami inundation. In *Tsunami: Progress in Prediction, Disaster Prevention and Warning (Advances in Natural and Technological Hazards Research)* (Tsuchiya Y. and Shuto N., eds.), volume 4, 129–149. Springer, Dordrecht.

Buforn E., López-Sánchez C., Lozano L., Martínez-Solares J., Cesca S., Oliveira C. and Udías A. (2019). Re-evaluation of seismic intensities and relocation of 1969 Saint Vincent Cape seismic sequence: A comparison with the 1755 Lisbon earthquake. *Pure and Applied Geophysics*, 1–20.

Calisto I., Miller M. and Constanzo I. (2017). Comparison between tsunami signals generated by different source models and the observed data of the Illapel 2015 earthquake. In *The Chile-2015 (Illapel) Earthquake and Tsunami*, 287–297. Springer.

Carrier G. and Greenspan H. (1958). Water waves of finite amplitude on a sloping beach. *Journal of Fluid Mechanics*, 4(1):97–109.

Chang Y.H., Hwang K.S. and Hwung H.H. (2009). Large-scale laboratory measurements of solitary wave inundation on a 1:20 slope. *Coastal Engineering*, 56(10):1022–1034.

Charvet I., Eames I. and Rossetto T. (2013). New tsunami runup relationships based on long wave experiments. *Ocean Modelling*, 69:79–92.

Chen Q., Kaihatu J.M. and Hwang P.A. (2004). Incorporation of wind effects into Boussinesq wave models. *Journal of Waterway, Port, Coastal, and Ocean Engineering*, 130(6):312–321.

Chen Q., Kirby J.T., Dalrymple R.A., Shi F. and Thornton E.B. (2003). Boussinesq modeling of longshore currents. *Journal of Geophysical Research: Oceans*, 108(C11).

Choi B., Kaistrenko V., Kim K., Min B. and Pelinovsky E. (2011). Rapid forecasting of tsunami runup heights from 2-D numerical simulations. *Natural Hazards and Earth System Science*, 11(3):707–714.

Clain S., Reis C., Costa R., Figueiredo J., Baptista M. and Miranda J. (2016). Second-order finite volume with hydrostatic reconstruction for tsunami simulation. *Journal of Advances in Modeling Earth Systems*.

Clawpack Development Team (2014a). Clawpack software. `http://www.clawpack.org`. Version 5.2.2.

Clawpack Development Team (2014b). GeoClaw—A variant of Clawpack for geophysical flows. `http://depts.washington.edu/clawpack/geoclaw/`. Version 5.2.1.

Custódio S., Lima V., Vales D., Cesca S. and Carrilho F. (2016). Imaging active faulting in a region of distributed deformation from the joint clustering of focal mechanisms and hypocentres: Application to the Azores–western Mediterranean region. *Tectonophysics*, 676:70–89.

Dao M. and Tkalich P. (2007). Tsunami propagation modelling—a sensitivity study. *Natural Hazards and Earth System Sciences*, 7:741–754.

Dean R.G. and Dalrymple R.A. (1991). *Water Wave Mechanics for Engineers and Scientists*, volume 2 de *Advanced Series on Ocean Engineering*. World Scientific Publishing Company.

Deng Z., Wang C., Yao Y. and Higuera P. (2019). Numerical simulation of an oscillating water column device installed over a submerged breakwater. *Journal of Marine Science and Technology*, 1–14.

Devolder B., Rauwoens P. and Troch P. (2017). Application of a buoyancy-modified k-ω SST turbulence model to simulate wave run-up around a monopile subjected to regular waves using OpenFOAM®. *Coastal Engineering*, 125:81–94.

Devolder B., Troch P. and Rauwoens P. (2018). Performance of a buoyancy-modified k-ω and k-ω SST turbulence model for simulating wave breaking under regular waves using OpenFOAM®. *Coastal Engineering*, 138:49–65.

Dias F. and Dutykh D. (2007). Dynamics of tsunami waves. In *Extreme Man-Made and Natural Hazards in Dynamics of Structures* (Ibrahimbegovic A. and Kozar I., eds.), 201–224. Springer Netherlands.

Dias F., Dutykh D., O'Brien L., Renzi E. and Stefanakis T. (2014). On the modelling of tsunami generation and tsunami inundation. *Procedia IUTAM*, 10:338–355.

Didenkulova I., Kurkin A. and Pelinovsky E. (2007). Run-up of solitary waves on slopes with different profiles. *Izvestiya, Atmospheric and Oceanic Physics*, 43(3):384–390.

Didenkulova I., Zahibo N., Kurkin A., Levin B., Pelinovsky E. and Soomere T. (2006). Runup of nonlinearly deformed waves on a coast. In *Doklady Earth Sciences*, volume 411 (1), 1241–1243. Springer.

Dingemans M.W. (1997). *Water Wave Propagation Over Uneven Bottoms (in 2 Parts)*, volume 13 de *Advanced Series on Ocean Engineering*. World Scientific Publishing Company.

Drähne U., Goseberg N., Vater S., Beisiegel N. and Behrens J. (2015). An experimental and numerical study of long wave run-up on a plane beach. *Journal of Marine Science and Engineering*, 4(1):1.

Duarte J., Riel N., Civiero C., Rosas F., Schellart W., Almeida J., Silva S. and Terrinha P. (2019). Delamination of oceanic lithosphere in sw iberia: a key for subduction initiation? In *Geophysical Research Abstracts*, volume 21.

Eaton J., Bateman D., Hauberg S. and Wehbring R. (2014). *GNU Octave Version 3.8.1 Manual: A High-Level Interactive Language for Numerical Computations*. CreateSpace Independent Publishing Platform. URL `http://www.gnu.org/software/octave/doc/interpreter`. ISBN 1441413006.

Erduran K., Ilic S. and Kutija V. (2005). Hybrid finite-volume finite-difference scheme for the solution of Boussinesq equations. *International Journal for Numerical Methods in Fluids*, 49(11):1213–1232.

Erhard P., Etling D., Muller U., Riedel U., Sreenivasan K. and Warnatz J. (2010). *Prandtl's Essentials of Fluid Mechanics*, volume 158 de *Applied Mathematical Sciences*. Springer Science & Business Media.

FEMA 55 (2000). *Coastal Construction Manual*. Res. Rep. FEMA 55, Federal Emergency Management Agency, Washington DC.

FEMA P646 (2008). *Guidelines for Design of Structures for Vertical Evacuation from Tsunamis*. Res. Rep. FEMA P646, Federal Emergency Management Agency, Washington DC.

Fenton J. (1972). A ninth-order solution for the solitary wave. *Journal of Fluid Mechanics*, 53(02):257–271.

Ferziger J.H. and Peric M. (2012). *Computational Methods for Fluid Dynamics*. Springer Science & Business Media.

Fukao Y. (1973). Thrust faulting at a lithospheric plate boundary the Portugal earthquake of 1969. *Earth and Planetary Science Letters*, 18(2):205–216.

Gayer G., Leschka S., Nöhren I., Larsen O. and Günther H. (2010). Tsunami inundation modelling based on detailed roughness maps of densely populated areas. *Natural Hazards and Earth System Sciences*, 10(8):1679–1687.

George D. (2006). *Finite Volume Methods and Adaptive Refinement for Tsunami Propagation and Inundation*. PhD Thesis, University of Washington.

George D. and Mandli K. (2012). Modeling hyperbolic problems in geophysics with GeoClaw. An International Workshop of Deep Geothermal Systems, Wuhan, China, June 29-30, 2012.

George D.L. (2008). Augmented Riemann solvers for the shallow water equations over variable topography with steady states and inundation. *Journal of Computational Physics*, 227(6):3089–3113.

George D.L. and LeVeque R.J. (2006). Finite volume methods and adaptive refinement for global tsunami propagation and local inundation. *Science of Tsunami Hazards*, 24(5):319–328.

Geraghty B. (2006). *Comparative Numerical Modelling of Tsunami Propagation Over Various Bathymetries*. PhD Thesis, University of Canterbury.

Gisler G.R. (2008). Tsunami simulations. *Annual Reviews of Fluid Mechanics*, 40:71–90.

Gjevik B., Pedersen G., Dybesland E., Harbitz C., Miranda P.A., Baptista M., Mendes-Victor L., Heinrich P., Roche R. and Guesmia M. (1997). Modeling tsunamis from earthquake sources near Gorringe Bank southwest of Portugal. *Journal of Geophysical Research: Oceans*, 102:27931–27949.

Glimsdal S., Pedersen G.K., Harbitz C.B. and Løvholt F. (2013). Dispersion of tsunamis: does it really matter? *Natural Hazards and Earth System Sciences*, 13:1507–1526.

Gomez-Gesteira M., Crespo A., Rogers B., Dalrymple R., Dominguez J. and Barreiro A. (2012a). SPHysics—development of a free-surface fluid solver—Part 2: Efficiency and test cases. *Computers and Geosciences*, 48:300–307.

Gomez-Gesteira M., Rogers B., Crespo A., Dalrymple R., Narayanaswamy M. and Dominguez J. (2012b). SPHysics—development of a free-surface fluid solver—Part 1: Theory and formulations. *Computers and Geosciences*, 48:289–299.

González F. and Kulikov Y.A. (1993). Tsunami dispersion observed in the deep ocean. In *Tsunamis in the World*, 7–16. Springer.

González F., LeVeque R., Chamberlain P., Hirai B., Varkovitzky J. and George D. (2011). *Validation of the GeoClaw Model, by the GeoClaw Tsunami Modeling Group*. Res. Rep., University of Washington. NTHMP MMS Tsunami Inundation Model Validation Workshop.

Goring D. (1978). *Tsunamis—The Propagation of Long Waves onto a Shelf*. PhD Thesis, W.M. Keck Laboratory of Hydraulics and Water Resources, California Institute of Technology.

Goring D. and Raichlen F. (1980). The generation of long waves in the laboratory. In *Proceedings of 17th Conference on Coastal Engineering, Sydney, Australia, 1980* (Edge B.L., ed.), 763–783. ASCE.

Grandin R., Borges J., Bezzeghoud M., Caldeira B. and Carrilho F. (2007). Simulations of strong ground motion in SW Iberia for the 1969 February 28 (Ms=8.0) and the 1755 November 1 (M 8.5) earthquakes-II. Strong ground motion simulations. *Geophysical Journal International*, 171(2):807–822.

Grilli A., Grilli S., David E. and Coulet C. (2015). Modeling of Tsunami Propagation in the Atlantic Ocean Basin for Tsunami Hazard Assessment along the North Shore of Hispaniola. In *Proceedings of the Twenty-fifth (2015) International Ocean and Polar Engineering Conference*. International Society of Offshore and Polar Engineers (ISOPE).

Grilli A.R. and Grilli S.T. (2013). *Far-field tsunami impact on the US East Coast from an extreme flank collapse of the Cumbre Vieja volcano (Canary Islands)*. Res. Rep. CACR-13-03, Center for Applied Coastal Research, University of Delaware, Newark, Delaware 19716, USA. NTHMP Award NA10NWS4670010.

Grilli S., Ioualalen M., Asavanant J., Shi F., Kirby J. and Watts P. (2007). Source constraints and model simulation of the December 26, 2004, Indian Ocean Tsunami. *Journal of Waterway, Port, Coastal and Ocean Engineering*, 133(6):414–428.

Grilli S.T. (1997). Fully nonlinear potential flow models used for long wave runup prediction. In *Long-Wave Runup Models, Proceedings of the International Workshop* (Yeh H., Liu P. and Synolakis C.E., eds.), 116–180.

Grilli S.T., Harris J.C., Bakhsh T.S.T., Masterlark T.L., Kyriakopoulos C., Kirby J.T. and Shi F. (2013). Numerical simulation of the 2011 Tohoku tsunami based on a new transient FEM coseismic source: Comparison to far-and near-field observations. *Pure and Applied Geophysics*, 170(6–8):1333–1359.

Grimshaw R. (1970). The solitary wave in water of variable depth. *Journal of Fluid Mechanics*, 42(03):639–656.

Gutscher M.A., Roger J., Baptista M.A., Miranda J. and Tinti S. (2006). Source of the 1693 Catania earthquake and tsunami (southern Italy): New evidence from tsunami modeling of a locked subduction fault plane. *Geophysical Research Letters*, 33(8):L08309.

Hanks T.C. and Kanamori H. (1979). A moment magnitude scale. *Journal of Geophysical Research: Solid Earth*, 84(B5):2348–2350.

Havelock T.H. (1929). LIX. Forced surface-waves on water. *The London, Edinburgh, and Dublin Philosophical Magazine and Journal of Science*, 8(51):569–576.

Hayes G.P., Wald D.J. and Johnson R.L. (2012). Slab1.0: A three-dimensional model of global subduction zone geometries. *Journal of Geophysical Research: Solid Earth*, 117:B01302.

Heidarzadeh M., Murotani S., Satake K., Ishibe T. and Gusman A.R. (2016). Source model of the 16 September 2015 Illapel, Chile, Mw 8.4 earthquake based on teleseismic and tsunami data. *Geophysical Research Letters*, 43(2):643–650.

Heidarzadeh M., Satake K., Murotani S., Gusman A. and Watada S. (2015). Deep-water characteristics of the trans-Pacific tsunami from the 1 April 2014 Mw 8.2 Iquique, Chile earthquake. *Pure and Applied Geophysics*, 172(3-4):719–730.

Higuera P. (2016). olaFlow - Reference Manual.

Higuera P. (2019). olaflow. `http://olaflow.github.io/`. Accessed: 2019-04-29.

Higuera P., Buldakov E., Stagonas D. et al. (2018a). Numerical Modelling of Wave Interaction With an FPSO Using a Combination of OpenFOAM® and Lagrangian Models. In *The 28th International Ocean and Polar Engineering Conference*. International Society of Offshore and Polar Engineers.

Higuera P., Lara J. and Losada I. (2013a). Realistic wave generation and active wave absorption for Navier–Stokes models: Application to OpenFOAM®. *Coastal Engineering*, 71:102–118.

Higuera P., Lara J. and Losada I. (2013b). Simulating coastal engineering processes with OpenFOAM®. *Coastal Engineering*, 71:119–134.

Higuera P., Lara J. and Losada I. (2014a). Three-dimensional interaction of waves and porous coastal structures using OpenFOAM®. Part I: Formulation and validation. *Coastal Engineering*, 83:243–258.

Higuera P., Lara J. and Losada I. (2014b). Three-dimensional interaction of waves and porous coastal structures using OpenFOAM®. Part II: Application. *Coastal Engineering*, 83:259–270.

Higuera P., Lara J. and Losada I. (2017). Ihfoam. `http://ihfoam.ihcantabria.com/`. Accessed: 2017-11-09.

Higuera P., Liu P.F., Lin C., Wong W.Y. and Kao M.J. (2018b). Laboratory-scale swash flows generated by a non-breaking solitary wave on a steep slope. *Journal of Fluid Mechanics*, 847:186–227.

Hirt C.W. and Nichols B.D. (1981). Volume of fluid (VOF) method for the dynamics of free boundaries. *Journal of Computational Physics*, 39(1):201–225.

Hornbach M.J., Braudy N., Briggs R.W., Cormier M.H., Davis M.B., Diebold J.B., Dieudonne N., Douilly R., Frohlich C., Gulick S.P.S., Johnson III H.E., Mann P., McHugh C., Ryan-Mishkin K., Prentice C.S., Seeber L., Sorlien C.C., Steckler M.S., Symithe S.J., Taylor F.W. and Templeton J. (2010). High tsunami frequency as a result of combined strike-slip faulting and coastal landslides. *Nature Geoscience*, 3(11):783–788.

Horrillo J. and Kowalik Z. (2006). Wave dispersion study in the Indian ocean tsunami of December 26, 2004. *Science of Tsunami Hazards*, 25(1):42.

Horrillo J., Kowalik Z. and Shigihara Y. (2006). Wave dispersion study in the Indian Ocean-Tsunami of December 26, 2004. *Marine Geodesy*, 29(3):149–166.

Horrillo J., Wood A., Williams C., Parambath A. and Kim G.B. (2010). *Construction of tsunami inundation maps in the guld of Mexico*. Res. Rep., Report to the National Tsunami Hazard Mitigation Program.

Hsu H.C., Chen Y.Y., Lin C.Y. and Cheng C.Y. (2012). Experimental study of the velocity field in solitary water waves. *Journal of Nonlinear Mathematical Physics*, 19(supp01):1240003.

Hughes S.A. (1993). *Physical Models and Laboratory Techniques in Coastal Engineering*, volume 7 de *Advanced Series on Ocean Engineering*. World Scientific.

Hunt I.A. (1959). Design of sea-walls and breakwaters. *Transactions of the American Society of Civil Engineers*, 126(4):542–570.

Imamura F. (1996). Simulation of wave-packet propagation along sloping beach by TUNAMI-code. In *Long-wave Runup Models* (Yeh H., Liu P. and Synolakis C., eds.), 231–241. World Scientific.

Jacobsen N.G., Fuhrman D.R. and Fredsøe J. (2012). A wave generation toolbox for the open-source CFD library: OpenFoam®. *International Journal for Numerical Methods in Fluids*, 70(9):1073–1088.

Jasak H. (1996). *Error Analysis and Estimation for the Finite Volume Method with Applications to Fluid Flows*. PhD Thesis, Imperial College London (University of London).

Jensen A., Mayer S. and Pedersen G.K. (2005). Experiments and computation of onshore breaking solitary waves. *Measurement Science and Technology*, 16(10):1913–1920.

Jensen A., Pedersen G.K. and Wood D.J. (2003). An experimental study of wave run-up at a steep beach. *Journal of Fluid Mechanics*, 486:161–188.

Kanamori H. (1977). The energy release in great earthquakes. *Journal of Geophysical Research*, 82(20):2981–2987.

Katell G. and Eric B. (2002). Accuracy of solitary wave generation by a piston wave maker. *Journal of Hydraulic Research*, 40(3):321–331.

Kazolea M. and Delis A. (2013). A well-balanced shock-capturing hybrid finite volume-finite difference numerical scheme for extended 1D Boussinesq models. *Applied Numerical Mathematics*, 67:167–186.

Kennard E.H. (1949). Generation of surface waves by a moving partition. *Quarterly of Applied Mathematics*, 7(3):303–312.

Kennedy A.B., Chen Q., Kirby J.T. and Dalrymple R.A. (2000). Boussinesq modeling of wave transformation, breaking, and runup. I: 1D. *Journal of Waterway, Port, Coastal, and Ocean Engineering*, 126(1):39–47.

Kim D.H. and Lynett P.J. (2011). Turbulent mixing and passive scalar transport in shallow flows. *Physics of Fluids*, 23(1):016603.

Kim D.H. and Son S. (2019). Role of shelf geometry and wave breaking in single N-type tsunami runup under geophysical-scale. *Ocean Modelling*, 138:13–22.

Kim J., Pedersen G., Løvholt F. and LeVeque R. (2017). A Boussinesq type extension of the GeoClaw model—a study of wave breaking phenomena applying dispersive long wave models. *Coastal Engineering*, 122:75–86.

Kirby J. (2003). Boussinesq models and applications to nearshore wave propagation, surf zone processes and wave-induced currents. In *Advances in Coastal Engineering* (Lakhan C., ed.). Elsevier, Amsterdam.

Kirby J., Wei G., Chen Q., Kennedy A. and Dalrymple R. (1998). *FUNWAVE 1.0, Fully nonlinear Boussinesq wave model. Documentation and users manual*. Res. Rep. CACR-98-06, Center for Applied Coastal Research, University of Delaware, Newark, Delaware 19716, USA.

Kirby J.T., Shi F., Grilli S.T., Nemati F. and Tehranirad B. (2017). *NTHMP Current Benchmark Workshop: FUNWAVE-TVD results*. Res. Rep. CACR-16-01, Center for Applied Coastal Research, University of Delaware, Newark, Delaware 19716, USA.; Department of Ocean Engineering University of Rhode Island.

Kirby J.T., Shi F., Tehranirad B., Harris J.C. and Grilli S.T. (2013). Dispersive tsunami waves in the ocean: Model equations and sensitivity to dispersion and Coriolis effects. *Ocean Modelling*, 62:39–55.

Kissling K., Springer J., Jasak H., Schutz S., Urban K. and Piesche M. (2010). A coupled pressure based solution algorithm based on the volume-of-fluid approach for two or more immiscible fluids. In *V European Conference on Computational Fluid Dynamics, ECCOMAS CFD*.

Klettner C., Balasubramanian S., Hunt J., Fernando H., Voropayev S. and Eames I. (2012). Draw-down and run-up of tsunami waves on sloping beaches. *Proceedings of the Institution of Civil Engineers—Engineering and Computational Mechanics*, 165(2):119–129.

Kowalik Z., Knight W., Logan T. and Whitmore P. (2005). Numerical modeling of the global tsunami: Indonesian tsunami of 26 December 2004. *Science of Tsunami Hazards*, 23(1):40–56.

Kulikov E. (2005a). *Dispersion of the Sumatra tsunami waves in the Indian Ocean detected by satellite altimetry*. Res. Rep., Rep. from P. P. Shirshov Institute of Oceanology, Russian Academy of Sciences, Moscow.

Kulikov Y. (2005b). The highly dispersive waves of the Indian Ocean Tsunami. *Russian Academy of Sciences*.

Laitone E. (1960). The second approximation to cnoidal and solitary waves. *Journal of Fluid Mechanics*, 9(03):430–444.

Larsen B.E. and Fuhrman D.R. (2018). On the over-production of turbulence beneath surface waves in Reynolds-Averaged Navier-Stokes models. *Journal of Fluid Mechanics*, 853:419–460.

Launder B. and Spalding D. (1974). The numerical computation of turbulent flows. *Computer Methods in Applied Mechanics and Engineering*, 3:269–289.

Le Méhauté B. (1976). Similitude in Coastal Engineering. *Journal of the Waterways, Harbors and Coastal Engineering Division*, 102(3):317–335.

Lee J.J., Skjelbreia J.E. and Raichlen F. (1982). Measurement of velocities in solitary waves. *Journal of the Waterway, Port, Coastal and Ocean Division*, 108(2):200–218.

LeVeque R. and George D. (2007). High-resolution finite volume methods for the shallow water equations with bathymetry and dry states. In *Proceedings of the Third International Workshop on Long-Wave Runup Models, Catalina, 2004 (Advances in Coastal and Ocean Engineering)* (Liu P.L.F., Yeh H. and Synolakis C., eds.), volume 10, 43–73. World Scientific.

LeVeque R.J. (1996). High-resolution conservative algorithms for advection in incompressible flow. *SIAM Journal on Numerical Analysis*, 33(2):627–665.

LeVeque R.J. (1997). Wave propagation algorithms for multidimensional hyperbolic systems. *Journal of Computational Physics*, 131(2):327–353.

LeVeque R.J. (2002). Finite-volume methods for non-linear elasticity in heterogeneous media. *International Journal for Numerical Methods in Fluids*, 40(1–2):93–104.

LeVeque R.J., George D.L. and Berger M.J. (2011). Tsunami modelling with adaptively refined finite volume methods. *Acta Numerica*, 20:211–289.

Li Y. (2000). *Tsunamis: Non-Breaking and Breaking Solitary Wave Run-Up*. PhD Thesis, Rep. KH-R-60, California Inst. of Technol., Calif.

Li Y. and Raichlen F. (2001). Solitary wave runup on plane slopes. *Journal of Waterway, Port, Coastal, and Ocean Engineering*, 127(1):33–44.

Li Y. and Raichlen F. (2002). Non-breaking and breaking solitary wave run-up. *Jounal of Fluid Mechanics*, 456:295–318.

Li Y. and Raichlen F. (2003). Energy balance model for breaking solitary wave run-up. *Journal of Waterway, Port, Coastal, and Ocean Engineering*, 47:47–59.

Lima V., Baptista M., Avilez-Valente P. and Miranda M. (2016). A combined model for tsunami generation and propagation. In *EGU General Assembly Conference Abstracts*, volume 18, EPSC2016–10028.

Lima V.V., Avilez-Valente P., Baptista M.A.V. and Miranda J.M. (2019). Generation of N-waves in laboratory. *Coastal Engineering*, 148:1–18. URL `http://www.sciencedirect.com/science/article/pii/S0378383918302060`.

Lima V.V., Miranda J.M., Baptista M.A., Catalão J., González M., Otero L., Olabarrieta M., Álvarez-Gómez J.A. and Carreño E. (2010). Impact of a 1755-like tsunami in Huelva, Spain. *Natural Hazards and Earth System Sciences*, 10(1):139–148.

Liu P.F., Cho Y.S., Briggs M., Kanoglu U. and Synolakis C. (1995). Runup of solitary waves on a circular island. *Journal of Fluid Mechanics*, 302:259–285.

Liu P.L.F., Yeh H. and Synolakis C. (2008). *Benchmark Problems in Advanced Numerical Models for Simulating Tsunami Waves and Runup*, volume 10 de *Advances in Coastal and Ocean Engineering*. World Scientific.

López-Venegas A., Horrillo J., Pampell-Manis A., Huérfano V. and Mercado A. (2015). Advanced tsunami numerical simulations and energy considerations by use of 3D–2D coupled models: the October 11, 1918, Mona Passage Tsunami. *Pure and Applied Geophysics*, 172(6):1679–1698.

Løvholt F., Pedersen G. and Gisler G. (2008). Oceanic propagation of a potential tsunami from the La Palma Island. *Journal of Geophysical Research*, 133:C09026.

Løvholt F., Pedersen G. and Glimsdal S. (2010). Coupling of dispersive tsunami propagation and shallow water coastal response. *The Open Oceanography Journal*, 4:71–82.

Løvholt F., Pedersen G., Harbitz C.B., Glimsdal S. and Kim J. (2015). On the characteristics of landslide tsunamis. *Philosophical Transactions of the Royal Society A: Mathematical, Physical and Engineering Sciences*, 373(2053):20140376.

Lynett P.J., Borrero J.C., Weiss R., Son S., Greer D. and Renteria W. (2012). Observations and modeling of tsunami-induced currents in ports and harbors. *Earth and Planetary Science Letters*, 327:68–74.

Lynett P.J., Wu T.R. and Liu P.L.F. (2002). Modeling wave runup with depth-integrated equations. *Coastal Engineering*, 46(2):89–107.

MacInnes B., Gusman A., LeVeque R. and Tanioka Y. (2013a). Comparison of earthquake source models for the 2011 Tohoku event using tsunami simulations and near field observations. *Bulletin of the Seismological Society of America*, 103:1256–1274.

MacInnes B.T., Gusman A.R., LeVeque R.J. and Tanioka Y. (2013b). Comparison of earthquake source models for the 2011 Tohoku event using tsunami simulations and near-field observations. *Bulletin of the Seismological Society of America*, 103(2B):1256–1274.

Madsen P. and Schäffer H. (2010). Analytical solutions for tsunami runup on a plane beach: single waves, N-waves and transient waves. *Journal of Fluid Mechanics*, 645:27–57.

Madsen P.A., Fuhrman D.R. and Schäffer H.A. (2008). On the solitary wave paradigm for tsunamis. *Journal of Geophysical Research: Oceans*, 113(C12).

Madsen P.A. and Sørensen O.R. (1992). A new form of the Boussinesq equations with improved linear dispersion characteristics. Part 2. A slowly-varying bathymetry. *Coastal Engineering*, 18(3-4):183–204.

Malek-Mohammadi S. and Testik F.Y. (2010). New methodology for laboratory generation of solitary waves. *Journal of Waterway, Port, Coastal, and Ocean Engineering*, 136(5):286–294.

Manighetti I., Campillo M., Bouley S. and Cotton F. (2007). Earthquake scaling, fault segmentation, and structural maturity. *Earth and Planetary Science Letters*, 253(3–4):429–438.

Mansinha L. and Smylie D. (1971). The displacement field of inclined faults. *Bulletin of the Seismological Society of America*, 61(5):1433–1440.

Matsuyama M. and Tanaka H. (2001). An experimental study of the highest run-up height in 1993 Hokkaido-Nansei-Oki earthquake tsunami. In *International Tsunami Symposium; Seattle, USA, August 7–10, 2001*.

McGovern D., Chandler I. and Rossetto T. (2016). Experimental study of the runup of tsunami waves on a smooth sloping beach. In *Proceeding of the 6th International Conference on Application of Physical Modelling to Port and Coastal Protection, Coastlab16*.

Mehauté L., Koh R.C. and Hwang L.S. (1968). A synthesis on wave run-up. *Journal of the Waterways and Harbors Division*, 94(1):77–92.

Melgar D. and Bock Y. (2013). Near-field tsunami models with rapid earthquake source inversions from land-and ocean-based observations: The potential for forecast and warning. *Journal of Geophysical Research: Solid Earth*, 118(11):5939–5955.

Melgar D. and Bock Y. (2015). Kinematic earthquake source inversion and tsunami runup prediction with regional geophysical data. *Journal of Geophysical Research: Solid Earth*, 120(5):3324–3349.

Melgar D., Fan W., Riquelme S., Geng J., Liang C., Fuentes M., Vargas G., Allen R., Shearer P. and Fielding E. (2016). Slip segmentation and slow rupture to the trench during the 2015, Mw 8.3 Illapel, Chile earthquake. *Geophysical Research Letters*, 43(3):961–966.

Menter F.R. (1994). Two-equation eddy-viscosity turbulence models for engineering applications. *AIAA journal*, 32(8):1598–1605.

Menter F.R., Kuntz M. and Langtry R. (2003). Ten years of industrial experience with the SST turbulence model. *Turbulence, heat and mass transfer*, 4(1):625–632.

Mesquita A. (2013). *Turbulência e Rebentação: Interacção Onda-Quebramar Submerso*. PhD Thesis, Faculdade de Engenharia da Universidade do Porto.

Miranda J., Luis J., Reis C., Omira R. and Baptista M.A. (2014). Validation of NSWING, a multicore finite difference code for tsunami propagation and run-up. In *American Geophysical Union (AGU) Fall Meeting, San Francisco*. S21A-4390.

Munk W.H. (1950). Origin and generation of waves. In *Proceedings of First Conference on Coastal Engineering, Long Beach, California, October, 1950* (Johnson J., ed.). 1, Council on Wave Research, The Engineering Foundation, copyrighted 1951.

Nadaoka K., Beji S. and Nakagawa Y. (1997). A fully dispersive weakly nonlinear model for water waves. *Proceedings of the Royal Society of London. Series A: Mathematical, Physical and Engineering Sciences*, 453(1957):303–318.

Narayanaswamy M., Crespo A., Gomez-Gesteira M. and Dalrymple R. (2010). SPHysics-FUNWAVE hybrid model for coastal wave propagation. *Journal of Hydraulic Research*, 48:85–93.

Nayar K., Panchanathan D., McKinley G. and Lienhard J. (2014). Surface tension of seawater. *Journal of Physical and Chemical Reference Data*, 43(4):043103.

Nouri Y., Nistor I., Palermo D. and Cornett A. (2010). Experimental investigation of tsunami impact on free standing structures. *Coastal Engineering Journal*, 52(01):43–70.

Nwogu O. (1993). Alternative form of Boussinesq equations for nearshore wave propagation. *Journal of Waterway, Port, Coastal, and Ocean Engineering*, 119(6):618–638.

Okada Y. (1985). Surface deformation due to shear and tensile faults in a halfspace. *Bulletin of the Seismological Society of America*, 75(4):1135–1154.

Okal E.A. (1982). Mode-wave equivalence and other asymptotic problems in tsunami theory. *Physics of the Earth and Planetary Interiors*, 30(1):1–11.

Okal E.A. and Synolakis C.E. (2004). Source discriminants for near-field tsunamis. *Geophysical Journal International*, 158(3):899–912.

Oliveira T.C.A., Sanchez-Arcilla A., Gironella X. and Madsen O.S. (2017). On the generation of regular long waves in numerical wave flumes based on the particle finite element method. *Journal of Hydraulic Research*, 55(4):538–556.

Omira R., Baptista M. and Lisboa F. (2016). Tsunami characteristics along the Peru–Chile trench: Analysis of the 2015 Mw 8.3 Illapel, the 2014 Mw 8.2 Iquique and the 2010 Mw 8.8 Maule tsunamis in the near-field. *Pure and Applied Geophysics*, 173(4):1063–1077.

OpenCFD Limited (2019). OpenFOAM® - The Open Source CFD Toolbox. `https://www.openfoam.com/`. Accessed: 2019-01-22.

Palermo D., Nistor I., Nouri Y. and Cornett A. (2009). Tsunami loading of near-shoreline structures: a primer. *Canadian Journal of Civil Engineering*, 36(11):1804–1815.

Pedersen G. and Gjevik B. (1983). Run-up of solitary waves. *Journal of Fluid Mechanics*, 135:283–299.

Pedersen G. and Løvholt F. (2008). Documentation of a global Boussinesq solver. *Preprint series. Mechanics and Applied Mathematics http://urn. nb. no/URN: NBN: no-23418*.

Pelinovsky E. and Mazova R.K. (1992). Exact analytical solutions of nonlinear problems of tsunami wave run-up on slopes with different profiles. *Natural Hazards*, 6(3):227–249.

Peregrine D. (1967). Long waves on a beach. *Journal of Fluid Mechanics*, 27(4):815–827.

Philip Liu Group (2014). COMCOT: A Tsunami Modeling Package. http://ceeserver.cee.cornell.edu/pll-group/comcot.htm. V1.7.

Pujiraharjo A. and Hosoyamada T. (2006). Dispersive Study on Tsunami Propagation of The Indian Ocean Tsunami, 26 December 2004. *International Journal of Civil and Environmental Engineering, IJCEE - IJENS*, 10(6):6–12.

Rivera P. (2006). Modeling the Asian tsunami evolution and propagation with a new generation mechanism and a non-linear dispersive wave model. *Science of Tsunami Hazards*, 25(1):18–33.

Roeber V., Cheung K.F. and Kobayashi M.H. (2010). Shock-capturing Boussinesq-type model for nearshore wave processes. *Coastal Engineering*, 57(4):407–423.

Rossetto T., Allsop W., Charvet I. and Robinson D. (2011). Physical modelling of tsunami using a new pneumatic wave generator. *Coastal Engineering*, 58(6):517–527.

Sandwell D., Gille S. and eds. W.S. (2002). *Bathymetry from Space: Oceanography, Geophysics, and Climate*. Res. Rep., Geoscience Professional Services, Bethesda, Maryland. 24 pp.

Schäffer H.A. and Klopman G. (2000). Review of multidirectional active wave absorption methods. *Journal of Waterway, Port, Coastal, and Ocean Engineering*, 126(2):88–97.

Schäffer H.A. and Madsen P.A. (1995). Further enhancements of Boussinesq-type equations. *Coastal Engineering*, 26(1-2):1–14.

Schnyder J.S., Eberli G.P., Kirby J.T., Shi F., Tehranirad B., Mulder T., Ducassou E., Hebbeln D. and Wintersteller P. (2016). Tsunamis caused by submarine slope failures along western Great Bahama Bank. *Scientific Reports*, 6:35925.

Scott Russell J. (1845). Report on waves. In *Report of the Fourteenth Meeting of the British Association for the Advancement of Science, York*, 311–390. John Murray, London.

Shi F., Kirby J. and Tehranirad B. (2012a). *Tsunami benchmark results for spherical coordinate version of FUNWAVE-TVD (Version 2.0)*. Res. Rep., Center for Applied Coastal Research, University of Delaware. Revised October 2012.

Shi F., Kirby J.T., Harris J.C., Geiman J.D. and Grilli S.T. (2012b). A high-order adaptive time-stepping TVD solver for Boussinesq modeling of breaking waves and coastal inundation. *Ocean Modelling*, 43:36–51.

Shi F., Kirby J.T., Tehranirad B., Choi Y.K. and Malej M. (2016). *FUNWAVE-TVD, Fully Nonlinear Boussinesq Wave Model With TVD solver, documentation and user's manual (Version 3.0)*. Res. Rep. CACR-11-03, Center for Applied Coastal Research, University of Delaware, Newark, Delaware 19716, USA.

Shi F., Kirby J.T., Tehranirad B., Harris J.C. and Grilli S. (2012c). *FUNWAVE-TVD, Fully Nonlinear Boussinesq Wave Model With TVD solver, documentation and user's manual (Version 2.0)*. Res. Rep. CACR-11-04, Center for Applied Coastal Research, University of Delaware, Newark, Delaware 19716, USA.

Shuto N., Goto C. and Imamura F. (1990). Numerical simulation as a means of warning for near-field tsunamis. *Coastal Engineering in Japan*, 33(2):173–193.

Shuto N., Imamura F., Yalciner A.C. and Ozyur G. (1997). The MOST (Method of Splitting Tsunami) model. http://nctr.pmel.noaa.gov/model.html.

Shuto N., Imamura F., Yalciner A.C. and Ozyur G. (2014). TUNAMI N2 Tsunami Modelling Manual. `http://tunamin2.ce.metu.edu.tr/`.

Sitanggang K. and Lynett P. (2009). Multi-scale simulation with a hybrid Boussinesq-RANS hydrodynamic model. *International Journal of Numerical Methods in Fluids*, 62:1013–1046.

Sraj I., Mandli K.T., Knio O.M., Dawson C.N. and Hoteit I. (2014). Uncertainty quantification and inference of Manning's friction coefficients using DART buoy data during the Tōhoku tsunami. *Ocean Modelling*, 83:82–97.

Sraj I., Mandli K.T., Knio O.M., Dawson C.N. and Hoteit I. (2017). Quantifying uncertainties in fault slip distribution during the Tōhoku tsunami using polynomial chaos. *Ocean Dynamics*, 67(12):1535–1551.

Sriram V., Didenkulova I., Sergeeva A. and Schimmels S. (2016). Tsunami evolution and run-up in a large scale experimental facility. *Coastal Engineering*, 111:1–12.

St-Germain P., Nistor I., Townsend R. and Shibayama T. (2013). Smoothed-particle hydrodynamics numerical modeling of structures impacted by tsunami bores. *Journal of Waterway, Port, Coastal, and Ocean Engineering*, 140(1):66–81.

Stagonas D., Higuera P. and Buldakov E. (2017). Simulating Breaking Focused Waves in CFD: Methodology for Controlled Generation of First and Second Order. *Journal of Waterway, Port, Coastal, and Ocean Engineering*, 144(2):06017005.

Synolakis C. (1987). The runup of solitary waves. *Journal of Fluid Mechanics*, 185:523–545.

Synolakis C., Bernard E., Titov V., Kanoglu U. and González F. (2007). *Standards, criteria, and procedures for NOAA evaluation of tsunami numerical models*. Res. Rep., NOAA, NOAA/Pacific Marine Environmental Laboratory, Seattle, Washington.

Synolakis C., Bernard E., Titov V., Kanoglu U. and González F. (2008). Validation and Verification of Tsunami Numerical Models. *Pure and Applied Geophysics*, 165:2197–2228.

Synolakis C., Liu P., Philip H.A., Carrier G. and Yeh H. (1997). Tsunamigenic sea-floor deformations. *Science*, 278(5338):598–600.

Synolakis C.E. (1990). Generation of long waves in laboratory. *Journal of Waterway, Port, Coastal, and Ocean Engineering*, 116(2):252–266.

Synolakis C.E. and Bernard E.N. (2006). Tsunami science before and beyond boxing day 2004. *Philosophical Transactions of the Royal Society A: Mathematical, Physical and Engineering Sciences*, 364(1845):2231–2265.

Tadepalli S. and Synolakis C. (1994). The run-up of N-waves on sloping beaches. *Proceedings of the Royal Society London: Mathematical and Physical Sciences*, A445:99–112.

Tanaka M. (1986). The stability of solitary waves. *The Physics of Fluids*, 29:650–655.

Tang L., Titov V.V., Moore C. and Wei Y. (2016). Real-time assessment of the 16 September 2015 Chile tsunami and implications for near-field forecast. *Pure and Applied Geophysics*, 173(2):369–387.

Tappin D.R., Grilli S.T., Harris J.C., Geller R.J., Masterlark T., Kirby J.T., Shi F., Ma G., Thingbaijam K. and Mai P.M. (2014). Did a submarine landslide contribute to the 2011 Tohoku tsunami? *Marine Geology*, 357:344–361.

Te Chow V. (1959). *Open-Channel Hydraulics*, volume 1. McGraw-Hill New York.

Tehranirad B., Shi F., Kirby J., Harris J. and Grilli S. (2011). *Tsunami benchmark results for fully nonlinear Boussinesq wave model FUNWAVE-TVD, Version 1.0*. Res. Rep., Center for Applied Coastal Research, University of Delaware.

Teixeira R.A.F. (2012). *Quebramares portugueses. Inventário e análise comparativa de soluções*. Masters Thesis, Faculdade de Engenharia da Universidade do Porto.

Teng M.H. (1997). Solitary wave solution to Boussinesq equations. *Journal of Waterway, Port, Coastal, and Ocean Engineering*, 123(3):138–141.

Teng M.H. and Wu T.Y. (1992). Nonlinear water waves in channels of arbitrary shape. *Journal of Fluid Mechanics*, 242:211–233.

Thompson D.B. (1992). Numerical methods 101—Convergence of Numerical Models. In *Hydraulic Engineering: Saving a Threatened Resource—In Search of Solutions: Proceedings of the Hydraulic Engineering sessions at Water Forum '92, Baltimore, Maryland, August 2–6, 1992*, 398–403. American Society of Civil Engineers.

Titov V. and Synolakis C. (1998). Numerical modeling of tidal wave runup. *Journal of Waterway, Port, Coastal, and Ocean Enginering*, 124(4):157–71.

Tonelli M. and Petti M. (2009). Hybrid finite volume–finite difference scheme for 2DH improved Boussinesq equations. *Coastal Engineering*, 56(5-6):609–620.

Toro E.F. (2009). *Riemann Solvers and Numerical Methods for Fluid Dynamics: A Practical Introduction*. Springer Science & Business Media, third ed.

Torrence C. and Compo G. (1998). A practical guide to wavelet analysis. *Bulletin of the American Meteorological Society*, 79(1):61–78.

Ursell F., Dean R.G. and Yu Y.S. (1960). Forced small-amplitude water waves: a comparison of theory and experiment. *Journal of Fluid Mechanics*, 7(1):33–52.

van Rossum G. (1995). *Python tutorial*. Technical Report CS-R9526, Centrum voor Wiskunde en Informatica (CWI), Amsterdam.

Vincenty T. (1975). Direct and inverse solutions of geodesics on the ellipsoid with application of nested equations. *Survey review*, 23(176):88–93.

Ward S.N. (1980). Relationships of tsunami generation and an earthquake source. *Journal of Physics of the Earth*, 28(5):441–474.

Watts P., Grilli S., Kirby J., Fryer G. and Tappin D.R. (2003). Landslide tsunami case studies using a Boussinesq model and a fully nonlinear tsunami generation model. *Natural Hazards and Earth System Sciences*, 3:391–402.

Watts P., Grilli S., Tappin D. and Fryer G. (2005). Tsunami generation by submarine mass failure, Part II: Predictive equations and case studies. *Jounal of Waterway, Port, Coastal, and Ocean Engineering*, 131:298–310.

Wei G. and Kirby J. (1995). A time-dependent numerical code for extended Boussinesq equations. *Journal of Waterway, Port, Coastal, and Ocean Enginering*, 120:251–261.

Wei G., Kirby J., Grilli S. and Subramanya R. (1995). A fully nonlinear Boussinesq model for surface waves: Part I. Highly nonlinear unsteady waves. *Journal of Fluid Mechanics*, 294:71–92.

White F.M. (2005). *Viscous Fluid Flow*. McGraw-Hill New York.

Whitham G. (1974). *Linear and Nonlinear Waves*. John Wiley & Sons.

Windt C., Davidson J., Schmitt P. and Ringwood J.V. (2019). On the Assessment of Numerical Wave Makers in CFD Simulations. *Journal of Marine Science and Engineering*, 7(2):47.

Yamamoto S., Kano S. and Daiguji H. (1998). An efficient CFD approach for simulating unsteady hypersonic shock–shock interference flows. *Computers & Fluids*, 27(5–6):571–580.

Yates G.T. (1995). Various Boussinesq solitary wave solutions. In *The Fifth International Offshore and Polar Engineering Conference*, 70–76. International Society of Offshore and Polar Engineers (ISOPE).

Zelt J. (1991). The run-up of nonbreaking and breaking solitary waves. *Coastal Engineering*, 15(3):205–246.

Zhang Y., Priest G., Allan J. and Stimely L. (2016). Benchmarking an unstructured-grid model for tsunami current modeling. *Pure and Applied Geophysics*, 173(12):4075–4087.

Zhao X., Wang B. and Liu H. (2011). Propagation and runup of tsunami waves with Boussinesq model. *Coastal Engineering Proceedings*, 1(32):9.

Zhou J.G., Causon D.M., Mingham C.G. and Ingram D.M. (2001). The surface gradient method for the treatment of source terms in the shallow-water equations. *Journal of Computational Physics*, 168(1):1–25.

Zijlema M. and Stelling G. (2008). Efficient computation of surf zone waves using the nonlinear shallow water equations with non-hydrostatic pressure. *Coastal Engineering*, 55(10):780–790.

Zijlema M., Stelling G. and Smit P. (2011). SWASH: An operational public domain code for simulating wave fields and rapidly varied flows in coastal waters. *Coastal Engineering*, 58(10):992–1012.

Zijlema M. and Stelling G.S. (2005). Further experiences with computing non-hydrostatic free-surface flows involving water waves. *International Journal for Numerical Methods in Fluids*, 48(2):169–197.

Zitellini N., Gràcia E., Matias L., Terrinha P., Abreu M., DeAlteriis G., Henriet J., Dañobeitia J., Masson D., Mulder T. et al. (2009). The quest for the Africa–Eurasia plate boundary west of the Strait of Gibraltar. *Earth and Planetary Science Letters*, 280(1–4):13–50.